Crystallography Reports, Vol. 47, Suppl. 1, 2002, pp. S1–S2.

Preface

Crystal Growth vol. 22, a collection of papers published as a supplement to the *Crystallography Reports*, is composed of the invited papers presented to the 9th All-Russian Conference on Crystal Growth, Moscow, October 2000, one of the regular All-Union Conferences to the effect held since 1956.

All but three articles are based on experimental results and are either reviews of the studies performed by their authors or the published data. The articles also contain numerous original results.

The papers were selected in a way that reflects the basic problems of crystal growth, the current methods of studying crystallization processes, the advances in the growth technologies of various crystals, mainly from melts, in particular, of profiled crystals and oxide fibers.

The first two papers are an attempt to look at the future and, in fact, are aimed at the 21st century. M.G. Mil'vidsky reviews the tendencies in growth of large dislocation-free single crystals up to 600 mm in diameter. T.T. Basiev, E.V. Zharikov, and V.V. Osiko consider possible application of numerous single crystals (halides, oxides, nitrates, carbonates, tungstenates, and molybdates) in photonics, one of the most rapidly developing high technologies.

The remaining articles are grouped into three sections.

The section *Crystal Growth from Melts* consists of five articles. It begins with the paper by Kh.S. Bagdasarov, who summarizes the experimental and theoretical data on directional high-temperature horizontal crystallization. The basic problems of this method are considered by an example of growth of Al_2O_3 single crystals. It is shown that one necessarily has to take into account the physicochemical properties of a substance to be crystallized and possible formation of complexes in a melt. It is the concentration of these complexes that determines the critical growth rate. It is also necessary to take into account the optical properties of a melt and a crystal when determining the optimal configuration of a thermal field.

Three other papers in this section deal with growth of profiled crystals from melts by the classical Stepanov method. V.A. Borodin and Yu.A. Osipyan consider the technologies used to grow crystals of the given shape and the design of the growth apparatus. P.I. Antonov and V.N. Kurlov analyze various modifications of the Stepanov method in the application to growth of profiled sapphire single crystals including those with doped spatial structures. V.N. Kurlov *et al.* describe the method of crystallization of fibers of various oxides and their combinations for heat-proof composites and discuss their microstructure and strength.

This section is concluded with the article by B.P. Sobolev, who reviews numerous published data and the results of his own studies concerning the chemical aspects of crystal growth of multicomponent fluorides from melts. The knowledge of these characteristics is necessary for purification of starting materials and the development of the growth technology of transparent materials extensively used in science and technology.

The section *Crystal Growth from Solutions* includes three experimental and two theoretical papers. Based on the chemical analysis of potassium dihydrogen phosphate crystals (KDP) grown from an aqueous solution, and computer simulation of the defect centers, T.A. Eremina *et al.* analyze the mechanism of incorporation into this crystal of di- and trivalent metals characterized by a wide range of ionic radii and also study the influence of these factors on the growth kinetics and face morphology. L.N. Dem'yanets *et al.* summarize experimental data on growth of ZnO single crystals under hydrothermal conditions and analyze the polar nature and nonstoichiometry of these crystals. They also studied the effect of Li impurities and the impurities of a number of di- and trivalent metals on the growth kinetics and some physical characteristics of ZnO crystals. The chemical reactions occurring on the (0001) and (000$\bar{1}$) faces are also analyzed. V.K. Yanovskiĭ *et al.* discuss the atomic structure and physical properties of Nb- and Sn-doped $KTiOPO_4$ crystals grown from flux. The above impurities strongly affect the configuration of (titanium, oxygen) polyhedra and, hence, the ferroelectric and nonlinear optical properties of these crystals.

Two theoretical articles of this section are written by I.L. Maksimov and E.B. Treĭvus, who analyzed the nucleation kinetics under high supersaturation and the equilibrium shape of crystals based on the Gibbs–Curie principle, respectively.

The third section is dedicated mainly to the real structure of crystals and the crystallization of films and tips. L.G. Lavrent'eva *et al.* discuss a nontraditional approach to controlling GaAs properties via the introduction of an excessive amount of arsenic into crystals during low-temperature molecular-beam epitaxy. V.P. Zlomanov *et al.* analyze the conditions of formation and characteristics of the real structure of Cr-, Co-, Ni-, and In-doped lead telluride single crystals grown

1063-7745/02/47S1-S0001$22.00 © 2002 MAIK "Nauka/Interperiodica"

from the vapor phase. Lead telluride is a promising material for receivers of the infrared radiation.

A.É. Voloshin, T. Nishinaga, and P. Ge describe experiments on the study of perfection of GaSb : Te crystals grown aboard a Chinese spacecraft. The crystals grown were studied by highly sensitive X-ray diffraction methods (single- and double-crystal X-ray topography, and high-resolution diffractometry). I.V. Yaminsky *et al.* applied atomic-force microscopy to the study of a protein lysozyme crystal, whose surfaces were investigated at a molecular resolution. The basic growth parameters (density of kinks at the steps, kink and step velocities, etc.) are determined.

E.I. Givargizov *et al.* study the mechanism of the deposition of the crystalline diamond particles onto single-crystal silicon tips grown on silicon substrates by the vapor–liquid–solid mechanism. It is shown that the epitaxial growth of diamond on silicon is possible despite essentially different lattice parameters. An example of the practical use of diamond-coated silicon tips in plane cathodoluminescence lamps.

A.E. Galashev applies the methods of molecular dynamics to studying the growth of a silicon nanocrystal in vacuum and in an atomic-oxygen atmosphere. The computer simulation of growth of silicon nanoparticles indicates possible oxygen condensation.

The concluding article by E.V. Rakova *et al.* is dedicated to analysis of the structure of epitaxial films of cadmium and lead sulfides on the Langmuir layers of fatty acids. They also consider the influence of the geometric and stereometric factors on the mutual orientation of a Langmuir monolayer and nanocrystals of cadmium and lead sulfides.

On the whole, this collection of articles fully reflects the level and the results of the studies of crystal growth performed at Russian research centers in the past decade since the previous conference on crystal growth.

The collection was prepared for publication by A.F. Konstantinova, doctor in physics and mathematics, who was assisted by S.F. Grigor'eva and I.N. Mironova.

E.I. Givargizov and E.A. Krivandina

Translated by R. Tyapaev

Crystallography Reports, Vol. 47, Suppl. 1, 2002, pp. S105–S115.

SOLUTION GROWTH

Nucleation Kinetics at Strong Supersaturation

I. L. Maksimov

Nizhniĭ Novgorod State University, pr. Gagarina 23, Nizhniĭ Novgorod, 630600 Russia

e-mail: ilmaks@phys.unn.runnet.ru

Received October 2, 2002

Abstract—Nucleation in an arbitrary *d*-dimensional system is considered. Two nucleation regimes are predicted within an original kinetic approach. The first regime (for a weak supersaturation) is characterized by the formation of a critical nucleus (critical nucleus regime). The second regime (for a strong supersaturation) corresponds to an uncontrollable growth of a cluster of any size (runaway nucleation regime). It is established that the nucleation regime is controlled by the metastability parameter *M* of the system under consideration. The analytical properties of the free energy of the nucleation system are investigated. It is demonstrated that a change in the parameter *M* leads to a considerable transformation of the nucleation barrier topography. The effect of the nucleation barrier height on the kinetics of nonstationary nucleation is described. © *2002 MAIK "Nauka/Interperiodica".*

INTRODUCTION

Investigation into the nucleation kinetics is an important problem in the statistical physics of nonequilibrium systems. In the majority of the papers concerned with this problem, consideration has been given to weakly nonequilibrium nucleation occurring under conditions of sufficiently weak supersaturation (superheating) of the system [1, 2]. Under these conditions, the nucleation is controlled by the Gibbs nucleation barrier. This process can be described by a characteristic exponential function involved in the expression for the nucleation rate. However, the use of new technological regimes can create strongly nonequilibrium nucleation conditions (strong supersaturation or superheating), whose description is outside the scope of universally accepted approaches. In this respect, analysis of the nucleation kinetics over a wide range of degrees of nonequilibrium is a topical problem in the statistical physics of condensed systems.

It is known that the possible structures and processes proceeding in a system essentially depend on its dimension. In particular, the nucleation on a substrate (formally, the two-dimensional case) can be considered a strictly two-dimensional process ($d = 2$) that is predominantly governed by the surface diffusion [3], a quasi-three-dimensional process ($d = 3$) that occurs through the Volmer–Weber growth mechanism [4], and an intermediate process ($2 < d < 3$) that corresponds, for example, to the growth of fractal nuclei [5]. An adequate quantitative description of the kinetic characteristics of nucleation can be accomplished only in terms of an efficient theory. In the present work, we will use a kinetically accented version of the classical nucleation theory. This theory is conveniently applied to an analytical description of nucleation processes (specifically of nonstationary processes), on the one hand, and, as was shown in [6], offers results virtually identical to those obtained within more advanced field-theoretical approaches [7–9], on the other hand.

In this paper, we consider the nucleation in an arbitrary *d*-dimensional case. The kinetic concept of a critical nucleus is formulated in the first part of the present survey. In this part, the evolution of the critical nucleus size is described as a function of the supersaturation and two nucleation regimes are predicted. One regime (for a weak supersaturation) is characterized by the formation a critical nucleus (the critical nucleus regime). The other regime (for a strong supersaturation) corresponds to the uncontrollable growth of a cluster of arbitrary size (the runaway nucleation regime). The effect of the nucleation barrier height on the kinetics of nonstationary nucleation is discussed in the second part of this survey. An approximate relationship for the distribution of clusters over sizes *n* is proposed in the case of a high barrier (for a weak supersaturation). This relationship provides a correct description of the cluster distribution in an arbitrary time interval $0 < t < \infty$. An asymptotically exact solution of the self-similar type is derived in the case of the runaway nucleation regime. This solution makes it possible to describe adequately the kinetics of an *d*-dimensional nucleation for a strong supersaturation (vanishingly low nucleation barrier).

CRITICAL NUCLEUS: THE KINETIC DESCRIPTION

In contrast with the universally accepted approaches, we will use the *kinetic* description of a critical nucleus. Essentially, the kinetic concept of a critical nucleus consists in applying the balance condition

to the rates K^+ of attachment of monomers to a cluster and their rates K^- of detachment from the cluster, that is,

$$K^+(n) = K^-(n), \quad (1)$$

which is satisfied at the critical nucleus size $n = n^k$ [10, 11]. Note that condition (1) does not coincide with the condition for an extremum of the quasi-equilibrium size distribution function for clusters [1–3]:

$$c_0(n) = N_1 \exp(-W_{rev}(n)/kT), \quad (2)$$

where N_1 is the normalization factor, k is the Boltzmann constant, T is the temperature of the system, and $W_{rev}(n)$ is the work done by the system to form a cluster containing n monomers, that is,

$$W_{rev}(n) = -\Delta\mu n + \gamma_d^* n^\nu. \quad (3)$$

Here, $\Delta\mu = \mu^\alpha - \mu^\beta(T)$ is the difference in the chemical potentials of the parent (α) and nucleating (β) phases separated by an interface (characterized by the effective interfacial surface tension γ_d^*) and $\nu = (d-1)/d$ is the exponent relating the surface area of the cluster and the cluster size n. Consequently, the quantity n is a fundamental parameter of the nonequilibrium system under consideration, which describes the main kinetic characteristics of the system. For further analysis, it is convenient to use the detailed balancing principle [12]

$$c_0(n)K^+(n) = c_0(n+\delta n)K^-(n+\delta n) \quad (4)$$

(where $\delta n \equiv 1$ for the attachment and detachment of monomers) and the universally accepted power expression for $K^+(n)$ [1–3]:

$$K^+(n) = K_0^+ n^r. \quad (5)$$

Here, r is the exponent characterizing the adsorption efficiency and varies (depending on the adsorption mechanism) from $r = \nu = (d-1)/d$ for the ballistic regime [2] to $r = (d-1)/2d$ for the diffusion mechanism of adsorption [3]. Below, we will analyze the case of nucleation controlled by ballistics, i.e., $r = \nu = (d-1)/d$.

Kinetic and thermodynamic critical nuclei. The ratio K^+/K^- is conveniently represented in the form

$$\ln\left(\frac{K^+(R)}{K^-(R)}\right) \equiv \Psi_d(R) = \frac{r}{M^{(d)}n^*}\frac{M^{(d)} + R^d - R^{(d-1)}}{R^d}. \quad (6)$$

In expression (6), we changed over to the variable $R = (n/n^*)^{1/d}$. Here, R is the reduced (to critical) dimensionless radius of the cluster involving n monomers and n^* is the critical nucleus size determined from the thermodynamic condition [1–3]

$$\left.\frac{\partial W_{rev}(n)}{\partial n}\right|_{n=n^*} = 0. \quad (7)$$

From this relationship, we obtain $n^* = \left[\frac{(d-1)\gamma_d^*}{d\Delta\mu}\right]^d$ and $W_{rev}(n^*) = n^*\Delta\mu/(d-1)$. In expression (6), we introduced the dimensionless parameter $M^{(d)} = rkT/\Delta\mu n^*$, which is inversely proportional to the nucleation barrier height $W_{rev}(n^*) \equiv W_d^*$ and, in essence, plays the role of a metastability parameter of the system under investigation. Actually, in the case of a high barrier (at $W_d^* \gg kT$), the metastability parameter is vanishingly small, i.e., $M^{(d)} \ll 1$. As a result, the classical nucleation theory can be applied successfully. In contrast, at $M^{(d)} \gtrsim 1$, the barrier is relatively small ($W_d^* \lesssim kT$); consequently, the classical nucleation theory becomes formally inapplicable. Below, we will demonstrate the qualitative effects characterizing a strongly nonequilibrium nucleation.

Equation (1) with the use of relationships (4)–(6) can be reduced to the simple algebraic equation

$$R^{(d-1)} - R^d = M^{(d)} = r\left(\frac{d}{d-1}\right)^d \frac{kT}{\gamma_d^*}\left(\frac{\Delta\mu}{\gamma_d^*}\right)^{(d-1)}. \quad (8)$$

As can easily be shown, this equation either possesses two real solutions $n_{1,2}^k = n^* R_{1,2}^d$ (at $M^{(d)} < M_c^{(d)}$) or has no solutions (at $M^{(d)} > M_c^{(d)}$) [11]. Here, the quantity $M_c^{(d)} = (d-1)^{-1}[(d-1)/d]^d$ corresponds to a maximum value on the right-hand side of Eq. (8): $M_c^{(2)} = 0.25$ at $d = 2$ and $M_c^{(3)} = 4/27 = 0.148$ at $d = 3$.

Thus, the system at $M^{(d)} < M_c^{(d)}$ actually contains two kinetically defined critical nuclei that characterize the averaged (over the time) competition between adsorption and desorption of monomers. This competition is illustrated in Fig. 1, which depicts the plots of the function $\Psi_d(n)$ at $d = 2$. It can be seen from Fig. 1 that the decay dominates over the growth when the cluster sizes fall in the range between the first and second critical nucleus sizes: $n_2^k < n < n_1^k$. In contrast, the growth dominates over the decays at $n < n_2^k$ and $n_1^k < n$; therefore, the quantity n_1^k is the critical nucleus size in the kinetic formulation. Indeed, in the case when the cluster overcomes the nucleation barrier, the cluster growth becomes uncontrollable, because, in this range, the

attachment of monomers to the cluster dominates over their detachment.

The kinetic nucleation potential. It is interesting to note that n_1^k and n_2^k are the extrema of the auxiliary kinetic potential

$$W_{\text{kin}}(n) = W_{\text{rev}}(n) - kT\ln K^+(n), \qquad (9)$$

which was introduced in our earlier works [11, 13] with the aim of analyzing critical nuclei. The kinetic potential profile depicted in Fig. 2 exhibits a nontrivial behavior. It can be seen that, at a weak supersaturation, the kinetic potential $W_{\text{kin}}(n)$ is characterized by a clearly defined nucleation barrier (Fig. 2, curve *1*). The height of this barrier is determined by the metastability parameter $M^{(d)}$. Note that the kinetic potential $W_{\text{kin}}(n)$ ($n = n_1^k$) at the maximum corresponds to an unstable state. An increase in the metastability parameter $M^{(d)}$ is accompanied by a qualitative transformation of the profile of the kinetic potential $W_{\text{kin}}(n)$; namely, the extrema of the potential W_{kin} gradually approach each other and merge together at $M^{(d)} = M_c^{(d)}$. As a consequence, the kinetic potential $W_{\text{kin}}(n)$ monotonically decreases with an increase in n (Fig. 2, curve *2*).

The nucleation diagram. From the above discussion, it follows that the nucleation kinetics is characterized by two ranges of parameters of the system: critical nuclei can arise in one range and cannot arise in the other range. This allows us to make the inference that the nucleation can occur in two radically different regimes. The former regime—the critical nucleus regime—is observed at weak nonequilibrium when the metastability parameter $M^{(d)}$ falls in the range $0 < M^{(d)} < M_c^{(d)}$. The latter regime—the kinetic runaway regime—is attained when the metastability parameter $M^{(d)}$ takes on supercritical values, i.e., $M^{(d)} > M_c^{(d)}$. In order to refine the characteristic features of these regimes, we consider the nucleation diagram of the studied system in the "chemical potential–temperature" (physically meaningful parameters) coordinate frame (Fig. 3). This diagram accounts for the appropriate conditions of attaining different nucleation regimes.

Apart from the aforementioned case, the runaway regime can be achieved under the following condition: the size of a kinetic critical nucleus n_1^k must be less than the minimum possible size $n_{\min}$. For definiteness, we assume that $n_{\min} = 1$; hence, the above conditions can be written in the from $n_1^k < 1$. This situation is similar to the well-known case in the classical nucleation theory, $n^* < 1$, which can be realized in the vicinity of the critical point when the surface tension can be ignored [2]. It should be emphasized that this situation is also closely similar to the spinodal decomposition

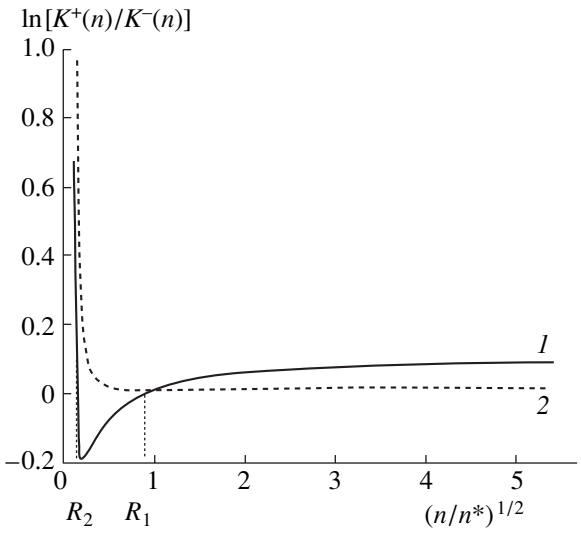

Fig. 1. Plots of the function $\ln[K^+(n)/K^-(n)]$ in the case of two-dimensional nucleation ($d = 2$) at (*1*) $M^{(d)} < M_c^{(d)}$ and (*2*) $M^{(d)} > M_c^{(d)}$.

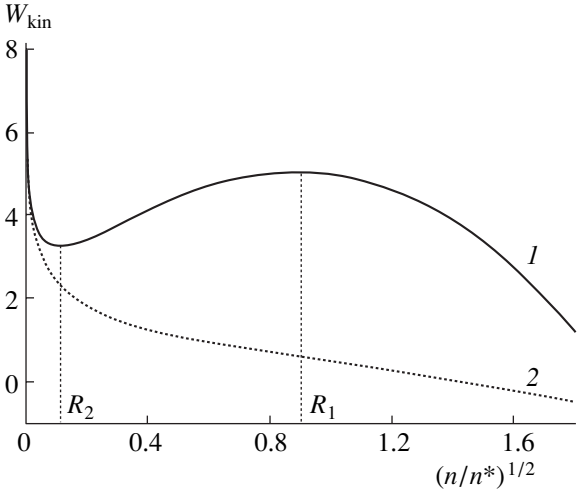

Fig. 2. Profiles of the kinetic potential $W_{\text{kin}}(n)$ for $d = 2$ at (*1*) $M^{(d)} < M_c^{(d)}$ and (*2*) $M^{(d)} > M_c^{(d)}$.

regime, because it is also characterized by an extremely low nucleation barrier height. The case under consideration can be conventionally treated as a quasi-spinodal nucleation regime.

In summary, we should note that the above kinetic description of a critical nucleus, in essence, only refines certain details of the classical theory. For rough estimates, the universally accepted thermodynamic definition of a critical nucleus can serve as a good starting approximation. At the same time, unlike the thermodynamic approach, the kinetic approach, as applied to the description of a critical nucleus, permits both a prediction of two nucleation regimes and a rigorous quantitative description of the conditions necessary for a cross-

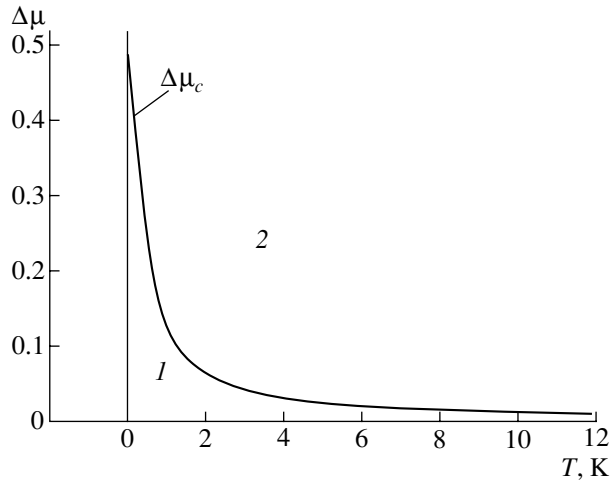

Fig. 3. Diagram of the two-dimensional nucleation ($d = 2$): (*1*) critical nucleus regime $M^{(d)} < M_c^{(d)}$ and (*2*) kinetic runaway regime $M^{(d)} > M_c^{(d)}$. The supersaturation and the temperature are normalized to the surface energy.

over between these nucleation regimes. As will be shown below, the kinetic concept of a critical nucleus is deeply connected with the analytical properties of the free energy of the nucleation system.

ANALYTICAL PROPERTIES OF THE FREE ENERGY OF A NUCLEATION SYSTEM

It is quite instructive to discuss the aforementioned assertions regarding the possible existence of the kinetically defined critical nuclei and different nucleation regimes from the viewpoint of the basic principles of statistical physics. As is known, the parent system originally resides in the metastable state. The degree of metastability is determined by the metastability parameter $M^{(d)}$, and the decay rate of the metastable state is governed by the attachment rate of monomers. In the course of phase transition, the system undergoes a number of transformations from one metastable state to another metastable state with a lower energy. Eventually, the system transforms into a stable, thermodynamically equilibrium state and the phase transition is completed.

The decay rate of the metastable state can be estimated by calculating the partition function and the free energy. In terms of the Mayer cluster expansion, the partition function of the system can be represented by the expression [8, 9]

$$Z = \frac{1}{N_1}\sum_{n=0}^{\infty} c_0(n), \qquad (10)$$

where $c_0(n)$ is the Gibbs distribution function (2) for clusters. When calculating the partition function (10), it is convenient to change over to the integral representation and to replace summation over n by integration over the variable $R = (n/n^*)^{1/d}$. As a result, the partition function Z can be written in the form

$$Z = n^* d\int_C \exp(-W(R)/kT)dR, \qquad (11)$$

where

$$W(R) = W_{\text{rev}}(R) - (d-1)kT\ln(R) \qquad (12)$$

and the integral is taken along the contour C coinciding with the real axis: $0 < R < \infty$. It is worth noting that the pseudopotential $W(R)$ in relationship (11) is equivalent to the previously introduced potential $W_{\text{kin}}(n(R)) \equiv W_{\text{kin}}(R)$ [see formula (9)], whereas the extrema of the pseudopotential $W(R)$ coincide with the extrema of the potential $W_{\text{kin}}(R)$, which are determined by Eq. (8). This coincidence takes place in the most actual case when $r = \nu = (d-1)/d$. It is easy to see that no degeneracy occurs in the more specific case when the kinetic exponent r is not equal to the geometric exponent ν ($r \neq \nu$). From relationship (10) with due regard for expression (2), it follows that the partition function is finite at $\Delta\mu < 0$ (an undersaturated solution) and that the series described by expression (10) is divergent at $\Delta\mu > 0$ (a supersaturated solution). In order to calculate the partition function (10), Langer [7, 8] proposed a method providing a means for avoiding physically meaningless divergence of the free energy. Indeed, the formally divergent expression (11) for the partition function can be rearranged to a finite expression through its analytic continuation to the complex plane $z = \rho e^{i\varphi}$ and the proper choice of the integration contour C' with allowance made for the specific features of the pseudopotential $W(z)$. This procedure ensures a finiteness of the partition function Z but leads to the appearance of the imaginary part in the function Z and, correspondingly, in the free energy $F = -kT\ln Z$.

Two-dimensional nucleation. As an example, the proposed approach will be applied to a simple two-dimensional nucleation ($d = 2$). For this purpose, in the two-dimensional case (at $z = x + iy$), the real (Re) and imaginary (Im) parts of the nucleation barrier pseudopotential $W(z)$ normalized to kT can be written as

$$\begin{aligned}\text{Re}\,W \equiv U &= (y^2 - (x-1)^2)/(2M^{(2)}) - 0.5\ln(x^2+y^2);\\ \text{Im}\,W \equiv V &= -(x-1)y/M^{(2)} - \arctan(y/x).\end{aligned} \qquad (13)$$

The positions of the extrema of the pseudopotential $W(z)$ can be obtained by a simple calculation: $z^*_{1,2} = 0.5[1 \pm \sqrt{1 - M^{(2)}/M_c^{(2)}}$, where $M_c^{(2)} = 0.25$. It is worth noting that, at $M^{(2)} < M_c^{(2)}$, the $z^*_{1,2}$ coordinates are real, i.e., $z^*_{1,2} = x_{1,2} \equiv R_{1,2}$. At $M^{(2)} > M_c^{(2)}$, the $z^*_{1,2}$ coordinates become complex.

The integration contour in the complex plane z is chosen using the procedure originally proposed by Langer [7]. First, we examine how the integration contour in the plane $z = x + iy$ varies upon changeover from $\Delta\mu < 0$ to $\Delta\mu > 0$. The direct changeover along the real axis is forbidden, because, as was shown above, the partition function Z involves the divergent integral. Therefore, after the analytic continuation to the complex plane, we continuously change over from $\Delta\mu < 0$ to $\Delta\mu > 0$ along a circumference of radius $|\Delta\mu|$. In this case, the motion along the contour in the $\Delta\mu$ plane is immediately attended by a change in the integration contour in the z plane. After this changeover from the negative semiaxis $\mathrm{Re}\Delta\mu < 0$ to its continuation $\mathrm{Re}\Delta\mu > 0$, the contour in the plane $z = x + iy$ passes rigorously along the imaginary axis. Note that, in the case of clockwise motion in the $\Delta\mu$ plane, we have $\varphi = \pi/2$, whereas the counterclockwise motion in the $\Delta\mu$ plane leads to $\varphi = -\pi/2$. It is evident that, in both cases, the relationships derived for the partition function are complex conjugate. It can easily be verified that, at arbitrary $d > 2$, the direction of the "true" path will make the angle $\varphi = \pi/d$ with the real axis $\mathrm{Re}z$.

By applying the Langer method [7–9], integral (11) at $d = 2$ can be represented as the sum of two terms:

$$Z^{(2)} = 2n^*\left\{\int_0^{\mathrm{Re}z_1^*} \exp(-W(R)/(kT))dR + i\int_0^{\infty}\exp[-W(\mathrm{Re}z_1^* + iu)/(kT)]du\right\}. \quad (14)$$

It should be noted that the first integral in relationship (14) is taken along the real axis, whereas the second (already convergent) integral is taken along the imaginary axis. The corresponding integration contour is indicated by arrows in Figs. 4a and 4b, which depict the surface profiles of the real part of the nucleation barrier pseudopotential $\mathrm{Re}\,W(z)$ for two metastability parameters $M^{(2)}$. After simple but cumbersome calculations, we can obtain an explicit expression for $Z^{(2)}$. It is reasonable to consider the asymptotic relationships for $Z^{(2)}$ and $F^{(2)}$ in the physically most important cases. Under the conditions of weakly nonequilibrium nucleation, i.e., in the case of a high barrier ($M^{(2)} \ll M_c^{(2)} = 0.25$), the relationship for $Z^{(2)}$ to the second order in $M^{(2)}$ can be written in the form

$$Z^{(2)} \approx 2n^*M^{(2)^2}\{3 + \exp[-1/(2M^{(2)})] - i\sqrt{9\pi/(8M^{(2)})}\exp[-1/(2M^{(2)})]\}/3. \quad (15)$$

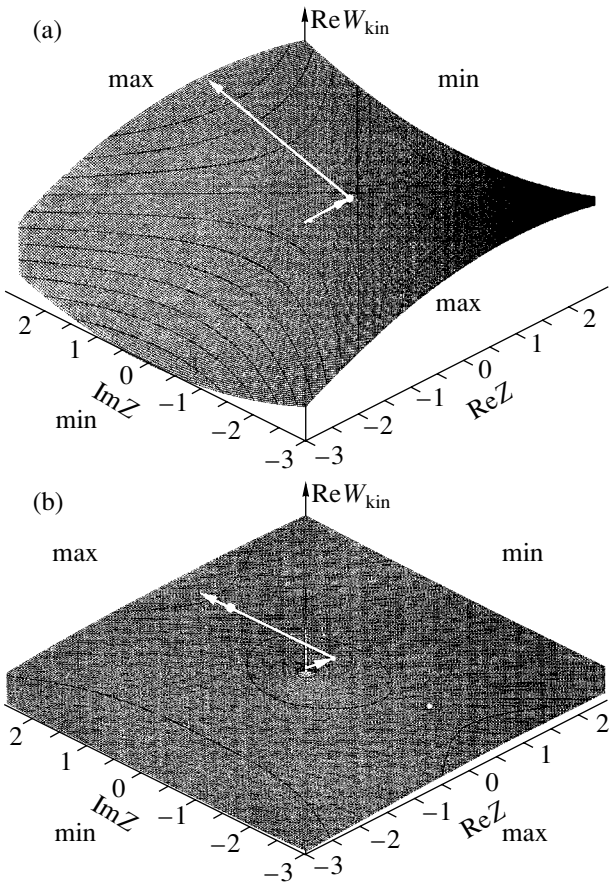

Fig. 4. Topology of the nucleation barrier $\mathrm{Re}\,W(z)$ [see relationship (13)] at $d = 2$ for (a) $M^{(2)} = 0.01$ and (b) $M^{(2)} = 3.0$.

In this relationship, we took into account that $R_1^{(2)} \approx 1 - M^{(2)}$. In the limit of a weak nonequilibrium ($M^{(2)} \ll M_c^{(2)}$), the imaginary part of $F = -kT\ln Z$ proves to be an exponentially small quantity, that is,

$$\mathrm{Im}\,F \approx kT\sqrt{\pi/4M^{(2)}n^*}\exp[-1/(2M^{(2)})]. \quad (16)$$

This corresponds to an exponentially long time τ of transition to the stable state: $\tau \propto \tau_0\exp[1/(2M^{(2)})]$, where τ_0 is the characteristic time of the evolution of the macrosystem under investigation. The surface profile of the real part of the nucleation pseudopotential $\mathrm{Re}\,W(z)$ at $M^{(2)} = 0.01$ is shown in Fig. 4a.

In the case when the system is in a strongly nonequilibrium state (the runaway regime at $M^{(2)} > M_c^{(2)}$), the profile of the nucleation barrier changes significantly. Judging from the profile of the nucleation barrier at $M^{(2)} = 3$ (Fig. 4b), the saddle point is absent when moving along the real axis $\mathrm{Re}z$, because the function $\mathrm{Re}\,W(z)$ monotonically decreases at $\mathrm{Re}z \longrightarrow +\infty$. Analysis demonstrates that, at $M^{(2)} > M_c^{(2)}$, the extrema or, more precisely, the complex conjugate saddle points of

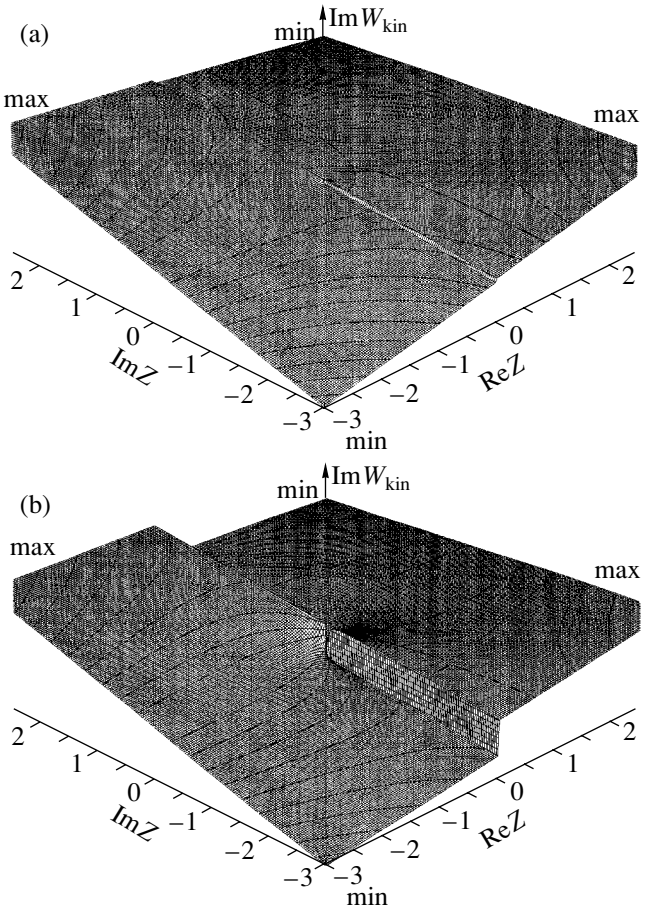

Fig. 5. Imaginary part Im $W(z)$ of the kinetic nucleation potential [see relationship (13)] at $d = 2$ for (a) $M^{(2)} = 0.25$ and (b) $M^{(2)} = 3.0$.

the pseudopotential $W(z)$ shift along the imaginary axis and are symmetrically arranged with respect to the real axis (Fig. 4b). Therefore, the crossover of the nucleation mechanism (from the barrier regime to the barrier-free regime) is accompanied by variations in the topography of the kinetic nucleation barrier, during which the double saddle point is as though split into two saddle points that are symmetrically arranged with respect to the real axis. This clearly illustrates the influence of the nonequilibrium [and, especially, the decisive role of the kinetic factor $K^+(n)$] on the specific features of the fine structure of the nucleation barrier. In the case when $M^{(2)} \gg M_c^{(2)}$, the imaginary part of the free energy $\mathrm{Im}F \approx kT/\sqrt{M^{(2)}n^*}$ proves to be a monotonically increasing function of the supersaturation $\Delta\mu$. For a strong supersaturation, this leads to a power decrease in the transition time: $\tau \propto (\Delta\mu kT)^{-1/2}$.

Let us now consider how the nonequilibrium parameter $M^{(2)}$ affects the topographic characteristics of the nucleation barrier. When calculating the partition function, the integration contour was chosen by analyzing the real part Re $W(z)$ of the surface profile of the nucleation barrier $W(x + iy)$. The evolution of the surface profile of the real part Re $W(z)$ with a change in the nonequilibrium parameter from $M^{(2)} = 0.01$ to $M^{(2)} = 3$ is illustrated Figs. 4a and 4b, respectively. The appearance of a sharp maximum in the function Re $W(z)$ at $z = 0$ (Fig. 4b) is noteworthy. This indicates an increase in the contribution of the kinetic factor, which is eventually responsible for the observed monotonic decrease in Re $W(z)$ along the real axis.

It should be noted that the surface profile of the imaginary part of the nucleation barrier Im $W(z)$ also noticeably changes away from equilibrium. The evolution of the imaginary part Im W with a change in the metastability parameter from $M^{(2)} = M_c^{(2)} = 0.25$ to $M^{(2)} = 3$ is illustrated in Figs. 5a and 5b, respectively. It can be seen that the imaginary part of W is very sensitive to a change in the metastability parameter $M^{(2)}$, as is the case with the real part of W. In actual fact, an increase in the metastability parameter $M^{(2)}$ results in the formation of a wrinkle in the surface profile of the imaginary part Im W. This wrinkle is aligned along the imaginary axis, and the wrinkle height is governed by the metastability parameter $M^{(2)}$. Consequently, we can make the inference that the height of the wrinkle in Im W accounts for the degree of nonequilibrium of the system. The presence of the imaginary term in the partition function and, correspondingly, the imaginary term in the energy F implies that the system tends to leave the initial metastable state and to transform into the adjacent state. Apparently, the rate of transition from one metastable state to another is determined by the height of the wrinkle in the function Im F, whereas the lifetime of the initial metastable state is characterized by a quantity inversely proportional to the wrinkle height.

For the three-dimensional case ($d = 3$), a similar treatment in the weak supersaturation limit was performed by Langer. Note that the derivation of exact analytical expressions for the functions $Z^{(3)}$ and $F^{(3)}$ at arbitrary parameters $M^{(3)}$ in the three-dimensional case presents considerable difficulties; for this reason, no such expressions have been obtained to date.

NONSTATIONARY NUCLEATION KINETICS

The nucleation theory provides a quantitative description of the evolution of the originally metastable system from an unstable state to a stable state. The nonstationary nucleation is conveniently analyzed using a set of Frenkel–Zel'dovich equations [14], that is,

$$\frac{\partial}{\partial t}c(n,t) = -\frac{\partial J(n,t)}{\partial n}, \tag{17}$$

$$J(n,t) = -K^+(n)c_0(n)\frac{\partial}{\partial n}\frac{c(n,t)}{c_0(n,t)}. \tag{18}$$

In this case, the initial and boundary conditions have the form

$$c(n, 0) = c_0(n)\delta_{n,1},$$
$$\frac{c(n,t)}{c_0(n)} \longrightarrow 1, \quad \text{at} \quad t \geq 0 \quad \text{and} \quad n \longrightarrow 1, \qquad (19)$$
$$\frac{c(n,t)}{c_0(n)} \longrightarrow 0, \quad \text{at} \quad t \geq 0 \quad \text{and} \quad n \longrightarrow \infty.$$

Here, $c_0(n)$ and $c(n, t)$ are the quasi-equilibrium and nonstationary size distribution functions [see expression (2)] for clusters, respectively, and $J(n, t)$ is the nucleation flux. The stationary distribution function $c_s(n)$ can be represented by the relationship [2, 12, 15]

$$\frac{c_s(n)}{c_0(n)} = J_s\int_n^\infty \frac{dn'}{c_0(n')K^+(n')}. \qquad (20)$$

This function is responsible for the stationary nucleation flux J_s, which can be written in the following form:

$$J_s^{-1} = \int_0^\infty \frac{dn'}{c_0(n')K^+(n')}. \qquad (21)$$

Let us now analyze how the degree of nonequilibrium (or, in other words, the nucleation barrier) affects the nonstationary nucleation kinetics.

The high barrier: an effective erfc approximation. First, we consider the most typical case of a high nucleation barrier ($W_d^* \gg kT$). This situation was treated by many authors [16–21], who applied different approaches to the solution of the set of equations (17)–(19). For the most part, the expressions derived earlier for the nonstationary distribution function can be reduced to a characteristic step relationship represented by the erfc-type function

$$\frac{c_j(n,t)}{c_0(n)} = \frac{1}{2}\mathrm{erfc}\left[\frac{a_j + b_j(n)\exp[t/t_i]}{\sqrt{\exp[2t/t_i] - \zeta_j}}\right], \qquad (22)$$

where the subscript j ($1 \leq j \leq 4$) refers to the specific solution. Note that the Shneidman solution [20, 21] makes it impossible to identify precisely the parameter ζ: $\zeta = 1$ at $n = n^*$ in accordance with the results obtained in [20] (this parameter ζ coincides with the parameters $\zeta = 1$ obtained in [16–19] at arbitrary n) and, according to [21], $\zeta = 0$ in distribution (22) at $n \neq n^*$.

The "asymptotic catastrophe." Unfortunately, the majority of the expressions [16–19] derived for the nonstationary distribution function have a substantial disadvantage; i.e., they exhibit an asymptotic catastrophe. This means that the nucleation flux at $t \longrightarrow \infty$ does not reach a steady-state value $J = J_s$ at arbitrary values of $n \neq n^*$. However, according to the nucleation theory, this is a necessary condition, because the steady flux at $t \longrightarrow \infty$ is attained along the entire axis of cluster sizes. In order to apply this theory in practice, we should determine the threshold cluster size n_c, beginning from which nuclei must necessarily reach macroscopic sizes. With due regard for the recommendations of the classical nucleation theory, we assume that the threshold cluster size n_c coincides with the cluster size n_c^+, which corresponds to the upper boundary of the critical region and is determined from the condition $W_{\mathrm{rev}}(n_c^+) = W_d^* - kT$. Indeed, within the classical nucleation theory, it is universally adopted that a cluster developing through thermal fluctuations grows with an absolute probability up to macroscopic sizes if it leaves the kinetic region. Taking into account expression (3), it can easily be found that $n_c = n_c^+ \approx n^*[1 + \sqrt{2d^2M^{(d)}/(d-1)}]$ at $M^{(d)} < M_c^{(d)}$. It should be remembered that, in the case of a sufficiently low barrier $W_d^* \leq kT$, the threshold cluster size n_c, by definition, coincides with the size $\overline{n_d} = r^{-d}n^*$, which satisfies the condition $W_{\mathrm{rev}}(\overline{n_d}) = 0$. Note that the following equalities holds: $\overline{n_3} = 3.375n^*$ and $\overline{n_2} = 4n^*$.

An effective erfc approximation. With the aim of eliminating the aforementioned asymptotic catastrophe, it is necessary to modify appropriately the erfc-type nonstationary distribution function

$$\frac{c(n,t)}{c_0(n)} = \frac{1}{2}\mathrm{erfc}\left[\frac{a + b(n)\exp[t/t_i]}{\sqrt{\exp[2t/t_i] - 1}}\right], \qquad (23)$$

where the parameter $b(n)$ is considered to be variational and the coefficient a can be determined from the initial condition: $a = -b(1)$. In view of relationship (23), the flux J can be expressed in the form

$$J(n,t) = \frac{c_0(n)K^+(n)}{\sqrt{1 - \exp(-2t/t_i)}}\frac{db}{dn}\exp\left[-\frac{[a + b(n)\exp(t/t_i)]^2}{\exp(2t/t_i) - 1}\right]. \qquad (24)$$

In the case when the condition $J(n, t) \longrightarrow J_s$ at $t \longrightarrow \infty$ is satisfied, we obtain the equation for finding the parameter $b(n)$, that is,

$$\int_b^\infty \exp(-u^2)du = J_s\int_n^\infty \frac{dn'}{c_0(n')K^+(n')} = c_s(n)/c_0(n). \qquad (25)$$

The solution of Eq. (25) gives the sought function $b(n)$; as a result, the nonstationary flux can be repre-

sented in the compact form

$$\frac{J(n,t)}{J_s} = \frac{1}{\sqrt{1-\exp(-2t/t_i)}} \times \exp\left[b^2(n) - \frac{[a+b(n)\exp(t/t_i)]^2}{\exp(2t/t_i)-1}\right]. \quad (26)$$

Expression (26) correctly describes the evolution of the nucleation flux in an arbitrary time interval $0 < t < \infty$. In a number of cases [22], it is convenient to represent the function $b(n)$ in the form of an effective approximant satisfying the necessary constraints.

The low barrier: runaway nucleation kinetics. As was shown above, the kinetic runaway regime is achieved in the case of strong supersaturation (at $M^{(d)} > M_c^{(d)}$) when the nucleation barrier plays no significant role. However, the nucleation in this situation cannot be considered explosive in character. Since it is as though an ensemble of clusters were an incompressible medium, the averaged kinetics of attachment and detachment of monomers is realized on the microscopic level at each point of the n axis. As a consequence, the nucleation proceeds at a finite rate and is completed in a finite time. It is quite reasonable that, in the runaway regime ($M^{(d)} > M_c^{(d)}$), the nucleation barrier becomes inefficient and the kinetics of the process under investigation is governed by the degree of disbalance between the rates of attachment and detachment of monomers to the cluster. As will be demonstrated below, the nucleation rate is actually controlled only by the kinetic exponent r, which, in turn, is determined by the dimension d of the problem. The most actual cases of three-dimensional and two-dimensional nucleation ($d = 2$ and 3) will be considered below.

The self-similar solution. In order to determine the nonstationary distribution function in the case under consideration, we use the Becker–Döring ansatz [15]

$$\frac{c_s(n)}{c_0(n)} = J_s\int_u^\infty \frac{dn'}{c_0(n')K^+(n')}, \quad (27)$$

where $u \equiv u(n, t)$ is the ancillary variable satisfying the following conditions: $u(n, t) = n$ (the stationary limit) at $t \longrightarrow \infty$ and $u(n, t) \longrightarrow \infty$ at $t \longrightarrow 0$. Substitution of expression (27) into relationship (21) gives the diffusion-type nonlinear partial differential equation [11]

$$\frac{D(n)}{D(u)}\frac{1}{K^+(n)}\frac{\partial u}{\partial t} = \frac{\partial}{\partial n}\left\{\frac{D(n)}{D(u)}\frac{\partial u}{\partial n}\right\}, \quad (28)$$

where $D(n) = c_0(n)K^+(n)$ is the effective diffusion coefficient.

The structure of Eq. (28), which is characterized by the power function $K^+(n)$, permits the self-similar change $u(n, t) = t^\alpha\Psi(n/t^\beta)$. In this case, we assume that the following conditions are satisfied: (i) the surface term in expression (3) is omitted, and (ii) clusters have sizes $n \gg kT/\Delta\mu$. These conditions impose severe constraints on the exponents α and β; more precisely, $\alpha = \beta = d$. As a result, the variable u takes the form

$$u(n, t) = t^d\Psi(\xi), \quad (29)$$

where $\xi = n/t^d$. The function $\Psi(\xi)$ obeys the first-order ordinary differential equation

$$\Psi - \xi\Psi' = Q_d\xi^r\Psi'(1-\Psi'), \quad (30)$$

where $Q_d = K_0^+\Delta\mu/(dkT)$. Equation (30) can be solved in the specific cases parametrized by the exponent r. It should be noted that the trivial solution $\Psi_{tr}(\xi) = \xi$ of Eq. (30) corresponds to the final state $u \equiv n$, whereas the nontrivial solution $\Psi_{ntr}(\xi)$ describes the transient process.

The variable $u(n, t)$ is conveniently expressed in the form $u(n, t) = n[1 + \phi(x)]$, where $x = \xi\tau^d = n\tau^d/t^d$ and $\tau = Q_d^{-1}$. The appropriate relationship for the nucleation flux has the following form:

$$\frac{J(n,t)}{J_s} = \frac{1}{(1+\phi(x))^{1-r}} \times \exp\left[-n\frac{\Delta\mu}{kT}\phi(x)\right]\left\{1 + \left[\phi(x) + x\frac{d\phi(x)}{dx}\right]\right\}. \quad (31)$$

According to this relationship, the nucleation flux reaches a steady-state value at $t = t_L(n) = \tau_d n^{1/d}$.

Specific cases. In the most interesting three-dimensional case ($d = 3$), the function $\phi(x)$ can be represented in the closed form

$$\phi_3(x) = \frac{1}{16}(x^{1/3}-1)^3(3x^{1/3}+1)H(x-1), \quad (32)$$

where $H(z)$ is the Heaviside function. As a consequence, the nucleation flux can be written in the compact form [22]

$$\frac{J(n,t)}{J_s} = \frac{1}{(1+\phi(x))^{2/3}} \times \exp\left[-n\frac{\Delta\mu}{kT}\phi(x)\right][1 + 0.25(x^{1/6} - x^{-1/6})^2H(x-1)]. \quad (33)$$

From this expression, it follows that the nucleation flux reaches a steady-state value, i.e., $J = J_s$ at $t = t_L(n) = \tau n^{1/3}$ (which corresponds to $x = 1$).

In the two-dimensional case ($d = 2$), the dependence $x(p)$ ($p > 1$) can be represented only in the parametric

form

$$x^{-1/2} = 2p - 1 + 2(p^2 - p)\ln(1 - 1/p);$$
$$\phi(p) = \Psi(p)/x(p) - 1 \quad (34)$$
$$= (p-1)^2[2p^2\ln(1-1/p) - (2p+1)]H(p-1),$$

where $x = \xi\tau^2 = n\tau^2/t^2$ and $\tau = Q_2^{-1}$. Here, the parameter p varies from $p = \infty$ (at $t = 0$) to $p = 1$ [at $t = t_L(n) = \tau n^{1/2}$]. This corresponds to the joining of the nontrivial solution of Eq. (34) and the trivial solution $\Psi_{tr} = \xi$ for $p \equiv 1$. Note that the joining of both solutions at the point $\xi = Q_2^2$ ($x = 1$) is so smooth that the first-order and second-order derivatives are continuous. The time a nucleus takes to reach this point (the time lag) can be defined by the expression $t_L(n) = n^{1/2}/Q_2$. At $t > t_L(n)$, the function ϕ becomes identically equal to zero (since $\Psi \equiv \xi$); hence, the stationary distribution (24) of clusters is attained automatically, because $u(n, t) \equiv n$. For $t \longrightarrow t_L(n)$, the nucleation flux can be described by the expression

$$J(n, t) \approx J_s[1 + \gamma_d(1 - (t/t_L(n))^2] \quad (35)$$

and is characterized by the "overshooting" effect, which was discussed in detail in [23]. The total number of nucleated clusters $N_p(n) = \int_0^t J(n, t')dt'$ exhibits an exponentially nonanalytic behavior at the initial stage of the nucleation process: $N_p \propto t^{(d-1)/d}\exp[-\tau_1^{(d)} n^{(d+1)/d}/t]$. Then, at $t \gg t_L(n)$, the behavior of the total number of nucleated clusters is represented by the linear time dependence $N_p \approx J_s[t - t_L(n)]$.

Thus, it is evident that, in the case of a vanishingly low nucleation barrier, the nucleation kinetics changes drastically. The characteristic exponential law gives way to a radically different, self-similar power time law of the evolution. Physically, this is associated with the fact that the nonequilibrium-induced crossover of the studied system to another thermodynamic branch must necessarily be attended by variations in the evolution of this system with time. Mathematically, this change can stem from the inapplicability of the parabolic expansion of $W_{rev}(n)$ in the vicinity of the maximum; as a result, we cannot use the method of matching asymptotics, which works very well in the limit of a high nucleation barrier.

DISCUSSION

In this work, we consistently considered the nucleation kinetics over a wide range of degrees of nonequilibrium of the metastable phase. It was revealed that the occurrence of different nucleation regimes is controlled by the sole controlling parameter $M^{(d)}$ of the problem. An increase in $M^{(d)}$ above the threshold value $M_c^{(d)}$ results in a bifurcation transition attended by variations in the nucleation barrier topology, which, in turn, leads to a crossover of the nucleation regime. The above scenario is consistent with the evolution concept that holds for states far from thermodynamic equilibrium. According to this concept [24], when the controlling parameter of the system (in our case, it is the metastability parameter M) exceeds a critical value, the evolution of the complex system can undergo qualitative transformations. As a result, the system transforms from a continuum of thermodynamically quasi-equilibrium states to a set of states of a radically different type. In our work, we examined a particular physical system, namely, a supersaturated solution. Moreover, we quantitatively characterized the conditions for a crossover

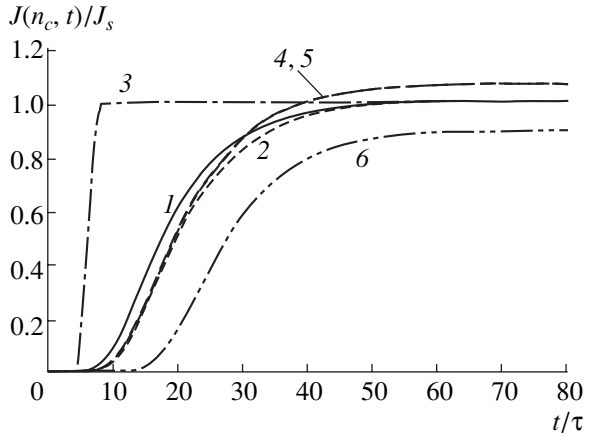

Fig. 6. Nucleation fluxes $J(n, t)$ determined at $n = n_c = 65$, $n^* = 50$, and $W_3^*/kT = 33.3$ ($M^{(3)} = 0.01$) according to (*1*) numerical calculation, (*2*) relationship (26) [22], (*3*) self-similar solution (33), (*4*) solution taken from [17], (*5*) solution taken from [18], and (*6*) solution taken from [19].

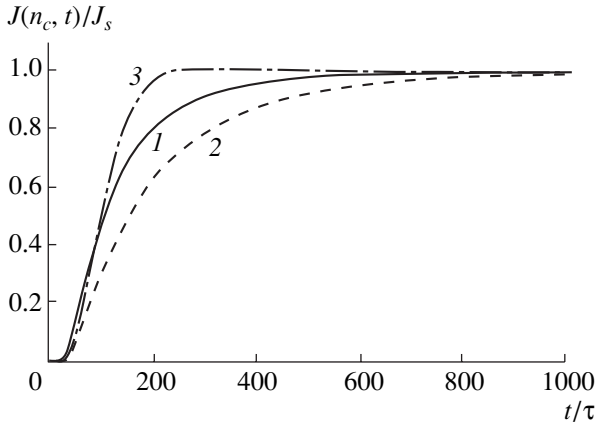

Fig. 7. Nucleation fluxes $J(n, t)$ determined at $n = n_c = 94$, $n^* = 30$, and $W_3^*/kT = 0.7$ ($M^{(3)} \approx 0.5$) according to (*1*) numerical calculation, (*2*) relationship (26) [22], and (*3*) self-similar solution (33).

between nucleation regimes and obtained an analytical description of the main kinetic characteristics of their evolution.

Let us now discuss the results obtained above. For this purpose, it is expedient to compare the time evolution of the nucleation flux, which was proposed in our work for different nucleation regimes, and the results of direct numerical calculations. In the case of a high nucleation barrier when $W_3^*/kT = 33.3$ ($M^{(3)} = 0.01$), the results obtained for a three-dimensional nucleation are presented in Fig. 6. A comparison of the data obtained at $n = n_c = 65$ and $n^* = 50$ demonstrates that our interpolation (23)–(26) has obvious advantages over the calculations performed by other authors. In the case of a low nucleation barrier when $W_3^*/kT = 0.7$ ($M^{(3)} \approx 0.5 > M_c^{(3)}$), only relationships (26) and (33) are physically correct at $n = n_c \neq n^*$. It can be seen from Fig. 7 that both solutions adequately (even though differently) approximate the calculated dependence $J(t)$. It can be expected that the self-similar solution will be more exact in the limit $M^{(3)} \gg M_c^{(3)}$.

The self-similar substitution (29) suggests that the size of a cluster with an arbitrary dimension $R \propto n^{1/d}$ varies linearly with time: $R \sim t$. This implies that the rate of increase in the cluster size R reaches a steady-state value ($\dot{R} = \text{const}$) with time, which was observed experimentally in [25]. It should be noted that our consideration of the nucleus growth is valid to the onset of the next (later) nucleation stage, at which the degree of supersaturation begins to change with time [26] and then the diffusion fields of growing nuclei overlap (i.e., interact) with each other. This diffusion interaction results in a crossover of the mechanism of the cluster growth to the Ostwald ripening mechanism [27]. Since the Ostwald ripening regime of nucleation is not considered here, the possible cluster sizes are limited from above.

CONCLUSIONS

The main inferences and results obtained in this work can be summarized as follows.

(i) It has been demonstrated that, in the framework of the classical nucleation theory, the degree of nonequilibrium of the metastable phase is the most important factor controlling the nucleation kinetics (quantitatively described by the metastability parameter $M^{(d)}$).

(ii) The effect of the nucleation barrier height on the possible nucleation regimes is investigated. It is shown that an increase in the metastability parameter $M^{(d)}$ above the threshold value leads to a crossover of the nucleation regime from the critical nucleus regime (observed at $M^{(d)} < M_c^{(d)}$) to the kinetic runaway regime (at $M^{(d)} > M_c^{(d)}$). This crossover is attended by a considerable transformation of the surface topology of the kinetic nucleation potential.

(iii) The demarcation line separating different nucleation regimes is constructed in the supersaturation–temperature coordinate frame.

(iv) In the case of a nonstationary nucleation and a high nucleation barrier, an approximate relationship is proposed for the distribution of clusters over sizes n. This relationship adequately describes the distribution of clusters on an arbitrary time interval $0 < t < \infty$. A comparison with the results of the direct numerical solution of the kinetic nucleation equation shows that the approximate solution is in close agreement with the exact solution.

(v) An asymptotically exact self-similar solution is derived for a low nucleation barrier. This solution indicates that the nonstationary cluster distribution changes in character in the region with high metastability.

ACKNOWLEDGMENTS

I am grateful to my friend and colleague Kazumi Nishioka† for his collaboration in formulating the main ideas underlying this investigation. I would like to thank A.S. Chernov, S. Fisenko, D. Kashchiev, S.A. Kukushkin, H. Kumomi, A. Mori, B. Mutafshchiev, L.N. Rashkovich, V. Shneidman, J. Wilemsky, and the other colleagues for their participation in discussions that provided a deeper insight into many problems under consideration. I also thank my young colleagues, postgraduate students, L.N. Balykov, J.-S. Lee, S.K. Saĭkov, and M. Sanada for their assistance and helpful discussions.

REFERENCES

1. J. Feder, K. C. Russel, J. Lothe, and G. M. Pound, Adv. Phys. **15**, 117 (1966).
2. K. Binder and D. Stauffer, Adv. Phys. **25**, 343 (1976).
3. A. S. Myerson and A. F. Izmailov, in *Handbook of Crystal Growth*, Ed. by D. T. J. Hurle (North-Holland, Amsterdam, 1993), Vol. 1, p. 250.
4. M. Volmer and N. Weber, Z. Phys. Chem. (Leipzig) **119**, 277 (1926).
5. A. Bunde, Philos. Mag. B **59**, 85 (1989).
6. L. V. Bravina and E. Z. Zabrodin, Phys. Lett. A **233**, 423 (1997).
7. J. S. Langer, Ann. Phys. **41**, 108 (1967).
8. J. S. Langer, in *Solids Far from Equilibrium*, Ed. by C. Godreche (Cambridge Univ. Press, New York, 1993), Vol. 21, p. 297.
9. J. D. Gunton, M. San Miguel, and P. S. Sahni, in *Phase Transitions and Critical Phenomena*, Ed. by C. Domb and J. L. Lebowitz (Academic, London, 1983), Vol. 8, p. 267.
10. K. Nishioka, Phys. Rev. E **52**, 3263 (1995).
11. I. L. Maksimov and K. Nishioka, Phys. Lett. A **264**, 51 (1999).

† Deceased.

12. E. M. Lifshitz and L. P. Pitaevski, *Course of Theoretical Physics*, Vol. 10: *Physical Kinetics* (Nauka, Moscow, 1979; Pergamon, Oxford, 1981).
13. K. Nishioka and I. L. Maksimov, J. Cryst. Growth **163**, 1 (1996).
14. Ya. B. Zel'dovich, Zh. Éksp. Teor. Fiz. **12**, 525 (1942).
15. R. Becker and W. Döring, Ann. Phys. **24**, 719 (1935).
16. D. Kashchiev, Surf. Sci. **14**, 209 (1969).
17. H. Trinkaus and M. H. Yoo, Philos. Mag. A **55**, 269 (1987).
18. G. Shi, J. H. Seinfeld, and K. Okuyama, Phys. Rev. A **41**, 2101 (1990).
19. P. Demo and Z. Kožišek, Phys. Rev. B **48**, 3620 (1993).
20. V. A. Shneidman, Phys. Rev. A **44**, 2609 (1991).
21. V. A. Shneidman and M. C. Weinberg, J. Chem. Phys. **97**, 3621 (1992).
22. I. L. Maksimov, M. Sanada, and K. Nishioka, J. Chem. Phys. **113**, 3323 (2000).
23. K. Kawamura, J. Phys. Soc. Jpn. **38**, 1259 (1975).
24. G. Nicolis and I. Prigogine, *Self-Organization in Non-Equilibrium Systems* (Wiley, New York, 1977; Mir, Moscow, 1979).
25. B. J. Ackerson and K. Schätzel, Phys. Rev. E **52**, 6448 (1995).
26. S. A. Kukushkin and A. V. Osipov, Usp. Fiz. Nauk **168**, 1083 (1998) [Phys. Usp. **41**, 983 (1998)].
27. I. M. Lifshitz and V. V. Slyozov, Zh. Éksp. Teor. Fiz. **35**, 479 (1958) [Sov. Phys. JETP **8**, 331 (1959)].

Translated by O. Borovik-Romanova

Crystallography Reports, Vol. 47, Suppl. 1, 2002, pp. S116–S117.

SOLUTION GROWTH

On the Equilibrium Crystal Habit as Predicted by the Gibbs–Curie Principle

E. B. Treĭvus

Institute of the Earth's Crust, St. Petersburg State University, Universitetskaya nab. 7/9, St. Petersburg, 199034 Russia

e-mail: treivus@cryst.geol.pu.ru

Received October 7, 2002

Abstract—It is pointed out that there is no physical mechanism for the change, dictated by the Gibbs–Curie principle, from a nonequilibrium habit of a macroscopic faceted crystal to the equilibrium habit. The reason why this principle is inapplicable to such a crystal is established. © *2002 MAIK "Nauka/Interperiodica".*

According to the Gibbs–Curie principle, established about 120 years ago [1, 2], a crystal at equilibrium must take a habit that minimizes its total surface free energy and is, therefore, determined by the relative values of surface tension on crystal faces. This principle has been discussed in many works and is often regarded as the main law governing the equilibrium crystal habit. There has been and continues to be considerable effort aimed at developing and perfecting it [3–6]. In deriving the Gibbs–Curie principle, no limitations are imposed on the crystal size. For this reason, most researchers consider it a universal rule, without paying attention to this point. At the same time, Gibbs himself treated this principle with a degree of caution, supposing that it applies to only very small crystals [1]. However, his explanation of why this principle is inapplicable to relatively large crystals is not quite correct because he considered crystal growth in supersaturated solutions (even though weakly supersaturated); that is, he did not differentiate between equilibrium and nonequilibrium crystal habits, while the principle in question refers only to the former.

A major question to be answered in this context is how a nonequilibrium (in terms of the Gibbs–Curie principle) habit transforms into the equilibrium one.

To provide a degree of generality, consider a crystal grown from a liquid solution. For definiteness, let it have the same habit as the one considered by Curie [2]: a combination of a tetragonal prism and pinacoid. The solution is supersaturated, and the crystal is macroscopic; that is, the thickness of the surface layer (several atomic planes [7]) is negligible in comparison with the crystal size, which is the case if the latter exceeds 30–50 nm. Let the crystal section parallel to two of the prism faces have the shape shown by the solid line in the figure. The crystal is single-component and can, therefore, be fully characterized by the chemical potential. It contains no impurities, and its chemical potential is the same for the growth pyramids of all its faces (ideal crystal).

Let the crystal be transferred to a solution which is in equilibrium with the crystal at a given temperature and pressure, whose oscillations do not exceed their possible spontaneous fluctuations. The relative values of surface tension on the crystal faces, σ_a and σ_b, are such that, according to the Gibbs–Curie principle, the crystal must take the habit shown by the dashed line in the figure. For this to take place, an amount of the crystal substance must be transferred from face *B* to face *A* via molecular transport. In this way, atomic layers on face *B* must disappear one after another. The length scale of the process is such that, macroscopically, it consists in local (selective) dissolution of the pinacoid face. However, this is only possible if the solution is undersaturated with respect to this face. At the same time, the crystal is at equilibrium and dissolution of face *B* is impossible. Accordingly, no macroscopic growth of face *A* can occur. Thus, there is no physical mechanism for changes in the areas of the two faces.

The Gibbs–Curie principle is based on the view that the crystal–solution interface should be thought of as a geometric surface, with no thickness, and that the surface energy refers to this surface. This approach appears unsatisfactory, at least in the case under consid-

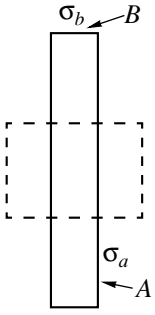

Outline of a crystal with a nonequilibrium habit (solid line) and the corresponding equilibrium habit (dashed line) according to commonly accepted views.

1063-7745/02/47S1-S0116$22.00

eration. There is another approach to analyzing surface phenomena, which goes back to van der Waals and is based on the notion that the interfacial layer between two phases has a certain thickness and may be regarded as a distinct phase (surface phase, or interphase) [8]. The boundaries of the interphase can be located only approximately. Clearly it must involve the surface layer of the crystal and the chemisorption layer. The interphase is characterized by thermodynamic parameters of its own. According to Rusanov [8, p. 5], "the method of finite-thickness layer restricts the possibility of misinterpretation."

If the interface is flat and the temperature and pressure in the two bulk phases are equal and constant, the equilibrium state of the surface phase is described by the well-known equation [8, p. 57]

$$Sd\sigma = -\Sigma m_i d\mu_i^{(\sigma)}, \quad (1)$$

which differs from the equation given in [8] in that it includes no terms containing differentials of temperature and pressure for the reason indicated above. For a crystal located in a saturated solution of the same substance, S is the surface area of an arbitrary macroscopic region on any of the crystal faces, $m_i^{(\sigma)}$ is the weight of the ith component in the interphase within this region (component 1 is the crystallizing substance, and component 2 is the solvent), σ is the surface tension coefficient, and $\mu_i^{(\sigma)}$ is the chemical potential of the ith component.

If the solution (phase α), crystal (phase β), and surface phase (σ) are in equilibrium at a given temperature and pressure in the system, the following conditions are fulfilled [8]:

$$\mu_1^{(\alpha)} = \mu_1^{(\beta)} = \mu_1^{(\sigma)}. \quad (2)$$

Both equations are valid for the growth pyramids of all the crystal faces. Since the chemical potential is taken to be the same for all the growth pyramids, and the solution is homogeneous, the chemical potential of the crystallizing substance in the surface phase, $\mu_1^{(\sigma)}$, is the same on all the faces, as is the chemical potential of the solvent in the surface phase, $\mu_2^{(\sigma)}$. Clearly, there is a single adlayer for all the crystal faces, with "breaks" at the crystal edges. Its components may be redistributed between different faces. Equation (1) can be thought of as describing changes in the state of the adlayer and surface layer in going from one face to another. Paradoxically, since the values of $\mu_i^{(\sigma)}$ are identical on all the faces, the surface tension is the same on the faces with simple Miller indices. In the case of a nonequilibrium crystal, σ_a differs from σ_b; however, if the crystal is transferred to the equilibrium conditions, the difference must decrease, which can be understood in terms of the physical processes occurring in a mobile adlayer on crystal faces. Thus, homogeneous macroscopic crystals with faces of low indices characteristic of them are "indifferent" to their habits taken under nonequilibrium conditions. Consequently, the Gibbs–Curie principle is inapplicable to macroscopic crystals with rational faces. In other words, this principle should not be treated as universal, as is common practice at present.

Analysis of the Gibbs–Curie principle with application to crystals whose dimensions are comparable to the surface layer thickness is beyond the scope of the present work. Crystals with nonsingular faces or curved surfaces also will not be discussed here.

ACKNOWLEDGMENTS

This work was supported by the Russian Foundation for Basic Research, project no. 00-05-65183.

REFERENCES

1. J. W. Gibbs, *The Scientific Papers*, Vol. 1: *Thermodynamics* (Dover, New York, 1961; Nauka, Moscow, 1982).
2. P. Curie, J. Chem. Educ. **47** (9), 636 (1970).
3. M. Failung, *Entwicklung Numerischer Algorithmen zur Computergrafischen Darstellung Spezieller Probleme der Differentialgeometrie und Kristallographie* (Shaker Verlag, Gießen, 1996).
4. A. S. Salomatov, Sib. Mat. Zh. **37** (5), 1135 (1996).
5. S. Osher and B. Merriman, Asian J. Math. **1** (3), 560 (1997).
6. M. V. Provotorov and R. V. Kazantsev, in *Proceedings of the 3rd International Conference "Crystals: Growth, Properties, Real Structure, Application," Aleksandrov, 1997*, p. 30.
7. M. J. Jaycock and G. D. Parfitt, *Chemistry of Interfaces* (Wiley, New York, 1981; Mir, Moscow, 1984).
8. A. I. Rusanov, *Phase Equilibriums and Surface Phenomena* (Khimiya, Leningrad, 1967).

Translated by O. Tsarev

Crystallography Reports, Vol. 47, Suppl. 1, 2002, pp. S118–S127.

REAL STRUCTURE OF CRYSTALS. GROWTH OF FILMS. NANOCRYSTALS. TIP STRUCTURES

Low-Temperature Molecular Beam Epitaxy of GaAs: Influence of Crystallization Conditions on Structure and Properties of Layers

L. G. Lavrent'eva*, M. D. Vilisova, V. V. Preobrazhenskiĭ***, and V.V. Chaldyshev******

** Faculty of Physics, Tomsk State University, pr. Lenina 36, Tomsk, 634050 Russia*
e-mail: lavr@ic.ic.tsu.ru
*** Siberian Physicotechnical Institute at Tomsk State University, pl. Novosobornaya 1, Tomsk, 634050 Russia*
**** Institute of Physics of Semiconductors, Siberian Division, Russian Academy of Sciences, pr. Lavrent'eva 13, Novosibirsk, 630090 Russia*
***** Ioffe Physicotechnical Institute, Politekhnicheskaya 26, St. Petersburg, 194021 Russia*

Received April 1, 1999

Abstract—A nontraditional approach to the control of GaAs properties via the introduction of an excessive amount of arsenic during growth of epitaxial layers under conditions of low-temperature molecular-beam epitaxy (LT-GaAs layers) is considered. The influence of excessive arsenic on the structure and properties of as-grown and annealed LT-GaAs layers is considered as well as the effect of layer doping on the "capture" of excess arsenic. © *2002 MAIK "Nauka/Interperiodica".*

INTRODUCTION

The traditional approach to the control of the properties of semiconductor materials is based on their doping with various elements. This approach requires the solution of various problems such as the choice of the appropriate dopants to create the necessary energy levels, the methods of introducing dopants into crystals or epitaxial layers, and also the optimum crystallization conditions to prevent possible strong influence of structural defects on the electronic properties of doped materials.

In recent decades, a nontraditional approach to control of semiconductor properties has been developed, which is based on the formation in the material bulk of an ensemble of point defects and clusters of nanometer dimensions consisting only of the material components, vacancies, and impurities [1, 2]. This approach was shown to be especially efficient for GaAs, where an excess of As in the solid phase was used as a factor determining the formation of the ensemble of point defects and the properties of the material. For the first time, this approach was used in the 1980s to grow single crystals from a solution containing excess arsenic. The use of this approach provided growth of GaAs ingots with semi-insulating properties.

In the late 1980s, the so-called LT-GaAs layers grown by the method of molecular beam epitaxy (MBE) in the excess of As at relatively low substrate temperatures (200–300°C in comparison with conventionally used 500–600°C) became the object of thorough studies [3, 4], which showed that the structure of LT-GaAs layers has a number of specific features. These layers contain superstoichiometric (excess) arsenic, whose concentration considerably exceeds the concentration of the homogeneity boundary). Upon annealing, arsenic precipitates (clusters) of nanometer dimensions are formed in the material bulk, whereas the GaAs matrix has a high degree of perfection. LT-GaAs layers have rather interesting properties—high conductivity ($>10^5$ Ω cm) and short lifetime of minor carriers (<1 ps)—and, therefore, are a rather promising material for the formation of buffer layers in device structures, design of photodetectors in electronics, etc. In turn, this gave an impetus for intense studies of this material [5–10].

At present, the properties of LT-GaAs layers and their analogues are actively studied by various groups in many countries. In Russia, this material is being studied by a group of researchers working at the Ioffe Physicotechnical Institute in St. Petersburg, the Institute of Physics of Semiconductors in Novosibirsk, Tomsk State University, and the Siberian Physicotechnical Institute at Tomsk State University. The basic results on the effect of excessive arsenic on the structure and properties of epitaxial GaAs and solid solutions on its basis [10–29] obtained by this group are reviewed below.

GROWTH TECHNOLOGY AND METHODS OF STUDYING LT-GaAs LAYERS

The new approach to the controlling GaAs properties became possible due to progress achieved by the

1063-7745/02/47S1-S0118$22.00 © 2002 MAIK "Nauka/Interperiodica"

technology of MBE. The advantages of the MBE method important for the technology of growth of LT-GaAs layers are as follows:

—the molecular flows of Ga and As and other components with the controlled flux densities are provided by individual sources;

—the method of preparing substrates provides high purity of the surfaces and includes polishing chemical etching of the substrates and their subsequent annealing to remove possible oxidation products still in the arsenic atmosphere of the MBE chamber at 550–600°C;

—the surface quality is controlled *in situ* by reflection high-energy electron diffraction (RHEED);

—the growth rate of the layers is controlled by RHEED, taking into consideration the period of the intensity oscillations of the reflected signal;

—the variation of the epitaxial-growth conditions over a wide range (deposition temperature, molecular-beam composition with respect to the main and the impurity components).

The typical values of the parameters used in growth of LT-GaAs layers in the MBE system are as follows:

—the substrate temperature t_g during growth varies from 300 to 150°C;

—the density of the gallium flux J_{Ga} ranges within 10^{14}–10^{15} atoms/(cm^2 s);

—the flux ratio of the arsenic and gallium fluxes, J_{As}/J_{Ga}, varies within 1–30;

—the growth rate of GaAs is limited by the gallium flux and is usually 1 μm/h (i.e., one monolayer per second). The total time of growth of GaAs layers is usually 1 h.

The method of growing LT-GaAs layers is described elsewhere [10–13]. The samples were grown on semi-insulating (001) GaAs substrates in a Katun MBE setup at the Institute of Physics of Semiconductors, Siberian Division, Russian Academy of Sciences (Novosibirsk).

The structure and the properties of the LT-GaAs layers grown were studied in St. Petersburg and Tomsk. Double-crystal X-ray diffractometry was used to determine the lattice parameters of the epitaxial layer and the substrate and the structural perfection of the layers. The concentration of excess arsenic in LT-GaAs layers was measured by X-ray spectral microanalysis. Arsenic clusters in the annealed GaAs layers were revealed by the transmission electron microscopy (TEM) method. The electrophysical parameters of GaAs layers were determined by measuring electrical conductivity and the Hall effect. The concentration of optically active point defects was calculated from the absorption spectra obtained in the near IR range and the photoluminescence spectra.

Other groups also used some additional methods for studying the structure and properties of LT-GaAs layers. In particular, the concentration of Ga vacancies was determined by the method of positron annihilation, the concentration of arsenic not incorporated into the structure (hereafter referred to as antisite arsenic) was determined by the EPR method, and interstitial As was established based on the effect of ion channeling. Other methods used included Auger spectroscopy, scanning tunneling electron microscopy, etc. Such a complex approach led to considerable progress in the studies of the influence of the crystallization conditions on the structure and properties of LT-GaAs layers.

STRUCTURE AND COMPOSITION OF LT-GaAs LAYERS

Detailed X-ray diffraction studies showed that lowering of the crystallization temperature of LT-GaAs layers below 300°C results in the tetragonal distortion of their lattice and an increase in the lattice parameter of the epitaxial layers. This effect is usually characterized by the $\Delta a/a = (a_L - a)/a$ ratio, where a and a_L are the lattice parameters of the substrate and the epitaxial layer, respectively. The $\Delta a/a$ ratio increases with a decrease in t_g to 150°C [8, 10, 30, 31]. The corresponding data on the variation of the lattice parameter of LT-GaAs layers with the growth temperature are indicated in Fig. 1. The results obtained in [8, 10, 30] are in good agreement. The data obtained in [31] show similar dependences, but slightly displaced with respect to the temperature, which seems to be associated with the specific methods of temperature measurements.

The studies performed by X-ray microanalysis show that growth of LT-GaAs layers is accompanied by capture of arsenic excessive with respect to its stoichiometric concentration, [As_{ex}], which increases with lowering of the substrate temperature and attains a value of ~1.5 at. % at t_g = 150°C [8, 10].

The analysis shows that the change in the lattice parameter $\Delta a/a$ correlates with [As_{ex}] concentration (Fig. 2). This correlation dependence can be used to estimate the total concentration of excessive arsenic from the data on the lattice parameter.

It is naturally expected that the [As_{ex}] and $\Delta a/a$ values would be dependent on the ratio of the As and Ga components in the molecular beam, J_{As}/J_{Ga}. Corresponding data were obtained in several studies [4, 10, 13, 30–32]. As a rule, the As_4 flux obtained by sublimation of solid arsenic was used. The most detailed studies in the temperature range 200–310°C were performed in [31].

At present, it has been established that the LT-GaAs layers grown at J_{As}/J_{Ga} = 1 have the stoichiometric composition, i.e., $\Delta a/a$ = 0 [31–35]. With an increase in the J_{As}/J_{Ga} ratio, i.e., with an increase in the J_{As} flux, the composition of the LT-GaAs layers starts deviating from stoichiometric, which is seen from an increase in $\Delta a/a$. Then, the lattice parameter attains its limiting value, which corresponds to the maximum possible concentration of excessive arsenic at the given t_g. According to [31], this character of the dependence of

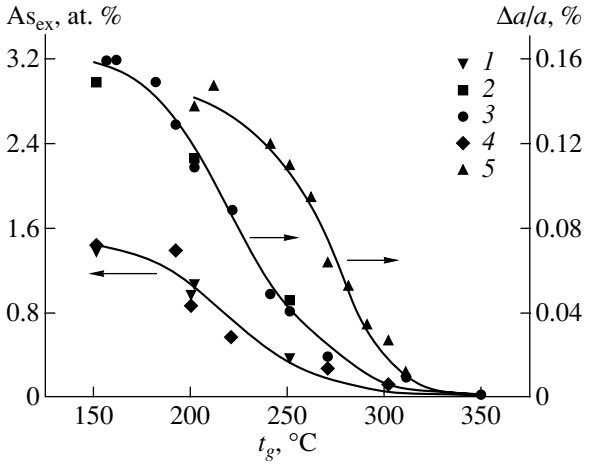

Fig. 1. Concentration of excessive arsenic and the variation of the lattice parameter of LT-GaAs layers as functions of growth temperature (*1*, *2*) according to data [10]; (*3*, *4*) according to data [8, 30]; and (*5*) according to data [31].

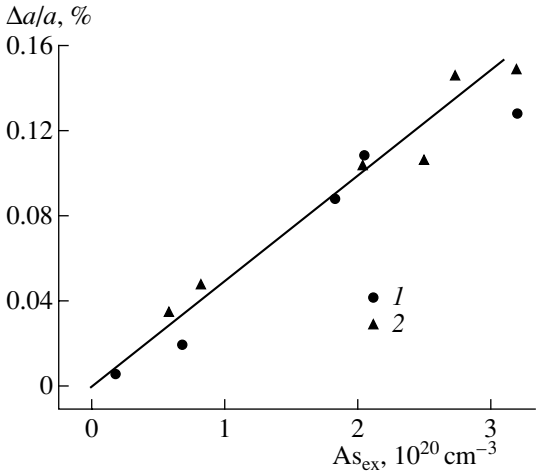

Fig. 2. Correlation of the changes in the lattice parameter and the concentration of excessive arsenic in LT-GaAs layers according to data *1* [8] and *2* [10].

$\Delta a/a$ on J_{As}/J_{Ga} is preserved within the temperature range $240 < t_g < 310$°C. At lower t_g, the dependence of $\Delta a/a$ on J_{As}/J_{Ga} becomes nonmonotonic and, upon the attainment of its maximum value, one observes a gradual decrease in $\Delta a/a$ [29, 31]. The dependence of the limiting values of $\Delta a/a$ on t_g obtained in [31] is shown in Fig. 1.

It was also shown [33–35] that the LT-GaAs layers of the stoichiometric composition grown at a rigorously established ratio of the As and Ga fluxes possess properties close to those of GaAs grown under conventional MBE conditions (t_g = 580–600°C).

FORMS OF INCORPORATION OF EXCESS As INTO THE LATTICE OF LT-GaAs LAYERS

The form of the incorporation of excess Ga and As atoms into the GaAs lattice has been studied both experimentally and theoretically since 1960. A review of studies to this effect and an analysis of the state of the problem were done in [36, 37].

According to the commonly accepted opinion, the "capture" of excess Ga into the GaAs lattice within the homogeneity range is accompanied by generation of vacancies in the arsenic sublattice [36, 37]. Beyond the homogeneity range, the excess Ga atoms are transformed into the microparticles of the second phase. They can be "captured" by a growing layer during crystallization from the gas phase [13, 38], which gives rise to a number of secondary effects. In particular, one can observe microwave absorption in the range of weak magnetic fields at low temperatures characteristic of inclusions of the superconducting phase. This effect was also observed in LT-GaAs layers [10–13].

Unlike gallium, excessive arsenic can occupy interstitials (As_i) and the "antisite" positions ("antisite defect" As_{Ga}) [36, 37]. The As_{Ga} defects are characterized by EL2 levels located in the vicinity of the middle of the band gap (E_c = 0.8 eV) responsible for the semi-insulating properties of GaAs single crystals. At the same time, gallium vacancies V_{Ga} appear in the GaAs lattice at a concentration uniquely related to the concentration of excess arsenic. The limiting equilibrium concentrations of intrinsic point defects in GaAs single crystals grown at high temperatures do not exceed 10^{19} cm^{-3}.

It is difficult to determine the composition of an ensemble of point defects in LT-GaAs layers because the process of low-temperature MBE is far from equilibrium. According to [2], an ensemble of intrinsic point defects in LT-GaAs layers grown in an excess of As includes As_{Ga}, V_{Ga}, and As_i, with the antisite As and Ga vacancies being either in the neutral (As^0_{Ga}, V^0_{Ga}) or in the ionized (As^+_{Ga}, V^-_{Ga}) states. The concentrations of all the defects depend on the epitaxial-growth temperature t_g and the ratio J_{As}/J_{Ga}, whereas the ionization degree depends on the position of the Fermi level. According to [30, 39–41], the concentrations of all the defects increase with a decrease in the growth temperature, which qualitatively agrees with the data on the capture of excessive As and indicates that the process of defect formation is not equilibrium. In the whole range of the epitaxial temperatures (150–300°C) and different flux ratios J_{As}/J_{Ga}, the defect concentrations remain different: $[As^0_{Ga}] > [As^+_{Ga}] > [V_{Ga}]$ [30, 39, 41].

Comparison of the observed changes in the lattice parameter with the concentration of antisite defects As_{Ga} in the LT-GaAs layers shows the existence of a correlation dependence which, according to [39], is of the linear character (Fig. 3) and can be approximated by

the ratio $\Delta a/a = 1.24 \times 10^{-23}[As_{Ga}]$, where the concentration of $[As_{Ga}]$ is given in at. cm^{-3}. The data obtained for GaAs single crystals fit this dependence quite well [39]. Therefore, it is assumed that the prevailing defects responsible for the observed increase in the lattice parameter in LT-GaAs layers are antisite As_{Ga} defects. The calculated length of the As–As bond in the structure of an As_{Ga}–$4As_{As}$ minicluster calculated from the correlation dependence equals 0.265 nm, i.e., substantially larger than the length of the Ga–As bond in GaAs (0.245 nm) and the length of the As–As bond in the rhombohedral arsenic lattice (0.251 nm). It is assumed that, in the vicinity of an antisite As_{Ga} defect, the As_{As} atoms are somewhat displaced from their conventional positions toward the closest interstitials. This gives rise to the additional scattering observed in the experiments on ionic channeling, which is assumed by some authors to be caused by interstitial arsenic. It should be mentioned that the pronounced value of the "tetrahedral As–As bond" in a minicluster agrees quite well with theoretical calculations [42, 43].

On the contrary, it is assumed in [33, 34] that the main contribution to the lattice deformation in LT-GaAs layers proceeds from interstitial arsenic. This conclusion was drawn from the existence of the linear correlation between $\Delta a/a$ and the total concentration of excess arsenic (Fig. 2) and also from the favorable ratio of the covalent radius of arsenic and the radius of the tetrahedral interstitial (0.104 nm) in the GaAs lattice. The ion channeling data also confirm this assumption. It is also believed [33, 34] that the formation of antisite As_{Ga} defects should not result in pronounced changes in the bond length, because the tetrahedral covalent radii of Ga and As vary only insignificantly (0.126 and 0.118 nm, respectively).

At present, the prevailing point of view is that the main defects in LT-GaAs layers are As_{Ga} defects, and, therefore, the linear correlation dependence shown in Fig. 3 can be used to recalculate the measured $\Delta a/a$ values into the concentration of As_{Ga} defects. However, the problem of the quantitative relation of the concentrations of antisite and interstitial arsenic in LT-GaAs layers is still open mainly because of the absence of reliable identification methods and measurements of As_i concentration.

It should also be mentioned that the linear correlation shown in Fig. 3 was constructed in [39] based on the data for LT-GaAs layers grown in the temperature range 200–270°C. The flux ratio J_{As}/J_{Ga} was not taken into account. One can assume that the values of this ratio were rather high and produced no significant influence on $\Delta a/a$. At lower growth temperatures, the dependence of $\Delta a/a$ on J_{As}/J_{Ga} becomes more complicated, which may affect the correlation dependence. Figure 3 also shows the data obtained in [29] for LT-GaAs layers grown at t_g = 150°C, with the J_{As}/J_{Ga} ratio ranging from 1.3 to 20.0. It is seen that this dependence is indeed nonlinear.

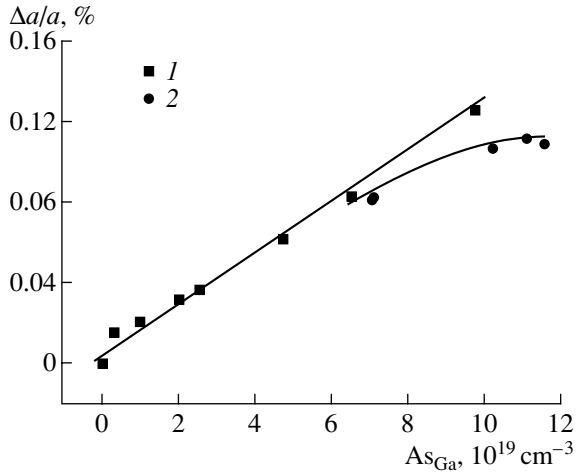

Fig. 3. Correlation between the changes in the lattice parameter $\Delta a/a$ and concentration of As_{Ga} defects determined from the IR absorption in LT-GaAs layers (*1*) grown at different temperatures [39] and (*2*) grown at different As fluxes but at constant temperature, 150°C [29].

INFLUENCE OF ANNEALING ON THE STRUCTURE AND PROPERTIES OF LT-GaAs LAYERS: CLUSTER FORMATION

The electrophysical measurements of the parameters of LT-GaAs layers show that as-grown layers have comparatively high resistivity ($\rho = 10^2$–10^3 Ω cm) and low electron mobility ($\mu \sim 10^{-1}$ $cm^2/(V\ s)$). Analysis of the temperature dependence of conductivity [44, 45] shows that, in the layers grown at $t_g < 250$°C, the hopping conduction over the deep layers takes place ($\log\sigma \sim T^{1/4}$). With an increase of t_g from 300 to 420°C, the contribution of the hopping conduction becomes unimportant, which is seen from the dramatic increase of the carrier mobility (from 500 to 6000 $cm^2/(V\ s)$).

Already, the early studies [4, 5] showed that annealing of LT-GaAs layers in the growth chamber at $t_a >$ 400°C considerably changes the structure and properties of the material. The resistivity of the annealed layers increases from 10^2–10^3 to 10^6–10^8 Ω cm, whereas the $\Delta a/a$ ratio decreases. The change in the lattice parameter of the layers grown at t_g and then subjected to isochronal annealing at t_a is shown in Fig. 4 [10]. Upon 15-min-annealing at t_a = 500°C, the lattice parameter acquires a value characteristic of the stoichiometric GaAs. The halfwidth of the diffraction lines from the annealed LT-GaAs layers ranges within 20–40″, which indicates that the matrix structure has a high degree of perfection. Annealing results in a decrease in the concentration of As_{Ga} defects. The activation energy of the process ranges from 1.4 eV [40] to 1.7 eV [45]. The concentration of gallium defects also decreases,

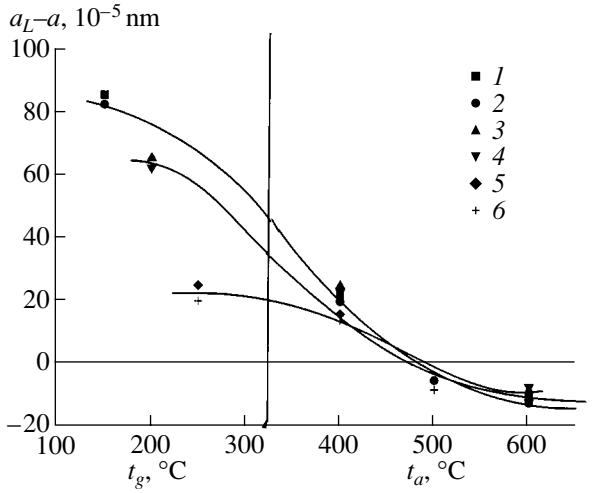

Fig. 4. Dependence of the parameter mismatch of the epitaxial layer, a_L, and the substrate, a, on t_g and the annealing temperature t_a [10]. Annealing time 15 min. Points *1, 3, 5* and *2, 4, 6* relate to two different values of the J_{As}/J_{Ga} ratio.

but still remains sufficiently high, so that they become the main defects in the annealed LT-GaAs layers [41]. Therefore, the lattice parameter of LT-GaAs layers annealed at t_a = 600°C becomes less than the lattice parameter of the substrate (Fig. 4).

The transmission electron microscopy (TEM) study of the structure of LT-GaAs layers reveals an ensemble of arsenic precipitates (clusters) in the annealed material randomly distributed over the bulk of the epitaxial layer. The typical concentration and the average linear dimension of the clusters are ~10^{17} cm^{-3} and ~5 nm, respectively. These quantities are related and depend on the J_{As}/J_{Ga} ratio and the growth, t_g, and annealing, t_a, temperatures and time. Figure 5a from [16] shows an example of the distribution of arsenic clusters in LT-GaAs layers. It is seen that the clusters are randomly distributed over the volume, with their dimensions varying within some limits. The moiré fringes show that the clusters have the crystal structures. The analysis of the moiré fringes showed [16] that the structure of these clusters depends on their dimensions. The clusters with a diameter exceeding 3 nm have the hexagonal lattice characteristic of arsenic, which is somewhat distorted by the elastic stresses at the cluster–matrix interface. For smaller clusters, the lattice is close to cubic. The data on the atomic structure of these clusters are used for modeling the electronic structure and properties of LT-GaAs layers [46].

Clusters of metal As incorporated into the matrix of LT-GaAs layers play the decisive role in the formation of the properties of the annealed material. The mechanism of such an influence is considered in [5]. It is well known that the Fermi level is fixed at the metal–semiconductor interface. At the GaAs-matrix–As-cluster interface, the Fermi level is fixed close to the middle of the band gap in GaAs, which results in the formation of the region of depletion of charge carriers around the cluster. Since the concentration of As clusters in annealed LT-GaAs layers is rather high (~10^{17} cm^{-3}), the average distance between the clusters is less than the double thickness of the depletion region. As a result, the GaAs matrix acquires the semi-insulating properties. Moreover, the electric fields in the vicinity of the matrix–cluster interfaces provide capture and a high recombination rate of nonequilibrium charge carriers, and, as a result, the lifetime of the charge carriers in the cluster-containing LT-GaAs layers does not exceed 1 ps. If the cluster-containing LT-GaAs layers are combined with conventional layers with *n*- or *p*-type conductivity [24, 25], some additional possibilities for the control of the electron distribution in epitaxial structures arise.

It was established in early studies [47–49] that it is possible to control the cluster distribution in the bulk of LT-GaAs layers by creating multilayer structures doped with silicon, beryllium, and indium. At present, δ-doping with In is the most popular. In the process of the growth of LT-GaAs layers, the Ga flow stops and, for several seconds, is replaced by the In flow. The nominal thickness of the In δ-layer varies within 0.5–1.0 monolayer. Because of the influence of the growth microrelief, In is distributed over three to four neighboring monolayers. The distance between the indium δ-layers ranges within 20–30 nm. In the process of postgrowth 10–15-min annealing at 500–600°C, As_{ex} is redistributed, which is accompanied by the formation of As-clusters concentrated in the δ-layers. As a result, one obtains a structure in which two-dimensional layers containing clusters are separated by layers having no such clusters [17–21]. The electron-microscopy image of the transverse cross section of such a structure is shown in Fig. 5b [18]. The position of cluster-containing layers coincides with the position of indium δ-layers. The cluster density in the layers is $(1–3) \times 10^{11}$ cm^{-2}; the average cluster size is 4–5 nm. If the distance between the indium δ-layers exceeds 30 nm, then annealing results in the formation of clusters both on δ-layers and between them. An increase in the annealing temperature results in an increase in the cluster dimensions. There exist an optimum annealing time and temperature that provide the accumulation of more than 90% of all the clusters in indium δ-layers [24–26].

To form layer structures, one can use not only indium but also some other isovalent dopants. In [21], the efficiencies of In and Sb δ-doping providing the accumulation of As clusters in the two-dimensional layer were compared. It was established that cluster formation in Sb-doped layers occurs much faster. In the samples with antimony-doped δ-layers, clusters were observed already after 15-min annealing at t_a = 400°C, whereas in indium-doped δ-layers, no clusters were observed upon such annealing. The average dimension of clusters upon annealing at t_a = 500 and 600°C was 3–7 nm at indium-doped δ-layers and 7 and 18 nm at antimony-doped δ-layers, respectively. These data indicate

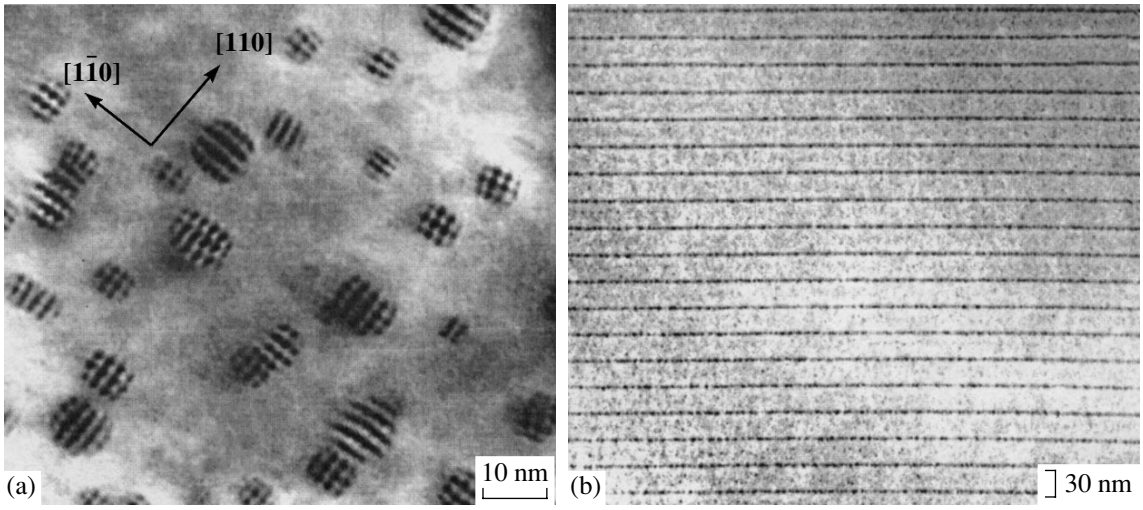

Fig. 5. Bright-field image of (a) undoped LT-GaAs layers grown at 200°C and (b) the same layers with In δ doping. The distance between the δ-layers is 30 nm. The annealing temperature is (a) 600 and (b) 500°C; the annealing time 15 min. The projections along the (a) [001] and (b) [110] directions [16, 18].

that the process of As_{ex} precipitation at δ-layers depends on the dopant type.

The redistribution of excessive arsenic occurs via diffusion. The diffusion of As_{Ga} is promoted by a high concentration of Ga vacancies. The additional difference between the chemical potentials necessary for heterogeneous nucleation of As_{ex} at two-dimensional δ-layers seems to be associated with the elastic stresses created by different lattice parameters of GaAs, InAs, and GaSb.

Annealing of doped δ-layers in LT-GaAs layers is accompanied not only by diffusion and precipitation of excessive As at the boundaries of the δ-layers, but also by mutual diffusion of In and Ga or Sb and As. The effective self-diffusion coefficients in LT-GaAs layers should considerably differ from those known for the stoichiometric GaAs, because of a high concentration of intrinsic point defects (V_{Ga}, As_i) affecting the rate of diffusion exchange over the sites of the cationic sublattice and providing the development of the dissociation mechanism of diffusion in the anionic sublattice [50–52]. The experimental study of the diffusion blurring of the boundaries of the In- and Sb-doped δ-layers and also the Al-doped δ-layers confirmed these expectations [21–23, 27]. It was established that the effective self-diffusion coefficients in the cationic and anionic sublattices of the LT-GaAs layers in the temperature range 400–700°C exceed by several orders of magnitude the values characteristic of the stoichiometric materials, whereas the activation energy of the In–Ga and Al–Ga mutual diffusion in LT-GaAs layers is considerably lower than in a GaAs single crystal. Thus, the activation energy of In–Ga mutual diffusion is 1.1 eV, which is much lower than the activation energy of migration of gallium vacancies in GaAs (1.9 eV). The substantial reduction of the activation energy of mutual-diffusion is provided by the fact that the concentrations of vacancies and other point defects can vary during annealing of LT-GaAs layers.

INFLUENCE OF DOPING ON THE CAPTURE OF EXCESS As AND THE PROPERTIES OF LT-GaAs LAYERS

Although the basic properties of LT-GaAs layers are provided by high concentration of clusters and intrinsic point defects, doping is an important factor, which allows one to change the charge state of these defects and influence the processes of the capture of excess arsenic and cluster formation.

The effect of doping and isovalent impurities (Si, Be, and In) on the composition, structure, and properties of LT-GaAs layers have been repeatedly studied [2, 15, 26, 33–35, 45, 53]. Consider in brief the important results obtained.

It was established experimentally that doping of LT-GaAs layers with Si and Be at the constant flux ratio J_{As}/J_{Ga} and growth temperature t_g (250°C) reduces the capture of excessive arsenic. With an increase of the impurity concentration, the reflections from the film and the substrate on the X-ray diffraction patterns approach one another, and, at concentrations of $\sim 1 \times 10^{19}$ cm^{-3}, the peaks of these reflections merge together, which indicates that the lattice parameters of the layer and the substrate become equal [33]. At the same time, one also observes a decrease in the concentration of antisite defects As_{Ga} (from 3×10^{19} to 4×10^{18} cm^{-3}) and the transition from the hopping to electron or hole conduction characteristic of Si- and Be-doped GaAs, respectively. Therefore, under conditions of competition for the sites of incorporation into the gallium sub-

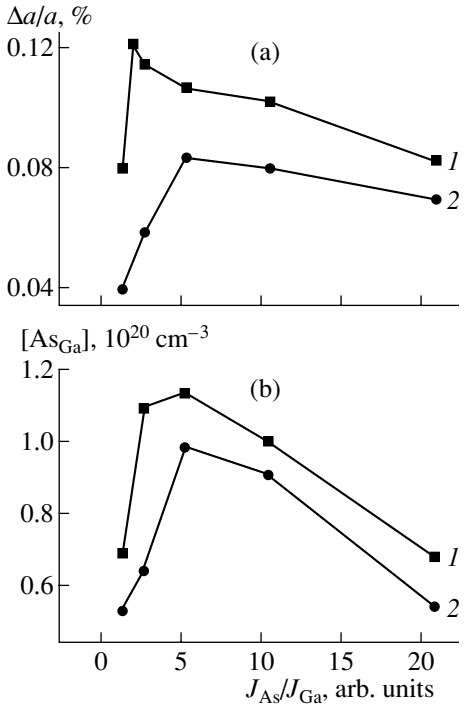

Fig. 6. Dependences of (a) the change in the lattice parameter of LT-GaAs layers and (b) the concentration of As_{Ga} defects on the flux ratio J_{As}/J_{Ga} at the growth temperature 150°C for (*1*) undoped and (*2*) doped layers; Si dopant (1×10^{19} cm^{-3}) [29].

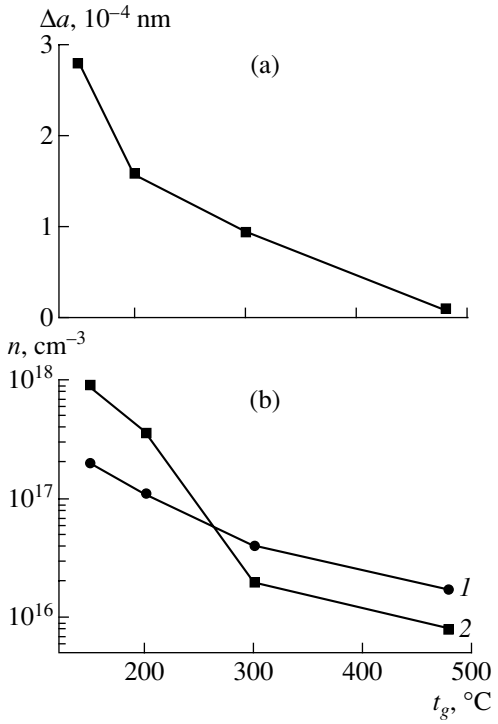

Fig. 7. Influence of annealing on the parameters of LT-GaAs layers grown at different temperatures: (a) variation of the lattice parameters and (b) variation of the electron concentration (*1*) prior to annealing and (*2*) upon it [28].

lattice, the Si and Be dopants have advantages over As and push excessive arsenic out.

The detailed studies showed that the effect of pushing As_{ex} away by the Si and Be dopants is observed over the wide range of growth conditions of LT-GaAs layers. Figure 6 shows the data demonstrating the influence of Si-doping on $\Delta a/a$ and the concentration of As_{Ga} defects in LT-GaAs layers grown at 150°C [29]. It is seen that doping with Si reduces the capture of As_{ex} over the whole range of the J_{As}/J_{Ga} ratio variation.

The situation is quite different in doping with indium [14]. At the indium concentration of 0.2 at. %, the concentration of antisite As_{Ga} defects increases by 15% in comparison with undoped LT-GaAs layers (from 5.7×10^{19} to 6.5×10^{19} cm^{-3}). Thus, the isovalent and the electrically active dopants influence the capture of As_{ex} in different ways.

SPECIFIC FEATURES OF THE STRUCTURE AND PROPERTIES OF LT-InGaAs LAYERS

The capture of excessive arsenic and deformation of the crystal lattice with lowering of the epitaxial temperature are also observed in the InGaAs [13, 28, 54–58] and AlGaAs [59, 60] solid solutions related to GaAs. Usually, AlGaAs layers are grown on GaAs substrates and the InGaAs layers with a higher indium content, on InP substrates. The composition of the $In_{0.53}Ga_{0.47}As$ solid solution (molar fraction of Ga equals 0.47 and molar fraction of In, 0.53) are chosen in such a way that the parameter of the InGaAs film would match that of the InP substrate.

It is established experimentally, that, similar to the case of LT-GaAs layers, the lattice parameter in the AlGaAs and InGaAs solid-solution layers increases with lowering of the growth temperature, but is restored to its standard value upon annealing. Figure 7a illustrates the influence of annealing on the variation in the lattice parameter of the LT-InGaAs layers grown at different temperatures t_g [28].

During annealing of LT-InGaAs layers, excess arsenic forms precipitates (clusters) uniformly distributed over the volume of the epitaxial layer [13, 28, 57]. The typical concentration of arsenic clusters is $\sim 5 \times 10^{17}$ cm^{-3} and their linear dimensions range within 2–5 nm. The volume of the clusters in the InGaAs lattice amounts to 0.4%. The study of cluster-containing material by the TEM methods reveals the moiré fringes indicating the crystalline state of the precipitate.

It should also be mentioned that the redistribution of excess arsenic in the crystal lattice of solid solutions is a rather complicated process and proceeds simultaneously with the diffuse redistribution of Ga and In over the respective sublattices. Therefore, the halfwidth

of the rocking curves of LT-InGaAs solid solutions considerably exceeds that of LT-GaAs layers, but it does not decrease upon annealing. Moreover, the line half-widths can increase upon annealing if they are accompanied by the decomposition of the solid solution into its main components [13].

Unlike GaAs, the LT-InGaAs layers have quite a high concentration of charge carriers increasing with lowering of the t_g temperature (Fig. 7b). Upon annealing, the electron concentration in the low-temperature layers decreases (from 10^{18} to 2×10^{17} cm^{-3} at a growth temperature of 150°C, Fig. 7b), but not so pronouncedly as in LT-GaAs layers [28]. The concentration of the "background impurity" in the layers does not exceed 10^{15} cm^{-3}. Thus, the high electron concentration in LT-InGaAs layers both before and after annealing is provided by intrinsic point defects, and, first of all, antisite arsenic. An antisite defect in the InGaAs solid solution is characterized by a relatively shallow donor level E_c = 0.032 eV. The formation of the Schottky barrier during annealing results in the fixation of the Fermi level in the upper part of the band gap. Therefore, the InGaAs layers grown at a low temperature are characterized by high conductivity and preserve it, to a large degree, also after annealing [28].

Doping of LT-InGaAs layers results in pushing-out excessive As by Si and Be dopants in a way similar to that described for the LT-GaAs layers [56].

MECHANISM OF FORMATION OF ANTISITE As_{Ga} DEFECTS IN LT-GaAs LAYERS

The accumulated experimental data provide a rather complete description of the main laws governing the capture of excessive arsenic during growth of GaAs layers in the MBE system at low temperatures. However, the mechanism of the processes responsible for the capture of the excessive arsenic into the GaAs lattice is studied insufficiently.

It is well known that growth of epitaxial layers from the gas phase is limited by the kinetics of surface processes consisting in a number of successive and parallel stages such as adsorption, desorption, surface diffusion, and incorporation of atoms into the kinks at the growth steps. Since LT-GaAs layers are usually grown on the atomically smooth (001) surface; the surface kinetics also includes the nucleation stage.

At present, the mechanism of the processes occurring during MBE of compound semiconductors are based mainly on the model suggested by Joyce [61]. However, applying this model to the description of growth of LT-GaAs layers, one has take into account some features characteristic of this process, namely:

—the capture of excessive arsenic into the epitaxial LT-GaAs layers begins at t_g < 300°C and attains the maximum at $t_g \approx$ 150°C;

—each growth temperature has a corresponding limiting value of excess arsenic concentration;

—the excess arsenic is in the nonequilibrium state and, upon short annealing, forms precipitates;

—the doping impurities suppress the capture of excess arsenic.

The character of the dependence of $\Delta a/a$ on J_{As}/J_{Ga} allows one to assume that the capture of As_{ex} is limited by the density of the adsorption sites. The Ga and As atoms compete with Be and Si impurities for sites in the Ga sublattice. The probability of the incorporation of As into the antisite As_{Ga} sites increases with lowering of the temperature. On the other hand, at $J_{As}/J_{Ga} < 1$, no incorporation of Ga into the As sites with the formation of Ga_{As} defects takes place in the temperature range considered, despite the fact that the energy of formation of As_{Ga} and Ga_{As} defects are rather close [37]. This fact indicates that the mechanisms of arsenic and gallium capture from the adsorbed layer into the crystal are different.

This difference is explained by the specific physicochemical properties of Ga and As. The molecular beam incident onto the substrate surface contains Ga in the monatomic form, whereas As, in the form of As_4 and As_2 molecules. The thermodynamic calculations show that these molecules are rather stable and dissociate very weakly even at temperatures ranging within 600–800°C [62]. Under the growth conditions of LT-GaAs layers, the heat transfer to the substrate at the temperatures 150–300°C cannot essentially influence the dissociation degree of a molecule during adsorption. It seems that the most favorable states for dissociation of As molecules are the adsorption states on a step. In fact, the activated complexes, which include Ga atoms and As molecules, are formed on the step. The rate of complex formation depends on the Ga flux, whereas the rate of step growth is determined by the probability of the dissociation of the complex into the GaAs molecule adsorbed at the kink and an As adatom. If no dissociation of the complex occurred during the time necessary for the incorporation of a GaAs molecule into the crystal lattice, then the second As atom can be captured by the defect position (As_{Ga} or As_i).

The possible implementation of this mechanism was shown by example of the capture of a number of diatomic molecules (As_2, S_2, Se_2, Te_2, and Si_2) during growth of GaAs under conditions of gas-phase epitaxy [63–65]. Similar processes of the incorporation of Te_2 molecules and the formation of antisite defects were observed in growth of CdHgTe in the MBE system [66]. This allows one to consider this mechanism as common for systems containing components from groups IV–VIA of the Periodic Table forming rather strong diatomic molecules.

During operation of this mechanism under conditions of the growth of LT-GaAs layers, the concentration of the excess As should depend not only on J_{As}/J_{Ga} and t_g, but also on the number of sites favorable for adsorption of As_2 molecules, i.e., on the number of steps on the growth surface. The meager experimental

data accumulated confirm, in the first approximation, the relation between the capture of As_{ex} and the stepwise structure of the surface [35, 67]. In addition, even the first experiments showed that the efficiency of the capture of As_2 molecules during GaAs growth is considerably higher than that of As_4 [6, 68].

The kinetic model of the formation of antisite As_{Ga} defects under conditions of low-temperature MBE [69] suggested recently takes into account the adsorption–desorption processes and the rate of incorporation of As into the defect position, but ignores the dissociation rate of arsenic molecules.

CONCLUSION

Thus, the experimental data obtained by various authors indicate that the low-temperature growth of GaAs in the MBE system is accompanied by the nonequilibrium capture of excess arsenic into the epitaxial layer in the form of As_{Ga} and As_i. Subsequent annealing results in the redistribution of excessive As, restoration of the equilibrium structure of the layers, and formation of an ensemble of arsenic precipitates (clusters). The GaAs matrix preserves its high degree of crystallinity both prior to and upon annealing. Analogous phenomena were also observed in low-temperature growth of the InGaAs solid solutions.

In the LT-GaAs layers grown with an excess of As, the main density of the impurity states is set by the donor levels of the antisite As_{Ga} defects. The considerable resistivity of the LT-GaAs layers is provided by the corresponding position of these levels and their high concentration, which results in the fixation of the Fermi level close to the middle of the band gap in GaAs.

The Fermi level in the annealed LT-GaAs layers is fixed at the cluster–matrix interface in the position close to the middle of the band gap in GaAs. The regions depleted of charge carriers around the clusters overlap if the concentration of these clusters is $\sim 10^{17}$ cm^{-3}, which provides a high resistivity of the material and high rate of charge-carrier recombination.

The specific features of the electrophysical properties of the LT-InGaAs solid-solution layer in comparison with the LT-GaAs layers are provided by the displacement of the point of the Fermi-level fixation towards the edge of the conduction band.

Doping of the layers with the Si and Be impurities results in a decrease of the capture of excess arsenic into the crystal lattice of LT-GaAs layers, whereas the introduction of the isovalent indium impurity, to its increase.

The GaAs layers obtained by the MBE at low temperature possess an unusual structure and a set of unique properties, namely, high (up to 10^8 Ω cm) resistivity, high electric-breakdown voltage, and ultrashort lifetime (<1 ps) of nonequilibrium carriers. This material is extremely attractive for its use as insulating and buffer layers in transistors and integrated microcircuits [70] and also as active layers in a wide class of superhigh-speed optoelectron devices [71].

ACKNOWLEDGMENTS

The authors are grateful to N.A. Bert, A.E. Kunitsyn, B.R. Semyagin, M.A. Putyato, I. V. Ivonin, M.P. Yakubenya, *et al.* for their cooperation over many years. This study was supported by the Russian Foundation for Basic Research, International Association for the Promotion of Cooperation with Scientists from the New Independent States of the Former Soviet Union (INTAS), and the Ministry of Science of the Russian Federation.

REFERENCES

1. M. G. Mil'vidskii and V. V. Chaldyshev, Fiz. Tekh. Poluprovodn. (St. Petersburg) **32** (5), 513 (1998) [Semiconductors **32**, 457 (1998)].
2. *Proceedings of the Symposium on Non-Stoichiometric III–V Compounds, Erlangen-Nurnberg, 1998*, PMH-6.
3. F. W. Smith, A. R. Calawa, Chen Chang-Lee, *et al.*, IEEE Electron Device Lett. **9**, 77 (1988).
4. M. Kaminska, Z. Liliental-Weber, E. R. Weber, *et al.*, Appl. Phys. Lett. **54** (19), 1881 (1989).
5. A. C. Warren, J. M. Woodall, J. L. Freeouf, *et al.*, Appl. Phys. Lett. **57**, 1331 (1990).
6. M. R. Melloch, K. Mahalingam, N. Otsuka, *et al.*, J. Cryst. Growth **111**, 39 (1991).
7. D. C. Look, D. C. Walters, M. O. Manasreh, *et al.*, Phys. Rev. B **42**, 3578 (1990).
8. Yu Kin Man, M. Kaminska, and Z. Liliental-Weber, J. Appl. Phys. **72** (7), 2850 (1992).
9. J. M. Baranowski, Z. Liliental-Weber, W. F. Yau, and E. R. Weber, Phys. Rev. Lett. **66** (23), 3079 (1991).
10. N. A. Bert, A. I. Veĭnger, M. D. Vilisova, *et al.*, Fiz. Tverd. Tela (St. Petersburg) **35** (10), 2609 (1993) [Phys. Solid State **35**, 1289 (1993)].
11. N. A. Bert, V. V. Chaldyshev, S. I. Goloshchapov, *et al.*, Mater. Res. Soc. Symp. Proc. **235**, 401 (1994).
12. A. I. Veĭnger, S. V. Kozyrev, V. V. Chaldyshev, *et al.*, Fiz. Tverd. Tela (St. Petersburg) **38** (10), 2897 (1996) [Phys. Solid State **38**, 1585 (1996)].
13. I. A. Bobrovnikova, A. I. Veĭnger, M. D. Vilisova, *et al.*, Izv. Vyssh. Uchebn. Zaved., Fiz., No. 9, 37 (1998).
14. N. A. Bert, V. V. Chaldyshev, A. E. Kunitsyn, *et al.*, Appl. Phys. Lett. **70** (23), 3146 (1997).
15. V. V. Chaldyshev, A. E. Kunitsyn, V. V. Preobrazhenskiĭ, *et al.*, Fiz. Tekh. Poluprovodn. (St. Petersburg) **32** (7), 778 (1998) [Semiconductors **32**, 692 (1998)].
16. N. A. Bert and V. V. Chaldyshev, Fiz. Tekh. Poluprovodn. (St. Petersburg) **30** (10), 1889 (1996) [Semiconductors **30**, 988 (1996)].
17. N. A. Bert, V. V. Chaldyshev, D. I. Lubyshev, *et al.*, Fiz. Tekh. Poluprovodn. (St. Petersburg) **29** (12), 2232 (1995) [Semiconductors **29**, 1170 (1995)].
18. V. V. Chaldyshev, N. A. Bert, A. E. Kunitsyn, *et al.*, Fiz. Tekh. Poluprovodn. (St. Petersburg) **32** (10), 1161 (1998) [Semiconductors **32**, 1036 (1998)].

19. V. V. Chaldyshev, N. A. Bert, V. V. Preobrazhenskiĭ, *et al.*, Mater. Sci. Eng. A **238** (1), 148 (1997).
20. V. V. Chaldyshev, N. N. Faleev, N. A. Bert, *et al.*, J. Cryst. Growth **202**, 260 (1999).
21. N. A. Bert, V. V. Chaldyshev, A. A. Suvorova, *et al.*, Appl. Phys. Lett. **74** (11), 1588 (1999).
22. N. A. Bert, V. V. Chaldyshev, Yu. G. Musikhin, *et al.*, Appl. Phys. Lett. **74** (10), 1442 (1999).
23. V. V. Chaldyshev, N. A. Bert, Yu. G. Musikhin, *et al.*, Appl. Phys. Lett. **79** (9), 1294 (2001).
24. P. N. Brounkov, V. V. Chaldyshev, A. A. Suvorova, *et al.*, Appl. Phys. Lett. **73** (19), 2796 (1998).
25. P. N. Brounkov, V. V. Chaldyshev, A. V. Chernigovskiĭ, *et al.*, Fiz. Tekh. Poluprovodn. (St. Petersburg) **34** (9), 1109 (2000) [Semiconductors **34**, 1068 (2000)].
26. A. E. Kunitsyn, V. V. Chaldyshev, S. P. Vul', *et al.*, Fiz. Tekh. Poluprovodn. (St. Petersburg) **33** (10), 1187 (1999) [Semiconductors **33**, 1080 (1999)].
27. N. A. Bert, Yu. G. Musikhin, V. V. Preobrazhenskiĭ, *et al.*, Fiz. Tekh. Poluprovodn. (St. Petersburg) **32** (7), 769 (1998) [Semiconductors **32**, 683 (1998)].
28. M. D. Vilisova, I. V. Ivonin, L. G. Lavrent'eva, *et al.*, Fiz. Tekh. Poluprovodn. (St. Petersburg) **33** (8), 900 (1999) [Semiconductors **33**, 824 (1999)].
29. M. D. Vilisova, A. E. Kunitsyn, L. G. Lavrent'eva, *et al.*, Fiz. Tekh. Poluprovodn. (St. Petersburg) (2002) (in press) [Semiconductors (2002) (in press)].
30. M. Luysberg, H. Sohn, A. Prasad, *et al.*, J. Appl. Phys. **83** (1), 561 (1998).
31. A. Suda and N. Otsuka, Surf. Sci. **458**, 162 (2000).
32. A. Suda and N. Otsuka, Appl. Phys. Lett. **73** (11), 1529 (1998).
33. M. Missous and S. O'Haghan, J. Appl. Phys. **75** (7), 3396 (1994).
34. S. O'Haghan and M. Missous, J. Appl. Phys. **75** (12), 7835 (1994).
35. M. Missous and S. O'Haghan, J. Cryst. Growth **175/176**, 197 (1997).
36. M. G. Mil'vidsky and V. B. Osvenskiĭ, *Structural Defects in Semiconductor Single Crystals* (Metallurgiya, Moscow, 1984).
37. D. T. J. Hurle, J. Appl. Phys. **85** (10), 6957 (1999).
38. V. V. Chaldyshev, I. V. Ivonin, A. E. Kunitsyn, *et al.*, in *Proceedings of the 23rd International Symposium on Compound Semiconductors, St. Petersburg, 1996* (Inst. of Physics Publ., Bristol, 1997); Inst. Phys. Conf. Ser. **155**, 251 (1997).
39. X. Liu, A. Prasad, J. Nishio, *et al.*, Appl. Phys. Lett. **67** (2), 279 (1995).
40. X. Liu, A. Prasad, W. M. Chen, *et al.*, Appl. Phys. Lett. **65** (23), 3002 (1994).
41. J. Gebauer, F. Borner, R. Krause-Rehberg, *et al.*, J. Appl. Phys. **87** (12), 8368 (2000).
42. J. D. Chady and K. J. Chang, Phys. Rev. Lett. **60**, 2187 (1988).
43. J. Dobrowsky and M. Scheffler, Phys. Rev. Lett. **60**, 2183 (1988).
44. J. Betko, M. Morvic, J. Novak, *et al.*, Appl. Phys. Lett. **69** (17), 2563 (1996).
45. D. E. Bliss, W. Walukiewicz, J. W. Ager, *et al.*, J. Appl. Phys. **71**, 1699 (1992).
46. S. N. Grinyaev and V. A. Chaldyshev, Fiz. Tekh. Poluprovodn. (St. Petersburg) **32** (9), 1094 (1998) [Semiconductors **32**, 980 (1998)].
47. M. R. Melloch, N. Otsuka, K. Machalingam, *et al.*, Appl. Phys. Lett. **61** (2), 177 (1992).
48. M. R. Melloch, N. Otsuka, K. Machalingam, *et al.*, J. Appl. Phys. **72** (8), 3509 (1992).
49. T. M. Cheng, C. V. Chang, A. Chin, *et al.*, Appl. Phys. Lett. **64**, 2517 (1994).
50. J. S. Tsang, C. P. Lee, S. H. Lee, *et al.*, J. Appl. Phys. **77** (9), 4302 (1995).
51. R. Geursen, I. Lahiri, M. Dinu, *et al.*, Phys. Rev. B **60** (15), 10 926 (1999).
52. I. Lahiri, D. D. Nolte, J. C. P. Chang, *et al.*, Appl. Phys. Lett. **67** (9), 1244 (1995).
53. P. Specht, R. Zhao, R. C. Lutz, and E. R. Weber, in *Proceedings of the Symposium on Non-Stoichiometric III–V Compounds, Erlangen-Nürnberg, 1998*, p. 15.
54. H. Kunzel, J. Bottcher, R. Gibis, and G. Urmann, Appl. Phys. Lett. **61**, 1347 (1992).
55. R. A. Metzger, A. S. Brown, L. G. McCray, *et al.*, J. Vac. Sci. Technol. B **11** (3), 798 (1993).
56. B. Grandidier, H. Chen, R. M. Feenstra, *et al.*, Appl. Phys. Lett. **74** (10), 1439 (1999).
57. J. P. Ibbetson, J. S. Speck, A. C. Gossard, and U. K. Mishra, Appl. Phys. Lett. **62** (18), 2209 (1993).
58. N. D. Zakharov, Z. Liliental-Weber, W. Swider, *et al.*, Appl. Phys. Lett. **63**, 2809 (1993).
59. W. H. Knox, G. E. Doran, M. Asom, *et al.*, Appl. Phys. Lett. **59**, 1491 (1991).
60. A. K. Verma, J. S. Smith, H. Fujioka, and E. R. Weber, J. Appl. Phys. **77**, 4452 (1995).
61. B. A. Joyce, in *Molecular Bean Epitaxy and Heterostructures*, Ed. by L. L. Chang and K. Ploog (Martimus Nishoff, Amsterdam, 1985; Mir, Moscow, 1989).
62. D. T. Harl and J. B. Malin, in *Metallurgy in Electronics*, Ed. by N. G. Ryabtsev and F. A. Kuznetsova (Metallurgiya, Moscow, 1970), p. 129.
63. L. G. Lavrent'eva and M. D. Vilisova, Izv. Vyssh. Uchebn. Zaved., Fiz., No. 5, 3 (1986).
64. I. A. Bobrovnikova, L. G. Lavrent'eva, M. P. Ruzaikin, and M. D. Vilisova, J. Cryst. Growth **123**, 529 (1992).
65. L. G. Lavrent'eva, I. A. Bobrovnikova, and M. D. Vilisova, Izv. Vyssh. Uchebn. Zaved., Mater. Élektron. Tekh., No. 4, 35 (1998).
66. Yu. G. Sidorov, S. A. Dvoretskiĭ, V. S. Varavin, and N. N. Mikhaĭlov, in *Matrix Photodetectors of Infrared Range*, Ed. by S. P. Sinitsa (Nauka, Novosibirsk 2001), p. 119.
67. T. M. Cheng, C. Y. Chang, and J. H. Hang, Appl. Phys. Lett. **66** (1), 55 (1995).
68. J. H. Neave, P. K. Larsen, J. F. van der Veen, *et al.*, Surf. Sci. **133**, 267 (1983).
69. S. Muthuvenkatraman, S. Gorantla, R. Venkat, and D. L. Dorsey, J. Appl. Phys. **83**, 5845 (1998).
70. V. V. Chaldyshev, M. A. Putyato, B. R. Semyagin, *et al.*, Élektron. Prom-st, Nos. 1–2, 154 (1998).
71. D. D. Nolte, J. Appl. Phys. **85**, 6259 (1999).

Translated by L. Man

Crystallography Reports, Vol. 47, Suppl. 1, 2002, pp. S128–S135.

REAL STRUCTURE OF CRYSTALS. GROWTH OF FILMS. NANOCRYSTALS. TIP STRUCTURES

Real Structures of Doped Lead Telluride Crystals

V. P. Zlomanov, T. A. Kuznetsova, S. G. Dorofeev, V. D. Volodin, and O. I. Tananaeva

Department of Chemistry, Moscow State University,
Vorob'evy gory, Moscow, 119899 Russia
e-mail: tak@inorg.chem.msu.ru

Received October 1, 2002

Abstract—A relationship between the real crystal structure and the doping level was proposed based on experimental data on the real structures of PbTe crystals with different Cr, Co, Ni, and In contents. Two composition regions were revealed for these crystals. One region is characterized by the presence of impurity atmospheres at dislocations as the main type of impurity inhomogeneity, whereas impurity-rich microprecipitates prevail in the second region. Possible reasons for the formation of solid solutions supersaturated with impurity ions were analyzed. The influence of thermal treatment on the real structure and galvanomagnetic properties of the crystals was investigated. © *2002 MAIK "Nauka/Interperiodica".*

INTRODUCTION

Lead telluride PbTe belongs to the group of IR-sensitive narrow-band semiconductors A^4B^6, which acquire new properties upon doping.

The real crystal structure is characterized by the presence of two- and three-dimensional crystal defects (dislocations, point-defect accumulations, local inhomogeneities, etc.).

The real structures of doped crystals depend not only on the synthesis conditions, but also on the doping level [1]. An impurity introduced in the course of the synthesis can lead to the formation of supersaturated solid solutions in the semiconductors thus formed. The degree of supersaturation determines the qualitative (the presence of particular types of lattice imperfections) and quantitative (density of these imperfections) characteristics of the real structure. The relationship between the doping level and the real structure was studied best for the A^3B^5 semiconductors [2].

In this study, we analyzed the conditions of formation and characteristic features of the real structure of PbTe crystals doped with different impurities. Crystals with a doping level varying from 10^{17} to 10^{21} atoms/cm^3 were grown under identical conditions. The real structure (dislocation density, presence of blocks, low-angle boundaries, cell substructure, and microprecipitates of doping components) was characterized as a function of the impurity contents in the melt and the crystal. The influence of isothermal annealing on the real structure was examined.

FORMATION OF REAL STRUCTURE OF DOPED CRYSTALS

Formulation of the problem. The real structure of a material is formed in the course of the crystallization and postcrystallization transformations. The real structure of a doped crystal depends substantially on the possibility of formation and decomposition of supersaturated solutions. An excess of an impurity (if the distribution coefficient k between the medium and crystal is smaller than unity) is incorporated into a crystal, giving rise to a supersaturated solid solution in the course of crystallization due to the difference in the rates of transport processes in the crystal, growth medium, and near the surface of the growing crystal. The situation near the growing surface depends on which step of the synthesis is rate limiting (the surface kinetics or mass transfer in the growth medium). When crystallization (surface kinetics) is the rate-limiting step, impurity cations are trapped in the crystal, because their concentration in two-dimensional (surface layer), one-dimensional (step), and null-dimensional (break) solid solutions can be several times higher (even in the equilibrium state) than the concentration in a three-dimensional solid solution. If the rate of crystallization is higher than the rate of bulk diffusion, impurity atoms are accumulated in near-interface layers at a concentration exceeding the equilibrium value typical of this temperature. The amount of excess atoms is determined both by the thermodynamic (the difference in the coefficients k_{surf} and k_{bulk}) and kinetic (the difference in the rates of crystallization and bulk diffusion) factors [3].

The processes involving the mass transfer in a growth medium as a rate-limiting step are more typical of crystallization from flux. In this case, impurity supersaturation occurs, because a diffusion layer enriched with impurity cations is formed in the melt near the crystallization surface (at $k < 1$). The formation of the diffusion layer results from the difference in the rates of incorporation of particles into the growing surface and diffusion in the growth medium. Generally, the composition of the near-surface layer remains unknown, although it is this layer, rather than the aver-

age composition of the medium, that determines the effective distribution coefficient k_{eff}. The composition and structure of the near-surface layer depend on the growth conditions (growth rate, medium composition, etc.). Correspondingly, this dependence extends to k_{eff}, the character of the crystal microstructure, and the impurity distribution. Generally, the difference between k_{eff} and k, the impurity amount, the mosaicity, and the dislocation density increase with increasing difference in the compositions of the medium and near-surface layer. In addition, a cell structure can appear. The situation where the mass transfer is a rate-limiting step is more probable for crystallization from viscous melts of metal chalcogenides.

In continuation of the growth cycle, further processes accompanied by changes in composition and structure occur in the inner layers below the crystallization surface. An important feature of these processes is high temperature and, consequently, high rates of exchange diffusion transformations. In this step, the tendency toward a lower internal-energy state can lead to a substantial change in the crystal matrix up to decomposition of supersaturated solutions [2]. It is difficult to separate the role of the postcrystallization step in the defect formation in the crystal. The changes in the galvanomagnetic properties of semiconductor crystals upon decomposition of solid solutions are studied by isothermal annealing [4]. This procedure can also be useful for examining changes in the real structure of a crystal matrix supersaturated with impurity atoms. Annealing experiments are generally performed with the use of small samples cut from crystals. Although the surface-to-volume ratio of the samples thus prepared is much larger than that in a bulk crystal, annealing can allow one to reveal the direction of further transformations of the crystal toward the minimum-energy state.

The degree of supersaturation of the crystal matrix correlates with the impurity concentration in the diffusion layer. The larger the difference in the compositions of the crystal and growth medium, the higher the supersaturation. The degree of supersaturation depends on the characteristic features (the relative positions of the liquidus and solidus and the coefficient k) of the corresponding compound–impurity phase diagram. If k increases with decreasing temperature, an excess of impurity atoms can find equivalent sites in the matrix in the course of initial cooling, when diffusion processes at a temperature close to the melting temperature occur at the maximum rate. When the coefficient k decreases, the matrix supersaturation is retained and, consequently, impurity atoms are arranged in the matrix in such a way as to reduce the internal energy of the crystal, for example, by forming associates (i.e., in PbTe(Bi) crystals [5]) or microprecipitates.

Hence, impurity atoms interact with the growing crystal throughout the growth cycle. The final features of the real crystal structure are determined by the characteristics of the corresponding phase diagram and the ratio between the rates of the individual synthesis steps.

Attempts to find the conditions for the direct investigation of the behavior of impurity atoms in different steps of crystal growth failed. Hence, only indirect evidence, model experiments, and calculations can be used.

In our study of the real structures of doped PbTe crystals, we synthesized a series of crystals, estimated the stability of the crystallization front, examined the effect of the doping level on the real structure, and evaluated the influence of isothermal annealing on the real structure.

Experimental conditions. Crystals of PbTe [6–9] were grown by the Bridgman method in evacuated sealed 12–15-mm quartz tubes with a cone shaped lower end by moving in the temperature gradient of 15–20 K/cm with a rate of 0.5–1 cm/day. To prevent supercooling of the melt at the beginning of crystallization, the tube with the starting mixture was heated above the melting point by no more than 20 K, and the crystal nucleation was repeated 2–3 times. The synthesis was performed for 10–12 days. In the course of the synthesis, the temperature of the crystal was increased by about 100 K, after which the crystal was cooled to 700–750 K at a rate of 10 K/h and then to room temperature in a switched-off furnace. To estimate the characteristic features of the crystallization surface, some experiments were carried out as follows. The crystals were quenched (i.e., rapidly cooled in air), the melt was removed from the crystal, and the crystal surface was investigated.

Crystals containing Cr (6×10^{17} atoms/cm^3) and In ($1.5–2 \times 10^{20}$ atoms/cm^3) were prepared by the vapor–liquid–crystal (VLC) method. This method was not used for doping with Co and Ni because of the low vapor pressure of the corresponding tellurides.

Tellurides with different compositions, namely, $Cr_{0.47}Te_{0.53}$, $Cr_{0.4}Te_{0.6}$, Ni_3Te_2, $NiTe_2$, CoTe, $CoTe_2$, InTe, and In_2Te_3, were used as dopants. The synthesis conditions were chosen from the T–x diagrams of the corresponding sections of the Pb–Cr–Te, Pb–Ni–Te, Pb–Co–Te, and Pb–In–Te ternary systems. All of the sections correspond to the eutectic type with a limited region of the $Pb_{1-x}M_xTe$ solid solutions (M = Cr, Co, Ni, or In). In all cases, the equilibrium distribution coefficients k for tellurides of dopant metals in PbTe were smaller than unity [6–9]. The sizes of the homogeneity regions for $Pb_{1-x}M_xTe$, where M = Cr, Co, or Ni, were determined only in the temperature range of 970–1070 K. More detailed data on the homogeneity regions for $Pb_{1-x}In_xTe$ were reported in the studies [10–12]. Indium telluride, InTe, is characterized by the maximum solubility in PbTe (up to 30 mol % at 913 K). Selected characteristics of the T–x diagrams used in this study are listed in Table 1.

The concentrations of the doping impurities in the crystals were determined by chemical analysis. In addi-

Table 1. Coordinates of the eutectic points in the *T*–*x* diagrams of binary systems, solubilities of different tellurides in PbTe, and results of calculations of the Tiller criterion [7, 8]

Section	Coordinates of eutectic points		Solubility		*T*, K	Calculated C_1 (mol %), at which the right side of inequality (2) becomes larger than its left side
	mol % of doping telluride	*T*, K	mol % of doping telluride	atoms of doping metal per cm^3, 10^{20}		
PbTe–$Cr_{0.47}Te_{0.53}$	15	1167	1.5	2.0	1000	3
PbTe–CoTe	25	1160	3.5	6.3×10^{-1}	973	5
PbTe–$CoTe_2$*	40	1150	1	1.7	973	12
PbTe–Ni_3Te_2	17	925	2	1.8	973	Inadequate data
PbTe–$NiTe_2$	60	1075	7	4.6	973	7
PbTe–InTe	75	640	10**	1.5×10	1070	18
PbTe–In_2Te_3	80	600	8**	8.2	1070	23

* The section is non-quasibinary; crystallization of $Pb_{1-x}Co_xTe$ was accompanied by the formation of solid CoTe.
** Data on solubility are given for the annealing temperatures.

tion, the compositions of In-doped crystals were evaluated by powder X-ray diffraction analysis from the known dependence of the unit-cell parameter of $Pb_{1-x}In_xTe$ on the composition. The *x* parameter is given in the molar percent of dopant metal telluride or as the number of metal atoms per cubic centimeter (Table 2).

The real crystal structure was analyzed by selective etching [13] of 15–20-mm latitudinal and longitudinal sections of the crystals. The compositions of inclusions and microprecipitates were determined using Auger-electron spectroscopy on a JAMP-10 (JEOL) instrument. The character of the longitudinal distribution of doping telluride in the crystals was estimated from the results of analysis [14].

The concentrations and mobilities of charge carriers in crystalline samples were determined from Hall measurements.

Isothermal annealing of the crystalline samples was carried out at 1070 K for 5 days followed by quenching in air. It was expected that the crystal matrix would continue to undergo postcrystallization rearrangements upon thermal treatment. Several annealing experiments were carried out at lower temperature (920 K) for 10 days. Annealing was performed with the use of rectangular samples ($\approx 10 \times 6 \times 1.5$ mm^3) suitable for Hall measurements. The samples were placed in quartz tubes (5–6 mm in diameter and 30–50 mm in length). The tubes were evacuated, filled with spectrally pure argon (3.9×10^4 Pa) to prevent evaporation of the samples, and sealed. Before and after annealing, the concentration of the main charge carriers, dislocation density, and characteristic features of the real structure were monitored according to the same procedures.

Results. The methods of investigation used in this study allowed us to reveal elements of the real structure on the surfaces of crystal sections, namely, low-angle boundaries, mosaic block boundaries, melt inclusions, and microprecipitates enriched with an impurity component. The low-angle boundaries were observed as chains of closely-spaced etch pits. The mosaic block boundaries separate crystal regions, in which etch pits on dislocations have different shapes (for example, a square and trapezium). The dislocation density (N_d) was estimated from the amount of dislocation etch pits oriented on the (100) surfaces of the crystal sections.

Crystals contained 1–3 blocks, in which inclusions of different types were observed. The inclusions with smoothed edges, which had a rounded shape on latitudinal sections (Fig. 1a) and an elongated shape on longitudinal sections, were assigned to melt inclusions. Rows of etch figures (Fig. 1b) observed on the latitudinal sections were defined as melt inclusions located parrallel to the crystallization surface and partially opened by etching. Inclusions of this type, which were completely opened by polishing, dissolved in etchants more rapidly than crystal matrices and did not appear in micrographs. An enrichment of inclusions with impurity atoms was demonstrated using Auger-electron spectroscopy. The Auger-electron spectra of the inclusions revealed the presence of an impurity, whereas the Cr, Co, and Ni contents in the crystal matrix were below the sensitivity of the method. The character of the Auger-electron spectra of a melt, crystal, and transition region was discussed in the study [8]. The synthesis of crystals from concentrated melts (20 mol % of CoTe, 40 mol % of $NiTe_2$, etc.) led to an increase in the amount of inclusions, and the composition of the melt became more similar to that of the solid phase [8].

Inclusions of another type were assigned to microprecipitates of impurity tellurides. These inclusions had a platelet-like shape. In the case of PbTe(Cr), these

Table 2. Results of isothermal annealing experiments for doped PbTe crystals

Sample	Composition of the starting mixture used in the synthesis of crystals: doping telluride	mol % of doping telluride	impurity content in the starting mixture, atoms/cm^3	Impurity content in the crystal, atoms/cm^3	Method for crystal growth	Hall measurements: before annealing: type and concentration of charge carriers		after annealing: type and concentration of charge carriers		Annealing temperature, K	Assignment of the sample to region I or II in Fig. 2	N_d, cm^{-2}: before annealing	N_d, cm^{-2}: after annealing
1	$Cr_{0.47}Te_{0.53}$	1	7.4×10^{19}	6.0×10^{17}	VLC	*p*	3×10^{18}	*p*	7×10^{18}	1070	I	1×10^4	3×10^4
2	"	4	3.0×10^{20}	2.0×10^{19}	Bridgman	*n*	6×10^{18}	*p*	3×10^{18}	1070	II	5×10^4	8×10^4
3	CoTe	3	1.9×10^{20}	1.2×10^{19}	Bridgman	*n*	7×10^{17}	*p*	1×10^{19}	1070	II		
4	"	5	3.1×10^{20}	1.3×10^{19}	Bridgman	*n*	6×10^{16}	*p*	4.5×10^{18}	1070	II		
5	"	5	3.1×10^{20}	2.0×10^{19}	Bridgman	*n*	5×10^{17}	*p*	4.5×10^{18}	1070	II	5×10^4	2×10^5
6	"	8	5.1×10^{20}	1.7×10^{19}	Bridgman	*n*	3×10^{17}	*p*	6.5×10^{18}	1070	II		
7	"	20	1.3×10^{20}	3.0×10^{19}	Bridgman	*n*	2×10^{18}	*p*	7×10^{17}	920	II	8×10^4	5×10^5
8	$CoTe_2$	2	1.9×10^{20}	6.3×10^{18}	Bridgman	*n*	9×10^{16}	*p*	3×10^{18}	1070	II		
9	"	8	3.8×10^{20}	8.4×10^{18}	Bridgman	*n*	5×10^{17}	*p*	3×10^{18}	1070	II		
10	"	8	3.8×10^{20}		Bridgman	*n*	3×10^{16}	*p*	2×10^{18}	920	II		
11	Ni_3Te_2	5	4.6×10^{20}	1.9×10^{19}	Bridgman	*n*	7×10^{16}	*n*	4.5×10^{17}	1070	II	5×10^4	7×10^5
12	"	5	4.6×10^{20}	2.0×10^{19}	Bridgman	*n*	6×10^{16}	*n*	2×10^{17}	920	II		
13	$NiTe_2$	5	3.3×10^{20}	1.0×10^{19}	Bridgman	*n*	4×10^{16}	*n*	4×10^{17}	1070	II		
14	InTe	10	7.6×10^{20}	2.0×10^{20}	VLC	*n*	2×10^{19}	*n*	3×10^{18}	920	I		
15	"	10	7.6×10^{20}	1.5×10^{20}	VLC	*n*	1×10^{19}	*n*	3.5×10^{18}	1070	I	6×10^4	7×10^4

inclusions were well-faceted (Fig. 1c). Depending on the mutual orientation of the crystal section and inclusion, the latter were observed as discs or strokes. On the longitudinal sections of the crystals rapidly cooled (quenched) to room temperature, inclusions of this type were observed throughout the bulk of the crystals, except for the region adjacent to the melts. We assigned these inclusions to impurity microprecipitates formed in the crystal over a period of time after crystallization (3–5 h, judging from the length of the region without precipitates and the pulling rate of the tube). Treatment of the crystal sections with chemical etchants led to dissolution of microprecipitates (particularly, in the PbTe(Co) and PbTe(Ni) crystals). To estimate the compositions of the microprecipitates, the surfaces of the crystal sections were mechanically repolished without chemical treatment and then the Auger-electron spectra of the surfaces were measured with a step of 10 μm. This procedure allowed us to find surface sites, in which the doping metal tellurides were detected in amounts close to those observed in the crystal matrix, whereas lead was absent (peaks of lead in the Auger-electron spectrum were at the background level). In the PbTe(Co) and PbTe(Ni) crystals, copper was also discovered in microprecipitates (copper was present as an impurity in the starting dopant metals), but it was not found in the crystal matrix. It can be assumed that large platelet-like microprecipitates resulted from merging smaller microprecipitates. Thus, a large inhomogeneity is spherically surrounded by small inhomogeneities revealed by selective etching (see Fig. 1d). The enlargement process is accompanied by a series of exchange processes giving rise, in particular, to an enrichment of the microprecipitates with copper.

Hence, the compositions of inclusions in the crystals were estimated and their classification into melt inclusions and impurity microprecipitates was made based on the Auger-electron spectra of the crystal sections prepared according to different procedures.

No cell structure of the crystallization surface under the conditions of concentration supercooling (Fig. 1e) was observed on the surface of etched sections. Smoothed traces of cells (Fig. 1f) sometimes appeared at sites of high strains (near the walls of tubes, etc.).

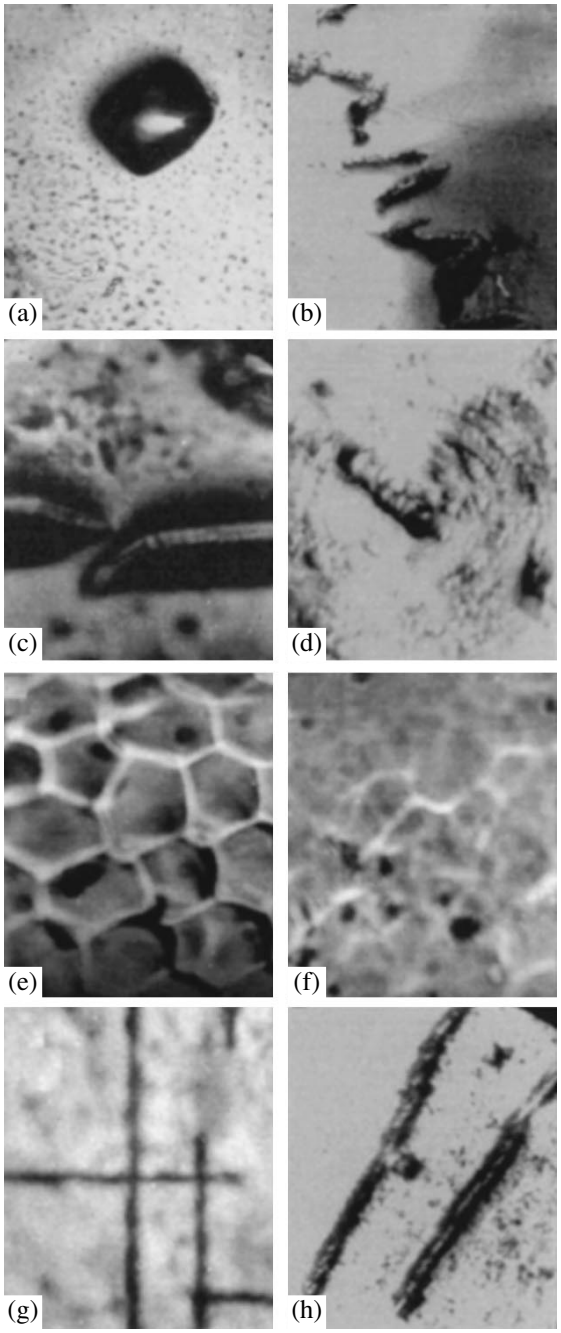

Fig. 1. Micrographs of the surfaces of doped crystals (all micrographs are shown on the same scale): (a) melt inclusions in the PbTe(Co) crystal; (b) the surface of the strongly doped PbTe(Ni) crystal (the starting melt contained 40 mol % of $NiTe_2$); traces of melt inclusions; (c) impurity microprecipitates in the PbTe(Cr) crystal prepared by flux crystallization; (d) a section of the PbTe(Cr) crystal, small microprecipitates spherically surround a large precipitate; (e) cells on the surface of the PbTe(Co) crystal, the melt was removed; (f) traces of a cell substructure on the surface of a section of the PbTe(Co) crystal (the same section is shown in micrograph 1e), the portion near the walls of the tube; (g) microprecipitates on the surface of a sections of the PbTe(Cr) crystal (the starting melt contained 1 mol % of CrTe); (h) large microprecipitates on the surface of a section of the strongly doped PbTe(Co) crystal (the starting melt contained 30 mol % of CoTe).

To examine the possibility of formation of a cell structure due to the instability of the flat crystallization front under the experimental conditions, we used the Tiller criterion. The simplest inequality is as follows:

$$G/R \geq [m(1-k)/Dk]C_1. \quad (1)$$

We also used the following inequality for concentrated melts [12]:

$$GD/R \geq m\Delta C, \quad (2)$$

where G is the temperature gradient in the melt; R is the growth rate; k is the distribution coefficient; D is the diffusion coefficient of an impurity component in the melt; m is the slope of the liquidus line; and $\Delta C = C_1 - C_s$, with C_1 and C_s as the concentrations of an impurity component at the crystallization front in the liquid and solid phases, respectively.

The concentrations of impurity atoms corresponding to inequality (2), i.e., to the maximum possible stability of the crystallization front, were evaluated as follows. First, the plots of the function $F(C) = m\Delta C$ vs. C_s were constructed. Then the limiting concentration of the impurity atoms for a crystal characterized by the flat crystallization front was determined with the use of the experimental G, D, and R values and inequality (2).

The influence of the doping level on the real crystal structure is schematically represented in Fig. 2. Two composition regions were revealed. In region I, low-angle boundaries, nearby longitudinal melt inclusions, and dislocations are the main elements of the real structure. The dislocation density gradually decreases from $N_d = (2–5) \times 10^5$ cm^{-2} to the minimum value, for example, to $N_d = 1 \times 10^4$ cm^{-2} at the chromium concentration of 6×10^{17} atoms/cm^3.

A decrease in the dislocation density N_d upon doping is associated with the formation of impurity atmospheres at dislocations, which hinder propagation and multiplication of dislocations upon cooling [2]. The formation of impurity atmospheres causes changes in the properties of a material, in particular, leads to an increase in its stability. Thus, the concentration dependence of the elastic modulus C_{44} for PbTe(Cr) showed a substantial increase in this property [15].

As the doping level was increased, small etch pits appeared on the surfaces of etched sections of the crystals belonging to region I (Fig. 2). Conceivably, this is evidence for an impurity inhomogeneity associated with the complex formation based on impurity atoms and intrinsic point defects.

An increase in N_d observed in region II (Fig. 2) results from the appearance of microprecipitates of dimensions $\sim 5 \times 50–5 \times 80$ μm enriched with a doping component and heterogeneously arranged on the section surfaces. For example, regions with grouped (Fig. 1g) or doubled (Fig. 1h) oriented platelet-like precipitates were observed in samples of PbTe(Cr). The oriented doubled platelet-like precipitates are more typical of PbTe(Co) and PbTe(Ni). The etched sections of

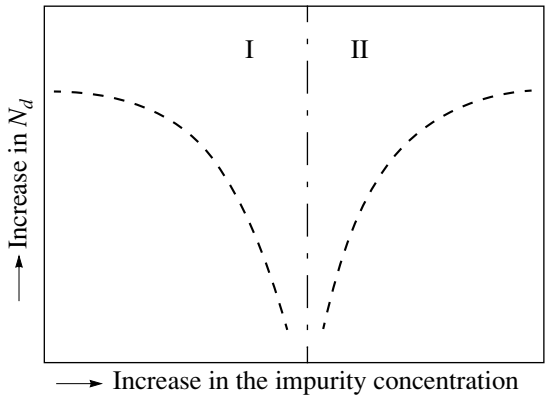

Fig. 2. Schematic representation of the qualitative characteristics of the real structure of doped PbTe crystals and dislocation density vs. the impurity concentration: region I corresponds to a decrease in N_d (low-angle boundaries); region II corresponds to an increase in N_d (impurity microprecipitates, cell structure, melt inclusions).

the crystals assigned to region II had smoother surfaces in the vicinity of the precipitates, due to the cleaning of the crystal matrix upon the coalescence of small precipitates into larger precipitates.

To estimate the influence of postcrystallization annealing on the real structure, crystals possessing different real structures were subjected to thermal treatment. Annealing led to changes in the surface compositions of the samples, the real structure of the crystal matrix, the concentration, and the type of charge carriers (Table 2). No substantial differences in the properties of the samples annealed at different temperatures were observed.

The surfaces and real structures of the samples assigned to region I underwent only slight changes upon annealing. Thus, annealing led to a slight increase in N_d (Table 2, samples 1 and 15) and the appearance of rare microprecipitates in the sample of PbTe(Cr) (sample 1). In the samples of PbTe(In), neither the surface nor crystal matrix contained impurity precipitates.

Much more substantial changes in the character of the surface and real structure were observed in the samples assigned to region II. Solidified drops of liquid enriched with Cr (according to Auger-electron spectroscopy) were observed on the surface of PbTe(Cr) (sample 2). Columnar microcrystals were produced on some drops through the vapor–liquid–crystal mechanism. In the crystals of PbTe(Cr), the density of dislocation etch pits decreased in the vicinity of microprecipitates. The surfaces of the PbTe(Co) and PbTe(Ni) crystals (samples 3–13) were subjected to gas etching. Impurity atoms were detected by Auger-electron spectroscopy at the edges and bottoms of pits. Small precipitates were grouped around larger precipitates in the bulk of the samples (N_d increases).

In all the samples under investigation, the concentrations of charge carriers changed. In the samples belonging to region II (Fig. 2), these changes are less pronounced. In sample 1, characterized by the lowest doping level, the concentration of holes increased, whereas the concentrations of electrons decreased in samples 14 and 15.

The crystals assigned to region II (Fig. 2) are characterized by a substantial supersaturation of the matrix with impurity atoms. In the PbTe(Cr) and PbTe(Co) samples, changes in the concentration of charge carriers were accompanied by a change in their type $n \longrightarrow p$.

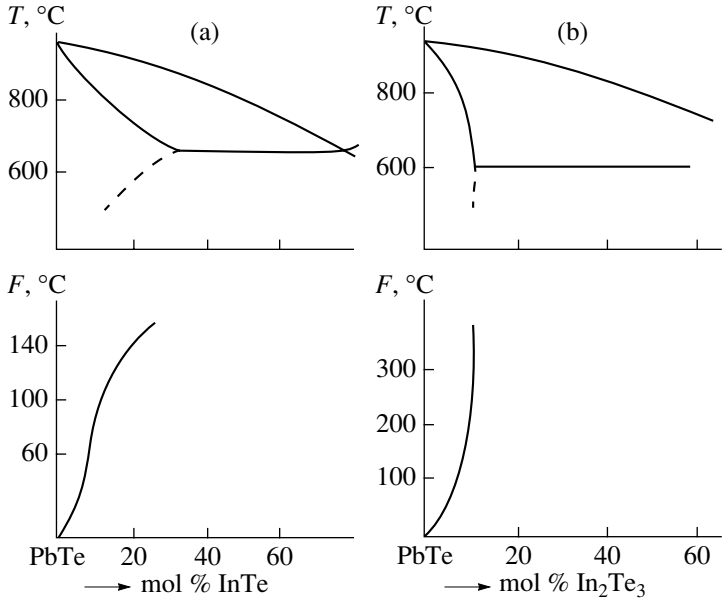

Fig. 3. Fragments of the *T*–*x* diagrams; (a) PbTe–InTe section and (b) PbTe–In_2Te_3 section of the Pb–In–Te ternary system and the calculated stability functions of the flat crystallization front of the PbTe-based solid solution.

Conceivably, this is associated with the formation of electrophysically neutral microprecipitates analogous to PbTe(Bi) [5], although the emergence of impurity atoms to the surface of the samples should also be taken into account. In the PbTe(Ni) samples, changes in the surface and real structure are analogous to those observed for PbTe(Cr) and PbTe(Co). However, not only a change in the sign of charge carriers, but also an increase in their concentration was found in samples 11–13 (Table 2). The difference in the behavior of chemically similar impurity atoms (Co and Ni) remains to be explained.

RESULTS AND DISCUSSION

The concentrations of the impurity atoms in the series of the crystals synthesized were varied from 10^{17} to 10^{21} atoms/cm^3. This range virtually overlaps the homogeneity range of the corresponding $Pb_{1-x}M_xTe$ solid solutions and gives rise to different states of the real structure (Fig. 2, regions I and II). The need to investigate a wide concentration range stems from the fact that doped PbTe crystals exhibit some properties only at high concentrations of impurity atoms, among which are the Fermi-level stabilization (In = 4×10^{19}–3×10^{20} atoms/cm^3) [9], the appearance of Shubnikov–de Haas oscillations with a high number of spin splitting (Cr > 10^{18} atoms/cm^3) [16], etc.

Retrograde solubility is non-typical of the *T*–*x* diagrams of PbTe-impurity telluride growth systems. The impurity inhomogeneities found in the crystals (microprecipitates, impurity atmospheres at dislocations) are, most likely, caused by nonequilibrium impurity trapping at the instant of crystallization. We did not obtain direct evidence for the mechanism of impurity trapping, except for the detection of a cell structure on the growth surface. The possibility of the cell formation in crystals at a particular concentration of impurity atoms in the melt was confirmed by the Tiller criterion (Fig. 3, Table 1). However, the calculations gave only an approximate estimate due to the lack of precise data on the positions of the solidus in the systems with Cr, Co, or Ni, the diffusion coefficients $D_{impurity}$ in the PbTe melt, and the temperature gradient in the crystals.

The reasons for the absence of cells in the bulk of the crystals, as opposed to their surface, remain unclear. It can be assumed that a high concentration of impurity atoms at the cell boundaries is diminished in the post-crystallization period at low growth rates.

Flux crystallization of $Pb_{1-x}In_xTe$ crystals with x = 0.5–0.6 gave rise to cell structures both on the growth surface and crystal sections, resulting in an increase in the concentration of melt inclusions, which were for the most part parrallel to the growth surface. In the $Pb_{1-x}Co_xTe$ and $Pb_{1-x}Ni_xTe$ crystals prepared by crystallization from flux with x = 0.2–0.4, the amounts of these inclusions were rather large. This fact can be considered as evidence for a dominant role of the diffusion layer in supersaturation and formation of the real structures of Co- or Ni-doped crystals.

At low doping levels, a different type of the real structure was observed (Fig. 2). This structure changed only slightly in the course of isothermal annealing (Table 2). Hence, the mechanism of impurity trapping described by the inequality $k_{surf} > k_{bulk}$ must not be ruled out.

It should be noted that the scheme shown in Fig. 2 is arbitrary. The overall sequence of the states of the real structure involved in this scheme was found upon doping of PbTe with transition metals Cr, Co, and Ni. These crystals are characterized by the narrow region I. Thus, the crystals contained impurity microprecipitates even at x_{melt} = 0.0025. By contrast, the $Pb_{1-x}In_xTe$ crystals are characterized by the broad region I. All the crystals synthesized in this study ($x \le 0.16$) contained no microprecipitates. However, a cell structure was found at $x \ge 0.03$. At $x \ge 0.15$, a high density of melt inclusions was observed.

To account for the observed differences, lets us analyze the *T*–*x* diagrams of growth systems involving transition metals and In. All diagrams have gently sloping liquidus curves. The *T*–*x* diagram of the PbTe–InTe system is characterized by a gently sloping solidus curve. The systems containing Cr, Co, or Ni are characterized by nearly vertical solidus lines. The coefficient k_{InTe} = 0.3, and it increases as the temperature decreases. For the systems containing Cr, Co, or Ni, the coefficient k, which was estimated from the data for the initial portions of the crystals [7, 8] as the ratio between the concentrations of the doping atoms in the crystal and melt, is much smaller than unity (0.1–0.3 for CrTe and smaller than 0.1 for CoTe, $CoTe_2$, Ni_3Te_2, and $NiTe_2$) and decreases with decreasing temperature. It can be assumed that the differences in the character of the temperature dependence of k and the value of the latter are responsible for different situations in the growth medium as the crystallization temperature is decreased. Thus, a decrease in k facilitates a rise of the impurity concentration in the diffusion layer and an increase in the degree of supersaturation in the crystal. By contrast, an increase in k gives rise to the opposite situation by decreasing the degree of impurity trapping.

The crystal matrix undergoes changes throughout the growth cycle. The results of annealing experiments gave an idea of the internal transformations occurring in the crystal. The characteristic feature of the annealing experiments is a change in the galvanomagnetic properties (see Table. 2). In all PbTe samples, except for those doped with Ni, the concentrations of electron carriers decreased, which is consistent with the results obtained for Ga-doped PbTe crystals [4]. Conceivably, a decrease in the amount of negatively charged impurity centers results from the formation of associates of impurity atoms involving, primarily, vacancies in the crystal matrix [2]. For example, taking into account the concentration dependence of the unit-cell parameter of

$Pb_{1-x}Bi_xTe$ and the results of Hall measurements for Bi-doped PbTe crystals, it was suggested that electroneutral complexes were formed [$Bi_2Te_3 + V_{Pb}^0$, where V_{Pb}^0 is a neutral lead vacancy in the lattice] [5]. Electron probe microanalysis also did not reveal any variations in the matrix composition. The investigation of such impurity inhomogeneities calls for other methods.

In the crystal lattice, impurity microprecipitates are electrically inactive and undergo changes in the course of annealing. In strongly doped annealed materials, impurity atoms tend to emerge from the bulk of the samples to the surface analogously to that described previously [4], and microprecipitates in the crystal matrix tend to be enlarged. In spite of the fact that the impurity contents in all the starting crystals were much smaller than the limiting solubility of an impurity component at the annealing temperature (as follows from the comparison of the data presented in Tables 1 and 2), no noticeable dissolution of microprecipitates was observed. Probably, there are kinetic factors hindering the disappearance of microprecipitates and equalization of the compositions of the sample, which appeared in the course of annealing. An increase in the dislocation density is apparently caused by the inhomogeneity of the composition.

According to the results of galvanomagnetic and X-ray diffraction studies, the Cr atoms in the PbTe crystal replace Pb atoms and create Cr_{Pb}^x defects [7]. The Co and Ni atoms in the +3 oxidation state presumably occupy interstitial positions [8].

In PbTe(Cr), the diffusion of Cr proceeds through Pb vacancies [7], whereas the impurity atoms in PbTe(Co) and PbTe(Ni) were assumed [8] to migrate through interstitial positions. The rate of migration of vacancies in the crystal is higher than that of interstitial atoms. Apparently, the difference in the rates is reflected in the degree of the completion of the exchange processes in the course of annealing, in particular, in the orientation, arrangement, and degree of segregation.

ACKNOWLEDGMENTS

This study was supported by the Russian Foundation for Basic Research, project no. 00-03-32388.

REFERENCES

1. V. I. Fistul', *Heavily Doped Semiconductors* (Nauka, Moscow, 1967; Plenum, New York, 1969).
2. M. G. Mil'vidskiĭ, *Semiconductor Materials in Modern Electronics* (Nauka, Moscow, 1986).
3. A. A. Chernov, in *Modern Crystallography*, Vol. 3: *Crystal Growth*, Ed. by B. K. Vainshtein, A. A. Chernov, and L. A. Shuvalov (Nauka, Moscow, 1980; Springer-Verlag, Berlin, 1984).
4. A. V. Novoselova, V. P. Zlomanov, A. M. Gas'kov, *et al.*, Vestn. Mosk. Univ., Ser. 2: Khim. **23** (1), 3 (1982).
5. M. Schenk, H. Bergen, C. Kleint, *et al.*, Phys. Status Solidi A **91,** K35 (1985).
6. P. V. Verteletskiĭ, T. A. Kuznetsova, V. P. Zlomanov, and O. I. Tananaeva, Élektron. Tekh., Ser. 6: Mater., No. 4 (241), 66 (1989).
7. P. V. Verteletskiĭ, V. P. Zlomanov, and O. I. Tananaeva, Neorg. Mater. **34** (4), 400 (1998).
8. T. A. Kuznetsova, V. P. Zlomanov, and O. I. Tananaeva, Neorg. Mater. **34** (9), 1055 (1998).
9. S. M. Kudryavtseva, T. A. Kuznetsova, V. P. Zlomanov, and O. I. Tananaeva, Neorg. Mater. **33** (3), 305 (1997).
10. E. I. Rogacheva, G. V. Gorne, and I. M. Panasenko, Izv. Akad. Nauk SSSR, Neorg. Mater. **15** (8), 1366 (1979).
11. E. I. Rogacheva, N. M. Panasenko, and P. P. Seregin, Izv. Akad. Nauk SSSR, Neorg. Mater. **16** (2), 265 (1980).
12. P. P. Fedorov, T. M. Turkina, V. A. Meleshina, and B. P. Sobolev, in *Crystal Growth* (Nauka, Moscow, 1988), Vol. 17, p. 198.
13. O. N. Krylyuk, A. M. Gas'kov, and V. P. Zlomanov, Vestn. Mosk. Univ., Ser. 2: Khim., No. 6, 571 (1986).
14. V. N. Vigdorovich, A. E. Vol'pyan, and G. M. Kurdyumov, *Oriented Crystallization and Physicochemical Analysis* (Khimiya, Moscow, 1976).
15. A. N. Vasil'ev, Yu. P. Gaĭdukov, V. P. Zlomanov, *et al.*, Izv. Akad. Nauk SSSR, Neorg. Mater. **24** (2), 227 (1988).
16. B. A. Akimov, V. P. Zlomanov, L. I. Ryabova, and D. R. Khokhlov, Vysokochist. Veshchestva, No. 6, 22 (1991).

Translated by T. Safonova

Crystallography Reports, Vol. 47, Suppl. 1, 2002, pp. S136–S148.

REAL STRUCTURE OF CRYSTALS. GROWTH OF FILMS. NANOCRYSTALS. TIP STRUCTURES

Perfection and Homogeneity of Space-Grown GaSb:Te Crystals

A. E. Voloshin*, T. Nishinaga, and P. Ge*****

** Shubnikov Institute of Crystallography, Russian Academy of Sciences, Leninskiĭ pr. 59, Moscow, 117333 Russia*

*** Department of Materials Science and Engineering, Faculty of Science and Technology, Meijo University, 1-501 Shiogamaguchi, Tenpaku-ku, Nagoya, 468-8502 Japan*

**** Institute of Physics, Chinese Academy of Sciences, Beijing, 100080 China*

e-mail: voloshin@ns.crys.ras.ru

Received April 1, 1999

Abstract—A Te-doped GaSb crystal grown by the method of directed crystallization under microgravitation has been studied by X-ray topography. It is shown that the structural perfection of the crystal part grown without contact with the ampule walls is substantially higher than the structural perfection of the crystals grown under terrestrial conditions. The distribution of a Te dopant in the crystal is studied by quantitative X-ray topography, and it is shown that, if the gap between the growing crystal and the ampule is small, the Marangoni convection in the melt can be less intense than the convection provided by residual microgravitation. The relation between the formation of a flat face on the crystallization front (faceting) and the formation of twins is also established.

INTRODUCTION

The advantages of crystal growth in space are associated with the fact that suppression of natural (thermogravitational) convection in weightlessness allows one to grow crystals without zonal inhomogeneity. Moreover, the reduced gravitation allows one to grow crystals without their contact with the container walls. Theoretically, this should considerably reduce the stresses in a growing crystal and, thus, also the dislocation density. However, the first experiments in space showed that the existence of a free melt surface can give rise to the so-called thermocapillary or Marangoni convection provided by the surface-tension gradient under the conditions of a temperature gradient. At a high intensity of the convective Marangoni flow, the process becomes unstable, which results in striation in the growing crystal. Therefore, all the attempts to grow dislocation-free crystals in the presence of a free melt surface have resulted in the formation of pronounced zonal inhomogeneity [1].

Below, we describe the study of a Te-doped GaSb single crystal grown under microgravitation aboard a Chinese spacecraft in 1992. The experiment was aimed at growth of a dislocation-free homogeneous crystal and the study of the characteristics of the dopant (Te) distribution in space-grown crystals. The details of growth of a GaSb:Te crystal by the method of cooling in the presence of a temperature gradient were considered earlier [2, 3]. The preliminary studies by the methods of chemical etching and photoluminescence [4, 5] showed that this crystal had rather high structural perfection: it had a large region with a small dislocation density and no striation, whereas the profile of the axial distribution of tellurium was close to diffuse, which indicated either a very low level of convection in the melt or even its complete absence.

We aimed to study in more detail this crystal and the specific features of the defect formation and dopant distribution by highly sensitive X-ray diffraction methods (single- and double-crystal X-ray topography) in order to establish their relation to the growth conditions. The space experiment considered below is one of a few experiments in which low dislocation density was combined with the absence of zonal inhomogeneity. In this connection, it was also of interest to establish the working growth mechanisms and their influence on the structure perfection.

EXPERIMENTAL

The starting material for the space experiment was a cylindrical sample (6 mm in diameter and 30 mm in length) cut from a GaSb crystal grown by the Czochralski method under the terrestrial conditions. The average Te concentration in the sample was 10^{18} cm^{-3}. The growth along the [111]*B* direction was performed in a sealed quartz ampule in the furnace with the temperature gradient. An unmelted region of the initial crystal of about 5 mm in length served as a seed.

The space-grown crystal is shown in Fig. 1. It is clearly seen that, at the first stage, growth proceeded without any contact of the crystal with the ampule walls, because the diameter of this part of the crystal

was less then the seed's diameter. The longitudinal section of the crystal made along the ingot axis parallel to the (110) plane was studied by the method of single-crystal projection and quantitative double-crystal X-ray topography.

Projection single-crystal X-ray topographs (Mo$K_{\alpha 1}$ radiation) were obtained in the reflection from the {220} planes on KhimFoto P-50 plates with 50-μm-thick emulsion used in nuclear research. Because of considerable sample thickness (1.5 mm) and strong absorption of the X-ray radiation in GaSb, the topographs had Borrmann-type contrast.

Double-crystal plane-wave X-ray topographs in the Bragg reflection geometry were obtained with the use of Cu$K_{\alpha 1}$ radiation, (440) GaSb reflection, and GaSb monochromator (440 reflection) with asymmetry coefficient of $b = 30$. Topographs were taken at the large-angle slope of the reflection curve at an intensity level of up to 50% of the peak value. The angular position of the sample during the experiment was stabilized with the aid of a special electronic system with an accuracy of ±1% of the halfwidth of the reflection curve. Topographs were recorded on the special X-ray-sensitive KhimFoto UVS-5 film coated with 10-μm-thick emulsion. For further processing, all the X-ray images were input into a computer with the aid of a CCD chamber via an optical microscope with a magnification of ×20.

To establish the quantitative variations in the lattice parameter of the sample, we obtained a pair of topographs at the azimuthal positions of the sample 0° and 180°. Upon image processing on a computer, the distribution of the lattice-parameter variations was obtained in the form of a map by a method described elsewhere [6–8].

EXPERIMENTAL RESULTS

Single-crystal X-ray topography. Three X-ray topographs of the sample obtained at different directions of the diffraction vector are shown in Fig. 2. The sample consisted of two parts separated by the twin boundary *T*. The (110) surface and the $(10\bar{1})$ plane were shared by both parts of the crystal, which provided a simultaneous record of both crystal parts in the $(20\bar{2})$ reflection (Fig. 2a). The topographs recorded in other {220}-type reflections showed either the upper or the lower parts of the crystal, because the (101)-type and $(1\bar{1}0)$-type planes are differently oriented in the parts of the crystals on different sides of the twin boundary. Therefore, the images in Figs. 2b and 2c are composed of topographs obtained for each part of the crystal separately.

The lower part of the crystal consists of the seed (*S*) and the portion of the crystal having a free surface during growth (I in Fig. 2). In the seeding part of the sample, which is part of the initial crystal grown under terrestrial conditions, one can clearly see striation *s* and the glide bands characteristic of Czochralski-grown crystals, whose dislocation density was evaluated as ~10^4 cm^{-2}. The large number of these dislocations is inherited by the crystal, however, after passing a distance of 1 to 2 mm; they outcrop on the side surface of the crystal so that only a few of these dislocations

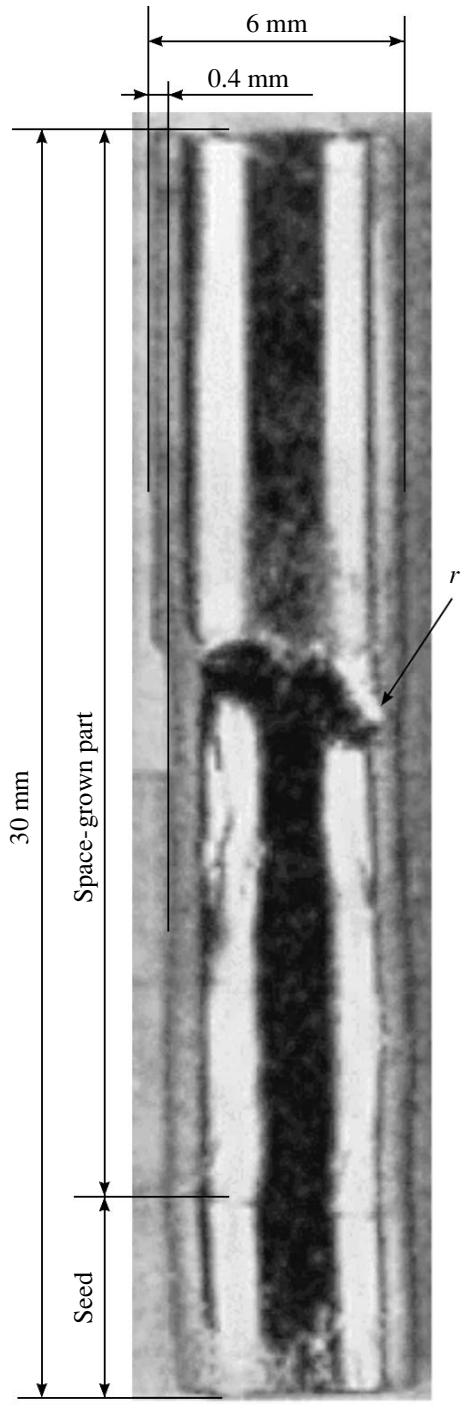

Fig. 1. Tellurium-doped GaSb crystal grown under the conditions of microgravitation (general view).

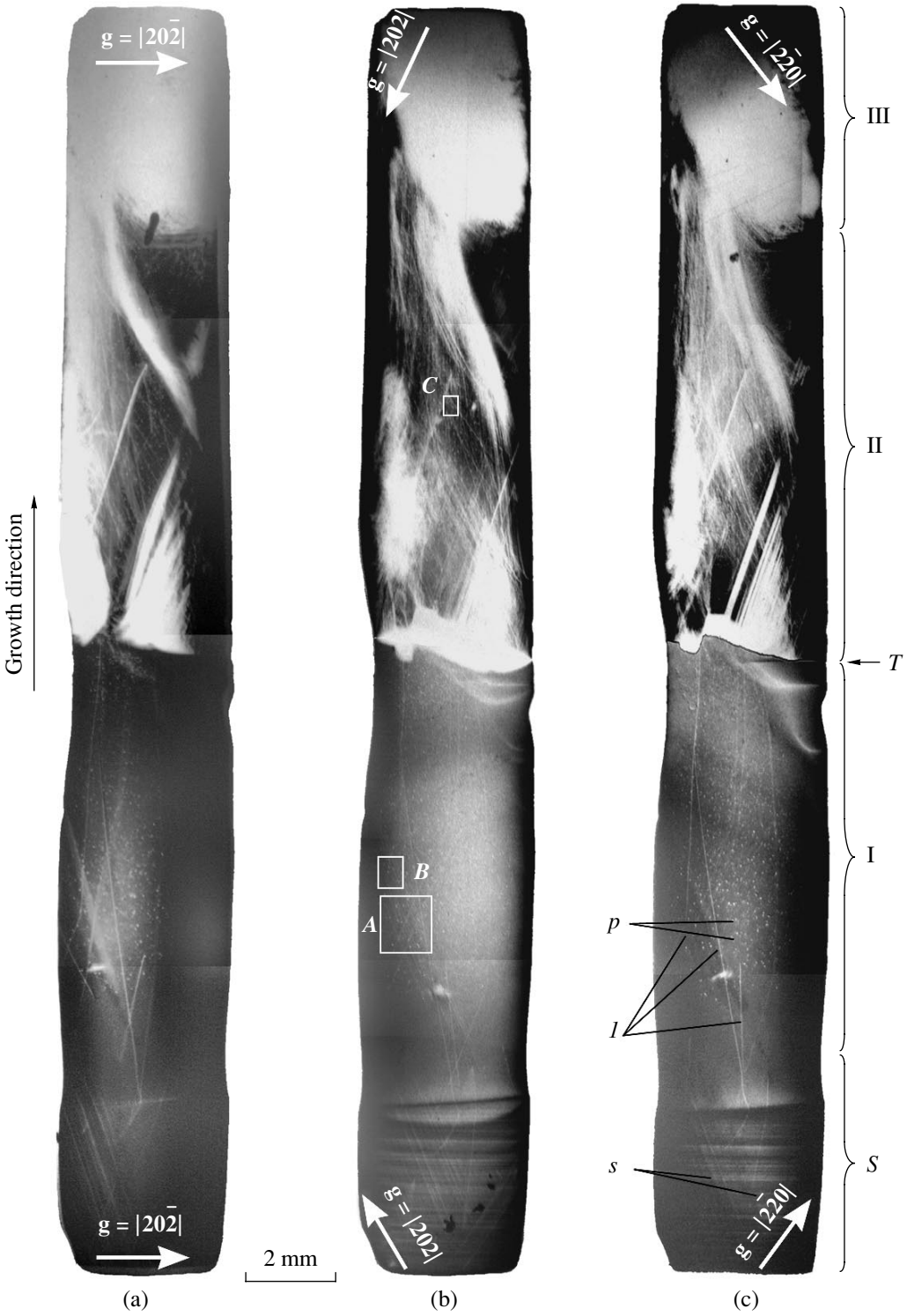

Fig. 2. Single-crystal projection X-ray topographs of a GaSb:Te crystal obtained in the (a) $20\bar{2}$, (b) 202, and (c) $2\bar{2}0$ reflections.

(*1* in Fig. 2) grow for a considerable distance into the crystal.

Thus, part I is the most perfect part of the crystal, because it has no striation, whereas dislocation density in this part does not exceed ~10^2 cm^{-2}. At the same time, the topograph of this part shows bright spots (*p*), which are images of defects whose nature is considered below. The average dimension of these images is about 50 μm and their concentration equals ~4 × 10^4 cm^{-3}.

The formation of these spots can be explained in two ways. First, they can be the images of dislocations normal (or almost normal) to the entrance surface of the sample. Second, they can be images of large microdefects. The nature of these images can be interpreted in accordance with the rules of projection geometry by comparing the images on the topographs obtained in different reflections. The mutual arrangement of the images of the objects equidistant from the entrance surface of the sample is the same irrespective of the diffraction vector, and, on the contrary, it varies with the change of the direction of the diffraction vector if defects are located at different depths of the crystal. Thus, the arrangement of the images of the points of the dislocation outcrop onto the crystal surface is the same on different topographs but is different for microdefects located in the crystal bulk.

Figures 3a–3c show two topographs of the same region of the crystal shown in the rectangle *A* (Fig. 2) obtained in different reflections and also the topograph obtained by the subtraction of the computer images. One can see that of the nine enumerated images in Figs. 3a and 3b, only the images of point *1* coincide. Therefore, Fig. 3c has no image of this point. The images of other defects could not be brought into coincidence, and, therefore, Fig. 3c for each of these defects shows a pair of images, with the bright image corresponding to Fig. 3a, and the dark one, to Fig. 3b. It is seen that the dark images are displaced with respect to the bright ones for different distances along different directions. This signifies that all the defects are located at different distances from the exit surface of the sample. In other words, taking into account the above, one can state that here we deal with microdefects.

Analyzing the image contrast, we see that the change in the location of the dark and the bright contrast does not follow the change in direction of the diffraction vector (Figs. 3a and 3b). This signifies that these microdefects induce spherically nonsymmetric strain fields and that their structures are rather complicated. They can include dislocation loops, or microtwins, or both these defects. Some of these defects generate dislocations, as seen in Fig. 3d.

The nature of these defects is still unclear. Similar defects were also observed in Te-doped InSb crystals [9]. The electron microscopy study provided the establishment of the inclusion composition which corresponded to the compounds formed in the In–Sb–Te system; around the inclusions, dislocation loops were formed.

A twin observed in the middle part of the crystal resulted in a dramatic increase in the number of dislocations: above the twin boundary, their density in part II ranged from $\sim 10^3$ cm^{-2} in region *L* (Fig. 2c) to $\sim 10^4$–10^5 cm^{-2} in region *H*. One can also see microdefects (Fig. 3e) similar to those observed in part I.

In part III, the dislocation density attains a value of $\sim 10^6$ cm^{-2}. These dislocations were formed at the concluding stage of crystallization when the sample was under pronounced pressure because of its contact with the ampule walls.

Double-crystal X-ray topography. A double-crystal plane-wave topograph of the sample is shown in Fig. 4a. Figure 4b shows the map of the lattice-parameter variation in part I of the sample, and Fig. 4c, the computer-assembled map of the lattice-parameter distributions and the single-crystal topograph of part I.

Unlike single-crystal topographs obtained in the transmission geometry, the double-crystal topographs were obtained in the reflection geometry. Therefore, double-crystal topographs show no images of dislocations or any other defects distributed over the crystal bulk. However, because of the high sensitivity of the plane-wave topography to lattice distortions, the topographs in Fig. 4a show weak deformations not seen in Fig. 2. In the upper part of the sample in Fig. 4a, the images of some regions are absent because of the pronounced misorientations of the lattice due to the presence of a large number of dislocations.

As seen from Fig. 4b, the sample is characterized by obvious, although smoothly distributed, nonuniformity in the lattice-parameter distribution mainly along the radial direction (the more intense green color corresponds to an increase in the lattice parameter, whereas the violet color, to its decrease). Considering the right-hand side of the sample in Figs. 4a and 4b, one can see in the vicinity of the twin boundary three regions *1*, *2*, and *3* separated by rectilinear boundaries. They are separated from the remaining part of the crystal by a broad light band. The lattice parameters in these regions differ only slightly, but they are pronouncedly different from the lattice parameters in the other regions of the crystal.

Because of rather high dopant concentration in the sample, it is expedient to assume that the nonuniformity observed in the lattice parameters is associated with the inhomogeneous Te distribution. To verify this assumption, we compared our results with the data on Te concentration determined by the photoluminescence method [5].

Figures 5a and 5b show the results of the measurements made in [5] and the variations in the lattice parameter along the same lines denoted as *a–a*, *b–b*, and *c–c* in Fig. 4b. The plots shown in Figs. 5a and 5b are very similar; however, to be able to compare them quantitatively, one has to reduce them to the same scale, because Fig. 5b shows the variations in the lattice parameter (i.e., the deviations of the lattice parameter from its value averaged over the sample), whereas Fig. 5a shows the logarithms of the absolute Te concentrations.

Thus, we recalculated the plots shown in Fig. 5a into the variations in the Te concentration on the linear scale. The variations in the lattice parameters shown in

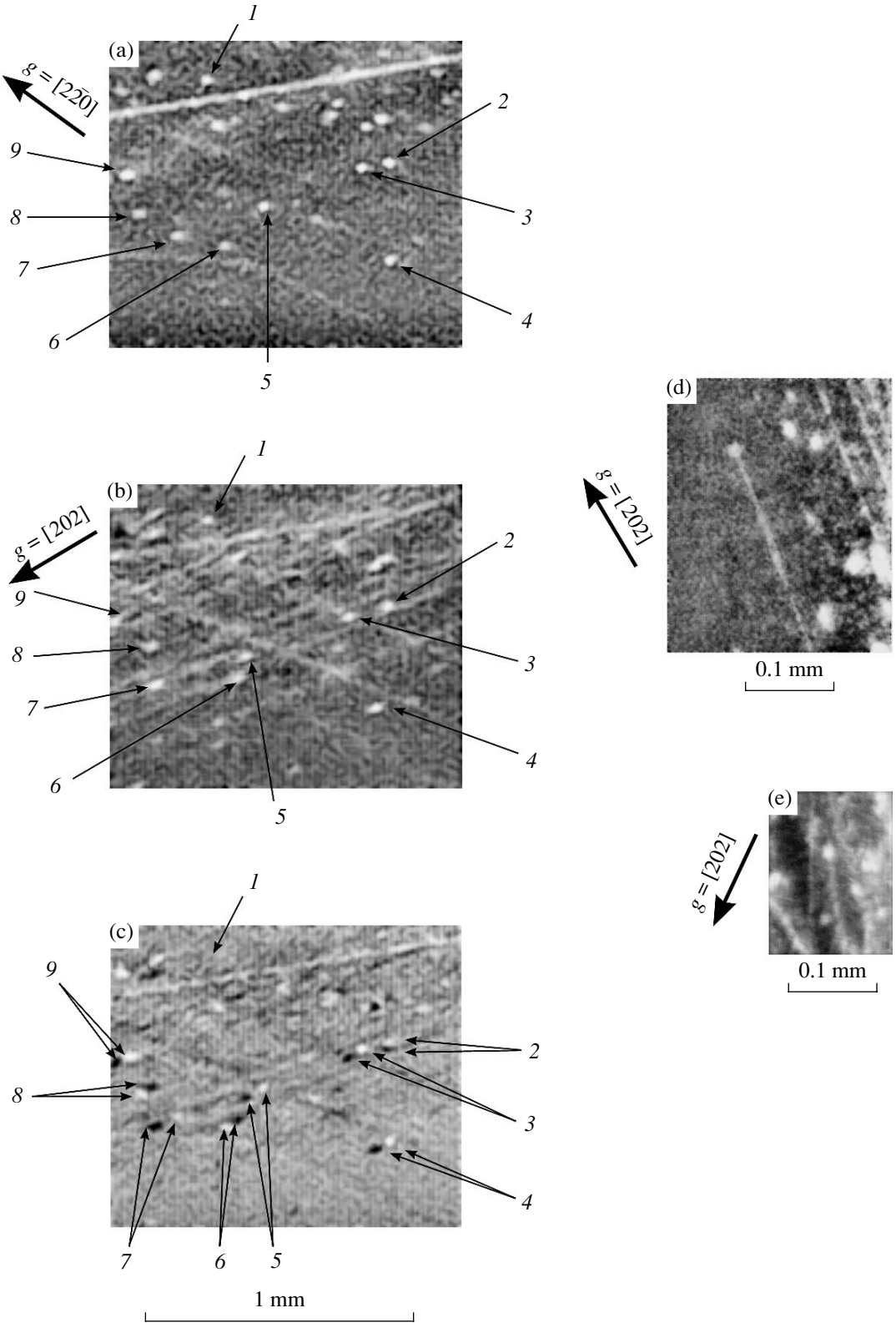

Fig. 3. Images of microdefects in a GaSb:Te crystal obtained in the (a) $2\bar{2}0$ and (b) 202 reflections, (c) the difference of the images (a) and (b) of the portion *A* in Fig. 2b, (d) the image of the portion *B* shown in Fig. 2b in the 202 reflection, (e) the image of the portion *C* shown in Fig. 2b in the 202 reflection, (*1–9*) images of microdefects.

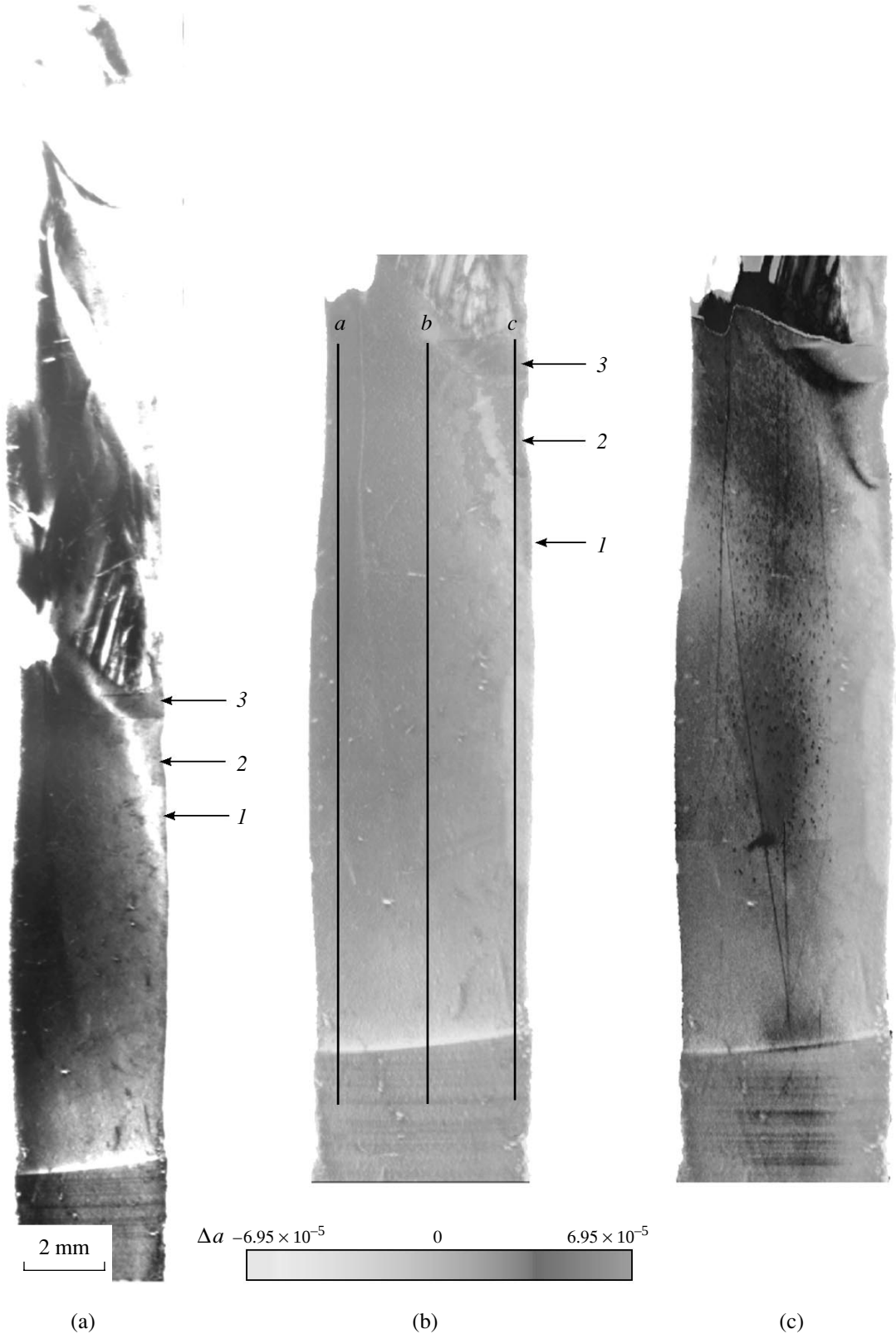

Fig. 4. (a) Plane-wave X-ray topograph of a GaSb:Te crystal obtained in the 220 reflection and (b) the map of the lattice-parameter variations for region I (Fig. 2) and (c) its matching with the projection topograph $g = [2\bar{2}0]$.

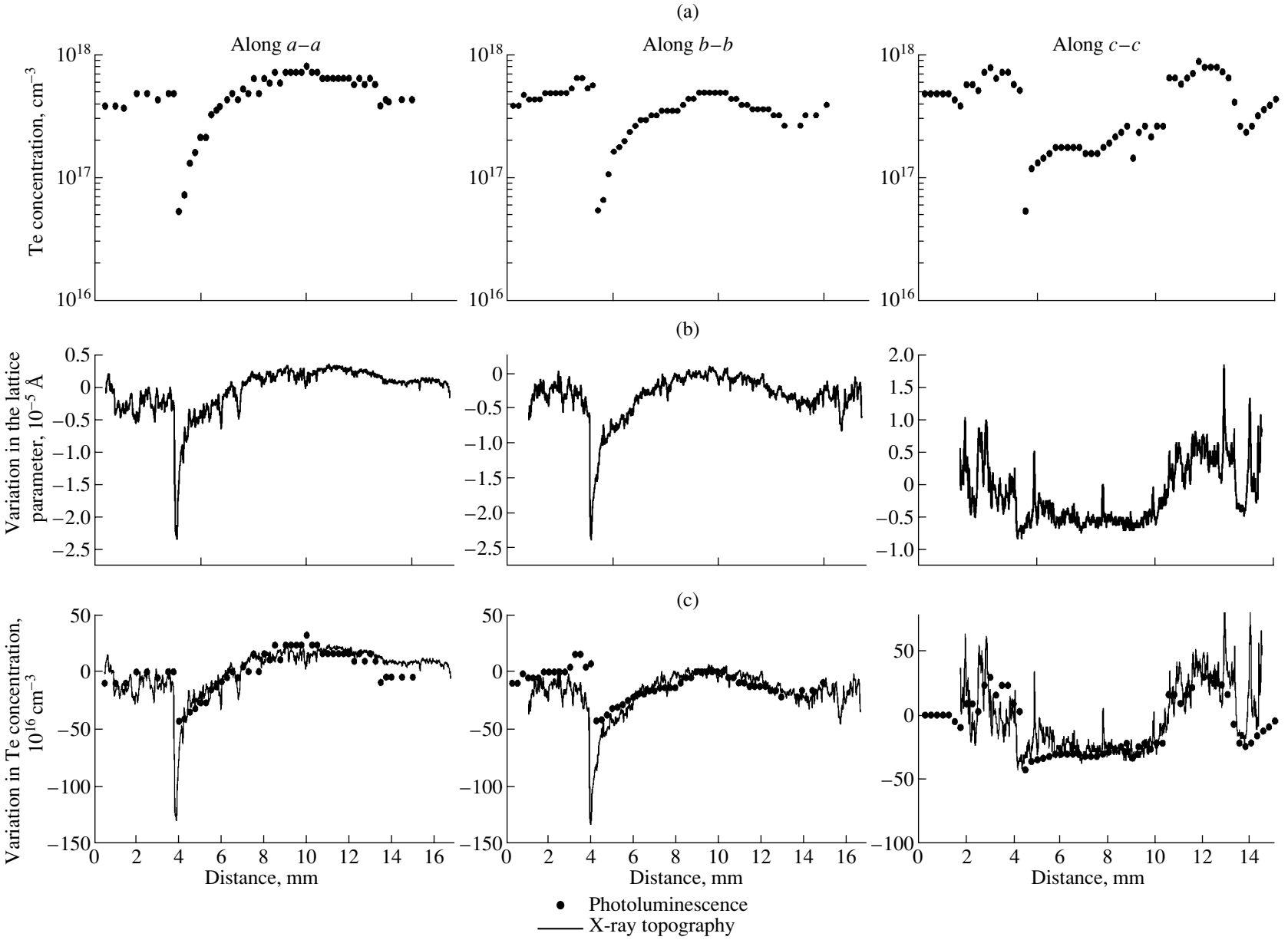

Fig. 5. Tellurium distribution in a GaSb crystal along the *a–a*, *b–b*, and *c–c* lines (Fig. 4b). (a) Te concentration measured by the method of spatially resolved photoluminescence method [4], (b) variations in the lattice parameter measured by the method of quantitative plane-wave topography, and (c) variations in the Te concentration recalculated from the concentrations given in (a) and (b).

Fig. 5b were recalculated into the variations of concentration by the formula

$$\Delta C(x) = s\alpha\Delta a(x), \quad (1)$$

where ΔC is the deviation of the Te concentration at the point x from its average value, s is the dimensional factor, α is the deformation coefficient of the GaSb lattice associated with the incorporation of Te atoms, and Δa is the change in the lattice parameter. One can obtain the approximate α value using the covalent radii of Ga, Sb, and Te under the assumption that Vegard's law is valid. However, a more rigorous evaluation of α can be made on the basis of the measured dependence of the GaSb lattice parameter as a function of Te concentration. Such measurements were made in [10], and the quantity $s\alpha$ was calculated from these data as 6.8×10^{22} Å^{-1} cm^{-3} with the Te concentration being of the order of 10^{18} cm^{-3}.

The luminescence data [5] and the recalculated lattice-parameter data reduced to the same scale are shown in Fig. 5c. One can see that these data are in good accord. Thus, we can justly state that all the changes in the lattice parameter in the sample are caused mainly by the inhomogeneous distribution of tellurium. Thus, the map in Fig. 4b showing the distribution of the lattice parameter can also be considered as the map of Te distribution, where the more intense green color indicates higher Te content.

Thus, Fig. 4b shows that the Te distribution in the sample is rather inhomogeneous, especially along the radial direction. Moreover, regions *1*, *2*, and *3* are enriched with Te. The latter fact explains the concentration maximum of Te on the curves measured along the *c*–*c* line located between 10 and 14 mm (Fig. 5).

Despite the fact that the Te distribution observed is characterized by a rather smooth concentration distribution (i.e., the deformation gradient is rather small), this results in the formation of certain elastic stresses in addition to the thermal ones. This, in turn, increases the intensity of the defect formation in the region with an elevated Te concentration (Fig. 4c).

DISCUSSION OF RESULTS

However, the inhomogeneous distribution of Te in the sample shows no striation, which indicates that crystal growth from melt was accompanied by the steady-state laminar convective flow [11]. At the same time, the profile of the axial distribution of Te indicates that the mass transfer in the melt occurred mainly in the diffusion mode [5], which, in turn, shows that the flow was rather weak. It could be caused by thermogravitational convection due to the residual microgravitation or by the thermocapillary Marangoni convection.

According to the widespread opinion that, under microgravitation conditions, the buoyancy-driven convection (convection due to the Archimedean force) is completely suppressed, so that in systems with a free surface, the Marangoni convection is prevalent with its intensity being the higher, the more pronounced the temperature change along the free surface of the melt. Sharing this standpoint and taking into account the above statement on a weak convective flow, we came to the conclusion that, in our case, the melt had a small portion of a free surface.

At the same time, it was shown [12] that even a rather low level of the residual gravitation could give rise to noticeable inhomogeneity of the crystal. Therefore, we took this factor into account and tried to estimate the effect of both types of convection on the Te distribution in the sample.

Inhomogeneity. Since crystal growth proceeded inside the ampule, in order to determine the zone of the free surface of the crystal, we had to consider the mutual arrangement of the ampule walls, the melt surface, and the crystal.

The free surface of a liquid drop under microgravitation conditions tends to acquire spherical shape. Therefore, if the diameter of this sphere exceeds the diameter of the ampule, as was the case in our experiment, then a considerable part of the melt filling the vessel would unavoidably acquire its shape. In this case, only a small part of its surface remains in the vicinity of the crystallization front—a meniscus.

In the process of crystal growth, the meniscus moves together with the crystallization front. This model was first suggested in [13, 14] and was discussed later (mainly the origin of the meniscus) in [15–17].

The height of the meniscus (Fig. 6) depends on its shape, the crystal–container distance d, the angle α of wetting the container wall with the melt, and the growth angle $\varepsilon = \varphi - \theta$ (where θ is the angle formed by the surface of the crystallization front and the side surface of the crystal and φ is the angle formed by the meniscus surface and the crystallization front). Point O is the point of the intersection of the three-phase line with the drawing plane. The angles α and ε and other parameters for GaSb are shown in the table.

The upper part of the crystal grew, being in the contact with the ampule walls; therefore, its diameter exceeds the diameter of the middle part of the crystal which grew without contact with the wall (Fig. 1). Thus, the gap between the surface of part I of the crystal and the ampule wall can be estimated as the distance between the side surfaces of the upper and the central parts of the sample. This estimate yields the values $d = 0.4$ and $d < 0.1$ mm on the left and the right, respectively. Approximating the generatrix of the meniscus surface by an arc of the circumference, we can estimate the height of the meniscus H by the formula

$$H = d\frac{\sin\alpha + \cos\varphi}{\cos\alpha + \sin\varphi}. \quad (2)$$

For growth of a crystal with constant diameter ($\theta = 90°$,

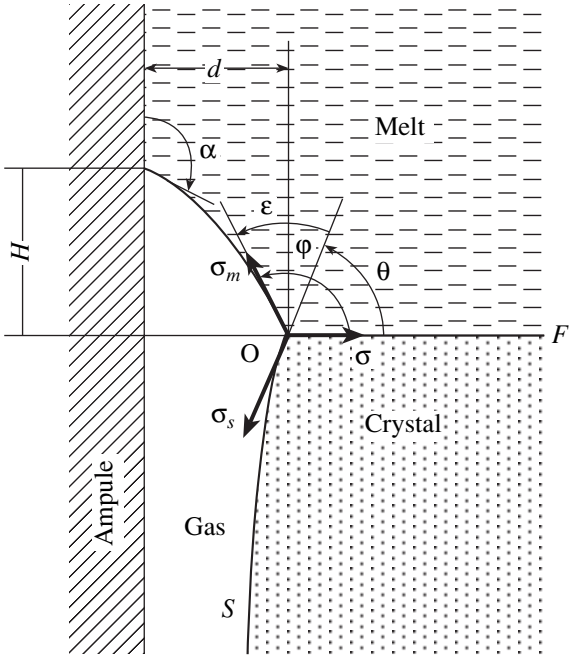

Fig. 6. Geometry of the interfaces in the vicinity of the growth front of the crystal grown without contact with the ampule walls.

$\varphi = 90° + \varepsilon$), we have

$$H = d\tan\frac{\alpha - \varepsilon}{2}. \quad (3)$$

At $\alpha = 121°$ and $\varepsilon = 15°$ (table), we obtain $H = 0.53$ mm for the left-hand side of the crystal and $H < 0.13$ mm for the right-hand side.

The temperature gradient along the meniscus surface gives rise to variations in the surface tension along its surface, which, in turn, gives rise to the Marangoni convection. The heat and mass transfer in which the melt flow is caused by the force acting only on some parts of the surface was used in [13, 14] to interpret the Te distribution in a space-grown InSb crystal. The experimental conditions taken into account in the calculations for the InSb crystal were as follows: crystal diameter 13 mm, axial temperature gradient 10 K/cm, and meniscus height $H = 2.5$ mm. As a result of the numerical solution of the Navier–Stokes equation, it was established that the convective flow propagated to the ampule center and occupied the region located at a distance from the crystallization front ranging from 3 to 4 H. The vortex center was spaced by 0.6 H from the crystallization front, and the maximum velocity of the melt flow was 2 mm/s, which provided the complete stirring in the liquid phase.

The physical properties of GaSb and InSb are rather close to the estimated ones and can be considered equivalent in calculations. The general scheme of the experiment performed in [9, 13, 14] is also similar to that used in our experiment, and therefore, we can attempt to compare the velocity of the Marangoni convection in our experiment on GaSb with the velocity calculated for InSb in [13, 14].

The Marangoni number (Ma) relating the driving forces of the thermocapillary convection and thermal conductivity can be written for our problem in the form [23]

$$\mathrm{Ma} = \frac{\partial\sigma_m}{\partial T}\frac{\Delta T H}{\rho\nu\lambda} = \frac{\partial\sigma_m}{\partial T}\frac{\partial T}{\partial z}\frac{H^2}{\rho\nu\lambda}, \quad (4)$$

where σ_m is the surface tension of the melt at the melt–gas interface, ρ is the melt density, λ is the thermal diffusivity, and ν is the kinematic viscosity. In our experiment, the axial temperature gradient $\frac{\partial T}{\partial z}$ and the meniscus height H were two and five times less than in [13], respectively, and, therefore, the Marangoni number in our case was about 50 times lower than in [13, 14]. The velocities of the convective flows, V_M, should be approximately in the same proportion, and thus, we obtained $V_M \approx 0.04$ mm/s for our case. This estimate is

Growth parameters for GaSb

Parameter	Notation	Value	Reference
Growth angle	ε	10°	[18]
		15°	[19]
Contact angle of the melt with the SiO_2 crucible	α	121°	[20]
Surface tension at the melt–gas interface at 725°C	σ_m	454 mN/m	[21]
Specific surface energy of the crystal–gas interface	σ_s		
Specific surface energy of the melt–crystal interface	σ	~150 mN/m	Estimated from the average atomic number
Temperature dependence of σ_m	$\partial\sigma_m/\partial T$	0.11 mN/mK	[21]
Melt density at 712	ρ	6.05×10^3 kg/m^3	[22]
and 1000°C		5.87×10^3 kg/m^3	
Volume thermal expansion coefficient of the melt	β	~1.0×10^{-4} K^{-1}	Estimated from [22]

made without taking into account the difference in the crystal diameters, and, therefore, the value thus obtained can change multiply; however, we assume that the above estimate is correct by an order of magnitude.

Since, in our case, the Marangoni convection is rather weak, it is possible that the contribution of the thermogravitational convection to the mass and heat transfer are pronounced and should be taken into account. The velocity of the thermogravitational convection can be estimated using the equation [23]

$$V_b = \sqrt{\beta g \Delta T L}, \quad (5)$$

where β is the volume thermal expansion coefficient of the melt, g is the acceleration of freefall, and L is the characteristic length. The velocity of this convective flow is essentially dependent on the orientation of the residual-gravitation vector. In the most unfavorable case, where this vector is normal to the crystallization front and directed from the crystal to the melt, we have $L = 25$ mm (the maximum height of the melt column) and $V_b = 0.13$ mm/s.

Thus, in our case, the flows of the thermocapillary and natural convections are comparable, with the latter being even more pronounced. At the same time, the traditional Bond number (the ratio of the Rayleigh number to the Marangoni number, Bo = Ra/Ma) taken from [23] acquires the form

$$\mathrm{Bo} = \frac{g\rho\beta L^2}{\partial\sigma_m/\partial T} \quad (6)$$

and, at $L = 25$ mm, has, in our case, the value $\mathrm{Bo} = 1.8 \times 10^{-3}$. This signifies that the Marangoni convection should be more intense by several orders of magnitude than the convection provided by the Archimedean force, which is inconsistent with the above estimates. This contradiction can readily be eliminated by an appropriate choice of the characteristic dimensions. In our growth experiment, the driving force of the thermogravitational convection is determined by the height of the melt column, whereas the driving force of the Marangoni convection is concentrated only at the meniscus surface. Therefore, for our case (and also for any other system with a limited free surface of the melt), the Marangoni number should be used in form (4), whereas the Rayleigh number in the form [23]

$$\mathrm{Ra} = \frac{g\beta\Delta T L^3}{\nu\lambda} = \frac{\partial T}{\partial z}\frac{g\beta L^4}{\nu\lambda}, \quad (7)$$

where L is the height of the melt column. Then,

$$\mathrm{Bo} = \frac{\rho g\beta L^4}{(\partial\sigma_m/\partial T)H^2}, \quad (8)$$

which, at $L = 25$ mm and $H = 0.53$ mm, yields Bo = 3.7. This value is consistent with the relation between the above estimates of V_M and V_b.

The above consideration shows that, at a sufficiently small surface of the meniscus, the Marangoni convection can be reduced to the level of the natural convection caused by the residual microgravitation. In our case, the resulting flow was also rather weak, which explains the above features of the radial and axial Te distributions. It can readily be seen from (8) that, in our case, the condition Bo > 1 is fulfilled at $H < 1$ mm, i.e., at such a height of the meniscus, the Marangoni convection is weaker than the thermogravitational convection. To preserve this relationship with a decrease in residual gravitation g, one has to decrease H proportionally to $\sqrt{g}$.

Faceting. Crystal regions *1*, *2*, and *3* in Fig. 4a demonstrate faceting in the right-hand part of the crystallization front. The face could be formed because of the following reasons. As seen from Figs. 2a and 4a, 4c, the boundary between the seed and the part of the crystal grown in space is slightly concave and is not normal to the growth direction. This indicates asymmetry of the thermal flow in the growth system. This face could be formed at the periphery of the concave growth front under a low axial temperature gradient. Its dimension D is described by the formula [24]

$$D = \frac{\Delta T}{\Sigma\cos\psi}, \qquad \Sigma = \left(\chi_s\frac{\partial T_s}{\partial z} + \chi_m\frac{\partial T_m}{\partial z}\right)/(\chi_s + \chi_m), \quad (9)$$

where ΔT is the supercooling at the crystallization front such that the faceted part of the front moves with a velocity equal to the growth rate of the unfaceted interface, ψ is the angle formed between the inclined isotherm at the interface periphery and the growth direction, Σ is the generalized axial temperature gradient at the interface, and χ_s and χ_m are thermal conductivities of the crystal and melt, respectively. It is seen from Fig. 4a that the crystallization front on the left was almost normal to the growth axis, whereas on the right, it was not, which provided the formation of a flat face on its surface. In the crystal–melt system, most of the heat from the crystallization front is removed via the crystal bulk. The rate of this removal was higher at the initial stage of growth and gradually decreased with the growth of the crystal. As a result, the temperature gradient at the interface decreased with time, thus increasing the probability of the face formation. At a certain moment, a flat portion of the (111) face was formed at the periphery of the crystallization front, whereas region *1* (Fig. 4a) was formed because of its propagation with the further growth of the crystal. With an increase in crystal length, the axial temperature gradient decreased with the simultaneous increase of the face dimensions, in accordance with Eq. (9) (regions *2* and *3* in Fig. 4a are wider than region *1*).

The supercooling ΔT necessary for growth of a smooth flat face with dislocation sources of steps,

which grows only due to two-dimensional nucleation, is considerably more pronounced than supercooling necessary for the propagation of a rough surface. Thus, growth of a rough surface in Si occurs under supercooling of about ~0.05 K, whereas growth of the flat (111)Si surface can occur under the supercooling of $\Delta T \geq 3.7$ K. With a decrease in the heat removal ΔT from the face with an increase in crystal length, the face growth decelerates, because it cannot grow at the rate of the rough interface. As a result, ΔT can decrease to a certain critical value necessary for two-dimensional nucleation. In this situation, the growth rate of a flat face drops practically to zero, and, therefore, the face dimensions increase. The "location" of such decelerations during the face propagation are indicated by the formation of flat boundaries (a kind of striation) between regions *1*, *2*, and *3* (Fig. 4a).

It is well known that the capture of impurities is more intense on flat surfaces than on rough ones. Thus, the coefficient of impurity distribution under the conditions of faceted growth is two to eight times higher than for normal growth [25]. This explains the increase in the Te concentration in the right-hand part of the crystal in the range between 10–14 mm (Fig. 5, along the *c*–*c* line).

Twinning. Twinning considerably deteriorates the crystal quality; therefore, measures should be taken to avoid twin formation. The twin boundary originating in the region of faceted growth is seen on both single- and double-crystal topographs (Fig. 7). We consider the mechanism of twin formation based on the Voronkov model [26–28], in which the evolution of the crystal shape and the formation of faces at the crystallization front and the side surface of the crystal are described in terms of the equilibrium processes occurring in the vicinity of the crystal–melt–gas interface.

In the isotropic approximation, the angles θ and φ (Fig. 6) are related as [26]

$$\cos\theta = \frac{\sigma + \sigma_m \cos\varphi}{\sigma_s}, \tag{10}$$

where σ and σ_s are the specific surface energy of the crystal–melt and crystal–gas interfaces, respectively. The above equation is valid under conditions close to equilibrium, i.e., if growth steps are absorbed by the three-phase interface *O*. Then the equilibrium growth angle is

$$\varepsilon_e = \arccos\left(\frac{\sigma_m^2 + \sigma_s^2 - \sigma^2 - \gamma_e^2}{2\sigma_m\sigma_s}\right), \qquad \gamma_e = -\sigma_m \sin\varphi + \sqrt{\sigma_s^2 - (\sigma - \sigma_m\cos\varphi)^2}, \tag{11}$$

where γ_e is the change in the total free surface energy of the system during the propagation of the crystal–melt interface *F* for a distance equal to growth-step height *h*.

As follows from Eq. (10), during growth of a crystal with a constant diameter ($\theta = 90°$), the angle φ depends on the ratio of the specific free surface energies of the melt (σ_m) and the crystal–melt interface σ,

$$\varphi = \arccos\left(-\frac{\sigma}{\sigma_m}\right). \tag{12}$$

The σ_m value for GaSb is given in the table; however, we failed to find a reliable σ value in the published data. Therefore, we made an attempt to estimate this value proceeding from the well-known fact that, for the diamond-like semiconductors, the σ and σ_s values depend on the average atomic number of the compound and obey a linear relationship [25]. Using the values $\sigma = 300$ mN/m for Si [27] and $\sigma = 200$ mN/m for Ge [29], we determined the σ-value for GaSb by the extrapolation method as $\sigma \approx 150$ mN/m. At this σ value, Eq. (12) yields $\varphi = 109°$ and, thus, the equilibrium growth angle for GaSb is $\varepsilon_e = 19°$, which is close to the experimental value of ε [18] (see table). This proves the validity of the Voronkov theory and shows its applicability to the analysis of the mechanism of the twin-boundary formation in our crystal.

As was indicated above, a twin was formed at the faceted portion of the growth front characterized by considerable supercooling under growth conditions far from equilibrium. In this case, Eq. (11) is invalid and should be corrected by introducing the term dependent on the growth rate of the face, *V*, and supercooling on it, ΔT, [28]

$$\varepsilon = \varepsilon_e - KV^{-1/3}\Delta T, \tag{13}$$

where *K* is the material constant. The introduced correction can have a considerable value. For the faceted growth of silicon by the Czochralski technique, it is about 20°; then, the growth angle $\varepsilon < 0$ [28]. This signifies that if a face is formed on the crystallization front, the crystal diameter increases considerably faster than in the case of the normal growth of a rough face under the condition that the meniscus shape is the same in both cases. In turn, this results in the formation of the characteristic ledges on the side surfaces of the crystal, where the region of the faceted growth front is in contact with the three-phase line. One such ledge is seen in Fig. 1.

The change in the crystal shape (local decrease and increase in its diameter) can result in the formation of inclined {111} faces on its side surface. If the crystal grows along the [111] direction, six inclined planes of the {111}-type are formed, with three of them being inclined at an angle of 70.5° and three other planes, at 109.5° to the growing (111) face (the angles were measured along the positive direction of measuring the angle θ, as shown in Fig. 6). Thus, if the value of angle θ is close to one of the above values, then the corresponding {111}-type face can be formed on the side surface of the crystal. It was shown [26, 28] that the formation of an inclined face forming an angle of 70.5°

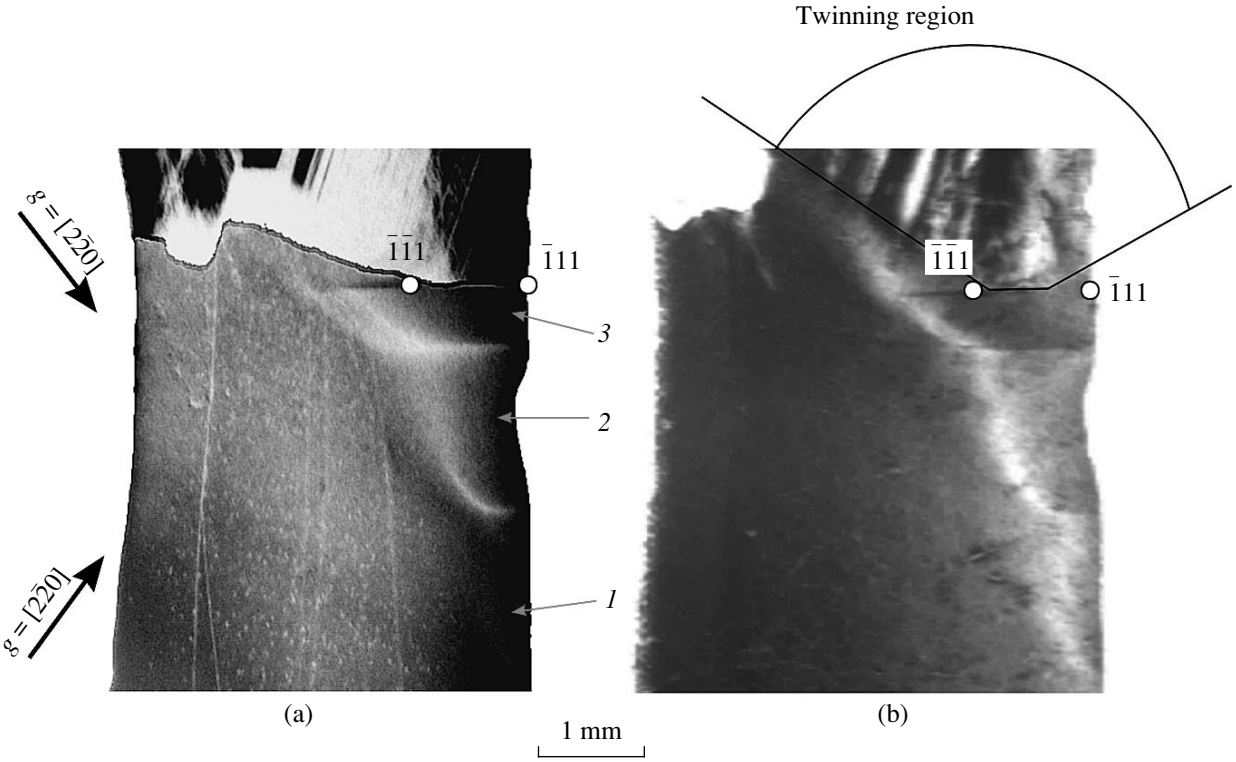

Fig. 7. The neighborhood of a twin in a GaSb crystal and the projections of the points at which the three-phase line is tangential to the $(\bar{1}\bar{1}1)$ and $(\bar{1}11)$ planes inclined to the face by angles of 109.5° and 70.5°, respectively. (a) Single-crystal projection X-ray topograph obtained in the $2\bar{2}0$ reflection and (b) double-crystal plane-wave topograph obtained in the 220 reflection.

with the (111) plane of the crystallization front is energetically favorable. If the angle φ is sufficiently large (for Si, φ > 70°), then it is more favorable for a crystal to form such a face than to have any other form of the side surface; in this case, the larger the φ angle, the more pronounced the gain in the energy associated with the formation of the face inclined at an angle of 70.5°. On the other hand, the formation of the face inclined at an angle of 109.5° is the least favorable, because it results in a dramatic increase of the free surface energy of the system. However, a decrease in the surface energy is provided by the formation of a twin at the point of the three-phase line where it is tangential to the {111} plane inclined at an angle of 109.5° [26]. If angle θ at this point is close to 109.5°, then during the formation of a twin with the twinning plane (111), its side face will be inclined by an angle of 70.5°, which would reduce the free surface energy of the system. The probability of formation of a twin increases with an increase in φ and θ: the closer the angle θ to 109.5°, the more pronounced the energy gain due to the twin formation.

As follows from Eq. (13), the formation of a face at the crystallization front increases the probability of twin formation. Faceting is accompanied by the change in crystal shape: if the periphery of the crystallization front has a face, the growth angle ε is smaller (because of a more pronounced supercooling), and angle θ is larger than in the absence of such a face. As a result, a crystal of constant diameter forms a face at the crystal–melt interface.

It should be indicated that the initial point of twin formation lies at the upper boundary of region *3* (Fig. 7). Based on Eq. (13), this can be explained as follows.

At the pronounced deceleration of the face (see section *Faceting*), whose growth provides the formation of region *3* (Fig. 7), *V* drops almost to zero, whereas ΔT remains quite high. Then, in accordance with Eq. (13), angle ε dramatically decreases, whereas angle θ increases, which explains the fact that the nucleation of a twin is the most probable during considerable deceleration of the face.

The mechanism of twin formation suggested above is confirmed by our observations. In the vicinity of the faceted portion of the crystallization front, there are two inclined {111}-type planes tangential to the three-phase line at the points whose projections are shown in Fig. 7. The $(\bar{1}\bar{1}1)$ plane is inclined to the (111) face at an angle of 109.5°, whereas the $(\bar{1}11)$ plane, at an angle of 70.5°. The twin starts growing when the face nearly ceases to move and its dimension increases to such an extent that its boundary becomes tangential to

the $(\bar{1}\bar{1}1)$ plane. At the same time, the formation of a twin changes the inclination angle of the $(\bar{1}11)$ plane from 70.5° to 109.5°. Therefore, the twin is nucleated in the vicinity of the tangential point and first occupies only a part of the face, whereas a small region of the initial crystal around the tangential point is still preserved for some time. Thus, twinning results in the formation of the energetically favorable configuration of the side surface of the crystal. In further growth, the twin propagates and, finally, occupies the whole section of the crystal.

CONCLUSIONS

The perfection of a Te-doped GaSb crystal grown under microgravitation has been studied by the method of X-ray topography. It is shown that a part of the ingot grown without contact with the ampule walls is characterized by a high degree of perfection: in this part no striation is observed and the dislocation density is lower by two to three orders of magnitude than in the crystals grown under terrestrial conditions. The use of quantitative X-ray topography provided the establishment of a number of important features in the formation of structural and compositional inhomogeneity of a space-grown GaSb:Te crystal. The relationship between the growth conditions, defect formation (faceting, twinning), and the Te distribution in the crystal is established. It is shown that at a sufficiently small height of the meniscus, the level of the Marangoni convection can be made lower than the level of the natural convection provided by residual microgravitation. Under these conditions, the crystal can grow without contact with the ampule walls mainly due to diffusion mass transfer. Faceting and twinning are interpreted based on theoretical models; it is also revealed that face growth promotes twinning.

ACKNOWLEDGMENTS

The authors are grateful to A.A. Chernov for discussion of the results. The study was supported by the Institute of Space and Aeronautical Sciences, Japan, and the Japan Space Forum.

REFERENCES

1. R. J. Naumann, in *Material Sciences in Space* (Springer-Verlag, Berlin, 1986; Mir, Moscow, 1989).
2. P. Ge, T. Nishinaga, C. Huo, *et al.*, Microgravity Q. **3**, 161 (1993).
3. P. Ge, T. Nishinaga, C. Huo, *et al.*, in *Proceedings of the 46th International Astronautical Congress, Oslo, Norway, 1995*, p. IAF-955-J.2.05.
4. T. Nishinaga, P. Ge, C. Huo, *et al.*, J. Cryst. Growth **174**, 96 (1997).
5. T. Nakamura, T. Nishinaga, P. Ge, *et al.*, J. Cryst. Growth **211**, 441 (2000).
6. J. Hartwig and V. Lerche, Phys. Status Solidi A **109**, 79 (1988).
7. A. E. Voloshin and I. L. Smolsky, Phys. Status Solidi B **192**, 73 (1996).
8. I. L. Smolsky, A. E. Voloshin, N. P. Zaitseva, *et al.*, Philos. Trans. R. Soc. London, Ser. A **357**, 2631 (1999).
9. V. S. Zemskov, M. R. Raukhman, I. V. Barmin, *et al.*, *Doped Semiconductor Materials* (Nauka, Moscow, 1985), p. 132.
10. V. T. Bublik and K. D. Shcherbachev, Kristallografiya **40**, 122 (1995) [Crystallogr. Rep. **40**, 110 (1995)].
11. R. A. Brown, in *Material Sciences in Space* (Springer-Verlag, Berlin, 1986; Mir, Moscow, 1989).
12. D. C. Gillies, S. L. Lehoczky, F. R. Szofan, *et al.*, J. Cryst. Growth **174**, 101 (1997).
13. I. V. Barmin, V. S. Zemskov, M. R. Raukhman, *et al.*, *Hydromechanics and Heat-and-Mass Transfer in Space* (Nauka, Moscow, 1982), p. 209.
14. V. S. Zemskov, M. R. Raukhman, I. V. Barmin, *et al.*, Fiz. Khim. Obrab. Mater., No. 5, 56 (1983).
15. W. R. Wilcox and L. L. Regel, Microgravity Sci. Technol. **8**, 56 (1995).
16. T. Duffar, I. Paret-Harter, and P. Dussere, J. Cryst. Growth **100**, 171 (1990).
17. T. Duffar, P. Boiton, P. Dussere, and J. Abadie, J. Cryst. Growth **179**, 397 (1997).
18. T. Duffar, P. Dussere, and J. Abadie, Adv. Space Res. **16**, 199 (1995).
19. I. Harter, T. Duffar, and P. Dussere, in *Proceedings of the 7th European Symposium on Materials and Fluid Sciences in Microgravity, Oxford, 1989* (European Space Agency, Paris, 1989), ESA SP-295, p. 69.
20. I. Harter, P. Dussere, T. Duffar, *et al.*, J. Cryst. Growth **131**, 157 (1993).
21. M. Ya. Dashevskiĭ, G. V. Kukuladze, V. B. Lazarev, and M. S. Mirgalovskaya, Izv. Akad. Nauk SSSR, Neorg. Mater. **3**, 1561 (1967).
22. Yu. G. Poltavtsev, *Structure of Semiconductor Melts* (Metallurgiya, Moscow, 1984).
23. S. Ostrach, in *Materials Sciences in Space with Application to Space Processing* (Princeton Univ. Press, Princeton, 1977; Mir, Moscow, 1989), Vol. 52.
24. A. A. Chernov, E. I. Givargizov, *et al.*, in *Modern Crystallography*, Vol. 3: *Crystal Growth*, Ed. by B. K. Vainshtein, A. A. Chernov, and L. A. Shuvalov (Nauka, Moscow, 1980; Springer-Verlag, Berlin, 1984).
25. S. S. Gorelik and M. Ya. Dashevskiĭ, *Materials Science of Semiconductors and Dielectrics* (Metallurgiya, Moscow, 1988), p. 576.
26. V. V. Voronkov, Kristallografiya **19**, 922 (1974) [Sov. Phys. Crystallogr. **19**, 573 (1974)].
27. V. V. Voronkov, Kristallografiya **17**, 909 (1972) [Sov. Phys. Crystallogr. **17**, 807 (1972)].
28. V. V. Voronkov, Kristallografiya **23**, 249 (1978) [Sov. Phys. Crystallogr. **23**, 137 (1978)].

Translated by L. Man

Crystallography Reports, Vol. 47, Suppl. 1, 2002, pp. S149–S158.

REAL STRUCTURE OF CRYSTALS. GROWTH OF FILMS. NANOCRYSTALS. TIP STRUCTURES

Atomic Force Microscopy Study of Lysozyme Crystallization

I. V. Yaminsky, N. V. Gvozdev, M. I. Sil'nikova, and L. N. Rashkovich

Physics Faculty, Moscow State University, Vorob'evy gory, 119992 Moscow

e-mail: yaminsky@nanoscopy.org

Received October 3, 2002

Abstract—Crystallization of lysozyme from solutions has been studied by the atomic force microscopy method. The surface morphology and the growth kinetics of several faces of the orthorhombic and monoclinic modifications of lysozyme crystals are considered. The surface images are obtained at molecular resolution. For the (010) face of orthorhombic lysozyme, the phenomenon of the surface reconstruction is established—doubling of the unit-cell parameter along the *a*-axis. The main growth parameters of lysozyme are determined—the kink density at steps, probabilities of the attachment and detachment of building blocks, the kink and step velocities, and the dependence of the fluctuation in the step position on time. © *2002 MAIK "Nauka/Interperiodica"*.

INTRODUCTION

Lysozyme is a protein with a well-known primary structure. It is a comparatively small protein with a molecular mass of about 14000; it consists of 129 amino acid residues forming one polypeptide chain. Tetragonal lysozyme has three water molecules per each amino acid, whereas two other lysozyme modifications have two water molecules per amino acid. A lysozyme molecule in solutions has an almost ellipsoidal shape with dimensions of $2.8 \times 3.2 \times 3.0$ nm [1] and a volume of 2.7×10^{-20} cm^3.

Lysozyme has six crystalline modifications—tetragonal, orthorhombic, monoclinic, trigonal, triclinic, and hexagonal. Crystallographic data for the first three modifications are listed in Table 1. The volume of a lysozyme molecule in an orthorhombic crystal equals 6×10^{-20} cm^3 and, in a monoclinic crystal, 10.7×10^{-20} cm^3. Two projections of an orthorhombic lysozyme structure, which includes about 40% of the solvent (the *ac*-projection and the *ac*-projection constructed in this study by the data of [4]) are shown in Fig. 1.

The tetragonal modification is studied in detail by the atomic force microscopy (AFM) method. The first attempt to study growth of tetragonal lysozyme by AFM was made by Durbin and Carlson [5], who observed the macrostep motion and two-dimensional nucleation on the crystal surface. Radmacher *et al.* used AFM to study adsorption of lysozyme molecules on mica; they also determined Young's modulus for a monomolecular layer (0.5 ± 0.2 GPa) [6]. Konnert *et al.* [7] and Kuznetsov *et al.* [8] managed to attain molecular resolution at the crystal surface. The growth mechanisms of tetragonal lysozyme crystals were also established by AFM [7, 9–11]. The defect formation at the surface of a growing lysozyme crystal was studied in [9, 12–14]. The building blocks of a tetragonal lysozyme crystal were considered by Wiechmann *et al.* [15], who also established that a kink at a step whose rise is equal to one unit-cell parameter (the unit cell containing four molecules) can travel for a distance of 90 nm for 0.08 s, which corresponds to the incorporation into the step of ten tetramers. They also assumed that such a fast tetramer incorporation is possible only if lysozyme molecules form aggregates in the solution which, later, are incorporated as a whole into the kink. Nevertheless, Wiechmann *et al.* [15] did not exclude possible incorporation of monomers and not aggregates into the kink, because, within the measurement time (0.08 s), individual molecules could also quickly fill the kink.

Table 1. Crystallographic data for lysozyme crystals

Symmetry	Sp. gr.	Unit-cell parameters	*Z*	Reference
Tetragonal	$P4_32_12$	$a = b = 78.73$ Å, $c = 38.56$ Å	8	[2]
Orthorhombic	$P2_12_12_1$	$a = 56.51$ Å, $b = 73.62$ Å, $c = 30.51$ Å	4	[2]
Monoclinic	$P2_1$	$a = 28.0$ Å, $b = 62.5$ Å, $c = 60.9$ Å, $\beta = 90.8°$	4	[3]

1063-7745/02/47S1-S0149$22.00 © 2002 MAIK "Nauka/Interperiodica"

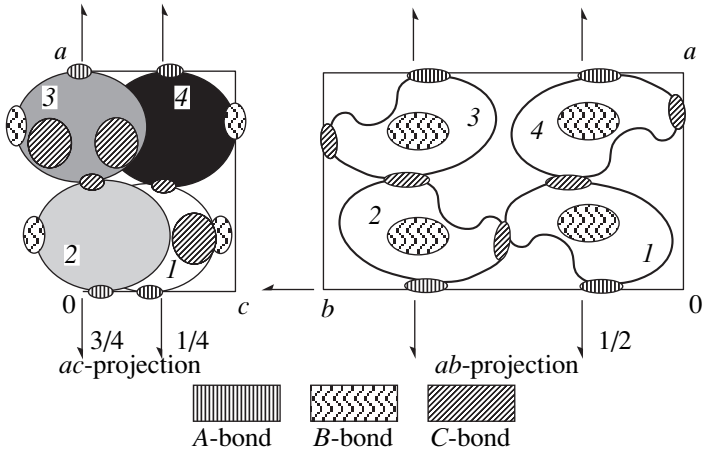

Fig. 1. Molecular packing in an orthorhombic lysozyme crystal. Schematic depiction of the unit cell with macrobonds. On the left, projection in the *ac* plane; on the right, projection in the *ab* plane. For a clearer representation, the molecules are numbered (from *1* to *4*).

Unlike previous works, we studied crystallization of orthorhombic and monoclinic lysozyme modifications. The point is that the formation of several lysozyme modifications under almost equivalent conditions and close temperatures is still unclear. One of the possible explanations for this fact is the formation in the solution of clusters with different dimensions and structures. Upon determination of the size of the kinks attaching building blocks, and, moreover, upon observing these building blocks in an atomic force microscope, one can attempt to verify the above hypothesis. Although we failed to answer this question unambiguously, we managed to reveal a number of other interesting phenomena.

STARTING MATERIALS AND METHODS

The working solutions for the synthesis of orthorhombic and monoclinic lysozyme crystals (5 wt % lysozyme, 5 wt % NaCl, pH 4.6, corrected with the aid of HCl or NaOH and 1 wt % lysozyme, 2 wt % $NaNO_3$ in 50 mM solution of an acetate buffer with pH 4.6, respectively) were prepared from sixfold recrystallized lysozyme (Seikagaku Corp., Japan). We used distilled water with a resistivity of 16 MΩ cm.

Orthorhombic crystals were obtained by the method of spontaneous crystallization as follows. Disklike glass substrates with a diameter of 1 cm and a thickness of 0.5 mm used in the AFM studies were placed into solution thermostated at $t = 40°C$. The substrates were suspended vertically to decrease nucleation. Then the solution temperature was slowly lowered (to avoid mass crystallization) to 35°C. Several hours later, the first crystals appeared on the disks (from several crystals to several dozens of crystals), whose dimensions ranged from dozens of microns to one to two millimeters. In some instances, prior to the formation of the orthorhombic phase, the working solution became turbid because of the formation of a large number of unidentified needlelike crystals. This effect was described in detail elsewhere [16].

Monoclinic lysozyme crystals were obtained in a similar way at room temperature. Later, we also grew lysozyme crystals by the sitting-drop method. With this aim we placed glass substrates on a support into a thermostated vessel in the horizontal position, poured the precipitant into the bottom of the vessel, and applied a droplet of the working solution to the upper surface of each substrate. This method provides growth of large higher quality crystals on the substrates. This method also considerably simplifies the transfer of crystals on the substrates into the growth cell of an atomic force microscope.

During the experiment, supersaturation s was varied by changing the solution temperature, $s = \exp(\Delta\mu/k_BT) - 1 = C/C_0 - 1$, where C and C_0 are the real and equilibrium solution concentrations, k_B is the Boltzmann constant, and $\Delta\mu$ is the chemical potential. The solubility data $C_0(T)$ for orthorhombic and tetragonal crystals in the solutions of the composition used in our experiments within a wide temperature range were taken from [17] and are presented in Fig. 2. As far as we know, there are no data on solubility of monoclinic lysozyme. Since the growth rate of lysozyme in our experiments was rather low, the solution concentration was assumed to be constant, and supersaturation could be varied by changing C_0. To determine the concentration, we took a 100-μl sample from the growth cell and diluted it in 10 ml of 5-wt % NaCl solution. The concentration was determined with the aid of the calibration curve by measuring the optical density of the solution at a wavelength of 281 nm.

The surface morphology of the crystals was studied in a liquid cell of a Nanoscope-3 atomic force microscope in the contact mode. The test measurements in the tapping mode yielded images of much worse quality.

The typical scanning frequency (512 lines) was 10 Hz. When scanning the sample, we maintained the minimum possible tip-sample force to avoid sample destruction. We used commercial Nanoprobe cantilevers (Si_3N_4 tips; mechanical rigidity of the cantilever 0.06–0.38 N/m; gold coated reflecting cantilever surface) and MikroMasch CSC12 cantilevers (Si tips, mechanical rigidity of the cantilever 0.03–0.08 N/m, aluminum coated reflecting cantilever surface). The images obtained with the use of different tips were of the same high quality. Gold-coated cantilevers provided a more pronounced total signal (more reflected light), whereas the aluminum-coated cantilevers provided a higher temperature stability because of a lower thermal bending of the two-layer cantilever.

The data obtained were processed with the use of specialized Femtoscan software (Center of Advanced Technologies, Moscow, Russia).

SURFACE STRUCTURE AT MOLECULAR RESOLUTION

The high-resolution surface image of the (010) face of an orthorhombic lysozyme crystal is shown in Fig. 3. The image is quite typical. To each protrusion, there corresponds one unit cell containing four lysozyme molecules. For this face, two molecules are located on the surface, and two other molecules are located under the former two. The cantilever tip of an atomic force microscope passes around two lysozyme molecules on the surface shown in Fig. 3. Therefore, the image shows not the individual molecules but the protrusions corresponding to these two molecules. The unit-cell dimensions practically coincide with the dimensions obtained by the X-ray diffraction method. It is rather difficult to compare quantitatively the unit-cell dimensions obtained by these two methods because, strictly speaking, a Nanoscope-3 microscope is not a metrological instrument and the accuracy of the corresponding measurements limited by the temperature-induced mechanical drift, nonlinearity, hysteresis, and creep of the ceramic is at a level of 10%.

The image in Fig. 3 was obtained at the minimum possible tip–sample force that can be achieved in a Nanoscope-3 microscope. The estimated value of this force was about 10^{-10} N. The quality images were obtained with the use of both rigid and soft cantilevers, which has a simple explanation. Rigid cantilevers are shorter than soft ones and, therefore, provide a more pronounced deviation of the light beam, which, in the final analysis, can result in a more "delicate" scanning by a cantilever over the surface profile.

Only in some instances did we manage to attain the molecular resolution and obtain the images of individual molecules. We believe that here the main part is played by the cantilever quality, so that only the finest cantilevers can provide the resolution of individual protein molecules.

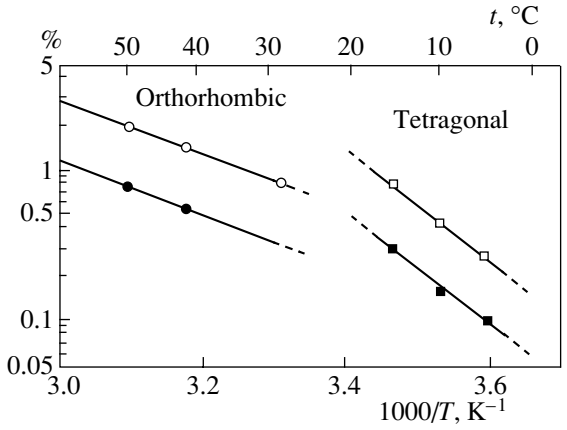

Fig. 2. Solubilities of two crystalline lysozyme modifications as functions of temperature (at pH 4.6). The NaCl content: 3 wt % (light symbols) and 5 wt % (dark symbols).

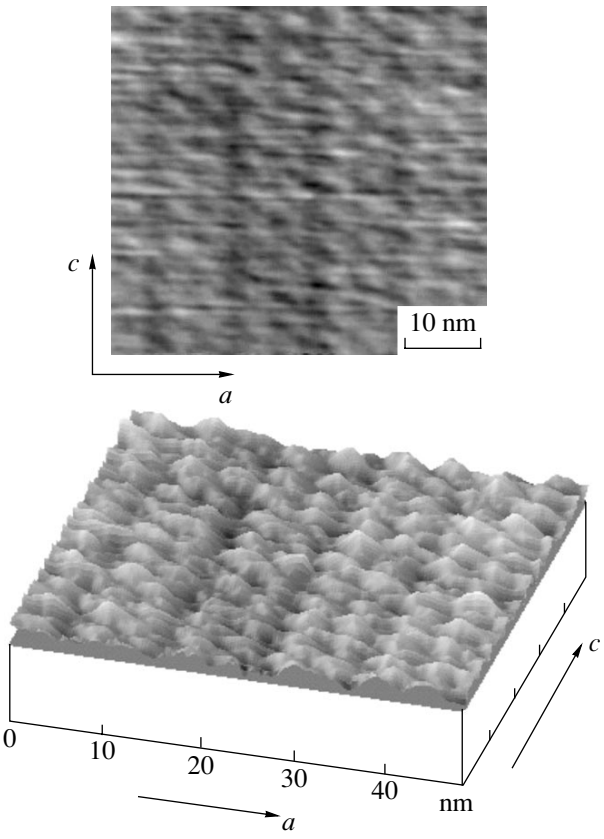

Fig. 3. Doubling of the parameter along the *a* axis on the (010) face of an orthorhombic lysozyme crystal. The original AFM image and its 3D reconstruction.

Doubling of the lattice parameter along the a-axis. If one slightly increases the tip–sample force a during scanning, an interesting phenomenon is observed. The neighboring rows of unit cells oriented along the *c*-axis are seen in the images as protrusions of different heights; the high rows alternate with the low rows. This phenomenon can be interpreted as doubling of the unit-

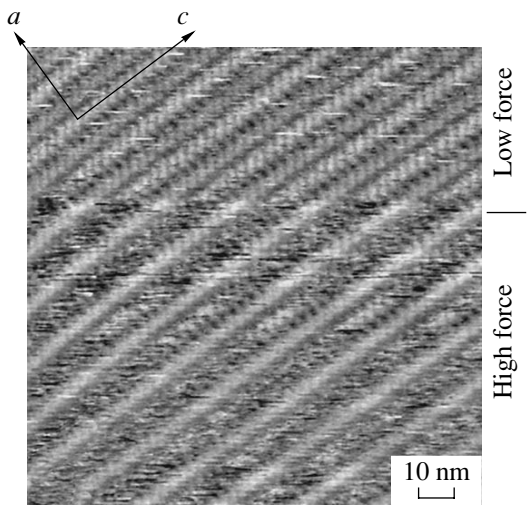

Fig. 4. The image of the regions of the (010) face of an orthorhombic lysozyme crystal at a molecular resolution obtained at different tip–sample forces.

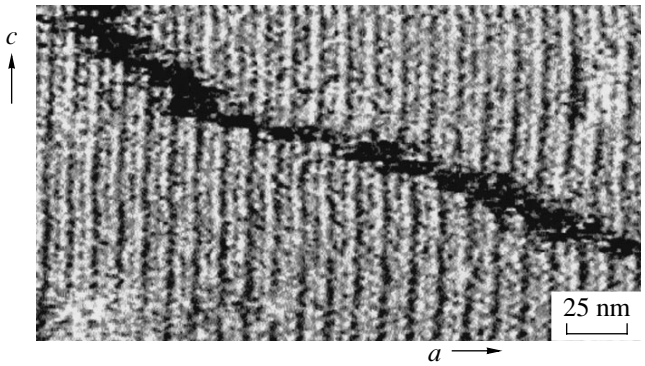

Fig. 5. Image of the region of the (010) face of an orthorhombic lysozyme crystal. The shift of the unit cell in the neighboring growth layers by a half-period. The *b* axis is normal to the drawing plane.

cell parameter along the *a* axis on the surface of the (010) face. Figure 4 shows a surface region at different values of the force applied to the cantilever at a high resolution. This force varied in the process of scanning (in the upward direction). One can clearly see that the neighboring unit-cell rows along the *c* axis are located at different heights ("the region of a high force"). This displacement practically disappears at a slightly lower force ("the region of a low force"). The estimated high force is 1.0×10^{-10} N, and the low force is 0.8×10^{-10} N. Thus, the properties of the neighboring unit cells along the *a* axis are essentially different. This phenomenon can be interpreted as molecule reorientation provided by the unsaturated bonds emerging to the surface. We assumed these bonds to be of *C*-type (Fig. 1). The phenomenon of molecule reorientation on the surface is analogous to the phenomenon of the surface reconstruction well-known for some inorganic materials. The phenomenon of surface reconstruction is, in fact, the process during which the molecules located on the surface are rearranged in comparison with their positions in the crystal bulk in a way that minimizes the free surface energy of the system. This phenomenon was first described for organic crystals in [18] and for tetragonal lysozyme crystals in [19].

In our case, the observed reconstruction depends on the applied force. The difference in the heights of the neighboring unit-cell rows increases with an increase in the force. With a further increase of the applied force, the cantilever seems to strike the molecules from a higher row because of more intense collisions. Indeed, with an increase in the applied force, the higher rows lose the periodicity of their structure and their heights decrease. The image becomes blurred, which can be explained by the "removal" of some protein molecules. Thus, one can draw the conclusion that the neighboring rows have different mechanical rigidity and, therefore, with an increase of the tip–sample force, they are elastically deformed to different degrees.

Doubling of the lattice parameter along the b axis. In neighboring layers in the *ac* plane, the doubled rows of building blocks are shifted by a half-period along the *a* axis, which is well seen if the step is located at an angle to the *c* axis. This situation is shown in Fig. 5 and can be interpreted as doubling of the lattice parameter along the *b* axis, at least, in two surface layers of the building blocks. The measured height of one of these layers equals $b = 7.3 \pm 0.4$ nm.

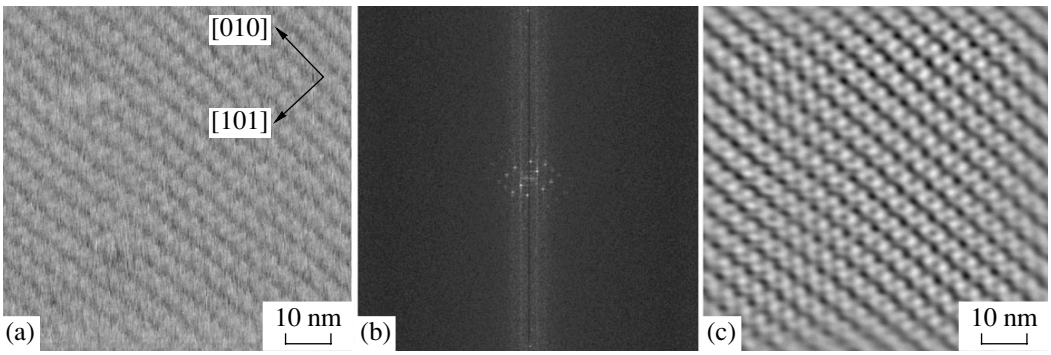

Fig. 6. The surface of a monoclinic lysozyme crystal: (a) initial image, (b) its Fourier transform, and (c) the filtered image.

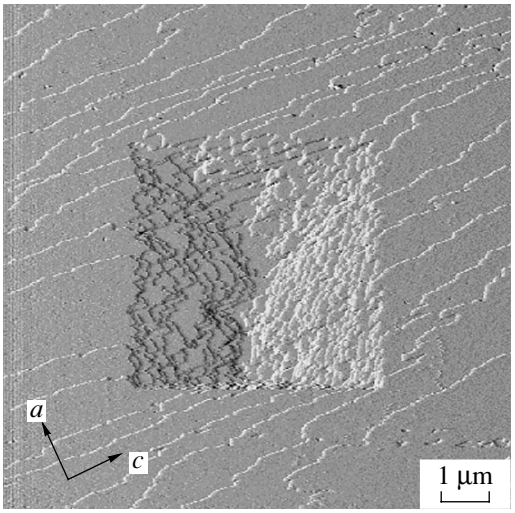

Fig. 7. Depression on the (010) face of an orthorhombic lysozyme crystal formed during long its scanning.

Figure 6 shows the structure of one of the faces of a monoclinic lysozyme crystal. We managed to attain a rather high resolution and visualize the unit cells. The characteristic unit-cell dimensions are 4.6 ± 0.2 nm along the "long" axis of the crystal and 8.5 ± 0.3 nm normal to it. The step rise at this face is 2.6 ± 0.3 nm. No surface reconstruction was observed in this case.

OBSERVATION OF LYSOZYME CRYSTALS SURFACE DESTRUCTION

Scanning in the contact mode at a force lower than 10^{-10} N does not lead to the destruction of the crystal surface. We managed to obtain stable images of a growing face, steps and kinks on this surface, and also the structure of defects. An increase in the force gives rise to the mechanical destruction of the surface including the removal of molecular layers and formation of depressions in the scanned region. Long scanning results in the formation of depressions on the scanned surface area (Fig. 7). The depression bottom formed upon short scanning is flat and has a large number of islands about 7 nm in height (which coincides with the elementary-step rise). With a decrease in the force, the depressions are quickly healed and the crystal face acquires its initial shape.

In some instances, where the force was close to the destruction threshold, the removal of a half-layer was observed. Figure 8a shows the surface region with elementary steps. If a scanning tip moves toward the steps (scanning from right to left), the cantilever "removes" a part of the growth layer and reveals the rougher part of the surface indicated by arrows in Fig. 8. The measured roughness heights showed that the depth of the removed half-layer is equal to the half-height of the growth layer, i.e., $b/2$. Upon the further scanning at a lower force, no destroyed region is seen anymore (Fig. 8b). Unfortunately, it is still unclear why the cantilever removes only a half-cell. It should also be indicated that healing of the damaged surface regions proceeds very quickly (the images in Fig. 8 were taken with an interval of 30 s). Strictly speaking, in this experiment, we did not rigorously control the tip–sample force. The point is that these images were obtained at slow scanning in the upward direction in the first image and in the downward direction in the second image. The different cantilever effect on the surface was caused by a small temperature drift in the downward direction. Also, we cannot exclude a possible effect produced by the tip asymmetry.

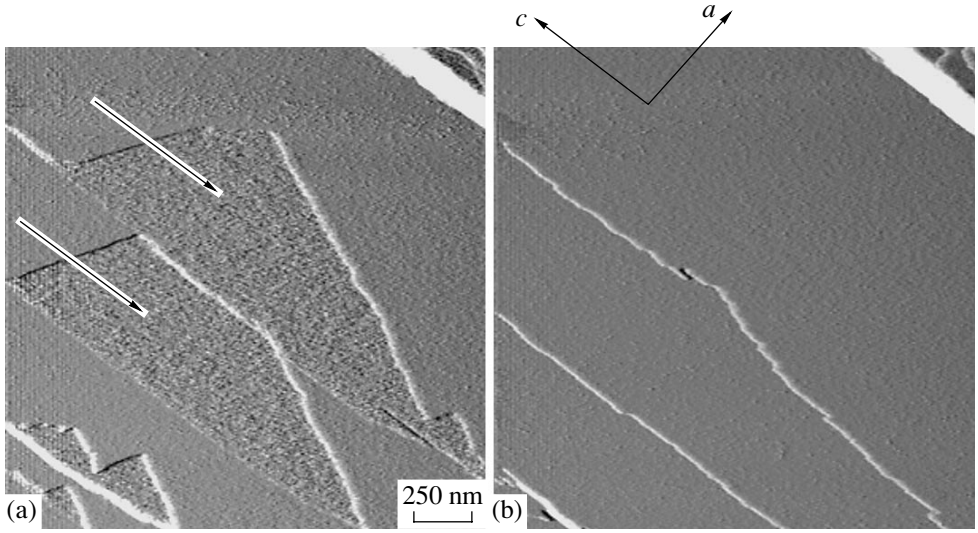

Fig. 8. Region of the surface of the (010) face of an orthorhombic crystal with the elementary steps scanned by the microscope cantilever: (a) scanning in the upward direction; (b) scanning in the downward direction.

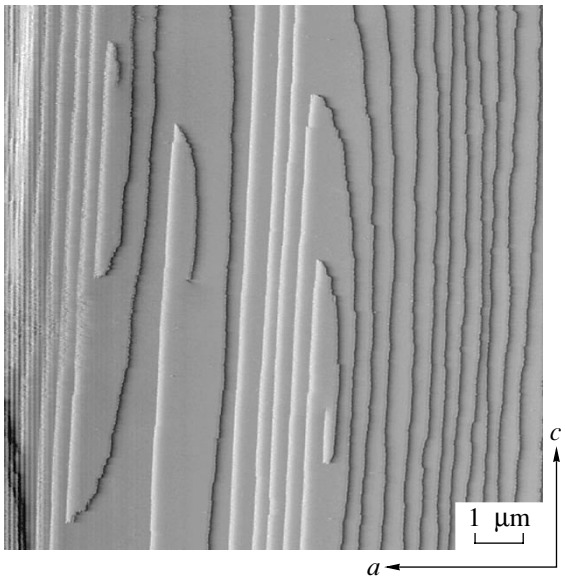

Fig. 9. Dislocation sources on the (010) face of an orthorhombic lysozyme crystal. The *c* axis is directed vertically.

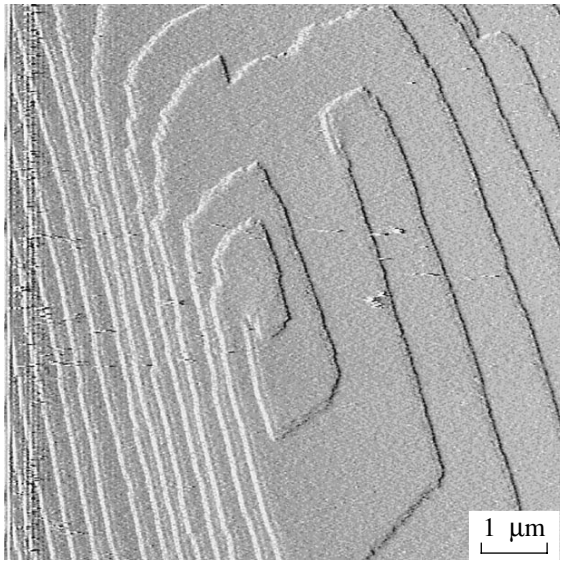

Fig. 10. Two dislocation sources on the face of a monoclinic lysozyme crystal.

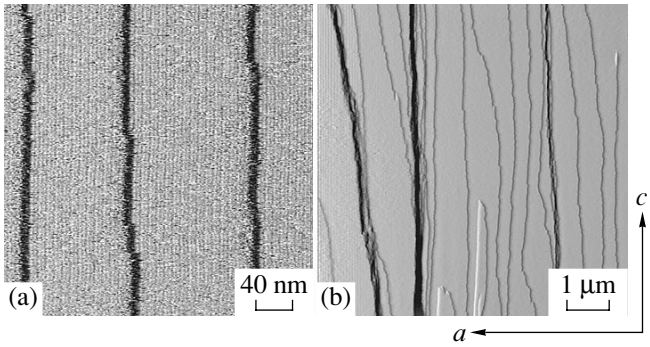

Fig. 11. Images of the surface regions of the (010) face of an orthorhombic crystal with growth steps: (a) elementary steps; (b) elementary steps and their bunching.

SHAPE OF DISLOCATION HILLOCKS

The maximum supersaturation in our experiments was of about 3; however, we observed two-dimensional nucleation in some rare instances. Crystals grew only by the dislocation mechanism. Dislocation hillocks on the (010) face of an orthorhombic lysozyme crystal were somewhat elongated. One of the hillock sides was almost rectilinear and coincided with the *c* axis, whereas the opposite side was bent as an arc and had a pronounced roughness (Fig. 9). The step velocities along the *a* and *c* axes differed by a factor of 7.2.

A dislocation hillock on one of the faces of a monoclinic lysozyme crystal is shown in Fig. 10. Here, the helix is less asymmetric and the ratio of the step velocities along the two perpendicular directions is about 1 : 3. The elementary-step rise equals 2.8 ± 0.3 nm.

OBSERVATION OF MOTION KINETICS OF STEPS AND KINKS

We obtained more than 2000 images of the (010) face of an orthorhombic lysozyme crystal on various scales. The face had both elementary steps and macrosteps. Figure 11a shows the image of the face region containing an echelon of elementary steps with a rise of 7.3 ± 0.4 nm, a value close to the lattice parameter along the *b* axis (Table 1). Figure 11b shows the region of the face not only with elementary steps but also with step bunching (macrosteps). The microstep rise was from two to ten times higher than the elementary-step rise. The velocity of the macrostep motion only slightly differs from the velocity of the elementary steps. Nevertheless, in some instances, the elementary steps caught up with macrosteps and merged into them (step bunching). At the same time, we also observed detachment of elementary steps from the macrostep base. Therefore, the macrostep rise is changed in the process of its motion.

The velocity of an elementary step is practically independent of the interstep distance (0.05–1.00 μm). This is confirmed by the sequence of three images taken with an interval of 50 s shown in Fig. 12. It is seen that the interstep distance is practically constant and, therefore, all the steps move with the same velocity. The steps move from left to right with velocity of about 0.45 nm/s. Therefore, one can conclude that supersaturation for closely located steps is the same as for steps separated by large distances.

We managed to obtain the image of kinks on a moving step at the molecular resolution. The kinks had different depths—from one lattice parameter along the *a* axis (about 80% of kinks) up to four lattice parameters. The existence of kinks only with different depths can be explained by the presence of noncontrolled impurities. The impurity stopper can decelerate the kink only for some time, then the kinks in the following building-block rows can catch up with the stopped kink. However, we have no proof of such a mechanism.

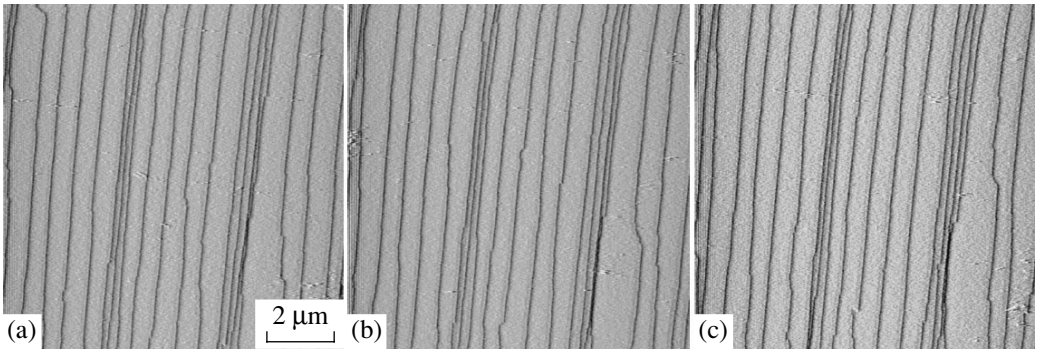

Fig. 12. (a–c) Motion of growth steps on the (010) face of an orthorhombic lysozyme crystal. The images are obtained with an interval of 50 s.

Figure 13 shows a portion of an elementary step with two positive and one negative kink. Their depths are equal to 5.8 ± 0.5 nm, which corresponds to one unit-cell parameter along the *a* axis. Thus, the kink is formed by four lysozyme molecules. However, the mechanism of kink formation is far from being clear. Possibly, the incorporation of only one molecule gives rise to very quick incorporation of the remaining three molecules. The alternative is the incorporation of a cluster of four molecules.

Concentration of kinks and their velocity. We measured the distances between almost 300 kinks at different steps. The average interkink distance is equal to a dimension comprised of about 180 unit cells, with the root-mean-square deviation being of the same order. The close values of these quantities indicate the exponential distribution function of the interkink distances characteristic of the random distribution of the interparticle distances along the line. The absence of any interaction between the kinks seems to be quite natural at such a low kink density.

At a low kink density, a step moves forward via the formation of rows of building blocks. The arrival of the kink at the given point of the step indicates its motion forward by a distance equal to the dimension of the building block. Therefore, the following relationship is valid:

$$V = b\rho v,$$

where V is the step velocity, v is the kink velocity, ρ is the kink density, and b is the dimension of the building block (the unit-cell parameter) along the direction of step motion. The step velocity can be readily determined from a sequence of its images. The above formula was used to calculate the kink velocity, which turned out to be 100 times higher than the step velocity.

Fluctuations in the step position. Since the building blocks cannot be attached only to the step but can also be detached from it, the step portion moves alternatively forward and backward. In order to observe this process, we switched off the slow-motion mode of the AFM cantilever and scanned only one line. On the step images of the (110) face thus obtained for orthorhombic lysozyme crystals (Fig. 14); the ordinate axis corresponded to time, the change in the coordinate of the chosen region of the step was measured along the abscissa. The same images can be used to determine the time intervals upon which the building blocks either arrive at or depart from the chosen point of the step. The step coordinate (x^*) as a function of time (t) is shown in Fig. 15. It is seen that, on the average, the step velocity is constant. Subtracting from the x^* values measured at moments t their average value, we arrive at the dependence of the fluctuations in the step position on time $x(t)$. Figure 16 shows the autocorrelation function of this dependence on the logarithmic scale:

$$W^2 = \langle [x(t) - x(t - \Delta t)]^2 \rangle.$$

Here, averaging was performed for all t at the constant Δt. The quantity $W(\Delta t)$ characterizes an increase in the

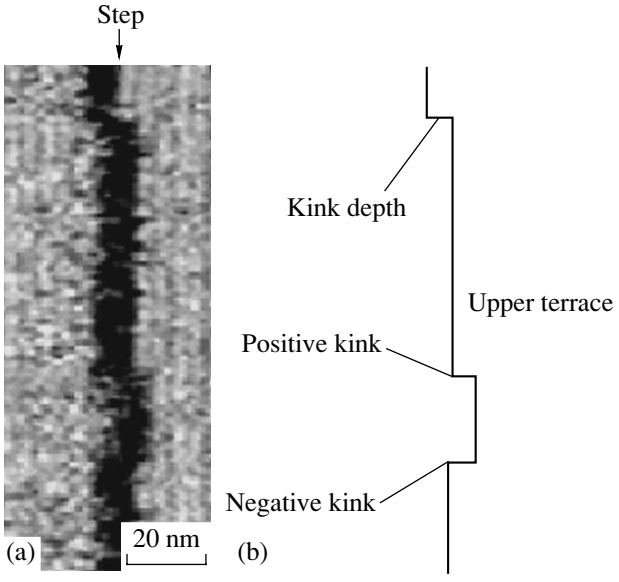

Fig. 13. (a) Portion of an elementary step with two positive and one negative kinks. (a) The step moves from right to left. (b) Schematic depiction of this portion. An orthorhombic lysozyme crystal.

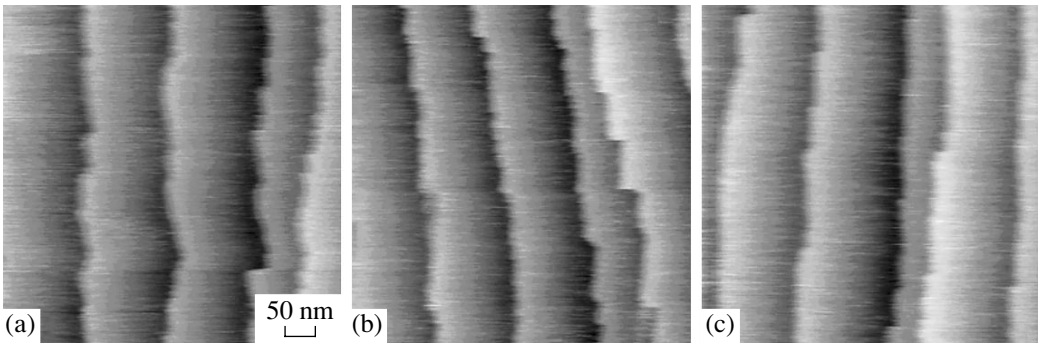

Fig. 14. (a–c) Images of steps on the (110) face of an orthorhombic lysozyme crystal obtained at switched-off scanning along the *y* axis. Scanning time 42 s; cantilever path 512 nm. Scanning frequency 12.2 Hz; scan number 512.

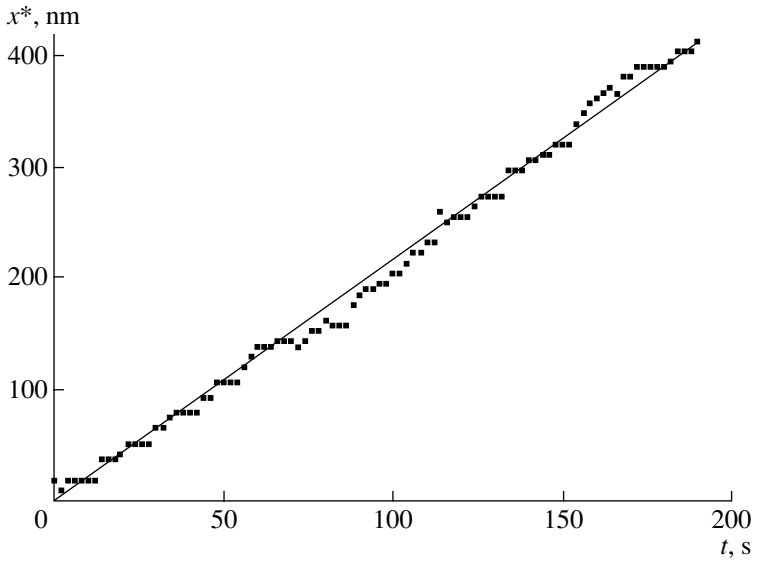

Fig. 15. Coordinate of the step position as a function of time.

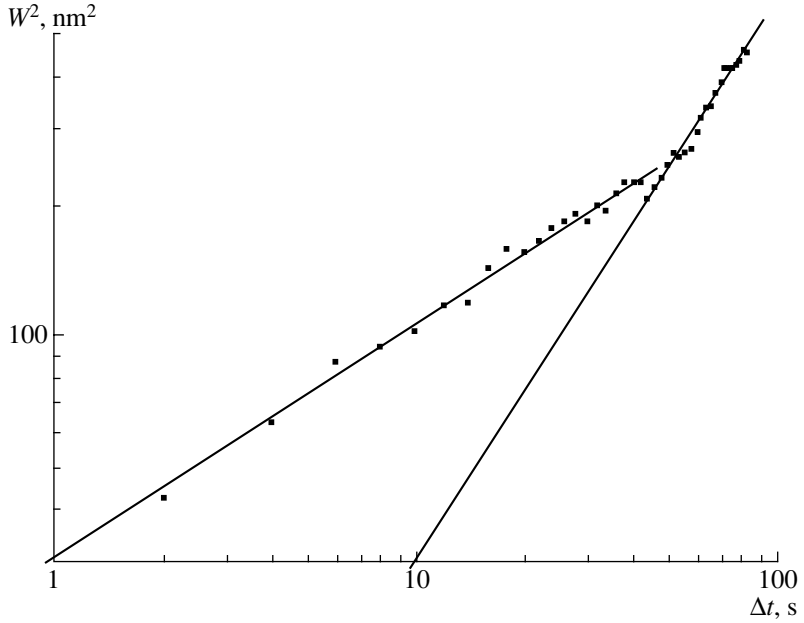

Fig. 16. Autocorrelation function for the dependence $x(t)$. The curve slope equals 0.53 ± 0.02 nm^2/s for the first region and 1.26 ± 0.04 cm^2/s for the second one.

Table 2. Parameters of lysozyme crystallization calculated from the data on step fluctuations

Parameters	Lysozyme, (110) face, step ‖ [001]
χ, cm^4/s	$(1.22 \pm 0.22) \times 10^{-25}$
a, cm	9.29×10^{-7}
c, cm	3.05×10^{-7}
h, cm	4.48×10^{-7}
$\omega^-(c\rho)^2$, s^{-1}	0.26
β/α_e, cm^2(erg s)	16.1
$c\rho$	0.087
ω^-, s^{-1}	34
β, cm/s	2.86×10^{-6}
α_e, erg/cm	1.71×10^{-7}
α_e/h, erg/cm^2	0.38

intensity of fluctuations (step roughness) for the time Δt. One can see two linear segments. The first one (at small Δt) has a slope equal to 1/2, the second one, 5/4. The second segment of the curve has not been interpreted as yet. However, the first one, which shows that fluctuations increase proportionally to the fourth root of time, confirms the model of the fluctuations in the step position suggested elsewhere [20, 21]. It is assumed in this model that the supersaturation at a step is constant, which agrees with our data that show that the step velocity is independent of the interstep distance. According to [21], we have

$$W^2 = (\chi t)^{1/2},$$

$$\chi = 2(\beta/\alpha_e)kTac/\pi = 2a^4\omega^-(c\rho)^2/\pi,$$

$$\beta = a(c\rho)\omega^-,$$

$$\alpha_e = kTc/(c\rho)a^2.$$

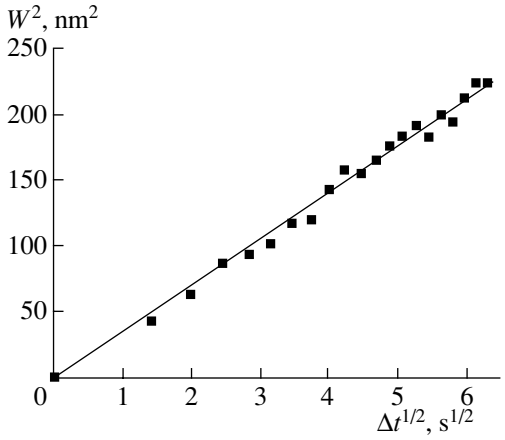

Fig. 17. The first portion of the autocorrelation function in the linearized form.

Here, β is the kinetic coefficient, α_e is the step rigidity, the quantity α_e/h is approximately equal to the free surface energy of the step end (where h is the step rise), k is the Boltzmann constant, T is the temperature, ω^- is the frequency of the detachment of the building blocks from the kinks, and c and a are the distances between the building blocks and their rows, respectively, calculated from the unit-cell dimensions at the given face.

Figure 17 shows the dependence $W^2(\Delta t^{1/2})$, whose slope equals 35.0 ± 0.3 nm^2/s$^{1/2}$ and determines the value of χ. The parameters calculated by the above formulas are listed in Table 2.

The $c\rho$, β, α_e, and ω^- values in the table depend on the building-block dimension. If this dimension differs from the unit-cell dimension, these values can readily be calculated with the use of the experimentally measured χ value.

CONCLUSION

In situ atomic force microscopy provided the study of surface morphology of orthorhombic and monoclinic lysozyme modifications.

A growing crystal face is visualized at molecular resolution. On the (010) face of an orthorhombic lysozyme crystal, the unit-cell parameters are doubled along the *a* and *b* axes, which indicates the reconstruction of the surface in the contact with the solution.

Lysozyme crystals grow by the dislocation mechanism, at least at supersaturations $s < 3$. The kinks at the steps, whose density is so low that they cannot interact with one another, are visualized. The steps move via row-by-row filling of the kinks with building blocks. The fluctuations in the positions of the step regions are studied. It is shown that they grow proportionally to the fourth root of time. This is in good accord with the predictions of the theory developed by V.V. Voronkov 30 years ago. The data on fluctuations allowed us to calculate some basic phenomenological and microscopic parameters of crystallization.

ACKNOWLEDGMENTS

This study was supported by the Russian Foundation for Basic Research, projects nos. 00-020-1670, 00-07-90016, and 00-04-055020 and the Ministry of Industry, Sciences, and Technologies of the Russian Federation, project. no. 1.11.99.

REFERENCES

1. L. K. Steinrauf, Acta Crystallogr. **12**, 77 (1959).
2. E. L. Forsythe, E. H. Snell, C. C. Malone, *et al.*, J. Cryst. Growth **196**, 332 (1999).
3. S. T. Rao and M. Sundaralingam, Acta Crystallogr., Sect. D: Biol. Crystallogr. **52**, 170 (1996).

4. H. Oki, Y. Matsuura, H. Komatsu, and A. A. Chernov, Acta Crystallogr., Sect. D: Biol. Crystallogr. **55**, 114 (1999).
5. S. D. Durbin and W. E. Carlson, J. Cryst. Growth **122**, 71 (1992).
6. M. Radmacher, M. Fritz, J. P. Cleveland, *et al.*, Langmuir **10**, 3809 (1994).
7. J. H. Konnert, P. D'Antonio, and K. B. Ward, Acta Crystallogr., Sect. D: Biol. Crystallogr. **50**, 603 (1994).
8. Yu. G. Kuznetsov, A. J. Malkin, T. A. Land, *et al.*, Biophys. J. **72**, 2357 (1997).
9. A. McPherson, A. J. Malkin, and Y. G. Kuznetsov, Structure (London) **3**, 759 (1995).
10. Yu. G. Kuznetsov, A. J. Malkin, W. Glantz, *et al.*, J. Cryst. Growth **168**, 63 (1996).
11. A. J. Malkin, Yu. G. Kuznetsov, and A. McPherson, J. Cryst. Growth **196**, 471 (1999).
12. A. J. Malkin, Yu. G. Kuznetsov, and A. McPherson, J. Struct. Biol. **117**, 124 (1996).
13. Yu. G. Kuznetsov, A. J. Malkin, and A. McPherson, Phys. Rev. B **58**, 6097 (1998).
14. Yu. G. Kuznetsov, A. J. Malkin, and A. McPherson, J. Cryst. Growth **196**, 498 (1999).
15. M. Wiechmann, O. Enders, S. Zeilinger, *et al.*, Ultramicroscopy **86**, 159 (2001).
16. M. Tanaka, M. Yamamoto, K. Kawashima, *et al.*, J. Cryst. Growth **168**, 44 (1996).
17. M. Ataka and M. Asai, J. Cryst. Growth **90**, 86 (1988).
18. A. A. Baker, W. Helbert, J. Sugiyama, *et al.*, J. Struct. Biol. **119**, 129 (1997).
19. H. Li, A. Nadarajah, and M. Pusey, Acta Crystallogr., Sect. D: Biol. Crystallogr. **55**, 1036 (1999).
20. V. V. Voronkov, in *Crystal Growth* (Nauka, Moscow, 1975), Vol. 11, p. 357.
21. V. V. Voronkov, in *Crystals*, Vol. 9: *Modern Theory of Crystal Growth I*, Ed. by A. A. Chernov and H. Müller-Krumbhaar (Springer-Verlag, Berlin, 1983), p. 7.

Translated by L. Man

Crystallography Reports, Vol. 47, Suppl. 1, 2002, pp. S15–S26.

CRYSTALS OF THE FUTURE

Crystals for Photonics

T. T. Basiev, E. V. Zharikov, and V. V. Osiko

Laser Materials and Technology Research Center, Institute of General Physics, Russian Academy of Sciences, ul. Vavilova 38, Moscow, 117942 Russia

e-mail: osiko@lst.gpi.ru

Received February 13, 2002

Abstract—The prospects of using crystals in photonics are discussed. Primary attention is focused on one of the topical problems of photonics—creation of sources of laser radiation with given wavelengths. Recent advances in the development of crystals for tunable lasers, as well as for the transformation of the radiation spectrum by means of the stimulated Raman scattering, are discussed. © *2002 MAIK "Nauka/Interperiodica".*

INTRODUCTION

Future prospects of using crystals in photonics, one of the rapidly developing fields of high technology, are discussed. It should be borne in mind that photonics is the technology for the generation and transformation of light and other kinds of electromagnetic radiation.

Recently, photonics has developed explosively, because, in particular, it largely determines the development of medical, ecological, and scientific instrument production; new technologies of materials processing; and military engineering. However, the main cause for this development is that photonics is extensively applied in information technologies, i.e., technologies for the acquisition, storage, processing, transmission, and reproduction of information. Moreover, many leading experts predict that photonics will determine the level of informatics in the near future. These predictions are based on the extremely high operation rate, information capacity, and robustness of photonic devices. Dielectric and semiconductor crystals, as well as structures based on them, serve as the material basis of photonics.

Crystals have the following advantages over other materials:

(i) the high density of operating particles (atoms, ions, molecules, atomic clusters), up to 10^{23} cm^{-3}, ensures a compact size of photonic devices, as well as further miniaturization and functional integration;

(ii) regular periodic packing of atoms (ions, molecules) in crystals gives rise to structural and energy degeneration and, as a result, to narrow resonances and large resonance cross sections for the absorption and emission of photons, as well as to high nonlinear optical coefficients;

(iii) rich variety of compositions and structures of crystals, in particular, a vast number of combinations of various crystal matrices and active dopants.

All materials and elements of photonics are divided into two types: (i) active, i.e., generating radiation (laser crystals, phosphors, scintillators) and (ii) passive, i.e., transforming the spectral and time parameters, phase, polarization or direction of wave propagation (various modulators, transformers of harmonics, transformers based on the stimulated Raman scattering of light, electro-optic deflectors, etc.).

Since the 1950s, the works of A.M. Prokhorov, N.G. Basov, and Ch. Townes, as well as the creation of lasers, led to the formation and further successful development of a branch of photonics that can be conditionally called macrophotonics, since it deals with decimeter- and centimeter-sized elements and structures. Macrophotonics is based on bulk single crystals that have very large sizes and are grown from their own melts, solution–melts, or aqueous solutions.

In the last decade, in connection with the already-mentioned tendency towards the photonization of informatics, the miniaturization and integration of photonic elements, as well as the application of microelectronic technological procedures in their technology, have been rapidly developed. Figure 1 shows the scheme of the so-called microchip laser and demonstrates the initial stage of the integration of photonic elements and the development from macrophotonics to microphotonics [1].

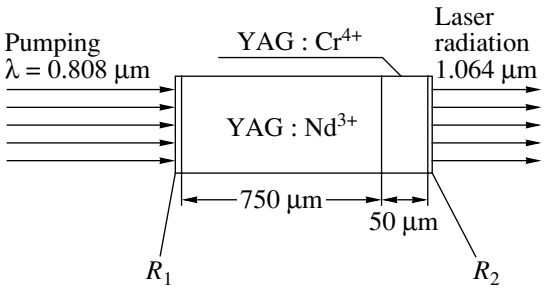

Fig. 1. Scheme of a microchip laser. A YAG : Cr^{4+} layer is grown over a IAG : Nd^{3+} layer by liquid-phase epitaxy, and the ends are covered by multilayer mirrors R_1 and R_2.

1063-7745/02/47S1-S0015$22.00

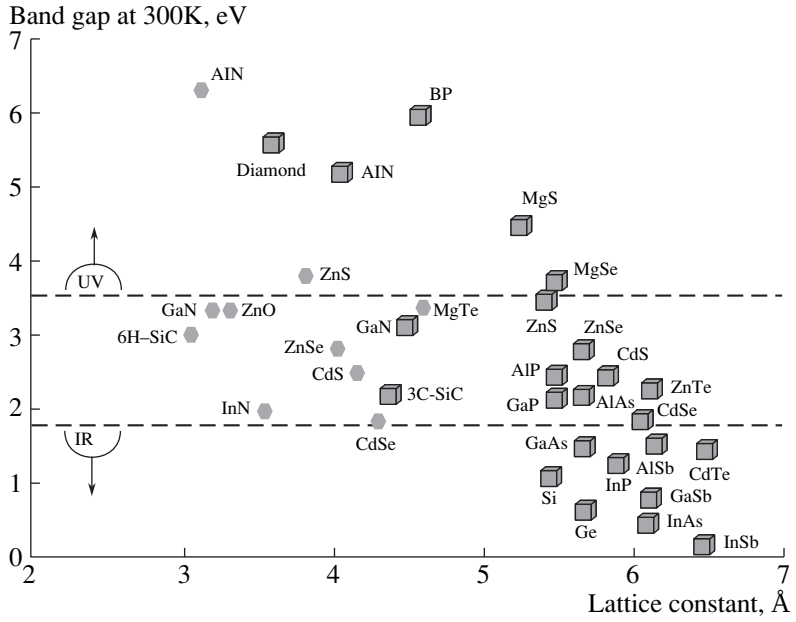

Fig. 2. Pure and binary semiconductors on which microphotonics is based. Semiconductor compounds with indirect *p–n* transitions are italicized, cubes are cubic-structure crystals, and hexahedrons are crystals with a hexagonal structure. Only the parameter *a* is indicated for the latter crystals. Dashed lines are the boundaries of the visible range.

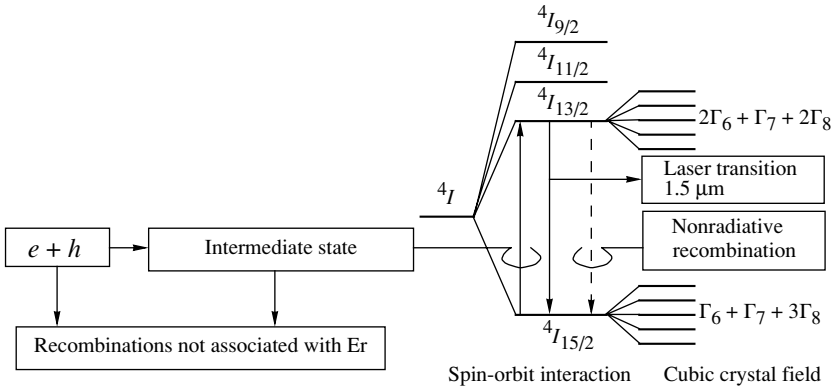

Fig. 3. Energy diagram of Si activated by Er^{3+} ions.

One of the main directions in photonic informatics is the application of structures based on semiconductor crystals. Figure 2 shows the lattice parameter and band gap for intrinsic semiconductors and semiconductor compounds which are current materials of semiconductor photonics.

The transition from macrophotonics to microphotonics, where the size of active and passive elements decreases to 10^{-4}–10^{-6} m, requires the transition to new technologies based on the epitaxial growth of single-crystal films, sputtering of thin layers, subsequent artificial drawing (lithography), and selective chemical etching. These processes provide the desired microchips.

From the standpoint of engineering and economics, the most promising and rational direction would be the creation of silicon photonics; i.e., photonic high-integrated chips involving active and passive elements produced by silicon microelectronic technologies. In this case, the direct transformation of electric signals to light and its further processing would be realized in technologically well-developed silicon chips. However, since electron transitions in Si are indirect, pure silicon cannot be used to generate light (nanocrystalline or amorphous Si is an exception). Nevertheless, silicon technologies might possibly be used to create passive elements of microphotonics.

The next logical step is an attempt to activate Si by rare-earth elements, e.g., Er (see Fig. 3). Erbium has strong radiation transitions near 1.54 μm (i.e., in the region of the spectral transmission of Si), which is the basic operation frequency in current fiber optics com-

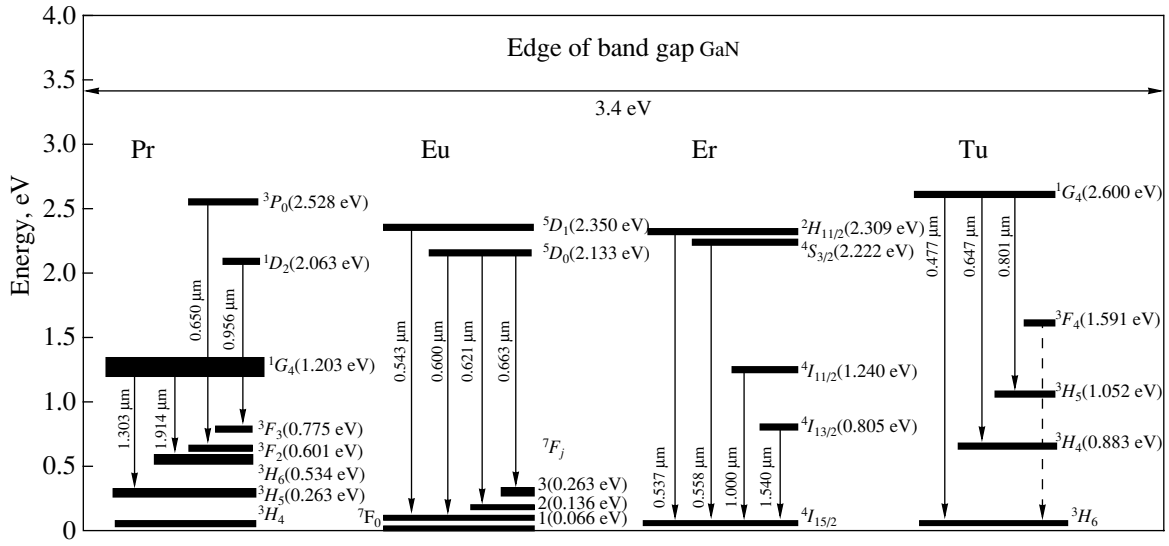

Fig. 4. Energy diagram of GaN activated by Pr^{3+}, Eu^{3+}, Er^{3+}, and Tm^{3+} ions.

munication lines. Although activated Si has been investigated for more than a decade, its generation has not been obtained yet and the maximum energy yield of electroluminescence is only equal to 0.05% [2].

Although research on GaN activated by rare-earth elements continue has been conducted for only five years, it has been much more successful at achieving (see Fig. 4) exciting results for the electroluminescence of Er ($\lambda \sim 0.55$ and 1.54 μm) and Pr ($\lambda \sim 0.65$, 0.96, 1.3, and 1.9 μm) in this crystal. The technology and study of films of pure and activated GaN on various substrates have been discussed at recent conference and symposiums. Numerous leading laboratories at universities and firms abroad [3] and in Russia have participated in this research.

In order to produce passive microphotonic elements, it is suggested that a phenomenon that was discovered in 1987 [4] be used. This phenomenon consists of the fact that photons in microperiodic structures with a certain scale and geometry have the properties of electrons in crystals: a frequency gap appears for modes propagating in these structures. These structures are called photonic crystals. Creating linear or point defects, one can produce various microphotonic elements: waveguides, splitters, filters, and resonators [5]. Another rapidly developing direction in the design of microphotonic elements is microring resonators with a high spectral selectivity and *Q* factor, which provide for a degree of integration of up to 10^5 elements per 1 cm^2 [6].

Most directions in microphotonics are still at the R&D stage. However, many laboratories have begun projects for the further miniaturization and integration of photonic elements, i.e., the transition from microscale to nanoscale (where an element size is 10^{-6}–10^{-8} m) [7]. These works are stimulated not only by further integration but also by the extension of the functional abilities of photonic chips due to new physical phenomena—the so-called quantum-well effects (e.g., the above-mentioned nanocrystalline silicon). Extension to the nanosize region encounters serious obstacles.

The statistical analysis of tendencies in developing microelectronics revealed regularities known as Moore's laws [8]. According to the first law, the number of transistors in chips is quadrupled every three years (this number was equal to 10^7 in 2000). The sizes of transistors decrease correspondingly. According to the second law, the cost of equipment for producing microchips is doubled every three years. Moore's laws concern the development of microelectronics. However, they are applicable to microphotonics as well, because microtechnologies are common. The extrapolation of Moore's laws to the next decade shows that the application of technologies developed for microphotonics to nanophotonics will inevitably lead to deadlock.[1] Therefore, the transition to the nanoscale requires absolutely novel technologies. Lithography of chips and selective etching must be replaced by the technology of chemical assembly. Chemical and physicochemical processes that will be used (and are already used) for this aim are as follows:

(i) initial stages of recrystallization of ultrathin films;

(ii) formation of surface and bulk clusters;

[1] Note that the second Moore's law points to the causes of the increasing lag of Russia in microelectronics and microphotonics. Economic factors hinder the wide practical realization of the brilliant fundamental works by academician N.G. Basov *et al.* on injector lasers and works by academician Zh.I. Alferov on semiconductor heterostructures, who recently was awarded the Nobel Prize.

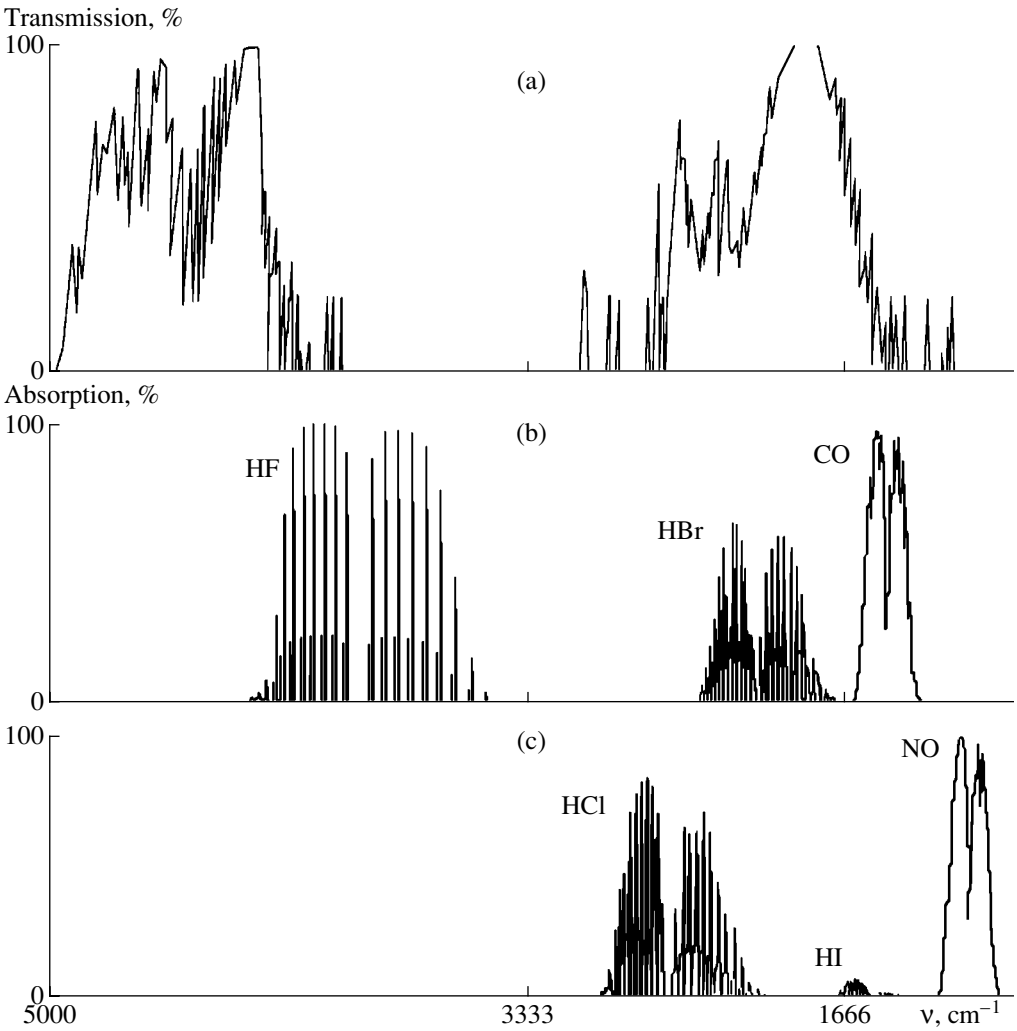

Fig. 5. (a) Transmission spectrum of the atmosphere in the infrared region and (b) and (c) absorption spectra of some gases.

(iii) nanocrystallization in glasses, liquid solutions, and gases.

The technology of nanostructures is at the very beginning of its development. Nevertheless, nanosize quantum dots on the surfaces of semiconductor crystals and one-dimensional quantum wires have already been obtained and actively used. These structures have sizes of 0.01 μm [9]. Nanoparticles with sizes of several nanometers have been obtained in solutions. Although many fundamental problems of nanotechnology, including the problem of coupling nanoelements, have yet to be solved, there is no doubt that nanophotonics will be created in the near future.

Current photonics is a wide and rapidly developing field in high technology. It is impossible to review even briefly the entire variety of directions and problems in this field in one paper. This paper focuses on one of the topical problems of macrophotonics—the creation of sources of radiation with given wavelengths.

SOURCES OF RADIATION WITH GIVEN WAVELENGTHS

Figure 5a shows the transmission spectrum of the Earth's atmosphere in the infrared region, whereas Figs. 5b and 5c show the absorption spectra of certain molecular gases. It is seen that the atmosphere spectrum has the so-called transmission windows; i.e., spectral regions where the atmosphere is transparent for electromagnetic radiation. One of these windows is in the visible spectral region responsible for the possibility of life on Earth. Such windows also exist in the infrared region, e.g., in the regions ~2–2.5 μm (~5000–4000 cm^{-1}) and ~4–5 μm (~2500–2000 cm^{-1}). The latter is interesting because it covers vibrational spectra of many molecules, including those whose content in the atmosphere we want to determine and monitor. Halohydrogens, carbon oxides, nitrogen oxides, etc., are among the latter molecules. The content of these molecules in the atmosphere can be remotely monitored via exciting them with spectrally selective radiation

sources. For this aim, it is necessary to have lasers emitting at strictly given wavelengths corresponding to the absorption spectra of each molecule; i.e., laser sources with given wavelengths are required.

Another example. Table 1 presents the wavelengths of the strong absorption and fluorescence lines of certain metal atoms. These so-called analytical spectral lines are used to determine very small amounts of metals via spectral methods. The remote determination of small amounts of metals in the atmosphere, water, or soil, e.g., for ecological monitoring, also requires sources with given wavelengths but which emit in the near ultraviolet region.

Radiation sources with given wavelengths are necessary for many problems, including ecology, ground-based communication with flying and cosmic objects, fiber optics communication systems, medicine, etc. The problem in question is formally similar to the problem of the generation and reception of radio waves when a radio receiver is exactly tuned to the wavelength of a radio transmitter. However, the analogy ends here. Radio equipment makes it possible to easily vary the radio frequency over a wide spectral region and, therefore, to tune to the resonance. Most laser sources generate radiation that has a fixed frequency and is close to monochromatic. Table 2 presents data on the most effective current laser crystals. Unfortunately, they are absolutely inapplicable to the above-listed problems, because their radiation frequencies are not in resonance with the most topical receivers. We emphasize that the lines in the absorption spectra of atoms, ions, and molecules are very narrow and have widths of 0.01–0.1 cm^{-1}. The radiation spectra of most lasers are also narrow and have widths of 0.1–1 cm^{-1}. Therefore, exact frequency coincidence between laser radiation and an absorption line of an atom or molecule is improbable. Solving this problem by broadening the variety of lasers is inefficient and hardly realizable, although works concerning the extension of crystal lasers to the middle infrared and near ultraviolet regions are being intensively carried out in a number of laboratories.

Laser sources emitting at exactly given wavelengths for remote action on atomic and molecular systems with narrow spectral resonances can be created by two methods:

(1) by using lasers with a variable generation frequency, i.e., by using the principle of tuning a radiator to the resonance frequencies of atoms or molecules;

(2) by transforming the radiation of existing lasers to shorter or longer wavelengths so that the spectrum of the transformed radiation corresponds to the required wavelength. In this case, the transformed radiation can be from both monochromatic and tunable lasers. The radiation wavelength is changed by crystals with pronounced nonlinear optical properties. In this case, physical phenomena such as the transformation of harmonics due to phase synchronism, parametric light generation, and stimulated Raman scattering of light (stimulated Raman scattering transformation) are used.

Table 1. Chemical elements having "analytical" electron transitions in the wavelength range 0.2–0.4 μm

Element	λ_{exc}, μm	λ_{fluor}, μm	Element	λ_{exc}, μm	λ_{fluor}, μm
Ag	0.3281	0.3383	Ni	0.3019	0.3101
Al	0.3082	0.3082	Pb	0.2833	0.4058
Au	0.2428	0.3123	Pt	0.2930	0.2998
B	0.2496	0.2497	Re	0.2896	0.4391
Be	0.2348	0.2348	Sb	0.2311	0.2311
Cd	0.3261	0.3261	Se	0.2974	0.5349
Co	0.3044	0.3405	Si	0.2514	0.2988
Cr	0.3352	0.4646	Sn	0.2863	0.3009
Cu	0.3247	0.5105	Sr	0.2931	0.7167
Fe	0.2967	0.3735	Ta	0.2873	0.3049
Ga	0.2874	0.2944	Te	0.2259	0.2530
Ge	0.2652	0.2754	Th	0.3060	0.3471
Hg	0.2536	0.2536	Ti	0.2933	0.2967
In	0.3039	0.3295	Tl	0.2768	0.3529
Ir	0.2951	0.3221	U	0.3115	0.3115
Li	0.3233	0.3233	V	0.2838	0.2864
Lu	0.2989	0.2989	W	0.2911	0.4028
Mg	0.2852	0.2852	Y	0.2974	0.3022
Mn	0.2795	0.2795	Zn	0.3076	0.3076
Mo	0.2944	0.4443	Zr	0.2961	0.3011
Nb	0.3742	0.3764			

Table 2. Crystals for lasers with monochromatic radiation

Crystal	Activator : sensitizer	Radiation wavelength, μm
$Y_3Al_5O_{12}$	Nd^{3+}	1.064 (0.94; 1.32; 1.444)
	Yb^{3+}	1.030
	Er^{3+}	2.940
	$Ho^{3+} : Tm^{3+}$	2.098
$Gd_3Ga_5O_{12}$	$Nd^{3+} : Cr^{3+}$	1.062
	$Er^{3+} : Cr^{3+}$	2.790
$Y_3Sc_2Ga_3O_{12}$	$Nd^{3+} : Cr^{3+}$	1.058
	$Er^{3+} : Cr^{3+}$	2.791
$Gd_3Sc_2Ga_3O_{12}$	$Nd^{3+} : Cr^{3+}$	1.061
$YAlO_3$	Nd^{3+}	1.079
$KGd(WO_4)_2$	Nd^{3+}	1.067
YVO_4	Nd^{3+}	1.064
$LiYF_4$	Nd^{3+}	1.047 (π) 1.053 (σ)

Table 3. Crystals for tunable lasers

Crystal	Activator	Radiation wavelength range, μm
Al_2O_3	Ti^{3+}	0.650–1.110
$Y_3Al_5O_{12}$	Cr^{4+}	1.340–1.570
Mg_2SiO_4	Cr^{4+}	1.130–1.367
$LiSrAlF_6$	Cr^{3+}	0.780–0.990
	Ce^{3+}	0.285–0.315
MgF_2	Co^{2+}	1.550–2.300
ZnSe	Cr^{2+}	2.200–2.812
LiF	F_2^- (color center)	1.060–1.300
	F_2^+ (color center)	0.800–1.100

CRYSTALS FOR TUNABLE LASERS

Table 3 presents two types of crystals for tunable lasers. In the first of these, lasing centers are formed by native point defects, the so-called color centers, and by impurity ions of transition elements Cr^{2+}, Cr^{3+}, Cr^{4+}, Ti^{3+}, Co^{2+}, and Ce^{3+}, respectively. In both cases, the luminescence spectra of crystals are wide (the width of luminescence bands reaches 1000 cm^{-1}), structureless, or slightly structured bands within which the generation frequency can vary.

Table 4 presents the basic physicochemical, mechanical, and optical characteristics of the most promising crystals with color centers. Lithium fluoride crystals are most extensively used in tunable lasers. Such a crystal has a cubic structure, is not hygroscopic, and has high thermal conductivity that exceeds the thermal conductivity of yttrium–aluminum garnet (YAG). Moreover, its nonlinear refractive index n_2 is low. Owing to these properties, the threshold for the laser destruction of LiF is as high as 3.6 GW/cm^2 (for λ = 1.06 μm and a pulse duration of 10 ns) and this crystal can be used in laser systems with a high average power. Comparatively low mechanical characteristics are among the drawbacks of LiF.

Lithum fluoride crystals are grown using the Kyropoulos method. Since this crystal has long been used as an optical material, its technology is well developed: LiF bools up to 50 cm in diameter are grown with a high homogeneity.

Figure 6 shows the structures of the basic color-center forms in LiF: F, F_2, F_2^+, and F_2^-. The basic color-center structure presents vacancies of anions that have an effective positive charge and, therefore, can absorb electrons. In addition, F vacancies under certain conditions tend to combine into pairs and more complex aggregates. The most active lasing centers are F_2 (pair

Table 4. Basic physicochemical, mechanical, and optical characteristics of promising crystals with color centers

Crystal	ρ, g/cm^3	*d*, Å	*H*, kg/mm^2	Solubility, 1 g/100 g H_2O	T_m, K	*K*, W/mK	α 10^6, K^{-1}	*n*	*dn*/*dT* 10^5, K^{-1}	I_{thr} 10^{-12} W/m^2	Transparency range for $k = 1$ cm^{-1}, μm
LiF	2.64	4.03	99–102	0.12	1121	14.2	33.7	1.387	–2.9	3600	0.11–6.6
NaF	2.791	4.62	60	4.2	1270	9.2	32.2	1.321	–1.8	1400	0.16–11.2
NaCl	2.17	5.64	15.2–18.2	36.0	1074	6.4	39.6	1.53	–3.7	200	0.17–18.0
KF	2.50	5.35		94.9	1130						0.2–15.0
KCl	1.99	6.29	7.2–9.3	37.4	1049	6.0	37.0	1.48	–3.3	700	0.18–23.0
KBr	2.75	6.60	6–7	70.9	1007	4.8	38.4	1.54	–3.2	500	0.21–28.0
KI	3.13	7.07	5	144.0	959	2.1	41.2	1.64	–4.5	200	0.3–35.0
PbCl	2.76	6.58		94.2	717		32.8				
MgF_2	3.18	a = 4.64 c = 3.06	576	0.0076	1.536	21⊥c 30∥c	9.4⊥c 13.4∥c	n_0 = 1.373 n_e = 1.385	11.2 5.8	1000	0.1–7.0
CaF_2	3.18	5.46	120–163	0.0016	1.676	9.7	18.8	1.429	–1.05	>1000	0.13–9.4
SrF_2	4.24	5.79	144	<0.1	1.190		19.6			1900	0.1–9.0
Al_2O_3	3.974	a = 4.76 c = 13.0	2100	0	2.313	35.0	5⊥c 6.7∥c	n_0 = 1.765 n_e = 1.757	1.3 0.97	12000	0.18–5.1
Diamond	3.515	3.57	8820	0	3.770	9000.0	1.0	2.40	0.4	2000	0.24–2.7
$Y_3Al_5O_{12}$	4.55	12.0	1350	0	2.223	13.0	7.8	1.815	1.05		0.21–5.3

Note: ρ is the density, *d* is the lattice constant, *H* is the Knoop hardness, T_m is the melting temperature, *K* is the heat transfer coefficient at 300 K, α is the thermal expansion coefficient at 300 K, *n* is the refractive index at λ = 1 μm, *dn*/*dT* is the thermal coefficient of the refractive index at λ = 1 μm, I_{thr} is the threshold of destruction by laser radiation with the wavelength λ = 1 μm for 10 ns, and *k* is the optical-absorption factor.

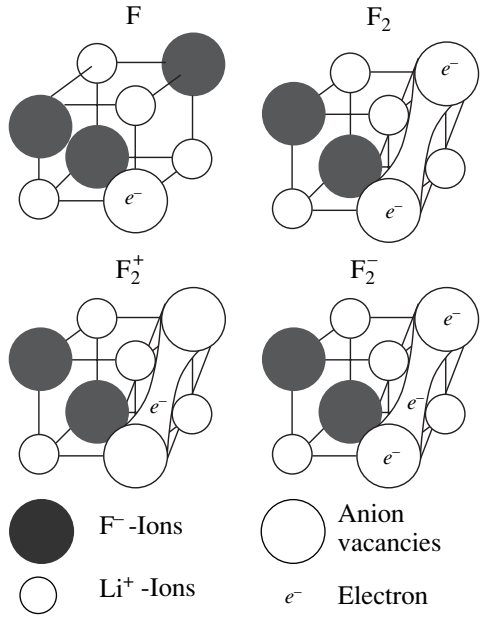

Fig. 6. Structure of the basic color centers in LiF crystals.

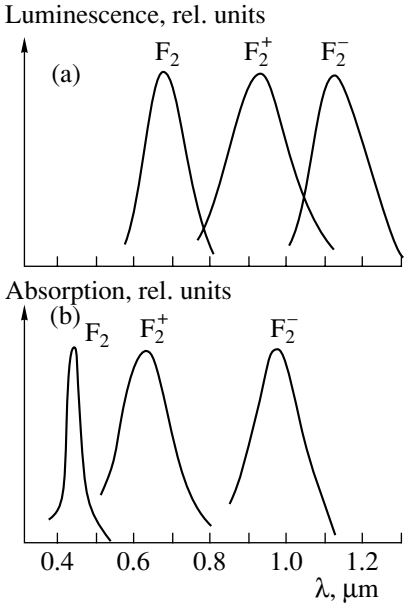

Fig. 7. Absorption and luminescence spectra of F_2, F_2^+, and F_2^- centers in LiF.

vacancy capturing two electrons), F_2^+ (pair with one electron), and F_2^- (pair with three electrons). Color centers are formed in originally colorless crystals either by heating crystals in the vapors of alkali or alkali-earth metals (so-called additive coloring) or by exposing them to hard radiation (γ rays, fast electrons, X-rays, or neutrons). In the first case, electrons for anion vacancies are supplied by hyperstoichiometric metal atoms. In the second case, radiation gives rise to the redistribution of electrons in the crystal and the corresponding number of holes are formed along with electrons localized at vacancies. Color centers formed by additive coloring are stable against heat and light, but particles that scatter light often appear in the crystals. Color centers formed by irradiation are unstable against heat and light, but the crystals maintain their original optical homogeneity. Moreover, a set of various color centers are simultaneously formed in both cases. The formation of aggregated color centers due to infrared radiation is a complex multistage process involving the formation of primary Fresnel pairs, their aggregation, and the recharging of aggregates by localizing electrons and holes at them. The basic processes leading to the formation of color centers in LiF can be schematically represented as follows [10]:

$$V_F + F \longrightarrow F_2^+,$$

$$F_2^+ + e \longrightarrow F_2,$$

$$F_2 + e \longrightarrow F_2^-,$$

where V_F is a fluorine vacancy, F is a fluorine vacancy capturing an electron (*F* center), and *e* is an electron.

Recently, technologies for producing photo- and thermostable LiF crystals with color centers have been developed. Crystals have a high optical density (the absorption coefficient reaches several inverse centimeters at the maxima of the absorption bands of color centers) and high contrast. The useful-to-background absorption ratio of color centers reaches 20–40. Crystals of LiF:F_2^+ described in [11] do not degrade under optical pumping in the range 0.62–0.75 μm up to an energy density of ~5 J/cm^2. The lifetime of these crystals is equal to 10 yr at 300 K. The efficiency of generating these elements reaches 50% (with respect to optical pumping). The use of LiF crystals slightly doped with Mg^{2+}, Li^+, and OH^{1-} and the use of various doses and intensities of radiation in combination with various temperatures at which irradiation is carried out are substantial features of the technologies proposed in [11]. Special multistage irradiation processes were also developed [12]. Figure 7 shows the spectra of the absorption and luminescence of basic color centers in LiF crystals. As is seen, a relatively wide spectral region can be covered by using various color centers with the same crystal.

In addition to tunable lasers based on crystals that have either transition elements or color centers and wide electron-vibration spectra of luminescence, the tuning of the radiation frequency of narrow-band laser crystals by changing their chemical composition has recently been developed.

VARIABLE-COMPOSITION TUNABLE SOLID-STATE LASERS

By changing the composition of a crystal via various isomorphic substitutions in the structure, one can regularly shift laser radiation wavelengths due to the nearest surrounding of active ions and to the corresponding change in the intensity of the crystal field acting on these ions. For crystals activated with transition-metal ions, this shift can be very substantial, because transitions are allowed and the action of the crystal field is strong. We emphasize that this feature allows the radiation frequency of crystals activated with transition-metal ions to vary over a wide wavelength range due to effective electron–phonon interaction.

Although crystals for lasers based on electron-vibration transitions, e.g., $LiSrAlF_6 : Cr^{3+}$, $Al_2O_3 : Ti^{3+}$, LiF : color center, etc., provide for widely tunable laser radiation, they have drawbacks typical of these systems: a low quantum yield and short half-lives of the upper laser level. At the same time, high quantum yield is necessary for the effective operation of a laser, whereas a long half-life considerably facilitates the diode pumping of the active medium.

The suitable level of these parameters is achieved in the case of using crystals activated by rare-earth ions. However, these crystals have narrow luminescence lines and their laser-radiation wavelengths cannot vary widely because their outer electron shells are effectively shielded. In this case, the laser radiation wavelength can be changed considerably by varying the composition of the matrix doped with an active ion. The discrete compositional change in laser radiation in the region near 1.06 μm was proposed in [13] for application in multichannel fiber optics communication lines with the use of a set of crystals with a garnet structure of various compositions: $Y_3Sc_2Ga_3O_{12}$ (λ = 1.0585 μm), $Gd_3Sc_2Al_3O_{12}$ (λ = 1.0602 μm), $Gd_3Sc_2Ga_3O_{12}$ (λ = 1.0612 μm), and $Gd_3Ga_5O_{12}$ (λ = 1.0621 μm). A finer compositional change ($\Delta\lambda$ = 0.003 μm) was proposed in [13] on the basis of solid solutions in a system of scandium garnets $Gd_3Sc_2Al_3O_{12}/Y_3Sc_2Ga_3O_{12}$.

The character and range of a compositional change induced in the radiation wavelength by isomorphic substitutions in the structure are determined by the laws of crystal chemistry and restricted by the range of existing solid solutions in a given system. In view of this circumstance, a recent attempt [14] to change the radiation wavelength in a $Y_3Ga_xAl_{5-x}O_{12}:Nd^{3+}$ system in the region of the 0.94411-μm absorption line of water vapors by varying the composition was doomed to failure, since the replacement of Al by Ga has special importance in this system [15] in connection with which $Y_3Ga_xAl_{5-x}O_{12}$ crystals of high optical quality can only be obtained for a very limited range of compositions.

Table 5. Crystals for variable-composition tunable lasers

Composition	λ_1–λ_2, μm	$\Delta\lambda$, μm
$YSAG_xGSGG_{1-x}$	1.06017–1.0612	0.00103
$YSGG_xYSAG_{1-x}$	1.0585–1.06013	0.00163
$YSGG_xGSAG_{1-x}$	1.0585–1.06017	0.00167
$GSAG_xGGG_{1-x}$	1.06017–1.0621	0.00193
$YSGG_xYAG_{1-x}$	1.0585–1.06415	0.00565

Note: Congruently melted compositions [15] were used as initial components of the solid solutions in the range $0 \le x \le 1$.

An important advantage of the solid solutions of scandium garnets is that, when the radiation wavelength varies over a wide (for rare-earth ions) range, other characteristics of the material change only slightly over the entire composition range [16]. In view of this circumstance, it is reasonable that Barnes *et al.* [14] later diverted from $Y_3Ga_xAl_{5-x}O_{12}$ crystals to gallium garnets [17]. Table 5 presents the compositions of the solid solutions based on rare-earth scandium garnets:

$$\text{YSAG: } \{Y_{2.89}Sc_{0.11}\}[Sc_{1.05}Al_{0.95}](Al_3)O_{12},$$

$$\text{GSAG: } \{Gd_{2.88}Sc_{0.12}\}[Sc_{1.77}Al_{0.23}](Al_3)O_{12},$$

$$\text{GSGG: } \{Gd_{2.95}Sc_{0.05}\}[Sc_{1.85}Ga_{0.15}](Ga_3)O_{12},$$

$$\text{YAG: } \{Y_3\}[Y_{0.01}Al_{1.99}](Al_3)O_{12},$$

$$\text{YSGG: } \{Y_{2.93}Sc_{0.07}\}[Sc_{1.36}Ga_{0.64}](Ga_3)O_{12}, \text{ and}$$

$$\text{GGG: } \{Gd_3\}[Gd_{0.05}Ga_{1.95}](Ga_3)O_{12},$$

as well as the corresponding ranges of varying the radiation wavelength of lasers based on the $^4F_{3/2}$–$^4I_{11/2}$ transition in Nd^{3+} ions.

CRYSTALS FOR WHICH STIMULATED RAMAN SCATTERING IS POSSIBLE

In 1962, studying the modulation of the *Q* factor of a ruby laser, Woodbury and Ng [18] first observed a kind of radiation that was later interpreted as the stimulated Raman scattering of light. Spontaneous Raman scattering can be treated as a two-photon resonance, where the difference in two optical frequencies, absorbed ν_L and emitted ν_S, is equal to the quantum vibration frequency of atoms in a molecule or crystal:

$$\nu_L - \nu_S = \nu_V.$$

The cross section for this two-photon optical process is very small ($\sigma \sim 10^{-30}$ cm^2). The intensity of stimulated Stokes scattering in the steady-state mode is

$$I_S(l) = I_S(O)\exp(gI_Ll),$$

where I_L is the intensity of incident laser radiation, l is the interaction length, I_S is the intensity of Stokes radiation, and g is the gain due to stimulated Raman scattering. Recent studies demonstrated that up to 50–80% of laser radiation incident on a medium can be transformed into stimulated Raman scattering radiation [19]. Because of such a high efficiency, stimulated Raman scattering can be used practically to create effective spectral transformers for laser-radiation sources. As was

mentioned in the Introduction, crystal transformers based on stimulated Raman scattering have a substantial advantage over gaseous and liquid transformers. High substance densities ensure the most compact interaction of exciting light with a substance, where stimulated Raman scattering is possible, and high gain [19]. Moreover, an ordered structure enhances the collective effect of the interaction with laser radiation, reduces the threshold of the effect, and raises the gain and efficiency of the transformation based on stimulated Raman scattering.

In view of an increasing interest in crystals where stimulated Raman scattering is possible it is necessary to extensively search for and comparatively analyze such crystals. Several tens of crystalline compounds have been recently examined. The basic parameters of Raman scattering were estimated from the results for spontaneous Raman scattering, which were obtained for both single crystals and polycrystalline samples [20]. Diamond and simple oxides are among crystalline compounds where Raman scattering is possible. However, compounds with complex anions involving oxygen present the widest group. Vibrations responsible for stimulated Raman scattering in these compounds are caused by centrally symmetric (breathing) motions of oxygen ions with respect to the central ion in the quasi-molecular groups $[CO_3]$, $[NO_3]$, $[PO_4]$, $[ClO_3]$, $[WO_4]$, $[NbO_6]$, $[IO_3]$, $[BrO_3]$, $[SiO_4]$, $[NbO_4]$, as well as hydrogen ions in $[NH_4]$ groups.

Table 6 presents the Raman scattering parameters of the basic compounds under consideration. The relative integrated and peak intensities and frequencies of Raman scattering, which characterize the frequency shift of incident radiation, were measured. The vibration frequencies in materials of various compositions are very different (from 250 to 1700 cm^{-1}). These data indicate that, having a set of numerous crystals where stimulated Raman scattering is possible, the laser radiation frequency can be discretely changed and shifted to the long-wavelength spectral region by values presented in Table 6. Among the listed crystals, diamond and compounds of tungstates, molybdates, niobates, and iodates have largest integrated scattering cross sections (600–900 cm^{-1}). On the other hand, the threshold and gain of stimulated Raman scattering when being pumped by short nano- and picosecond pulses are determined by a peak in the scattering cross section. In this parameter, crystals of nitrates, tungstates, and molybdates, along with diamond, stand out. Further analysis demonstrated that crystals simultaneously having large integrated cross sections for Raman scattering and narrow lines are the most preferable. Crystals of tungstates and molybdates of alkali-earth elements are of considerable interest in this respect [21]. Taking into account that the broadening of Raman scattering lines is associated with the interaction of high-frequency vibrations responsible for stimulated Raman scattering with lattice phonon modes, it is necessary to reduce the frequencies of these modes by choosing crystals with the heaviest ions among the homologous series. In particular, the width of the Raman scattering line of the familiar crystal $CaWO_4$ of the scheelite group is equal to $\Delta_\nu = 6.95$ cm^{-1}. The replacement of Ca^{2+} ions with Sr^{2+} and Ba^{2+} ions enables one to sharply retard relaxation and to narrow the Raman scattering line to 1.63 cm^{-1} (for $BaWO_4$). A rise in the ionic radius in the series Ca^{2+}, Sr^{2+}, Ba^{2+} and in the parameters of the crystal lattice increases the frequency of completely symmetric vibrations of group $[WO_4]$. These factors lead to both a considerable rise in the peak of the scattering cross section and in the gain due to stimulated Raman scattering. Similar regularities were also found in the homologous series of alkali-earth molybdates (see Table 6). The predictions based on studying spontaneous Raman scattering were corroborated by direct measurements of the gain [21] and generation of stimulated Raman scattering.

In our opinion, the above results indicate that the search for and creation of numerous new crystals for transformers based on stimulated Raman scattering are promising.

In addition to the above-discussed crystals for tunable lasers and transformers based on stimulated Raman scattering, nonlinear optical crystals are also extensively used in photonics. Among these crystals are noncentrosymmetric crystals such as lithium niobiumate and lithium tantalumate and their derivatives; a group of crystals based on potassium-titanyl phosphate; a wide group of borates of Groups I, II, and III, which includes metha-, ortho-, and oxoborates; a rich group of aqueous soluble hydrophosphates; and crystals of lithium iodate and some organic compounds. These crystals provide the following:

(i) the generation of higher harmonics, i.e., doubling, tripling, etc., the frequencies of the fundamental harmonics of lasers; e.g., the 1.064-μm radiation frequency of a YAG : Nd^{3+} laser can be sequentially transformed into 0.532, 0.355, 0.266, and 0.213 μm;

(ii) the mixing of frequencies, i.e., the production of the sum and difference of the radiation frequencies of different lasers;

(iii) the smooth variation of frequency, the so-called parametric light generation.

Nonlinear optical crystals were studied in numerous papers and monographs (see, e.g., [22]). In this paper, only the capabilities of nonlinear optical crystals as the sources of laser radiation with given wavelengths are compared.

A comparative analysis of the possibility of transforming the laser-radiation spectrum by means of the above methods provides the following conclusions.

In contrast to transformation based on stimulated Raman scattering, the generation of harmonics shifts the frequency to the short-wavelength spectral region by a value multiple to the fundamental frequency. This means that the transformation of harmonics cannot ensure the spectral variety inherent in transformation based on stimulated Raman scattering. Nevertheless, a shift to the blue and near ultraviolet spectral region is

Table 6. Crystals for the laser-radiation transformation based on stimulated Raman scattering

Crystal	Space group	Molecular group	Raman-scattering frequency ν, cm^{-1}	Raman-scattering line width Δν, cm^{-1}	Total scattering cross section, rel. units	Peak intensity, rel. units
Diamond	O_h^7		1332.9	2.7	100	100
		Nitrates and carbonates				
$Ba(NO_3)_2$	T_h^6	$[NO_3]$	1048.6	0.4	21	63
$NaNO_3$	D_{3d}^6	$[NO_3]$	1069.2	1.0	23	44
$CaCO_3$	D_{3d}^6	$[CO_3]$	1086.4	1.2	6.0	10.6
		Tungstates				
$CaWO_4$	C_{4h}^6	$[WO_4]$	910.7	6.95	47	18.6
$SrWO_4$	C_{4h}^6	$[WO_4]$	92.5	3		
$BaWO_4$	C_{4h}^6	$[WO_4]$	926.5	1.63	47	64
$NaGd(WO_4)_2$	C_{4h}^6	$[WO_4]$	919	14		
$NaY(WO_4)_2$	C_{4h}^6	$[WO_4]$	918	15		
$Sc_2(WO_4)_3$		$[WO_4]$	1024	15		
$In_2(WO_4)_3$		$[WO_4]$	1023	13		
$LiIn(WO_4)_2$		$[WO_4]$	920	8		
$NaSr(WO_4)_2$			924	2.5		
Na_2WO_4	O_h^7		929.2	1.8		
$KGd(WO_4)_2$	C_{2h}^6	$[WO_6]$	901	5.4	50	35
$KY(WO_4)_2$	C_{2h}^6	$[WO_6]$	905.6	7	46	35
$KYb(WO_4)_2$	C_{2h}^6	$[WO_6]$	908	7.4	48	34
		Molybdates				
$CaMoO_4$	C_{4h}^6	$[MoO_4]$	879.3	5.0	64	34
$SrMoO_4$	C_{4h}^6	$[MoO_4]$	887.7	2.8	55	51
$BaMoO_4$	C_{4h}^6	$[MoO_4]$	892.4	2.1	52	64
		Iodates and niobates				
$LiIO_3$	C_6^6	$[IO_3]$	821.6	5.0	54	25
$LiNbO_3$	C_{3v}^6	$[NbO_6]$	872	21.4	44	5
$LiNbO_3$	C_{3v}^6	$[NbO_6]$	632	27	166	18
$LiNbO_3$	C_{3v}^6	$[NbO_6]$	250	28		22
$LaNbO_4$	C_{2h}^3	$[NbO_4]$	805	9	22	7.1
		Phosphates				
$Ca_5(PO_4)_3F$	C_{6h}^2	$[PO_4]$	964.7	2.8	3.4	3.8
$Sr_5(PO_4)_3F$	C_{6h}^2	$[PO_4]$	950.3	2.8	3.4	3.8
$Li(PO_4)$		$[PO_4]$	951	7.7		
		Others				
$NaClO_3$		$[ClO_3]$	937	4.9		
$NaBrO_3$		$[BrO_3]$	799.5	2.5		
NH_4Cl	O_h^1	$[NH_4]$	1712	6		

very topical, because this spectral region is lacking in laser frequencies. The transformation based on stimulated Raman scattering has the following advantages over parametric light generation:

(i) higher quantum efficiency;

(ii) higher stability of energy parameters;

(iii) higher spatial uniformity of radiation and the absence of induced birefringence.

Fixed-frequency lasers in combination with tunable lasers based on stimulated Raman scattering and other nonlinearly optical transformers densely cover the near ultraviolet, visual, and near infrared spectral regions and provide a rich set of laser wavelengths for creating radiation sources having given wavelengths and required parameters (Fig. 8).

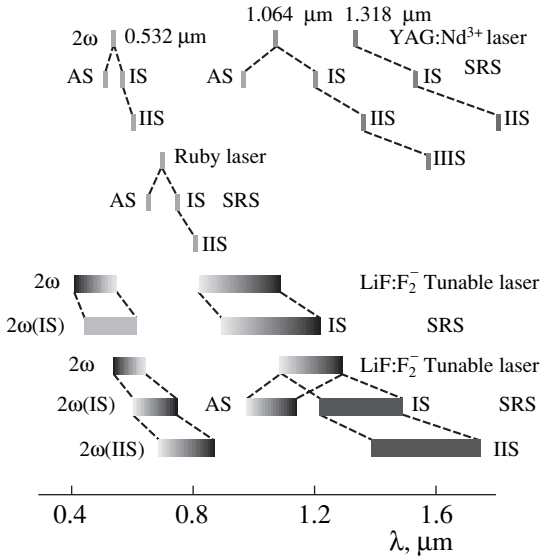

Fig. 8. Shifts of the radiation wavelengths of lasers by nonlinear crystals and crystals, where stimulated Raman scattering (SRS) is possible: 2ω is the second harmonic; IS, IIS, and IIIS are the first, second, and third Stokes component of stimulated Raman scattering; and AS is the anti-Stokes component.

CRYSTALS FOR THE PROJECT OF A LASER-EXCITED SODIUM STAR

The project of a laser-excited sodium star seems to be the greatest indication of the urgency of radiation sources with given wavelengths.

It is well known that the atmospheric optical aberration of celestial objects is the basic problem of ground-based astronomical observations. For this reason, astronomical instruments are situated on mountain peaks or in space. The project of a laser-excited sodium star aims at minimizing atmospheric distortions and returning telescopes and other instruments to the ground. In 1982, Happer suggested using the sodium-atom layer surrounding the Earth for this aim. The average altitude and thickness of this layer are equal to ~95 and ~10 km, respectively. The density of Na atoms is equal to only 5×10^{13} m^{-3}. Atmospheric sodium vapors have two narrow absorption lines at frequencies of $\lambda = 0.5892$ and 0.5896 μm corresponding to the transitions $3^2S_{1/2} \longrightarrow 3^2P_{3/2}$ and $3^2P_{1/2}$, respectively, and, correspondingly, two close emission lines.

If a laser emitting in resonance with one of the absorption lines of Na could be created, an artificial yellow star, whose light, passing to a ground-based, observer, undergoes the same distortions as that of the observed celestial objects would be illuminated at an altitude of about 100 km. Using special, the so-called additive, optics, it would be possible to compensate aberrations and, therefore, to refine images. Calculations indicated that this goal requires a laser with an average radiation power of 20 W, which can be realized [23].

There are several proposals for solving this problem. Humphreys *et al.* [24] suggested exciting the D_2 line of Na by a tunable dye laser. For this aim, Jeys *et al.* [25] later engineered a solid-state laser, where the frequencies 1.064 and 1.319 μm were mixed in lithium triborate [25].

An effective tunable laser that is based on LiF:F_2^- centers, has a frequency range of 1.08–1.27 μm, and is pumped by a YAG:Nd laser, whose radiation is generated with an efficiency of 30%, was engineered in 1982 [26]. The effective quasi-continuous generation of such a laser with pulse-repetition frequencies of 1–20 kHz was demonstrated in [27]. The transformation of a tunable harmonic to the second harmonic made it possible to tune it to the wavelength of the D_2 line of Na.

Recently, Zverev *et al.* [28] proposed a laser system that is based exclusively on crystals and can entirely satisfy the requirements of the laser-excited sodium star project with respect to energy parameters, the accuracy of spectral tuning, and the stability of a generated spectrum, which is especially important. The system involves a $BaWO_4$ crystal as a transformer based on stimulated Raman scattering and the $Gd_3Ga_5O_{12}$:Nd^{3+} crystal of Gd–Ga garnet with Nd (GGG:Nd^{3+}) as the active medium of a master laser. There are two variants of the laser scheme. In the first variant, the 1.0621-μm radiation of the GGG:Nd^{3+} laser is modulated by a LiF:F_2^- crystal. The modulated radiation with an pulse energy of 70 mJ and a duration of 15 ns is used to pump an element that is based on stimulated Raman scattering and is comprised of a $4 \times 4 \times 40$-mm $BaWO_4$ crystal situated between two planar dichroic mirrors of a cavity. For a pumping pulse energy of 65 mJ, the energy after the transformation that is based on stimulated Raman scattering and leads to the first Stokes component is equal to 15 mJ, which corresponds to a pump efficiency of 23%. After doubling the frequency via a $K(TiO)PO_4$ crystal, the radiation spectrum corresponds to the D_2 absorption line of Na.

In the second variant, the modulated radiation of the GGG:Nd^{3+} laser is first transformed to the second harmonic by means of a $K(TiO)PO_4$ crystal and, then, to the second Stokes component via the $BaWO_4$ crystal. The output pulse energy is equal to 4 mJ for the transformation efficiency of ~30% of the first Stokes component to the second one. Both schemes generate a 0.58895-μm line and have approximately identical energy parameters. The final fine tuning of the resonance was carried out by varying the temperature of the active GGG:Nd^{3+} element. The above-described setup has a high energy efficiency, has the desired generation spectrum, and satisfies the basic requirements of the project of a laser-excited sodium star. In addition to the above advantages, the proposed scheme can be scaled.

CONCLUSION

Macrophotonics is the most studied field among the three areas of photonics discussed in this paper. The technologies of growing many crystals and creating microphotonic elements based on these crystals have been developed considerably. Many specific problems of macrophotonics have already been solved. For this reason, we discussed advances in radiation sources with given wavelengths for applications to the problems of macrophotonics. In so doing, the results are of interest for microphotonics and (in certain extent) for nanophotonics, since we are dealing with the same physical phenomena and processes as in the case of macroobjects. At the same time, micro- and especially nanophotonics have their own specific problems associated with a scale factor.

The mechanisms of self-organization and self-assembly, which are associated with chemical thermodynamics, are of substantial or even determining importance for nanophotonics incipient at present and nanotechnologies that satisfy the demands of nanophotonics. In particular, crystallization is a promising example of this self-assembly. Advances in studying these mechanisms and understanding these processes open wide prospects for developing new technologies for creating nanocrystalline elements and nanophotonic devices.

ACKNOWLEDGMENTS

We are grateful to L.M. Ershova, K.A. Subbotin, and D.A. Lis for invaluable help in preparation of the manuscript.

REFERENCES

1. Y. Isyanova, J. G. Manni, and D. Welford, in *Advanced Solid-State Lasers, Seattle, 2001*, Ed. by Ch. Marshall (Optical Society of America, Washington, 2001), p. 107.
2. T. Gregorkievicz and J. M. Langer, MRS Bull. **24** (9), 27 (1999).
3. A. J. Steckl and J. M. Zavada, MRS Bull. **24** (9), 33 (1999).
4. S. John, Phys. Rev. Lett. **58**, 2486 (1987).
5. Sh. Fan and J. D. Joannopoulos, Opt. Photonics News **11** (10), 28 (2000).
6. B. E. Little and S. T. Chu, Opt. Photonics News **11** (11), 24 (2000).
7. A. P. Alivisatos, MRS Bull. **23** (2), 18 (1998).
8. J. Birnbaum and R. S. Williams, Phys. Today **53** (1), 38 (2000).
9. D. Bimberg, M. Grundman, and N. N. Ledentsov, MRS Bull. **23** (2), 31 (1998).
10. C. J. Delbecq, Z. Phys. **171**, 560 (1963).
11. T. T. Basiev, I. V. Ermakov, V. V. Fedorov, *et al.*, in *Proceedings of International Conference on Tunable Solid State Lasers* (Inst. Molecular and Atomic Physics, Minsk, 1994), Vol. 64, p. 64.
12. S. V. Mirov and A. Yu. Dergachev, Proc. SPIE **2986**, 162 (1997).
13. V. V. Firsov, N. V. Kravtsov, O. E. Nanii, *et al.*, in *Proceedings of the Optical Society of America* (Optical Society of America, Washington, 1993), p. 96.
14. N. P. Barnes, K. E. Murray, E. B. Ertur, *et al.*, in *Advanced Solid-State Lasers*, Ed. by S. A. Payne and C. Pollock (Optical Society of America, Washington, 1996), OSA Trends in Optics and Photonics Series, Vol. 1, p. 522.
15. E. V. Zharikov, Proc. SPIE **1839**, 46 (1992).
16. G. B. Lutts, V. I. Vlasov, E. V. Zharikov, *et al.*, Preprint No. 115, Inst. Obshcheĭ Fiziki Ross. Akad. Nauk (General Physics Institute, Russian Academy of Sciences, Moscow, 1990).
17. F. S. Ermeneux, R. W. Equall, R. L. Hutchison, *et al.*, in *Advanced Solid-State Lasers* (Optical Society of America, Washington, 1996), OSA Trends in Optics and Photonics Series, Vol. 26, p. 242.
18. E. J. Woodbury and W. K. Ng, Proc. IRE **50**, 2367 (1962).
19. T. T. Basiev and R. S. Powell, Opt. Mater. **11**, 301 (1999).
20. T. T. Basiev, Usp. Fiz. Nauk **169** (10), 1149 (1999).
21. P. G. Zverev, T. T. Basiev, and A. A. Sobol', Kvantovaya Élektron. (Moscow) **30**, 55 (2000).
22. A. M. Prokhorov and Yu. S. Kuzminov, *Physics and Chemistry of Crystalline Lithium Niobate* (Adam Hilger, Bristol, 1990).
23. W. Happer, G. J. Mac Donald, C. E. Max, and F. J. Dyson, J. Opt. Soc. Am. A **11**, 263 (1994).
24. R. A. Humphreys, C. A. Primmerman, L. C. Bradley, and J. Hermann, Opt. Lett. **16**, 1367 (1991).
25. T. H. Jeys, A. A. Brailove, and A. Mooradian, Appl. Opt. **28**, 2588 (1989).
26. T. T. Basiev, S. B. Mirov, and V. V. Osiko, IEEE J. Quantum Electron. **25**, 1052 (1988).
27. T. T. Basiev, P. G. Zverev, A. G. Papashvili, *et al.*, Kvantovaya Élektron. (Moscow) **27**, 759 (1997).
28. P. G. Zverev, T. T. Basiev, M. E. Doroshenko, and V. V. Osiko, in *Advanced Solid-State Lasers*, Ed. by H. Injevan, U. Keller, and Ch. Marshall (Optical Society of America, Washington, 2000), OSA Trends in Optics and Photonics Series, Vol. 34, p. 348.

Translated by R. Tyapaev

Crystallography Reports, Vol. 47, Suppl. 1, 2002, pp. S159–S168.

Nucleation and Growth of Crystalline Diamond Particles on Silicon Tips

E. I. Givargizov*, A. N. Stepanova*, L. L. Aksenova*, E. V. Rakova*, J. L. Hatchison, N. A. Kiselev*, E. S. Mashkova***, and V. A. Molchanov***†**

** Shubnikov Institute of Crystallography, Russian Academy of Sciences, Leninskiĭ pr. 59, Moscow, 117333 Russia*

e-mail: cvdlab@ns.crys.ras.ru

*** Department of Materials, University of Oxford, Parks Road, Oxford, OX1 3PH, UK*

**** Institute of Nuclear Physics, Moscow State University, Vorob'evy gory, 119489 Russia*

Received April 1, 1999

Abstract—The data on the deposition, structure, and electric properties of crystalline diamond particles at silicon tips grown on single-crystal silicon substrates obtained over the last decade, mainly at the Institute of Crystallography of the Russian Academy of Sciences, have been reviewed. It is shown that silicon emitters coated with crystalline diamond are highly electrically stable. They are used to prepare long-life cathodoluminescence light sources. *© 2002 MAIK "Nauka/Interperiodica".*

INTRODUCTION

Himpsel *et al.* [1] obtained experimental data on photoluminescence of diamond and came to the conclusion that this material is characterized by a broad forbidden gap and can possess a negative affinity to an electron; i.e., the emission of electrons from this material can considerably be facilitated. Since then, this material has attracted the ever increasing attention of researchers studying electron and, first and foremost, field electron emission. Within the last three decades, several dozens of publications have been devoted to the emission properties of diamonds.

At the same time, it is clear that the use of single crystal diamond as a material for emission is not expedient because of its extremely high cost. Therefore, it was suggested to use for the field emission of electrons, silicon tips coated with crystalline diamond particles [2, 3].

Below, we briefly review studies to this effect.

EXPERIMENTAL METHOD

Preparation of Silicon Tips

Silicon tips were prepared from silicon whiskers grown from the vapor phase by the vapor–liquid–solid (VLS) mechanism suggested by Wagner and Ellis in 1964 [4] and then further developed in [5, 6].

In essence, the method for growing whiskers on crystallographically oriented single-crystal silicon substrates reduces to the following. A single-crystal silicon substrate is oriented along the (111) close-packed face. Then a metal (gold, copper, silver, nickel, iron, platinum, etc.) particle is deposited to the substrate. During contact melting, a particle can form the liquid phase of the low-melting eutectics with the substrate. Heating to moderately high temperatures, e.g., up to 800–900°C, results in the formation of a droplet of silicon–gold alloy at the site of a particle. The interaction in the reactive mixture (e.g., silicon tetrachloride and hydrogen) that is passed above this substrate can result in the separation of silicon. At not too high temperatures, the corresponding reaction proceeds mainly at the liquid-phase surface. This is explained by the fact that although the reaction above the crystalline surface is thermodynamically possible, it is kinetically decelerated. At the same time, the ideally rough liquid surface intensely adsorbs the reaction components and catalyzes the reaction. As a result of silicon deposition on the surface of the droplet, the supersaturation of silicon with respect to its equilibrium concentration in the silicon–gold flux takes place; the excess silicon diffuses to the droplet–surface interface and crystallizes there. Upon further silicon deposition, the droplet is displaced from the substrate so that a single-crystal silicon column (whisker) grows under the droplet and epitaxially continues the substrate. If numerous catalyst particles are deposited onto the substrate, e.g., form a regular array of particles, then they provide the growth of a regular array of whiskers (Fig. 1). At the apex of each whisker, one can see a hemispherical particle ("globule"), which is, in fact, the crystallized liquid alloy formed by the mixture of silicon and gold microcrystallites.

The whiskers thus grown are used for the preparation of tips by chemical etching in the solution, which

† Deceased.

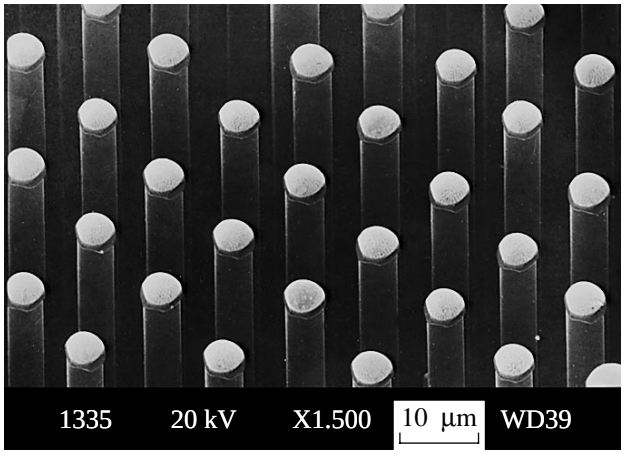

Fig. 1. Regular array of silicon whiskers. The micrograph obtained in a scanning electron microscope.

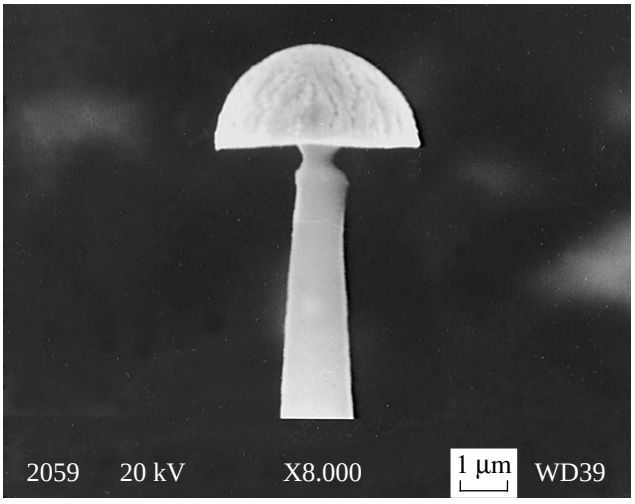

Fig. 2. Transient stage of the transformation of whiskers into tips upon chemical etching.

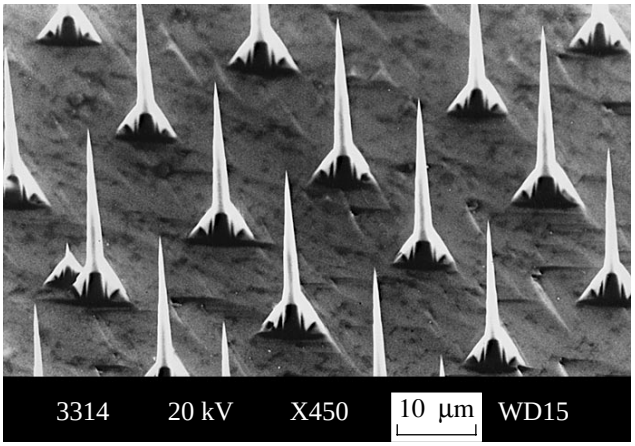

Fig. 3. Array of silicon tips prepared from the array of silicon whiskers.

reacts with silicon relatively slowly. In this case, etching proceeds from the globule–whisker interface with the formation of a mushroomlike structure (Fig. 2). At one of the subsequent stages of the process, the mushroom cap falls off and a silicon tip is formed. Figure 3 shows the system of silicon tips formed as a result of such a process.

Usually, the curvature radii of the tips do not exceed 20–30 nm. Some scatter in the curvature radii, hindering the use of these tips as field emitters because the emission is strongly dependent on the curvature radius of the tips.

The tips can be considerably sharpened by the method suggested by Marcus *et al.* [7]. The method consists in the alternating use of thermal oxidation of the tip and etching-off of the oxide in the solution with a considerable amount of the hydrofluoric acid. If oxidation of a silicon tip is performed in a certain temperature range (e.g., 900–950°C), then, at a certain curvature radius, the tip oxidation ceases because of the formation of pronounced mechanical stresses at the tip apex, since the SiO_2 oxide formed is characterized by a much lower thermal expansion coefficient than that of the silicon under it. Figure 4 shows the micrograph obtained in a transmission electron microscope of a silicon "ultratip" obtained by the oxidation–etching procedure. The silicon whisker was grown along the [111] crystallographic direction; the ultratip was oriented in the visual field of a microscope in such a way that the electron beam was transmitted along the atomic rows in the (111) plane. Thus, it was possible to achieve the atomic resolution. Each point on the micrograph corresponds to the atomic row in the silicon lattice, whereas the arrow at the apex indicates a single atom. The distance between the atomic planes of silicon along the [111] direction is 0.31 nm. Thus, the curvature radius of the tip is evaluated as 2–3 nm.

Deposition of Diamond Particles on Silicon Tips

As was indicated above, the field emission properties of diamond can be observed if one deposits diamond on silicon tips. It was established [2] that, under certain conditions, the diamond particles have the tendency to be deposited on the apices of silicon tips (Fig. 5).

Diamond particles are deposited by the standard hot-filament method of the chemical deposition of diamond from the vapor phase [8]. The chamber is filled with a methane–hydrogen mixture. At the hot filament, molecular hydrogen partly dissociates into atomic hydrogen, which reaches the silicon substrate with the tips onto which the diamond particles are deposited. The filament–substrate distance should not be too large in order to preserve as much as possible the dissociated state of hydrogen. The characteristic growth conditions are considered elsewhere [2].

In these experiments, the diamond particles were formed via spontaneous nucleation. A possible explanation of the preferable deposition of diamond particles on the silicon-tip apices will be given somewhat later.

Structure of Diamond Particles

The electron diffraction patterns from spherical diamond particles shown in Figs. 5a and 5b were obtained with an electron microscope.

One of the typical electron diffraction patterns is shown in Fig. 6 [9]. One can see the 111, 220, and 311 Debye rings characteristic of the diamond lattice (sp. gr. $Fd3m$); the lattice parameter equals $a = 3.56$ Å. The system of the recorded spot reflections belongs to the [110] zone of silicon.

The type of the reflections recorded on this electron diffraction pattern indicates that the spherical diamond particles consists of fine crystallites 3–5 nm large. Obviously, this microstructure is associated with pronouncedly nonequilibrium growth conditions of diamond particles provided by their relatively low crystallization temperatures (about 700°C) and high diamond supersaturations in the vapor phase.

As is well known, the hot-filament method used in this study for diamond crystallization is based on the fact that, at high temperatures, some hydrogen molecules H_2 dissociate into hydrogen atoms. Atomic hydrogen is a very active reagent, which can efficiently dissolve the nano- and microscopic particles of amorphous carbon formed during methane dissociation (in fact, these are particles of carbon black). Carbon in this form can suppress growth of crystalline diamond, which, as is well known, is a metastable carbon phase. This fact prevented the crystallization of diamond from the vapor phase for quite a long time, until it was shown [8] that this difficulty can be overcome by introducting of atomic hydrogen into the process. In fact, the method of diamond crystallization with the use of the microwave discharge suggested later [10] is also based this discharge creating a rather high concentration of atomic hydrogen. Atomic hydrogen can also dissolve crystalline diamond, but this process occurs at a rate lower by several orders of magnitude than the dissolution rate of carbon forming carbon black; i.e., we have here kinetically favorable conditions for deposition of diamond and not amorphous carbon. Then, it follows that the concentration of atomic hydrogen in the vapor phase is one of the factors determining the supersaturation during diamond crystallization: the higher the concentration of atomic hydrogen, the lower this supersaturation.

The degree of molecular-hydrogen dissociation into atomic hydrogen is strongly dependent on the temperature of the hot filament. At the temperatures used in our experiment, the degree of dissociation was 5–10%. The data on the dissociation of molecular hydrogen in the temperature range used for diamond deposition indicated in the table were obtained in accordance with the calculations performed by B.V. Spitsyn from the Institute of Physical Chemistry of the Russian Academy of Sciences. In accordance with these data, we performed

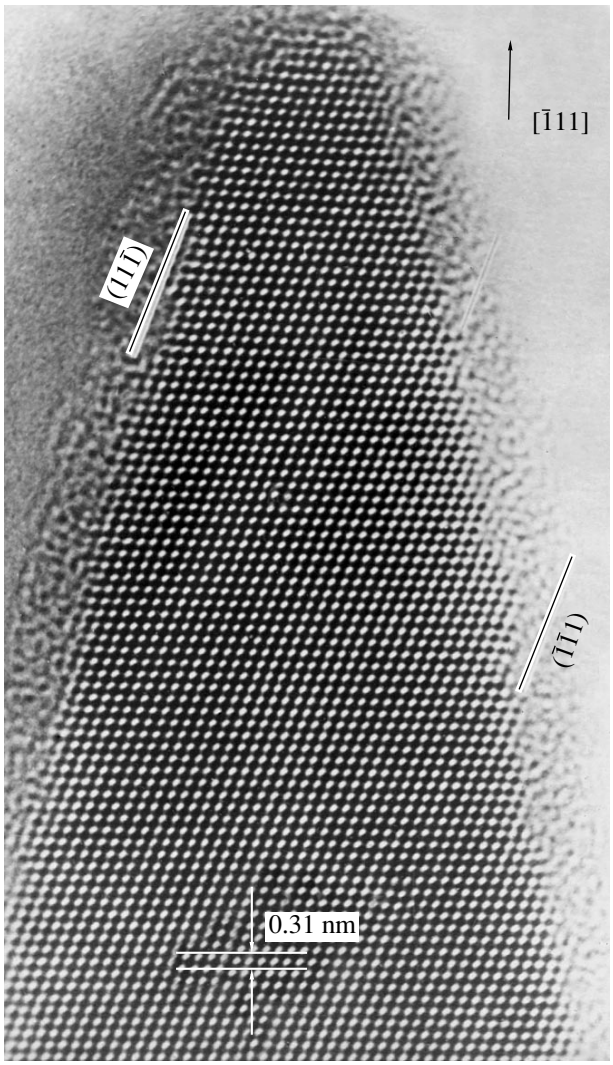

Fig. 4. Image of silicon "ultratip" obtained in a high-resolution transmission electron microscope. The coating is a layer formed from the vacuum-oil vapor deposited on the ultratip in the electron-microscope column. Figures in brackets indicate the crystallographic planes seen as the traces of the atomic rows. The arrow in the square brackets indicates the direction of growth of the whisker which provided the formation of the tip. The figures at the tip indicate the interplanar spacing in silicon along the ⟨111⟩ direction.

Fraction of atomic hydrogen (H) formed during dissociation of molecular hydrogen (H_2) under a total pressure of 25 torr

Temperature, °C	Fraction of H, %
1800	2
2000	6
2200	15

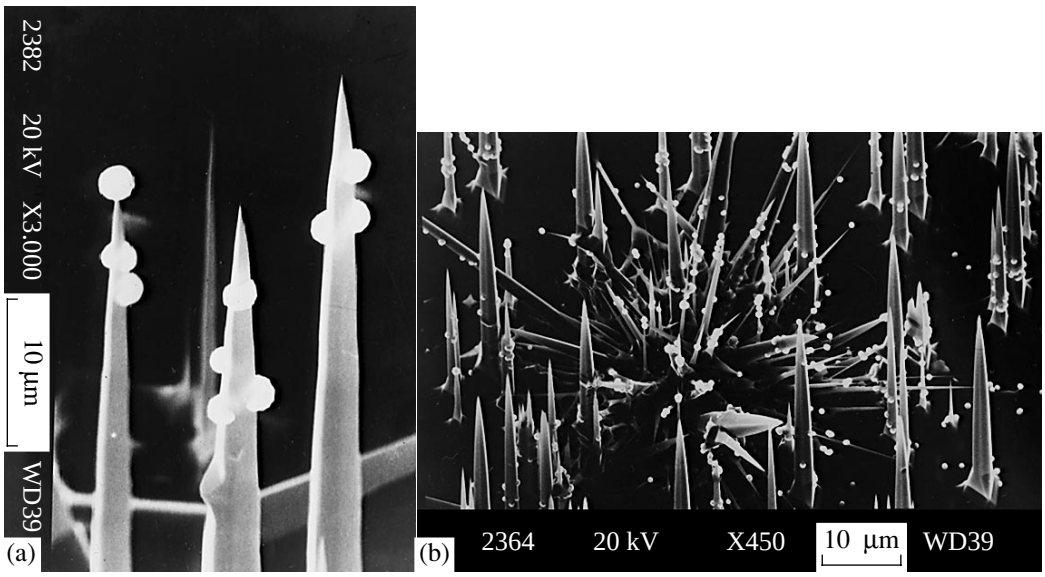

Fig. 5. (a, b) Deposition of diamond particles mainly at the apices of the silicon vertices or in the vicinity of these apices.

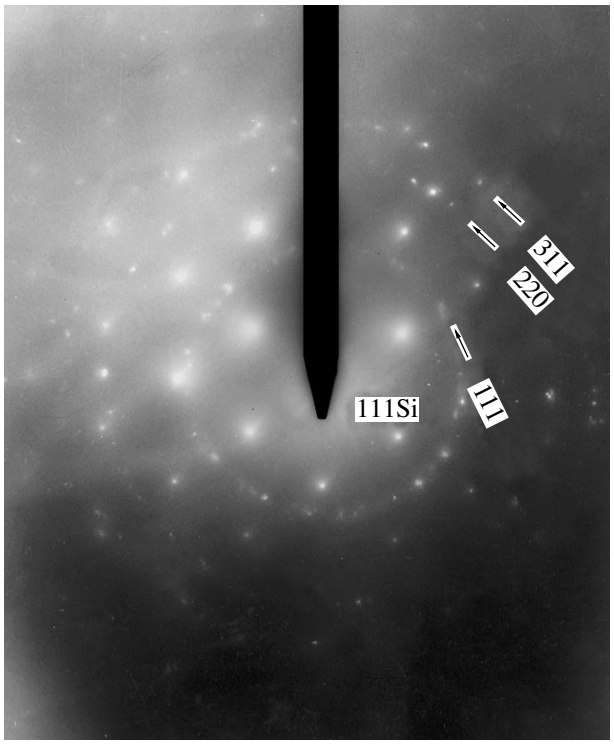

Fig. 6. Electron diffraction pattern from diamond particles analogous to those shown in Figs. 5a and 5b which were obtained with an electron microscope; 111 Si indicates that the whisker used to prepare the tip was grown along the [111] direction.

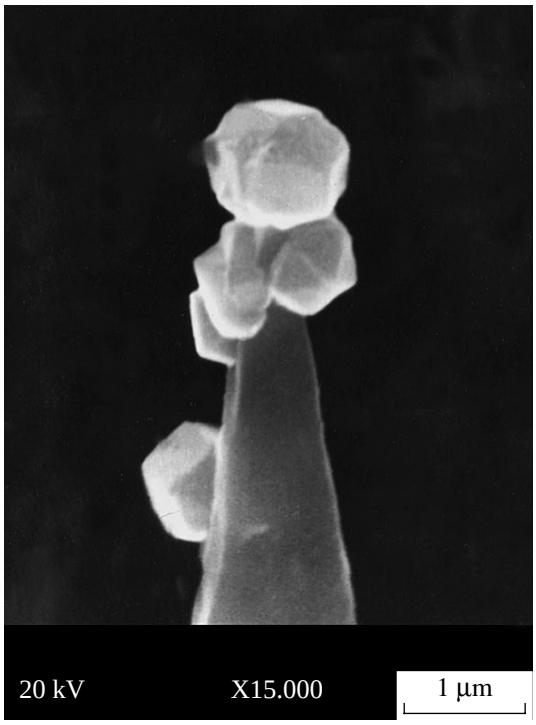

Fig. 7. Faceted diamond particles formed at the apex of a silicon tip at the elevated hot-filament temperatures.

the experiments on diamond crystallization at elevated filament temperatures (~2000°C). It turned out that, in this case, the nature of growth was considerably different—instead of fine spherical crystalline diamond particles, well-faceted single-crystal diamond crystals were formed (Fig. 7). At still higher hot-filament temperatures, well-faceted diamond single crystals were formed (Fig. 8) with the crystallographic shape corresponding to the ideal equilibrium shape of the diamond. It is important that, according to the position of this diamond crystal with respect to the silicon tip–substrate, we observed epitaxial growth of diamond on silicon,

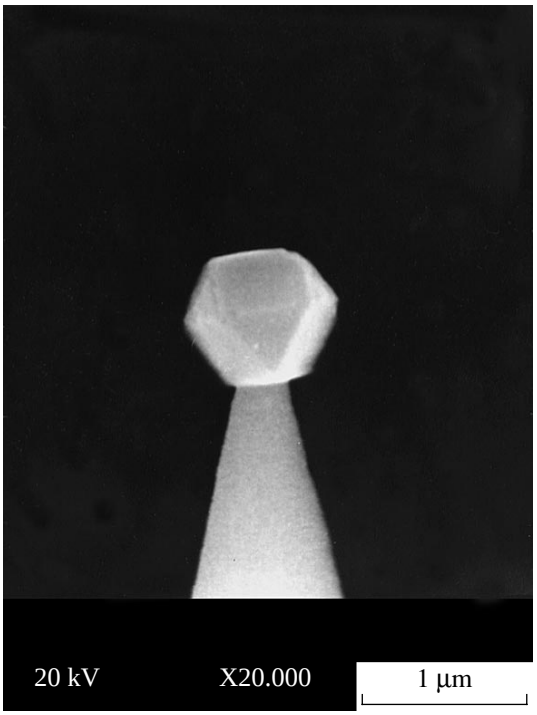

Fig. 8. Single-crystal diamond particle at the apex of a silicon tip.

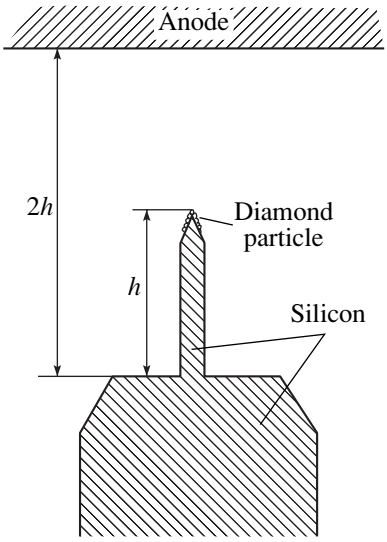

Fig. 9. Scheme for measurement of the field-emission properties of diamond particles; h is the tip height, $2h$ is the double (in comparison with the tip height) cathode–anode distance used in such measurements.

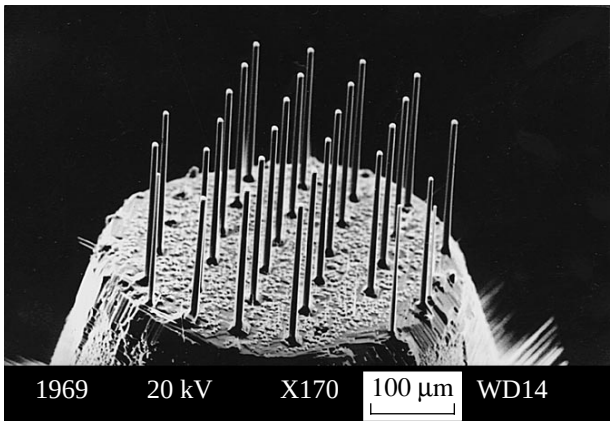

Fig. 10. Array of silicon whiskers grown at the end of a single-crystal silicon rod.

despite fact that the geometrical parameters of these related materials differ by about 34% [11]. This difference considerably exceeds the lattice mismatch between the substrate and the film theoretically admissible in epitaxial growth (about 10%). This can be explained by the fact that the geometric conditions for epitaxial growth considerably differ if one considers two crystal lattices on very small areas. In this case (Fig. 8), the areas are about 0.25 μm^2.

Study of Field Emission from Diamond Particles

These experiments were performed in the apparatus of the diode configuration schematically shown in Fig. 9. The system of silicon whiskers was grown on a plane end of a single-crystal silicon rod along the [111] direction (Fig. 10). The whiskers were sharpened by the methods considered above and coated with diamond particles. Then all the tips except one were mechanically removed by a steel or tungsten needle. The remaining tip with diamond particles was positioned as shown in Fig. 9. The field emission was measured in a vacuum of 10^{-7}–10^{-8} torr, and the corresponding current–voltage characteristics of the emitter was plotted (Fig. 11). The results obtained are discussed below.

DISCUSSION OF RESULTS

Deposition of Diamond Particles

As was indicated above, the diamond particles shown in Fig. 5 were formed via spontaneous nucleation. At first glance, deposition of diamond particles at the tip apices contradicts the classical concepts of crystal growth from the vapor phase: one would expect that, during spontaneous nucleation, the crystals would have been deposited, first and foremost, at the tip base (root), where there are numerous reentrant angles favorable for both nucleation and further growth of nuclei. Here, we interpret the preferable nucleation and growth of particles at the tips of silicon whiskers. At least two important circumstances should be taken into account:

—the behavior of atomic hydrogen present in considerable amounts (about several percent) in the vapor phase;

—relatively low heat conductivity of silicon as a semiconductor material.

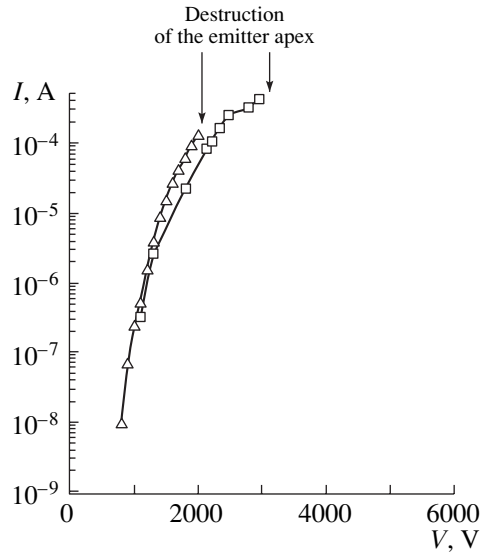

Fig. 11. Current–voltage characteristics of silicon tips coated with diamond prior to their destruction by the transmitted electric current. △, sample 1; □, sample 2.

These two factors are responsible for a considerably higher temperature of the tip relative to the substrate (measured by a thermocouple).

An increase in the tip temperature is explained mainly by possible efficient recombination of atomic hydrogen into molecular hydrogen with the accompanying evolution of a large amount of energy—the transformation heat has quite a high value—103 kcal/mol. The tip is characterized by a considerable geometric factor; i.e., it receives a large amount of atomic hydrogen from the sphere with a radius of the order of the free path length of molecules in the methane–hydrogen mixture. In the mixtures used in our experiments, this factor was equal to about 10 μm. At the same time, the conditions for recombination of atomic hydrogen in the molecular vapor phase (i.e., under homogeneous conditions) are rather unfavorable, because the law of conservation of the mechanical pulse is not maintained. Thus, intense recombination is observed at the apex. However, the evolved energy cannot be readily removed from the tip apex because the thermal conductivity of silicon is not high enough (it is lower by an order of magnitude than that of classical metals).

We estimated an increase in the temperature of the silicon tip, which showed that the temperature of the tip apex exceeds the temperature of its base by about ~200°C, which gives rise to the preferable deposition of diamond at the tip apex (the dependence of the diamond growth rate on temperature is considered in [12–14]). The model of preferable deposition of diamond at the tip

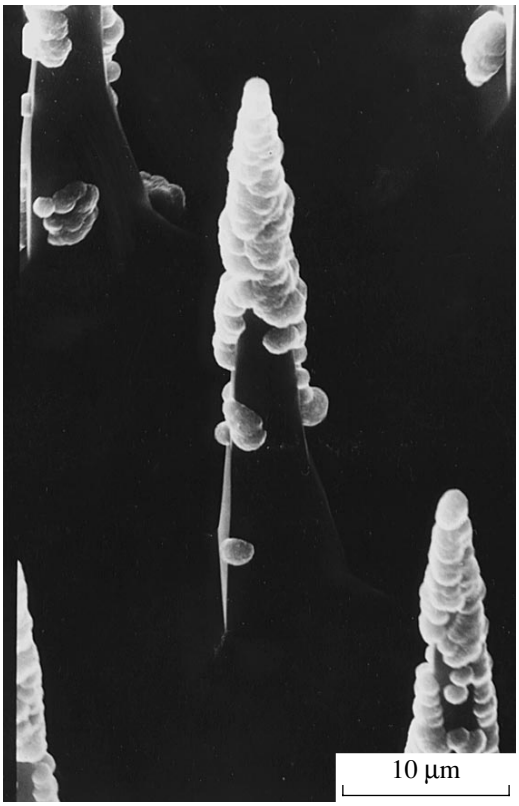

Fig. 12. Preferable deposition of diamond particles at the upper parts of silicon tips.

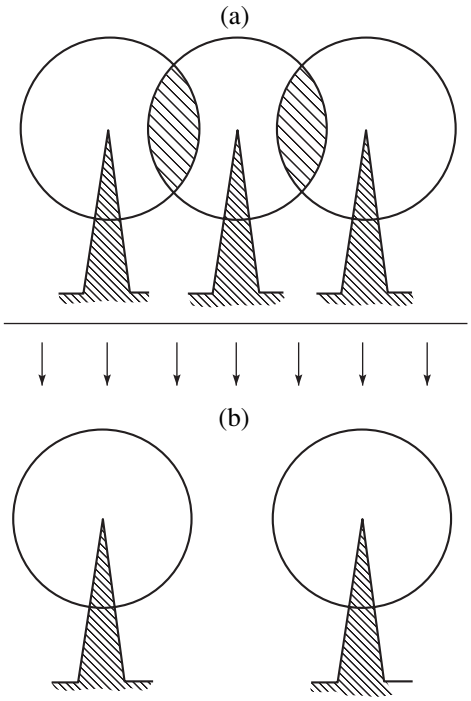

Fig. 13. Schemes of feeding of two different tip systems. (a) Tips located rather close to one another: the feeding spheres of neighboring tips overlap; i.e., feeding of the lower parts of the tips is hindered. (b) Tips spaced at large distances from one another; individual tips are fed independently of one another.

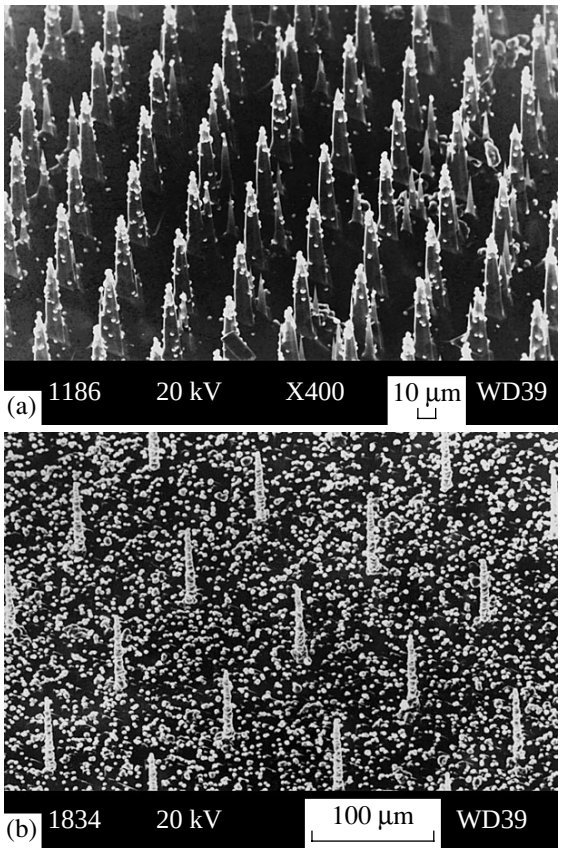

Fig. 14. Overgrowth of silicon tips depending on the spacings separating these tips. (a) The tips located comparatively close to one another; overgrowth occurs only at their upper portions. (b) Tips spaced by considerable distances from one another; overgrowth proceeds everywhere from their apices to their bases.

apex or in the vicinity of it is also confirmed by our experiments with forced diamond nucleation.

Growth of diamond particles on such substrates showed that, under certain conditions (see below), the overgrowth of diamond particles on the tips is initiated at the tip apices and decreases to the tip base. This is clearly seen in Fig. 12.

This phenomenon is explained by the specific features of crystallization from the vapor phase. We have already indicated that the average free path of the molecules in the methane–hydrogen mixture used in our experiments under a total pressure of 25 torr is about 10 μm. In this case, the sphere of feeding of the tips with the diamond material is about 10 μm.

If the distances between such tips are of this order of magnitude or less, they can compete with one another to be fed with the diamond material (see the scheme in Fig. 13a). In this case, only the diamond nuclei deposited close to the tip apices grow intensely. If the distances between the neighboring tips are much larger, the deposition of the diamond particles on different tips proceeds independently of deposition on other tips

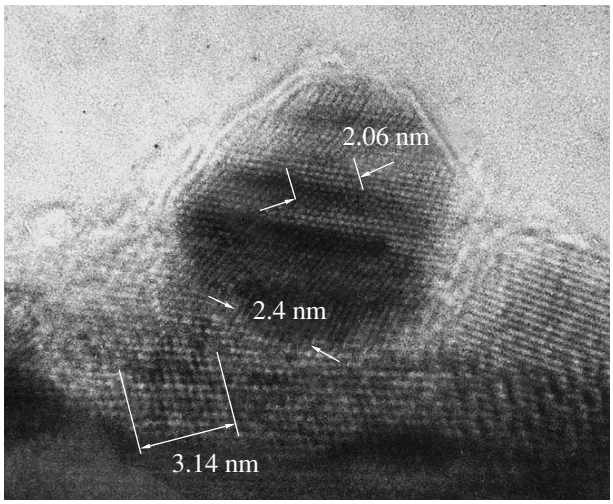

Fig. 15. Diamond particle formed at the silicon tip with the formation of an intermediate silicon carbide layer. The region indicated by 2.4 nm relates to silicon carbide. The regions indicated by 2.06 and 3.14 nm relate to diamond and silicon, respectively (these figures correspond to tenfold lattice constants of these materials).

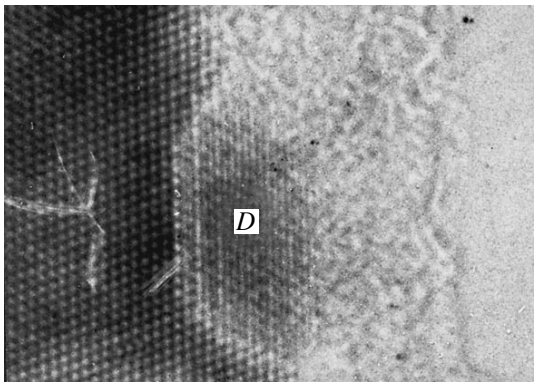

Fig. 16. Epitaxial growth of diamond lattice on silicon; *D* is a diamond crystallite overgrown on the silicon tip shown on the left.

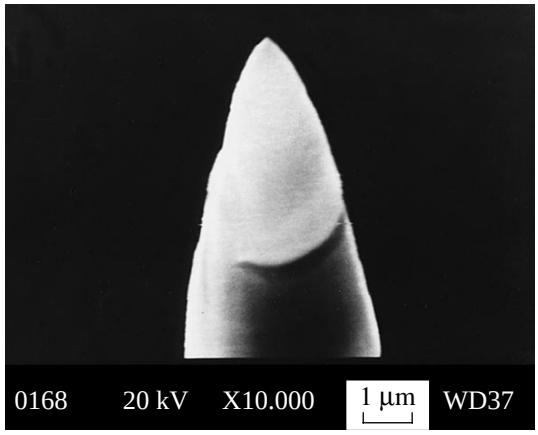

Fig. 17. Diamond particle on a silicon tip upon etching by 30 keV argon or nitrogen beams.

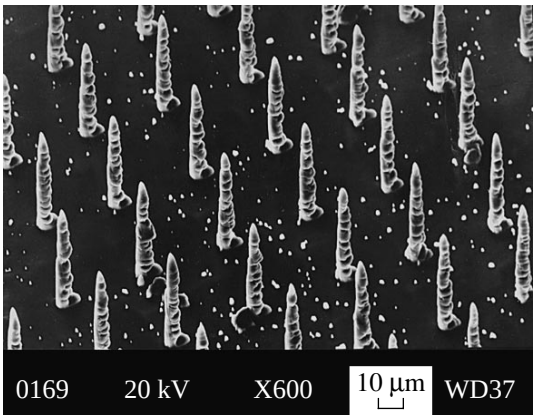

Fig. 18. System of diamond particles on silicon tips sharpened by a high-energy ion beam.

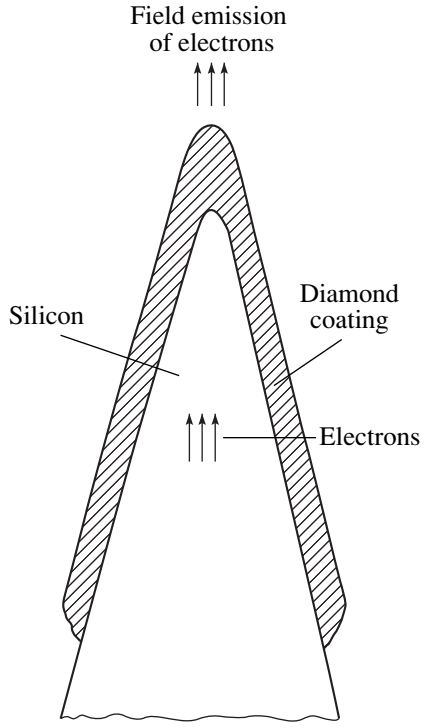

Fig. 19. Illustrating the action of a silicon emitter coated with a layer of crystalline diamond.

(scheme in Fig. 13b). This interpretation is confirmed by overgrowth of two different tip systems with diamond particles (Figs. 14a and 14b).

Structure of Diamond Particles Formed on Silicon Tips. Possible Epitaxial Growth

Studies using a high-resolution transmission electron microscope revealed at least three variants of possible growth of diamond particles on silicon tips [9]:

—The formation of an amorphous layer between the diamond particle and the silicon tip without the formation of any specific orientational relationships between the crystal lattices of diamond and silicon.

—The formation of an intermediate silicon carbide layer between the diamond particle and the silicon tip (Fig. 15). Here, an 8-nm-large diamond particle and the silicon tip are separated by a crystalline layer. The lattice parameter of this layer (about 0.25 nm) is very close to the lattice parameter of silicon carbide. Moreover, one can also see twinning in the diamond particle in Fig. 15.

—It is also possible to observe the direct overgrowth of a diamond particle on silicon. One can conclude from the micrograph in Fig. 16 that the diamond particle is grown directly on silicon (without the formation of an intermediate layer), although one cannot conform this statement because of the insufficient resolution of the micrograph.

Ion Etching of Diamond Particles on Silicon Tips

It is well known that the field emission is strongly dependent on the curvature radius of the emitter. At the same time, the deposition of diamond particles on a silicon tip considerably increases its curvature radius. Therefore, it is very desirable to sharpen the diamond particle grown.

It is well known that diamond is a chemically stable material and, therefore, chemical etching can hardly be used to sharpen diamond particles.

The problem was solved using ion sharpening, i.e., the treatment of diamond particles by directed beams of argon ions or molecular nitrogen [15]. The 30 keV Ar^+ or N_2^+ beams were directed along the tip axis. As a result, the diamond particle was sharpened up to a curvature radius of about 50 nm (Fig. 17). In a similar way, one can also obtain a system of diamond tips (Fig. 18).

As was established by high-resolution transmission electron microscopy, sharpening with high-energy ions results in amorphization of the surface layers of diamond particles with the preservation of some inclusions of crystalline diamond. These sharpened tips were used in field-emission measurements [15].

Electrical Characteristics and Some Applications of Diamond Emitters

The possibility of coating silicon tips with diamond particles and then sharpening the tips by ion bombardment (reducing the curvature radii) make these emitters rather promising for various applications in emission electronics.

Figure 11 shows the current–voltage characteristics of two silicon tips–emitters coated with diamond. It is

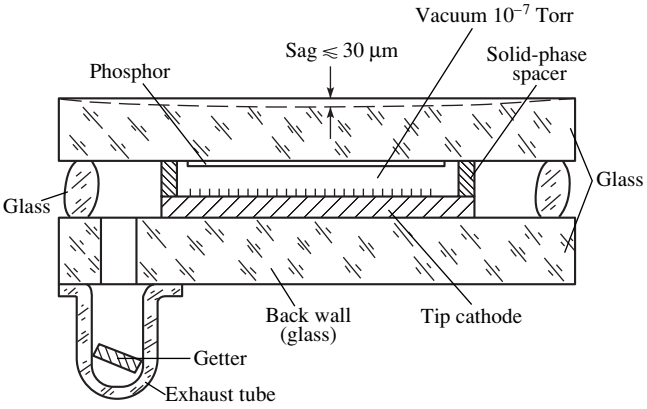

Fig. 20. Scheme of a plane cathodoluminescence lamp based on an array of diamond emitters.

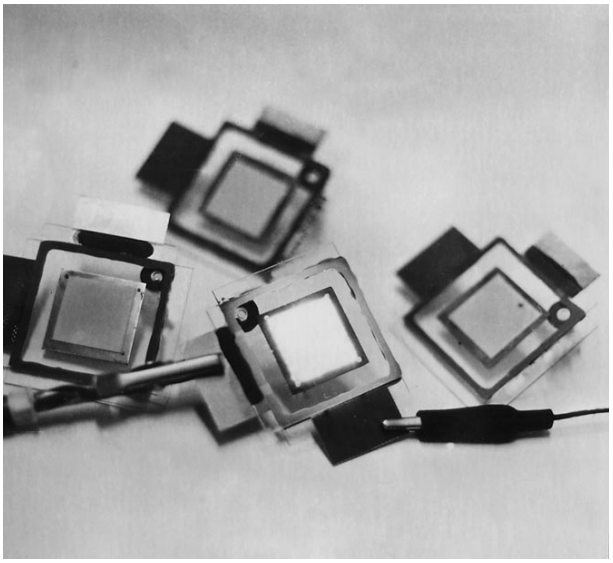

Fig. 21. Cathodoluminescence lamps prepared in accordance with the scheme in Fig. 20. The luminescent part of the tip cathode of the lamp has dimensions of 25×25 mm.

seen that one of the emitters can sustain a current of up to 150 μA, whereas the other, up to 450 μA. For comparison, the silicon-tip emitter not coated with diamond can sustain a current of several tens of microamperes A [16, 17], i.e., much lower (by an order of magnitude). Stronger currents result in a discharge at the tip apex and destruction of the emitter. In our case, the silicon tip was coated with diamond. The scheme of such a coating, corresponding to Fig. 17, is shown in Fig. 19. It is well known that diamond possesses extremely high mechanical strength. Diamond is also characterized by heat conductivity considerably exceeding the heat conductivity of copper.

Figure 19 illustrates the operation of this electron emitter. The maximum density of the emission current is observed at the tip apex. The electric current heats the tip, which results in the discharge mentioned above.

In the case of diamond coating, the high heat conductivity of diamond provides heat removal, and the tip becomes stable and is not destroyed.

The detailed electrical characteristics of diamond emitters can be found in [18].

An emitter consisting of a system of silicon tips coated with diamond can be used as long-life cathodes in plane cathodoluminescence lamps [19, 20], schematically shown in Fig. 20. The application of 2000–3000 V between the tip cathode and the anode coated with phosphor results in the electron emission from the tips and their acceleration to high energies. These electrons impinge the phosphor and give rise to its luminescence.

Some of such lamps are shown in Fig. 21; to one of them (in the center) the voltage is applied and the luminescence arises.

CONCLUSION

The method of deposition of diamond particles onto the apices of silicon tips prepared from whiskers grown on a single-crystal (111) oriented substrate by the vapor–liquid–solid mechanism has been developed. Diamond particles were deposited from a methane–hydrogen mixture by the hot-filament method. It is established that at relatively low filament temperatures, the deposited diamond particles are spherical and have fine crystalline structure, whereas at high filament temperatures (~2000°C), the particles are faceted and have single-crystal structure. The single-crystal diamond particles were sharpened to nanometer curvature radii by their bombardment with directed argon or nitrogen ions accelerated up to 30 keV. The silicon emitters coated with crystalline diamond are (by an order of magnitude) stable to strong emission currents. The diamond particles deposited on regular systems of silicon tips are used to prepare long-life cathodoluminescence light sources.

ACKNOWLEDGMENTS

The authors are grateful to their colleagues who participated in this study: A.N. Kiselev for obtaining high-resolution electron-microscopy images, V.I. Muratova and V.G. Galstyan for obtaining images on a scanning electron microscope, L.N. Obolenskaya for growing silicon whiskers, N.A. Verezub for the calculating tip temperatures, and O.B. Vol'skaya for micrographs.

REFERENCES

1. F. J. Himpsel, J. A. Knapp, J. A. van Vechten, and D. A. Eastman, Phys. Rev. B **20**, 624 (1979).
2. E. I. Givargizov, V. V. Zhirnov, A. V. Kuznetsov, and P. S. Plekhanov, Mater. Lett. **18**, 61 (1993).
3. E. I. Givargizov, J. Vac. Sci. Technol. B **13**, 414 (1995).
4. R. S. Wagner and W. C. Ellis, Appl. Phys. Lett. **4**, 89 (1964).

5. E. I. Givargizov, J. Cryst. Growth **31**, 20 (1975).
6. E. I. Givargizov, J. Vac. Sci. Technol. B **11**, 449 (1993).
7. R. B. Marcus, T. S. Ravi, T. Gmitter, *et al.*, Appl. Phys. Lett. **56**, 236 (1990).
8. B. V. Spitsyn, L. L. Bouilov, and B. V. Derjaguin, J. Cryst. Growth **52**, 219 (1981).
9. E. I. Givargizov, L. L. Aksenova, V. G. Galstyan, *et al.*, J. Cryst. Growth **162**, 73 (1996).
10. S. Matsumoto, Y. Sato, M. Kamo, and N. Setaka, Jpn. J. Appl. Phys. **21**, L183 (1982).
11. A. N. Stepanova, L. L. Aksenova, A. V. Kuznetsov, *et al.*, Mater. Lett. **22**, 285 (1995).
12. E. Kondoh, T. Ohta, T. Mitomo, and K. Ohtsuka, Appl. Phys. Lett. **59**, 488 (1991).
13. K. A. Snail and C. M. Marks, Appl. Phys. Lett. **60**, 3135 (1992).
14. A. Yamaguchi, M. Ihara, and H. Komiyama, Appl. Phys. Lett. **64**, 1306 (1994).
15. E. S. Mashkova, V. A. Molchanov, A. N. Stepanova, *et al.*, Poverkhnost, No. 3, 64 (1997).
16. I. Brodie and C. A. Spindt, Adv. Electron. Electron Phys. **83**, 1 (1992).
17. H. F. Gray and J. L. Shaw, Vide, Suppl. **271**, 29 (1994).
18. V. V. Zhirnov, A. B. Voronin, E. I. Givargizov, and A. L. Meshcheryakova, J. Vac. Sci. Technol. B **14**, 2034 (1996).
19. E. I. Givargizov, V. V. Zhirnov, A. N. Stepanova, and N. N. Chubun, in *SID International Symposium: Digest of Technical Papers, 1997*, p. 369.
20. T. E. Felter, A. A. Talin, D. A. A. Ohlberg, *et al.*, in *SID International Symposium: Digest of Technical Papers, 1998*, p. 577.

Translated by L. Man

Crystallography Reports, Vol. 47, Suppl. 1, 2002, pp. S169–S176.

REAL STRUCTURE OF CRYSTALS. GROWTH OF FILMS. NANOCRYSTALS. TIP STRUCTURES

Growth of a Si Nanocrystal in an Oxygen Atmosphere. Computer Simulation

A. E. Galashev

Institute of Thermal Physics, Ural Division, Russian Academy of Sciences, ul. Pervomaĭskaya 91, Yekaterinburg, 620219 Russia

e-mail: galashev@itp.uran.ru

Received April 1, 1999

Abstract—Growth of a Si nanocrystal in vacuum and in atomic-oxygen atmosphere was simulated on the basis of molecular dynamics. SiO_x nanoparticles (x = 0–0.42) containing up to 302 atoms were obtained. The shape of the nanocrystals was primarily determined by the amount of oxygen contained in them. The growth of nanocrystals in an oxygen atmosphere was accompanied by the formation of oxygen clusters inside a nanoparticle, which gave rise to considerable internal stresses. In most cases, structural relaxation increases the volume of SiO_x nanocrystals and decreases internal pressure. The angular and topological statistical characteristics of Voronoi polyhedra are indicative of a structural irregularity in oxygen clusters formed inside Si nanoparticles.

INTRODUCTION

The initial stage of crystal growth remains poorly studied, because nanoscale experiments are difficult. Nevertheless, a theory of the growth of macroscopic crystals [1] was developed on the basis of experimental data. For layer and normal growths of crystals, the surface of a growing crystal is smooth and rough, respectively. In semiconductor crystals (Si, Ge), isolated smooth faces can coexist with rough surfaces. Growth from a gaseous phase usually proceeds via layer crystallization. In this case, adsorbed atoms diffuse over the crystal surface. Rough-surface crystals usually have round shape, whereas smooth atomic surfaces form faces. Layer growth is accompanied by the nonequilibrium capture of impurities. In the absence of gravity, the convective removal of gas from the crystallization front is hindered, and the crystal is enriched with gas inclusions. Impurities are responsible for internal stresses, dislocations, and cracks.

In this study, the growth of Si nanoparticles in the absence of gravity is simulated in the case where the Si ions necessary for growth are supplied to a cooled zone from an ion beam, and the condensation region is either initially under vacuum or contains atomic oxygen.

MOLECULAR DYNAMICS MODEL

Two-stage calculations were carried out in the framework of the NVT ensemble. At the first stage, the growth of Si nanocrystals via the condensation of Si vapor either in vacuum or in oxygen atmosphere was simulated. Silicon from ion beams was supplied to the cooled zone held at a constant temperature of 300 K by the thermal-bath algorithm proposed in [2]. At the second stage, the structural relaxation of nanocrystals obtained at the first stage was studied at the same temperature. The set of equations of motion was solved by the Beeman finite-difference algorithm [3] with the time step Δt = 0.038317 fs, which is one-tenth of the step used in simulating large (extended) pure-silicon systems [4]. The first and second stages are completed in (1.5–1.7) $\times$ 10^6 Δt and 10^6 Δt, respectively. The flux of ions is simulated as their motion through a cylindrical channel with a radius of 5σ that is initially divided by equidistant sections spaced by σ, where σ = 0.20951 nm is the characteristic size used to describe interactions in silicon [2]. Five Si ions were randomly distributed over the volume of every cylindrical region bounded by two neighboring sections. All Si ions in the channel at the initial time had identical velocities, which were directed to the condensation region and correspond to 3000 K. The condensation region was a 9.0σ-radius sphere whose center was at the axis of the cylindrical channel through which Si ions moved. The condensation region was initially either empty (under vacuum) or randomly filled with oxygen atoms. Arriving at the condensation region, Si ions were randomly distributed so that they were spaced by no less than 0.304 nm, whereas distances between them and oxygen atoms located in this region were no larger than 0.160 nm [5]. At regular intervals of 10 000 Δt, we used a procedure aimed at distributing a successive group of ions located in the condensation zone so that they were attached to the cluster. The entire condensation region was divided into cells by accomodating in it a fictitious diamondlike lattice whose constant a = 0.542 nm coincided with the corresponding value for a Si crystal. The lattice site nearest to the center of the condensation region was the first candidate for being occupied by

ions located in the condensation region at a given time. Further, for every ion, we found an optimal free lattice site, i.e., a site closest to both this ion and the center of mass of the cluster. This ion was placed at a random point of the 0.25σ-radius sphere whose center was at the corresponding site. When the condensation region was initially filled with oxygen, oxygen atoms were similarly attached to the cluster in agreement with the above cluster-forming procedure.

The growth of the nanoparticle was simulated with the Jiang–Brown interatomic potential [6], which includes both the pair and the triple interactions and accounts for competition between ionic and covalent chemical bonds. In essence, the Jiang–Brown potential is a combination of the improved Beest–Kramer–Santen potentials [7] used to simulate a SiO_2 system and the Stillinger–Weber potential [4] used in computer simulations for the Si model. Thus, the total potential energy of the system is given by

$$E(\{\mathbf{r}_i\}) = \sum_i e_i(q_i) + \sum_{i<j}[\nu_2(i,j) + \phi_{ij}] + \sum_{i<j<k}\nu_3(i,j,k), \quad (1)$$

where $\{\mathbf{r}_i\}$ is the set of the radius vectors of particles; (i, j) and (i, j, k) are the sets of distances between corresponding pairs and triples of atoms, respectively; and the other quantities defined below. The energy and length units are $\varepsilon = 11.94$ J/mole and $\sigma = 0.20951$ nm, respectively. Both values are used in the Stillinger–Weber potential for silicon. Formula (1) involves the Beest–Kramer–Santen potential

$$\phi_{ij} = q_i q_j / r_{ij} + A_{ij}\exp(-b_{ij} r_{ij}) - c_{ij}/r_{ij}^6. \quad (2)$$

Here, r_{ij} is the distance between the ith and jth atoms; A_{ij}, b_{ij}, and c_{ij} are the parameters depending on the kind of atoms (Si or O); and

$$q_i = \begin{cases} \sum_{j\subset O} q_O H(r_{ji}), & i \subset \mathrm{Si} \\ \sum_{j\subset \mathrm{Si}} q_O H(r_{ji}), & i \subset \mathrm{O} \end{cases} \quad (3)$$

is the effective charge of the ith atom. Here, q_O is a constant and

$$H(r) = \begin{cases} 1, & r < r_0 \\ \frac{1}{2} + \frac{1}{2}\cos\left(\pi\frac{r - r_0}{r_s - r_0}\right), & r_0 \le r \le r_s \\ 0, & r > r_s \end{cases} \quad (4)$$

is the charge transfer function, where r_s and r_0 are the parameters.

The remaining part of the pair interaction in (1) is related to the Stillinger–Weber potential as

$$\nu_2(i,j) = \begin{cases} g_{ij} f_2(r_{ij}), & i \subset \mathrm{Si}, \quad j \subset \mathrm{Si} \\ 0, & \text{otherwise}, \end{cases} \quad (5)$$

where

$$f_2(r) = \begin{cases} A(Br^{-p} - r^{-q})\exp[(r-a)^{-1}], & r < a \\ 0, & r \ge a \end{cases} \quad (6)$$

is the function used in the Stillinger–Weber potential with the same constants A, B, p, q, and a.

The bond weakening function

$$g_{ij} = \begin{cases} \exp\left(\frac{1}{q_s}\right)\exp\left[\frac{1}{q_i + q_j - q_s}\right], & q_i + q_j < q_s \\ 0, & q_i + q_j \ge q_s, \end{cases} \quad (7)$$

appearing in Eq. (5) decreases steadily from 1 to 0 as the sum of charges $q_i + q_j$ increases from zero to the cutoff parameter determined by the q_s value.

The three-body part of interaction (1) has the form

$$\nu_3(i,j,k) = \begin{cases} g_{ij}g_{ik}h(r_{ij}, r_{ik}, \theta_{jik}) + g_{ji}g_{jk}h(r_{ji}, r_{jk}, \theta_{ijk}) + g_{ki}g_{kj}h(r_{ki}, r_{kj}, \theta_{ikj}), & i,j,k \subset \mathrm{Si} \\ 0, & \text{otherwise}. \end{cases} \quad (8)$$

Here, the function $h(r_{ij}, r_{ik}, \theta_{ijk})$ is defined in the same manner as in the Stillinger–Weber potential; i.e.,

$$h(r_{ij}, r_{ik}, \theta_{jik}) = \begin{cases} \lambda\exp[\gamma(r_{ij} - a)^{-1} + \gamma(r_{ik} - a)^{-1}]\left(\cos\theta_{jik} + \frac{1}{3}\right)^2, & r_{ij} < a, \quad r_{ik} < a \\ 0, & \text{otherwise}, \end{cases} \quad (9)$$

where θ_{jik} is the angle between $\mathbf{r}_{ij}$ and $\mathbf{r}_{ik}$, and the function is the one used in the Stillinger–Weber potential with the same constant γ and λ.

The ionization energy of Si and O atoms are specified as

$$e_i(q_i) = \begin{cases} e_0\exp[-1/(q_i - q_{\mathrm{Si}}^0)], & q_i > q_{\mathrm{Si}}^0 \\ 0, & q_i < q_{\mathrm{Si}}^0 \end{cases} \quad i \subset \mathrm{Si} \quad (10)$$

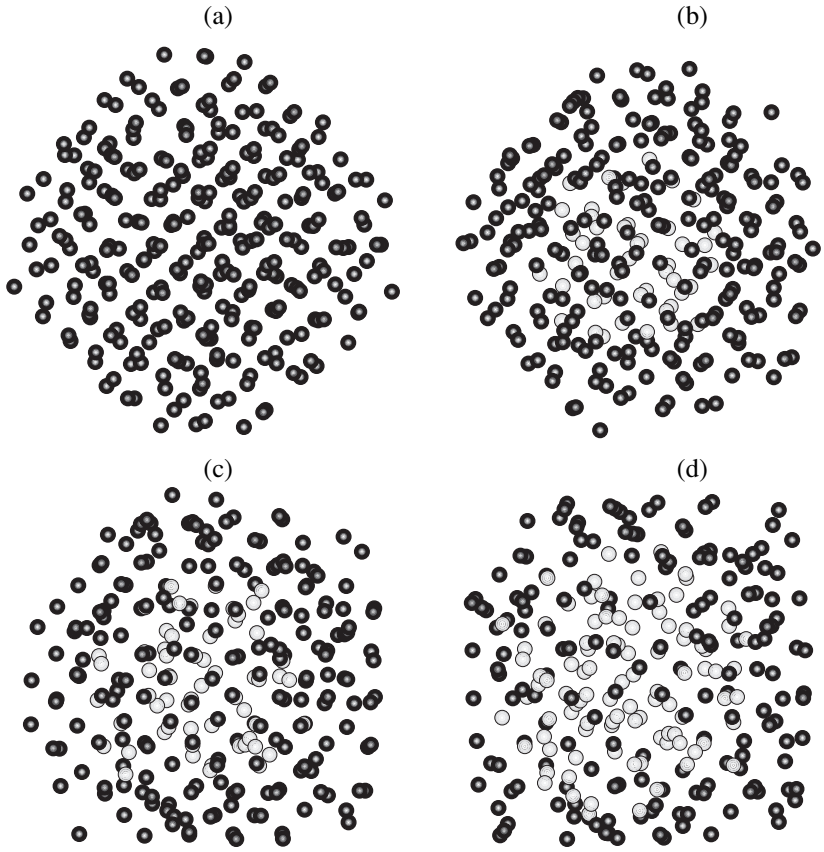

Fig. 1. Projection of the configurations of SiO_x nanoparticles grown at a temperature of 300 K and the rate u = 30 m/s for x = (a) 0, (b) 0.17, (c) 0.27, and (d) 0.42.

and

$$e_i(q_i) = \begin{cases} e_0 \exp[1/(q_i - q_O^0)], & q_i < q_O^0 \\ 0, & q_i > q_O^0, \end{cases} \quad i \subset O, \quad (11)$$

respectively, where q_O^0 and q_{Si}^0 are the fixed charges used in the Beest–Kramer–Santen potential.

FORMATION OF NANOCRYSTALS

Figure 1 shows the projections of nanoparticles obtained at the stage of crystal-growth simulation. A Si nanoparticle has the diamondlike crystal structure with numerous point defects (Fig. 1a), including vacancies and interstitial atoms. A large area of the surface of this nanocrystal involving 300 Si atoms is formed by close-packed {111} faces. A relatively small area of the surface is formed by {100} faces. The next three nanoparticles were grown up to $N \le 302$ in the oxygen atmosphere and entrapped 53, 85, and 126 oxygen atoms, respectively, which comprise 0.17, 0.27, and 0.42 of the total numbers of atoms in the respective nanoparticles. During the growth of the first nanoparticle, oxygen atoms were trapped more frequently for small N values. For this reason, the distribution of oxygen atoms in the central part of the first nanoparticle (Fig. 1b) is more compact than the distribution in nanoparticles enriched with oxygen to a greater extent (Figs. 1c, 1d).

The habit of the nanocrystal with an oxygen content of 0.17 differs considerably from the habit of the pure-silicon nanoparticle, because a part of the nanoparticle grown is rounded due to the formation of an atomic rough surface. The other part of the nanocrystal is bounded by {111} and {100} faces (Fig. 1b). Oxygen atoms can occupy both voids and interstices. Oxygen distorts the regular rows of Si atoms beyond the oxidant location as well.

The shape of the nanoparticle with an oxygen content of 0.27 changes further (Fig. 1c) and is primarily formed by large {100} faces and smaller atomic rough {111} faces. The shape of the nanoparticle is roundish, which manifests itself in smoothing edges formed by the intersection of {100} faces. Oxygen in this nanoparticle is present in a wider region than in the x = 0.17 case.

As the oxygen content increases to 0.42, the fraction of {100} faces in the nanocrystal surface increases, whereas the fraction of small {111} faces decreases (Fig. 1d). As in the preceding case, the edges are

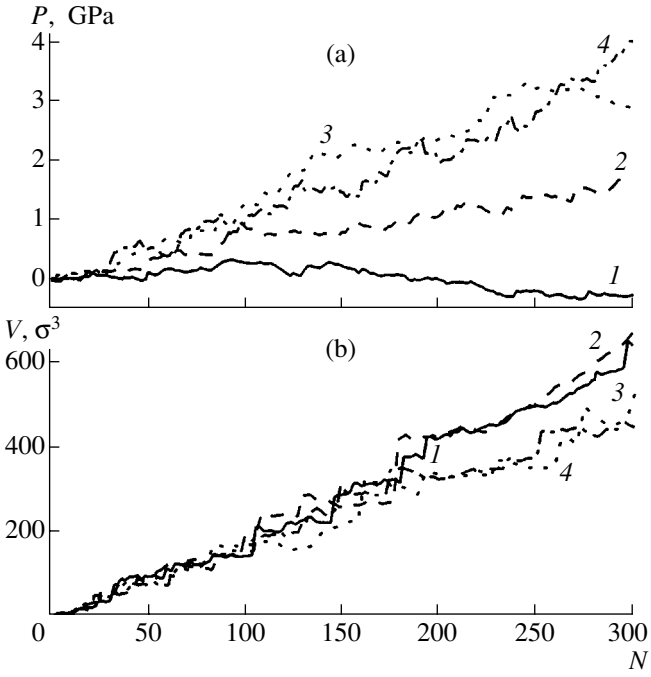

Fig. 2. (a) Pressure and (b) volume of a growing SiO_x nanocrystal for x = (*1*) 0, (*2*) 0.17, (*3*) 0.27, and (*4*) 0.42 vs. the number of atoms in the cluster N.

smoothed, and oxygen atoms are absent on the nanocrystal faces.

Figure 2 shows the (a) pressure P and (b) volume V calculated according to [2] for growing nanocrystals in relation to the number of atoms in the cluster. When growing, all nanoparticles under investigation had internal stresses, which indicates that this process is substantially nonequilibrium. Stresses were lowest in the pure-silicon cluster (line *1*). In this case, the internal pressure in the nanoparticle is negative for $N \geq 203$. The internal stresses increase with the oxygen content in a nanocrystal. Pressure is highest in the 301-atomic $SiO_{0.42}$ cluster. Pressure in nanoparticles with $x \neq 0$ is high, because oxygen atoms concentrate in a limited region of the crystal aggregate; i.e., a sufficiently large oxygen cluster squeezed by the Si crystal lattice was formed.

Oxygen content (x) in nanoparticles, as well as the density (ρ) and specific internal energy E of nanoparticles (subscript 0) before and after structural relaxation

No.	x	ρ_0, 10^3 kg/m^3	ρ, 10^3 kg/m^3	$-E_0$, eV/atom	$-E$, eV/atom
1	0	2.36	2.24	2.27	2.12
2	0.17	2.10	2.06	0.98	1.95
3	0.27	2.32	2.34	0.75	1.20
4	0.42	2.78	2.40	0.07	0.82

The fluctuations of V in the growing pure-silicon nanoparticle (line *1* in Fig. 2b) are more frequent and uniform than fluctuations in other nanocrystals. For $N \geq 183$, the nanoparticle with $x \leq 0.17$ has the largest volume among all clusters. The internal stresses in the cluster with $x = 0$ are accumulated at a much lower rate than stresses in clusters growing in the oxygen atmosphere and, beginning with $N = 203$, are completely relaxed. Volume fluctuations in the cluster with $x = 0.27$ (line *3*) are similar to fluctuations in the cluster with $x = 0.42$ (line *4*), but have a higher amplitude for $N > 230$. As a result, the final cluster volume for the $x = 0.27$ cluster is larger than the volume for the $x = 0.42$ cluster. The table lists the densities of the final nanoparticles. The density of the Si nanocrystal is slightly lower than the experimental density 2.42×10^3 kg/m^3 of an extended Si crystal [7].

STRUCTURAL RELAXATION OF NANOPARTICLES

High internal stresses in the nanoparticles were caused by the high crystallization rate, which was equal to 30 m/s on the average. The table lists the oxygen content, as well as the density and specific internal energy E of nanoparticles (subscript 0) before and after the structural relaxation occurring in an interval of $10^6\,\Delta t$. The energy of nanoparticles containing oxygen decreases with time, whereas the energy of pure silicon ($x = 0$) increases. In the latter case, the magnitude of negative pressure decreases more than four times. As a rule, the structural relaxation of a nanoparticle causes its volume to increase, except the $x = 0.27$ nanoparticle, whose volume decreases by 1.2%. The extension of nanoparticles containing oxygen is induced by the diffusion of oxygen atoms toward the nanoparticle surface. The contraction of the $SiO_{0.27}$ cluster is associated with the transfer of vacancies to the cluster surface. A decrease in the nanoparticle density is indicative of the tendency to amorphization, because the density (2.35×10^3 kg/m^3) of extended amorphous silicon is lower than the density of crystalline silicon [8]. The final configurations of nanoparticles after structural relaxation were more disordered than configurations shown in Fig. 1, but do not correspond to the complete amorphization of the nanocrystals.

The self-diffusion coefficients were calculated from the Einstein equation

$$D = \frac{1}{6\tau N}\left\langle \sum_{i=1}^{N} [\mathbf{r}_i(\tau) - \mathbf{r}_i(0)]^2 \right\rangle, \qquad (12)$$

where τ is the diffusion time interval, $[\mathbf{r}_i(\tau) - \mathbf{r}_i(0)]^2$ is the squared displacement of the ith atom in time interval τ, N is the number of silicon or oxygen atoms in the nanoparticle, and the pointed brackets indicate the averaging over different time intervals.

The displacements of atoms in a spherical cluster have two components: the radial component $\langle(\Delta\mathbf{r})^2\rangle_r$ directed to (or from) the cluster center and the tangential component $\langle(\Delta\mathbf{r})^2\rangle_\tau$ perpendicular to the radial direction. Therefore,

$$D_r = \frac{1}{3}\lim_{\tau\to\infty}\frac{\langle\mathbf{r}^2(\tau)+\mathbf{r}^2(0)-2\mathbf{r}(\tau)\mathbf{r}(0)\rangle}{\tau}, \quad (13)$$

$$D_\tau = \frac{1}{3}\lim_{\tau\to\infty}\frac{\langle\mathbf{r}(\tau)\mathbf{r}(0)[1-2\mathbf{u}(\tau)\mathbf{u}(0)]\rangle}{\tau}, \quad (14)$$

where $\mathbf{u} = \mathbf{r}(\tau)/|\mathbf{r}(\tau)|$ is the unit vector [9].

Figure 3a shows the total, radial, and tangential mean-square displacements of atoms in the Si nanoparticle. As can be seen, the slope of the curve for the tangential component $\langle(\Delta\mathbf{r})^2\rangle_\tau$ exceeds the slope for the radial component $\langle(\Delta\mathbf{r})^2\rangle_r$. The behavior of the $\langle(\Delta\mathbf{r})^2\rangle(t)$ curve and its components differs from the monotonically increasing behavior for a liquid. Indeed, the portions of steep rise (or sometimes drop) and plateaus are pronounced in each curve. The step dependence is attributed to the motion and recombination of point defects produced in the nanocrystal-growth process.

The coefficient D characterizes the mobility of atoms in nanoparticles. The mean and partial (for Si and O atoms) values of D, D_r, and D_τ were determined. Furthermore, the radial distributions of these quantities averaged over the concentric layers of a spherical cluster were calculated. The cluster layers were formed according to the radii of the coordination spheres of crystalline silicon with the diamondlike structure. The $\overline{D}$ value for the 300-atomic Si cluster agrees well with a value of 10^{-9} m^2/s obtained in [10] for the 480-atomic cluster.

Figure 3b shows the distributions of D, D_r, and D_τ over the spherical layers of the Si nanocrystal, where the values of $D_r^{(i)}$ and $D_\tau^{(i)}$ are largest in the third and twelfth layers, respectively. The coefficient D and its components vanish in the outer 20th layer, because covalent bonds existing in the nanocrystal strongly restrict diffusion on the surface. The behavior is opposite for metallic bonds. In particular, $D^{(i)}$ for a crystalline lead cluster is largest in the outer layer [11], which is a liquidlike film.

Since $\langle(\Delta\mathbf{r})^2\rangle = \langle(\Delta\mathbf{r})^2\rangle_r + \langle(\Delta\mathbf{r})^2\rangle_\tau$, the self-diffusion coefficients are related as $D = D_r + D_\tau$. The coefficients $\overline{D}$ for the entire cluster are related as $\overline{D}_r < \overline{D}_\tau$. The same inequality is satisfied for the coefficients $D^{(i)}$ characterizing the mobility of atoms in the spherical cluster layers, except the outer (tenth) oxygen layer in the clusters with $x = 0.17$ and 0.28, where $D_r^{(10)} > D_\tau^{(10)}$; i.e., oxygen tends to approach the cluster surface. Oxygen atoms in SiO_x nanoparticles are much more mobile than

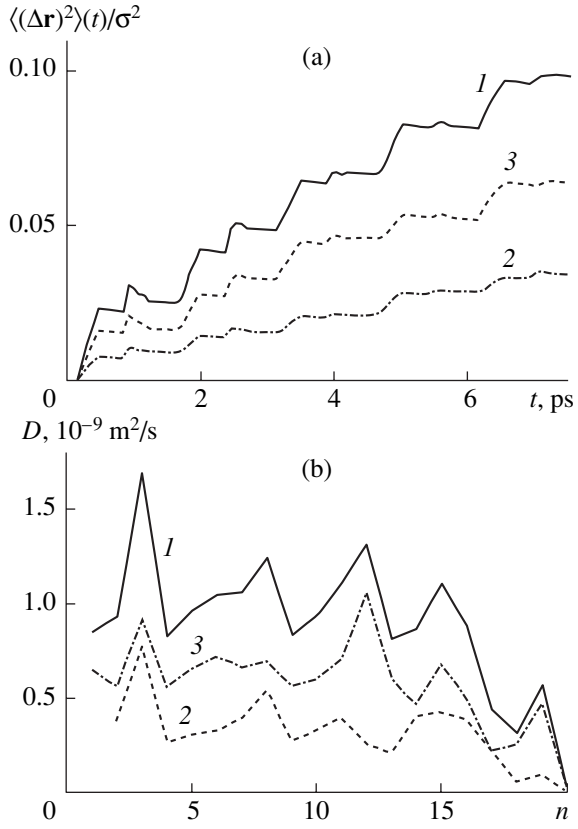

Fig. 3. The (a) mean squared displacement of atoms and (b) self-diffusion coefficient in coordination layers of the 300-atomic Si nanocrystal vs. the coordination-layer number n: (*1*) the total coefficient and its (*2*) radial and (*3*) tangential components.

Si atoms. The coefficients $D^{(i)}$ for silicon are largest in the tenth–fourteenth layers, where the kinetic energy is transferred from oxygen to silicon.

Figure 4 shows the distribution of the coefficient D and its components over the spherical layers of the $SiO_{0.42}$ nanoparticle. As a rule, zero values of $D^{(i)}(z)$ mean the absence of z-type atoms in the ith spherical layer. In this nanoparticle, the diffusion coefficient for oxygen is larger than the coefficient for silicon by a factor of 5.6 on average. The coefficients D for oxygen and silicon are largest in ninth and thirteenth layers, respectively. The coefficient D in the outer, twentieth, layer is no longer zero, although the radial component D_r in this case is close to zero. Thus, the oxygen core affects the kinetic properties of the outer layer.

METHOD OF STATISTICAL GEOMETRY

The structure of the nanoparticles after their relaxation, which removes the internal pressure created during growth, were studied in detail using the statistical-geometry analysis of Voronoi polyhedra. These polyhedra were constructed for 50 z-type atoms closest to the center of mass of a nanoparticle by using the atomic

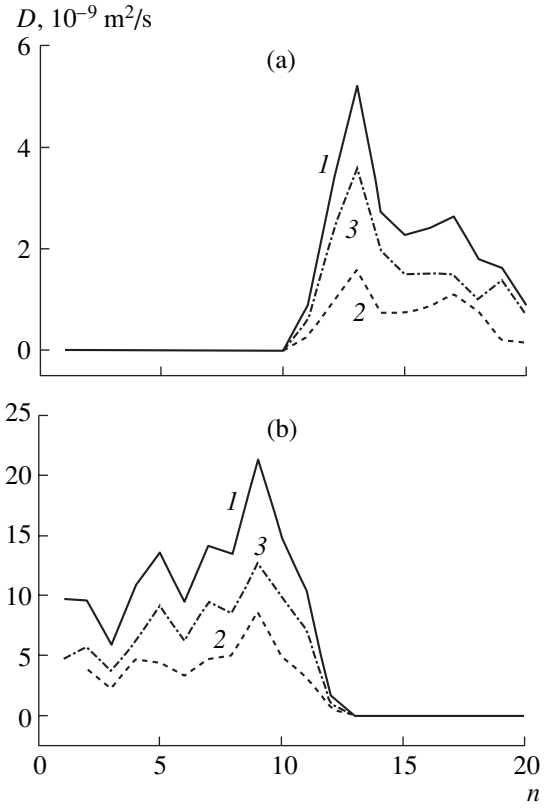

Fig. 4. The same as in Fig. 3b, but for (a) silicon and (b) oxygen in the 300-atomic $SiO_{0.42}$ nanoparticle grown at the rate u = 30 m/s.

coordinates recorded every 1000 time steps. Thus, the resulting statistical characteristics were obtained by analyzing 50 000 polyhedra.

In conventional statistical analysis, the distributions of Voronoi polyhedra in the number n of faces and distributions of faces in the number m of sides are constructed. Information about the average cluster structure can be acquired by removing thermal noise. The amplitude of atomic vibrations in a crystal nucleus growing in a supercooled metallic melt is as large as $\delta \sim 0.1\ a$ [12], where a is the lattice constant. Therefore, it is reasonable to eliminate thermal noise by excluding the edges of Voronoi polyhedra with length $l < \delta$. The angular distribution of the nearest neighbors, i.e., the distribution in the angles between a pair of neighbors that form faces of Voronoi polyhedra and the atom at the polyhedron center (vertex of the angle θ), is the characteristic most sensitive to the crystal structure [13]. An analysis of the θ, n, and m distributions indicates that there are imperfect crystalline structure in the Si nanoparticle and amorphous-crystalline structure in SiO_x nanoparticles for $0.17 \le x \le 0.42$.

For a multicomponent system, partial Voronoi polyhedra can be constructed in addition to polyhedra to the type of atoms. Voronoi polyhedra involving the Si–Si, O–O, and Si–O bonds were constructed to analyze the

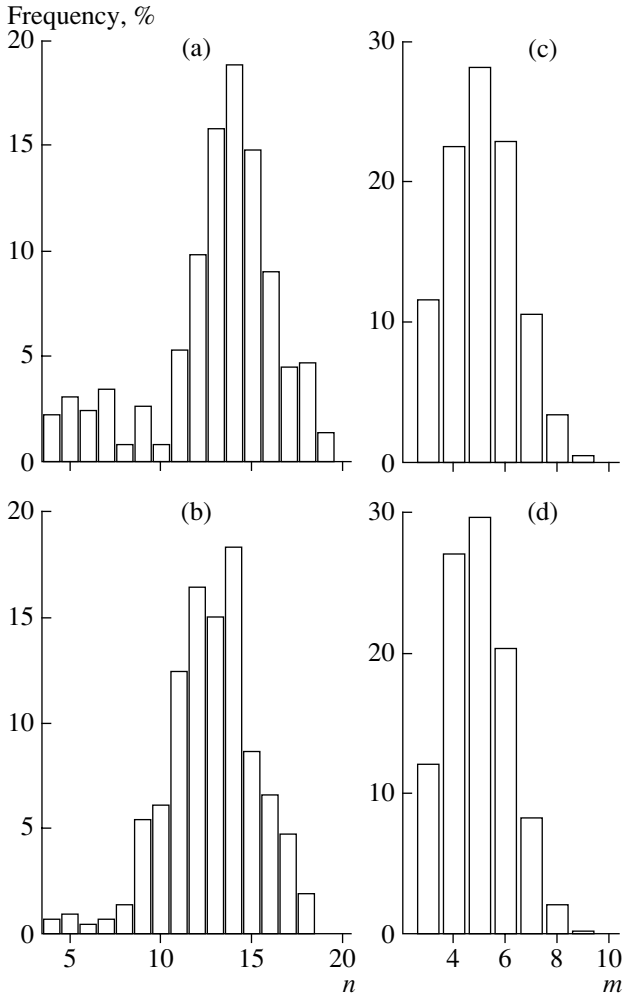

Fig. 5. Distributions of (a, b) Voronoi polyhedra in the number of faces and (c, d) faces in the number of sides as calculated for the 300-atomic $SiO_{0.42}$ nanoparticle undergoing structural relaxation; (a, c) exact Voronoi polyhedra and (b, d) Voronoi polyhedra with small edges excluded.

structure of SiO_x nanoparticles. Let us consider the case x = 0.42 in detail. Figure 5 shows the n and m distributions for Voronoi polyhedra constructed while disregarding the type of atoms. The distribution of Voronoi polyhedra in the number of faces has a peak at n = 14 (Fig. 5a). This peak is not shifted when small edges are excluded from Voronoi polyhedra (Fig. 5b). Pentagonal faces are dominant in the distributions of faces in the number of sides (Fig. 5c) before and (Fig. 5d) after removing edges whose lengths $l < \delta$. Since the m spectrum represents the rotational symmetry, the predominance of the fifth-order symmetry indicates that the nanoparticle as a whole likely has the amorphous, rather than crystalline, structure. This conclusion is also corroborated by the fact that 14-hedra dominating here prevail also in the n spectrum of a simple liquid [14]. The angular distribution of the nearest neighbors, which is based on polyhedra to the type of atoms, has

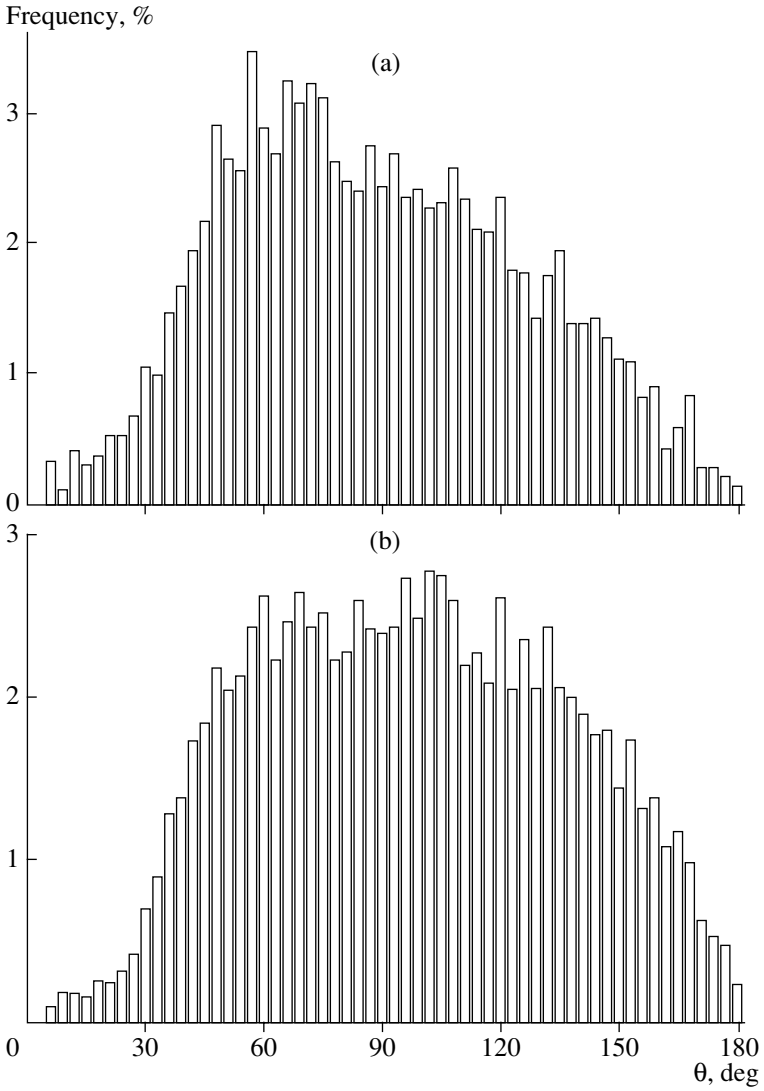

Fig. 6. Angular distribution of the nearest neighbors as calculated for the 300-atomic $SiO_{0.42}$ nanoparticle undergoing structural relaxation; calculations with exact Voronoi polyhedra involving (a) Si–Si and (b) O–O bonds.

two pronounced peaks at 63° and 99°. A similar distribution for the simple-liquid model has peaks at 60° and 110° [14]. The angular distributions constructed for the (Fig. 6a) Si and (Fig. 6b) O subsystems indicate that angular ranges $57° \le \theta \le 66°$ and $96° \le \theta \le 118°$, respectively, are most probable. The angular distribution characterizing Si–O bonds has three peaks at 63°, 87°, and 109°. Thus, the first and second peaks in the angular distribution equivalently representing both subsystems (Si and O) are primarily attributed to Si–Si, Si–O and O–O bonds, respectively.

In summary, the molecular dynamics method in combination with the model of statistical geometry of growth makes it possible to construct SiO_x nanoparticles that have the amorphous–crystalline structure and surface similar to macroscopic crystals. The core of nanoparticles is an irregular oxygen cluster, and the outer crystalline part is formed by covalently bonded Si atoms. The characteristic defects of the structure originate at the nanoparticle formation stage. In this respect, the situation is similar to the appearance of defect structures in metallic glasses, nanocrystalline bodies, amorphous nanocrystalline composites, thin-film solid systems, and nanoscale quasi-crystalline materials [15]. The difference is that defects formed in the SiO_x nanoparticles under investigation are point rather than linear. Defects in the form of vacancies and interstitial atoms facilitate the inward motion of oxygen in the cluster and the accumulation of oxygen near the center of the nanoparticle. Oxygen atoms and their associations serve as effective sinks for free vacancies. Thus, virtually all the oxygen trapped during the growth of a nanoparticle is concentrated in the central region of the nanocrystal. The formation of oxygen clusters in a Si crystal was observed when crystals were obtained by Czochralski method, where the pulling rate was sufficiently high

and supersaturated oxygen was condensed [6]. However, upon annealing, large clusters separated into smaller clusters containing from 3 to 20 oxygen atoms. The basic result of this study is that the simulation of the growth of nanosize Si particles reveals oxygen condensation.

ACKNOWLEDGMENTS

This study was supported by the Russian Foundation for Basic Research (project no. 01-02-96425–Ural) and the Program for the Support of Leading Scientific Schools (project no. 00-15-96719).

REFERENCES

1. A. A. Chernov, in *Modern Crystallography*, Vol. 3: *Crystal Growth*, Ed. by B. K. Vainshtein, A. A. Chernov, and L. A. Shuvalov (Nauka, Moscow, 1980; Springer-Verlag, Berlin, 1984).
2. H. J. C. Berendsen, J. P. M. Postma, W. F. van Gunsteren, *et al.*, J. Chem. Phys. **81**, 3684 (1984).
3. D. Beeman, J. Comput. Phys. **20** (2), 130 (1976).
4. F. H. Stillinger and T. A. Weber, Phys. Rev. B **31** (8), 5262 (1985).
5. J. D. Kubicki and A. C. Lasaga, Am. Mineral. **73**, 941 (1998).
6. Z. Jiang and R. A. Brown, Chem. Eng. Sci. **49** (17), 2991 (1994).
7. B. W. H. van Beest, G. J. Kramer, and R. A. van Santen, Phys. Rev. Lett. **64**, 1955 (1990).
8. *Tables of Physical Quantities*, Ed. by I. K. Kikoin (Atomizdat, Moscow, 1976).
9. C. L. Briant and J. J. Burton, Nature **243**, 100 (1973).
10. M. R. Zachariah, J. Carrier, and E. Blaisten-Barojas, J. Phys. Chem. **100**, 14856 (1996).
11. A. E. Galashev, Kristallografiya **44** (2), 203 (1999) [Crystallogr. Rep. **44**, 171 (1999)].
12. A. E. Galashev and I. P. Chernysheva, Neorg. Mater. **35** (1), 53 (1999).
13. A. E. Galashev, Kristallografiya **43** (4), 739 (1998) [Crystallogr. Rep. **43**, 690 (1998)].
14. J. Bernal and S. King, in *Physics of Simple Liquids*, Ed. by H. Temperley, G. Rowlinson, and G. Rushbrooke (North-Holland, Amsterdam, 1968; Mir, Moscow, 1971), p. 116.
15. M. Yu. Gutkin and I. A. Ovid'ko, *Defects and Mechanisms of Plasticity in Nanostructural and Noncrystalline Materials* (Yanus, St. Petersburg, 2001), p. 6.

Translated by R. Tyapaev

Crystallography Reports, Vol. 47, Suppl. 1, 2002, pp. S177–S182.

REAL STRUCTURE OF CRYSTALS. GROWTH OF FILMS. NANOCRYSTALS. TIP STRUCTURES

Epitaxy of CdS and PbS on Langmuir Layers

E. V. Rakova, V. V. Klechkovskaya, N. D. Stepina, and L. A. Feĭgin

Shubnikov Institute of Crystallography, Russian Academy of Sciences, Leninskiĭ pr. 59, Moscow, 119333 Russia

Received October 3, 2002

Abstract—The results of a structural study of CdS and PbS nanocrystals grown from solutions under a Langmuir monolayer of a fatty acid are presented, and the influence of the geometric and stereochemical factors on the mutual orientation of the monolayer and the nanocrystals grown are considered. © *2002 MAIK "Nauka/Interperiodica".*

INTRODUCTION

The use of a Langmuir monolayer as an orienting substrate for growth of inorganic nanocrystals opens new possibilities for the formation of nanometer heterostructures. The oriented growth of nanocrystals on Langmuir layers combines some elements of biomineralization [1, 2] and artificial epitaxy (graphoepitaxy) [3]. Such growth is similar to artificial epitaxy because the orienting substrate (in this case, an organic Langmuir monolayer) is prepared by an experimentalist directly during the growth process. The experimentalist chooses an appropriate amphiphilic organic compound consisting of a hydrophilic functional group (carboxylic or amino group) and a hydrophobic part (a hydrocarbon chain). Then, using the barrier compression, one forms an ordered Langmuir monolayer on the surface of the aqueous solution containing the reagents necessary for the synthesis and growth of crystals (a subphase). The hydrophilic groups in this monolayer form a periodic two-dimensional network at the air–water interface, whereas the hydrophobic chains are directed either along the surface normal or form a small angle with it.

In essence, growth of inorganic crystals under a Langmuir monolayer is a simplified model of the biomineralization process widespread in nature (formation of bones, teeth, protective shells, etc.). In this case, nucleation of crystals occurs on a biopolymer matrix, which is responsible for the biological control of their growth. The use of biomineralization principles for the synthesis and growth of crystals is called biomimetics [4].

The prerequisite for heteroepitaxial growth of films and crystals is match of lattice parameters of the atomic networks of the substrate and the film in the conjugated plane. If this requirement is met, the oriented growth can take place; however, it is impossible to predict *a priori* orientation because of the complex molecular interaction at the interface. At present, our knowledge of the structure of a nucleus in crystal growth from a solution, in general, and biomineralization, in particular, is still insufficient. The role of clusters and their composition and the contribution that comes from the stereochemical and electrostatic factors to the nucleation process are still unclear. Better understanding of these problems requires the study of crystallization under a Langmuir monolayer, because the latter is sufficiently well characterized and, if necessary, can readily be modified. The study of growth under a monolayer is also important for the development of new methods for obtaining highly dispersed materials of the nanometer range, in particular, of semiconductor CdS and PbS nanoparticles possessing quantum–size properties [5]. The conventional chemical deposition of sulfide nanoparticles from aqueous solutions is hindered by their coagulation and Ostwald ripening. Growth of sulfides under Langmuir monolayers by the method suggested in [6, 7] yields nanoparticles in the monolayer plane, which excludes their coagulation. This method, in combination with the Langmuir–Blodgett technique, allows one to obtain periodic layer structures consisting of organic dielectric layers with the nanoparticle of a semiconductor material packed in the interlayer space, which is of great importance for molecular electronics.

Below, we generalize the results of the structural and orientational studies of nanoparticles of cadmium and lead sulfides under Langmuir monolayers of fatty acids. These cubic crystals have rather close lattice parameters but belong to different structure types, possess different physical properties, and are differently oriented with respect to the monolayers. We also suggest here an orientational model that takes into account the close geometry and the stereochemical similarity of monolayers of fatty acids and the grown CdS and PbS nanocrystals.

EXPERIMENT

The growth process was performed either in a Joyce-Loebl Langmuir trough or a Petri dish by a method described elsewhere [6, 7]. Unlike the procedure in [6, 7], we introduced into the subphase lead or

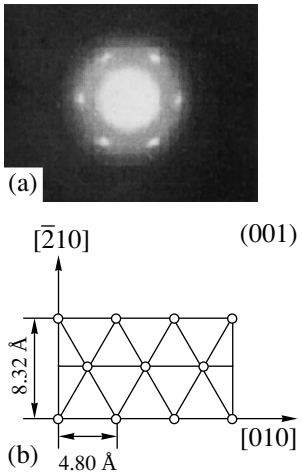

Fig. 1. (a) Electron diffraction pattern and (b) packing of the fatty acid molecules in the hexagonal phase of the monolayer.

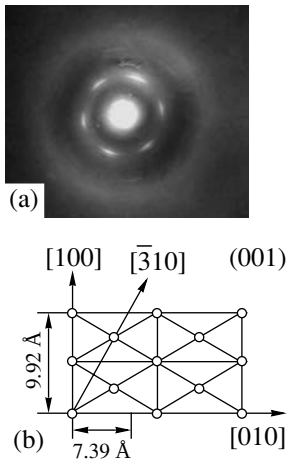

Fig. 2. (a) Electron diffraction pattern and (b) packing of the fatty acid molecules in the orthorhombic phase of the monolayer.

cadmium nitrates at concentrations of 3×10^{-5} M for $Pb(NO_3)_2$ and 5×10^{-4} M for $Cd(NO_3)_2 \cdot 4H_2O$ at pH = 5.5, since we established earlier that cadmium chloride in the solution gives rise to disorder of the structure at the monolayer–subphase interface because of the propensity of cadmium halides to form various complexes [8]. A solution of $C_nH_{2n+1}COOH$ fatty acid in chloroform at a concentration of 1 mg/l was applied to the subphase surface at room temperature. We used stearic, arachidic, and behenic acids with 17, 19, and 21 carbon atoms in the chain, respectively. In order to obtain the ordered structure of the monolayer, we compressed the layer until the attainment of a surface pressure of 28 mN m^{-1} in the Langmuir trough or added an excessive amount of the fatty acid to the Petri dish (if the barrier-free compression was used). To provide the necessary reaction, we introduced into the subphase some hydrogen sulfide that evolved during hydrolysis of sodium sulfide from the close volume via diffusion through the monolayer. Since the solubility of cadmium and lead sulfides in water is rather poor (the product of the ion concentrations equals $[Cd^{+2}] \cdot [S^{-2}] = 10^{-27}$ and $[Pb^{+2}] \cdot [S^{-2}] = 10^{-28}$ at room temperature), it was necessary to provide a sufficiently low rate of the hydrogen sulfide inflow in order to prevent the homogeneous formation of clusters in the solution and provide heterogeneous nucleation of crystals under the monolayer. The growth time varied from 0.5 to 72 h. The structure was studied using an EMR-102 electron diffraction camera and a JEM-100 C electron microscope. The samples were applied onto copper grids coated with a thin layer of amorphous cellulose, which is transparent to an electron beam. It should be indicated that the electron diffraction camera permitted observation for several minutes of a rather stable diffraction pattern from an organic monolayer, whereas using an electron microscope, the samples exposed to an electron beam deteriorated within several seconds at $T = 4.2$ K [9]. A rather intense diffraction pattern can be obtained in an electron diffraction camera at lower beam currents because of the illumination of a larger area of the sample. The electron diffraction patterns can be recorded at various azimuth and tilt angles of the sample (up to 80°), which makes it possible to collect the complete set of reciprocal-lattice sections.

RESULTS AND THEIR DISCUSSION

Structure of a Monolayer–Substrate

Hydroxyl groups of fatty acid form a two-dimensional ordered network at the water surface. Cadmium cations introduced into the subphase are adsorbed from the solution and form a monolayer of the respective cadmium salt—stearate, arachidate, or behenate. The electron diffraction patterns from such monolayers show that they consist mainly of domains having either hexagonal (Fig. 1) or orthorhombic (Fig. 2) molecular packings with vertically oriented hydrocarbon chains. This result is consistent with the data obtained from the phase diagram [10] and the known X-ray data [11]. The parameter of the hexagonal unit cell equals $a = 4.80$ Å, and the parameters of the two-dimensional orthorhombic unit cell $a = 4.96$ Å and $b = 7.39$ Å. Under the controlled surface pressure of 28 mN m^{-1}, the domains of the hexagonal phase are almost parallel to one another, which is confirmed by the electron diffraction pattern with six strong 110-type reflections in Fig. 1a. The hexagonal domains form two-dimensional mosaic crystals with the area ranging within 2–4 mm^2.

The domains of the orthorhombic phase are rotated with respect to one another by an angle of 120°. The corresponding electron diffraction pattern (Fig. 2a) has a sixfold axis and is the superposition of three reciprocal-lattice sections normal to the [001]-axis. The reflections of the 110-, 020-, 120-, and 200-types are seen.

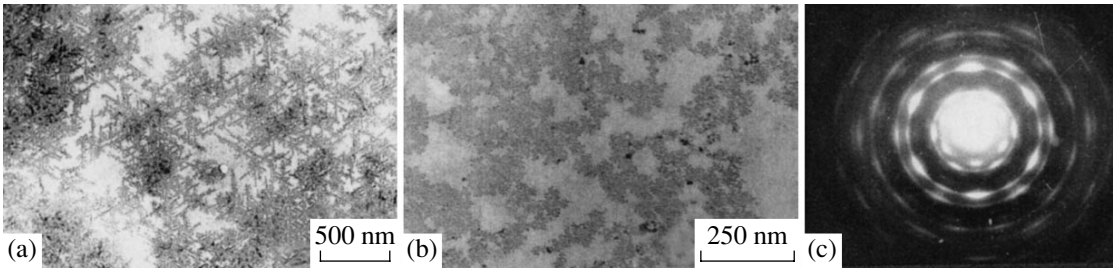

Fig. 3. Micrograph of a CdS sample (a) grown for 30 min in the Langmuir trough and (b) Petri dish and (c) the electron diffraction pattern from the sample shown in Fig. 3a.

The domain size estimated from the halfwidth of the diffraction lines is about 150 Å; the domains are misoriented with respect to each other by an angle of the order of 10°. It is usually assumed that this structure arises in monolayers of fatty acids because of the orthorhombic distortion of the two-dimensional hexagonal lattice. Under noncontrolled pressure in the Petri dish, the domains in the monolayers are pronouncedly misoriented and form a texture with the [001]-axis.

Growth of CdS Nanoncrystals under a Cadmium Behenate Monolayer

Cadmium sulfide was grown under a monolayer of behemic acid, $C_{21}H_{43}COOH$, on a cadmium nitrate–containing subphase. The crystals are formed at the monolayer–subphase interface as a result of the reaction between H_2S and the adsorbed Cd^{+2}-ions playing the role of nucleation centers of CdS. During this process, the surface acquires a yellow color. Figure 3 shows the electron micrographs of a CdS sample grown for 30 min under the cadmium behenate monolayer in the Langmuir trough (Fig. 3a) and the Petri dish (Fig. 3b). It is seen that under the controlled surface pressure (Fig. 3a), the CdS particles form a dendrite-like structure with the dendrite branches forming an angle of 120° with one another. If the surface pressure is not controlled, the cadmium behenate domains are misoriented in the monolayer plane and the CdS particles form small islands (Fig. 3b). With an increase in growth time, the islands become larger and, finally, form a continuous layer.

The electron diffraction data indicate that, in both cases, cadmium sulfide has a sphalerite-type cubic structure, with the particles being oriented mainly with the (110) face parallel to the monolayer. Figure 3b shows the electron diffraction pattern from the sample shown in Fig. 3a with the 110- and 020-type reflections of the orthorhombic cadmium behenate (the reflections closest to the primary beam) and the cadmium sulfide reflections of the 111-, 200-, 220-, 113-, and 331-type. Similar to the case in Fig. 2a, the electron diffraction pattern in this case is the superposition of three diffraction patterns rotated by an angle of 120° with respect to one another. This signifies that the domains in the substrate and the CdS particles grown on it occupy three equivalent positions rotated by an angle of 120° to one another.

The analysis of the electron diffraction patterns shows that, in all the positions, cadmium sulfide grows epitaxially on the monolayer and that the mutual orientation of the crystals and the substrate is described by the relationships $(110)[\bar{1}10]CdS \parallel (001)[\bar{3}10]CdBeh$. This orientation is observed in the majority of the samples irrespectively of the way of monolayer formation on the subphase surface. The degree of nanoparticle order depends on the degree of the monolayer order. Thus, the CdS particles grown in the Petri dish form the texture with the [110]-axis and are azimuthally misoriented in a way similar to that of the monolayer of the corresponding fatty acid salt.

The result obtained is inconsistent with the data presented in [12], where cadmium sulfide particles were grown from the cadmium chloride–containing subphase under a monolayer of the arachidic acid. In [12], the oriented growth of cadmium sulfide with the wurtzite structure was observed. This discrepancy can be explained by the influence of various anions in the subphase. As is known, during CdS deposition from solutions, the NO_3^- anions promote the formation of the cubic modification of cadmium sulfide, whereas the Cl^- anions give rise to the formation of the hexagonal modification [13]. The discrepancy between our results and the data in [12] can also be explained by the fact that the phase composition necessary for precision structural determination was established in [12] from micrographs, whereas we used with this aim the diffraction patterns obtained in the electron diffraction camera. In the latter case, we used the averaged distribution of the reflection intensities (because of a larger cross section of the beam) and more precise interplanar spacings.

We should like to remind that the initial monolayer consisted of the domains with the hexagonal and orthorhombic molecular packings. Upon growth of CdS, no hexagonal phase of cadmium behenate was recorded on the electron diffraction patterns. This seems to be explained by the fact that the hexagonal molecular packing in the monolayer is less stable and undergoes the phase transition into the orthorhombic

phase caused by elastic deformations arising during cadmium sulfide nucleation and growth because of the lattice mismatch at the interface. This transition should be related to a new type of elastic-stress relaxation during epitaxial growth, on organic matrices that should have taken place in biomineralization processes.

The dimensions of individual crystals forming CdS particles (Fig. 3b) are about 5 nm (high-resolution electron microscopy data) [14]. These particles manifest here the quantum-size effect—the boundary of the photoconductivity band is shifted to the short wavelength range of the spectrum and is observed in the vicinity of 470 nm.

Orientational Relationships between Cadmium Behenate and Cadmium Sulfide

Figure 4 shows the scheme of the Cd and S networks in the (110)CdS plane. According to the electron diffraction data, the coinciding directions are $[\bar{1}10]$ in CdS and $[\bar{3}10]$ in cadmium behenate (indicated by an arrow in Fig. 2b). The lattice mismatch along these directions is less than 1%. One can readily see that along other directions, there is some lattice mismatch between the substrate and the crystals; in other words, we deal here with the so-called one-dimensional epitaxy. Obviously, the oriented crystallization in this case results from the collective interactions and not from the successive attachment of the atoms of the growing crystal to the points of the two-dimensional network of the monolayer. It is these interactions that are most probable in growth of inorganic crystals on a biopolymer matrix.

In the sphalerite-type crystal lattice (sp. gr. $F\bar{4}3m$), the atoms are tetrahedrally coordinated and have four covalent bonds with an angle of 109°28′ between them. In the (110)CdS plane, the zigzag –Cd–S– chains with the covalent bonds located along the $[\bar{1}10]$ direction are parallel to the $[\bar{3}10]$ direction of cadmium behenate, with each sixth chain coinciding with the atomic rows of the monolayer network. Another system of –Cd–S–chains in the crystal is located in the $(\bar{1}10)$CdS plane normal to the (110)CdS plane and the monolayer surface.

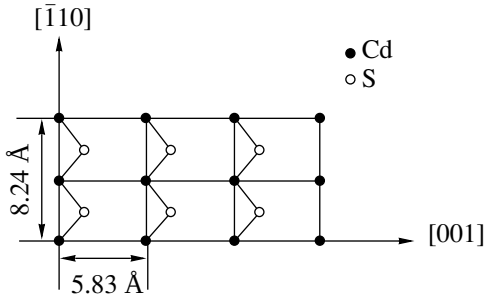

Fig. 4. Arrangement of Cd and S atoms in the (110)CdS plane.

Now, consider the structure of the molecules of a fatty acid salt forming a monolayer in more detail. The constituent carbon atoms of the hydrocarbon chain C_nH_{2n+1} form bonds among themselves and also covalent tetrahedral bonds with hydrogen atoms in a way similar to the bonds between the sulfur and cadmium atoms in the cadmium sulfide lattice. In the orthorhombic phase (according to the electron diffraction data, the monolayer upon the overgrowth of CdS consists of the orthorhombic phase), the chains are directed vertically along the surface normal. The angle between the tetrahedral covalent –C–C–C– bonds equals 112°; the angle between the H–C–H bonds lying in the normal plane is about 108°.

This signifies that at mutual orientation of the monolayer and the crystals described as $(110)[\bar{1}10]\text{CdS} \parallel (001)[\bar{3}10]\text{CdBeh}$, there exists a stereochemical similarity of the structure of the components of the given epitaxial pair. This similarity was reduced to the fact that the tetrahedral covalent bonds in the molecules of the fatty acid salt forming a monolayer and the tetrahedral covalent bonds in the grown cadmium-sulfide nanocrystals are located in parallel planes.

The role of the stereochemical factor has already been discussed in [15], where growth of calcium carbonate under a calcium stearate monolayer was studied. It was concluded [15] that the orientation of one of the calcite $CaCO_3$ modifications is determined by the joint action of the geometric match of the atomic networks in the integrowth plane and the stereochemical similarity of the carboxyl and carbonate groups. Moreover, one also has to take into account the charge state of the monolayer surface.

Orientation of PbS Crystals Grown in the Langmuir Trough under a Lead Stearate Monolayer

The PbS crystals under a monolayer of the stearic acid, $C_{17}H_{35}COOH$, on the subphase containing lead nitrate were grown in the Langmuir trough under the controlled surface pressure of 28 mN m^{-1}.

The structure of the initial monolayer of lead stearate was similar to the structure of cadmium behenate described in the previous section. A monolayer transferred to the copper grid to be studied in an electron diffraction camera consisted mainly of the domains with the orthorhombic packing of the molecules and a few regions with hexagonal packing. The parameters of the two-dimensional lead stearate network were very close to those of cadmium behenate.

Growth of PbS nanocrystals occurred on the surface of a monolayer, and the surface acquired a gray color; no homogeneous nucleation in the solution was

observed in this case. It should be indicated that noticeable coloration of the surface took considerably more time than in the case of cadmium sulfide growth. This becomes quite clear if one compares the morphologies of PbS and CdS nanocrystals. Figure 5 shows the micrograph of a lead stearate monolayer kept for 2.5 h in the H_2S atmosphere. It is seen that the morphology of lead sulfide nanocrystals considerably differs from the morphology of cadmium sulfide nanocrystals. In this case, individual triangular crystals are formed, which indicates that they are oriented with the (111) face parallel to the surface. We should like to remind that in the absence of the orienting substrate, PbS crystals are usually faceted by the {001} planes possessing the minimum surface energy. The particles are twinned with respect to the [111]-axis, which is characteristic of the epitaxial growth of semiconductor A^4B^6-type compounds with cubic structures, because their nucleation at all the twin positions is equiprobable. The crystal dimensions range within 10–40 nm, with the average density being 2×10^{10} cm^{-2}. In addition to the crystals oriented with the (111) face parallel to the monolayer, there are also some PbS particles of other orientations. Keeping particles in the H_2S atmosphere longer increases their size and results in conjugation of crystals of different orientations. This can be the consequence of deformation of the Langmuir monolayer under the action of PbS nanocrystals grown at the initial stages of epitaxial growth. Moreover, the kinetic conditions of nucleation and growth vary with time because of a decrease of the concentration of lead ions in the vicinity of the growth front and the diffusion limitations existing in the solution.

Lead sulfide has a cubic NaCl-type structure (sp. gr. $Fm3m$) with a lattice parameter of 5.94 Å and octahedral atomic coordination. The coordination number equals six; the covalent–ionic Pb–S bonds form 90° angles with one another. This is the most important difference between the PbS and CdS structures determining their different orientations under the monolayer.

The electron diffraction patterns from PbS samples confirm the preferable orientation of nanocrystals with the (111) plane parallel to the monolayer; however, these patterns are insufficient for determining the coinciding directions as was the case with CdS. The mutual orientation of nanocrystals in PbS samples was established from the comparison of the atomic networks at the monolayer–crystal interface.

In the (111) plane, the lead or sulfur atoms form the alternating hexagonal networks (Fig. 6), which can readily be brought into coincidence with the two-dimensional network of the carboxyl groups in the monolayer in the case of hexagonal molecular packing (Fig. 1b). The mutual orientation is described by the relationship $(111)[\bar{1}10]\text{PbS} \parallel (001)[210]\text{PbSt}_{\text{hex}}$, the lattice mismatch is about 1%, and the layer is somewhat extended. For orthorhombic packing, the mutual orientation of the crystal and monolayer is described by the

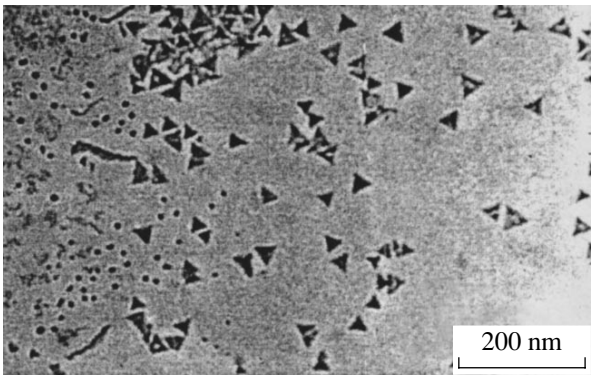

Fig. 5. Micrograph of the PbS sample grown for 2.5 h in the Langmuir trough.

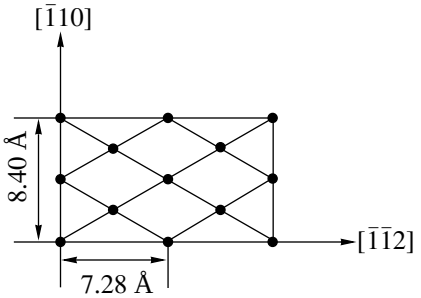

Fig. 6. Arrangement of Pb atoms in the (111) PbS plane.

relationship $(111)[\bar{1}10]\text{PbS} \parallel (001)[\bar{3}10]\text{PbSt}_{\text{rhomb}}$. Here, the pronounced lattice mismatch is observed.

Obviously, in growth of lead sulfide under a fatty acid monolayer, of key importance is the geometric match of the atomic lattices in the conjugated plane. Lead cations adsorbed by carboxyl groups from the subphase form the ordered system of the centers of lead sulfide nucleation during the interaction with hydrogen sulfide from the vapor phase diffusing through the monolayer.

CONCLUSION

The above structural studies show that the orientation of inorganic crystals grown from solutions under an ordered fatty acid monolayer is determined not only by the geometric mismatch of the atomic networks in the conjugated plane but also by the spatial arrangement of the bonds in the crystal and monolayer. Cadmium sulfide is characterized by tetrahedral atomic coordination similar to coordination in a hydrocarbon chain. This provides orientation of the crystals with the (110) plane parallel to the (001) plane of the monolayer. In growth of lead sulfide with octahedral atomic coordination, the decisive role in the orientation is played by the geometric match of the lattices in the conjugated plane, which is the best for crystal orientation with the

(111) plane parallel to the (001) plane of the monolayer with the hexagonal molecular packing.

ACKNOWLEDGMENTS

This study was supported by the Russian Foundation for Basic Research, project no. 00-15-96580

REFERENCES

1. A. H. Heuer, D. Fink, V. J. Laraia, *et al.*, Science **255**, 1098 (1992).
2. B. C. Bunker, P. C. Rieke, B. J. Tarasevich, *et al.*, Science **264**, 48 (1994).
3. E. I. Givargizov, *Artificial Epitaxy* (Nauka, Moscow, 1988); *Oriented Crystallization on Amorphous Substrates* (Plenum, New York, 1991).
4. J. H. Fendler, *Membrane-Mimetic Approach to Advanced Materials* (Springer-Verlag, Berlin, 1994).
5. R. Rosetti, J. L. Ellison, J. M. Gibson, and L. E. Brus, J. Chem. Phys. **40**, 4464 (1980).
6. X. K. Zhao, Y. Yang, L. D. McCormick, and J. H. Fendler, J. Phys. Chem. **96**, 9933 (1992).
7. X. K. Zhao and L. D. McCormick, Appl. Phys. Lett. **61**, 849 (1992).
8. V. Klechkovskaya, M. Anderle, R. Antolini, *et al.*, Thin Solid Films **284–285**, 208 (1996).
9. T. Inoue, K. Yase, M. Okada, *et al.*, Jpn. J. Appl. Phys. **28**, L2037 (1989).
10. S. Stallberg-Stenhagen and E. Stenhagen, Nature **156**, 239 (1945).
11. R. M. Kenn, C. Bohm, A. M. Bibo, *et al.*, J. Phys. Chem. **95**, 2092 (1991).
12. J. Yang, F. C. Meldrum, and J. H. Fendler, J. Phys. Chem. **99**, 5500 (1995).
13. R. Sato, Acta Crystallogr. **15**, 1109 (1962).
14. E. V. Rakova, N. D. Stepina, V. V. Klechkovskaya, *et al.*, Izv. Akad. Nauk, Ser. Fiz. **65** (9), 1268 (2001).
15. S. Mann, B. R. Heywood, S. Rajam, and J. B. A. Walker, J. Phys. D **24**, 154 (1991).

Translated by L. Man

Crystallography Reports, Vol. 47, Suppl. 1, 2002, pp. S27–S34.

MELT GROWTH

Fundamentals of High-Temperature Crystallization

Kh. S. Bagdasarov

Shubnikov Institute of Crystallography, Russian Academy of Sciences, Leninskiĭ pr. 59, Moscow, 117333 Russia

e-mail: secr@ns.crys.ras.ru

Received October 3, 2002

Abstract—The fundamental problems of high-temperature crystallization are considered. It is shown that, unlike low-temperature crystallization, high-temperature crystallization proceeds under nonequilibrium conditions, which complicates consideration of related problems. © *2002 MAIK "Nauka/Interperiodica".*

INTRODUCTION: FORMULATION OF THE PROBLEM

High-temperature crystallization is one of the comparatively new fields based on the fundamental laws of high-temperature physics and chemistry and has the following important problems:

—methodological,

—chemical processes accompanying crystallization,

—heat and mass transfer,

—kinetics at the growth front, and

—processes occurring in the grown crystal during its cooling.

Since, in many instances, there are no reliable data on the physical and chemical processes occurring at high temperatures, the rate of the development of this field of crystallography is insufficient, so that the theory often lags behind the practical needs for the synthesis of refractory single crystals.

To diminish the gap between the theory and practice of high-temperature crystallization, we make here an attempt to generalize the known theoretical and experimental data accumulated in this field. Obviously, it is impossible to consider all the problems within one article; therefore the focus is only on key problems.

Unlike low-temperature crystallization, high-temperature crystallization proceeds under nonequilibrium conditions. The process is characterized by high temperature gradients (up to 100 K/mm) and comparatively high growth rates (of the order of 10–100 mm/h). Moreover, the formation of the real structure of single crystals at high temperatures is not completed with the completion of crystal growth and is continued during single-crystal cooling.

We consider the main problems of high-temperature crystallization using an example of sapphire single crystals (Al_2O_3), a good model for such consideration. Aluminum oxide has been studied rather well [1] because it is very important for many practical applications [2]. Because of the unique combination of its physical and chemical properties, sapphire single crystals play the leading role in refractory dielectrics.

METHODOLOGICAL ASPECT OF THE PROBLEM

The development of high-temperature crystallization is closely associated with the synthesis of jewelry-quality ruby crystals. The first attempts in this direction were undertaken by the French chemist M.A. Gandin in the middle of the 19th century [3]. Melting together alumina and potassium chromate, he managed to synthesize one-carat (0.2 g) ruby crystals. Only in searching half a century did O. Verneuil manage to develop a method appropriate for industrial growth of ruby single crystals [4]. The maximum weight of these crystals did not exceed 6 g. The outstanding contribution made by Verneuil to high-temperature crystallization is confirmed by the fact that, despite numerous attempts to improve his method [5], it has not undergone any important changes over the subsequent hundred years.

The gas-flame method suggested by Verneuil is based on crystallization of aluminum oxide in air (Fig. 1). The method allows one to conduct crystallization at temperatures ranging from 2400 to 2500°C. The upper temperature limit is determined by the endothermic reaction of water molecules, because the heat source is an oxygen–hydrogen flame. Varying the ratio of the flame components, it is possible to create either oxidative or reducing conditions of crystallization.

The Verneuil method allowed one to perform the first systematic studies of high-temperature crystallization. The study of the grown crystals reveled the defects of their real structure such as mechanical inclusions, zonal and sectorial structures, and also linear and point defects. In fact, the studies of the relation between the

1063-7745/02/47S1-S0027$22.00

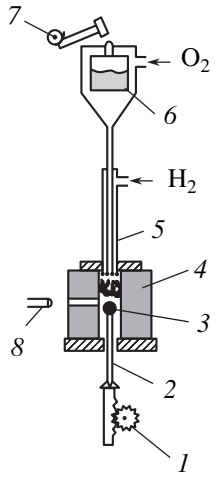

Fig. 1. Schematic of the Verneuil method. (*1*) Mechanism of crystal translation, (*2*) crystal holder, (*3*) growing crystal, (*4*) muffle, (*5*) burner, (*6*) bunker, (*7*) mechanism of bunker shaking, (*8*) cathetometer.

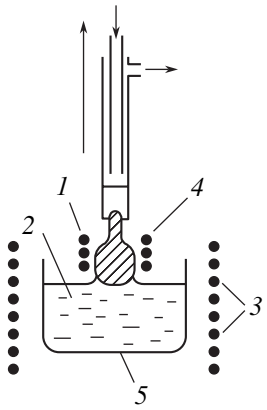

Fig. 2. Schematic of the Czochralski method. (*1*) Growing crystal, (*2*) melt, (*3*) heater, (*4*) additional heater, (*5*) crucible.

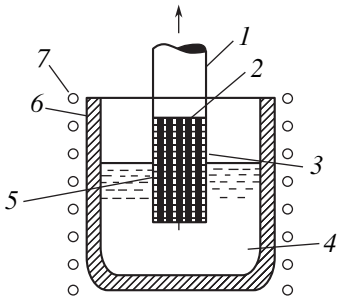

Fig. 3. Schematic of the Stepanov method. (*1*) Growing crystal, (*2*) melt film, (*3*) capillary tubes, (*4*) melt, (*5*) draw plate, (6) crucible, (*7*) heater.

growth conditions and the real structure of single crystals were started on the basis of the Verneuil method.

The necessity of increasing the nomenclature of refractory single crystals permitted the development of new growth methods that differed from the Verneuil method. Thus, in 1917, I. Czochralski suggested pulling a crystal from the melt in a crucible (Fig. 2) [6]. The crystallization conditions in his method were provided by the rigorous control of temperature and atmosphere. It is the use of this method that allowed one to perform crystallization in vacuum. The development of the Czochralski method allowed one to pass to growth of large high-quality sapphire single crystals. Later, the method underwent substantial changes. Thus, in 1926, Kyropoulos substituted pulling a crystal from the melt by directional crystallization in a crucible by slowly lowering the temperature [7]. However, in this case, some difficulties arose, which were associated with the removal of the grown crystal from the crucible. The problem was solved with the introduction of a new procedure at the concluding stage of crystallization—pulling a crystal for a distance that excluded any contact between the crystal and the crucible walls [8].

The revolutionary modifications of the Czochralski method were made by A.V. Stepanov, who suggested pulling a crystal through a draw plate, which provided growth of the single crystals with the set shape (Fig. 3) [9].

Nearly simultaneously with I. Czochralski, P. Bridgman suggested growing single crystals in a crucible with a conic bottom (Fig. 4) [10]. During the transfer of this crucible through the melting zone, a seeding crystal is formed in its conical part (the geometrical selection [11]), which provides growth of a single crystal in the crucible. The method was further improved by D. Stockbarger, who noticed that with an increase in the axial temperature gradient, the quality of the grown crystal becomes much higher. To implement this dependence in practice, Stockbarger suggested using a special thermal aperture in the melting zone, which considerably increased the axial temperature gradient (Fig. 4).

By analogy with the Kyropoulos method, it was suggested to use instead of crucible transfer a slow lowering of the temperature [12] by decreasing the local temperature of the crucible bottom by blowing on it with a cooled gas.

In 1964, Bagdasarov [13] suggested a new method of growing refractory single crystals based on the transfer of a boatlike container with the material through the melting zone (Fig. 5). In this case, the creation of controlled extended temperature fields necessary for growing large and extra large high-quality single crystals presents no technical difficulties. This method provides growth of large platelike single crystals.

Thus, the methodological problem of high-temperature crystallization seems to be completely solved. The successful solution of the main methodological problems provided the creation of the necessary conditions for solving the fundamental problems of the synthesis of refractory single crystals.

CHEMICAL PROCESSES ACCOMPANYING CRYSTALLIZATION

A.V. Shubnikov defined crystallization as a partly physical and partly chemical process [14]. In our opinion, the physical nature of crystallization is studied quite well, whereas its chemical nature is studied insufficiently. The contribution of the chemical processes to high-temperature crystallization is seen from the empirical dependence of growth rate of single crystals on the chemical composition of the substance crystallized—the more complicated the crystal composition, the lower its growth rate.

In practice, the growth rate of monatomic substances (metals and elemental semiconductors) is about 100 mm/h; the growth rate of diatomic substances (oxides and other compounds), 10 mm/h; and the growth rate of multiatomic compounds, only 1 mm/h. We consider this dependence with an example of the synthesis of sapphire single crystals. During melting of this compound, our attention was drawn to the jumpwise change of some of its physical properties. Thus, the density changed from 3.98×10^4 kg/m in crystals up to 3.01×10^4 kg/m in the melt. Even more surprising is the temperature dependence of electric conductivity (Fig. 6) [15]. The behavior of these physical characteristics indicates the occurrence of the critical structural processes accompanying melting of aluminum oxide. The character of this process can be estimated if one determines the average size of the particles (complexes) in the melt, r_k. The particle size is determined by the Fürthtz formula [16]

$$r_k = 0.62(kT/\sigma)^{3/2}$$

(where k is the Boltzmann constant, T is the melt temperature, and σ is the surface tension) with due regard for the temperature dependence of the surface tension, $\sigma(T)$ [17]. For the Al_2O_3 melt, $r_k = 1.2$ Å, which, according to the X-ray diffraction data [18], is close to the ionic radius of AlO^+ (1.82 Å) but is substantially different from the ionic radius of Al^+ (0.53 Å).

It seems that the aluminum-oxide melt contains, in addition to Al^+ and O^- ions, AlO^+, AlO_2^-, Al_2O^+, and $Al_2O_2^+$ suboxides, whose existence was repeatedly indicated by scientists who studied thermal stability of this material [19]. This is also confirmed by the estimations of r_k with due regard for the energy of the viscous flow of the melt, E_η:

$$r_k = \sqrt{E_\eta}/4\pi\sigma.$$

The corresponding data listed in Table 1 indicate the presence of relatively large particles in the melt—complexes. The analogous conclusion also follows from the activation theory developed by Eyring [20]:

$$r_k = kT(2D\eta),$$

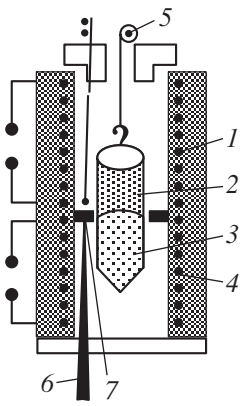

Fig. 4. Schematic of the Bridgman method. (*1*) Container, (*2*) melt, (*3*) growing single crystal, (*4*) heater, (*5*) translation mechanism, (*6*) thermocouple, (*7*) thermal aperture.

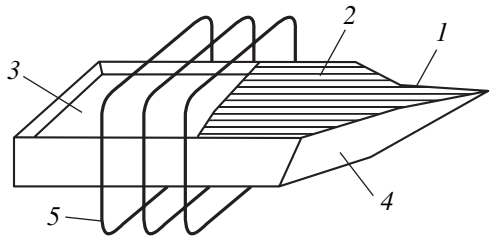

Fig. 5. Schematic of the Bagdasarov method. (*1*) Seeding crystal, (*2*) growing single crystal, (*3*) melt, (*4*) container, (*5*) heater.

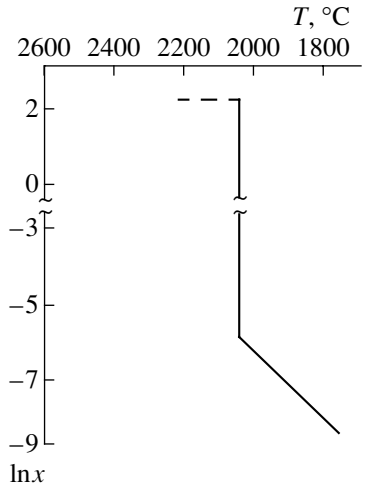

Fig. 6. Temperature dependence of conductivity [15].

where D is the diffusion coefficient and η is the melt viscosity. The thus estimated particle sizes are indicated in Table 2.

Generalizing the above data, one can draw the conclusion that the Al_2O_3 melt is an ionic liquid formed as a result of thermal dissociation processes [19]. The occurrence of the reactions of thermal dissociation was

Table 1. Average particle size r_k calculated at several melt temperatures

t, °C	r_k, Å
2050	2.28
2300	1.52
2500	1.40

Table 2. Average particle size r_k calculated with due regard for melt viscosity

t, °C	$D \times 10^5$, cm^2/s	η, Pa	r_k, Å
2050	1.95	0.58	1.50
2100	2.05	0.52	1.52
2130	2.15	0.45	1.70
2150	2.35	0.39	1.82

assumed by comparing the experimental and the calculated conductivities of the melt, χ, and the use of the Einstein relationship [21]:

$$\chi = Dz^2F^2c/NR,$$

where z is the ion charge, F is the Faraday number, c is the ion concentration, N is the Avogadro number, and R is the gas constant.

The results of this estimation are indicated in Table 3, according to which the most probable reactions of thermal dissociation are

$$Al_2O_3 \rightleftharpoons AlO^+ + AlO_2^+,$$

$$2Al_2O_3 \rightleftharpoons Al^+ + 3AlO_2^-.$$

Generalizing the above data, one can draw the conclusion that the existence in the melt of complexes with different diffusion mobility should produce the decisive effect on the growth kinetics and the limiting growth rate of high-quality single crystals. In fact, the excessive components behave as impurities and provide the concentration supercooling [22]. Under these conditions, various inhomogeneities, including the point defects, can be formed in a growing single crystals [23].

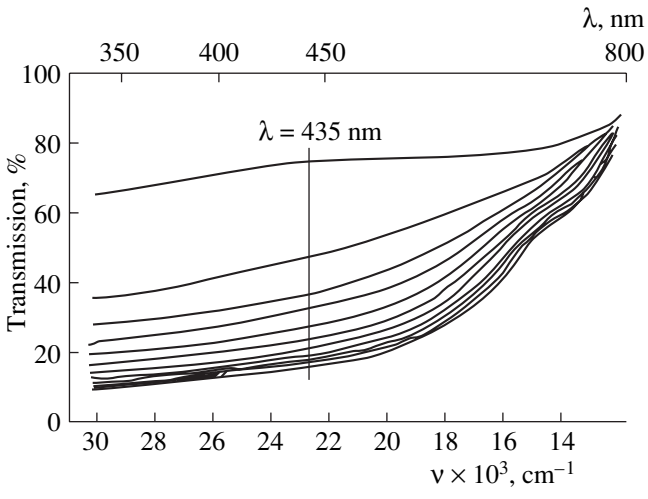

Fig. 7. Transmission curves of a multiply UV-irradiated (λ = 254 nm) single-crystal sapphire specimen.

The above is confirmed by the studies of the real structure of single crystals. Thus, studying the nature of point-defect formation, one can establish the state of the melt at the moment of its crystallization. The defects observed in the real structure of single crystals can be considered as the indicators of the existing growth conditions.

It is well known that sapphire single crystals irradiated with ultraviolet (λ = 254 nm) at wavelengths ranging within λ = 250–800 nm are characterized by a broad absorption band (Fig. 7) [24] provided by the formation of optical centers and point defects (vacancies) in the crystal lattice. The absorption intensity depends on the irradiation time. The curves in Fig. 7 correspond to the successive cycles of 1-min UV-irradiation of a crystal. These transmission curves are similar to the saturation curves; in other words, the number of optical centers is finite. Heating of the UV-irradiated specimens up to 500°C removes the absorption bands, which indicates the destruction of the optical centers.

The study of the above effect shows that the intensity of the absorption band induced by the ultraviolet irradiation is essentially dependent on the nature of the atmosphere in which a crystal grows. The absorption-band intensity is maximal for crystals grown in vacuum and hydrogen atmosphere and minimal for crystals grown in air and in inert atmosphere (Ar) (Fig. 8). The temperature dependence of the intensity of aluminum-oxide evaporation behaves in a similar way (Fig. 9) [2], maximal in vacuum and hydrogen atmosphere and minimal in an inert gas.

The similar behavior of two different dependences indicates their close relation. Indeed, the nature of point defects in sapphire single crystals depends on the evaporation of the Al_2O_3 melt. Studying the nature of the point defects, one can also establish the nature of evaporation. Since point defects are electrically charged, we studied their nature by the electrodiffusion method.

The experiments on electrodiffusion were performed on $10 \times 10 \times 10$ mm^3-large polished specimens under the following conditions: t = 1200°C, V = 100 V/cm, and τ = 6 h. These experiments gave the following results:

—the diffusion flow of point defects is always directed toward the positively charged electrode, which proves that point defects are charged negatively;

—the electrodiffusion rate along the ⟨0001⟩ direction is higher than along other crystallographic directions;

—electrodiffusion is completed with the formation of aggregates of point defects in the vicinity of the pos-

Table 3. Possible dissociation reactions in aluminum oxide with due regard for melt conductivity

t, °C	$D \times 10^5$, cm^2/s	Conductivity χ, Ω^{-1} cm^{-1}			
		experimental	conductivity calculated by the following reactions of thermal dissociation		
			$Al_2O_3 \rightleftarrows Al^+ + 3O^-$	$2Al_2O_3 \rightleftarrows Al^+ + 3AlO_2^-$	$Al_2O_3 \rightleftarrows AlO^+ + AlO_2^-$
2050	1.95	0.71	4.50	2.25	0.25
2100	2.05	0.78	5.20	2.60	0.29
2130	2.15	0.91	5.95	3.00	0.33
2150	2.35	1.03	6.00	3.25	0.36

itively charged electrode, and these defects do not leave the crystal;

—the portion of the crystal having no point defects is insensitive to subsequent ultraviolet irradiation.

The above experimental data clearly show that the nature of point-defect formation is determined by the selective evaporation of the melt. Taking into account the nature of the formation and disappearance of the optical centers and their charge, one can state that the sought component is aluminum, whose vapor elasticity at the melting point of Al_2O_3 is rather high. Obviously, this process depends on the nature and pressure of the crystallization atmosphere. The process is especially intense in vacuum and hydrogen atmosphere (where the reduction of aluminum by hydrogen is possible) and is rather weak in air and inert atmospheres.

HEAT TRANSFER IN NONTRANSPARENT, SEMITRANSPARENT, AND TRANSPARENT MEDIA

Another important characteristic of high-temperature crystallization is the nature of heat transfer. Here, one has to take into account not only thermal and physical properties of the medium to be crystallized, but also its optical properties, especially in the spectrum range, where the Planck function has the maximum value. For a blackbody (the materials used as heating elements such as graphite, tungsten, and molybdenum, can be considered as blackbodies), the maximum of the Planck function lies in the vicinity of 3 μm [25], i.e., in the range where the transparency of many refractory materials is quite pronounced. Thus, three cases of heat transfer should be distinguished:

$$\alpha L \gg 1, \quad \alpha L \approx 1, \quad \alpha L \ll 1,$$

where α is the absorption coefficient of the medium and L is the characteristic length along the heat flow, i.e., the distance at which the heat flow completely attenuates.

The first case, $\alpha L \gg 1$, corresponds to nontransparent media in which the radiation from a heat source is absorbed by the surface; further heat transfer proceeds by the mechanism of phonon heat transfer λ_{ph}. This case is characteristic of monatomic substances, e.g., metals and elemental semiconductors. The heat flux q is described by the Fourier law,

$$q = -\lambda_{ph} \operatorname{Grad} T,$$

and the heat conductivity equations.

The second case, $\alpha L \approx 1$, is typical of semitransparent media. The radiation incident onto the melt and crystal gradually attenuates. The heat transfer occurs by

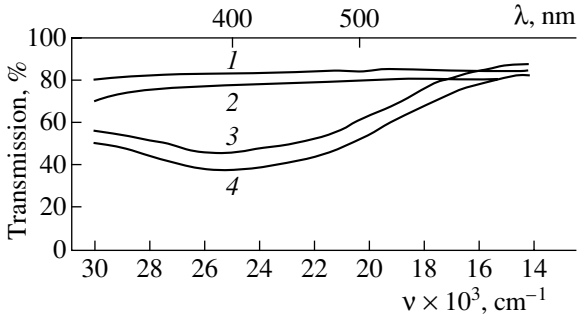

Fig. 8. Transmission curves of the single-crystal sapphire specimens grown in (*1*) air, (*2*) inert argon atmosphere, (*3*) vacuum, (*4*) hydrogen atmosphere.

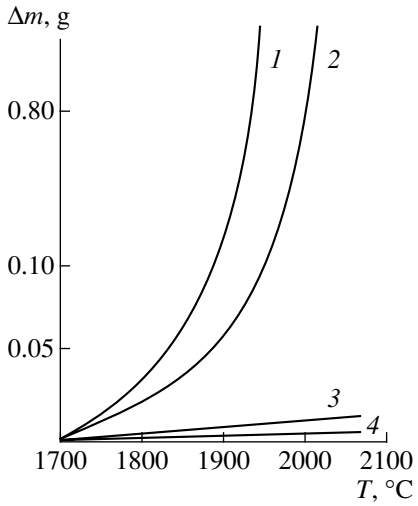

Fig. 9. Intensity of Al_2O_3 evaporation as a function of temperature in (*1*) hydrogen atmosphere, (*2*) vacuum, (*3*) inert nitrogen atmosphere, (*4*) air.

Table 4. Homogeneity criterion for $Y_3Al_5O_{12}(Nd^{3+})$ single crystals along different crystallographic directions

Growth form	Chemical element	Average fluorescence intensity J for 100 s	$\sqrt{J}$	$Z_k = [\Sigma(J_i - J)^2/(n-1)]^{1/2}$	Homogeneity criterion $Z_k/2\sqrt{J}$
(100) face	Nd	6200	79	700	4.40
	Y	60980	247	3149	6.37
	Al	183205	428	1521	8.80
Nonfacial	Nd	5518	74	115	0.80
	Y	61941	249	507	1.10
	Al	188540	434	869	1.00

Note: Z_k is the quantity proportional to the fluorescence intensity.

the mechanism of reradiation. The Fourier law and the heat conductivity equations are valid in this case as well. However, the heat conductivity coefficient here is understood as the sum

$$\lambda_0 = \lambda_{ph} + \lambda_r,$$

where λ_{ph} and λ_r are the heat conductivities of the phonon and radiation components, respectively, $\lambda_r = 16n^2kT^3/3\alpha$, and n is the refractive index of the medium.

When determining the configuration of the temperature field, one has necessarily to take into account the optical properties of the melt and the crystal. Doing so for the melt layer showed that, because of the finite transparency of the crystal in the range of the Planck-function maximum, the temperature gradient is not constant and, upon approach to the growth front, increases by several times [26]. It is these conditions that are most often implemented in the practice of growth of refractory single crystals.

The third case, $\alpha L \ll 1$, is that of the transparent medium. The radiation from a heat source in this medium does not completely attenuate; it is multiply reflected from the container walls and other elements of the crystallization furnace. In this case, the Fourier law is no longer fulfilled and the heat conductivity equations become invalid. Instead, one has to use the integral radiative transfer equation. In this case, the heat conductivity coefficient is, in fact, the effective coefficient λ_{eff}, because it depends on the shape of the crystallization front and the boundary conditions,

$$\lambda_{eff} = 4\pi kT^3 n\varphi_k,$$

where φ_k is a factor dependent on the optical properties and the system configuration.

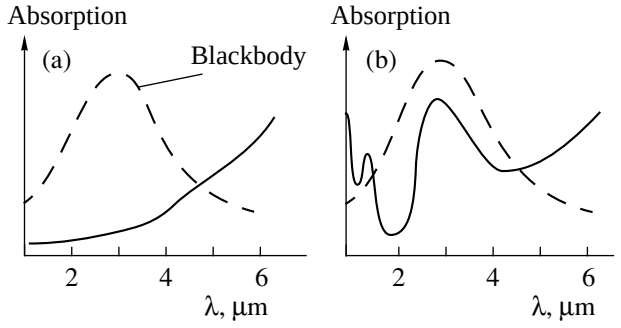

Fig. 10. Absorption curves of (a) $Y_3Al_5O_{12}$ and (b) $Dy_3Al_5O_{12}$ single crystals in the range of the Planck-function maximum (dashed curve).

As an example, consider two chemically similar garnets ($Y_3Al_5O_{12}$) and ($Dy_3Al_5O_{12}$) possessing different optical properties in the range of the Planck-function maximum (Fig. 10) [25]. It is seen that for $Y_3Al_5O_{12}$, condition $\alpha L \ll 1$ is fulfilled, whereas for $Dy_3Al_5O_{12}$, condition $\alpha L \approx 1$ is fulfilled. This is the only difference in the thermal growth conditions for these two single crystals. In the second case, no faceted growth is observed and the growth rate of high-quality single crystals is considerably higher than in the first case.

KINETICS AT GROWTH FRONT

High-temperature crystallization is also characterized by the specific growth kinetics. The atomic roughness of the growth front depends on the axial temperature gradient. Two limiting cases were established experimentally: a growth front consisting of atomically smooth surfaces (faces) and an atomically rough growth front (which almost repeats the isothermal growth surface). Both cases take place in the growth of single crystals [27].

The X-ray microanalysis of the crystal portions formed by the above growth mechanisms (see Table 4) showed that the homogeneity of the crystal composition is essentially dependent on the degree of atomic roughness of the growth front. The homogeneity criterion for an atomically rough front is higher than for an atomically smooth front. On the contrary, the coefficient of Nd-ion distribution in $Y_3Al_5O_{12}$ crystals is higher for an atomically smooth surface.

The above experimental facts dictated the necessity in the control of the atomic roughness of the growth

front. This can be attained using the dependence [28]

$$d_f = 2\sqrt{r_{fr}}\Delta T_{max}/\mathrm{Grad}\,T,$$

where d_f is the average face dimension, r_{fr} is the curvature radius of the growth front, ΔT_{max} is the maximum admissible supercooling at the growth front, $\mathrm{Grad}\,T = (a_c\partial T_c/\partial x + a_m\partial T_m/\partial x)/(a_c + a_m)$ is the generalized temperature gradient, where a_c and a_m are the heat-conductivity coefficients of the crystal and the melt, and $\partial T_c/\partial x$ and $\partial T_m/\partial x$ are the temperature gradients in the crystal and the melt, respectively.

Thus, the transition to a rough growth front occurs with an increase of Grad$T$, which is consistent with the experimental data [27]. The transition to a rough growth front can also be achieved by decreasing ΔT. However, the latter method is limited by the degree of the chemical stability of the substance to be crystallized. In particular, for chemically stable substances, ΔT can be decreased by using deep chemical cleaning of impurities. In the case of chemically unstable compounds, this is almost impossible and, therefore, the control of the front roughness is implemented either by increasing the axial temperature gradient or by flattening the growth front.

PROCESSES OCCURRING IN GROWN CRYSTAL DURING ITS COOLING

One of the characteristic features of high-temperature crystallization is the fact that the formation of its real structure is not completed with an event of a phase transition. This process continues in a certain temperature range because, at temperatures close to the melting point, both micro- and macroparticles move to the growth front. The possible mechanism of particle motion in a single crystal was studied earlier [29]. The motion of macroparticles in a high-gradient temperature field occurs because of recondensation of the substance inside an inclusion. Therefore, for micron and submicron particles, the above mechanism is hardly probable. Our experiments show that, in the vicinity of the melting point of Al_2O_3, microparticles move with rather high velocities (several mm/h). This fact also indicates the possible occurrence of some other mechanisms and, in particular, of the mechanism provided by the temperature dependence of the density of the substance to be crystallized. However, in this case, the mechanical inclusions would be empty. Then, in high-gradient temperature fields, the temperature dependence of the density of the basic material would provide the motion of these particles with a velocity almost independent of the particle size.

CONCLUSIONS

The methodological problem of the high-temperature crystallization has almost been solved.

The high-temperature crystallization has a fundamental characteristic associated with the necessity of rigorous account for the physical and chemical properties of the substance to be crystallized. Here, an essential part is played by the degree of the chemical stability of the substance to be crystallized—the more stable the substance, the higher its growth rate.

Allowance for the possible formation of complexes in the melt is necessary for the determination of the critical growth rate of single crystals.

When determining the temperature-field configuration, one has necessarily to take into account also the optical properties of the melt and the crystal.

The process of real-structure formation is not completed with the event of the phase transition but continues in the grown single crystal during its cooling.

REFERENCES

1. M. A. Maurakh and B. S. Mitin, *Liquid Refrectory Oxides* (Metallurgiya, Moscow, 1979).
2. Kh. S. Bagdasarov, Itogi Nauki Tekh., Ser. Kristallokhim. **21**, 3 (1987).
3. M. A. Gandin, C. R. Hebd. Seances Acad. Sci., No. 4, 999 (1857).
4. O. Verneuil, C. R. Hebd. Seances Acad. Sci. **135**, 791 (1902).
5. K. T. Vil'ke, *Methods of Crystal Growth* (Nedra, Leningrad, 1968).
6. I. Czochralski, Z. Phys. Chem. (Leipzig) **92** (2), 219 (1917).
7. S. Kyropoulos, Z. Anorg. Allg. Chem. **154**, 308 (1926).
8. M. I. Musatov, Izv. Akad. Nauk SSSR, Neorg. Mater. **15**, 1806 (1979).
9. A. V. Stepanov, Izv. Akad. Nauk SSSR, Ser. Fiz. **33** (12), 1946 (1969).
10. Kh. S. Bagdasarov, in *Modern Crystallography*, Vol. 3: *Crystal Growth*, Ed. by B. K. Vainshtein, A. A. Chernov, and L. A. Shuvalov (Nauka, Moscow, 1980; Springer-Verlag, Berlin, 1984).
11. A. V. Shubnikov, E. E. Flint, and G. B. Bokiĭ, *Foundations of Crystallography* (Akad. Nauk SSSR, Moscow, 1940).
12. F. Schmid and D. Viechnicki, J. Am. Ceram. Soc. **53** (9), 528 (1970).
13. Kh. S. Bagdasarov, in *Proceedings of the Fourth All-Union Conference on Crystal Growth, Tsakhkadzor, 1972* (Akad. Nauk Arm. SSR, Yerevan, 1972), p. 6.
14. Kh. S. Bagdasarov, Kristallografiya **32** (3), 764 (1987) [Sov. Phys. Crystallogr. **32**, 449 (1987)].
15. V. I. Aleksandrov, V. V. Osiko, and V. M. Tatarintsev, Izv. Akad. Nauk SSSR, Neorg. Mater. **8** (5), 956 (1972).
16. R. Fürthtz, Proc. Cambridge Philos. Soc. **37**, 255 (1941).
17. Yu. V. Zubarev, V. I. Kostikov, B. S. Mitin, *et al.*, Izv. Akad. Nauk SSSR, Neorg. Mater. **5** (9), 1563 (1969).
18. G. B. Bokiĭ, *Introduction to Crystal Chemistry* (Mosk. Gos. Univ., Moscow, 1954).
19. I. S. Kulikov, *Thermal Dissociation of Compounds* (Metallurgiya, Moscow, 1969).

20. S. Glasstone, K. J. Laidler, and H. Eyring, *Theory of Rate Processes* (McGraw-Hill, New York, 1941; Inostrannaya Literatura, Moscow, 1948).

21. O. A. Esin and P. V. Gel'd, *Physical Chemistry of Pyrometallurgical Processes* (Metallurgiya, Moscow, 1966), Part 2.

22. R. Laudise and R. Parker, *The Growth of Single Cristals; Crystal Growth Mechanisms: Energetics, Kinematics and Transport* (Prentice-Hall, Englewood Cliffs, 1970; Mir, Moscow, 1974).

23. Kh. S. Bagdasarov, A. I. Munchaev, and M. V. Remizov, Kristallografiya **36** (2), 463 (1991) [Sov. Phys. Crystallogr. **36**, 253 (1991)].

24. Kh. S. Bagdasarov, A. I. Munchaev, S. A. Kobzareva, and V. F. Karyagin, Perspekt. Mater., No. 2, 32 (2001).

25. B. Cockayne, M. Chesswas, and D. B. Gasson, J. Mater. Sci. **2**, 7 (1967).

26. Kh. S. Bagdasarov, Yu. K. Lingart, and S. N. Smirnov, Kristallografiya **28** (6), 1194 (1983) [Sov. Phys. Crystallogr. **28**, 701 (1983)].

27. Kh. S. Bagdasarov, L. M. Dedukh, I. A. Zhizheĭko, *et al.*, Kristallografiya **15** (2), 334 (1970) [Sov. Phys. Crystallogr. **15**, 278 (1970)].

28. A. A. Chernov, in *Modern Crystallography*, Vol. 3: *Crystal Growth*, Ed. by B. K. Vainshtein, A. A. Chernov, and L. A. Shuvalov (Nauka, Moscow, 1980; Springer-Verlag, Berlin, 1984).

29. Kh. S. Bagdasarov, J. Adv. Mater. **1** (2), 173 (1994).

Translated by L. Man

Crystallography Reports, Vol. 47, Suppl. 1, 2002, pp. S3–S14.

CRYSTALS OF THE FUTURE

Semiconductor Silicon at the Threshold of Twenty-First Century

M. G. Mil'vidsky

Institute of Chemical Problems of Microelectronics,
Bolshoĭ Tolmachevskiĭ per. 5, Moscow, 109017 Russia
e-mail: icpm@mail.girmet.ru

Received October 3, 2002

Abstract—The strategy of the further development of silicon technology in the near future is analyzed in light of the problems of semiconductor electronics. The main tendencies in synthesis of dislocation-free single crystals of large dimensions with a controlled concentration of microdefects are considered. Promising directions of future development of the technology for manufacturing thin epitaxial films, including $Si_{1-x}Ge_xSi$ heteroepitaxial films with low dislocation concentrations, are discussed. Considerable attention is paid to the prospects for technologies used in synthesis of high-quality silicon-on-insulator structures. The problems of silicon-based optoelectronics associated with manufacturing device structures for highly efficient radiation sources are analyzed in terms of materials science. The characteristic features of the present state in technology and materials science of silicon, the most important semiconductor material, are discussed. © *2002 MAIK "Nauka/Interperiodica".*

INTRODUCTION

For nearly 50 years, semiconductor silicon has been the number one material for solid-state electronics. Enormous investments have been made into the development of silicon industry and its scientific basis, and the results obtained in this field are rather impressive. Today, single-crystal silicon is the best crystalline material of all the numerous natural and synthetic materials. Every year, about 20 000 tons of high-quality dislocation-free single crystals are synthesized. Most of these unique products, about 80% of all the single crystals synthesized in the world, are consumed in microelectronics.

The influence of microelectronics on scientific and technological progress is incredible and, to a large extent, determines the solution of the problems associated with the widespread use of computers and information technologies, the creation of new communication and television systems, various medical and special-purpose equipment, and household appliances. Silicon microelectronics enters the 21st century with very large-scale integrated (VLSI) circuits with 256 Mbit–1Gbit dynamic memory and microprocessors operating at 0.5–1.0 GHz master-clock frequencies. In 2012, the creation of 64-Gbit-dynamic memory and 10 GHz-microprocessors is expected. In 1998, the total volume of the output of silicon microelectronics exceeded 140 billion dollars, whereas the income from the sales of modern microelectronics products (computers, mobile telephones, video- and TV apparatus) approached the record sum of one billion dollars [1].

Single-crystal silicon is also the main material of high-current (high-power) electronics. The nomenclature of high-current devices increases every year and includes powerful diodes and thyristors and a wide spectrum of powerful transistors and various integrated circuits, which substantially increases the possibilities provided by powerful semiconductor devices. Today, high-current silicon-based electronic devices are successfully used in long-distance power transmission systems with minimum energy losses, in power-intensive metallurgic and chemical industries, in means of transport, and in systems of electric drive and power consumption. Even the most modest estimates show that the optimum saturation of power engineering with the means of modern high-current electronics would provide savings of not less than 10–15% of all the electrical energy produced in the world, the amount approximately equivalent to the energy produced by all nuclear power stations [2].

Silicon also plays a decisive role in the development of semiconductor solar engineering. The total amount of electrical energy produced by silicon solar batteries has already exceeded the level of a thousand megawatts. It is expected that in the nearest future, this figure would be multiplied by a factor of several tens and would be accompanied by a simultaneous decrease in the price of electrical energy to a level comparable to or even lower than the price of electrical energy from traditional power sources such as electrical heating plants and nuclear and hydroelectrical stations. The widespread use of solar batteries in power engineering is also very promising in terms of ecology. Undoubtedly, the 21st century will see new nontraditional energy

1063-7745/02/47S1-S0003$22.00

sources, and semiconductor solar-energy converters would play an important role in this process.

Recent studies allow one to see the real prospects of silicon optoelectronics, the possibilities provided by the widespread effective use of silicon in various sensor devices, precision micromechanical systems, and in many other fields of modern technology.

Nowadays, the industry of semiconductor silicon is an excellent example of the impressive achievements of the human intellect in the development of world civilization. Its further progress is closely related to the solution of ever more complex scientific and technological problems. Below, we consider some of these.

1. GENERAL STRATEGY OF SILICON TECHNOLOGY DEVELOPMENT

The strategy of silicon technology is determined, first and foremost, by the requirements of microelectronics. Beginning in 1994, the Semiconductor Industry Association has regularly published the prognoses of the development of this most important direction. A fragment of such a prognosis made in 1994 on the use of silicon-based VLSI circuits in dynamic memory is given in the Table.

The prognosis made in 1998 indicates a transition to the topological dimension of the working element in VLSI circuits equal to 0.035 μm in 2012 and a further increase in the wafer diameter up to 675 mm by 2015 [1].

The increasing complication of VLSI circuits is accompanied by more severe requirements on the wafer quality (total and local planarity, reduction of the level of surface contamination, increase in the structural quality and homogeneity of the initial single crystal) and a simultaneous increase in wafer diameter and a considerable reduction in their cost. The latter requirement is very important. At the same time, with an increase in the wafer diameter, their cost considerably increases. Thus, the transition from wafers with a diameter of 150 mm to wafers with a diameter of 200 mm increased their cost by about 30%; still, a considerable economic gain was achieved because of the increased efficiency of VLSI circuit production. The preliminary estimates show that a further transition to wafers with a diameter of 300 mm can result in an additional economic gain at a level not lower than 25%. What will be the economic effect of the transition to wafers with a diameter of 400 mm or more is still unknown. In any case, it is obvious that the production of high-quality wafers with such a diameter would require enormous additional investments in their production.

Economic reasons can introduce considerable corrections into the strategic planes of silicon-based microelectronics and force silicon manufacturers to significantly revise the traditional approaches to the synthesis of single crystals and production of wafers of the necessary quality. On the other hand, one has to bear in mind that with a decrease of the topological dimensions of the working elements of integrated circuits, the depth of location of *p–n* junctions, and the layer thickness of a SiO_2 gate insulator, the working characteristics of transistors become more dependent on the characteristics of the surface and subsurface layers of wafers. Therefore, one can expect that some requirements on the bulk properties of wafers will soon be revised. Additional requirements on the wafer quality, in particular, to their nonplanarity, can also be dictated by the use of shorter ultraviolet range and X-ray radiation in the traditional technology of lithography and the application of mask-free electron-beam lithography [1, 3]. Today, as never before, we need to create a unified ideology (in terms of materials science) for solving the scientific and technological problems in the whole single crystal–wafer–integrated circuit technological cycle. In turn, this requires the close cooperation of silicon manufacturers with the users of their products.

A considerable increase in the assemblage density and a decrease in the dimensions of the working elements of VLSI circuits dictate a reduction of the working currents and voltages. Under these conditions, the negative role of various noises substantially increases. In this connection, the requirements on purity, structural quality, and microhomogeneity of the active region of the device structure become considerably more severe,

Fragment of technology road map on VLSI

Planned parameter	Year					
	1995	1998	2001	2004	2007	2010
Memory	64 Mbit	256 Mbit	1 Gbit	4 Gbit	16 Gbit	64 Gbit
Dimensions of working element, μm	0.35	0.25	0.18	0.13	0.10	0.07
Depth of *p–n* junction, μm					0.05	0.03
Thickness of oxide layer, nm			3	2.5	2	1.5
Diameter of silicon wafer, mm	200	200	300	300	400	400
Number of particles on the wafer surface	50	40	50	40	35	20
Dimensions of particles, μm	0.12	0.08	0.06	0.04	0.03	0.02

especially the requirements on the level of contamination with various impurities giving rise to electrically and recombination-active centers. This makes purity one of the global problems [4]. High purity should be maintained at all the stages of integrated-circuit manufacturing beginning with the synthesis of extra pure polycrystalline silicon. This problem is especially important for the manufacture of wafers and elements of integrated circuits. The admissible level of surface contamination of wafers changed with time in the following sequence: 5×10^{10} in 1995, 2.5×10^{10} in 1998, 1×10^{10} in 2000, and is predicted to be 5×10^{9} in 2004. Special attention is given to the purity of the starting and auxiliary materials. One has to develop efficient ecologically pure technologies and equipment for production of a large number of technological gases, materials for containers, metals, and chemical reagents, in which the content of the residual impurities does not exceed values ranging from 10^{-7} to 10^{-8}%. This, in turn, requires the creation of highly sensitive methods of analysis of the corresponding materials, which would detect contamination with impurities at a level of 10^{-9} to 10^{-10}%, and the use of extraclean production areas.

The creation of absolutely pure industries is hardly probable, because it would require enormous investment. Thus, gettering of the residual impurities and defects and creation of efficient gettering media also become urgent tasks. The solution of this problem requires, in turn, the development of efficient methods for control of the defect state of the system and, first of all, the state of ensembles of intrinsic point defects in the crystal matrix at the stages of growth of single crystals, preparation of wafers, and formation of individual elements of the VLSI circuits themselves.

An important role in the solution of the purity problem and higher quality of the device structures is played by the inclusion of low-temperature fast technological processes into the general industrial chain, especially at the stage of epitaxial growth, plasma–chemical treatment, film deposition, formation of *p–n* junctions, insulation, and thermal and photon annealing. Special attention should be given to nonthermal stimulation of technological processes.

An important place in the general scheme of creation of VLSI circuits of ever increasing complexity is occupied by the creation of precision, highly efficient, technological equipment and automation of the main technological processes. This requires more sophisticated technological equipment and more exacting standards for individual production lines.

New, serious problems also arise in controlling the ready production of new industries. Here, the control of wafer quality is especially important. With an increase in the degree of integration, the need for new high-resolution and high-speed highly informative and automated contact-free methods of quality control dramatically increases. The requirements imposed on the number of admissible defects and their dimensions on the wafer surface become stricter every year, whereas the possibilities of traditional optical and electrophysical methods of their control have already been exhausted. It is necessary to pass to a higher level metrology which would use all the possibilities provided by scanning tunneling and atomic-force microscopy and other modern methods of control for the structure and the properties at a submicron and nanometer resolution. These new methods of control should also fit the ideology of the creation of flexible, continuous, highly productive automated technological lines. These rapid methods of surface control should be sensitive to contaminations with metal impurities as low as ~10^8 at/cm^2.

Under the conditions of ever increasing complexity of the industrial processes and the transition to highly productive large-charge technological equipment, one has to pay special attention to the modeling of heat and mass transfer, elementary crystallization processes, and real defect formation. The qualified modeling of these processes at minimum expenses should provide the optimization of the main technological processes and the corresponding technological apparatus.

2. DISLOCATION-FREE SINGLE CRYSTALS WITH LARGE DIAMETERS

Single-crystal growth is one of the most important stages in the creation of device structures. The wafers cut out from the grown single crystal are used either for manufacturing integrated circuits on their basis and creating discrete devices or else as substrates in manufacturing epitaxial thin-film structures. In both cases, the requirements on the quality of single-crystal wafers are very high.

As a rule, silicon single crystals are grown by the Czochralski method. The technology of growing dislocation-free silicon single crystals is developed along the lines of increasing crystal diameters and improving their quality and the uniformity of the electrophysical characteristics in the material bulk. To provide the necessary economic efficiency of the technological process in the chain single crystal–wafer, the length of the cylindrical part of the ingot should not be less than 100 cm [1]. This signifies that growth of a crystal with a diameter of 200 mm requires the minimum weight of the material loaded into the crucible not less than 110 kg (in actual fact, the crucibles are loaded with about 150 kg of the starting material). In growth of crystals with a diameter of 300 mm, this weight should be about 200 kg (in practice, 250–300 kg). For crystals with a diameter of 400–450 mm, furnaces loaded with 550–600 kg of initial material would be used. The diameter of the widely used quartz crucible is already close to one meter.

When growing crystals with large diameters, one has to considerably reduce the pulling rates, which increases the duration of the technological process with all the subsequent negative consequences. It is also nec-

essary to provide efficient control for heat and mass transfer in the large mass of the melt. It seems that this can be achieved most efficiently with the use of magnetohydrodynamic factors and rather intense (from three to four thousand gauss) fields. Another important task is the precision control of heat fields, which requires the optimum design of thermal units used in the growth setups. One should not forget the additional difficulties associated with the necessity of providing a very low level of contamination in growing crystals (the total content of rapidly diffusing metal impurities should not exceed 10^{11} cm^{-3} and of carbon impurities, 1×10^{15} cm^{-3}) and also rigorous control of the uniformity of oxygen distribution in the ingot volume. Moreover, the necessity of reliable support of a very heavy crystal in the process of its pulling also considerably complicates the design of growth setups. Under these conditions, an increase in the economic efficiency of growth of single crystals at each new stage of an increase in their diameter becomes more and more difficult, especially, of single crystals with a diameter exceeding 200 mm.

One of the most serious problems encountered in growth of dislocation-free single crystals with large diameters is the necessity of reduction of the concentration of growth microdefects and their dimensions. Recent studies show that it is growth microdefects contained in wafers that considerably deteriorate the working characteristics of VLSI circuits [5, 6]. Therefore, a decrease in the topological dimensions of the working elements of integrated circuits makes the requirements imposed on the number of submicron defects on the wafer much more severe.

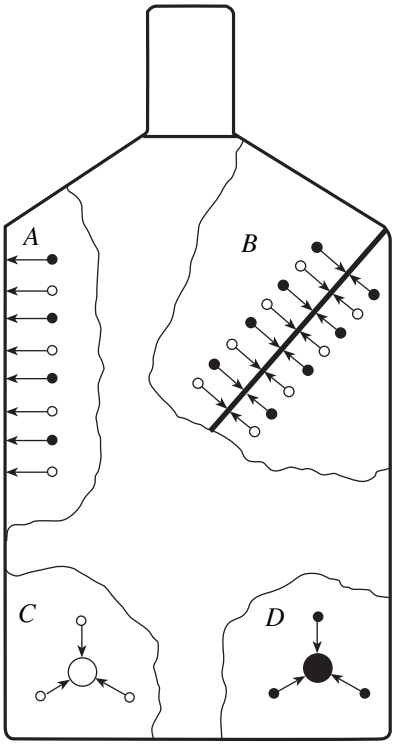

Fig. 1. Possible sinks for excessive intrinsic point defects in grown single crystals. (*A*) sink to the side surface, (*B*) sink to dislocation, (*C*) formation of aggregates of vacancies, (*D*) formation of aggregates of interstitial atoms (○ denotes a vacancy, ● denotes an interstitial atom).

The main role in the formation of growth microdefects in Czochralski-grown single crystals is played by intrinsic point defects (vacancies, interstitial atoms) and also oxygen impurities [7–12]. Under real growth conditions, considerable supersaturations with intrinsic point defects are observed at rather small distances from the crystallization front caused by the drastic temperature dependence of their equilibrium concentrations in the silicon crystal lattice. The excessive nonequilibrium intrinsic point defects thus formed are annihilated at sinks whose role is played by the side surface of the ingot and larger defects present in the ingot bulk, and, first of all, dislocations (Fig. 1). However, dislocation-free single crystals have no such efficient internal sinks, the side surface of the ingot cannot provide the complete removal of the "supersaturation with defects" because of a limitation of purely diffusion nature. As a result, solid solutions supersaturated with intrinsic point defects are formed in the crystal bulk and then decompose in the process of postcrystallization cooling with the formation of micron and submicron spherical aggregates, which are called microdefects. Another source of growth microdefects is oxygen, whose concentration in growing single crystals is usually sufficient for the formation of supersaturated solid solutions in the process of postcrystallization cooling. Despite the fact that the oxygen concentration in a crystal is much higher than the concentration of intrinsic point defects, it is the latter defects that play the key role in the processes of defect formation. The point is that the driving force of aggregation is not the absolute concentration of point defects (intrinsic or extrinsic), but the supersaturation of the corresponding solid solution, which is substantially higher for intrinsic point defects because of a drastic decrease in their equilibrium concentration with lowering of the temperature.

The enthalpies of formation of interstitial atoms and vacancies in the silicon crystal lattice are comparatively close. Therefore, the equilibrium concentrations of these defects are comparable in a rather wide temperature range, and, therefore, the process of their recombination plays an essential part in the formation of microdefects. As was shown in [13], under the conditions of fast recombination of interstitial atoms and vacancies, the key parameter determining the type of the surviving intrinsic point defects and also the nature, dimensions, and concentration of growth microdefects in a growing crystal is the ratio of the growth rate V to the axial temperature gradient G in the vicinity of the crystallization front in the ingot, $\xi = V/G$. At a certain critical value of this parameter, ξ_t, and the limited content of oxygen in the crystal, no growth defects should form at all. At $\xi < \xi_t$, the crystals after recombination still have some interstitial atoms and, therefore, the interstitial-type

microdefects are formed as aggregates of interstitial atoms and interstitial-type dislocation loops. Usually, these crystals are called interstitial-type. At $\xi > \xi_t$, some vacancies survive in single crystals and, therefore, the typical defects are vacancy pores and of oxygen-vacancy aggregates. These crystals are called vacancy-type (Fig. 2).

The most pronounced negative effect on the parameters of VLSI circuits is produced by interstitial dislocation loops and pores (Fig. 3), whose formation occurs under considerable deviations from ξ_t (regions II in Fig. 2). In this case, the formation of aggregates of interstitial atoms deteriorates the characteristics of transistors and increases the leak currents via the *p–n* junction, whereas the vacancy-type pores deteriorate, first of all, the quality of the SiO_2 gate insulator. At present, the synthesized single crystals with large diameters are vacancy-type crystals and, therefore, at the present stage of the technology's development, the main task is growth of crystals without vacancy-type pores.

To grow single crystals without microdefects, which can influence the working characteristics of VLSI circuits, one has to maintain the growth conditions with small deviations from ξ_t (regions I in Fig. 2) and also the necessary modes of postcrystallization cooling of the ingot. To meet these requirements under a gradient *G* varying both along its length and in the transverse section of the single crystal is far from easy. As was established in [14], the additional doping of crystals with nitrogen up to concentrations of $\sim 10^{15}$ cm^{-3} allows one to considerably increase the range of the admissible variations of the growth conditions. Similar results were also obtained for crystals doped with boron up to rather high concentrations [15]. However, the additional doping does not completely solve the problem, because the necessary results can be achieved only at considerably lower pulling rates, which increases the duration and the cost of the technological process.

Considerably larger possibilities for improving the structural quality of single crystals with growth defects are provided by thermal treatment of wafers cut out of such ingots. The wafer surface is a good sink for intrinsic point defects and impurities present in its bulk. The modes of thermal treatment (temperature, ambient atmosphere) are selected proceeding from the nature of microdefects present in the wafer [9]. Thus, good results for the wafers prepared from vacancy-type crystals are provided by their high-temperature treatment in a H_2 or Ar atmosphere or in a mixture of both gases [16, 17]. In the process of such treatment, an almost defect-free layer is formed in the vicinity of the wafer surface, whereas in its bulk, the conditions are favorable for the formation of an inner getter consisting of oxygen precipitates.

The disadvantages of the traditional, rather long, high-temperature treatment are an additional increase in wafer cost, deterioration of the wafer surface, possible wafer bending, and contamination with metal impurities and dislocations. Thus, the most advantageous method seems to be fast thermal annealing, which, providing almost the same results, has almost none of the above disadvantages [18, 19].

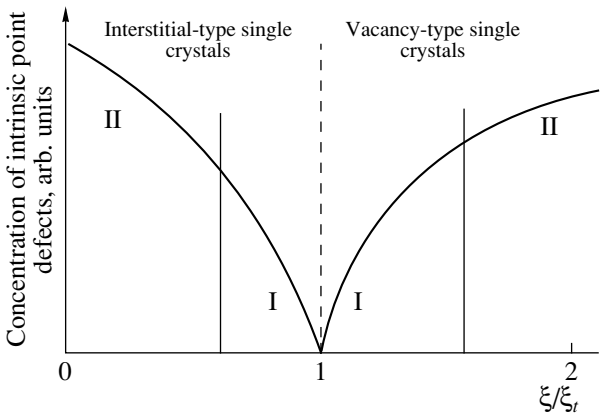

Fig. 2. Qualitative dependence of the concentrations of intrinsic point defects that have survived upon recombination and "growth" microdefects on the growth conditions. No microdefects exist in regions I.

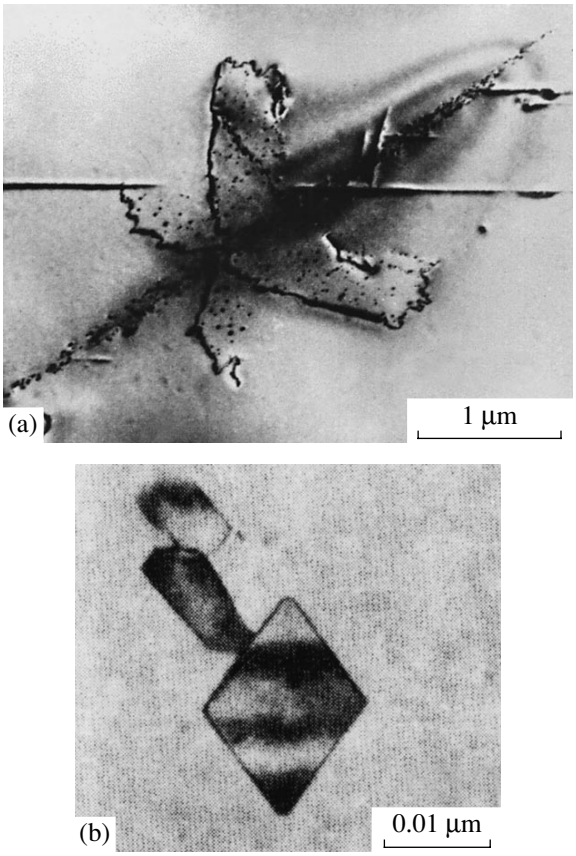

Fig. 3. (a) Interstitial-type dislocation loops and (b) octahedral vacancy-type pores formed in silicon single crystals grown under conditions of pronounced deviations from ξ_t (transmission electron microscopy data).

3. EPITAXIAL STRUCTURES

A serious alternative to polished wafers in manufacturing VLSI circuits is epitaxial structures if only because of the fact that the epitaxial layers hardly contain growth microdefects because of the specific conditions of their manufacture. The main cause of the increased attention in epitaxial technologies is the transition of microelectronics to the submicron, and in the nearest future, even to the nanometer level of fabricating device structures and the real prospects for creating VLSI circuits based on the epitaxial heterostructures in the system of Si—SiGe solid solutions.

In recent years, epitaxial growth in combination with ion implantation and pulsed irradiation of materials has started playing an important part in the formation of the most complex silicon-based device structures. Very thin (at a nanometer level) single-layer and multilayer homo- and heteroepitaxial films with pronounced planar *p–n* junctions and interfaces and preset (sometimes very complicated) doping profiles are widely used in technologies of VLSI circuit production. The severe demands are prescribed on the allowable content of residual impurities and structural defects in the epitaxial layer (which can considerably deteriorate the working characteristics of various devices) and on the uniformity of the electrophysical properties within the epitaxial layer. With the complication of the geometry of device structures, the local epitaxial processes have also become important [20].

The main tendency in the development of the technology of traditional gas-phase epitaxy is a further substantial decrease of working temperatures. To a large extent, the successful development of low-temperature methods of gas-phase epitaxy is determined by the increased sterility of the technological process, first of all, because of new vacuum equipment that ensures the stable operation of the equipment under reduced pressures in the working reactor and the extensive use of radiation heating. It is also very important to use new readily dissociating gaseous sources of extra pure silicon (SiH_4, Si_2H_6, SiH_2Cl_2, and SiH_2F_2) and also nonthermal (optical, plasma, electromagnetic, etc.) stimulation of epitaxial processes. To provide the conditions for stable layer growth, considerable attention is paid to the control of epitaxial-layer growth at the atomic level [21]. We mean here the manufacture of high-quality dislocation-free epitaxial films on substrates with a diameter ranging from 300 to 450 mm. This dictates the development of new approaches to epitaxial growth and design and construction of new, precision, highly productive equipment.

Along with the further elaboration of traditional epitaxial processes, the method of molecular beam epitaxy (MBE) has become very popular. This method has been developed not only to create ultrathin multilayer homo- and heteroepitaxial structures on the substrates with a large surface area but also to synthesize epitaxial metal–dielectric–semiconductor (MIS) structures, including the use of various variants of local epitaxy within one technological cycle. The apparatus designed for this method provides the combination of the processes of epitaxial growth and ion implantation of the given impurities to the synthesized layer and also its laser or electron-beam treatment or rapid thermal annealing in one technological cycle. All these innovations considerably extend the possibilities of the molecular beam epitaxy. High-vacuum chemical epitaxy is also developing at a rapid pace. Another important aspect of the development of technological processes is the study of the mechanisms of the processes occurring at the crystallization front in the gas phase and on the growth surface and also defining the nature of various factors stimulating epitaxial growth.

Epitaxial processes open new vistas for widespread use of SiGe solid solution-based heterostructures in silicon technology. These heterostructures would allow one to create superhigh-speed transistors based on SiGe/Si heterojunctions. The possible considerable variations of the band structure of multilayer heteroepitaxial structures allow one to increase the injection efficiency, drift velocity, and spatial limits of carriers in the transistor structures. In this case, the technology of manufacturing heteroepitaxial SiGe/Si structures is very consistent with the basic epitaxial technological processes of silicon growth, whose fast development provides the comparatively easy manufacture of heterostructures of nanometer dimensions and creation of quantum-dimensional structures with quantum wells and stressed superlattices, including heterostructures with a two-dimensional electron gas.

Heterojunction-based bipolar and field transistors with nanometer-thick working layers, 200-Hz-frequencies, and excellent noise characteristics have already become reality, and this is still far from the limit of heterojunction-based devices. These results considerably surpass the parameters obtained on traditional silicon-based metal–oxide–semiconductor (MOS) structures. The transition to heterojunction-based transistors instead of the traditional silicon structures in VLSI circuits allow one to obtain the same results at considerably larger topological dimensions of the working elements (250 instead of 130 or 130 instead of 70 nm) and to attain higher frequency characteristics, delay time, and noise level at the same topological dimensions [22]. All these factors also promise considerable technological and economic gains. Encouraging prospects are also opened by the use of multilayer quantum-dimensional SiGe/Si heterostructures for creating fast, highly sensitive photodetectors operating in the IR range [23].

To obtain thin films of SiGe solid solution-based heteroepitaxial structure, one can successfully use traditional gas-phase hydride epitaxy, the molecular-beam epitaxy, and high-vacuum chemical epitaxy at 750–800°C. Here, the main problem in manufacturing high-quality heterostructures is the necessity to reduce the

dislocation density in the working layers of the films and smoothen the heteroboundaries giving rise to additional carrier scattering.

The lattice mismatch for silicon and germanium is about 4%, which can give rise to pronounced misfit stresses during growth of epitaxial heterostructures. With an increase in the epitaxial-layer thickness, these stresses can partly or completely relax. Relaxation proceeds either at the expense of the formation of a characteristic roughness on the surface of a growing layer or because of the appearance of misfit dislocations, or else because of the simultaneous action of both these mechanisms [24]. The critical thicknesses of the layers necessary for generation of misfit dislocations in epitaxial SiGe/Si heterostructures are very small. Thus, in growth of epitaxial layers of the composition $Si_{0.7}Ge_{0.3}$ on silicon substrates, this thickness is about 10 nm. In the case of complete relaxation of misfit stresses, the density of inclined dislocations in such layers ranges within 10^{10}–10^{11} cm^{-2}, which excludes the use of these structures in various devices. To create high-quality transistors, the dislocation density in the active region of the epitaxial device structure should not exceed 10^4–10^5 cm^{-2}.

To obtain heterostructures with low dislocation density, the method of growth of intermediate (buffer) layers between the substrate and the working layers is used. The buffer layer can be that of a solid solution with the Ge concentration gradually increasing up to the given values or that of a solid solution grown at temperatures lower than the temperatures used for growth of working layers (usually, about 550°C). These "low-temperature layers" have elevated concentrations of clusters of point defects, which are the effective centers of heterogeneous nucleation of dislocations, which, in turn, promote the relaxation of misfit stresses in the growing heterostructure [25]. Good results are also obtained on substrates prepared from silicon structures on insulators with a very thin (of the order of nanometers) layer of dislocation-free single-crystal silicon applied to the oxide surface (Fig. 4, [26]). At present, these structures are successfully obtained by the method of direct wafer bonding (see below). In this case, a thin silicon layer on an insulator surface plays the role of an elastic substrate, which accumulates a considerable fraction of misfit stresses in the process of heteroepitaxial-structure growth. Simultaneously with a decrease of the dislocation density, the above methods also improve the situation with rough heteroboundaries. The successful use of the methods of manufacturing SiGe/Si heterostructures with low dislocation density and planar heteroboundaries allows one to positively estimate the real prospects for their wide use in microelectronics in the nearest future.

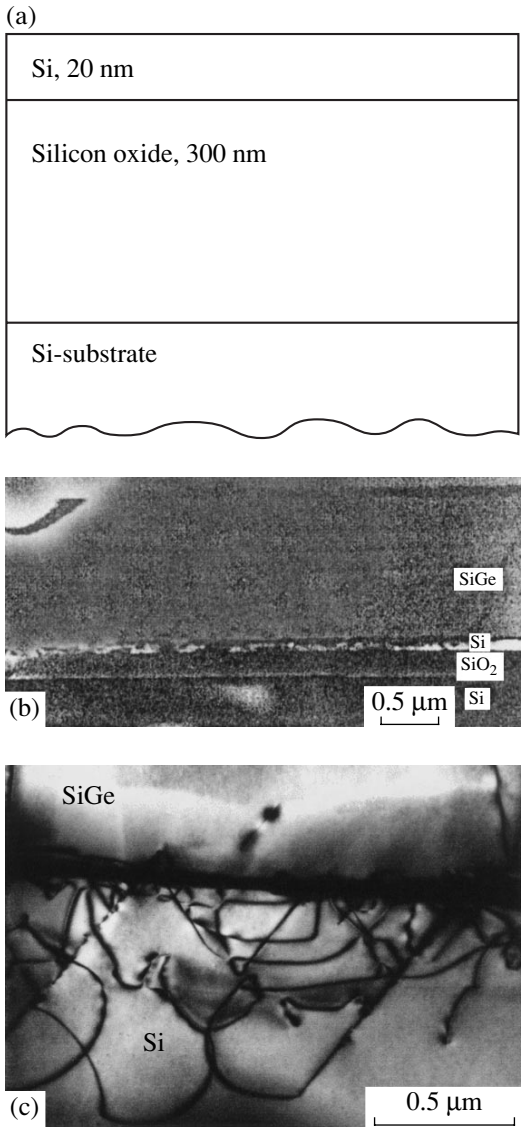

Fig. 4. (a) Schematic depiction of the substrate (silicon structure on insulator) for growing epitaxial $Si_{1-x}Ge_x$ layers, (b) electron micrograph of the transverse section of the epitaxial $Si_{0.6}Ge_{0.4}$ layer grown on such a (001)-oriented substrate [26], and (c) electron micrograph of the epitaxial layer of the same composition grown on a traditional silicon substrate of the same orientation.

4. SILICON STRUCTURES ON INSULATORS

For more than 30 years, silicon structures on insulators have been the focus of attention of designers of discrete devices and integrated circuits. This is dictated, first and foremost, by such advantages of these structures as possible considerable reduction of stray capacitance, reliable insulation of the devices used in integrated circuits, comparatively simple control of current modes, and possible reduction of working voltages and powers. Initially, silicon structures on insulators were created for high-temperature radiation-stable integrated circuits necessary for electronic devices in aerospace, automobile, atomic, and defense industries. However, in recent decades, the main attention is attracted to the use of these structures for designing

low-voltage and low-power high-frequency VLSI circuits for portable electronic devices such as mobile telephones, notebooks, minicomputers, etc. The structures necessary for VLSI circuits should have a defect- and stress-free thin working single-crystal silicon layer and insulator with thicknesses uniform over the whole structure area and an interface with low density of surface states.

At present, high-quality silicon structures on insulators are manufactured using three main processes: (1) separation by implantation of oxygen (SIMOX), (2) direct bonding and etching back silicon-oxide insulator (BESOI) with the subsequent thinning of one of the bonded wafers by polishing its reverse side, and (3) direct bonding of the oxidized wafer with a thin layer of single-crystal silicon separated from the second wafer by implanting it with hydrogen ions (the Smart-Cut process) [27].

In the SIMOX process, oxygen ions are implanted into a single-crystal wafer which, when interacting with silicon atoms, form a buried oxide layer at a certain distance from the surface above which a thin single-crystal silicon layer is formed. At the early stage of the method's development, a continuous buried insulator layer was formed because of high doses of ion implantation (oxygen dose, $\sim 2 \times 10^{18}$ cm^{-2}) at accelerating voltages of about 200 keV, which then was subjected to high-temperature annealing. The process proceeds in the mode of multiple successive implantation–postimplantation annealing cycles, which allows one to attain a dislocation density in the working single-crystal silicon layer at a level of $\sim 10^5$ cm^{-2}. Further considerable progress was achieved because of the use of low-dose implantation modes (oxygen dose of about 4×10^{17} cm^{-2}, accelerating energies of about 180 keV, and postimplantation annealing at temperatures exceeding 1300°C). It was possible to prepare a continuous buried layer of an insulator and reduce the dislocation density in the subsurface silicon layer down to $\sim 10^2$ cm^{-2}. Subsequent studies were directed at attaining a higher quality of buried insulator layer. Then, an additional cycle was introduced at a temperature of 1350°C. In the process of this annealing, a thermal-oxide layer was formed on the surface and, simultaneously, the characteristics of the buried insulator layer were considerably improved and the microroughness of the single-crystal silicon layer was smoothened. This technique is called the internal thermal oxidation (ITOX) process [28].

As a result, today we possess a well-developed low-dose SIMOX process, which provides the manufacture of silicon structures on insulators with a wafer diameter of 200 mm and the following characteristics: thickness of a silicon layer 170 ± 5 nm, thickness of the buried oxide layer 115 ± 10 nm, dislocation density in the silicon layer $< 1 \times 10^3$ cm^{-2}, surface microroughness 0.4 nm, interface microroughness < 2 nm, and contamination with metal impurities $< 5 \times 10^{10}$ cm^{-2}. The structures of such high quality are appropriate for creation of VLSI circuits of the submicron level. At present, intense studies are directed to the further improvement of the quality of structures manufactured by the SIMOX process and the achievement of better technical and economic characteristics.

A process competing with SIMOX in manufacturing high-quality silicon structures on insulators is the method of direct wafer bonding [29, 30]. The successful development of this new technology is promoted by the achievements in manufacturing wafers with large diameters and high-quality working surfaces and ultrathin (nanometer) wafers prepared by the Smart-Cut process [31]. The direct bonding technology is considerably simpler and has a number of serious ecological advantages. Also, it substantially reduces the energy consumption and provides high-quality device structures. In this case, no additional efforts are necessary for preparing a working dislocation-free silicon layer. The technology for manufacturing high-quality layers of thermal oxide on the surfaces of wafers with large diameters is also well developed. Up to recently, the most labor-consuming operation has been polishing of the reverse side of one of the wafers to be bonded in order to achieve the necessary thickness of a working silicon layer (bonded and etched back silicon oxide insulator, BESOI). However, the advent of the technology of separation of ultrathin thickness-uniform nanometer layers from bulky silicon wafers by implanting hydrogen ions into the wafer and their subsequent low-temperature thermal treatment has promoted the successful solution of this problem. Moreover, the initial wafer remains undamaged and can be used in the process several times (Fig. 5).

A rather difficult and still unsolved problem is the reduction of the level of surface microroughness of a thin silicon layer without the use of any additional thorough polishing. The study of the mechanism of the separation of thin layers with the aid of hydrogen implantation of the wafers and the development of the low-dose variant of this process are new promising directions for these studies.

Today, the technology of direct wafer bonding is widely used both in microelectronics and in power instrument engineering. The estimates show [32] that the need for silicon structures on insulators with a diameter of 200 mm attains the enormous figure of about two billion in 2000. About 80% of these structures are manufactured by direct wafer bonding. Silicon structures on insulators are still much more expensive than high-quality wafers obtained by conventional methods. Therefore, one of the basic problems in the development of the technology of manufacturing these structures in the near future is the essential increase in the technical and economic indices.

The direct-bonding technology opens new possibilities for creation of complex device structures with the use of other semiconductor materials, including those based on heterostructures which can hardly be pro-

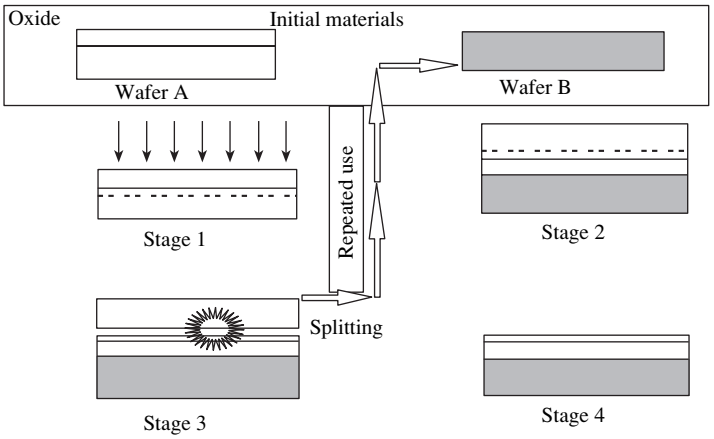

Fig. 5. Schematic of the technological cycle of manufacturing silicon structure on an insulator with the use of the Smart-Cut process. Stage 1: implantation of oxygen into the wafer; stage 2: cleaning and direct bonding of A and B wafers; stage 3: thermal treatment; stage 4: final polishing of the surface.

duced by the epitaxial methods, i.e., GaAs/Si, InP/Si, SiC, and GaAs on oxidized silicon, etc.

5. SILICON-BASED OPTOELECTRONICS

An increase in the assemblage density of working elements with the improvement of VLSI circuits has resulted in the considerable extension and complication of the architecture of the traditional wire contacts. The wire connections are one of the major difficulties encountered in attempts to increase the response speed of VLSI circuits, which makes their manufacture an ever more expensive operation, which, in turn, also increases the costs of integrated circuits. Under these conditions, the use of new principles for making contacts between individual elements in VLSI circuits and chips and between various functional units of a complex electronic apparatus becomes quite urgent. Today, when we see the widespread use of computers in all fields and the creation of global communication and information networks, this problem becomes especially important.

A very promising alternative to traditional connections of elements are optoelectronic systems, which provide generation, modulation, amplification, transmission, and detection of light signals. The potential possibilities of these systems can hardly be overestimated. An individual cell of a monolithic optoelectronic device is a result of the integration within one wafer of a radiation source, a waveguide, and a photodetector. The necessary condition for the successful use of optoelectronic devices is their geometrical and functional compatibility with other elements of VLSI circuits. The technology of their manufacture should also be compatible with the technology of manufacturing VLSI circuits themselves; moreover, this technology should also use the well-developed processes and equipment used in silicon-based instrument industry [33, 34].

The central problem of silicon optoelectronics is the creation of efficient radiation sources whose role is usually played by a light diode or a laser. The point is that silicon is a non-direct-band semiconductor, and the efficiency of the interband radiative recombination in it is rather low. An exit from this situation is doping of silicon with erbium, forming effective centers of radiative recombination with the participation of 4*f*-electrons of the impurity atom in the crystal lattice. This recombination yields radiation with a wavelength of 1.54 μm for which silicon is an almost transparent material. This radiation also corresponds to the window with the maximum transparency in the optical waveguides prepared from quartz glass. Unfortunately, erbium solubility in silicon is rather low, $\sim 10^{16}$ cm^{-3} at 1300°C, which is insufficient for generation of more intense radiation. To increase the erbium content in the crystal lattice, one has to use nonequilibrium methods for preparing heavily doped silicon layers such as ion implantation, molecular-beam epitaxy, ion-beam evaporation, etc. A higher content of erbium in the layer is also promoted by additional doping of the layer with oxygen and fluorine, forming rather stable complexes with erbium. The best results are achieved by the method of ion implantation [35] in the following sequence. A silicon substrate is simultaneously doped with erbium and oxygen ions in the proportion 1 : 10. Then, the amorphized layer thus formed is annealed for 3 h at 620°C to provide its recrystallization. The final stage is fast (30 s) annealing of the recrystallized layer at 900°C, which provides annihilation of the residual defect in the layer. As a result, high-quality single-crystal layers with an erbium concentration of up to $\sim 10^{20}$ cm^{-3} are obtained. It is expected that, in the nearest future, this breakthrough in increasing the doping level will result in manufacturing erbium-doped silicon-based light-emitting diodes with the quantum efficiency of emission at a level of 1% at room temperature and with the frequency characteristics appropriate for integration. The

prospects for creating Er-doped silicon-based lasers are also rather good.

Another promising direction in the production of efficient light emitters is growth of heteroepitaxial structures of direct-band $A^{III}B^{V}$ compounds (GaAs, InGaP, etc.) on silicon substrates [33]. As in the case of SiGe/Si heterostructures (see Sect. 3), the use of intermediate buffer layers in the form of stressed superlattices, structures with the composition gradient along the thickness, or layers grown at relatively low temperatures in combination with multiple cycles of intermediate thermal treatment allows one to grow, e.g., epitaxial GaAs layers on silicon substrates with dislocation densities of the order of $N_d \approx 10^5$ cm^{-2}. However, this is not sufficient for the creation of lasers that would efficiently operate at room temperature, but is quite sufficient for the formation of light-emitting diodes. Further progress in the reduction of the dislocation density in such heterostructures can be achieved by epitaxial growth of structures on profiled substrates (mesastructures, porous wafers) and by the use of the direct wafer bonding (see Sect. 4).

In recent years, numerous attempts have been made in designing light-emitting structures on the basis of epitaxial layers of semiconductor iron disilicide (β-$FeSi_2$), a direct-band material with an optical gap of 0.8 eV (corresponding to a wavelength of 1.5 μm). The main methods for producing such structures are molecular-beam epitaxy and ion implantation in combination with various variants of thermal treatment. Today, we already have seen the appearance of the first light-emitting diodes based on these structures [36].

The promising materials for creating emitters are also epitaxial layers of solid solutions of group-IV elements of the Periodic Table such as $Si_{1-x-y}Ge_xC_y$, $Si_{1-y}C_y$, and Sn_xGe_{1-x}. Some of these solid solutions can provide the formation of structures possessing the direct-band structure [37], quantum-dimensional silicon-based structures (superlattices with multiple quantum wells in the SiGe/Si system, quantum wires and quantum dots formed in the silicon matrix based on direct-band semiconductors [38], and also silicon nanocrystals [39]).

The studies of new solid solutions of group-4 elements and silicon-based quantum-dimensional light-emitting structures are only at their initial stage. Nanocrystals are studied on a wider scale, first of all, because of the enormous interest in porous silicon-based structures.

The structures of porous silicon are usually obtained by traditional electrochemical etching of single-crystal wafers. In the etching process a structure consisting of thin single-crystals fibers separated by pores is formed. If the diameter of these fibers attains the quantum-dimensional (nanometer) level, the porous matrix can generate radiation in the visible range of the spectrum. Today, the nature of this luminescence is not quite clear. Many other phenomena observed in porous silicon during the passage of an electric current or its optical excitation are also not completely understood. The reproducibility of the results of electrochemical etching of fiber structures (and, first of all, fiber diameters) is also far from being perfect. The same is true for the degradation characteristics. All these facts stimulate further intense studies of this very interesting and, no doubt, promising material.

Lately, we have also seen the advent of new methods for the synthesis of silicon nanocrystals with rather well-reproducible dimensions such as electric-spark treatment, selective etching in combination with photolithography, direct chemical synthesis, silicon-ion implantation into SiO_2 films with the subsequent formation of nanocrystals in the process of the decomposition of supersaturated solid solutions thus formed, etc. It was believed that upon the attainment of certain dimensions, nanocrystals would have acquired direct-band structure. Unfortunately, at dimensions exceeding 2 nm, nanocrystals are still non-direct-band semiconductors with all the undesirable consequences this implies. Nevertheless, the interest in silicon nanocrystals has not diminished. If we manage to attain the reliable passivation of the nanocrystal surfaces, then it will become possible to create on their basis light-emitting diodes with an external quantum efficiency of about 1% [39], which, no doubt, would be of great practical interest.

As for waveguides, Si/SiO_2 structures with a difference in the refractive indices of the components of $\Delta n = 2$ seem to be very promising, because they can provide conditions for reliable optical limitation. The light in such a waveguide propagates along a thin single-crystal silicon layer transparent to radiation with a wavelength of λ = 1.30–1.55 μm. To manufacture a waveguide structure, one uses the method of direct wafer bonding in combination with the Smart-Cut process (see Sect. 4). The waveguide structure thus obtained provides reliable communication (with minimum optical losses) with the emitter and photodetector and satisfies all the requirements set for microwaveguide structures to be used in monolithic optoelectronic devices [33, 34].

The most appropriate materials for radiation detectors operating at wavelengths of 1.3–1.5 μm are Ge, SiGe solid solutions with high Ge content, stressed superlattices in the SiGe/Si system, and also GaAs [33]. As was mentioned above, growth of multilayer heterostructures with high-quality working single-crystal layers of these materials grown on silicon substrate meets no difficulties.

Thus, today there are all the necessary prerequisites for the successful creation of monolithic silicon-based optoelectronic devices compatible with silicon-based integrated circuits.

It would also be logical to consider here the problems of silicon-based solar power engineering in terms of materials science and systems for processing and

mapping information on the basis of thin-film structures of hydrogenated amorphous silicon and related materials. However, these problems are beyond the scope of this article.

CONCLUSION

The ever increasing rate of progress in the creation of global computer, informational, and communication networks increases the role of solid-state electronics in the development of world civilization. Semiconductor silicon has always been, and will always be, at least in the coming decades, the main material for electronic instrument engineering.

Increasing complexity of VLSI circuits caused by the transition to nanometer topological dimensions of the working elements is accompanied by the transition to single-crystal wafers, epitaxial structures, and multilayer heterostructures with ever increasing diameters and, simultaneously, by considerably more and more severe demands on their quality. This, in turn, substantially increases the price of the existing technological processes and does not allow one to reduce the price of the products to satisfy consumers. Economic considerations play an important role in estimating the expediency of further development of some industries and impose considerable limitations on the rate of increase of the elemental base of electronics.

The way out of all these difficulties lies, on the one hand, in revising traditional approaches to the manufacture of wafers and structures of the necessary high quality (including the technologies used) and, on the other hand, in revising the demands on their quality with the transition to new technologies of producing of VLSI circuits.

With the new requirements on the operative speed of VLSI circuits and growing production of low-voltage and low-power integrated circuits, the ever increasing attention of consumers is paid to the heteroepitaxial SiGe/Si and silicon structures on insulators.

The attainment of the possible physical limits in the existing approaches to manufacturing VLSI circuits based on traditional transistors predicted for the nearest future dictates the creation of a new elemental base and the use of quantum-dimensional and tunneling effects in nanometer silicon-based multilayer structures. Under these conditions, the role of advanced low-temperature epitaxial methods (molecular beam epitaxy, high-vacuum chemical epitaxy, etc.) in the formation of device structures considerably increases.

It can be expected that the optoelectronic approaches to integration with the use of materials and technological processes compatible with the technologies used in silicon-based instrument engineering will play a more important part in the formation of silicon-based VLSI circuits of next generations and electronic devices based on these circuits.

ACKNOWLEDGMENTS

The author expresses his deep gratitude to V.Ya. Reznik and A.L. Gromadin for their help in the preparation of this article for publication.

REFERENCES

1. A. P. Mozer, Solid State Phenom. **69–70**, 1 (1999).
2. I. V. Grekhov, Izv. Vyssh. Uchebn. Zaved., Ser. Mater. Élektron. Tekh., No. 3, 9 (2000).
3. K. V. Ravi, Solid State Phenom. **69–70**, 103 (1999).
4. L. C. Kimerling, Solid State Phenom. **57–58**, 1 (1997).
5. J. G. Park, J. M. Park, K. C. Cho, *et al.*, Proc.–Electrochem. Soc. **97–22**, 173 (1997).
6. J. G. Park and G. A. Rozgonyi, Solid State Phenom. **47–48**, 327 (1996).
7. H. Takeno, M. Kato, and Y. Kitagawa, in *Proceedings of the 2nd International Symposium on Advanced Science and Technology of Silicon Materials, Osaka, 1996*, Ed. by M. Umeno, p. 294.
8. N. I. Puzanov and A. M. Eidenzon, J. Cryst. Growth **178**, 459 (1997).
9. M. G. Mil'vidsky, Izv. Vyssh. Uchebn. Zaved., Ser. Mater. Élektron. Tekh., No. 3, 4 (1998).
10. H. Furuya, K. Harada, and J. G. Park, Solid State Technol., No. 11, S25 (2000).
11. V. V. Voronkov and R. Falster, J. Cryst. Growth **204**, 462 (1999).
12. J. Vanhellemont, Solid State Phenom. **69–70**, 111 (1999).
13. V. V. Voronkov, J. Cryst. Growth **59**, 625 (1982).
14. K. Nakai, Y. Jnoue, H. Yokota, *et al.*, in *Proceedings of the 2nd International Symposium on Advanced Science and Technology of Silicon Materials, Osaka, 2000*, Ed. by M. Umeno, p. 88.
15. M. Suhren, G. Grof, U. Lambert, *et al.*, Proc.–Electrochem. Soc. **96–13**, 132 (1996).
16. S. Nadahara, H. Kubota, and S. Samata, Solid State Phenom. **57–58**, 19 (1997).
17. D. Graf, R. Wahlich, P. Krottenthaler, *et al.*, Proc. – Electrochem. Soc. **97–22**, 18 (1997).
18. R. Falster, *Semiconductor Fabtech* (2000, 13th ed.), p. 187.
19. J. Vanhellemont, J. Esfandyari, G. Obermeier, *et al.*, Proc.–Electrochem. Soc. **98–13**, 101 (1998).
20. M. G. Mil'vidsky, Materialovedenie, No. 5, 36 (1997).
21. V. V. Voronkov, L. A. Zhukova, and M. G. Mil'vidsky, Kristallografiya **42** (6), 1114 (1997) [Crystallogr. Rep. **42**, 1038 (1997)].
22. U. Konig, Solid State Phenom. **69–70**, 121 (1999).
23. S. C. Jain and W. Hayes, Semicond. Sci. Technol. **6**, 547 (1991).
24. L. J. Schowaller, MRS Bull. **21** (4), 18 (1996).
25. A. N. Larsen, Solid State Phenom. **69–70**, 43 (1999).
26. Z. Yang, J. Alperin, K. L. Wang, *et al.*, J. Vac. Sci. Technol. B **16**, 1489 (1998).
27. J. B. Colinge, MRS Bull. **23** (12), 16 (1998).
28. K. Jzumin, MRS Bull. **23** (12), 20 (1998).

29. M. G. Milvidsky, K. L. Enisherlova, V. Ja. Reznick, *et al.*, Adv. Perform. Mater. **4**, 165 (1997).
30. C. A. Desmond-Colinge and U. Gosele, MRS Bull. **23** (12), 30 (1998).
31. M. Bruel, MRS Bull. **23** (12), 35 (1998).
32. W. P. Maszara and P. K. Vasudev, in *Extended Abstracts of the Symposium 20th Anniversary of the 145th Committee on Processing and Characterization of Crystals of JSPS, Tokyo, 1997*, p. 28.
33. E. A. Fitzerald and L. C. Kimerling, MRS Bull. **23** (4), 39 (1998).
34. L. C. Kimerling, Solid State Phenom. **69–70**, 131 (1999).
35. S. Coffa, G. Franzo, and F. Priolo, MRS Bull. **23** (4), 25 (1998).
36. T. Suemasu, Y. Negishi, and K. Takakura, Jpn. J. Appl. Phys. **39**, L1013 (2000).
37. J. C. Sturm, MRS Bull. **23** (4), 60 (1998).
38. R. Soref, MRS Bull. **23** (4), 20 (1998).
39. L. Tsybeskov, MRS Bull. **23** (4), 33 (1998).

Translated by L. Man

Crystallography Reports, Vol. 47, Suppl. 1, 2002, pp. S35–S42.

MELT GROWTH

Development of Shaping Technologies for Crystals Grown from Melts

V. A. Borodin* and Yu. A. Osipyan**

** Experimental Factory of Scientific Instrument Engineering, Russian Academy of Sciences, Chernogolovka, Moscow oblast, 142432 Russia*

e-mail: bor@ezan.ac.ru

*** Institute of Solid State Physics, Russian Academy of Sciences, Chernogolovka, Moscow oblast, 142432 Russia*

Received October 1, 2002

Abstract—The development of technologies for growing crystals with a given shape and designing the growth equipment for the Czochralski and conventional and modified Stepanov methods have been considered. The reviewed experimental data lead to the conclusion that it is possible to provide three-dimensional control of the crystal geometry with the aid of a die in the growth process. © *2002 MAIK "Nauka/Interperiodica".*

METHODS OF CRYSTAL SHAPING

Today, the Czochralski method is the most widespread technique for industrial growth of semiconductor and dielectric single crystals. Crystal shaping in the Czochralski method is reduced to growth of a seed to a crystal of the set diameter, further growth of the cylindrical part of this crystal, and then narrowing of the crystal to the set diameter. In this process, one not only has to maintain the given diameter of the cylindrical part of the crystal, but also to maintain an experimentally certain profile of the side surface of the crystal at the stages of crystal broadening and narrowing. This problem is solved with the aid of an automatic system of control of the growth process with feedback, with the object of such a control being the crystal diameter.

The method suggested by Stepanov allows one to grow various shaped crystals with the given transverse cross section along the growth axis. The geometry of the transverse cross section is set by the geometry of the die edges. It is much easier to maintain the given crystal shape in the Stepanov method than in the Czochralski technique and, if the crystal radius is much less than the radius of a crucible with the melt (e.g., in growth of a thin rod), then it is possible to conduct the growth process under a fixed heating power and pulling rate. However, in most instances, the given crystal shape can be maintained by controlling the above parameters. Therefore, the development of the growth technology for profiled crystals by both the Czochralski and Stepanov methods requires automation of the growth process.

An increased range of application of profiled crystals dictates the creation of new technologies that might provide growth from melt of the crystals with the variable transverse cross sections along the growth axis. The studies started in 1982 at the Institute of Solid State Physics of the Russian Academy of Sciences resulted in the development of two main technologies. The first one, the so-called variable shaping technique [1, 2], provides discrete changes of the cross-section shape of a pulled crystal. The second, the so-called local dynamic shaping technique, provides the growth of crystalline articles with the programmed continuously varying side surface of the crystals [3–6, 8, 9].

Variable shaping technique. There are several technological possibilities for changing the shape of the transverse cross section of a crystal pulled from the die. It is well known [10] that "anchoring" of the melt meniscus from which the crystal grows by the die edges provides the steady-state growth process. In essence, all the methods referred to as "variable shaping techniques" are reduced to the detachment of the meniscus base from the edges of the die, which sets the initial shape of the transverse cross section of the crystal, with the aid of various technological techniques and its anchoring at the edges of another die, which sets the next shape of the transverse cross section. In this case, the mass of the melt that reached the crystallization front is also controlled by varying the melt temperature and the pulling rate. In the simplest case, the variable shaping technique allows one to pass from growing a hollow profile (e.g., a tube) to growing a solid rod. In this case, the external meniscus remains fixed at the external edges of the former, whereas the internal meniscus disappears. In the general case, the variable shaping technique can be considered as a sequence of the operations of pulling the crystal from different dies.

Growth of each specific article requires the choosing the appropriate technology. Taking into account the achievements of other groups working in this field, it is expedient to classify all the engineering developments

1063-7745/02/47S1-S0035$22.00

into seven groups according to the following main technological and construction characteristics:

(1) The change of the melt position with respect to the working edges of the dies separated by capillary gaps.

(2) The vertical projection of the capillary channels of the dies (at least of one die) should exceed the vertical projection of the capillary gap separating this die from the neighboring one [11].

The developments along this direction were made in our studies [12, 13] and also in [14]. The die used in [14] consisted of the immobile and mobile parts separated by a capillary gap. The mobile part was connected to a crucible moving along the vertical. Unlike the devices used in [12, 13], the movable part of the shaping device could be either connected or not connected to the crucible depending on its rotation.

(3) Supply of the melt to the individual edges of a complex shaping device consisting of a set of dies with different widths of the capillaries. The meniscus moves from one edge to another because of the change of the melt level in the capillaries [15].

(4) The regulation or the change of the ambient-gas pressure at the internal and external sides of the meniscus of a hollow profile.

This principle underlies several developments made by various groups. Pressure leveling inside and outside the sapphire tube upon growth of the first solid partition in this tube allowed us to pass from growth of the cylindrical rod to growth of a tube [16]. The reliable method of growth of hollow sapphire articles with partitions, which, unlike the previous growth methods, does not require the use of mobile parts, was suggested in [17]. A seed placed onto the top of a die with the inner cavity completely closed this cavity. During pulling of a profiled crystal tightly closed with the seed, the pressure in the die cavity dramatically decreased, and the melt, under the action of the difference in the pressures outside and inside the die, came up to the internal working edges. As a result, the hollow profile was transformed into a solid rod during pulling.

Several years later, this method was also used in [18] and was called "a new method for growth of profiled crystals with the use of additional noncapillary feeding."

(5) Several-stage growth of articles from several separated individual dies. An element of the article grown at the previous stage of the process plays the role of a seeding crystal at the following stage of growth. This group also includes the developments made in [19, 20].

(6) The use of the relief of the top surface of a die [21, 22]. Varying either the temperature mode or the pulling rate of the crystal, it is possible to make the meniscus base pass from one die edge to another. However, these methods are not widely used because of the difficulties associated with the choice of the mode of meniscus passage and the low reproducibility of the results.

(7) Horizontal motion of the elements of the shaping device independent of one another. In particular, such a motion can occur via crucible rotation. The examples of growing various articles by this method are considered in [23].

We believe that one of the most universal techniques ensuring variable shaping reproducible results is our development [11], illustrated in Fig. 1. The sequence of the operations used to change the crystal shape is shown from left to right. The package of dies is not connected to the crucible that can move along the vertical direction with respect to the static dies of different lengths separated from one another by capillary gaps. As a result, one can move the crucible along the vertical and, thus, either introduce the individual dies into the melt and remove them from it. Filling the capillary gaps between the neighboring dies with the melt during the immersion of the base of an additional die into the melt smoothly varies the shape of the meniscus of a growing crystal and, thus, also the shape and the dimensions of its transverse cross section. The immersion of the crucible into the melt and the removal of one of the dies from it result in the depletion of the melt in the capillary gap, whereas the base of the meniscus starts transforming unless the meniscus acquires the geometry of the working edges of the die contacting with the melt in the crucible.

Sapphire products grown by this method were described elsewhere [1, 2].

The local shaping technique allows one to grow tubular and cylindrical crystals. Unlike in the traditional Stepanov method, the die in this method creates only a certain local melt meniscus, whereas, on the whole, the final shape of the article is formed due to crystal rotation (Fig. 2).

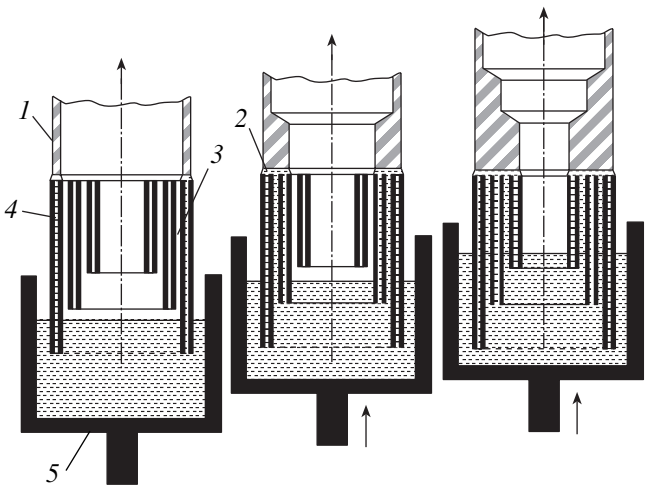

Fig. 1. Scheme of crystal growth by the variable shaping technique. (*1*) Crystal, (*2*) meniscus, (*3*) die, (*4*) capillary channel, and (*5*) crucible.

The method was first described in [24], where it was used for growing LiF tubes. We also used this method to grow sapphire tubes on rod seeds [4–7] and also tubes and rods of an Al_2O_3–$ZrO_2(Y_2O_3)$-based eutectic composite. In these works, the growth of sapphire tubes, its stability, and the crystal structure were studied, and the model of the corresponding growth process called "local shaping" was suggested.

Local dynamic shaping technique for growing complex articles in the form of bodies of rotation with continuously varying shape of the side surface was first described in our study in 1985 [3]. Some types of the crystals grown by this new method were demonstrated in [6, 8]; the method itself was considered in detail in [4, 5, 9].

The internal r_1 and external r_2 radii of the tube are determined by the expressions $r_1 = R - p/2$ and $r_2 = R + p/2$, where R is the distance between the rotation axis of the crystal and the center of the top surface of the die and p is the diameter of the die top (Fig. 2). The process is characterized by three parameters: the melt temperature T_m, the rotation speed n, and the pulling rate V with the corresponding values of the degrees of freedom of the process (the so-called phase variables). The degrees of freedom (phase variables) in this case are the radii r_1 and r_2 of the tube and the meniscus height h. Since the process is steady-state, the small deviations of the parameters ΔT_m, Δn, and ΔV result in small variations of the internal and external radii of the tube. Assuming that the distance between the rotation axis of the crystal and the center of the top surface of the die, R, is a slowly varying (with time) parameter, then it follows from the fact that the process is steady-state that each $R(t)$ value has the corresponding values of $r_1(t)$ and $r_2(t)$. Physically, it is possible only under the conditions that $R \geq r_1(t)$ and $R \leq r_2(t)$. These conditions signify that the crystallization process is possible only if the set velocity of R variation does not exceed the velocity of an increase (decrease) of the external and internal radii of the crystal, $dR/dt \geq dr_1/dt$ and $dR/dt \leq dr_2/dt$. Proceeding from this fact, we developed the method for growing bodies of rotation with continuous programmed change of the side-surface shape [3–5], which consists in the following. In the course of pulling of a rotating crystal from the die, which sets only the local region of the transverse cross section of the crystal, one also changes the distance between the die and the rotation axis of the crystal. Unlike in the method of local shaping, in this method, the die and the rotating seed holder move with respect to one another in the horizontal plane. The method is called the *local dynamic shaping technique*. The programmed side-surface profile along the direction Z of the crystal pulling is determined by the set of all the process parameters and $r_{1,2} = f(T_m, n, V, R, t)$. In principle, the die can move along the rectilinear trajectory in the horizontal plane, along the arbitrary trajectory, or along the circumference arc. Obviously, the shape of the product can also

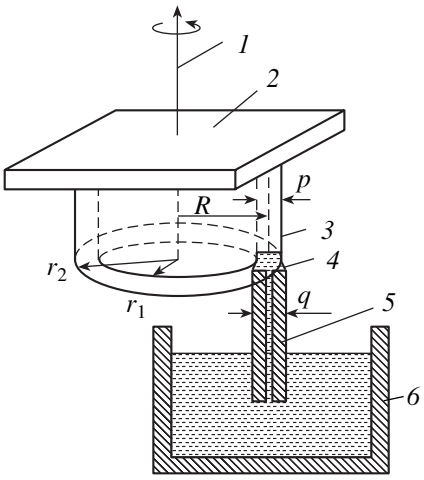

Fig. 2. Scheme of crystal growth by the local shaping technique. (*1*) Rotation axis, (*2*) seeding crystal, (*3*) crystal in the shape of a tube, (*4*) meniscus, (*5*) die, and (*6*) crucible.

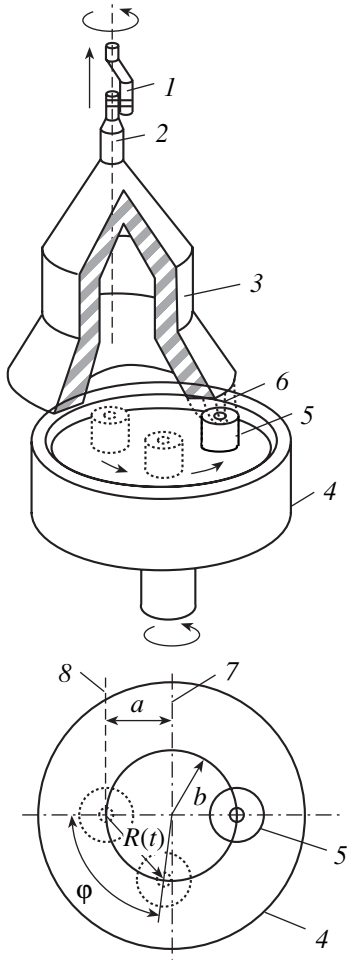

Fig. 3. Scheme of growth of crystals by the local dynamic shaping technique. The variant of the horizontal displacement of the die via the crucible rotation. (*1*) Seed holder, (*2*) seeding crystal, (*3*) growing article, (*4*) crucible, (*5*) die, (*6*) meniscus, (*7*) rotation axis of the crucible, and (*8*) rotation axis of the seed holder.

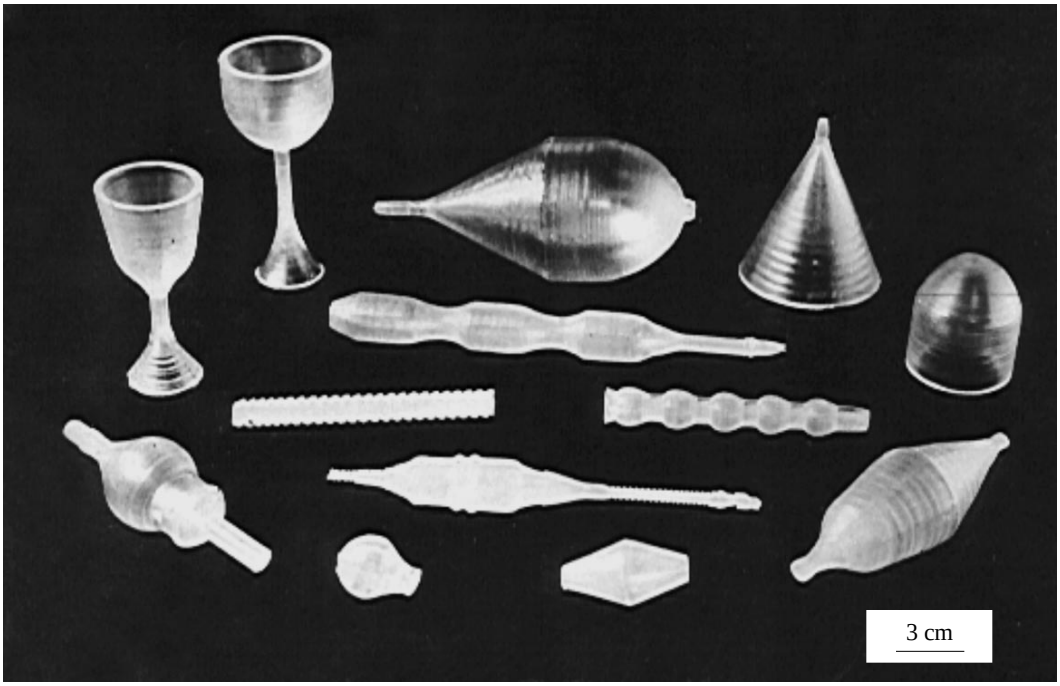

Fig. 4. Sapphire articles of complicated shapes manufactured in the programmed growth by the local dynamic shaping technique.

be changed by moving the seed holder in the horizontal plane.

The most efficient technological scheme of crystal growth by the local dynamic shaping technique is shown in Fig. 3. In this case, the die is translated in the horizontal plane via crucible rotation. Die *5* is rigidly connected to rotating crucible *4* (the lower rotating rod of the setup is used) and is displaced with respect to its rotation axis *7* by the distance *b*. The rotation axis of upper rod *8* does not coincide with the rotation axis of the crucible and is displaced with respect to this axis by the distance *a*. In this device, the rotation of the crucible by angle φ gives rise to horizontal translation of the die with respect to the rotation axis of the crystal, with $R(t)$ and $\varphi(t)$ being related as

$$R(t) = [a^2 + b^2 - 2ab\cos\varphi(t)]^{1/2}. \quad (1)$$

Let the diameter of the working surface of the die be q. If $R(t) > q/2$, we obtain a hollow crystal with the internal radius $r_1 = R - p/2$. If $R(t) < q/2$, we obtain a crystal in the shape of a solid body of rotation. The solid article can be transformed into a hollow one and back with the aid of a device where $|a - b| < q/2$, and therefore, the use of the device in which $a = b$ would provide growth of both hollow and solid products.

Some sapphire products grown by the set program on a setup called the "crystallization center" by the local shaping technique are shown in Fig. 4.

DEVELOPMENT OF SHAPING TECHNIQUES

The further development of the crystal shaping techniques is required by an ever increasing nomenclature of the articles grown from melts. One of the promising directions here is the Stepanov method and the variable and local dynamic shaping techniques used in one growth cycle [25]. The apparatus used allows the arbitrary change of the growth techniques during the growth process. With this aim, some of the dies used, e.g., for designing the scheme of the variable shaping technique (Fig. 1), were installed on a platform separated from the crucible, whereas the other dies were mounted in the crucible, which could be rotated and moved with respect to the platform. The dies on the platform and in the crucible can be located asymmetrically with respect to the rotation axis of the crucible. Moving the crucible along the vertical, one can place the working edges of the dies on the platform and in those of the dies mounted in the crucible which are at the same level or else change their positions with respect to one another along the vertical, thus providing variable shaping. Moreover, the variable shaping can also be achieved by horizontal displacement of the dies mounted in the crucible with respect to the dies mounted on an immobile platform by rotating the crucible about the vertical axis. The local shaping in this device is attained at the asymmetric position of the rotation axis of the seed holder and the vertical axis of the die providing the growth process. If this die is mounted in the crucible, then, at the appropriate rotation velocity of the crucible, growth proceeds by local

dynamic shaping. The choice of the corresponding ranges of pulling rates, the velocity of the rotation of the crystal and the crucible, and the determination of the necessary thermal mode are the key factors in all the methods and also in the transition from one growth method to another one.

The local dynamic shaping technique provides growth of the products in the shape of bodies of rotation. The results obtained in [25] and in the mathematical simulation of the growth process with the translation of the dies in the horizontal plane with respect to the rotation axis of the crystal allow one to state that there should exist such modes of crystal rotation, pulling rates, and the die trajectories of the die and the velocities motion along the trajectories that provide the three-dimensional changes in the shape of a growing crystal. In fact, this signifies the creation of a new promising technology that will allow a considerable increase in the nomenclature of the articles that can be grown from melt.

An apparatus providing the implementation of new technologies and the reproducible results, on the one hand, should be a precision instrument, which would allow the active studies of growth of various crystals and crystals of different profiles and also would provide the possibility of setting the necessary growth parameters determining the crystal quality. On the other hand, it should have reliable exploitation characteristics corresponding to the level of commercial equipment. One of the conditions necessary for meeting these two requirements is the creation of a complex that combines the use of modern computer-controlled growth technologies and the most advanced software.

Such a complex was created at the Experimental Factory of Scientific Instrument Engineering of the Russian Academy of Sciences, the company ROSTOKS-N, Ltd., and the Institute of Solid State Physics of the Russian Academy of Sciences and includes the acquisition and processing of analog and discrete signals, displaying and recording of the information necessary for personnel, a technological signaling system, recording of emergency situations and other events, and accumulating and storing information in archives. The block scheme of the controlling system is shown in Fig. 5.

The controlling functions of the complex include automatic regulation, logic control, and remote control. The NIKA 2000 controlling program has been developed in the Microsoft Visual C++6.0 medium for the Windows'95, Windows'98, and Windows'NT operating systems. The modular structure of the program provides its fast adaptation to various methods of crystal growth from melts and new growth setups. The program consists of the following modules: the module for representation of growth-process data, the module for manual control of the growth process, and the module dealing with the mathematical model of the growth process and automatic control of the heating power. The apparatus part consists of a block for measuring the force acting on the growing crystal, a block for control of a high-frequency generator, a block for control of the electric motors providing the rotation and translation of the upper and lower water-cooled rods.

The block for measuring forces consists of a strain sensor providing the transformation of the weight of a growing crystal into an electric signal, an analog-to-digital (AD) converter with a digital infrared transmitter–receiver, and a light diode connected to a computer via the RS-232 channel. The light diode provides the rotation of the strain sensor and the analog-to-digital converter with respect to the light diode; the power to the analog-to-digital converter is supplied via sliding contacts.

The block for the generator control includes a digital-to-analog (DA) converter. The power and control circuits of the converters are electrically isolated from the computer circuit.

In the automatic mode, the control of the generator is provided by a special program. The transition from manual to automatic control and back can be performed by an operator either from the keyboard of a personal computer or with the aid of a switcher mounted on the indicator.

The block for control of the rod translation and rotation consists of the control block proper and a three-phase step electric motor. The control of the block operation is provided by a computer via the RS-232 channel.

The program controlling the crystal growth can operate in the following main modes:

—control of a high-frequency generator;

—control of the electric motors of the pulling and rotating drives of the rod;

—the automatic control of the process of crystal growth with the use of a force sensor;

—the mode providing the necessary information and alarm signals for an operator;

—the mode of displaying the process parameters on the monitor screen in the form of the dynamic plots and numerical data;

—the mode of recording the necessary process parameters into a file.

The program envisages the display of the graphical information about all the growth parameters and their control, namely, the force recorded by the strain sensor, the real and the model weights of the crystal, the length of the model crystal, the generator power, etc. The program has a flexible adjustable graphic interface providing the arbitrary adjustment of the information displayed in accordance with the requirements set by an operator.

The automatic system with feedback includes algorithms for estimating the state of an object and the control of the heater temperature and pulling rate (control channels). The controlled object is transverse dimensions of a pulled crystal usually determined by simple

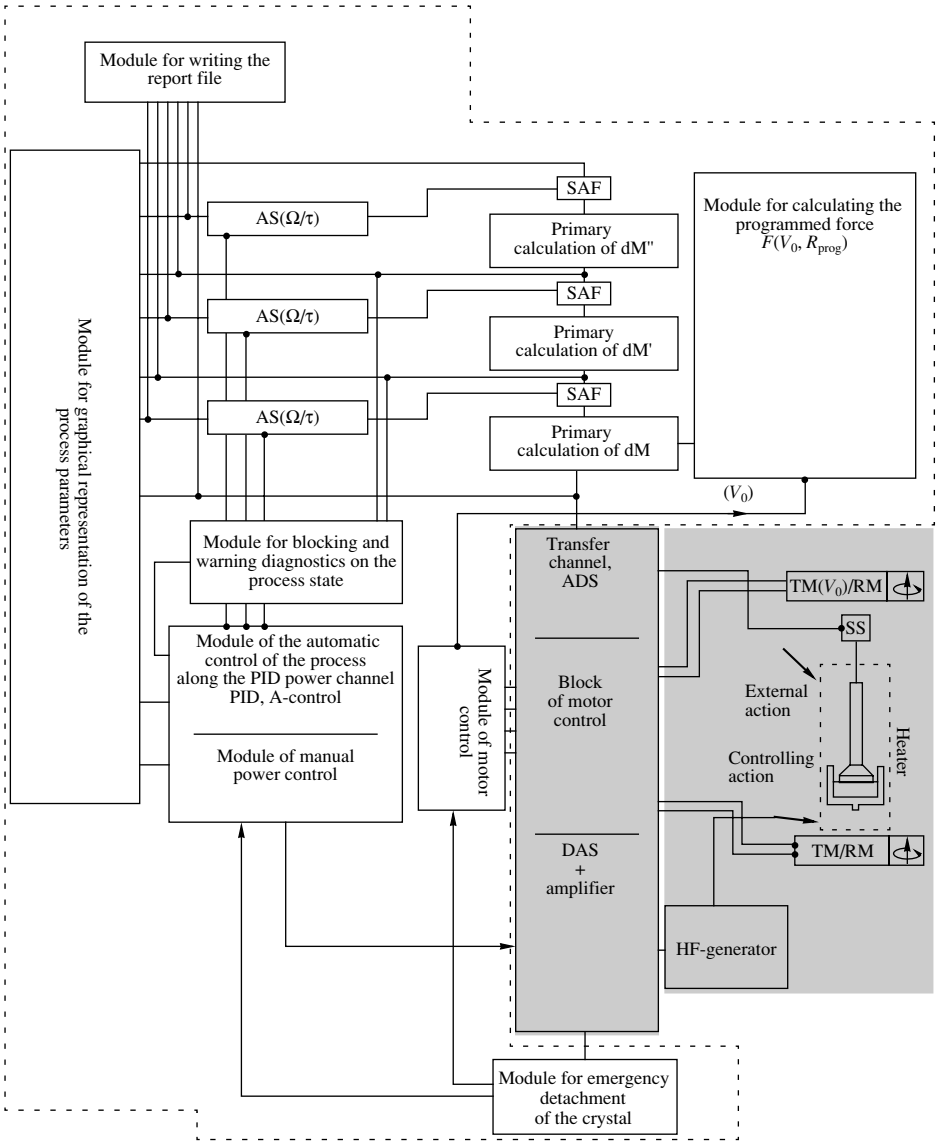

Fig. 5. Block-diagram of the controlling system. Notation: [AS(Ω/τ)] averaging summation for the controlled period; (SAF) sliding-averaging filter, (dM) the change in the crystal mass, (TM) electric motor of rod translation, (RM) electric motor of rod rotation, (SS) strain sensor, (ADC) analog-to-digital converter, (DAC) digital-to-analogue converter; (PID) proportional integro-differential regulator, (A-control) the amplitude control in the "combined method," ($F(V_0, R_{prog})$) programmed force acting onto the growing crystal with the transverse dimensions R_{prog}, and V_0 is the pulling rate.

calculation based on the signal of a sensor which measures the total force acting onto a pulled crystal. The computational device (or the program block) calculates the value of the force corresponding to the maintained radius of the ingot. The main regulator records the sensor readings and the calculated-force value, determines their difference, and generates the signal controlling the heater power. The programmed force is calculated by an observation equation, in which the phase variables (crystal radius and meniscus height) are either constant or vary in accordance with the functions indicated above.

The well-known observation equation for the Czochralski method obtained from the analysis of the forces acting onto the crystal has the form

$$W(t) = \int_0^t \rho_S g \pi r^2 V(t) dt + \pi r^2 \rho_L g h + 2\pi r \sigma_{LG} \cos\varepsilon, \quad (2)$$

where $W(t)$ is the modeled value of the force-sensor reading, ρ_S and ρ_L are the densities of the crystal and the melt, r is the crystal radius, σ_{LG} is the surface-tension coefficient of the melt, ε is the growth angle, V is the pulling rate of the crystal, and h is the meniscus height. The first term corresponds to the crystal mass grown for time t; the second one, to the mass of the meniscus of height h; and the latter term, to the surface-tension force acting onto the crystal.

In the automatic mode, the value of the force (programmed force) is calculated in the corresponding module of the program according to the observation equation with a transverse cross section of the crystal having the desirable area (determined *a priori*). Then the real and the modeled forces are compared and their difference ΔW is determined. This procedure is performed by interrogating the force sensor with an interval τ. To reduce the measurement noise, the results obtained are subjected to digital filtration by the method of sliding averaging,

$$\Delta W_j^* = \left\{ \sum_{k=j-n}^{k=j} \Delta W_k \right\}/n. \quad (3)$$

The first and the second derivatives of the difference ΔW are also calculated and digitally filtered,

$$\Delta \dot{W}_j = (\Delta W_j^* - \Delta W_{j-1}^*)/\tau,$$
$$\Delta \dot{W}_j^* = \left\{ \sum_{k=j-n}^{k=j} \Delta \dot{W}_k \right\}/n, \quad (4)$$

$$\Delta \ddot{W}_j = (\Delta W_j^* - 2\Delta W_{j-1}^* + \Delta W_{j-2}^*)/\tau^2,$$
$$\Delta \ddot{W}_j^* = \left\{ \sum_{k=j-n}^{k=j} \Delta \ddot{W}_k \right\}/n. \quad (5)$$

Then the averaging summation is made over the control period Ω,

$$\Delta W_i^* = \frac{\sum_{j}^{j+\frac{\Omega}{\tau}} \Delta W_j^*}{\Omega/\tau}, \quad \Delta \dot{W}_i^* = \frac{\sum_{j}^{j+\frac{\Omega}{\tau}} \Delta \dot{W}_j^*}{\Omega/\tau},$$
$$\Delta \ddot{W}_i^* = \frac{\sum_{j}^{j+\frac{\Omega}{\tau}} \Delta \ddot{W}_j^*}{\Omega/\tau}, \quad (6)$$

and the value of the controlling action (ΔP_i) along the power channel is calculated,

$$\Delta P_i = K_I \Delta W_i^* + K_P \Delta \dot{W}_i^* + K_D \Delta \ddot{W}_i^*, \quad (7)$$

where $\Delta \dot{W}_i^*$ and $\Delta \ddot{W}_i^*$ are the first and the second derivatives with respect to time. All the operations performed by the program are controlled by a program timer.

The developed complex was successfully tested on Czochralski-grown yttrium–aluminum garnet (YAG) 40 mm in diameter and more than 200 mm in length.

However, observation equation (2) is inapplicable to the Stepanov method and its modifications using dies. Our experimental studies of the influence of the process parameters on readings of the force sensor during growth of profiled crystals [27] and the mathematical simulation of the heat and mass transfer in the crystal–melt system [28] showed that the deviation from the stationary growth process gives rise to the changes in the hydrodynamic pressure in the melt meniscus, which, in turn, changes the force acting onto the crystal. As a result, we obtain the following observation equation for crystals grown with the use of dies:

$$W(t) = \int_0^t \rho_S g S(t) V_0 dt + S(t)\rho_L g h + \Gamma(t)\sigma_{LG}\cos\varepsilon + H_{\text{eff}}(t)\rho_L S(t) + K_R V_0 + \int_S p(h, V_0) ds, \quad (8)$$

where $S(t)$, $\Gamma(t)$ are the area and the perimeter of a growing crystal, V_0 is the pulling rate, h is the meniscus height, K_R is the coefficient of the resistance of the capillary die to the melt flow, and $p(h, V_0)$ is the hydrodynamic pressure under the crystallization front.

The positional oscillations of the crystallization front are caused by the temperature fluctuations in its vicinity and the mechanical noise of the apparatus. An analysis of observation equation (8) for the Stepanov method with due regard for the results obtained in [27, 28] shows that an increase in the meniscus height is accompanied by a dramatic increase in the oscillation amplitude of the force-sensor readings (ΔW). Indeed, attempts of automatic growth of profiled crystals with the use of the classical proportional integro-differential (PID) control showed that the melt supercooling accompanied by a decrease in the meniscus height gave rise to a dramatic increase in the measurement noise. The numerical differentiation of the deviation of the sensor reading from the modeled-force value with respect to time allowed us to reveal this effect much better. At an oscillation-amplitude value $\Delta \dot{W}$ higher than a certain limiting value, the control became unstable, which made necessary the intervention of an operator. Usually, the steady-state mode was maintained by an operator who increased the heating power or corrected the programmed force value manually.

The most efficient simple method of automatic control, the so-called "combined method," was suggested in [29]. As follows from the stated above, in order to provide the continuous process of the automatic control with the constant adjustment of the regulator, one has to maintain the dynamic characteristic of the controlled object constant, i.e., in our case, to maintain the meniscus height within a certain range. The experimental data and the results of modeling showed that the parameter of the indirect information on the meniscus height is the amplitude value $\Delta \dot{W}$. If the value of this parameter exceeds the experimentally established critical value, then the program blocks the PID regulator and

gradually increases the heating power up to the moment when the amplitude $\Delta\dot{W}$ attains the necessary limits. A decrease in $\Delta\dot{W}$ to the given value is the signal for switching on the PID regulator, which then controls the growth up to the moment when $\Delta\dot{W}$ becomes higher than the established value once again. The combined method is successfully used within the complex described above for simultaneous growth of about 30 sapphire rods with circular and rectangular transverse cross sections and a package of 10 ribbons.

The designed apparatus and software, and the experimental results obtained in the experiments on the automatic control of crystal growth from melts form the necessary basis for further experiments on growth of profiled crystals with three-dimensional variation of their shape during crystallization.

REFERENCES

1. V. A. Borodin, T. A. Steriopolo, V. A. Tatarchenko, and T. N. Yalovets, Izv. Akad. Nauk SSSR, Ser. Fiz. **47**, 368 (1983).
2. V. A. Borodin, V. V. Sidorov, T. A. Steriopolo, and V. A. Tatarchenko, J. Cryst. Growth **82**, 89 (1987).
3. V. A. Borodin, V. V. Sidorov, T. A. Steriopolo, and V. A. Tatarchenko, USSR Inventor's Certificate No. 1415820, C 30B 15/34 (1985).
4. V. A. Borodin, Doctoral Dissertation (Institute of General Physics, Russian Academy of Sciences, Moscow, 1991).
5. V. V. Sidorov, Candidate's Dissertation (Institute of Solid State Physics, Russian Academy of Sciences, Chernogolovka, 1992).
6. V. A. Borodin, V. V. Sidorov, T. A. Steriopolo, *et al.*, Izv. Akad. Nauk SSSR, Ser. Fiz. **52**, 2009 (1988).
7. V. A. Borodin, V. V. Sidorov, and T. N. Yalovets, Kristallografiya **35** (1), 185 (1990) [Sov. Phys. Crystallogr. **35**, 111 (1990)].
8. V. A. Borodin, V. V. Sidorov, S. N. Rossolenko, *et al.*, J. Cryst. Growth **104**, 69 (1990).
9. V. A. Borodin, V. V. Sidorov, S. N. Rossolenko, *et al.*, J. Cryst. Growth **198/199**, 201 (1999).
10. V. A. Tatarchenko, *Steady-State Crystal Growth* (Nauka, Moscow, 1988), p. 72.
11. V. A. Borodin, T. A. Steriopolo, and V. A. Tatarchenko, USSR Inventor's Certificate No. 1064660, C 30B 15/34 (1981).
12. V. A. Borodin, T. A. Steriopolo, and V. A. Tatarchenko, USSR Inventor's Certificate No. 917575, C 30B 15/34 (1980).
13. V. A. Borodin, T. A. Steriopolo, and V. A. Tatarchenko, USSR Inventor's Certificate No. 999675A, C 30B 15/34 (1980).
14. L. P. Egorov, L. M. Zatulovskiĭ, D. Ya. Kravetskiĭ, *et al.*, USSR Inventor's Certificate No. 1358483A1, C 30B 15/34 (1985).
15. B. B. Pel'ts, L. M. Zatulovskiĭ, D. Ya. Kravetskiĭ, *et al.*, USSR Inventor's Certificate No. 1271150A, C 30B 15/34 (1984).
16. N. V. Abrosimov, V. A. Borodin, T. A. Steriopolo, and V. A. Tatarchenko, USSR Inventor's Certificate No. 1075761A, C 30B 15/34 (1984).
17. I. V. Alyab'ev, S. V. Artemov, V. S. Papkov, and V. F. Perov, USSR Inventor's Certificate No. 1362093A1, C 30B 15/34 (1986).
18. V. N. Kurlov, Izv. Akad. Nauk, Ser. Fiz. **23**, 5 (1994).
19. V. A. Borodin, T. A. Steriopolo, and V. A. Tatarchenko, USSR Inventor's Certificate No. 1251592A, C 30B 15/34 (1984).
20. V. A. Borodin, V. V. Sidorov, T. A. Steriopolo, and V. A. Tatarchenko, USSR Inventor's Certificate No. 1360269A, C 30B 15/34 (1985).
21. V. A. Borodin, T. A. Steriopolo, and V. A. Tatarchenko, USSR Inventor's Certificate No. 1228527A, C 30B 15/34 (1984).
22. V. A. Borodin, T. A. Steriopolo, and V. A. Tatarchenko, USSR Inventor's Certificate No. 1238428A, C 30B 15/34 (1984).
23. V. A. Borodin, T. A. Steriopolo, and V. A. Tatarchenko, USSR Inventor's Certificate No. 1408815A, C 30B 15/34 (1985).
24. P. I. Antonov, Yu. G. Nosov, and S. P. Nikanorov, Izv. Akad. Nauk SSSR, Ser. Fiz. **49**, 2295 (1985).
25. V. A. Borodin, V. V. Sidorov, and T. A. Steriopolo, RF Patent No. 2160330, C 30B 15/34 (1997).
26. W. Bardsley, J. Cockayne, G. B. Green, *et al.*, J. Cryst. Growth **24/25**, 369 (1974).
27. A. V. Borodin, V. A. Borodin, V. V. Sidorov, and I. S. Petkov, J. Cryst. Growth **198/199**, 215 (1999).
28. A. V. Borodin, V. A. Borodin, and A. V. Zhdanov, J. Cryst. Growth **198/199**, 220 (1999).
29. A. V. Borodin, V. A. Borodin, I. S. Petkov, and V. V. Sidorov, J. Korean Assoc. Cryst. Growth **4**, 437 (1999).

Translated by L. Man

Crystallography Reports, Vol. 47, Suppl. 1, 2002, pp. S43–S52.

MELT GROWTH

New Advances and Developments in the Stepanov Method for the Growth of Shaped Crystals

P. I. Antonov* and V. N. Kurlov**

** Ioffe Physicotechnical Institute, Russian Academy of Sciences, Politekhnicheskaya ul. 26, St. Petersburg, 194021 Russia*

*** Institute of Solid State Physics, Russian Academy of Sciences, Chernogolovka, Moscow oblast, 142432 Russia*

e-mail: kurlov@issp.ac.ru

Received October 1, 2002

Abstract—The main recently developed versions of the Stepanov method are analyzed, and a brief review of the main achievements in the growth of shaped crystals is given. © *2002 MAIK "Nauka/Interperiodica".*

INTRODUCTION

The ideas and publications of A.V. Stepanov on crystal growth gave rise to a new line of research in this field and laid a foundation for the industry of shaped crystals. The new principle of crystal shaping is formulated in the following way: "A shape or an element of a shape that we need to form is created in the liquid state owing to different effects allowing the liquid to retain its shape; then, this shape or its element can be transformed to the solid state by choosing the appropriate crystallization conditions" [1].

The technique of Stepanov differs from the other methods of crystal growth from the melt in the presence of a new element, namely, a shaper, which provides an opportunity to form a liquid column of the melt in a free state without any contact with the crucible walls. Different types of single-crystal products with complicated cross-section shapes, geometry, and various sizes are obtained due to the crystallization of the liquid melt column formed by the shaper. Stepanov paid special attention to the latter. In his manuscripts, we found the following note: "A shaper should be distinguished from a die. A die is the embodiment of a brute force; its action can be described by the proverb 'It cries but crawls through.' A shaper is a more spiritual system. Its aim, first of all, is to provide a delicate effect on the curvature and shape of the mobile column of the liquid melt stretching itself behind the crystal by creating new boundary conditions along its contour."

The technique of Stepanov should be considered a natural extension of the Czochralski method. Conscious implementation of the shaping concept for liquids and the usage of shapers give rise to qualitatively new results. Hence, the technique of Stepanov gains importance and a life of its own. In this case, one could say that the crystallization is performed under the most controlled conditions, in comparison to all other methods.

Stepanov was the first person to realize the significant advantages of manufacturing shaped products: economizing on materials, automation of the process, and the creation of novel engineering materials. It is not an accidental fact that his book, published in the USSR in 1963, was entitled *The Future of Metal Processing* [1]. On the basis of the classical works of Stepanov, new versions of his technique are being developed; both the range of materials and the scope of applications for shaped crystals and products have become more and more broad. Stepanov paid considerable attention to the development of his technique in 1998. He initiated in 1967 the First All-Union Meeting on Manufacturing Shaped Products and Their Applications in Industry. The last, 11th, meeting was held, as always, at the Ioffe Institute of Physics and Technology, Saint Petersburg, Russia, and was dedicated to the 90th Anniversary of Stepanov. The proceedings of all the meetings were published in the journal *Bulletin of the Russian Academy of Sciences, Ser. Physics*, and in separate collections of papers of the Ioffe Institute.

Papers on the growth of shaped single crystals were also published in a separate issue of the *Journal of Crystal Growth* (1980, vol. 50). The Stepanov technique has been the subject of review articles and books [2–9]. The International Conferences on the Growth of Shaped Single Crystals were held in Budapest in 1986 and 1989.

As early as in his first papers, Stepanov clearly formulated the shaping concept: the design and operation of shapers wetted and not wetted by the melt. Many versions of the Stepanov technique have been tested and applied in industry.

However, some researchers revised the Stepanov technique and introduced new terms. Therefore, we would like once more to draw attention to certain aspects concerning the sense of the different versions of

1063-7745/02/47S1-S0043$22.00

the Stepanov technique and to the disputes on the problems of priority.

In the present paper, we analyze the main recently developed versions of the Stepanov technique and give a brief review of the main results achieved in shaped crystal growth.

THE GROWTH OF SHAPED CRYSTALS WITH A CONSTANT CROSS-SECTION USING A CAPILLARY FEED

The worldwide boom in the research concerning the growth and analysis of shaped single crystals was initiated by the papers of LaBelle and Mlavsky [10–12] at the end of the 1960s and the beginning of the 1970s. They proposed edge-defined, film-fed growth (EFG), which turned out to be very convenient for the growth of shaped sapphire when molybdenum was used as a material for the shaper. The main original idea of this method is that the melt wets the shaper and is fed to the edges through capillaries manufactured in the shaper bulk. As a result, in the course of the melt consumption, the melt is continuously supplied from the crucible. However, the authors of these papers completely avoided any reference to the Stepanov technique. N.N. Sheftal', acting on behalf of the Institute of Crystallography, USSR Academy of Sciences, Moscow, sent a letter [13] wherein he pointed out the role and the priority of Stepanov in connection with the EFG method, which had just appeared at that time. In his reply to this letter, Mlavsky noted that "the Stepanov method deals with shapers that are *not wetted* by the melt, whereas the EFG technique employs *wetted* shapers" (underlined by Mlavsky). This is schematically represented in Figs. 1a and 1b. Such a classification demonstrates a misunderstanding or a reluctance to understand the essence of the Stepanov method.

The EFG technique is one version of the Stepanov method that implements shapers wetted by the melt, where the catching by the outer edges is engaged and the melt column is fed through the capillary channel in the course of pulling the crystal (see Fig. 1b). This version became especially popular in the crystal growth of oxides (of sapphire, above all), silicon, germanium, alkali halides, metal fluorides, etc.

The efforts of different laboratories contributed to solving the problem of manufacturing different forms of shaped crystals directly in the process of their growth. The EFG technique was used to grow thin filaments, bars of various cross section, tapes of different thickness and width, tubes, bars and tapes with capillary channels, etc. As an example, we can mention the growth of silicon tubes up to 50 cm in diameter (14) and sapphire tapes up to 30 cm in width [15].

One of the most topical problems is improvement of the quality of the grown crystals. This would help to broaden significantly the range of application for shaped crystals.

An automated control system implementing a weight sensor was developed to monitor the state of the crystallization front and to avoid the formation of defects caused by supercooling. The design features of the control system for monitoring the state of the crystallization front in the course of the growth process are discussed in detail in paper [16].

The main parameter used to control the state of the crystallization front was the amplitude of the oscillations in the deviations of the actual mass variation rate from that specified. It was the analysis of the oscillation amplitude and its adjustment by the corresponding changes in the heating power and/or the crystal pulling

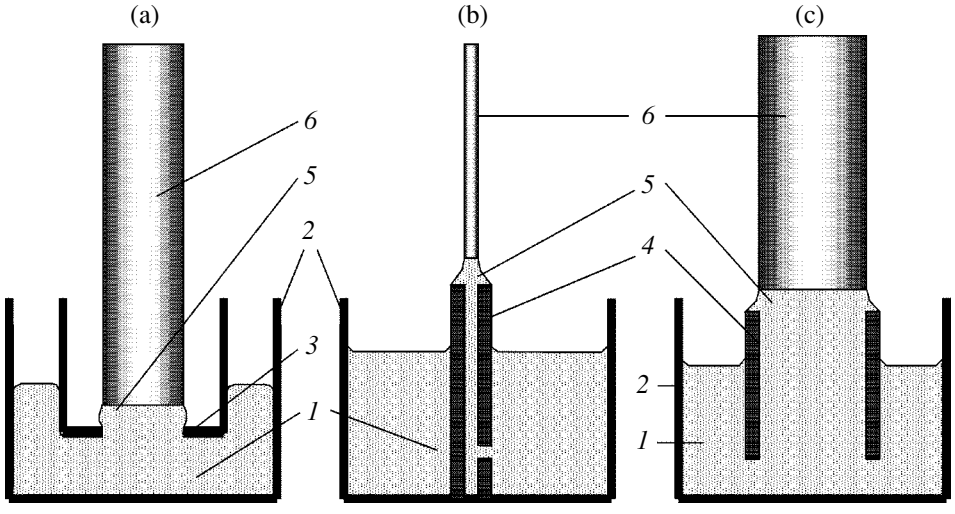

Fig. 1. The layout of different versions of the Stepanov method: (a) the classical version with the use of the shaper not wetted by the melt; (b) the EFG method; (c) the method with the use of the noncapillary feeding; (*1*) melt; (*2*) crucible; (*3*) shaper not wetted by the melt; (*4*) shaper wetted by the melt; (*5*) meniscus; (*6*) crystal.

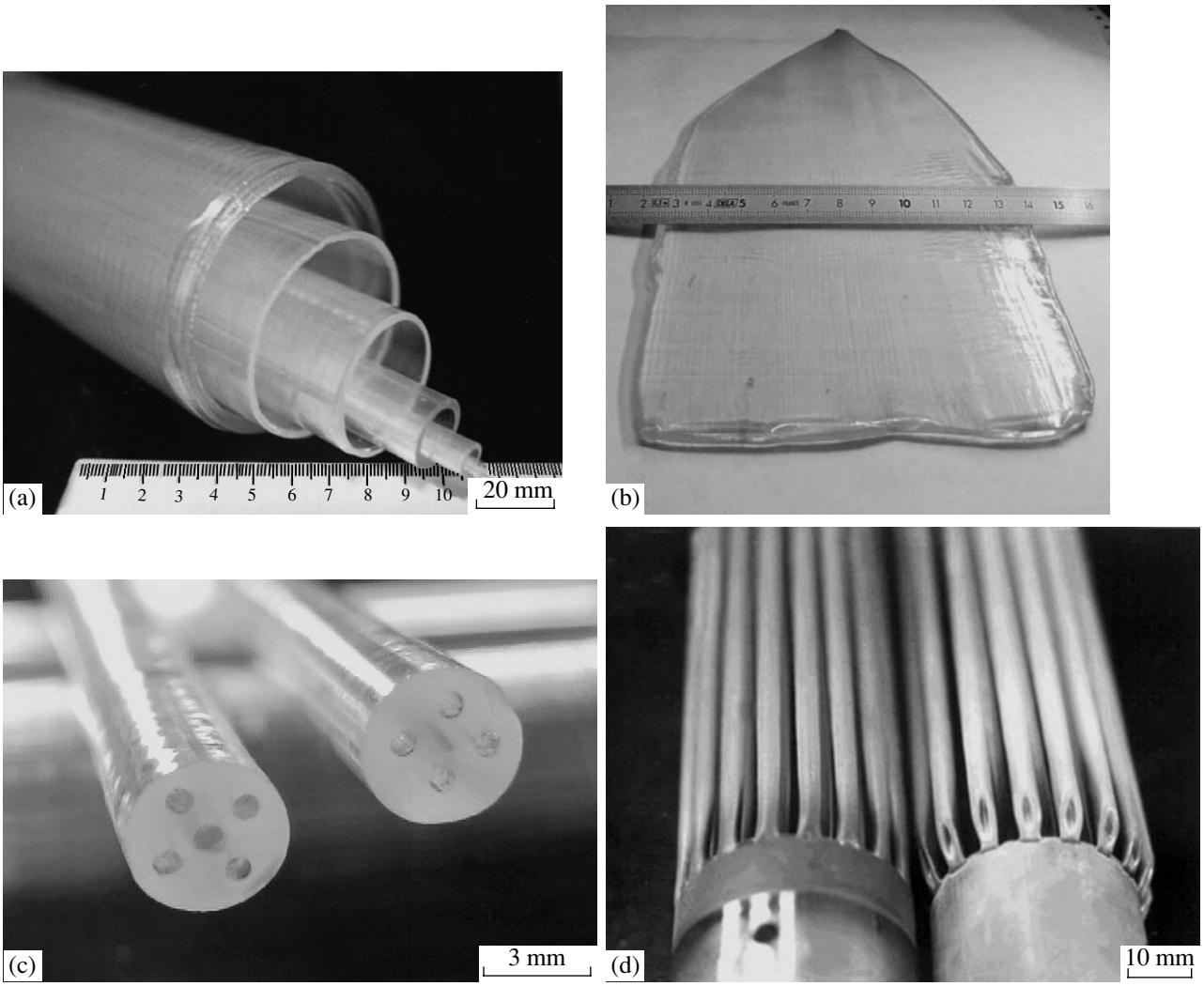

Fig. 2. The shaped crystals grown by the Stepanov method (EFG with the weight control): (a) tube up to 85 mm in diameter; (b) tape 120 mm wide; (c) bar with channels 0.7 mm in diameter; (d) bars and tubes grown in the group mode.

rate that provided the opportunity to control the shape and quality of growing crystals. The developed system was successfully implemented for the growth of large size sapphire tubes [17] and tapes [18], bars with capillary channels, filaments, bulk shaped crystals, and bars and tubes in the group growth mode (up to 50 crystals simultaneously) [16].

The shaped sapphire crystals with different shapes of their cross-section grown through the use of the automated control system are shown in Fig. 2.

THE METHOD OF VARIED SHAPING

A very important problem is the development of technologies allowing one to change the shape and size of crystals in the course of their growth. First of all, it is related to the use of shaped sapphire crystals in the form of complete products such as crucibles, boats, etc.

Different versions of changing the profile of the growing crystal which could be considered under such common name as “varied shaping” were developed based on the Stepanov method. In this technique, the base of the melt meniscus is torn off the edges of one shaper specifying the initial shape and then it catches on the edges of another shaper specifying the subsequent shape of the cross-section. The mass flow rate of the melt supplied to the crystallization front is controlled by different technological means: the change in the relative position of different parts of the shaper, the change in the shaper position with respect to the melt level, the subsequent use of different shapers, the temperature variation in the crystallization zone, the changes of pressure, crystal pulling rate, etc. [19–22].

In Fig. 3, we show the sapphire crucibles, boats, and other shaped crystals with varying cross-section grown by the method of varied shaping.

Fig. 3. Shaped crystals with varying cross section grown by the method of varied shaping.

THE CRYSTAL GROWTH WITH THE USE OF NONCAPILLARY SHAPING (NCS) METHOD

The noncapillary shaping (NCS) method was developed for the growth of high-quality shaped crystals with a large cross-sectional area. The essence of the NCS method is the feeding of the crystallization front by the melt from the crucible via a noncapillary channel (the channel cross-sectional size exceeds the value of the capillary constant for the melt). This promotes melt motion in the meniscus from the center to the periphery. Such an approach allows one to eliminate the formation of counterflows in the melt under the crystallization front, which are characteristic of the growth of a bar with a large cross-sectional area through the use of the EFG technique with capillary feeding. In the regions where the melt flows in the meniscus meet each other, the components of the flow rate have a minimum value. The regions adjacent to these are those with an enhanced content of gas impurities pushed off by the interface between the phases. Such regions are the most probable locations of the nucleation and capture of gas inclusions.

The NCS method implements a version of the Stepanov technique with the shaper wetted by the melt where the melt is fed under a negative pressure, whereas in the classical version of the Stepanov technique with the shaper not wetted by the melt, the melt is fed under a positive pressure (Fig. 1c).

For the growth of bulk crystals, different kinds of the initial growth stage and the subsequent feeding via a noncapillary channel can be used: with a pointlike seed (Fig. 4a), bulk seed (Fig. 4b), and ring-shaped capillary channel (Fig. 4c) [8, 9, 23]. The seed rotation can be used simultaneously with its advance at the stages of seeding, transient growth, and steady-state growth. In all these cases, the shape of the bulk crystal is determined by the catching at the outer edge of the shaper.

In the case of the pointlike seeding (Fig. 4a), after the transient growth stage, when the crystal dimensions coincide with those of the shaper, the melt becomes caught in the shaper edges. This actually corresponds to a transition from the Czochralski method to the NCS method. The version with the bulk seed (Fig. 4b) allows one to avoid the transient growth stage. Both cases are implemented when the level of the working edges in the shaper coincides with the melt level in the crucible.

The version with the ring-shaped capillary channel (Fig. 4c) is described in detail in [23]. The melt lifting in the shaper to the crystallization zone was performed via the noncapillary channel owing to the pressure difference between the growth chamber and the closed volume under the seeding plate. An analogous technique for the lifting of the melt to the crystallization front was used for the growth of sapphire crucibles.

In the NCS method, the optimum relationship of the diameter of the noncapillary channel to the cross-sectional size of the growing crystal, the pulling rate, and the end face geometry of the shaper makes it possible to feed the crystallization front through the melt strictly from the center to the periphery of the crystal cross section. In this case, the free surface of the meniscus is a sink for gas impurities. Thus, we can produce shaped crystals of a large diameter without gas inclusions in their bulk (Fig. 5).

The NCS method has been successfully applied also to the growth of monolithic sapphire crystals with different cross-sectional shapes, thick-wall tubes, plates, and threaded joints [23]. Noncapillary feeding was used to grow sapphire crucibles up to 65 mm in diameter without any inclusions in the bottom part of the crystals. The NCS method also provides an opportunity to control the shape of the crosspiece at the crossover between the hollow and monolithic parts of the crystal and vice versa by using a certain end face geometry of the working edge in the shaper. This is important for the growth of sapphire hemispherical blanks for high-temperature optical devices [24].

The development of the above version of the Stepanov method confirms once more the diversity of the techniques used to produce shaped crystals.

CRYSTALLIZATION FROM AN ELEMENT OF SHAPE

When the growth from an element of shape (GES) was first implemented [25], it seemed to be a technique rather different from the Stepanov method. However, it soon became clear that the sagacity of Stepanov manifested itself in this case also. His formulation of the capillary shaping principle also contained this version: “a shape or an element of the shape is created in the liquid state… .”

In the GES technique, the shaper does not entirely determine the form of the crystal cross section; it specifies only its thickness. The crystal growth is performed

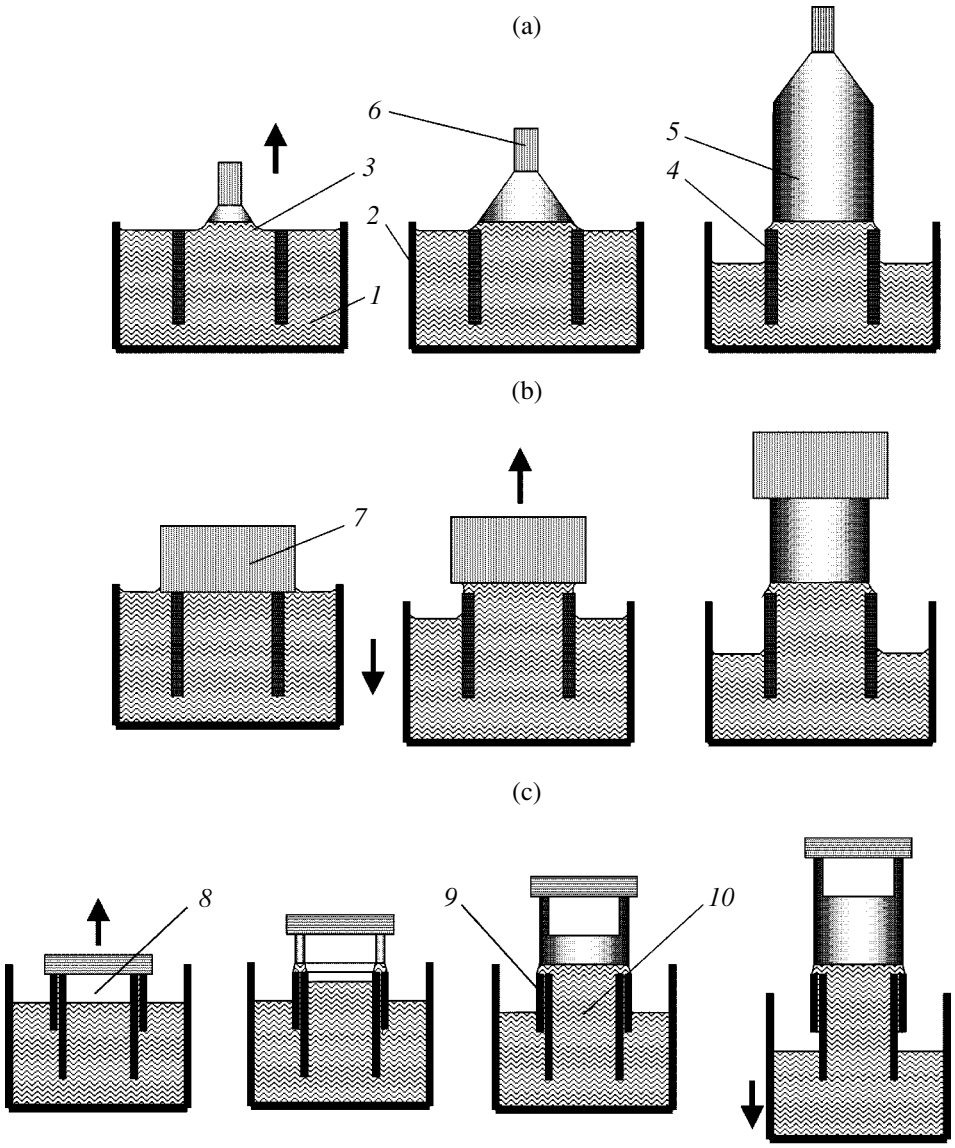

Fig. 4. Schematic picture illustrating the growth of shaped bulk crystals by the NCS technique: (a) with the use of pointlike seed; (b) with the use of bulk seed; (c) with the use of a capillary channel; (*1*) melt; (*2*) crucible; (*3*) meniscus; (*4*) shaper; (*5*) crystal; (*6*) pointlike seed; (*7*) bulk seed; (*8*) closed volume under the seeding plate; (*9*) capillary channel; (*10*) noncapillary channel.

layer by layer, and in the simplest case of simultaneous rotation and pulling of the crystal, its length increases during one turn by the value $l = V/\omega$, where V is the pulling rate and ω is the rotation frequency of the crystal (Fig. 6). By creating a relatively small melt volume and promoting various displacements of it with respect to the seed, it is possible to produce crystals of the most complicated shape. In the course of crystallization, a displacement can be given either to the seed crystal or to the shaper, or even to both of them simultaneously. The term "local shaping" introduced later [26] is not quite adequate. The authors of this technique [25] do not see any reason to change its name and argue that it is more correct to use the terminology suggested by Stepanov himself, namely, growth from an element of shape (GES).

The growth of sapphire hemispheres by the GES technique turned out to be the most advantageous application of this technique. The sapphire hemispheres were grown by the GES technique due to the integrated solution of a number of different problems: the formation of the initial stage of the hemisphere growth and maintaining a constant wall thickness of the blank during the whole growth process, optimization of the growth conditions for producing crystals free from gas and solid inclusions in their bulk, obtaining block-free crystals, reduction of thermoelastic stresses, and prevention of cracking in the hemispheres in the course of the growth process [27, 28].

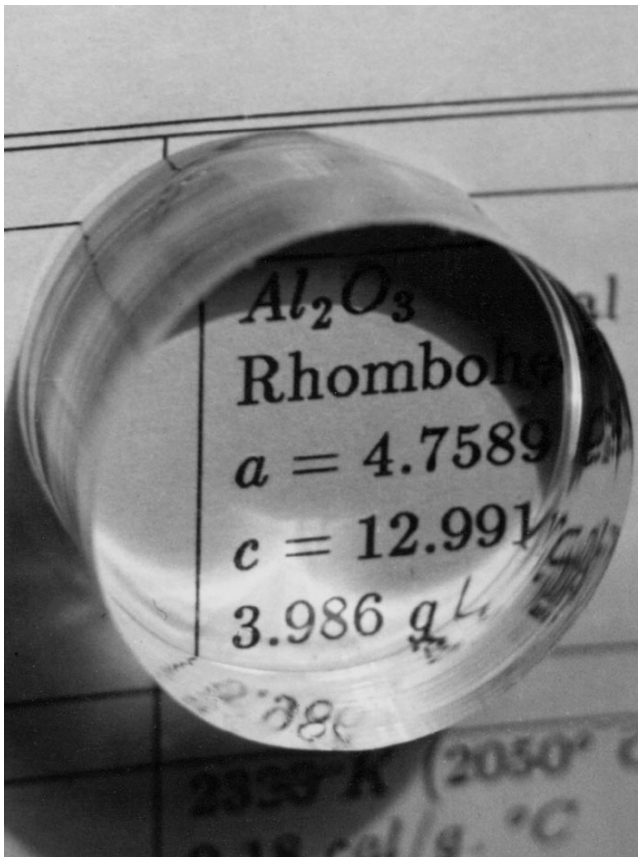

Fig. 5. Sapphire bar 40 mm in diameter grown by the NCS technique.

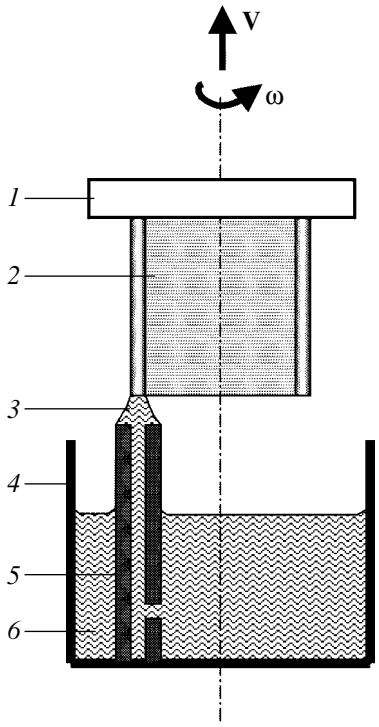

Fig. 6. Schematic picture illustrating the growth of crystals by the GES technique: (*1*) seeding plate; (*2*) crystal; (*3*) meniscus; (*4*) crucible; (*5*) shaper; (*6*) melt.

At the initial stage of the hemisphere formation, when after seeding, the pulling is performed nearly along the horizontal direction, the size of the crystal cross section tends to zero if the shaper with the plane horizontal end face is used. In this case, crystal growth is impossible because the melt meniscus is not caught by the edges of the shaper. The way to solve this problem is based on the use of a shaper with an inclined end face [27], which provides an opportunity to grow hemispherical blanks with a slightly variable wall thickness upon simultaneous displacement and rotation of the seed crystal both in the vertical and horizontal directions. The molybdenum shaper with a working end face placed at an angle of 45° with respect to the vertical axis is optimum for pulling crystals in a wide range of inclination angles characterizing the direction of the pulling.

An important parameter characterizing the growth of hemispherical sapphire blanks by the GES technique is the height of the layer grown during one 180-degree turn of the crystal. Its value is determined by the relationship between the rates of vertical and horizontal displacements and the crystal rotation rate. For a large thickness of the grown layer (20–120 μm), there appear periodically arranged clusters of gas and solid inclusions in the crystal bulk. These inclusions cause a significant lowering of the optical quality of the grown crystals. Experiments involving the growth of crystals with complicated shapes by the GES technique have demonstrated that a layer thickness of the order of 3–5 μm is the optimum thickness for manufacturing crystals free of gas and solid inclusions in its bulk [28]. The angular rotation rate was varied in such a way as to meet two conditions: maintaining a constant layer thickness and constant linear velocity of the rotation in order to prevent the nucleation of cracks in the course of the growth and cooling of the crystals.

The manufacture of sapphire hemispheres by using GES technique posed the problem of crack formation in the course of the crystal growth [27]. The crack arose directly above the shaper where a local distortion of the temperature field and the related enhancement of stresses took place. To estimate the thermoelastic stresses in crystals and to find the optimum modes for the growth of the crack-free sapphire hemispheres, the temperature measurements were performed using thermocouples grown into the crystals [29].

The temperature distribution for the GES technique demonstrated that the melted layer thickness above the shaper was 0.2–0.6 mm. This value far exceeds the value of $L = V/\omega$. For the crystals grown following the GES technique, the temperature distribution in the vicinity of the crystallization front demonstrated that the temperature peak corresponding to the melt meniscus passing under the thermocouple can be as high as 18°C.

Thus, we see that the shaper significantly affects the temperature distribution in the crystal. This, in turn,

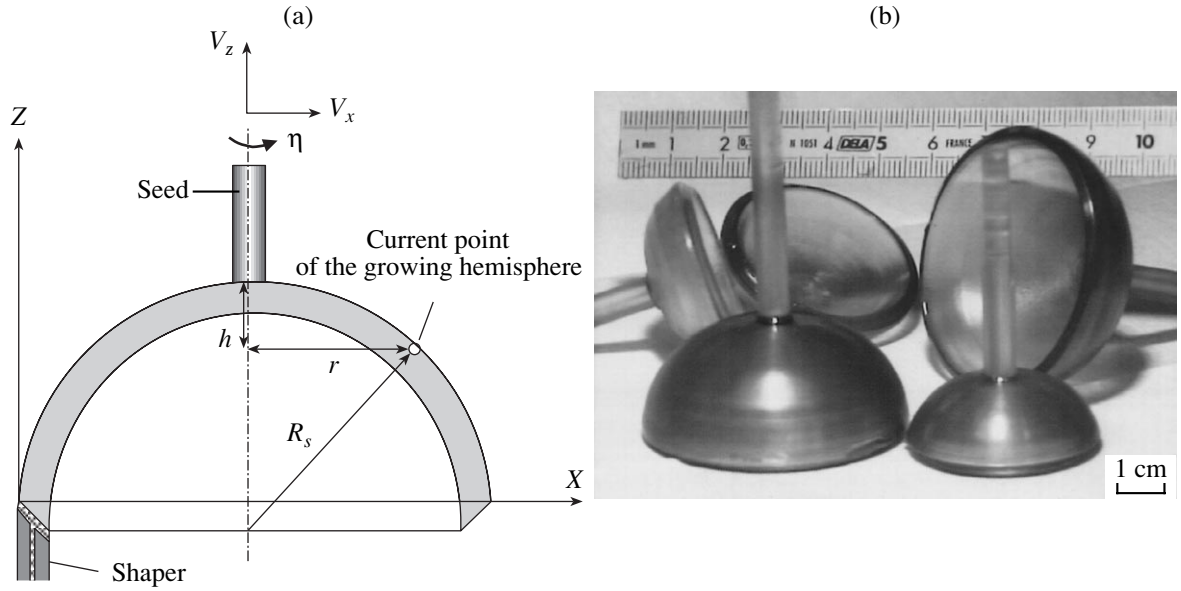

Fig. 7. The growth of hemispheres by the GES technique: (a) the growth scheme using the shaper with an inclined end face; (b) photos of sapphire hemispheres up to 50 mm in diameter with walls up to 4 mm thick.

should produce a certain effect on the level of thermally induced stresses. The EFG technique gives rise only to a nonlinear temperature distribution along the crystal growth axis, whereas in the GES technique, it is additionally supplemented by distortion of the temperature field above the shaper, which moves in the course of the crystal rotation.

Despite all this, the performed estimates of thermoelastic stresses calculated using the method of finite elements in the isotropic approximation for the case of planar stresses demonstrate that the stress level for the GES technique is not higher than that characteristic of the EFG technique [29]. To analyze the possible mechanisms of the stress formation in the crystals grown by the GES technique, the results of the numerical simulation for the time-dependent stressed and strained state of the growing crystal were used [27]. The model involved calculations of the temperature field, as well as elastic and viscoplastic stresses. The nucleation of the initial crack parallel to the crystal growth direction can stem from a high positive value (tensile force) of the hoopential component $\sigma_{\theta\theta}$ of the stress tensor. Further evolution of the crack takes place occurs gradually with the crystal growth and is related to the relaxation of the thermoplastic stresses continuously increasing with the crystal size. Based on this model, the optimum modes for the growth of sapphire hemispheres were chosen to eliminate the cracking in the course of their growth. To attain this optimum in the temperature range under study, it is necessary to have a plastic deformation rate that is not lower than the rate characterizing the growth of elastic stresses with the crystal size. The approximate estimates of these rates for the hemispheres allowed us to find the relationships between the growth parameters corresponding to the case when the condition of the plastic relaxation is met for thermoelastic stresses. In Fig. 7, we present a schematic illustration for the growth of hemispheres by the GES technique using a shaper with an inclined end face, as well as photos of sapphire hemispheres up to 50 mm in diameter with walls up to 4 mm thick [27].

SHAPED CRYSTALS WITH DOPED SPATIAL STRUCTURES

A topical task in the field of optoelectronics is the development of novel materials combining several functions. One way to fulfill this task to grow shaped crystals with modulated spatial structures. Different versions of the Stepanov technique have paved the way not only to the manufacture of crystals of any complicated shape but also to the creation of a new class of materials, namely, crystals with doped spatial structures.

Manufacturing of periodic structures. To produce shaped crystals with periodic spatial structures, a version of the GES technique was implemented wherein two or more kinds of melt with different impurity content were used (Fig. 8a).

The first layered crystals were produced based on the LiF–LiF:Mg^{2+} system (Fig. 8b) [25]; these crystals were used as a model material for the study of mechanical characteristics. These studies demonstrated that the nucleation of plastic shears occurs near the interface between layers. This leads to a more uniform distribution of strains in the samples and hence to enhancement of their plasticity. The plastic shears always nucleate in the impurity-free layers near the interfaces both at the

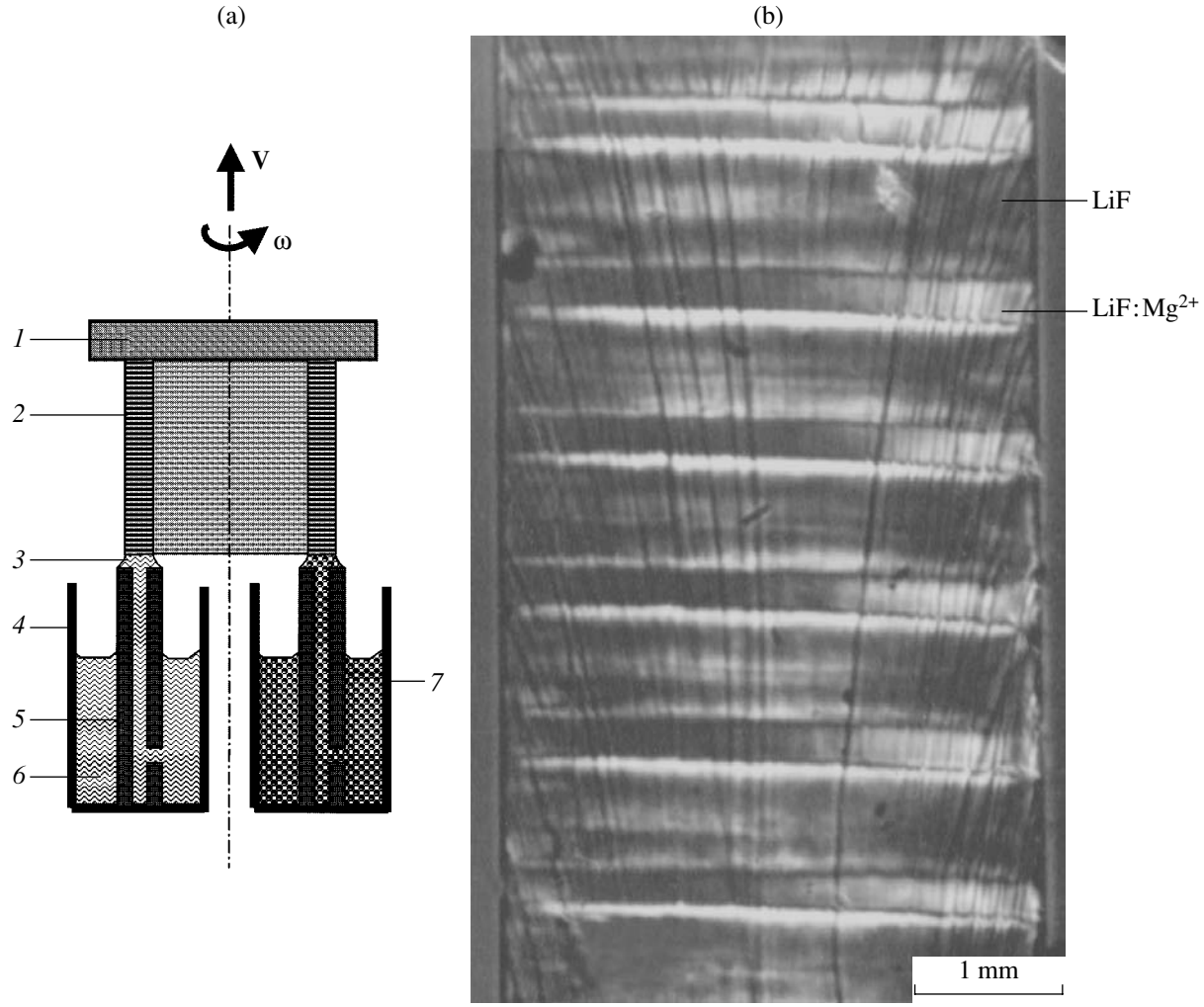

Fig. 8. Manufacturing of periodic structures by the GES technique: (a) layout of the growth setup ((*1*) seed; (*2*) crystal with the periodic structure; (*3*) melt meniscus; (*4*) crucible; (*5*) shaper; (*6*) undoped melt; (*7*) doped melt); (b) LiF–LiF:Mg^{2+} crystal with the periodic structure (the photo is taken in polarized light).

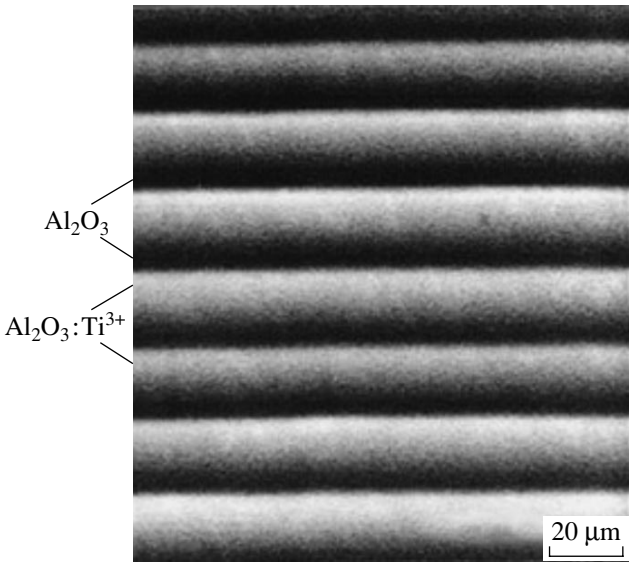

Fig. 9. Periodic Al_2O_3–Al_2O_3:Ti^{3+} structure produced by the GES technique.

sample surface and in the bulk. The layered transparent crystals are highly anisotropic in two mutually perpendicular directions; therefore, one should expect they be applied in the generation of modulated signals for beam transmission.

Further studies in the field of producing shaped crystals with periodic spatial structures were performed using the Al_2O_3:Ti^{3+} system [30, 31]. These crystals contain spatial resonant structures, i.e., periodic structures of variable chemical composition. This causes a drastic lowering of the generation thresholds and makes them nearly independent of the parameters of the external resonator. Al_2O_3–Al_2O_3:Ti^{3+} structures with a period of 5–100 μm were produced (Fig. 9). The Ti^{3+} content in the structures produced in such a way differed by 2–3 orders of magnitude, ranging from 10^{-4} wt % in the undoped part of the crystal to 0.2 wt % in its doped part. The width of the transient region has a value of the order of several tenth parts of *l*, where *l* is the increase in the crystal length during its 360° rotation.

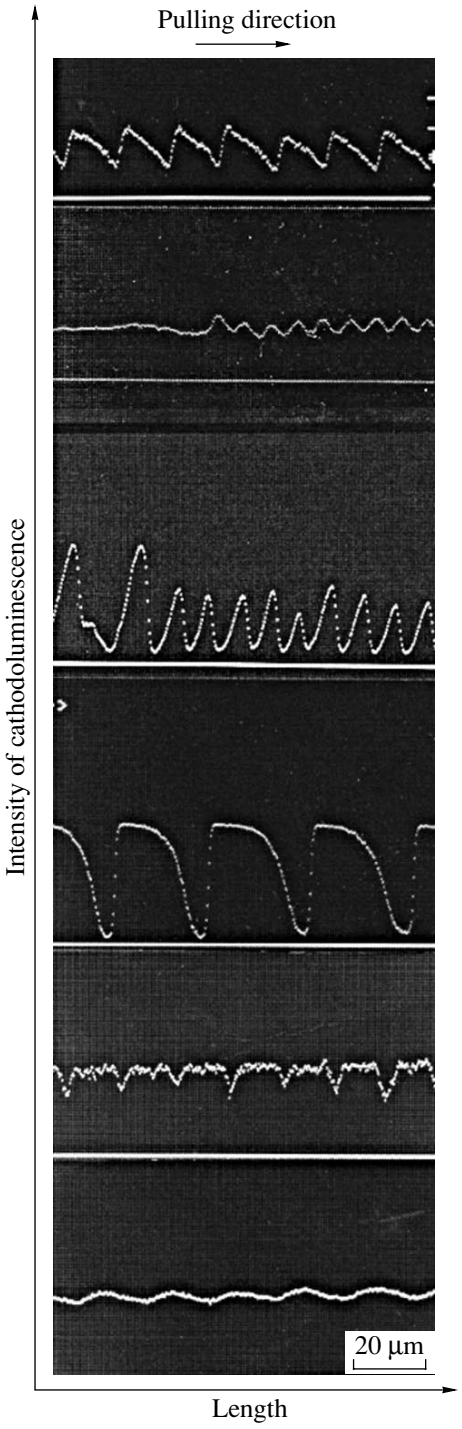

Fig. 10. The intensity distribution for the cathodoluminescence corresponding to the content of the luminescent impurity for different kinds of Al_2O_3–Al_2O_3:Ti^{3+} structures produced by the GES technique.

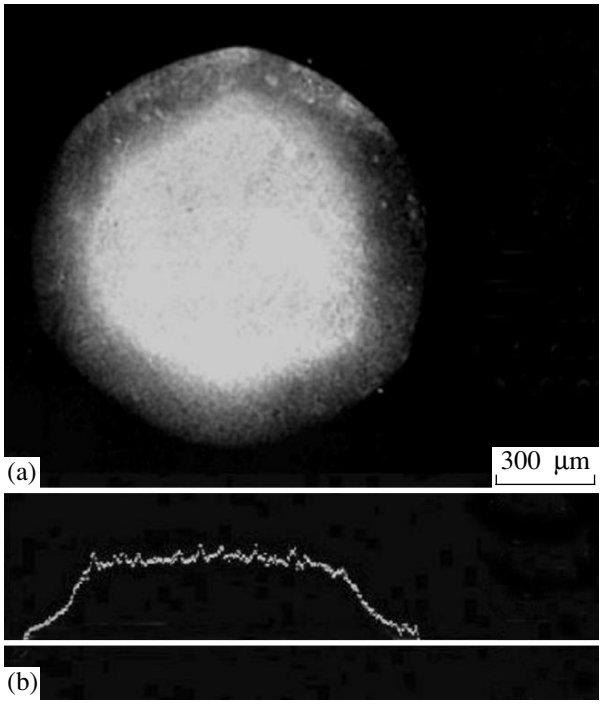

Fig. 11. (a) The cross section of an Al_2O_3–Al_2O_3:Ti^{3+} filament grown with the use of the weight control system and (b) the corresponding intensity distribution for the cathodoluminescence.

The implementation of the GES technique provides an opportunity to substantially broaden the range of the various periodic spatial structures produced *in situ*. The following structures were produced: with a crossover from one period to another owing to the variation in the relationship between the pulling rate and the frequency of rotation; with a crossover from periodic structures to homogeneously doped or undoped regions owing to the "switching off" of the melt feed to one of the shapers during the growth process; with a specified ratio of layer heights within one period; etc. In Fig. 10, we show the intensity distribution for the cathodoluminescence corresponding to the content of the luminescent impurity for different kinds of structures produced by the GES technique. The developed techniques allow us also to control the characteristic features of the frequency distribution in the crossover region.

Filaments with a central doped region. The high-quality single-crystalline filaments with the central part doped by activating ions are of special interest. In such crystals, the energy of optical pumping is absorbed only within the central region. This results in enhancement of the transformation efficiency and in a decrease in thermal losses.

For the growth of sapphire filaments of variable composition, a crucible with two vessels (for the doped and undoped melt) was used. In addition, a special shaper was developed, which provided an opportunity to feed the meniscus using these two melts simultaneously [32]. The main task in this growth scheme is to feed the meniscus by melts with varying composition at fixed flow rates and to maintain the spatial distribution of concentration dictated by this method. The main problems involved, which were solved in producing

these filaments, were optimization of the growth parameters and maintaining the temperature within a narrow range, first, to prevent the mixing of melts in the meniscus and, second, to eliminate the formation of defects related to the supercooling of the crystallization front. In Fig. 11, we show the cross section of the Al_2O_3–Al_2O_3:Ti^{3+} filament and the corresponding intensity distribution for the cathodoluminescence.

CONCLUSIONS

The ideas of Stepanov are being intensively developed. New versions of his method are being suggested, and the range of materials used is growing. Intensive research is being carried out in the following directions: improvement of the structure and quality of grown crystals, cost saving, growth of large shaped crystals and crystals with a complicated shape, and production of crystals with a specified doping structure. Shaped crystals are widely used as constructional, optical, and functional materials in science, technology, medicine, microelectronics, and laser technology.

ACKNOWLEDGMENTS

We are grateful to S.I. Baholdin for his help in the preparation of the manuscript for publication.

REFERENCES

1. A. V. Stepanov, *The Future of Metal Processing* (Lenizdat, Leningrad, 1963).
2. P. I. Antonov, L. M. Zatulovskiĭ, A. S. Kostygov, *et al.*, *Production of Profiled Single Crystals and Production by Stepanov Method* (Nauka, Leningrad, 1981).
3. P. Rudolph, *Profilzuchtung von Einkristalle* (Akademie Verlag, Berlin, 1982).
4. V. A. Tatarchenko, *Shaped Crystal Growth* (Kluwer, Dordrecht, 1993).
5. P. I. Antonov, S. I. Bakholdin, and S. P. Nikanorov, Prog. Cryst. Growth Charact. Mater. **16**, 19 (1988).
6. P. Rudolph and T. Fukuda, Cryst. Res. Technol. **34**, 3 (1999).
7. V. A. Tatarchenko, in *Encyclopedia of Materials: Science and Technology*, Ed. by K. H. J. Buschow *et al.* (Elsevier, Amsterdam, 2001), p. 3697.
8. V. N. Kurlov, in *Encyclopedia of Materials: Science and Technology*, Ed. by K. H. J. Buschow *et al*. (Elsevier, Amsterdam, 2001), p. 8259.
9. P. I. Antonov and V. N. Kurlov, Prog. Cryst. Growth Charact. Mater. (in press).
10. H. E. LaBelle and A. I. Mlavsky, Nature **216**, 574 (1967).
11. H. E. LaBelle and A. I. Mlavsky, Mater. Res. Bull. **6**, 571 (1971).
12. H. E. LaBelle, Mater. Res. Bull. **6**, 581 (1971).
13. N. N. Sheftal, Mater. Res. Bull. **7**, 345 (1972).
14. D. Garcia, M. Ouellette, B. Mackintosh, and J. P. Kalejs, J. Cryst. Growth **225**, 566 (2001).
15. P. H. Tibbets, Saphikon Insights **2**, 1 (2001).
16. V. N. Kurlov and S. N. Rossolenko, J. Cryst. Growth **173**, 417 (1997).
17. V. N. Kurlov and B. M. Epelbaum, J. Cryst. Growth **187**, 107 (1998).
18. V. N. Kurlov and S. N. Rossolenko, Izv. Akad. Nauk, Ser. Fiz. **63**, 1711 (1999).
19. A. I. Mlavsky and N. Pandiscio, US Patent No. 3868228 (1975).
20. H. E. LaBelle, US Patent No. 3 915 662 (1975).
21. D. Ya. Kravetskiĭ, L. P. Egorov, L. M. Zatulovskiĭ, *et al.*, Izv. Akad. Nauk SSSR, Ser. Fiz. **44**, 378 (1980).
22. V. A. Borodin, V. V. Sidorov, T. A. Steriopolo, and V. A. Tatarchenko, J. Cryst. Growth **82**, 89 (1987).
23. V. N. Kurlov, J. Cryst. Growth **179**, 168 (1977).
24. V. N. Kurlov and B. M. Epelbaum, J. Cryst. Growth **179**, 175 (1997).
25. P. I. Antonov, Yu. G. Nosov, and S. P. Nikanorov, Izv. Akad. Nauk SSSR, Ser. Fiz. **49**, 2295 (1985).
26. V. A. Borodin, V. V. Sidorov, T. A. Steriopolo, *et al.*, Izv. Akad. Nauk SSSR, Ser. Fiz. **52**, 2009 (1988).
27. F. Theodore, T. Duffar, J. L. Santailler, *et al.*, J. Cryst. Growth **204**, 317 (1999).
28. V. N. Kurlov and F. Theodore, Cryst. Res. Technol. **34**, 293 (1999).
29. V. M. Krymov, V. N. Kurlov, P. I. Antonov, *et al.*, Izv. Akad. Nauk, Ser. Fiz. **63**, 1745 (1999).
30. V. N. Kurlov and S. V. Belenko, Adv. Mater. **7**, 539 (1998).
31. V. N. Kurlov and S. V. Belenko, J. Cryst. Growth **191**, 779 (1998).
32. V. N. Kurlov, S. N. Rossolenko, and S. V. Belenko, J. Cryst. Growth **191**, 520 (1998).

Translated by K. Kugel

Crystallography Reports, Vol. 47, Suppl. 1, 2002, pp. S53–S62.

MELT GROWTH

Growth of Oxide Fibers by the Internal Crystallization Method

V. N. Kurlov, S. T. Mileĭko, A. A. Kolchin, M. Yu. Starostin, and V. M. Kiĭko

Institute of Solid State Physics, Russian Academy of Sciences, Chernogolovka, Moscow oblast, 142432 Russia

e-mail: kurlov@issp.ac.ru

Received October 2, 2002

Abstract—A new approach is developed for growing relatively inexpensive single-crystal and eutectic oxide fibers suitable for the fabrication of high-temperature composite materials. Sapphire (Al_2O_3), YAG ($Y_3Al_5O_{12}$), mullite ($3Al_2O_3 \cdot 2SiO_2$), YAP ($YAlO_3$), and eutectic (Al_2O_3–$Y_3Al_5O_{12}$, Al_2O_3–$ZrO_2(Y_2O_3)$, and Al_2O_3–Gd_2O_3) fibers are produced by the internal crystallization method, and their mechanical strength and microstructures are studied. © *2002 MAIK "Nauka/Interperiodica".*

INTRODUCTION

The development of high-temperature materials retaining good mechanical properties above 1100°C is vital for improving the performance of heat engines, in particular, gas turbines (raising their efficiency, reducing exhaust emission, etc.). It is becoming increasingly evident that this problem can only be solved by devising advanced fiber-reinforced metal-, intermetallic-, and ceramic-matrix composites. For this purpose, structurally reliable fibers with a high creep resistance at working temperatures are required. The available reinforcing fibers for high-temperature applications, based mainly on oxides and silicon carbide, are not structurally stable above 1200°C [1]. For this reason, efforts are focused on melt-grown single-crystal and eutectic oxide fibers.

Figure 1 schematically illustrates the main methods for the melt growth of single-crystal fibers. Edge-defined film-fed growth (EFG) [2] is a modification of the Stepanov technique [3], as is micro pulling down (μ-PD) [4]. Wide use is also made of laser heating for crucibleless crystal growth: the laser-heated floating zone (LHFZ) technique [5] and laser-heated pedestal growth (LHPG) [6].

The oxide fibers grown from melt by the above techniques find application for the most part in optics but are too costly to be used in composites. It is the lack of inexpensive oxide fibers that impedes the development of oxide-fiber-reinforced metal- and ceramic-matrix composites. Therefore, one of the challenges in this area is to devise new fabrication techniques that would notably reduce the cost of fibers.

The internal crystallization method (ICM) is a new approach to producing single-crystal and eutectic oxide fibers. A key feature of this method is directional melt solidification in capillary channels made in a metallic block. The method was first employed to produce molybdenum-matrix composites [7, 8]. Later, efforts were focused on the growth and subsequent extraction of fibers from the matrix.

This paper outlines the use of the ICM for producing relatively cheap oxide fibers. Data are presented on the microstructure and mechanical strength of various ICM fibers.

GROWTH AND MICROSTRUCTURE OF ICM FIBERS

Continuous cylindrical channels in an accessory (molybdenum) matrix can be formed in a number of ways. At present, use is commonly made of diffusion bonding under special conditions to give an assembly of alternating foils and wires. The growth process, schematized in Fig. 1d, yields fibers of cross-sectional size *t*. Diffusion bonding conditions depend on the matrix material and geometry. To grow oxide fibers, molybdenum assemblies with a wire diameter of d = 0.05–0.2 mm are commonly used.

Infiltration and fiber growth are carried out in induction-heated units (Kristall-603 and RUMO-1S) in an argon atmosphere at a pressure of 1.1–1.3 atm or in a resistance-heated vacuum unit (ChIR). The induction-heated units are equipped with graphite susceptors and molybdenum crucibles; the largest possible assembly length is 100 mm. In the ChIR unit, fitted with a tungsten resistance heater, the assembly length can be up to 250 mm. The high-temperature zones of these units enable growth of up to 150 g of fibers per run.

Sapphire (Al_2O_3) fibers possess a unique combination of physical properties for use in composites: a melting point as high as 2053°C, good resistance to aggressive attack, and high strength at temperatures above 1000°C.

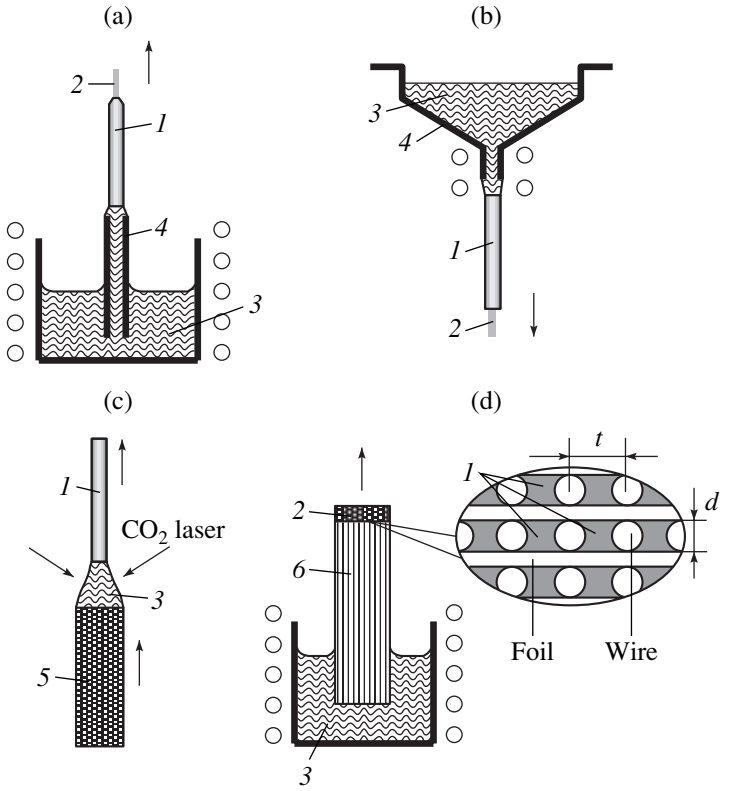

Fig. 1. Main methods for melt growth of fibers: (a) edge-defined film-fed growth (Stepanov technique), (b) micro-pulling-down, (c) laser-heated pedestal growth, (d) internal crystallization method; (*1*) crystal, (*2*) seed, (*3*) melt, (*4*) die, (*5*) polycrystalline rod, (*6*) oxide–molybdenum composite.

It was shown in the very first studies dealing with the ICM [7, 8] that Al_2O_3 crystallization in channels of a molybdenum matrix yields, under certain conditions, single-crystal sapphire fibers. However, their crystallographic orientation may vary even within the same sample. Composites reinforced with such fibers have a low creep resistance above 1000°C since a fraction of the fibers ("ill-oriented" ones) may experience creep. This gives rise to stress redistribution, raising the stress in "well-oriented" fibers, which begin to fracture at relatively low loads. Consequently, sapphire fibers in high-temperature composites must be uniform in crystallographic orientation, preferably with their *c* axis parallel to the fiber axis.

To achieve uniform orientation of ICM fibers, use can be made of oriented seeds [9]. The main steps of the top-seeded growth process are schematized in Fig. 2a. Initially, a molybdenum assembly with empty channels is placed above the melt contained in a crucible and a seed cut from a pregrown sapphire ribbon is mounted on top of the assembly. The crucible is heated to the temperature, determined experimentally, at which the underside of the sapphire seed begins to melt, and the seed subsides. The crucible is then raised to bring the melt into contact with the assembly, and the melt ascends the channels under the action of capillary forces.

The next step is directional solidification of the melt in the channels, which takes place as the assembly and seed are elevated to the low-temperature zone at a pulling rate of 1 to 30 mm/min. Fiber growth begins at the seed, and the growth front moves down the channels. The assembly is pulled until uniformly oriented sapphire fibers are grown throughout the channels (the assembly is above the molybdenum ring). Next, the temperature is lowered at 30°C/min. Figure 3 shows a set of assemblies (with platelike seeds on top) after fiber growth, and Fig. 4 shows sapphire fibers after dissolving away the molybdenum matrix in a mixture of HCl, HNO_3, and H_2O.

Examination by optical microscopy reveals two salient features of the fiber microstructure. First, the flat fiber surface is a negative replica of the surface of the molybdenum foil. Since Mo recrystallizes during fiber growth, its surface contains ~1-μm-high steps along grain boundaries (Fig. 5). Second, the fibers contain linear arrays of pores just below the surface.

Polarized-light images demonstrate that the ICM-grown sapphire fibers are single-crystal throughout their length, independent of the solidification rate. As the rotation angle of a flat bundle of fibers relative to crossed nicols changes from 0° to 45°, complete extinction is observed [9]. The orientation of the grown fibers coincides with that of the seed.

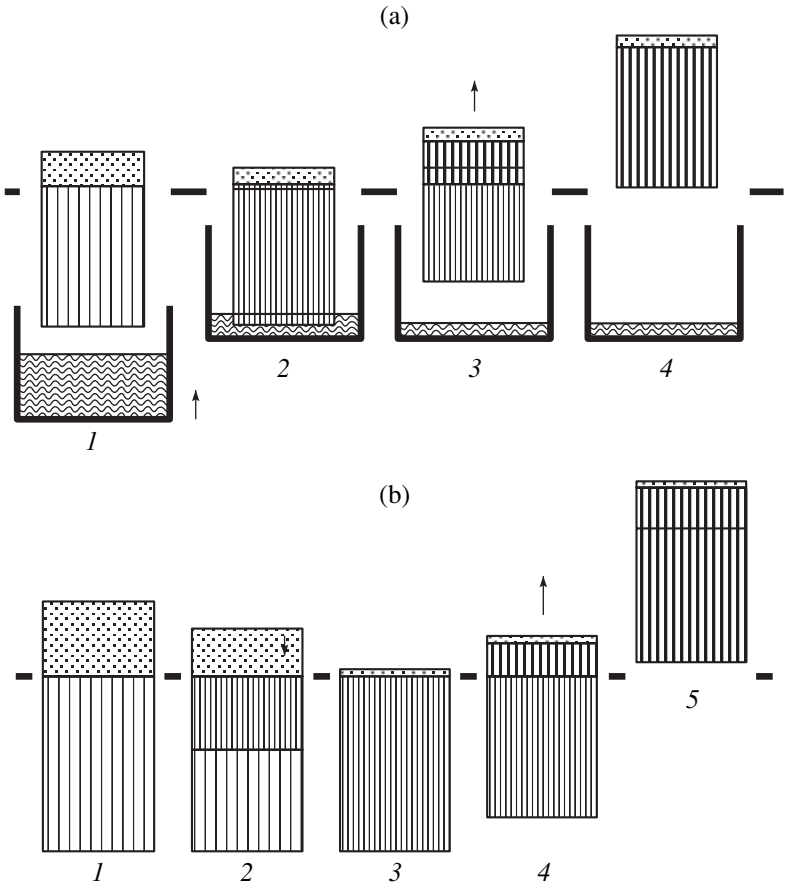

Fig. 2. Sequence of steps (*1–5*) in seeded fiber growth: (a) melt supply from a crucible, (b) crucibleless process. The schematics show the seed (▨), empty capillary channels (▯), melt-filled channels (▮), channels containing grown fibers (▮), and melt (▨).

Yttrium aluminum garnet (YAG), $Y_3Al_5O_{12}$, fibers were grown by the infiltration–solidification process described above with application to sapphire fibers (Fig. 2a) and also by a crucibleless process (Fig. 2b). In the latter case, during partial melting of a YAG crystal mounted on top of the molybdenum assembly, the melt fills the channels from the top down. The remainder of the crystal serves as a seed during subsequent melt solidification to yield uniformly oriented single-crystal YAG fibers (Fig. 6), as in the case of melt supply from a crucible.

Typical of the ICM, the surface of YAG fibers is a negative replica of the Mo foil surface. Phase analysis of powder samples indicates that the predominant phase in the fibers is YAG. Rarely do the fibers contain trace levels of Al_2O_3 and $YAlO_3$, which may result from melt overheating.

Eutectics crystallize from the melt without seeding. The creep resistance of eutectic fibers is independent of the crystallographic orientation of the constituent phases and seems to be determined by the deceleration of dislocations at interfaces. Eutectic fibers are fabricated by a process similar to the one schematized in Fig. 2a, but without seeding. In this way, Al_2O_3–$Y_3Al_5O_{12}$, Al_2O_3–$ZrO_2(Y_2O_3)$, Al_2O_3–$AlGdO_3$, and other eutectic fibers were produced. The surface morphology of eutectic fibers is characteristic of the ICM. Figure 7 shows the cross-sectional image of an Al_2O_3–$Y_3Al_5O_{12}$ fiber, which has a Chinese script eutectic microstructure with a characteristic cross-sectional colony size of 2–4 μm. At the curved fiber surfaces, the eutectic microstructure may be rougher (7–10 μm), pointing to a reduced solidification rate in those regions owing to the influence of the molybdenum wire.

Mullite ($3Al_2O_3 \cdot 2SiO_2$) in the form of single-crystal fibers can also be prepared by the ICM [10]. Given that mullite melts incongruently, such fibers can hardly be produced by other melt growth processes. Single-crystal mullite fibers exhibit the best creep behavior above 1400°C. The preparation of such fibers opens up a possibility of raising the working temperature of composites by replacing nickel alloys with higher temperature matrices, probably intermetallics or oxides.

Polarized-light images demonstrate that ICM-grown mullite fibers are single-crystal throughout their length (Fig. 8), although some of them are cut across by Al_2O_3 grains. The influence of these flaws on the strength of the fibers seems, however, to be significant

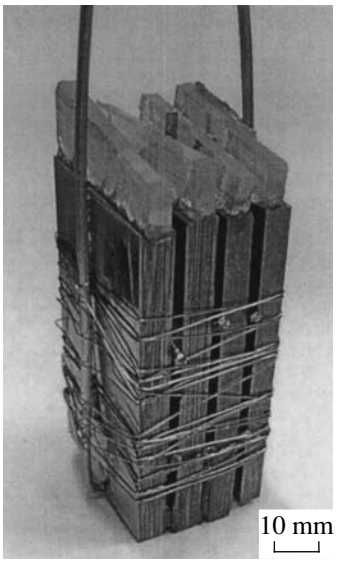

Fig. 3. Molybdenum assemblies and seeds after fiber growth in the channels.

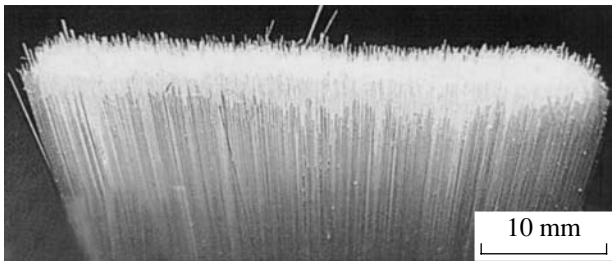

Fig. 4. A bundle of uniformly oriented ICM-grown sapphire fibers after dissolving away the molybdenum matrix.

only on a fairly large length scale, which is of little importance to the mechanical properties of the composite, provided it has been adequately designed.

STRENGTH OF FIBERS

Determination of Strength Characteristics

The cross-sectional shape of ICM fibers hampers the use of conventional testing techniques. In view of this, a special procedure was devised to assess the room-temperature strength of fibers [11]. A fiber with a cross section similar to the one shown in Fig. 1d, of thickness d, is bent around a rigid cylinder with a relatively large radius R, and the number of breaks is counted. If the number of breaks is sufficiently small, i.e., the average separation between neighboring breaks exceeds d (Fig. 1d) by more than a factor of 10 (end effects can be neglected), the fiber is then bent around a smaller radius cylinder. The procedure is repeated until the average separation between breaks is approximately $10d$. Typically, five to seven fibers chosen at random are tested.

The highest stress in a fiber bent around a rigid cylinder is given by

$$\sigma = E\frac{d}{2R}, \quad (1)$$

where E is Young's modulus of the fiber material. It can be taken as a first approximation that σ is the bending strength of the fiber measured over a gauge length equal to the average separation between fiber breaks. Clearly, this will lead, in subsequent calculations, to a fiber strength somewhat higher than the actual value. However, by reducing the cylinder radius in small steps, the error can be made sufficiently small.

To determine the Weibull parameters describing the tensile strength σ of fibers, use is made of experimental data obtained as described above. The distribution function is used in the form

$$P(\sigma, g) = 1 - \exp\left(-\frac{g}{g_0}\left(\frac{\sigma}{\sigma_0}\right)^{\beta}\right), \quad (2)$$

where g is a geometric parameter equal to the fiber

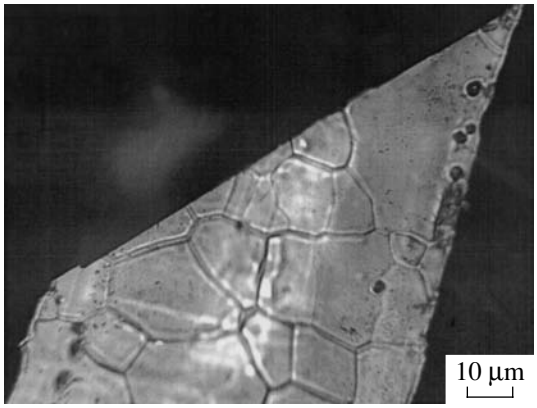

Fig. 5. ICM-grown sapphire fiber reproducing the surface contour of the molybdenum foil and containing pores in the surface region.

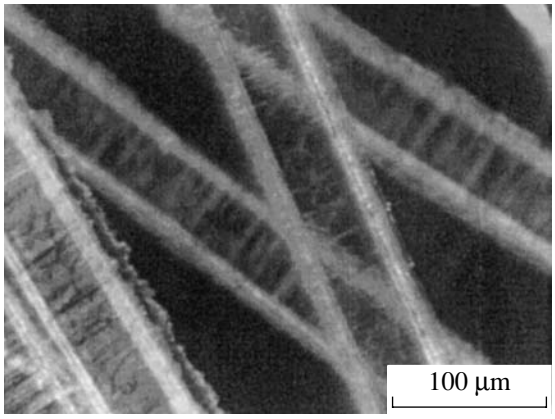

Fig. 6. Single-crystal YAG fibers.

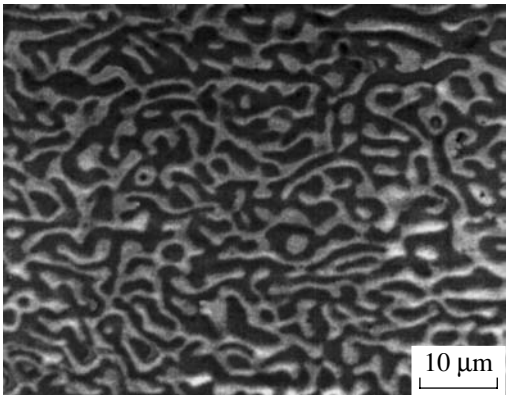

Fig. 7. Cross-sectional microstructure of an Al_2O_3–$Y_3Al_5O_{12}$ eutectic fiber.

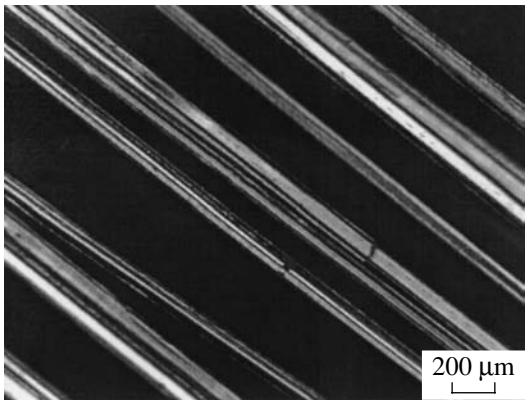

Fig. 8. Polarized-light image of mullite fibers.

length l, surface area S, or volume V, depending on the particular distribution of characteristic defects in the fiber; g_0 is the corresponding constant (l_0, S_0, and V_0 are constants having the dimensions of length, area, and volume, respectively); and σ_0 and β are the other two Weibull parameters. Clearly, one of the three parameters can be chosen arbitrarily. The average strength of a fiber with a geometric parameter g can be obtained from Eq. (2) in the form

$$\langle \sigma(g) \rangle = \int_0^\infty \sigma dP(\sigma) = \sigma_0 \left(\frac{g}{g_0}\right)^\beta \Gamma\left(1 + \frac{1}{\beta}\right), \qquad (3)$$

where Γ is the gamma function.

As shown recently [11], the assumption that defects form linear arrays on the fiber surface is inconsistent with experimental data. At the same time, mechanical tests, taken alone, provide no sufficient evidence to conclude whether a surface or volume defect distribution is actually the case. Moreover, it cannot be ruled out that there are two or more distinct defect systems responsible for fiber failure.

Let l^0 be a characteristic fiber length. Then, for a group of fibers, g is equal either to $V_0 = l^0 A_{av}$ or to $S_0 = l^0 P_{av}$, where A_{av} and P_{av} are, respectively, the average cross-sectional area and average perimeter of the fibers. V_0 and S_0 appear in the scaling relations

$$\sigma^*(V) = \sigma^b_{0V}\left(\frac{V}{V_0}\right)^{-1/\beta}, \quad \sigma^*(S) = \sigma^b_{0S}\left(\frac{S}{S_0}\right)^{-1/\beta},$$

where the pairs of Weibull parameters [β, σ^b_{0V}] and [β, σ^b_{0S}] referring to bending can be determined from experimental data using Eq. (2).

The Weibull parameters for tensile strength can be determined in a similar way, by integrating Eq. (2) under the assumption that defects are present only in the surface layer or throughout the fibers [11]. This procedure yields the following expressions for the tensile strength σ^t in the cases of volume (0V) and surface (0S) distributions, respectively:

$$\sigma^t_{0V} = M_V(\beta)\sigma^b_{0V}, \quad \sigma^t_{0S} = m_S(\beta)\sigma^b_{0S}.$$

Here, $M_V = \left(\gamma - \frac{\pi}{4}\right)^{-1/\beta} \left[\int_0^1 \xi^\beta (\gamma - \sqrt{1-\xi^2}) d\xi\right]^{1/\beta}$ and $M_S = \left(\frac{(\beta+1)(\pi+2\gamma)}{2}\right)^{-1/\beta}$, where $\gamma = t/d$ (Fig. 1d).

The effective characteristics of high-temperature tensile strength were determined by testing oxide-fiber-reinforced molybdenum-matrix composites. The experimental procedure and results were described in detail in [12].

Measurement Results

Sapphire fibers. Figure 9 shows a log–log plot of bending strength σ^* versus average distance between fiber breaks. Such data are used to evaluate the characteristics of tensile strength as described above. The results for oxide fibers prepared at pulling rates of 1.3, 3.3, and 30 mm/min are summarized in Table 1. The pulling rate was found to have an insignificant effect on the strength of the fibers.

The experimental data in Fig. 9 and Table 1 demonstrate that an ~1-μm-thick metal, ceramic, or pyrolytic carbon coating notably raises the strength of the fibers. This finding suggests two important conclusions. First, it is clear that a substantial fraction of the characteristic defects, which determine the strength of the fibers, reside in the surface layer. Second, since the effect of the matrix would be expected to be similar to that of a coating, the composite strength cannot be assessed by measuring only the strength characteristics of individual fibers. The same refers to the strength characteristics determined by testing fibers removed from the matrix—the procedure sometimes used to analyze the effect of fiber–matrix interaction on fiber strength [13].

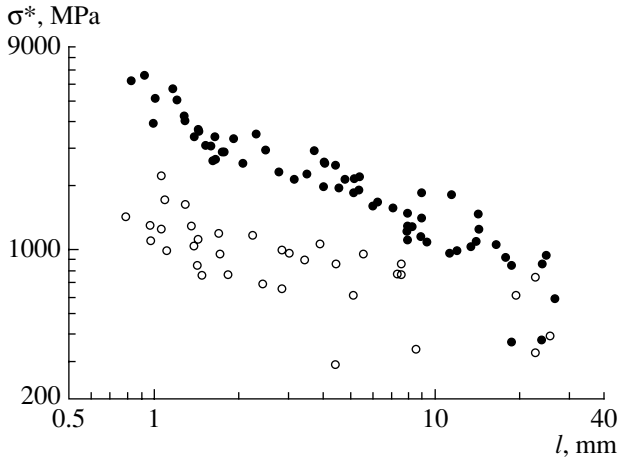

Fig. 9. Log–log plot of bending strength vs. fiber length for two groups of sapphire fibers (Table 1): no. 1 (uncoated, open circles) and no. 1SCO (coated with ~1-μm $SiC_{1-x}O_x$, filled circles).

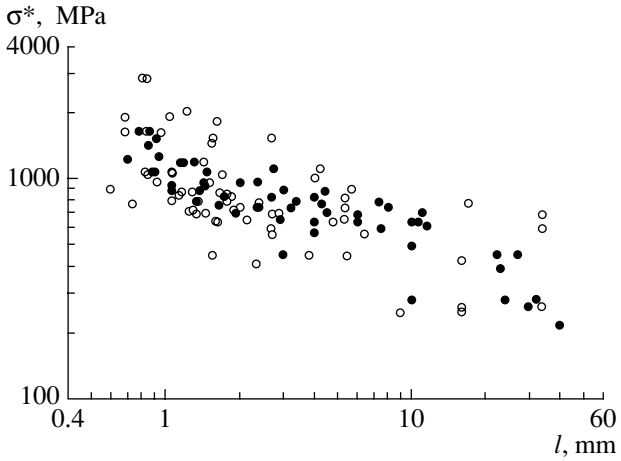

Fig. 10. Log–log plot of bending strength vs. fiber length for two groups of YAG fibers (Table 1): no. 4 (filled circles) and no. 5 (open circles).

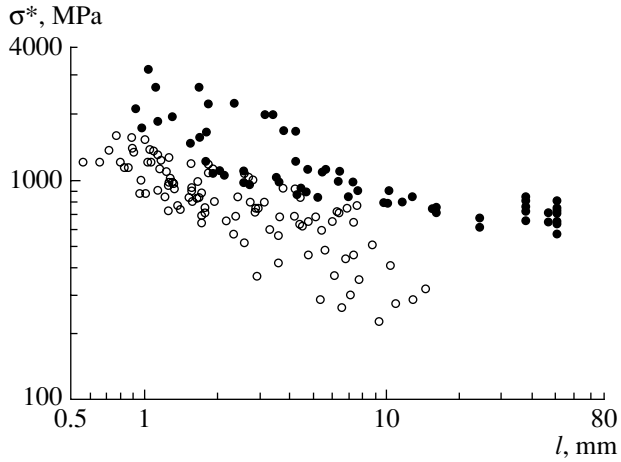

Fig. 11. Log–log plot of bending strength vs. fiber length for uncoated (open circles) and ~1-μm $SiC_{1-x}O_x$ coated (filled circles) sapphire–YAG fibers.

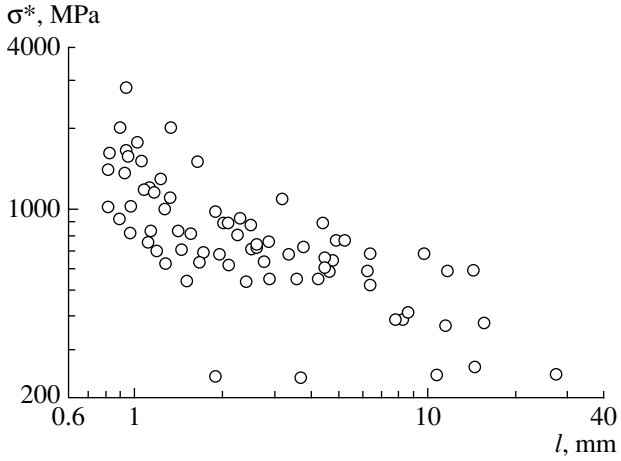

Fig. 12. Log–log plot of bending strength vs. average distance between fiber breaks for mullite fibers (Table 1, no. 6).

YAG fibers. The experimental data are displayed in Fig. 10. Table 1 lists the Weibull parameters for four groups of fibers. The strength characteristics are seen to be independent of the pulling rate and vary little.

YAG–sapphire eutectic fibers. A set of experimental data on the strength of such fibers is presented in Fig. 11. As in the case for sapphire fibers, coatings notably increase fiber strength. Typical Weibull parameters are listed in Table 1.

Single-crystal mullite fibers. The experimental data are shown in Fig. 12, and the Weibull parameters for the group of fibers tested are listed in Table 1.

Other fibers. We also determined the strength characteristics of some other fibers, in particular, Al_2O_3-based eutectic fibers. The experimental data and Weibull parameters for Al_2O_3–ZrO_2 and Al_2O_3–$GdAlO_3$ eutectic fibers are presented in Table 1. Note the rather high strength of Al_2O_3–ZrO_2 fibers.

SOME OBSERVATIONS ABOUT THE COST OF FIBERS

At this stage, the actual cost of fibers cannot be evaluated precisely. Some estimates are nevertheless possible. Under the assumption that the cost of crystals is dominated by the power consumption for crystal growth, the substantial difference in cost between large oxide crystals (hundreds of US dollars per kilogram) and sapphire fibers (tens of thousands of US dollars per kilogram) is determined by the productivity of the growth process and, hence, the associated power losses.[1] Since the ICM is comparable in productivity to the growth of bulk single crystals, the processes involved must be comparable in power consumption.

[1] In spite of its rather low efficiency in electric power–light–heat conversion, laser heating and local melting (LHPG method) is viewed as a viable approach to fiber fabrication, which lends support to the above assumption.

Table 1. Strength characteristics of oxide fibers; l^0 = 1 mm; E = 450 (fibers 1–3), 392 (4), 362 (5), 320 (6), and 300 GPa (7)

No.	Fiber material	β	σ^b_{0V}, MPa	σ^t_{0V}, MPa	V_0, mm^3	β	σ^b_{0S}, MPa	σ^t_{0S}, MPa	S_0, mm^3
		volume defects				surface defects			
1	Al_2O_3	3.07	1783	1457	0.00158	3.17	1133	536	1.782
1 SCO	Al_2O_3	3.25	2709	2221	0.00148	3.27	1262	607	5.242
2 Ni	Al_2O_3	2.81	1345	861	0.01336	2.85	843	296	2.669
2 NiO	Al_2O_3	1.82	1986	1162	0.01370	1.98	933	235	2.853
3	Al_2O_3	3.00	2146	1402	0.01718	3.00	1360	517	3.171
3 C	Al_2O_3	2.95	3273	2172	0.01199	2.96	1523	612	6.782
4	$Y_3Al_5O_{12}$	4.74	1013	728	0.0091	4.74	681	352	3.93
5	$Y_3Al_5O_{12}$	2.71	1225	796	0.0089	2.74	693	260	2.81
6	$3Al_2O_3 \cdot 2SiO_2$	3.42	1113	759.1	0.007766	3.44	783.7	346.1	1.861
7	Al_2O_3–ZrO_2	2.63	1674	1073	0.0101	2.63	788	280	4.434
8	Al_2O_3–$GdAlO_3$	3.52	567	393	0.0063	3.37	495	221	0.864

Note: SCO, C, Ni, and NiO designate ~1-μm-thick $SiC_{1-x}O_x$, pyrolytic carbon, Ni, and NiO coatings, respectively.

Table 2. Nickel-based matrix composites (*X* marks the fiber–matrix combinations studied)

Fiber⇒ Matrix⇓	Al_2O_3	$Y_3Al_2O_{12}$	$Al_2O_3/Y_3Al_5O_{12}$ eutectic	$Al_2O_3/ZrO_2(Y_2O_3)$ eutectic
VKNA-4U	*X*	*X*	*X*	*X*
ZhS-32	*X*	*X*	*X*	

The increase in the cost of fibers due to the use of molybdenum does not radically change the situation. Consequently, ICM fibers must be comparable in cost to bulk single crystals and can be used in various structural and, of course, high-temperature composites.

SOME APPLICATIONS OF OXIDE FIBERS

The range of potential applications of single-crystal oxide fibers, exhibiting various physical properties, is extremely broad. Here, we focus on the use of oxide fibers in structural composites. The corresponding fabrication processes were described in detail in a previous publication [14]. Microstructural analysis of the composites is beyond the scope of this article.

Application of Fibers in High-Temperature Nickel-Based Matrix Composites

Preliminary Remarks. Table 2 lists some of the composites studied, which were prepared by injection molding in the form of either cylindrical rods for bend tests or dumbbell-shaped specimens for tension tests. Note that almost all the composites were also tested by a pushout technique to evaluate the fiber–matrix bond strength.

To achieve high strength of ICM fibers in a composite, one must ensure a sufficiently high fiber–matrix bond strength for short fibers to be fully loaded [15]. Control over interfacial bonding in oxide-fiber-reinforced nickel-based matrix composites produced via liquid-phase processing is the most important technical problem in composite fabrication.

Creep tests and interpretation of results. Most mechanical tests on nickel-matrix composites were performed in the range 1100–1200°C because the creep resistance of composites in this range determines their potential for high-temperature applications. At these high temperatures, even short-term strength tests are, in essence, creep tests, even though they involve fairly high strain rates (high crosshead speeds in the testing machine). In view of this, in interpreting the results, we will not differentiate between "short-term" and "normal" creep tests at creep rates of, e.g., 10^{-4} to 10^{-2} h^{-1}. All tests were performed in vacuum. The load was measured by a dynamometer mounted in a glass bell jar. The crosshead speed was 2 mm/min. Vacuum testing allows one to exclude the effect of the ambient atmosphere on the creep behavior of composites. Clearly, real materials must be protected by coating to prevent oxidation of the matrix and produce a thermal barrier.

The results of creep tests in bending can be used to assess tensile creep characteristics expressed through the n and σ_n parameters in the power-law relation

$$\dot{\varepsilon} = \eta_n\left(\frac{\sigma}{\sigma_n}\right)^n, \quad (4)$$

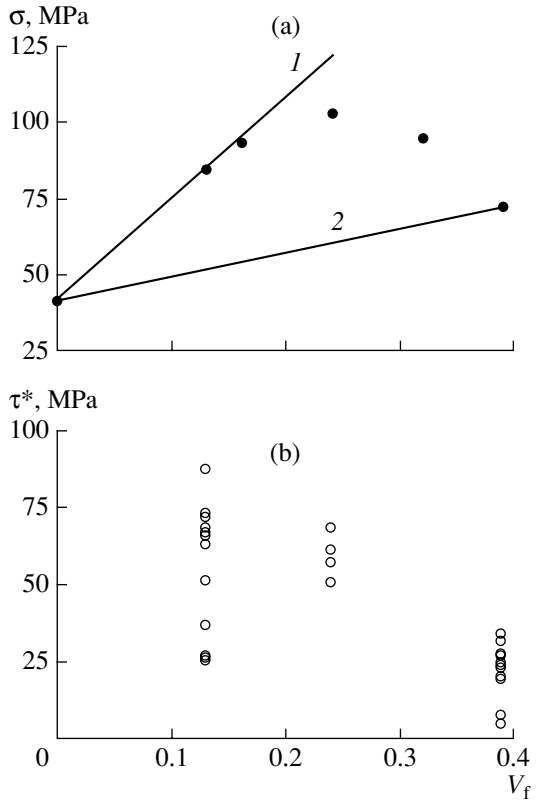

Fig. 13. Creep data for composites consisting of Al_2O_3–$Y_3Al_5O_{12}$ fibers and a ZhS-32 matrix. (a) 1150°C creep resistance vs. volume fraction of fibers. The solid lines show calculation results for a matrix with $\eta_m = 10^{-4}$ h^{-1}, $m = 2.8$, and $\sigma_m = 41.5$ MPa; (*1*) strong interfacial bonding and high fiber strength: $\alpha = 0.5$, $\beta = 3$, $\sigma_f^0 = 450$ MPa; (*2*) weak interfacial bonding and low fiber strength: $\alpha = 0.1$, $\beta = 3$, $\sigma_f^0 = 150$ MPa. Fiber geometry: $l_0 = 1$ mm, $d = 0.1$ mm. (b) Interfacial strength τ^* vs. volume fraction of fibers.

where $\dot{\varepsilon}$ is the steady-state creep rate of the composite and $\eta_n = 10^{-4}$ h^{-1} is a constant found by approximately solving the problem of bending creep in a rod and determining exponent n by stepwise loading of each specimen. The solution of the problem in question was reported previously [16].

To analyze testing results, we use a model describing creep in a composite consisting of brittle elastic fibers (Young's modulus E_f) and a viscous matrix [16]. The strength of the fibers can be described by Eq. (2) (Weibull statistics). The constitutive relation is taken to have a power-law form, like Eq. (6), with parameters m, σ_m, and $\eta_m = 10^{-4}$ h^{-1}. The fiber–matrix interface is an island-type boundary with a continuity coefficient α. At $\alpha = 0$, the interfacial shear strength is zero; at $\alpha = 1$, the interfacial shear strength is equal to that of the matrix (ideal interface). The steady-state creep rate $\dot{\varepsilon}$ of the composite and the applied stress σ are related by

$$\sigma = \lambda\sigma_m\left[\left(\frac{\sigma_0^{(f)}}{\lambda\sigma_m}\right)^{\beta}\left(\frac{l_0}{d}\right)\right]^{\frac{m+1}{n}}\left(\frac{\dot{\varepsilon}}{\eta_m}\right)^{\frac{1}{n}}V_f + \sigma_m\left(\frac{\dot{\varepsilon}}{\eta_m}\right)^{\frac{1}{m}}V_m, \quad (5)$$

where V_f and V_m are the volume fractions of the fibers and matrix, respectively; d is the characteristic cross-sectional size of the fibers; and λ is a known function, $\lambda(m, \alpha)$.

The results were described in full detail elsewhere [10, 14, 16]. Here, we consider the most important result: the dependence of the creep resistance (the stress which produces a creep strain of 1% over a period of 100 h) on the volume fraction of fibers and interfacial strength (Fig. 13). When the volume fraction of fibers in the composite attains about 25%, the interfacial strength drops sharply, presumably because the matrix becomes deficient in doping elements responsible for interfacial bonding. As a result, the dependence of the creep resistance on the volume fraction of fibers, essentially linear at low V_f, deviates from the one calculated in the above model.

To interpret such a dependence of the creep resistance on the volume fraction of fibers in the model in question, it is necessary to estimate α as a function of V_f from experimental data (Fig. 13b). For high volume fractions of fibers, we take $\alpha = 0.1$ and use the parameters of fiber strength similar to those obtained in an independent experiment. The corresponding calculated curve (Fig. 13a) passes through the data point for the highest V_f. The behavior of the composite at low V_f cannot be described by merely increasing α by about a factor of 5. Adequate results can only be obtained under the assumption that the effective strength of the fibers in the composite with a high interfacial strength exceeds the strength of free-standing fibers by about a factor of 3 (Fig. 14). This implies that, at a high fiber–matrix bond strength, the matrix material fills defects on the fiber surface, which have a strong effect on the strength of the fibers. The healing of defects is accompanied by an increase in the effective strength of the fibers in the composite. A similar effect is produced by coating the fibers, as illustrated in Fig. 9 and reported earlier for eutectic fibers [10].

This finding is of key importance not only in describing the properties of ICM fibers but also for the potential applications of these and other oxide fibers. Another important result is that high-temperature composites were obtained. The working temperature of the composites under consideration reaches about 1150°C [16], which is about 75°C higher than that of the best high-temperature alloys.

Application of Fibers in High-Temperature Titanium-Aluminide-Based Matrix Composites

The rather low cost of ICM fibers makes them candidate reinforcing agents for relatively low-temperature

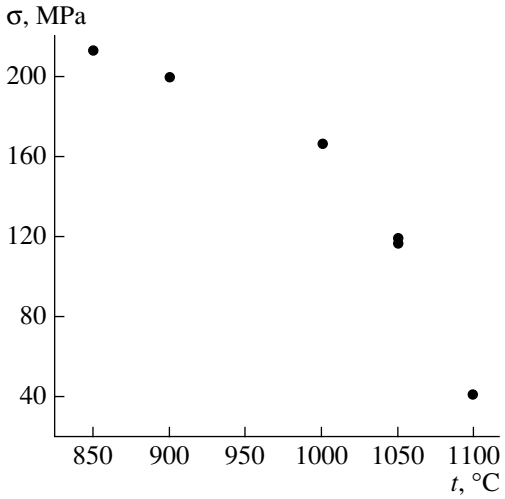

Fig. 14. Creep resistance (100 h) as a function of testing temperature for sapphire-fiber-reinforced TiAl-matrix composites.

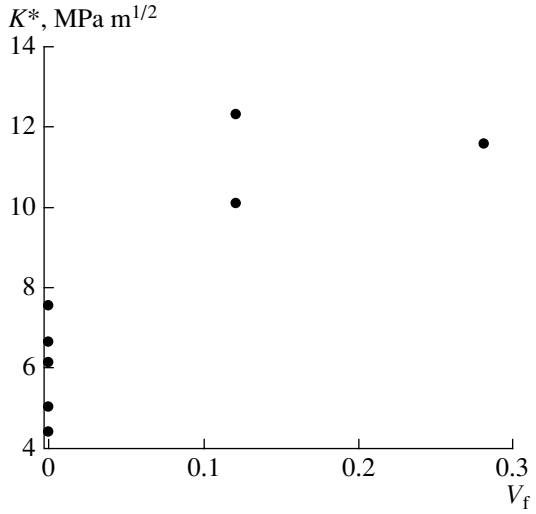

Fig. 15. Critical stress intensity factor vs. volume fraction of fibers for sapphire-fiber-reinforced polycrystalline corundum matrix composites.

matrices, e.g., those based on titanium aluminides. Preliminary experimental results (Fig. 14) [17] demonstrate that such composites, having a density as low as ~4.5 g/cm^3, retain an acceptable creep resistance up to ~1050°C, the working temperature of state-of-the-art high-temperature alloys.

Application of Fibers in Oxide–Oxide Composites

Fracture toughness, a key characteristic of ceramic–ceramic composites, is rather sensitive to the characteristics of the constituent materials and interfacial bonding (it should not be very high) [15]. To assess the serviceability of ICM-fiber-reinforced ceramic (polycrystalline oxide) matrix composites, we carried out model experiments on sapphire–corundum composites containing interfacial pyrolytic carbon layers [18]. The results, displayed in Fig. 15 as fracture toughness versus V_f data, appear encouraging, which is of practical importance because, as pointed out above, ICM fibers exhibit the best creep characteristics at temperatures above 1400°C.

CONCLUSIONS

A new approach was developed for producing single-crystal and eutectic oxide fibers cheap enough to be utilized in the fabrication of composite materials for use at temperatures as high as 1200–1300 (metallic and intermetallic matrices) and 1500–1700°C (ceramic matrices).

Sapphire (Al_2O_3), YAG ($Y_3Al_5O_{12}$), mullite ($3Al_2O_3 \cdot 2SiO_2$), YAP ($YAlO_3$), and eutectic (Al_2O_3–$Y_3Al_5O_{12}$, Al_2O_3–$ZrO_2(Y_2O_3)$, and Al_2O_3–Gd_2O_3) fibers were produced by the internal crystallization method, and their strength and microstructures were studied.

It is shown that, by using such fibers in metal-matrix composites, the working temperature of the composites can be raised by at least 75°C. The fibers can also be used in ceramic-matrix composites.

Clearly, ICM-grown oxide fibers, exhibiting a variety of physical properties, can be used to fabricate composites combining high strength with advantageous piezoelectric, optical, and other properties.

ACKNOWLEDGMENTS

The research described in this review article was supported by the International Science and Technology Center (project no. 507-97) and the Russian Foundation for Basic Research (grant nos. 99-01-01160, 00-02-16531, and 01-03-33193).

REFERENCES

1. F. Deleglise, M. H. Berger, and A. R. Bunsell, in *Proceedings of European Conference on Composite Materials* (Woodhead Publ., Cambridge, 1998), Vol. 4, p. 175.
2. H. E. LaBelle and A. I. Mlavsky, Nature **216**, 574 (1967).
3. A. V. Stepanov, *The Future of Metalworking* (Lenizdat, Leningrad, 1963).
4. D. H. Yoon, M. Hashimoto, and T. Fukuda, Jpn. J. Appl. Phys. **33**, 3510 (1994).
5. J. S. Haggerty and W. P. Menashi, Final Report Contract No. NAS 3-13479 (NASA, February, 1971).
6. R. S. Feigelson, J. Cryst. Growth **79**, 669 (1986).
7. S. K. Mileĭko and V. I. Kaz'min, Mekh. Kompoz. Mater., No. 5, 898 (1991).
8. S. T. Mileiko and V. I. Kazmin, J. Mater. Sci. **27**, 2165 (1992).

9. V. N. Kurlov, V. M. Kiiko, A. A. Kolchin, and S. T. Mileiko, J. Cryst. Growth **204**, 499 (1999).
10. S. T. Mileiko, V. M. Kiiko, M. Yu. Starostin, *et al.*, Scr. Mater. **44**, 249 (2001).
11. V. M. Kiiko and S. T. Mileiko, Compos. Sci. Technol. **59**, 1977 (1999).
12. S. T. Mileiko, V. M. Kiiko, N. S. Sarkissyan, *et al.*, Compos. Sci. Technol. **59**, 1763 (1999).
13. R. Asthana, S. N. Tewari, and S. L. Draper, Metall. Mater. Trans. A **29**, 1527 (1998).
14. S. T. Mileiko, V. M. Kiiko, A. A. Kolchin, *et al.*, Compos. Sci. Technol. **62**, 167 (2002).
15. S. T. Mileiko, *Metal and Ceramic Based Composites* (Elsevier, Amsterdam, 1997).
16. S. T. Mileiko, Compos. Sci. Technol. **62**, 195 (2002).
17. S. T. Mileiko, K. B. Povarova, A. V. Serebryakov, *et al.*, Scr. Mater. **44**, 2463 (2001).
18. A. A. Kolchin, V. M. Kiiko, N. S. Sarkissyan, and S. T. Mileiko, Compos. Sci. Technol. **61**, 1079 (2001).

Translated by O. Tsarev

Crystallography Reports, Vol. 47, Suppl. 1, 2002, pp. S63–S75.

MELT GROWTH

Chemical Aspects of Crystal Growth of Multicomponent Fluoride Materials from the Melt[1]

B. P. Sobolev

Institute of Crystallography, RAS, Moscow

e-mail: sobolevb@crossovers.com

Received August, 2002

Abstract—Chemical aspects of crystal growth of fluoride materials from the melt are considered. The high aptitude of fluorides to pyrohydrolysis (reaction with water vapour at high temperatures) to a large extent accounts for the specific chemical features of the conditions of preparing their single crystals. The processes of pyrohydrolysis in the well-known industrial techniques used to prepare crystals of alkaline-earth fluorides (MF_2) are reported. The review provides data on the stage mechanism of fluorite pyrohydrolysis, fluorite being the main fluoride optical material. The forms of external manifestation of pyrohydrolysis in crystals are considered. Classification of the techniques of fluoride purification from the oxygen impurity is given in reference to the extent of purification. The fluorinating atmospheres used in fluoride crystal growth are described. The review reports data on the interaction between gaseous fluorinating agents and fluoride melts with graphite, which is the main construction material used in crystal growth devices. *© 2002 MAIK "Nauka/Interperiodica".*

INTRODUCTION

The demand for crystals of optical fluoride materials emerged in the 1930s–1940s; these materials were fluorides of alkaline and alkaline earth elements. By the mid-1960s, single crystals of less than a dozen single-component fluorides had been produced. This assortment remained unchanged to the present; it is represented by crystals of LiF, CaF_2, BaF_2, MgF_2, LaF_3 and some other metal fluorides. The constant composition and, as a consequence, fixed set of properties of these compounds limit the practical application of simple fluorides.

The scope of engineering and technical tasks that require fluoride crystals is constantly widening. The properties of fluoride single crystals manufactured today often do not satisfy the requirements imposed by new technical tasks. A search for new fluoride materials is thus necessary.

Analysis of the available methods of preparing new single-crystalline simple fluorides indicates that in the future, the need for new fluoride materials will only be satisfied by making their chemical composition more complex. For this goal to be reached, a search for new phases formed in multicomponent systems must be undertaken [1–6].

Preparation of single crystals of simple, single-component (MF_m) and multicomponent fluoride materials is complicated due to one common property of their melts, high chemical activity. This is a typical feature of the techniques of synthesis and growth of fluoride crystals, which distinguishes them from other chemical classes of substances. The aggressive behavior of fluoride melts and vapours sets forth specific requirements for construction materials, such as heaters, crucibles, thermo-insulators, and other materials used in crystal growth devices. The intention to prepare fluoride crystals of high purity grade sometimes requires costly measures be taken. For example, some publications report on crystal growth devices whose heating elements can be made only of platinum.

Usually, the preparation of a substance in crystalline form from the melt, solution, or gaseous phase is recognized as a physical process. This approximation is true to the extent to which the definition of crystallization as a phase transition of a substance from one aggregate state to another holds. It is supposed that the chemical composition of the substance remains unchanged throughout the process.

However, changes in the aggregate state quite often give rise to chemical changes in the system upon an increase in temperature. In regard to the substance, these changes can be both "internal" (dissociation, incongruous evaporation, etc.) and "external." The latter are accounted for by chemical reactions of the melt with the environment.

Fluorides of many metals and of rare earth elements (REE–*R*) especially are compounds for which phase transitions upon heating (polymorphism and melting)

[1] This article was submitted by the author in English.

1063-7745/02/47S1-S0063$22.00 © 2002 MAIK "Nauka/Interperiodica"

are often accompanied by chemical processes which occur in real systems. These reactions cannot be neglected because in the case of inorganic fluorides, they directly and sometimes significantly affect the parameters of phase transitions.

Pyrohydrolysis of fluorides (reaction with H_2O vapors at high temperature) in the solid state upon heating does not only change its chemical composition but in some cases also changes the structure of the formed product. Pyrohydrolysis also occurs in melts that come in contact with the atmosphere for a long period of time during crystal growth.

This report supplies data on specific features in the chemical processes of growing fluoride crystals that have not been previously considered comprehensively. A significant part of the review is devoted to fluoride materials based on RE trifluorides. This is accounted for by the fact that RF_3 are highly apt to pyrohydrolysis; moreover, this reaction has been studied quite sufficiently.

The significant influence of pyrohydrolysis on the quality of fluoride single crystals has been well known for a long time. However, there are no available reviews on this topic and any researcher who starts working in this field is required to obtain information on pyrohydrolysis from scattered sources. Researchers in foreign countries cannot gain access to all the available information, because many of the basic investigations were published in Russian in scientific journals and publications of research institutions to which access is limited.

Alongside single crystals, in recent years, other forms have also become widely used: amorphous (fluoride glasses), ceramic (including optical ceramics), thin films, etc. All these technologies make use of heating or melting of fluorides. That is why the knowledge of and account of pyrohydrolysis processes is as important in these technologies as in crystal growth. Moreover, in the case of optical ceramics, pyrohydrolysis is the main factor, which accounts for the main quality of this material, namely, its optical transparency. In this review, it is impossible to consider the technologies of preparation of all of these promising forms of fluoride materials. We shall confine ourselves only to the preparation of single crystals from melts.

1. Pyrohydrolysis in the preparation technology of fluoride materials. Any researcher or technologist comes across the pyrohydrolysis of inorganic fluorides during their thermal treatment (sintering and melting). This fact should have resulted in a large body of relevant information on pyrohydrolisis being available in the literature; however, studies of the pyrohydrolysis of fluorides are scarce mostly due to the difficulties involved in oxygen detection.

Methods of suppressing pyrohydrolysis are similar in studies of the high-temperature chemistry of inorganic fluorides (thermal analysis of the systems) and in the course of preparation of single-crystalline fluorides from melts. The high quality of crystalline fluorides is directly connected with the advances made in the high-temperature chemistry of fluorides [5, 6]. In the aforementioned publications, the present author first attempted to report and generalize data on the chemical processes that accompany the growth of crystals of refractory and hydrolyzed fluorides.

1.1. Manifestations of partial pyrohydrolysis in single crystals. Results of partial fluoride pyrohydrolysis can be manifested in crystals in two forms.

The first one can be called "hidden," as it requires chemical detection of O_2; this consists in isomorphic incorporation of oxygen into the crystal, which remains single phase but transforms from fluoride into oxyfluoride. The sample does not scatter light; this is not, however, prove the absence of O_2. The properties of oxygen containing crystal differ from those of pure fluoride. The literature reports many examples for which the characteristics of partially hydrolyzed fluoride materials do not correspond to the characteristics of pure fluorides.

The second form of oxygen presence in crystals are particles of an oxygen-containing phase. This is evidence of deep pyrohydrolysis, when the solubility limit of metal oxide (or oxyfluoride) in the fluoride is surpassed. Since the main bulk of the crystalline rod that does not scatter light contains dissolved oxygen, the properties of the materials differ from the characteristics of pure fluoride. Externally, this is manifested in light scattering from particles of oxygen-containing phases. This technique has a principal restriction in that the minimum size of the detected particles depends on the wavelength of the light source. Distribution of oxygen between the solid solution and the independent phase is determined by specific metal oxide–metal fluoride (MO_m–RF_n) systems, which as a rule have not been studied.

The influence of oxygen impurity on the properties of fluoride materials has not been studied in detail. It can be both positive and negative. However, even in the rare case of positive changes in the characteristics of crystals, pyrohydrolysis remains an unwanted process, as it cannot be controlled and the properties of hydrolyzed materials cannot be reproduced.

Thus, light scattering can be considered an effective means of detecting oxygen only in the case of a very low solubility of oxygen-containing phases in the fluoride matrix. Fluorides of alkaline-earth metals, which do not scatter light, have low MO solubility in MF_2. The absence of light scattering is evidence of high MF_2 crystal purity from oxygen.

Light scattering in fluoride crystals can also be due to chlorine and sulfur compound impurities in amounts of several dozen ppm [7–9]. Due to the high volatility of sulfides and chlorides, these impurities can be removed during annealing of the starting reagent powders.

1.2. Principal sources of oxygen contamination of commercial fluorides. Of all industrially manufactured

metal fluorides, possible sources of oxygen contamination have been studied in detail only for RE trifluorides (RF_3). The commonly accepted idea that the source of oxygen in RF_3, prepared by "wet" methods, is hydrate water is disputable. In [10–14], it was shown that dehydration and pyrohydrolysis are two processes that are separated by a wide temperature range. According to [10], RF_3 are contaminated with oxygen due to impurities of $R(NO_3)_3$ or RCl_3, which are entrapped by gel-like precipitants. Upon thermal decomposition, they yield R_2O_3. Thus, uncareful washing of fluorides prepared by "wet" techniques results in uncontrolled RF_3 contamination with RE salts dissolved in water (chlorides, sulfates, nitrates). This source of oxygen in fluorides in "wet" methods cannot be controlled.

The above-mentioned explains why "wet" methods of many metal fluoride synthesis have been replaced in recent years either by water-free on combined methods. In the latter, the technological process ends with a "dry" stage, when additional purification from oxygen is used. This results in powder fluoride reagents that are quite pure of oxygen. However, such reagents are not always suitable for crystal growth in an inert atmosphere and the resulting samples contain light-scattering particles. Below, we shall consider methods of additional (deep) fluorination of the starting reagents during crystal growth.

One should be very careful in choosing MF_4 reagents for chemical (or any other) study. We can refer to [15], wherein five commercial products called "zirconium fluoride" were studied. Only one of them was actually monoclinic ZrF_4. The rest were partially hydrolyzed "ZrF_4" (stabilized by an O_2 tetragonal form), a hydrated amorphous mass, and even hydrate $ZrF_4 \times H_2O$. One can imagine how many "discoveries" have been or will be made by those researchers who do not control the quality of the starting reagents.

Water vapors, which are normally contained in the atmosphere or in inert gases, are a source of oxygen contamination of fluorides heated to high temperatures or when they are molten. Purifying the atmosphere of H_2O in special devices is a method of pyrohydrolysis suppression.

Fluoride powders actively absorb water from air. Suppression of the absorbing capacity is accomplished by melting powders of commercial fluorides in active (fluorinating) atmospheres. Storage and usage of thus prepared compact forms of RF_3 significantly reduce the contents of oxygen impurity in crystals prepared from these reagents.

In order to prepare crystal samples with low oxygen impurity content, it does not suffice to have starting reagents that are highly pure. Oxygen contamination occurs actively in the process of crystal growth.

Chemical features and temperature conditions for pyrohydrolysis are different for metal fluorides of the 2nd group and REE and other metal fluorides. Therefore, we will consider two groups of fluorides devoted to pyrohydrolysis during crystal growth: based on MF_2 and other MF_m (in particular, RF_3).

2. Pyrohydrolysis of MF_2 under conditions of crystal growth from the melt. Apparently, the first research into the interaction of the mineral CaF_2 with H_2O at high temperatures was performed in [16], wherein pyrohydrolysis was conducted up to CaO. The kinetics of pyrohydrolysis of CaF_2 at 1050–1250°C was studied in [17]. A significant difference between the pyrohydrolysis of alkaline earth fluorides and RF_3 is the fact that it is a one-stage process due to the absence of intermediate oxyfluoride phases in the MF_2–MO systems.

CaO solubility in CaF_2 at eutectic temperatures is assessed to be 1–1.5 mol % and decreases down to several dozen ppm upon a decrease in temperature. The CaO particles formed upon decomposition of the solid solution can be detected using light scattering, which is visible beginning from as low as 60 ppm O_2 [18]. An oxygen content of over 50 ppm in fluorite single crystals, according to [19, 20], makes them unsuitable for lasers.

Thus, due to the single-stage mechanism and low MO solubility in fluorite melts, the processes of MF_2 pyrohydrolysis are visually detected at lower oxygen contents than in the case of RF_3 pyrohydrolysis.

Below, we shall consider the conditions under which pyrohydrolysis can occur in the main industrial techniques of preparing single crystals of alkaline earth fluorides. These compounds were used as a model for developing methods for suppressing pyrohydrolysis when growing crystals from melts.

2.1. Stockbarger Technology (USA). The first experiments on preparing CaF_2 crystals from natural raw materials were conducted by Stockbarger in 1927 (see [21]). Nitrogen gas was used as an inert atmosphere. The experiments failed due to pyrohydrolysis.

The experiments conducted in [22] also failed; natural and synthetic CaF_2 were used. The reason behind the resulting nontransparent ingots was pyrohydrolysis. The ingots contained 3% CaO.

Stockbarger was the first researcher whose success in preparing synthetic CaF_2 was published. Stockbarger's search for methods to suppress pyrohydrolysis succeeded only in 1940–1945. The long period required to master the technology reflects the difficulties that occurred in the process of selecting the starting material and reactions to suppress melt pyrohydrolysis. The results of the research led to an industrial technology of preparing CaF_2 single crystals. This technology is reported in the classical work [21]. As the contemporary methods of industrial production of single crystals of alkaline earth fluorides are based on this technology, with a few exceptions, we shall consider it here in more detail.

Natural CaF_2 is considered to be the best starting material. It was prepared as a result of manual separation (floatation was unacceptable) of the natural fluorite

concentrate into three fractions: perfect single crystals (**A** fraction), crystals of medium quality with a moderate amount of gaseous-liquid and solid inclusions (**B** fraction) and poor samples with various inhomogeneities (**C** fraction).

The **A** fraction yielded good quality crystal samples. The **B** fraction could be used for crystal growth, but optical quality of its crystal samples was attained only after second crystallization. The **C** fraction was used for removing carbon particles from new crucibles by way of their washing in the melt.

Even perfect crystals have two kinds of inhomogeneities: isometric particles of the oxygen-containing phase and platy hexagonal inclusions, i.e., CaS particles yielded by inclusions of sulfide minerals (PbS, FeS, ZnS) in natural CaF_2 [7–9].

The author of [21] introduced PbF_2 into the starting CaF_2 in the ratio 1 : 50 in order to remove oxygen. This addition was termed "scavenger." The action of PbF_2 is based on the reaction

$$PbF_2 + CaO \longrightarrow CaF_2 + PbO\uparrow.$$

The reaction was moved to the right due to PbO evaporation. A plot of mixture (CaF_2 + PbF_2) heating and melting was constructed to ensure completeness of the "scavenger" reaction and removal of PbF_2 and PbO from the melt. The Pb content in the crystals was from 1 ppm to 10 ppm.

The full removal of Pb from CaF_2 has to be controlled for each crystal. Pb^{2+} ions have an intensive absorption band at 220 nm, which is manifested at contents of only 2 ppm [23].

CaF_2 crystals were prepared whose characteristics were as good as those of natural ones or better. The main advantages of the technology suggested in [21] are the following:

—A sharp temperature gradient (two heaters, divided by a thermal screen). A two-zone heater became a feature of the Stockbarger method (only one zone is used in the Bridgman method). The use of two zones also ensured good conditions for crystal annealing;

—The use of "scavenger" (PbF_2) to remove oxygen from the melt;

—Purification of inert gas (Ar) from oxygen by metals (heated Cu, W-getters);

—"Freezing" of water vapours and carbon dioxide using liquid N_2;

—Purification of new crucibles by washing them in CaF_2 melt from finely dispersed graphite particles entrapped by crystals during crystal growth.

2.2. Shamovskii Technology. At the All-Union Institute of Mineral Raw Materials (VIMS), Moscow, experiments aimed at preparing fluorite crystals were started in the 1930s by L.M. Shamovskii and coworkers. According to Yurgenson, 1980 (ref. [24], p. 62), the first synthetic crystals of optical fluorite were prepared in the USSR in 1937. The history of these studies, which proceeded Stockbarger's works in achieving successful results, was later described in [25]. In order to remove water vapor, the growth was conducted in a 10^{-4} mm Hg vacuum. Later, CdF_2 was suggested for we as a "scavenger."

2.3. Stepanov–Feofilov Technology (Russia). This technology was developed for fluorides of alkaline earth elements at the State Optical Institute (GOI), St. Petersburg, Russia. It is described in detail in [7, 26].

This technology unites elements of the Stockbarger and Shamovskii technologies: traces of oxygen are removed with the addition of 0.25 wt % PbF_2, and the growth is undergone in a 10^{-4}–10^{-5} mm Hg vacuum. Initially, heaters made of Mo and Ni crucibles were used. Heated Mo is a good O_2 chemical absorber (getter), and its usage contributed to purification of the gas medium. Nickel crucibles did not only incorporate impurities into the crystals but also hampered their removal due to wetting of Ni with the melt. Later, metals were replaced by graphite. Crystals of natural CaF_2 were initially used as the starting material. Now, synthetic CaF_2 is also used; its preparation technology is described in [27].

2.4. Technology of growing alkaline earth fluoride crystals of "plate" shape. The difficulties of mechanical treatment of crystals of alkaline earth fluorides due to their perfect cleavage and the need to reduce loss of the material used to fill the seed cone of the crucible, lead to an unusual solution. The authors of [28, 29] suggested growing MF_2 crystals in containers shaped like a cup with a flat bottom ("plate"). The cylindrical billets were close to in size to the optical elements prepared from them. The remaining conditions were the same as those used in the above technologies (vacuum and PbF_2).

The platy structure of the crucible without the seed cone became a major industrial technology for manufacturing optical fluoride materials in Russia. In terms of the sizes of the prepared crystals, with a diameter of up to 600 mm [26], the crystallization devices remain unique to date.

The main restriction in using natural raw materials for preparing CaF_2 crystals is insufficient and poorly controlled purity due to cationic impurities. Therefore, in addition to the industrial technologies employed further attempts to use synthetic CaF_2 instead of mineral raw materials were made.

The problem of transferring to synthetic raw materials for preparing optical-grade single crystals of alkaline earth fluorides was solved differently by different producers of single crystals. Most results remained at the level of "know-how." Some data on preparing CaF_2, SrF_2, and BaF_2 through ammonium complexes (similar to the synthesis of dehydrated RF_3) are reported in [30, 31]. At present, some companies produce raw materials that can be directly used for growing optical-

grade crystals of alkaline earth fluorides in vacuum or with the addition of some "scavengers."

2.5. Mechanism of CaF_2 pyrohydrolysis. Let us consider the few quantitative data available on the mechanism of CaF_2 pyrohydrolysis under conditions close to the conditions of crystal growth. The author of [32] showed that the source of oxygen in CaF_2 is not O_2 from the air but H_2O vapors. Interaction of CaF_2 with H_2O at 950–1150°C processed in three stages.

At the first stage, the IR spectra of the products exhibit (OH^{1-}) frequencies, which disappear at the second stage. $2F^{1-}$ replacement by O^{2-} yields the formation of anionic vacancies. The third stage, which arises when the equilibrium concentration of anionic vacancies in the crystal is attained, is characterized by coagulation of these particles with the release of CaO particles (detected by X-rays).

Changes in the lattice parameters of CaF_2 at different stages of pyrohydrolysis were found for the first time. This effect was later observed by the authors of [33], but they interpreted it in a different way.

Penetration of oxygen into CaF_2 crystals was studied by the authors of [34]. At the diffusion temperature (1000°C) the crystals were transparent, but upon cooling down to 725°C, they contained CaO particles 0.5–1 μm in diameter. Apparently, the authors observed decomposition of the CaO solid solution in CaF_2. The milky-white parts of the rod contained 2000–2400 ppm O_2, while the transparent part contained 20 ppm O_2.

A similar oxygen content in CaF_2, which caused light scattering, was detected by the authors of [8]. They observed light scattering directly introduced into the CaF_2 starting mixture containing 60 to 200 ppm CaO. The effect of light scattering by CaF_2 crystals occurred when sulfur in the form of 20 ppm CaS or $CaSO_4$ was introduced or chlorine in the form of 50 ppm $CaCl_2$ was introduced. These effects can be suppressed by introducing 100 ppm PbF_2 into the melt.

Introduction of R_2O_3 in amounts of up to 3% into the starting mixture does not lead to the formation of particles in $Ca_{1-x}R_xF_{2+x}$ single crystals. This observation was the first proof of high solubility of the products of RF_3 pyrohydrolysis, their oxyfluoride, in alkaline earth fluorides. Later, this was strictly shown in [35], were quasi-binary sections MF_2–ROF of the corresponding ternary systems were studied.

Decoration of dislocations in CaF_2 by CaO particles was observed in [32]. Oxygen penetrates into BaF_2 crystals through dislocations [36, 37].

3. Pyrohydrolysis of other metal fluorides MF_m. Pyrohydrolysis is a common reaction for inorganic fluorides; it complicates crystal growth of fluoride materials from the melt and studies of high-temperature chemistry of inorganic fluorides.

Intensive studies of the pyrohydrolysis of metal fluorides were part of the Manhattan project. Fluorides of U were prepared from uranium oxides by HF fluorination. Control over the completeness of the reaction required fast and accurate fluorine detection. Fluoride pyrohydrolysis was one of the suggested methods.

The authors of [38] studied the pyrohydrolysis of a large number of fluorides of elements of the Groups II–V of the Periodic Table, including RE trifluorides. They showed that pyrohydrolysis at 1000°C in a H_2O vapor flow can be recommended as a quantitative method of fluorine detection for most studied fluorides. The mean error for pure fluorides was ±0.05%. At the same time, a qualitative difference in the aptness of these compounds to pyrohydrolysis was found.

On the basis of studies of the kinetics of pyrohydrolysis, the authors of [38] distinguish between easily and not easily hydrolyzed. This distinction is conditional.

The first group contains fluorides for which hydrolysis (1000°C) in a H_2O flow vapor takes less than 20 minutes. This group includes the following members in order of increasing stability:

AlF_3, BiF_3, MgF_2, ThF_4, UF_4, UF_3, UO_2F_2,

VF_3, ZnF_2, ZrF_4, $ZrOF_2$, and RE fluorides.

The second group are fluorides of alkaline, alkaline earth elements, and Be, reaction with which is slower and does not always terminate. For example, after 7 h of treatment, CaF_2 converts into CaO by 94.7%. Some catalytic additives were suggested to speed up the reaction.

Pyrohydrolysis of RE trifluorides was studied in [39] as a method for detecting fluoride content. Differences in the reaction kinetics for different RF_3 were found. Pyrohydrolysis was conducted at 975 ± 25°C in a flow of humid air. Some RE fluorides, in turn, can be divided into easily and not easily hydrolyzed, according to the pyrohydrolysis rate.

The easily hydrolyzed RF_3 (hydrolysis takes less than 30 min.) are

ScF_3, LuF_3, CeF_3, YbF_3, HoF_3,

TbF_3, TmF_3, GdF_3, and DyF_3

(in order of increasing duration of full hydrolysis).

Not easily hydrolyzed fluorides, with a duration of hydrolysis from 45 to 150 minutes, are

SmF_3, YF_3, NdF_3, EuF_3, PrF_3, and LaF_3.

Thus, there are qualitative data on many metal fluorides stable to pyrohydrolysis. A few minutes of RF_3 heating in humid air is sufficient for the full transformation into R_2O_3. During crystal growth, the fluoride melt is affected by high temperatures for a longer time than in the experiments performed in [39]. Fluorides of alkaline earth elements are more stable to pyrohydrolysis; however, in this case, crystal growth from melts creates conditions for their conversion into MO.

4. Pyrohydrolysis of multicomponent melts containing fluorides of alkaline earth and RE elements. The forms of oxygen compounds contained in fluoride

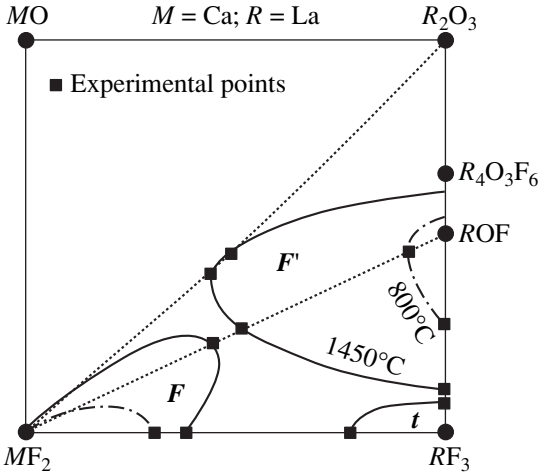

1450 and 800°C isothermal sections of the CaF_2–CaO–La_2O_3–LaF_3 system according to the data for MF_2–ROF [35], parts of the system LaF_3–La_2O_3 according to our data, and of the system CaF_2–La_2O_3 according to [40].

materials are determined by the composition, temperature, and equilibrium phase relations in the systems MF_2–MO–R_2O_3–RF_3. The phase relations in one of these systems are shown schematically in the figure, which shows two isothermal sections corresponding to phase formation in the system CaF_2–CaO–La_2O_3–LaF_3 at 1450 and 800°C. They are built on the basis of results of studies of the systems MF_2–ROF [35], part of the phase diagram of the system LaF_3–La_2O_3 according to our data, and the system CaF_2–La_2O_3 according to [40].

The scheme reflects processes that occur upon melt cooling in systems containing fluorides and oxides of alkaline earth and RE elements. The systems in which the phase relations were typical for most multicomponent fluoride materials were chosen.

4.1. Behavior of melts of the systems MF_2–MO. On the side of the square representing the system CaF_2–CaO, solid solutions are limited by 1–2% and there are no binary compounds. The only product upon oxygen contamination is a finely dispersed CaO phase. The crystals become milky-white with different degrees of transparency up to its full loss.

4.2. Behavior of melts of the systems RF_3–R_2O_3. Depending on the degree of pyrohydrolysis, i.e., the total oxygen content in the system RF_3–R_2O_3, a few different oxygen containing phases can be the products of pyrohydrolysis. In the LaF_3–La_2O_3 system shown in the figure, there will be a maximum of four such phases: a solid solution of $La_{1-y}F_{3-2y}O_y$ with the LaF_3 structure (phase ***t***), extended solid solutions with the fluorite-related structure (phases ***F*** and ***F***') (derived at low temperature), the oxyfluoride phase $La_4O_3F_6$, and the final product of pyrohydrolysis La_2O_3.

At the minimum degree of pyrohydrolysis, one can confine discussion to the phase (***t***), which is the first product [41, 42]. With decreasing temperature, it decomposes into RF_3 and ROF or $R_4O_3F_6$ depending on the RE and the temperature.

4.3. Behavior of melts of the systems MF_2–RF_3. Such melts are typical in preparing MF_2 crystals doped with REE. As the figure shows, in the stability areas of the phase ***F*** ($M_{1-x}R_xF_{2-2x}O_x$) and the phase with the tysonite (LaF_3) structure ***t***, certain amounts of oxygen do not disturb the single-phase character of the system. Temperature lowering sharply decreases oxygen solubility in $M_{1-x}R_xF_{2-2x}O_x$. This was shown in [35] and is evident on the 800°C isotherm. As a result, the considered case of oxygen simultaneously present in two forms is observed: as part of the oxygen-containing phase and in the dissolved form in the main crystal.

Thus, depending on the qualitative and quantitative composition of the systems MF_2–MO–R_2O_3–RF_3, the temperature and cooling regimes, the depth of pyrohydrolysis of fluorides, and the external manifestation of pyrohydrolysis can be different. Pyrohydrolysis occurs in most of the inorganic fluorides chosen as components of fluoride materials, and it is absolutely necessary to take it into account during crystal growth.

5. Purification of fluorides from oxygen. Let us consider the main techniques used for reducing oxygen impurity in fluoride crystals, which is the final product of interest. Some of these techniques were considered above. Thus, to reduce oxygen content in fluorides, the following main techniques are used:

—starting powder reagents are treated upon heating by HF, NH_4F, or $NH_4F \cdot HF$ with the aim of additional fluorination;

—scavengers (PbF_2 [21] or CdF_2 [25]) are incorporated into fluoride melts, as well as some others (see below);

—the melt is isolated from contact with damp gases by low-melting fluoride mixtures (fluxes), which react with oxides in the starting mixture and in the melt [43, 44]. Crystallization from solution in the melt is similar to this method [45];

—the melt or the powder is heated in an active (fluorinating) atmosphere. This method is commonly used in the course of the preliminary preparation of the starting mixtures, as well as in crystal growth, [46–56]. A separate section is devoted to active atmospheres (see below);

—zone melting purification, and related processes, is used for physical separation of particles of oxygen-containing phases [57–59].

In practice, different techniques are often combined. All are not universal; for this reason, under specific conditions, a specific method is required to ensure the best purification. Let us consider them in more detail.

5.1. Additional fluorination of commercial fluorides by NH_4F or $NH_4F \cdot HF$ is often used when preparing single crystals. These fluorinating agents are used in industrial methods of preparing RF_3 from R_2O_3 and in laboratories. Both compounds contain active HF in the

bonded (inert) form. However, due to specific mechanisms of interactions of NH_4F, $NH_4F \cdot HF$ with R_2O_3 and oxides of other metals, their fluorinating action is not identical to the reaction between R_2O_3 and HF (see below).

There are several works in which oxygen content is reported in the final product of fluorinating oxides by NH_4F and $NH_4F \cdot HF$. According to the authors of [60], who referred to reports by the Spedding group on F_2, NH_4F, and $NH_4F \cdot HF$, the latter yields the best results of interaction with R_2O_3 (300 ppm O_2 in the final product).

As reported in [61], the treatment of YF_3 hydrate by 30% excess $NH_4F \cdot HF$ at 250°C for 5 h with subsequent heating to 600°C for two hours yields a product with a higher oxygen content (0.16–0.51 wt %) than in the case of fluorinating R_2O_3.

Close values for oxygen impurities were obtained by the authors of [10, 13] for dehydration of $RF_3 \cdot xH_2O$ without fluorinating agents. The loss of water by hydrates of RE trifluorides, according to [13], is continuous and terminates at 300–400°C when the released water does not hydrolyze RF_3. However, the O_2 content in dehydrated RF_3 attains 0.4–0.5 wt %.

The oxygen content remains high in MgF_2, SrF_2, and BaF_2 in the course of their preparation using $NH_4F \cdot HF$ [62]. Two-stage purification (reaction at 250°C with subsequent removal of the fluorinating agent at 600°C) yielded MF_2 with contents of 0.11, 0.28, and 0.38 wt % O_2, respectively. This contradicts the results of analysis of the starting mixtures MF_2 for growing crystals from alkaline-earth carbonates and $NH_4F \cdot HF$ [30].

The mechanism of interaction of NH_4F and $NH_4F \cdot HF$ with R_2O_3 has been studied by several authors. This has made it possible to assess the conditions of effectively conducting reactions.

The authors of [63] used thermo-gravimetric analysis to study the interaction of Y_2O_3 and La_2O_3 with NH_4F. In the mixture $NH_4F + R_2O_3$ at 167–190°C decomposition occurs: $2NH_4F \longrightarrow NH_4F \cdot HF + NH_3$. The melting and boiling points of $NH_4F \cdot HF$ are 126°C and ~238°C, respectively [64]. At 220–240°C, the formation of ammoniates of RE fluorides starts. Upon heating up to 290–323°C the ammoniates interact with the excess R_2O_3. Depending on the proportion of the reagents, the process stops at the oxyfluoride formation stage or can be conducted up to RF_3. Assuming that in NH_4F and $NH_4F \cdot HF$ the fluorinating agent is HF, the fluorination reaction is as follows:

$$MO_{n/2(\text{solid})} + nHF_{(\text{gas})} \longrightarrow MF_{n(\text{solid})} + n/2H_2O_{(\text{gas})}.$$

However, upon fluorination of the oxides, according to [64, 65], NH_4F and $NH_4F \cdot HF$ are more active (in terms of fluorination speed and its completeness) than HF. Apparently, this is the case only when there are different mechanisms of the fluorination reactions. For NH_4F and $NH_4F \cdot HF$, the following reactions of oxide fluorination are suggested:

$$MO_{n/2(\text{solid})} + nNH_4F_{(\text{gas})} \longrightarrow MF_{n(\text{solid})} + n/2H_2O_{(\text{gas})} + nNH_{3(\text{gas})},$$

$$MO_{n/2(\text{solid})} + nNH_4F \cdot HF_{(\text{gas})} \longrightarrow MF_{n(\text{solid})} + n/2H_2O_{(\text{gas})} + n/2NH_{3(\text{gas})}.$$

Thermodynamic estimations of the probability of these processes for the elements of groups II–VI are reported in [64].

These reactions do not provide information on the mechanisms which would make it possible to study the intermediate products of interaction between NH_4F and $NH_4F \cdot HF$ with R_2O_3. Below, we report data from [64] for intermediate stages:

(1) Sc_2O_3 starts reacting with $NH_4F \cdot HF$ at 60°C, the process ends at 180°C with the formation of $(NH_4)_3ScF_6$;

(2) Y_2O_3 reacts with $NH_4F \cdot HF$ with an exothermal effect at 80°C and an endothermal effect at 170°C. With an excess of $NH_4F \cdot HF$, initially $NH_4Y_2F_7 \cdot NH_4F$ is formed, which then decomposes into YF_3. If the amount of $NH_4F \cdot HF$ is low, yttrium oxyfluoride is formed. According to [63], ammoniates of RE fluorides can be intermediate products;

(3) oxides of Pr, Nd, Sm, and Gd at the initial stage form NH_4RF_4, while oxides of Dy, Ho, Er, Tm, Yb, and Lu form the compounds $(NH_4)_3R_2F_9$. A further increase in temperature decomposes ammonium fluoromethallates, with the formation of RE fluorides.

According to different data reported in [64], the decomposition temperatures of these complexes are different. Below, the data from different papers will be referred in accordance with [64]:

(1) $(NH_4)_3R_2F_9$ with R = La, Pr, Sm, or Eu decomposes to $NH_4R_2F_7$ with R = Sm or Eu at 200–215°C or to NH_4RF_4 with R = La or Pr at 170–185°C. Higher temperatures are required to prepare RF_3.

(2) $(NH_4)_3NdF_6$ decomposes to NH_4NdF_4 at 350–400°C and to NdF_3 at about 500°C. $(NH_4)_3Ce_2F_9$ decomposition in vacuum at 430°C yields NH_4CeF_4 and CeF_3, respectively. According to other data, heating up to 450°C is required in order to prepare CeF_3.

(3) For the series of compounds NH_4RF_4, $NH_4R_2F_7$, and $(NH_4)_3R_2F_9$ with an increase in the atomic number R, two tendencies are found: for the first two types of compounds, the decomposition temperatures increase from 200 to 340°C from La to Lu, respectively. For $(NH_4)_3R_2F_9$, a maximum is found at R = Tb (275°C), after which the temperatures drop down to 220°C.

Thus, fluorination of R_2O_3, similar to additional fluorination of RF_3 with involvement of NH_4F and $NH_4F \cdot HF$, requires relatively low temperatures. It is recommended to conduct this reaction in an inert gas atmosphere. In the course of fluorinating R_2O_3 with account taken of evaporation losses, a six fold (in molar ratio) excess of the fluorinating agent is taken. Preparation of RF_3 from R_2O_3 or hydrated RF_3 using NH_4F and $NH_4F \cdot HF$ is applicable for all REE. However, this does not

ensure purity from oxygen, which is needed for synthesis of crystals of laser quality. The method is commonly used in laboratories because it allows preparation of RF_3 that is suitable for studies of the chemistry of RE trifluorides. Deep RF_3 purification from oxygen requires the use of other techniques (see below).

5.2. Treatment of fluoride melts by scavengers. Melt purification using this method was considered before for CaF_2. There are no data on the oxygen content in RF_3 crystals grown with the addition of CdF_2; however, it is known that the crystals are of laser quality. In MF_2 single crystals grown with PbF_2, hundreds and thousands of fractions of wt % O_2 were found. Thermodynamic assessments showed that many MF_m can be used for removing oxygen from fluoride melts according to the exchange reaction [66].

Constraints occur due to the necessity of removing excess scavenger from the melt as products of the interaction as well. Only PbF_2, CdF_2, SnF_2, and ZnF_2 are suitable for purification. These compounds are volatile themselves, and their oxides are also volatile. The use of MnF_3 and CoF_3 [67] did not become a common method.

The authors of [68] made a thermodynamic assessment of the efficiency of fluorinating action of PbF_2, CdF_2, HF, C_2H_4, and F_2. To transform CaO and CdO into fluorides at high temperatures, F_2, as well as the products of tetrafluoroethylene pyrolysis, is the most effective. Approximated calculations showed that in the range 1000–1800 K, CdF_2 fluorinates R_2O_3 from La to Dy, while "heavier" R_2O_3 require other scavengers.

The completeness of the removal of Pb and Cd from the melt has been studied insufficiently. The remaining amounts of Pb in BaF_2 crystals, beginning from contents of several ppm, exhibit strong absorption in the UV region. There is no data on CdO and PbO solubility in the melts and fluoride crystals. It should be stressed, therefore, that though the method of oxygen removal from fluoride melts using scavengers is technically simple, it should be applied very carefully. The resulting single crystals of REE and alkaline earth fluorides can have some characteristics determined by micro-impurities of heavy metal cations (Pb, Cd, etc.).

5.3. Physical methods of oxygen removal (zone crystallization, sublimation). Sublimation is used for physical methods of RF_3 purification from oxide impurities. Its application is restricted due to the low volatility of RF_3. An exception is ScF_3, for which the authors of [58] described purification by vacuum sublimation. As a result, the oxygen content was reduced from 325 to 30 ppm; this is the value that is attained upon fluorinating Sc_2O_3 using HF at 750°C.

The authors of [59] reported YF_3 purification by vacuum sublimation. According to the reported temperature of polymorphic transformation of the YF_3 obtained (1040°C), oxygen contamination is significant.

Vacuum RF_3 sublimation is a technological method of preparing thin film condensers and optical protecting and reflecting coatings. The kinetics of the sublimation, thermolysis, and reactions which occur when RF_3 interacts with a substrate have been studied insufficiently. There are even less data on the evaporation of multicomponent compositions with RF_3.

The use of directed crystallization as a physical method of purifying fluorides from particles of oxygen-containing phases (oxides and oxyfluorides) has been studied insufficiently. The efficiency of this method is restricted by the case of a full absence of oxygen solubility in fluoride crystals.

The formation of opal-like scattering, nontransparent parts at the end of crystalline rods is described quite often. Unfortunately, parts of the crystals were not analyzed to identify the oxygen contents (as compared to transparent parts) and their phase composition could not always be determined. The only quantitative data on purification of LaF_3 by zone melting were reported in [57]. According to the authors, oxygen is moved towards the end of the ingot and the transparent zone of the crystal contains 0.00n wt % O_2.

Particles of oxide or oxyfluoride as the second phase in the melt can differentiate (precipitate) due to a difference in specific weight. In order to separate the precipitating oxygen impurities, it suffices to remove the milky-white, nontransparent part of the rod resulting from fast cooling of the melt.

The method of "selection" for preparing high-quality crystals using repeated crystallization of selected transparent parts while sorting out opal-like parts is quite common in crystal growth experiments.

5.4. Application of fluxes. Low melting mixtures of fluorides and other compounds (fluxes) play a two-fold role. On the one hand, they should (as scavengers) interact with oxides contained in the starting mixture and form fluorides. On the other hand, they isolate the fluoride melt from contact with atmospheric moisture. The use of fluxes in the synthesis of minerals was quite common in the 19th century; this is why such additives were called "mineralizators".

The authors of [45] prepared $Sr_{1-x}La_xF_{2+x}$ ($0.1 \le x \le 0.3$) crystals from an $Sr(NO_3)_2$ melt in $La(NO_3)_3$ by precipitation of KF or KHF_2. Crystals of the most refractory binary fluoride of all the known fluorides (the composition $Sr_{0.69}La_{0.31}F_{2.31}$ melts at 1570°C [69]) were first prepared from solution in the melt at relatively low temperatures. This excluded pyrohydrolysis, which is inevitable upon melting of a refractory SrF_2 and LaF_3 mixture.

The authors of [44] suggested using fluxes of BeF_2, MgF_2, and AlF_3 in order to prepare large crystals of RF_3 and some other crystals of more complex composition. Complex fluxes ensured high purity of RF_3 with regard to oxygen and quite large crystal samples. Pyrohydrolysis in this case was reduced to a minimum. An indispensable condition in choosing the chemical composi-

tion of fluxes is a full absence of their solubility in RF_3. Unfortunately, there is no such data for most low-melting metal fluorides. This is a constraint for using fluxes in the practice of preparing pure crystals of REE fluorides.

Chlorides can be used as fluxes when preparing RF_3. NdF_3 crystals were grown from an eutectic mixture of KCl with $NdCl_3$ following [43]. According to qualitative estimates, they contained no more than 10 ppm O_2. The phase NdOCl was found in the products, which is evidence of a reaction between $NdCl_3$, as a composition more apt for pyrohydrolysis, and the main part of H_2O in the atmosphere.

5.5. Use of active fluorinating gaseous atmospheres. Long storage of the melt before crystal growth is the stage necessary for homogenization, gas removal, etc. It can be used for purification from oxygen as well. To achieve this, active (fluorinating) gas atmospheres should be ensured. Using such atmospheres became a common method of oxygen removal from fluoride materials.

According to the chemical compositions and mechanisms of fluorinating actions, active atmospheres can be divided into two categories, single-component (HF, BF_3, SF_4, etc.) and multi-component. The latter contain an active atmosphere in which the starting form of the fluorinating agent is solid, while active compounds, which are released upon heating, are gaseous.

5.5.1. The use of a gaseous form of HF. Dehydrated HF was used as a fluorinating agent for transforming R_2O_3 into RF_3 on industrial and laboratory scales of fluoride synthesis. The whole series of RF_3 was synthesized for X-ray diffraction studies upon interaction of their oxides with HF [70].

The authors of [52, 58] described a two-stage method of transforming R_2O_3 into RF_3. Its efficiency has been well documented for all 16 RF_3 by chemical analysis. At the first stage, R_2O_3 are treated at 750°C by HF. The resulting product contains up to 100–300 ppm O_2. At the second stage, the temperature is raised by 150°C above the melting point of RF_3 and the melt contacts with the flow of the HF and Ar mixture. After such treatment, RF_3 contains 20 ppm on less O_2 (the limit of analysis sensitivity).

These studies showed that upon transition of the main mass of R_2O_3 into RF_3, there is no significant difference among the use of NH_4F, $NH_4F \cdot HF$, and HF (in the static regime) from the viewpoint of oxygen content in the final products. In all cases, this content is high. A significant reduction of oxygen impurity can be attained by subsequent fluorination of HF melts in the dynamic regime.

The use of HF at all the stages of the high-temperature treatment of fluorides in the course of crystal growth was first described in [49, 50]. In the same years, the technique of crystal growth of fluorides in an HF atmosphere was developed in Russia (Kh.S. Bagdasarov, E.G. Ippolitov, B.P. Sobolev). Purification is based on the heterogeneous reaction

$$OH^{1-}_{(crystal)} + HF_{(gas)} \longrightarrow F^{1-}_{(crystal)} + H_2O_{(gas)}.$$

In this case, H_2O is formed, which is the source of pyrohydrolysis.

The author of [49] used treatment of the starting mixture of fluorides by HF at 800°C for a course of 18 h. However, the subsequent growth process yielded crystals with a significant oxygen content. The next step was a new technological scheme, which comprised preparation of the starting compounds MF_m, melting of its mixture, and growth and annealing of crystals in a dynamic fluorinating atmosphere (a flow of the HF mixture with dehydrated He) [50].

The author of [71] reported laser quality crystals of $LaF_3:Nd^{3+}$ grown in an HF atmosphere. The author of [72] reported (without describing the technology) preparation of $MF_2:Nd^{3+}$ and $LaF_3:Nd^{3+}$ crystals of laser quality by the Optovac company. Laser LaF_3 crystals were prepared by the authors of [73], who treated the starting mixture using HF at 1000–1300°C for 10 h. A shorter duration of storage of the melt results in the occurrence of scattering particles.

Dynamic fluorinating atmospheres where studied by a team from the Hughes Research Laboratory (California, USA). The advantage of an HF flow is based on the low values of the equilibrium constants in the case of its reaction with oxides at high temperatures. The HF flow moves equilibrium towards the formation of RF_3.

The first paper on the use of RAP (Reactive Atmospheric Processing) when growing fluorides [46] was devoted to the preparation of CaF_2, SrF_2, and BaF_2 using the Bridgman technique from melts treated by HF with 10 mol % He (flow 2 l/min) for 8 h (RAP-I). In fact, this is the same single-component (in terms of the fluorinating agent) atmosphere used by Guggenheim. The method was patented in [48] for RF_3 growth for lasers and materials used in constructing optics.

A comparative determination of melting points of alkaline-earth fluorides before and after treatment of their melts with an HF flow was conducted by the authors of [74]. In order to fully remove oxygen, a dynamic atmosphere of HF with Ar mixture was used, which was barbotized into melts overheated by 50–150°C. When removing CaO impurity from the CaF_2 melt using HF, contents of 10 ppm CaO can be attained. In the case of the studied fluorides, elevation of the melting points of the fluorinated samples by 1–14°C was found (the maximum increments were obtained for MgF_2, CaF_2, SrF_2, and BaF_2).

The authors of [75] described the method and the device for preliminary treatment of the starting mixture using an Ar flow with 60 vol % HF at 700–800°C for 24–48 h. After this, the starting mixture was melted. The flow of the gas mixture was transmitted above the melt or barbotized through it using Mo tubes. Such

purification ensured the growth of laser quality crystals in an inert crystal growth atmosphere.

Dehydrated HF is not suitable for use as a fluorinating agent because of the problems posed by transporting it in tanks, its high aggressiveness, and the danger of leaking. A more convenient form of HF conservation is hydro fluorides of alkaline and alkaline-earth elements which split HF at rather low temperatures [76]. In contrast to NH_4F and $NH_4F \cdot HF$, these sources should release HF if they do not contact with the objects of fluorinating. The use of such HF sources is limited by their high price.

5.5.2. Multicomponent (combined) fluorinating atmospheres. The reaction of R_2O_3 with HF releases H_2O, which is retained in the reaction volume and results in pyrohydrolysis. The search for methods of H_2O removal has led to multicomponent gas atmospheres.

The works on combined active atmospheres conducted by the team from the Hughes Research Laboratory, USA, in addition to preparing high-quality fluoride crystals, were connected to studies on oxygen impact on phase transitions in RF_3. By using a dynamic HF atmosphere (RAP-I), the authors of [77] prepared crystals of GdF_3, TbF_3, DyF_3, HoF_3, and ErF_3 (>1 cm^3). They considered this fact to be evidence of crystallization from the melt of orthorhombic (β-YF_3 type) forms of all the above RF_3. This conclusion was true only for TbF_3, DyF_3, and HoF_3 [41, 42].

After the work of [46], where HF was used in mixture with He (RAP-I), a series of studies of importance in the technology of growing RF_3 crystals followed. Below, we shall consider RAP studies of several compositions in historical sequence.

Combined RAP-II was suggested by the authors of [47]. It is a mixture of two fluorinating agents, HF and CF_4, with inert He. The logic of complicating an active component in RAP-II is as follows. If (following the authors) F^{1-} is replaced by OH^{1-}, and not by O^{2-}, which is more probable at high temperatures, the pyrohydrolysis equation in the general case can be written as

$$F^{1-}_{(solid)} + H_2O_{(gas)} \longrightarrow OH^{1-}_{(solid)} + HF_{(gas)}.$$

The relation between equilibrium contents of OH^{1-} and F^{1-} in the crystal is set by the equation $C = kP_{(H_2O)}/P_{(HF)}$, where k is the equilibrium constant and P are the corresponding partial pressures of H_2O and HF vapors. The HF flow moves the reaction to the left. The same effect is attained by incorporation into the gas mixture of a reagent, which removes water from the reaction sphere. This is attained by a conversion of H_2O into HF. To achieve this, a homogeneous reaction in the gas phase was suggested:

$$CF_{4(gas)} + 2H_2O_{(gas)} \longrightarrow CO_{2(gas)} + 4HF_{(gas)}.$$

At 1200 K, the equilibrium constant of this reaction is 6.8×10^{-27}, while at 1500 K, it is 1.9×10^{-25} atm^2. This reaction was studied experimentally for 900 and 1000°C. For 900°C, 100% conversion of H_2O into HF requires a ratio of H_2O to CF_4 of 1 to 10^3. With an increase in temperature, this ration grows. For full conversion at 1300°C, the ratio 1 : 10 is sufficient, while for 1450°C (the typical temperature for crystal grow of many MF_2 and RF_3), the ratio 0.63 : 1 is sufficient.

Another publication [78] from this series is devoted to a comparison of two secondary RAP agents, CF_4 and C_2F_4. The latter is prepared as a result of thermolysis of tetrafluoroethylene $(C_2F_4)_n$ (teflon). According to the data of thermo-gravimetric analysis, upon teflon heating, two processes occur: a reversible process, that is, melting at 321°C (according to other data, 324–327°C) and an irreversible process, that is, thermolysis of $(C_2F_4)_n \longrightarrow nC_2F_4$, which starts at 550°C. In addition to C_2F_4, C_3F_6 and C_4F_8 are formed in the course of teflon thermolysis. The presence of CF_4 is evidence that the process $C_2F_4 \longrightarrow CF_4 + C$ occurs already at the first stages of the thermolysis. The release of finely dispersed graphite in this case is well known to all those who have worked with teflon thermolysis atmospheres.

The instability of C_2F_4 did not allow the authors of [78] to study its reactions with R_2O_3. It was shown that for CF_4, the reaction with La_2O_3 does not proceed until 970°C. Higher temperatures (>1000°C) are required for fluorinating oxides using CF_4. Thermodynamic estimates suggest a possibility of direct reactions:

$$O^{2-}_{(solid)} + 1/2C_2F_{4(gas)} \longrightarrow 2F^{1-}_{(gas)} + CO_{(gas)},$$

$$O^{2-}_{(solid)} + 1/2CF_{4(gas)} \longrightarrow 2F^{1-}_{(solid)} + 1/2CO_{2(gas)}.$$

In actual fact, the compound C_2F_4 is unstable and the atmosphere of the products of teflon thermolysis is almost identical to the atmosphere with CF_4. As CF_4 reacts more efficiently with H_2O, and HF, with oxides, the authors recommend using a combined RAP-II comprising HF, CF_4, and a gas carrier.

5.5.3. Fluorinating with the products of tetrafluoroethylene pyrolysis (combined atmosphere with a solid source). In 1965, the authors of [54] suggested a simple and practical method of creating a fluorinating environment from thermal decomposition of tetrafluoroethylene at 400–500°C in an ~10^{-1} mm Hg vacuum. In [47], the priority of using teflon was erroneously assigned to another team of Russian scientists [79], who published the results of their research seven years later. Owing to the convenience of using an inert plastic material (teflon) as the source of active gas, the method suggested in [54] has been commonly used in the practice of crystal growth of fluorides.

When growing crystals of refractory fluorides, the use of products of teflon pyrolysis is equal to the use of the fluorinating agent CF_4. In the course of reaction between CF_4 and the oxygen-containing melt, HF is formed. Qualitatively, the same gas mixture ($HF + CF_4$) is formed as in the case of the combined atmosphere

[47], only with another ratio, HF : CF_4 (CF_4 prevails). When using products of teflon pyrolysis, there is no need to conduct drying of the chamber atmosphere because CF_4 interacts with H_2O.

The technology of using teflon product pyrolysis produces by-products (mainly finely dispersed carbon) which sometimes penetrate the crystal bulk. Another significant disadvantage similar to the case of using the mixture HF:CF_4 is that CF_4 above 1400°C reacts with graphite (the heated parts of the crystal growth device). This leads to an accelerated "burning" of graphite parts.

When choosing the crystal growth method for a specific fluoride material, one should bear in mind that the high chemical aggressiveness of melts is not confined to reaction with H_2O. Contact of the melt with the container can be accompanied by unwanted chemical reactions, which also should be reduced to a minimum.

The chemical aggressiveness of fluoride melts also concerns the vapor phase of these compounds. Fluoride vapors can interact with parts of the crystallization chamber: heaters, heat screens, internal grids, etc. The vapor pressure of many fluorides is low; however, even in this case, corrosion of the parts, particularly heated ones, can occur quickly. Fluorine is an active agent of many transport chemical reactions whose possibility cannot be excluded. Chemical transport in the fluoride crystal growth process has not been analyzed so far.

6. Interaction of fluorinating gaseous agents with graphite. Graphite is used for preparing fluoride single crystals as crucibles, heaters, and thermal screens. Therefore, the choice of the fluorinating atmosphere upon crystallization will be determined by its corrosion capacity with regard to heated graphite. The authors of [78] showed that above 1400°C, CF_4 interacts with graphite parts.

Increases in the rate of graphite corrosion correlate with the decrease in dissociation energy of the *M*–F bond over the series of compounds BF_3–CF_4–SF_6 (133, 121, 70 kcal). Thus, BF_3 is the least rusting fluorinating agent, while SF_6, in terms of rusting capacity, exceeds CF_4 by more than an order of magnitude. In the course of the reaction with carbon, BF_3 makes the surface passive (due to unknown reasons) and the burning is decreased by several times. Thus, the authors of [80] showed that CF_4 is not the best fluorinating agent for crystal growth at high temperatures.

It is important that BF_3 in a bonded form (complex compounds of the type MBF_4, etc.) is more accessible and cheaper than CF_4. The described technological processes during crystallization of hydrolyzed fluorides can place RAP with BF_3, in the near future, at the leading position among active fluorinating atmospheres.

The authors of [80] studied the interaction with graphite of all three types of combined fluorinating atmospheres:

(1) RAP-I consisting of 90% HF with 10% He,

(2) RAP-II consisting of three gases in the ratio HF : CF_4 : He = 0.5 : 0.05 : 1, and

(3) RAP-III consisting of HF : BF_3 : He = 0.5 : 0.05 : 1.

To compare RAP-I, RAP-II, and RAP-III, crystallization of SrF_2 and BaF_2 was conducted with preliminary storage of the melt for two hours at 1800°C (for RAP-II, at 1700°C). Transmission spectra in the IR region showed improvement of the optical quality of crystals for mixtures with CF_4 and BF_3 [80]. In the case of RAP-II in BaF_2, five absorption bands are found in the region 3.5–9 μm. For SrF_2, there is no such obvious effect.

Among fluoride materials, optical ceramics are of interest. The method of their preparation (hot pressing) and a highly dispersed starting mixture create favorable conditions for pyrohydrolysis. The same fluorinating agents, NH_4F, $NH_4F \cdot HF$, and HF, are used to improve ceramic transparency. In order to remove the absorbed gasses on the surface, H_2 is added; the powders are treated directly in the forms for hot pressing (see, for instance, [81, 82]).

Fluorinating atmospheres play an important role in the preparation of materials in such fields as quantum electronics, construction optics in spectral devices, the space and aviation industry, cinema- and photo-engineering, etc. Analysis of the results of research devoted to active fluorinating atmospheres shows that impact was studied for RE fluorides as a case of compounds apt to pyrohydrolysis.

The section concerning atmospheres in the course of crystal growth is directly related to the RF_3 chemistry. This area has been essentially enriched with new data in recent years due to a larger demand for fluoride materials of a high optical grade.

7. Interaction of fluoride melts with graphite. This includes two possible processes: reaction between carbon and the melt with the formation of gaseous compounds of fluorine and carbon and reduction of metal ions to the lowest oxidation states including the metallic state. We shall consider these reactions for metal fluorides under conditions of crystal growth.

The authors of [12] used mass spectrometry to show the absence in gaseous reactions of products, of melts (YF_3, CaF_2, and SrF_2) with graphite crucibles upon heating up to 1600–1800°C.

Among the 34 elements whose fluorides can be considered components of crystals and glasses, full transition into lower oxidation states under the conditions of preparing these crystals is typical of trivalent Sm, Eu, Yb, and In and tetravalent U. For some divalent (Pb, Cd) and trivalent (Bi) cations reduction can proceed until metal. The reduction degree varies depending on the chemical element and the conditions. Usually, full reduction is not attained during crystal growth even in the cases when, under special conditions, the process can be conducted with a 100% preparation of metal fluoride with a lower valence.

Metallic Pb, Cd, and Bi are often found in the course of crystal growth of their fluorides in graphite crucibles. The reduction degree is controlled by a number of kinetic factors, such as the porosity of the crucible walls, melt overheating, duration of melt keeping, presence of water, etc. Since the preparation of some ions with lower oxidation states is required to provide crystals with the required characteristics, studies of the methods of controlled ion oxidation states in fluorides are of particular importance. Unfortunately, there are very few such works [83].

CONCLUSIONS

Analysis of the literature data and the experience of the author and his colleagues at the Institute of Crystallography suggest the following general conclusions about the application of methods of purifying metal fluorides from oxygen impurities:

—All the methods of solid-state additional fluorination of commercial reagents (simple metal fluorides, MF_m) which are contaminated with oxygen ensure approximately the same level of purification, several hundreds ppm. This does not depend on the fluorinating agents. This purification degree is insufficient for some applications of fluoride materials.

—A deep purification degree is ensured by the melting of the starting mixture with a solid fluorinating agents (scavengers) or the use of active gaseous atmospheres for fluorinating melts, as well as physical purification methods (sublimation, zone crystallization). Oxygen contents in this case are lowered, on the average, by an order of magnitude as compared to the previous group of purification methods, providing dozens of ppm (the limit of sensitivity in the analysis for oxygen).

—Preparation of highly transparent single crystals of refractory fluorides and fluorides hydrolyzed at high temperatures is possible only with account taken of specific features in the chemical behavior of these compounds under the conditions of crystal growth from melts.

This work was supported by the International Association for the Promotion of Cooperation with the Former Soviet Union (INTAS), project no. 97-32045, and by the Russian Foundation for Basic Research, project no. 01-03-33000.

REFERENCES

1. B. P. Sobolev, Butll. Soc. Catalana Cienc. Fis., Quim. Mat. **12** (2), 275 (1991).
2. B. P. Sobolev, Zh. Vses. Khim. O–va im. D. I. Mendeleeva **36** (6), 726 (1991).
3. B. P. Sobolev, in *Growth of Crystals* (Consultants Bureau, New York, 1992), Vol. 18, p. 197.
4. B. P. Sobolev, in *Crystals: Growth, Structure, Properties* (Nauka, Moscow, 1993), p. 167.
5. B. P. Sobolev, *The Rare Earth Trifluorides*, Part 1: *The High Temperature Chemistry of Rare Earth Trifluorides* (Institut d'Estudis Catalans, Barcelona, 2000).
6. B. P. Sobolev, *The Rare Earth Trifluorides*, Part 2: *Introduction to Materials Science of Multi-Component Metal Fluoride Crystals* (Institut d'Estudis Catalans, Barcelona, 2001).
7. I. V. Stepanov and P. P. Feofilov, in *Growth of Crystals* (Akad. Nauk SSSR, Moscow, 1957), p. 229.
8. W. Bardsley and G. W. Green, Br. J. Appl. Phys. **16** (6), 911 (1965).
9. E. A. Simun, in *Proceedings of the 2nd All-Union Symposium on the Chemistry of Inorganic Fluorides, Moscow, 1970* (Nauka, Moscow, 1970), p. 134.
10. N. V. Barishnikov, Yu. A. Karpov, and T. I. Guschina, Izv. Akad. Nauk SSSR, Neorg. Mater. **4** (4), 532 (1968).
11. G. G. Glavin and Yu. A. Karpov, Zavod. Lab. **30** (3), 306 (1964).
12. G. G. Glavin, Yu. A. Karpov, and B. A. Olzhataev, Zavod. Lab. **35** (2), 172 (1969).
13. N. V. Barishnikov, T. V. Golstein, and Yu. A. Karpov, Nauchn. Tr., Gos. Nauchno-Issled. Proéktn. Inst. Redkomet. Prom-sti **45**, 61 (1972).
14. E. I. Smagina, V. S. Kutsev, and I. E. Krauze, Nauchn. Tr., Gos. Nauchno-Issled. Proéktn. Inst. Redkomet. Prom-sti **20**, 58 (1968).
15. R. M. Atkins, M. M. Broer, and A. J. Bruce, Mater. Sci. Forum **32–33**, 81 (1988).
16. M. E. Fremy, Ann. Chim. Phys. **47** (3), 5 (1856).
17. M. A. Mikhailov, Izv. Vost. Fil. Akad. Nauk SSSR, No. 9, 64 (1957).
18. W. Bardsley and G. W. Green, Br. J. Appl. Phys. **16** (6), 911 (1965).
19. M. Robinson and D. M. Cripe, J. Appl. Phys. **37** (5), 2072 (1966).
20. M. Robinson, G. Hills, and D. M. Cripe, US Patent No. 3649552 (1972).
21. D. S. Stockbarger, J. Opt. Soc. Am. **39** (9), 31 (1949).
22. E. V. Zhekhnovitser, Zh. Fiz. Khim. **10** (1), 88 (1937).
23. P. Schotanus, P. Dorenbos, C. W. E. van Eick, and R. W. Hollander, IEEE Trans. Nucl. Sci. **36** (1), 132 (1989).
24. N. P. Yushkin, N. V. Volkova, and G. A. Markova, *Optical Fluorite* (Nauka, Moscow, 1983).
25. L.M. Shamovskii, P. M. Stepanukha, and A. D. Shushkanov, in *Spectroscopy of Crystals* (Nauka, Moscow, 1970), p. 160.
26. V. A. Sokolov, E. A. Simun, and A. N. Sinev, Opt.-Mekh. Prom-st. **46** (5), 29 (1979) [Sov. J. Opt. Technol. **46**, 279 (1979)].
27. E. D. Kaplan, V. M. Reiterov, L. M. Trofimova, and R. N. Yashvina, Opt.-Mekh. Prom-st. **44** (9), 36 (1977) [Sov. J. Opt. Technol. **44**, 545 (1977)].
28. E. G. Chernevskaya, E. A. Simun, and A. I. Stozharov, Opt.-Mekh. Prom-st., No. 2, 42 (1970).
29. E. G. Chernevskaya, USSR Inventor's Certificate No. 321279, Byull. Izobret., No. 35, 26 (1971).
30. A. A. Luginina, L. A. Olkhovaya, D. D. Ikrami, *et al.*, Zh. Neorg. Khim. **26** (2), 332 (1981).

31. A. A. Luginina, L. A. Olkhovaya, and D. D. Ikrami, USSR Inventor's Certificate No. 998352, Byull. Izobret., No. 7, 40 (1983).
32. W. Bontinck, Philos. Mag. **2** (16), 561 (1957).
33. H. Hann, W. Seeman, and H. L. Kohn, Z. Anorg. Allg. Chem. **369** (1–2), 48 (1969).
34. W. L. Phillips and J. E. Hanlon, J. Am. Ceram. Soc. **46** (9), 447 (1963).
35. V. A. Gorbulev, P. P. Fedorov, and B. P. Sobolev, in *Proceedings of the 6th International Conference on Crystal Growth (ICCG-6), Moscow, 1980*, Vol. 3, p. 180.
36. A. M. Aronova and G. V. Berezkova, Krist. Tech. **14** (2), 173 (1979).
37. A. M. Aronova and G. V. Berezkova, Krist. Tech. **15** (5), K39 (1980).
38. J. C. Warf, W. D. Cline, and R. D. Tevebaugh, Anal. Chem. **26** (2), 2342 (1954).
39. C. V. Banks and K. E. Bruke, Anal. Chim. Acta **19** (2), 239 (1958).
40. H. Iwahara, T. Esaka, and T. Takahashi, J. Appl. Electrochem. **14** (6), 687 (1984).
41. B. P. Sobolev, P. P. Fedorov, D. V. Steinberg, *et al.*, J. Solid State Chem. **17** (2), 191 (1976).
42. B. P. Sobolev, P. P. Fedorov, K. B. Seiranian, and N. L. Tkachenko, J. Solid State Chem. **7** (2), 201 (1976).
43. J. Aride, J. P. Chaminade, and M. Pouchard, J. Fluorine Chem. **15**, 117 (1980).
44. W. H. Grodkiewicz and L. G. van Uitert, US Patent No. 3667921 (1972).
45. J. A. A. Ketelaar and P. J. H. Willems, Recl. Trav. Chim. Pays-Bas. **56** (1), 29 (1937).
46. R. S. Pastor and K. Arita, Mater. Res. Bull. **10** (6), 493 (1975).
47. R. C. Pastor and K. Arita, Mater. Res. Bull. **11** (8), 1037 (1976).
48. M. Pastor, K. Arita, and M. Robinson, US Patent No. 3935302 (1976).
49. H. J. Guggenheim, J. Appl. Phys. **32** (7), 1337 (1961).
50. H. J. Guggenheim, J. Appl. Phys. **34** (8), 2482 (1963).
51. V. H. Sirgo, Bull. Am. Phys. Soc. **8** (6), 475 (1963).
52. F. H. Spedding and D. C. Henderson, J. Chem. Phys. **54** (6), 2476 (1971).
53. M. Robinson, G. Hills, and D. M. Cripe, US Patent No. 3649552 (1972).
54. Yu. K. Voron'ko, V. V. Osiko, V. G. Udovenchik, and M. M. Fursikov, Fiz. Tverd. Tela (Leningrad) **7** (1), 267 (1965) [Sov. Phys. Solid State **7**, 204 (1965)].
55. B. Joukoff, J. Primot, and C. Tallot, Mater. Res. Bull. **11** (10), 1201 (1976).
56. M. N. Brekhovskikh, A. I. Popov, Yu. M. Kiselev, *et al.*, Visokochist. Mater. **1** (5), 83 (1987).
57. B. V. Sinitsyn, V. A. Kasyanov, and T. V. Uvarova, Nauchn. Tr., Gos. Nauchno-Issled. Proéktn. Inst. Redkomet. Prom-sti **45**, 101 (1972).
58. F. H. Spedding, B. J. Beaudry, D. C. Henderson, and J. Moorman, J. Chem. Phys. **60** (4), 1578 (1974).
59. K. Recker and F. Wallrafen, Ber. Dtsch. Keram. Ges. **50** (3), 68 (1973).
60. R. E. Thoma, C. F. Weaver, H. A. Friedman, *et al.*, J. Phys. Chem. **65** (7), 1096 (1961).
61. R. H. Nafziger, R. L. Lincoln, and N. Riazance, J. Inorg. Nucl. Chem. **35** (2), 421 (1973).
62. S. Cantor and W. T. Ward, J. Phys. Chem. **67** (12), 2766 (1963).
63. L. Ya. Markovskii, E. Ya. Pesina, L. M. Loev, and Yu. A. Omel'chenko, Zh. Neorg. Khim. **15** (1), 5 (1970).
64. E. G. Rakov and E. I. Mel'nichenko, Usp. Khim. **53** (9), 1463 (1984).
65. E. G. Rakov, in *Proceedings of the 7th All-Union Symposium on the Chemistry of Inorganic Fluorides, Leninabad, 1984* (Nauka, Moscow, 1984), p. 10.
66. O. G. Polachenok, Izv. Akad. Nauk SSSR, Neorg. Mater. **2** (6), 958 (1966).
67. M. Sfiligoj, US Patent No. 3282641 (1966).
68. M. F. Dubovik, A. I. Promoskal', and I. I. Smirnov, Izv. Akad. Nauk SSSR, Neorg. Mater. **4** (9), 1580 (1968).
69. B. P. Sobolev and K. B. Seiranian, J. Solid State Chem. **39** (2), 17 (1981).
70. A. Zalkin and D. H. Templeton, J. Am. Chem. Soc. **75** (10), 2453 (1953).
71. V. H. Sirgo, Bull. Am. Phys. Soc. **8** (6), 475 (1963).
72. L. F. Johnson, J. Appl. Phys. **34** (4), 897 (1963).
73. P. F. Weller and J. A. Kucza, J. Appl. Phys. **35** (6), 1945 (1964).
74. H. Kojima, S. G. Whiteway, and C. R. Masson, Can. J. Chem. **46** (18), 2968 (1968).
75. S. J. Warshaw and R. E. Jackson, Rev. Sci. Instrum. **36** (12), 1774 (1965).
76. D. D. Ikrami, S. Oripov, V. S. Sidorov, and S. A. Fassakhov, in *Proceedings of the 7th All-Union Symposium on the Chemistry of Inorganic Fluorides, Leninabad, 1984* (Nauka, Moscow, 1984), p. 156.
77. R. C. Pastor, M. Robinson, and K. T. Miller, Mater. Res. Bull. **9** (4), 449 (1974).
78. R. C. Pastor and M. Robinson, Mater. Res. Bull. **11** (10), 1327 (1976).
79. E. G. Chernevskaya and Z. N. Korneva, Opt.-Mekh. Prom-st. **39** (4), 30 (1972).
80. R. C. Pastor, M. Robinson, and M. Braunstain, Mater. Res. Bull. **15** (4), 469 (1980).
81. C. F. Swinehart and H. Parker, US Patent No. 4089937 (1978).
82. E. Carnall, US Patent No. 3437724 (1969).
83. A. D. Kirschenbaum, J. A. Cahill, and C. S. Stokes, J. Inorg. Nucl. Chem. **15** (3/4), 297 (1960).

Crystallography Reports, Vol. 47, Suppl. 1, 2002, pp. S76–S85.

SOLUTION GROWTH

Characterization of Defects Generated by Di- and Trivalent Cations in the Potassium-Dihydrophosphate Structure and Their Influence on Growth Kinetics and Face Morphology

T. A. Eremina*, N. N. Eremin, V. A. Kuznetsov*, T. M. Okhrimenko*, N. G. Furmanova*, E. P. Efremova*, and V. S. Urusov****

** Shubnikov Institute of Crystallography, Russian Academy of Sciences, Leninskiĭ pr. 59, Moscow, 117333 Russia*

e-mail: kuznetsov@ns.crys.ras.ru

*** Department of Geology, Moscow State University, Vorob'evy gory, Moscow, 119899 Russia*

Received October 4, 2002

Abstract—Different types of defect sites generated by the impurities of divalent (M^{2+}) and trivalent (M^{3+}) metals in the structure of potassium dihydrophosphate KH_2PO_4 (KDP) were revealed by crystal-chemical analysis and computer simulation. These sites cause different deformations of the crystal matrix by generating different local strains, which enhance the inhibiting effect of impurity atoms adsorbed on the surface. This fact accounts for the different influence of di- and trivalent cations on the growth kinetics and face morphology of KDP crystals. The effect of the M^{3+} ions is associated primarily with their adsorption on the face surfaces, whereas the influence of the M^{2+} ions results from their insertion into the surface layer of the crystal. *© 2002 MAIK "Nauka/Interperiodica".*

INTRODUCTION

In the theory and practice of crystal growth, the effect of impurity atoms on crystallization is related primarily to their adsorption on the surface of growth faces [1, 2]. Less attention has been given to the role of impurity particles introduced into the surface layer of the crystal [3], although they can have a profound effect under particular conditions. The lifetime of impurity atoms within the surface layer is much larger than that of adsorbed particles, due to which they more actively hinder the step motion. In addition, the insertion of impurities into the crystal lattice is accompanied by its deformation and cleavage of some chemical bonds, resulting in the generation of local strains in the vicinity of impurity ions [4]. The presence of local strains leads to an increase in the chemical potential of the material in the deformed regions of the crystal. Hence, when considering stoppers for the step motion, not only impurity atoms (which serve as stoppers in the case of surface adsorption), but also the regions of the crystal lattice deformed by the impurity atoms should be taken into account. The sizes of these regions are no smaller than that of the first coordination sphere around the impurity atom (ion). It was assumed [4] that local strains induced by impurities could substantially reduce the rate of crystal growth. A decrease in the rate of growth of strained crystals was demonstrated experimentally [5, 6].

Investigation of the influence of local strains induced by impurities on crystallization (the structural mechanism of impurity influence) calls for a knowledge of the structures of defect regions and the resulting deformations induced in the crystal matrix. The aim of this study is to analyze the mechanism of incorporation of impurities of di- and trivalent metals, which span a wide range of ionic radii, into the structure and examine the effect of these impurities on the growth kinetics and face morphology of KDP crystals. For this purpose, we performed a crystal-chemical analysis of the structure of potassium dihydrophosphate (KDP) and carried out a computer simulation of defect sites.

PROCEDURE FOR SIMULATION OF THE KDP STRUCTURE

The KDP structure containing impurities of divalent (Ni^{2+}, Co^{2+}, Fe^{2+}, Mn^{2+}, Ca^{2+}, Sr^{2+}, Ba^{2+}) and trivalent (Al^{3+}, Fe^{3+}, Mn^{3+}, Y^{3+}, La^{3+}) metals was simulated by energy minimization of interatomic interactions with the use of the GULP program package [7]. In calculations, we used the results of simulation of the ideal KDP structure obtained previously [8]. The effective charges of the impurity ions were taken equal to +2.7 and +1.9 e for M^{3+} and M^{2+}, respectively. The ionic radii after Shannon and Prewitt [9] were used in the discussion. In most of the calculations, the radius of the zone of substantial shifts in the direct vicinity of an impurity atom was taken equal to 4.5 Å, and the radius of the

exterior region was set equal to 11.5 Å. Outside the latter region, the structure can be assumed as nondistorted. The exceptions are the calculations of three-particle impurity clusters. In these calculations, the radii of the zones were increased to 6.5 and 16.5 Å, respectively.

The crystal-chemical analysis of the KDP structure performed by us previously [10] demonstrated that the interstitial cavities denoted as *M*1 and *M*2 with the coordinates (0.25, 0.35, 0.125) and (0.75, 0.22, 0.125), respectively, are the most probable positions for impurity cations. Large cations can replace the K^+ ions. For all ions under examination, both modes of their incorporation into the KDP structure were considered (for details of calculations, see the studies [11, 12]). Unlike the calculations performed earlier [11, 12], we carried out analogous calculations within the framework of a partially covalent model (taking into account the Morse potential). For crystals containing divalent impurity atoms, a harmonic component of the pair interaction potential for M^{2+}–O was also included. For a number of trivalent metals, the potassium position was not considered, because it cannot be occupied due to the small ionic radii of these elements. The calculations demonstrated that the introduction of the covalent component into the potential of the M^{3+}–O interatomic interaction (Morse potential) led to a change in the energy of defect formation but did not cause radical changes in the general pattern of the insertion of M^{3+} into the KDP structure considered in the study [12].

The calculations of the energy of the defects induced by divalent cations are more intricate. This homologous series involves cations, whose radii are close to the ionic radius of potassium. Hence, the K^+ cavity must be considered as a possible position along with the *M*1 and *M*2 positions. Because of this, an ionic model cannot adequately describe the M^{2+}–O interaction, and the latter was treated only in the partially covalent approximation. The introduction of the Morse potential as a covalent component imparts a particular rigidity to the metal–oxygen configuration, because this potential does not monotonically decrease with increasing distance but has a minimum at a distance optimum for this ionic pair. The Morse potential is described by two coefficients, namely, the weighting coefficient D_{ij} and the soft-core component σ_{ij}. In addition to these coefficients, the Morse potential is characterized by the optimum distance between the components of the M^{2+}–O bond. The latter parameter is approximated as the sum of the corresponding radii. The D_{ij} parameter can be estimated as the energy of cleavage of a single covalent bond corrected for the coordination number [13]. In the equation for the Born–Meyer potential, the soft-core parameter σ_{ij} is related to the corresponding hard-core parameter ρ_{ij} by the equation $\sigma_{ij} = 1/(2\rho_{ij})$ [14]. The ionicity of the bond *f* necessary for the Morse potential can be easily estimated based on the charges of the atoms involved in the bond. Thus, the ionicity of a divalent metal atom with a charge of +1.9 e is 95%, and the ionicity of the oxygen atom (–1.14 e) is 57%. Hence, the ionicity of the M^{2+}–O bond is 76%.

However, even the introduction of the Morse potential does not allow one to adequately describe interactions at distances larger than the optimum values. Let us exemplify this situation (Fig. 1). Let us assume that the *A* cation is in a tetrahedral environment formed by oxygen atoms, and all bond lengths (*r*) are equal to the optimum distance. This ideal situation corresponds to a minimum in the curve of the pairwise Morse potential. A distortion of the polyhedron (two distances are shortened and two are elongated by the same value Δr) leads to a rise of the energy by $2\Delta E_1 + 2\Delta E_2$. It should be noted that this distortion has virtually no effect on the volume of the coordination polyhedron, and this polyhedron is still rather suitable for the *A* cation. However, if all four distances are elongated and the volume of the polyhedron becomes unfavorable for this cation, the energy will increase (because the Morse potential is substantially nonsymmetrical) by a smaller value $4\Delta E_2$, which defies the physical sense.

To solve this problem, we additionally introduced a second-order harmonic component into the potential. This component was described by a symmetric quadratic parabola

$$V_{ij} = k(R_{ij}^0 - R_{ij})^2. \quad (1)$$

The harmonic potential involves the optimum distance between the interacting ions (R_{ij}^0) and the weighting coefficient *k* as the parameters. The latter coefficient was taken equal to 2.36 eV/Å^2 based on the results of calculations. In addition, it was necessary to determine the parameter, which allows only atoms of the first coordination sphere to be involved in the zone of action of the harmonic potential. Taking into account the results of crystal-chemical analysis of the structure, the latter parameter was taken equal to 3 Å. Hence, the total interaction potential for trivalent cations (within the framework of a partially covalent model) assumes the

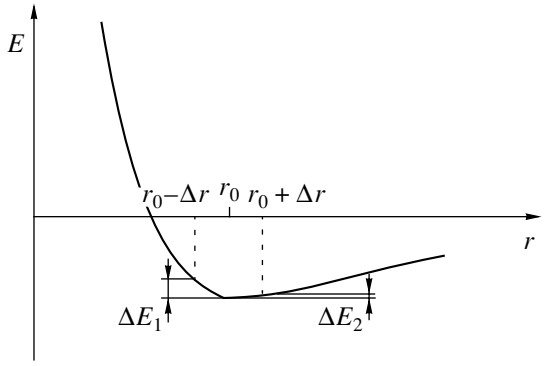

Fig. 1. Schematic representation of the Morse potential vs. the bond length *r*.

Table 1. Parameters of the $V_{ij}(R_{ij}, f)$ interatomic interaction potential for M^{3+}–O and M^{2+}–O calculated according to Eqs. (2) and (3), respectively

Cation	B_{ij}, eV	ρ_{ij}, Å	D_{ij}, eV	σ_{ij}, Å^{-1}	R_{ij}^0, Å
Al^{3+}	580.93	0.3118	0.412	1.604	1.91
Fe^{3+}	636.35	0.3239	0.425	1.516	2.11
Mn^{3+}	655.48	0.3214	0.441	1.556	2.03
Y^{3+}	700.92	0.3588	0.604	1.432	2.40
La^{3+}	701.96	0.3651	0.676	1.369	2.53
Ni^{2+}	1582.5	0.2882	0.43	1.7349	2.11
Co^{2+}	1491.7	0.2951	0.48	1.6943	2.14
Fe^{2+}	1207.6	0.3084	0.53	1.6213	2.16
Mn^{2+}	1007.4	0.3262	0.55	1.5328	2.21
Ca^{2+}	1090.4	0.3437	0.60	1.4546	2.40
Sr^{2+}	959.1	0.3721	0.59	1.3437	2.58
Ba^{2+}	905.7	0.3976	0.69	1.2575	2.76

Table 2. Energies of defect formation E generated by trivalent metals in the $M1$ and $M2$ positions

Cation	Radius of the cation, Å	E, eV	
		$M1$	$M2$
Al^{3+}	0.53	–15.84	–14.67
Fe^{3+}	0.55	–14.89	–13.32
Mn^{3+}	0.58	–14.38	–13.12
Y^{3+}	0.90	–12.11	–10.49
La^{3+}	1.03	–11.26	–9.49

following form:

$$V_{ij}(R_{ij}, f) = f^2[Z_iZ_j/R_{ij} + B_{ij}\exp(-R_{ij}/\rho_{ij})] - (1 - f^2)D_{ij}\{\exp[2\sigma_{ij}(R_{ij}^0 - R_{ij})] - 2\exp[\sigma_{ij}(R_{ij}^0 - R_{ij})]\}. \quad (2)$$

For divalent cations, the potential takes the following form:

$$V_{ij}(R_{ij}, f) = f^2[Z_iZ_j/R_{ij} + B_{ij}\exp(-R_{ij}/\rho_{ij})] - (1 - f^2)D_{ij}\{\exp[2\sigma_{ij}(R_{ij}^0 - R_{ij})] - 2\exp[\sigma_{ij}(R_{ij}^0 - R_{ij})]\} + k(R_{ij}^0 - R_{ij})^2, \quad (3)$$

where Z_i and Z_j are the charges of the atoms, R_{ij} is the distance between the corresponding ions, and B_{ij} is the weighting coefficient of the repulsion potential.

The parameters of the interatomic interaction potential for M^{n+}–O are given in Table 1. The defect energies calculated with the use of these parameters are listed in Tables 2 and 3 and presented in Fig. 2. It should be noted that there is no independent criterion for estimating the reliability of the interaction potential for M^{n+}–O involving the Morse potential and the harmonic component. The lack of such a criterion somewhat reduces the reliability of the absolute energies of defect formation but has no effect on their ratio in the series of di- and trivalent metals.

COMPARATIVE CHARACTERIZATION OF DEFECTS INDUCED BY DI- AND TRIVALENT METAL IONS

As can be seen from Tables 2 and 3 and Fig. 2, the $M1$ position corresponds to the minimum energies of defect formation for all trivalent cations and small divalent cations. The electroneutrality condition requires that the insertion of M^{3+} be accompanied by the removal of two K^+ cations and one proton, whereas the introduction of M^{2+} be accompanied by the displacement of only two K^+ cations [8, 11]. The calculations demonstrated that any other mode of valence compensation leads to the destabilization of the structure. The insertion of M^{2+} causes a shift of the nearest hydrogen atom from the position (0.125, 0.161, 0.125). For example, the hydrogen atom is displaced to the position (0.25, 0.099, 0.125) upon the insertion of Fe^{2+}, resulting in a distortion of a hydrogen bond (the O–H bond length increases from 1.27 to 1.29 Å, and the O···H–O angle decreases to 149°).

The introduction of impurity cations into the $M1$ position giving rise to vacancies leads not only to serious changes in the chemical composition, but also to substantial deformations of the nearest environment about the impurity ion A (Fig. 3). In addition, the detailed analysis of the geometry of its environment revealed distortions (sometimes substantial) of analogous adjacent pseudocavities. The sophisticated analysis of the environment about the Fe^{2+} ions [11] demonstrated that one of the adjacent voids (or cavities) B or C (Fig. 3a), which are equivalent with respect to the initial void, changes its configuration, so that it becomes more suitable for the incorporation of yet another impurity ion [11, 12]. If the B (or C) void is, in turn, occupied by the Fe^{2+} ion, the favorable conditions are created for the introduction of the next impurity ion into the D cavity. Hence, the chain can be propagated at an angle to the y-axis (or to the x-axis) (Fig. 3b). The geometric analysis demonstrated that these conclusions are true for all trivalent and small divalent cations. The linear chains ($ABDF\ldots$) are oriented at an angle of ~60° with respect to the z-axis of the crystal (Fig. 3b). The average angles for different types of bent chains (such as $ABDE\ldots$) can assume different values up to 75° and even somewhat larger.

However, although both di- and trivalent impurities can form such chains from a geometric standpoint, the electroneutrality principle does not preclude the formation of these chains only for divalent metals. Actually, the electroneutrality principle is retained upon intro-

duction of an M^{3+} ion into the *A* position (primary defect) [11]. The insertion of an impurity trivalent ion into the next unit of the chain (for example, into the *B* position) gives rise to an excess of the positive charge. The same situation is observed upon the introduction of an impurity M^{3+} ion into the *D* position. If the impurity is propagated further along the chain (the *E* or *F* position), the defect unit becomes again electroneutral. When occupied by impurity trivalent atoms, the next two units of the chain acquire excessive positive charges and so forth. In other words, although the formation of "clusters" by the impurity M^{3+} ions is favorable from a geometric standpoint, the accumulation of an excessive positive charge in certain regions of the chain hinders this process and requires the formation of additional vacancies, which is energetically unfavorable. For divalent cations, the situation is radically different. Thus, the impurity chain remains electroneutral throughout its length.

Hence, trivalent cations incorporated into the KDP crystal structure do not form clusters, and isolated *M*1 regions with the coordinates (0.25, 0.35, 0.125) are the main type of defects generated by trivalent cations over a wide range of ionic radii. The energy of formation of these defects increases with the growth of the ionic radius of impurity cations (Table 2), which indicates that larger cations have difficulties in incorporating into the structure. Since the *M*1 positions in the KDP structure are located in the {100} planes [8], the M^{3+} ions partially occupying these positions form loose networks parallel to the {100} and {010} planes. Let us call these networks as "impurity networks" of the *first type*. When intersecting, these networks form channels extended along the *z*-axis of the crystal and occupied by impurity ions (positions *A*, *G*, …, in Fig. 3b).

A more complex situation occurs in the homologous series of divalent cations. The calculations demonstrated that an increase in the ionic radius leads to a change in the defect type (Fig. 2, Table 3). Thus, the isolated *M*1 position is energetically most favorable for Ni^{2+}, which is the smallest of all cations under consideration (as in the case of M^{3+} ions). By contrast, chain clusters of the *ABDE*…, *ABDF*…, etc. types are most favorable for the Fe^{2+} and Mn^{2+} cations. As mentioned above, the chains can form angles of 60°–75° and larger with the *z*-axis. In the crystals, systems of these chains form "impurity networks" of the *second type*. The Co^{2+} cations are, apparently, statistically distributed over isolated positions and chains because of the close values of corresponding formation energies.

The calculations of the energies of defect formation giving rise to chains revealed a number of characteristic features. Thus, the Co^{2+} cations remain in the *M*1 positions upon the formation of three-particle clusters. In the case of formation of chains consisting of the Fe^{2+} or Mn^{2+} cations, the third member of the cluster is shifted in the course of energy minimization from the *D* position to the potassium vacancy. In systems containing

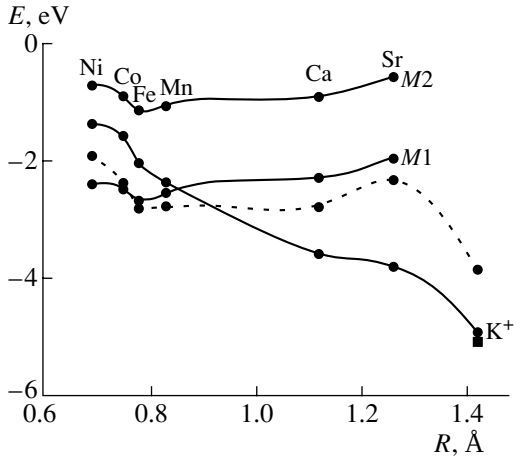

Fig. 2. Energies of defect formation in the *M*1, *M*2, and K^+ positions (with the removal of two K^+ cations) generated by divalent metal ions vs. the ionic radius *R*. The energies of formation of single defects and clusters are indicated by solid and dashed lines, respectively; ■ denotes the replacement of K^+ by Ba^{2+} through the mechanism of heterovalent isomorphism.

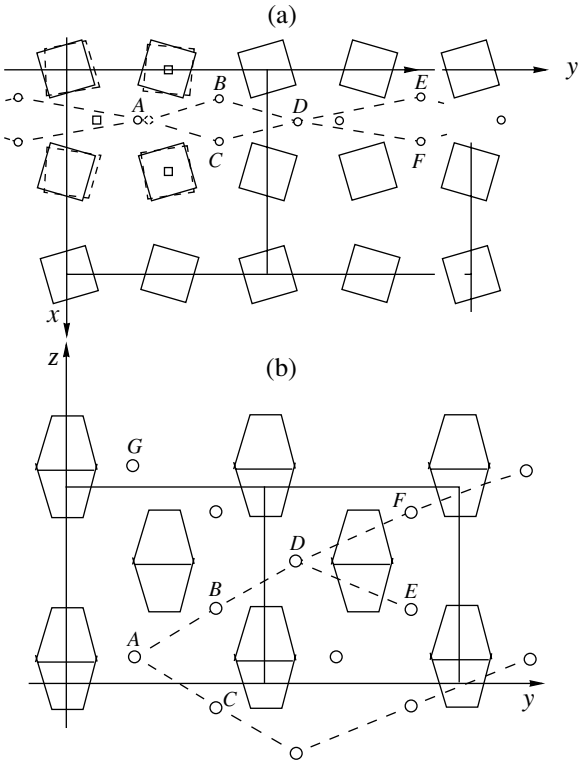

Fig. 3. The positions of the phosphorus–oxygen tetrahedra and the *A*…, *B*…, and *C* impurity ions in the *M*1 positions in the (a) (001) and (b) (100) planes.

the Ca^{2+}, Sr^{2+}, or Ba^{2+} cations, all the components of three-particle clusters are displaced to the potassium vacancies.

The shifts of small cations (Fe^{2+} and Mn^{2+}) to the potassium vacancies are attributable to the fact that the

Table 3. Energies of defect formation *E* generated by divalent metals in different positions

Cation	Radius of the cation, Å	*E*, eV				
		V_K ($K^+ + H^+$)*	V_K ($K^+ + K^+$)**	*M*1	*M*2	chain and "cluster" fragments
Ni^{2+}	0.69	0.63	−1.39	−2.40	−0.71	−1.94
Co^{2+}	0.75	0.14	−1.58	−2.50	−0.92	−2.39
Fe^{2+}	0.78	−0.31	−2.04	−2.69	−1.16	−2.82
Mn^{2+}	0.83	−0.63	−2.37	−2.57	−1.08	−2.82
Ca^{2+}	1.12	−1.75	−3.61	−2.32	−0.96	−2.81****
Sr^{2+}	1.26	−2.01	−3.83	−2.01	−0.62	−2.38****
Ba^{2+}	1.42	−3.17	−4.98	−3.17***	−3.17***	−3.92****

* Introduction into the potassium position accompanied by the removal of a potassium cation and a proton.

** Introduction into the potassium position accompanied by the removal of two potassium cations.

*** Displacement to the potassium position.

**** "Clusters" consisting of three impurity atoms in the potassium positions.

removal of a large amount of K atoms upon the formation of a chain gives rise to a local low-density region, in which most of the empty space is comprised of the former potassium polyhedra. Hence, it is more favorable to fill the low-density region with impurity ions by locating a portion of them (one of every three) in the potassium vacancies, in spite of the fact that the *M*1 cavities are favorable for the latter ions from a crystal-chemical standpoint. However, in the real crystal, the migration of the cation from the *D* cavity (*M*1 position) to the potassium vacancy is limited by the kinetic factors. Actually, the stepwise formation of impurity chains is most probable, e.g., only the insertion of the impurity ion *A* (Fig. 3) provides favorable conditions for the adjacent *B* pseudo-void to be occupied. Once the latter position is occupied, the *D* (or *E*) cavity, in turn, can be readily occupied. Hence, it is most likely that the cation from the *D* cavity is initially introduced into the *M*1 position and then migrates along the channels (which appear due to the absence of the K^+ and H^+ cations) to the K^+ position. An analogous migration in the crystal can be hindered, which means that most of impurity cations involved in clusters can remain in the *M*1 position that is favorable from a crystal-chemical standpoint. Nevertheless, these cations are in the energetically non-equilibrium state, and external factors, for example, the heating of the crystal, can facilitate their migration to the potassium vacancies. Conceivably, this is one of the reasons for the improvement of the optical properties of KDP crystals and the removal of internal strains in the course of annealing at 140–180°C [15, 16]. In the studies [15, 16], the improvement of the crystal quality was assigned to a change in the structure of internal defects, without going into the details of their structure.

For the bulky Sr^{2+} and Ba^{2+} cations with radii larger than 1.1 Å, the introduction into the *M*1 position is energetically unfavorable (Fig. 2, Table 3), and these cations replace the K^+ ions to form defects of the *third type*. In this case, the valence balance is achieved through the formation of either potassium or hydrogen vacancies, the former type being preferable (Table 3). In addition, the replacement of K^+ with Ba^{2+} according to the mechanism of heterovalent isomorphism $K^+ + P^{5+} = Ba^{2+} + Si^{4+}$ often occurs in natural minerals. The possibility of this replacement under laboratory conditions was confirmed by the fact that Si is always present in mother solutions of KDP. The corresponding calculations were carried out for the Ba^{2+} cations. The results of calculations demonstrated that the energy of formation of this double defect site is −5.12 eV, which corresponds to the energy minimum for the barium cation. The energy of the defect, which is generated by the simple replacement of K^+ by Ba^{2+} to form a potassium vacancy, is −4.98 eV (Table 3), which is only slightly higher than that corresponding to heterovalent isomorphism. Apparently, defects of both types are simultaneously present in the crystal. Hence, the K^+ position is more favorable for large impurity cations, which occupy this position either by replacing the K^+ ion to form an additional potassium vacancy or by forming complex defect sites through the mechanism of heterovalent isomorphism that is widespread in natural minerals. Apparently, the introduction of impurity ions into real crystals proceeds simultaneously through two mechanisms of replacement.

To summarize, impurity di- and trivalent metal ions form three types of defect sites in the KDP structure:

(1) isolated defect sites giving rise to "channels" along the *z*-axis of the crystal (the M^{3+} and Ni^{2+} cations and, partially, the Co^{2+} cations);

(2) impurity chains of the "cluster" type oriented at angles of 60°–75° and larger with respect to the *z*-axis of the crystal (cations with $r \sim 0.75$–1.1 Å; Fe^{2+} and Mn^{2+} cations and, partially, Co^{2+} cations);

(3) defect sites in the K^+ positions generated both through the formation of potassium vacancies and the mechanism of heterovalent isomorphism.

The formation of different types of defect sites is responsible for different degrees of deformation of the KDP crystal lattice. A comparison of the energies of defect formation and analysis of local distortions in the KDP structure caused by impurity ions [11, 12] demonstrated that M^{3+} ions generate weaker local strains in the structure as compared to those induced by M^{2+} ions.[1] Although the Ni^{2+} (partially, Co^{2+}) ions generate defect sites analogous to the M^{3+} sites, they cause stronger local strains in the structure. Even more substantial strains occur upon the formation of impurity chains of M^{2+} ions. In contrast, the incorporation of M^{2+} into the potassium position with the formation of an additional potassium vacancy or through the mechanism of heterovalent isomorphism (for example, $K^+ + P^{5+} = Ba^{2+} + Si^{4+}$) causes weaker strains. In the latter case, the somewhat smaller radius of the Ba^{2+} ion is compensated by the larger size of the $[SiO_4]$-tetrahedron.

INFLUENCE OF M^{3+} AND M^{2+} IMPURITIES ON THE GROWTH KINETICS AND FACE MORHOLOGY OF KDP CRYSTALS

Crystals of KDP were grown in the kinetic mode according to a procedure described previously [17] at ~50°C and by the evaporation of a solvent at room temperature. The surface morphology of the crystal faces was studied on a Neophot microscope.

Impurity di- and trivalent cations exert essentially different effects on the kinetics of growth of the KDP faces [18]. In the former case (Ni^{2+} or Co^{2+}), the growth rate of the faces (R) either weakly depends on the concentration of impurities C_{imp} ({101} faces) or monotonically decreases as C_{imp} is increased ({100} faces) (Fig. 4). This character of the $R(C_{imp})$ dependence is retained within the supersaturation σ range up to 0.06.

Trivalent cations (Fe^{3+} or Cr^{3+}) are characterized by another type of $R(C_{imp})$ dependence (Fig. 5). The growth rate of the {101} faces first increases as the concentration of impurity atoms is increased and then sharply decreases (the "catalytic" effect of impurities). In the case of Fe^{3+}, the catalytic effect is observed only at high supersaturations (σ is ~0.063) and is absent at lower σ (Fig. 5b). The growth rates of the {100} prism faces monotonically decrease as C_{imp} is increased at all supersaturations.

The M^{2+} and M^{3+} impurities also have different effects on the face morphology of the KDP crystals.

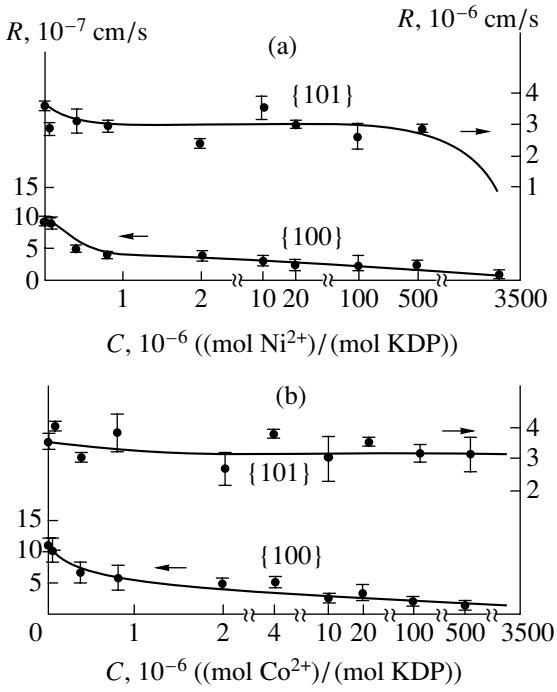

Fig. 4. Growth rate of the crystal faces vs. the concentrations of (a) Ni^{2+} and (b) Co^{2+} ions; $\sigma = 0.029$.

The addition of small amounts of Fe^{3+} or Cr^{3+} ($\leq 10^{-6}$ mol/mol) to the initial solution leads to only slight changes in the face topography and is manifested in a somewhat larger irregularity of thin growth layers. An increase in C_{imp} leads to the formation of thin extended macrosteps on the surfaces of the {100} faces, which are clearly seen under an optical microscope. These macrosteps move along the [001] direction (Fig. 6a). Small peaked or flattened growth hillocks are observed on terraces. Most of these hillocks are elongated with the long axes forming angles of ~63°–84° with the z-axis of the crystal. A further increase in C_{imp} leads to tapering typical of KDP crystals, the {100} face assuming a stepwise shape, and macrosteps separating into individual fragments (Fig. 6b).

Radically different changes in the morphology of the {100} faces are observed in the presence of Co^{2+} and Ni^{2+} impurities. These impurity cations cause virtually no tapering of KDP crystals. Thus, the tapering angle is no larger than 1.5°–2.5° even at high concentrations of Ni^{2+} and Co^{2+} (~10^{-2} mol/mol). Large ellipsoidal growth hillocks are important elements of the surface topography of the {100} faces. The long axes of most of these hillocks form angles of 65°–79° with the z-axis of the crystal. The density of growth hillocks increases as the impurity concentration is increased (Figs. 7a and 7b). The growth layers generated from the centers of the growth hillocks give rise to macrosteps grouped into echelons of steps with rounded faces. The

[1] For example, the energies of formation of single defects caused by di- and trivalent iron cations in the $M1$ position within the framework of the same partially covalent model (without considering the harmonic component) are –2.73 and –14.89 eV, respectively; within the same model, the calculated energy of defect formation upon the replacement of K^+ by Ba^{2+} with the simultaneous formation of one more K^+ vacancy is –3.29 eV.

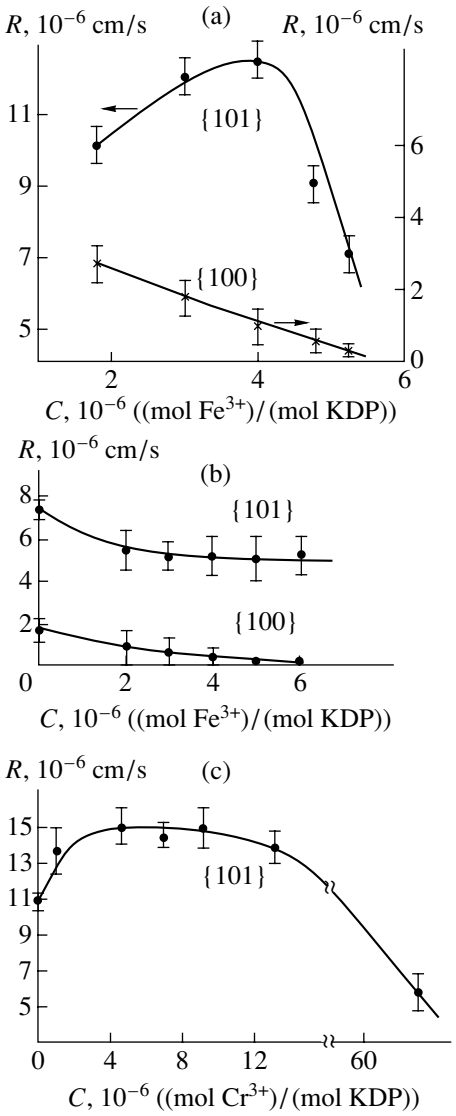

Fig. 5. Growth rate of the crystal faces vs. the concentrations of Fe^{3+} ions for (a) $\sigma = 0.063$ and (b) $\sigma = 0.03$ and (c) the concentration of Cr^{3+} ions for $\sigma = 0.063$.

formation of broad terraces containing rare thin macrosteps on the surface is typical of the KDP crystals.

Another characteristic feature of the surface morphology of the {100} faces in the presence of Co^{2+} or Ni^{2+} impurities is the formation of a "ribbon" topography (Fig. 7c). Thus, the echelons of steps are split into narrow bands parallel to the *z*-axis of the crystal. Weak evidence for the "ribbon" topography is observed under an optical microscope even at $C_{imp} \sim 10^{-5}$ mol/mol, but this topography becomes more pronounced at higher impurity concentrations. The formation of the rough {100} surface at high concentrations of impurity Ni^{2+} cations (>10^{-2} mol/mol) (Fig. 7d) and the formation of a columnar texture in the crystals are extreme manifestations of this effect. The columnar texture can even be split into needle-like individuals with a thickness up to 1 mm.

The effect of large divalent cations (Ba^{2+}) is most clearly manifested in the morphology of the {101} faces and imperfections of growth pyramids of these faces. Even a low concentration of Ba^{2+} ions in a crystallization solution (~10^{-5} mol/mol) leads to a substantial roughness of the {101} surface. This surface has a bumpy texture in the reflected light. The formation of high growth macrosteps is typical of the KDP crystals. At $C_{Ba} = \sim 5 \times 10^{-5}$ mol/mol, thin milk white interlayers parallel to the {101} faces and consisting of finest inclusions of the mother liquor appear in the {101} growth pyramids. A further increase in the concentration of the Ba^{2+} ions leads to turbidity of the bulk of the KDP crystal.

RESULTS AND DISCUSSION

The effect of impurities on the growth kinetics and face morphology of KDP crystals is determined by the simultaneous action of impurity cations adsorbed on the surface and introduced into the surface layer [18]. Due to the combined action of the thermodynamic factor responsible for an increase in the growth rate of faces and kinetic factors causing a decrease in the growth rate, the presence of adsorbed impurities can lead to a complicated $R(C_{imp})$ dependence with the maximum R at low concentrations of C_{imp} [19, 20]. Halting the moving growth steps, impurities present in the surface layer of the crystal enhance the inhibiting effect of ions adsorbed on the surface. The larger the local strains generated in the crystal, the more substantial the influence of the impurities. Correspondingly, the contribution of the thermodynamic factor to the total impurity effect is reduced. In the presence of strong strains in the crystal lattice, the role of the thermodynamic factor can be reduced to zero, and the $R(C_{imp})$ dependence becomes monotonically decreasing [18].

All of the aforesaid provide the basis for the discussion of our results, because the above-considered defect sites cause different deformations of the surrounding crystal space and generate different strains. Although the impurity sites were simulated in the bulk of the crystals, it can be assumed that the main characteristic features of their formation are also true for the surface layers. In particular, strains in the surface layers generated by different defect sites are increased in the same order as they appear in the bulk of the crystal. From this viewpoint, the experimental results can be interpreted as follows.

The effect of trivalent cations on the growth kinetics and face morphology of the KDP crystals is determined primarily by their adsorption on the crystal faces. This assumption is evidenced by the pronounced tapering of KDP crystals attributed to adsorption of impurities [21, 22] and the "catalytic" effect observed for the {101} faces. Apparently, the M^{3+} cations incorporated into the surface layer are of minor importance, which is in good agreement with small deformations of the crys-

tal lattice caused by the introduction of these cations. However, the situation somewhat changes when supersaturation σ is smaller than 0.06. Thus, the "catalytic" effect is absent, and the growth rates of the {101} and {100} faces monotonically decrease as the impurity concentration is increased. This change in the $R(C_{imp})$ dependence can be attributed to an increase in the concentration of Fe^{3+} in the crystal, because the trapping coefficient of Fe^{3+} in the KDP crystals substantially increases at low σ [23]. This increase in the concentration is accompanied by an enhancement of local strains in the crystal lattice, which become, apparently, sufficiently large that they completely suppress the contribution of the thermodynamic factor.

Another situation is observed in crystals containing Co^{2+} or Ni^{2+} impurities, which cause stronger deformations of the crystal matrix. The effects associated with adsorption of impurities (tapering and the "catalytic" effect) are either absent or weak. The $R(C_{imp})$ dependences for the {100} faces are monotonically decreasing, and the observed change in the surface topography of the {100} faces is typical only of these cations. Hence, it was concluded that the Co^{2+} and Ni^{2+} ions introduced into the surface layer of the crystal have a determining effect, whereas impurity cations adsorbed on the surface are of minor importance. Thus, the appearance of a "ribbon" surface topography probably results from the retarding action of impurities located in the "channels" parallel to the [001] direction. A high density of these centers in the bulk of the crystal provokes the development of block boundaries along the (100) and (010) planes followed by the formation of a columnar texture. This situation is observed in the presence of the Ni^{2+} ions. The weaker effect of the Co^{2+} ions as compared to the Ni^{2+} ions (at their equal concentrations in solutions) is, apparently, associated with the fact that the Co^{2+} ions are statistically distributed between networks of the first and second types, and these ions are present at a lower concentration in the "channels" parallel to the [100] direction.

It is noteworthy that the orientations of the long axes of ellipsoidal growth hillocks (which form angles of 65°–79° with the *z*-axis) differ from those of the *ABD*… impurity chains (60°–75° and larger). Previously, analogous ellipsoidal growth hillocks have been observed in the KDP crystals grown from pure solutions without special additives [24, 25]. According to the results of the study [24], the angle between the long axis of the growth hillock and the *z*-axis of the crystal was 67°. This orientation of growth hillocks cannot be related to the own structure of the KDP crystals [25]. Presumably, this effect is associated with the hindering action of impurity chains. It is known that growth hillocks have a rounded shape at a low supersaturation, and this fact was accounted for by adsorption of impurities from the solution [25]. At higher supersaturations, the hindering barrier is overcome, and the step motion is accelerated. Evidently, the growth steps would move more rapidly along impurity chains, whereas their motion in the perpendicular direction would be hindered. As a result, growth hillocks attain a shape that is elongated along the impurity chains. According to the results of the study [24], impurities can have a noticeable effect on the crystallization process even at very low impurity concentrations (~0.3 ppb), which are much lower than their concentrations in the solutions of KDP used for crystallization. Hence, impurity chains in crystals grown from "pure" solutions can be formed by background impurities of divalent metals with the ionic radii varying from ~0.75 to ~1.1 Å.

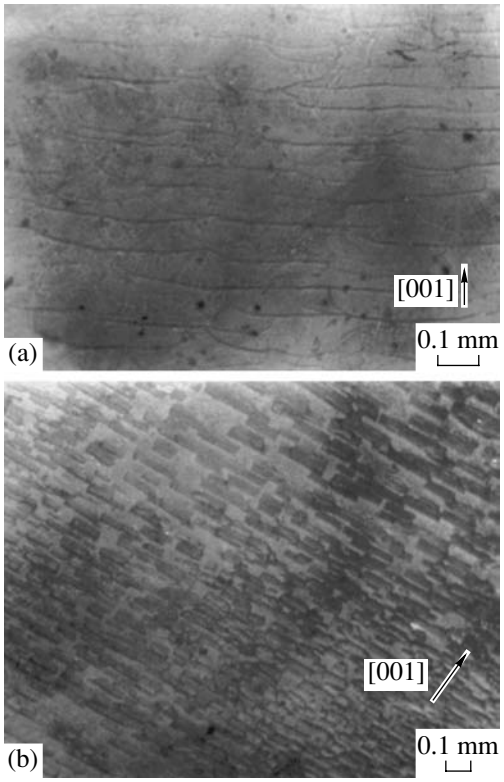

Fig. 6. Surface of the {100} faces of the KDP crystal grown in the presence of Cr^{3+}: (a) $C_{Cr^{3+}} = 10^{-6}$ and (b) 9.3×10^{-6} mol of Cr^{3+}/mol of KDP.

The proposed mechanism provides an explanation for the specific orientation of ellipsoidal growth hillocks on the {100} faces. It is noteworthy that we found no growth hillocks whose long axes form angles smaller than 60° with the *z*-axis of the crystal. This angle is the minimum for the *ABDF*… chains.

A strong influence of the Ba^{2+} impurity on the morphology of the {101} faces primarily results from the structure of these faces and also from the fact that the large Ba^{2+} cations occupy the K^+ positions in the KDP structure. According to the results of the study [26], the (101) surface is always composed of the K^+ cations forming a positively charged layer. On the one hand, this hinders the adsorption of positively charged impurity ions present in the solution on the (101) surface and

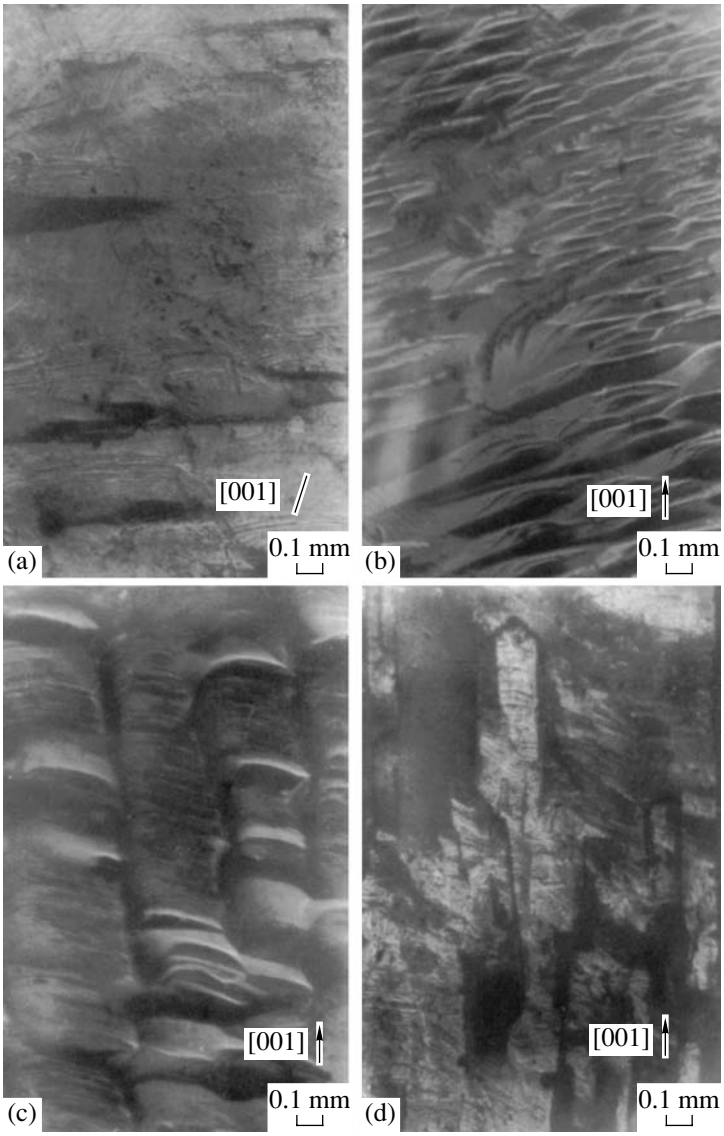

Fig. 7. Surface of the {100} faces of the KDP crystal grown in the presence of Co^{2+} or Ni^{2+} ions: $C_{Co^{2+}}$ = (a) 10^{-7}, (b) 4×10^{-6}, and (c) 10^{-2} mol of Co^{2+}/mol of KDP; (d) $C_{Ni^{2+}} = 2 \times 10^{-2}$ mol of Ni^{2+}/mol of KDP.

accounts for their lower concentration in the {101} growth pyramid, as compared to that in the growth pyramids of the prism faces. On the other hand, this structure of the (101) surface facilitates the replacement of K^+ by Ba^{2+} and generation of defect sites either with the formation of additional potassium vacancies or through the mechanism of heterovalent isomorphism. These processes occur very vigorously, because (according to our estimates) the effective coefficient of trapping of the Ba^{2+} cations in the KDP crystals is ~13 (under the conditions of our experiments) [13], which is much larger than the trapping coefficients of Fe^{3+}, Cr^{3+}, Ni^{2+}, and Co^{2+}. Because of this, the concentration of defect sites generated by Ba^{2+} is high, which leads to the surface roughening of the {101} faces and, finally, to the active trapping of solution microinclusions in these faces.

CONCLUSIONS

The results of our study demonstrated that impurities of di- and trivalent metals generate different types of defect sites in the KDP structure. These defect sites cause different deformations of the crystal matrix by generating local strains. The calculated energies of defect formation and analysis of distortions of the crystal lattice in the nearest environment around the impurity ions provide evidence that the minimum strains occur upon the introduction of trivalent metal cations. Divalent metal cations, which form both isolated sites

(including the mechanism of heterovalent isomorphism) and impurity chains in the structure, generate stronger strains in the crystal lattice. Impurity atoms in the surface layer of the crystal and local strains generated by these atoms enhance the inhibiting effect of impurities adsorbed on the surface. This is responsible for the different effects of di- and trivalent ions on the growth kinetics and face morphology of the KDP crystals. The experimental data suggest that the effect of M^{3+} impurities is determined primarily by the ions adsorbed on the surface, whereas the influence of M^{2+} impurities is mainly associated with their introduction into the surface layer of the crystal.

ACKNOWLEDGMENTS

This study was supported by the Russian Foundation for Basic Research, project no. 99-03-32557.

REFERENCES

1. A. A. Chernov, E. I. Givargizov, Kh. S. Bagdasarov, *et al.*, in *Modern Crystallography*, Vol. 3: *Crystal Growth*, Ed. by B. K. Vainshtein, A. A. Chernov, and L. A. Shuvalov (Nauka, Moscow, 1980; Springer-Verlag, Berlin, 1984).
2. K. Sangwal, Prog. Cryst. Growth Charact. **32**, 3 (1996).
3. V. V. Voronkov, Kristallografiya **19** (3), 475 (1974) [Sov. Phys. Crystallogr. **19**, 296 (1974)].
4. N. T. Barrett, G. M. Lamble, K. J. Roberts, *et al.*, J. Cryst. Growth **94**, 689 (1989).
5. H. L. Bhat, J. H. Sherwood, and T. Shripathi, Chem. Eng. Sci. **42** (4), 609 (1987).
6. R. I. Ristic, J. N. Sherwood, and K. Wojciechowsci, J. Cryst. Growth **91**, 163 (1988).
7. J. D. Gale, *GULP, User Manual* (Royal Institution and Imperial College, London, 1992–1994).
8. T. A. Eremina, V. A. Kuznetsov, T. M. Okhrimenko, *et al.*, Kristallografiya **43** (5), 906 (1998) [Crystallogr. Rep. **43**, 852 (1998)].
9. R. D. Shannon and C. T. Prewitt, Acta Crystallogr., Sect. B: Struct. Crystallogr. Cryst. Chem. **25**, 925 (1969).
10. T. A. Eremina, V. A. Kuznetsov, T. M. Okhrimenko, *et al.*, Kristallografiya **41** (4), 717 (1996) [Crystallogr. Rep. **41**, 680 (1996)].
11. T. A. Eremina, N. N. Eremin, N. G. Furmanova, *et al.*, Kristallografiya **46** (1), 82 (2001) [Crystallogr. Rep. **46**, 75 (2001)].
12. T. A. Eremina, V. A. Kuznetsov, N. N. Eremin, *et al.*, Kristallografiya **46** (6), 1072 (2001) [Crystallogr. Rep. **46**, 989 (2001)].
13. A. I. Efimov, *Properties of Inorganic Compounds: a Handbook* (Khimiya, Leningrad, 1983).
14. V. S. Urusov and N. N. Eremin, Phys. Chem. Miner. **22** (3), 151 (1995).
15. K. Fujioka, S. Matsuo, T. Kanabe, *et al.*, J. Cryst. Growth **181**, 265 (1997).
16. Y.-J. Fu, Z.-S. Gao, S.-L. Wand, *et al.*, Cryst. Res. Technol. **35** (2), 177 (2000).
17. V. A. Kuznetsov, T. M. Okhrimenko, and M. Rak, J. Cryst. Growth **193**, 164 (1998).
18. V. A. Kuznetsov, T. A. Eremina, N. N. Eremin, *et al.*, Kristallografiya **45** (6), 1120 (2000) [Crystallogr. Rep. **45**, 1035 (2000)].
19. R. J. Davey, in *Industrial Crystallization 78*, Ed. by E. J. de Jong and S. J. Jančić (North-Holland, Amsterdam, 1979).
20. I. Owczarek and K. Sangwal, J. Cryst. Growth **102**, 574 (1990).
21. B. Dam, P. Bennema, and W. J. P. Enckevort, J. Cryst. Growth **74**, 118 (1986).
22. I. Owczarek and K. Sangwal, J. Cryst. Growth **99**, 827 (1990).
23. C. Belouet, E. Dunia, and J. F. Petroff, J. Cryst. Growth **23**, 243 (1974).
24. A. A. Chernov and L. N. Rashkovich, Preprint No. 01/1986, IK AN SSSR (Institute of Crystallography, Academy of Sciences of USSR, Moscow, 1986).
25. J. W. Noor and B. Dam, J. Cryst. Growth **76**, 243 (1986).
26. S. A. de Vries, P. Goedtkindt, S. L. Bennett, *et al.*, Phys. Rev. Lett. **80** (10), 2229 (1998).

Translated by T. Safonova

Crystallography Reports, Vol. 47, Suppl. 1, 2002, pp. S86–S98.

SOLUTION GROWTH

Mechanism of Growth of ZnO Single Crystals from Hydrothermal Alkali Solutions

L. N. Demianets, D. V. Kostomarov, I. P. Kuz'mina, and S. V. Pushko

Shubnikov Institute of Crystallography, Russian Academy of Sciences, Leninskiĭ pr. 59, Moscow, 117333 Russia

e-mail:demianets@ns.crys.ras.ru

Received October 4, 2002

Abstract—The results obtained in experiments on the growth of zinc oxide, ZnO, under hydrothermal conditions are generalized. The polar growth and nonstoichiometry of ZnO crystals are analyzed in terms of crystal chemistry with due regard for the physicochemical conditions of the growth medium. The effect of the Li^+ and of di- and trivalent metal (Co^{2+}, Fe^{2+}, Mn^{2+}, Fe^{3+}, Mn^{3+}, Sc^{3+}, In^{3+}) impurities on the kinetics and some physical characteristics of ZnO crystals are studied, and the chemical reactions occurring on the surfaces of the (0001) and $(000\bar{1})$ faces are considered. © *2002 MAIK "Nauka/Interperiodica".*

INTRODUCTION

Zinc oxide (zincite, ZnO) is one of the well-known compounds in which interest has not diminished for several recent decades because of the wide spectrum of its possible applications in various modern technologies and medicine [1–4]. Zinc oxide crystals can be prepared in the form of nanopowders, films, ceramics, and single crystals. The latter can be grown from vapor phase, flux, and aqueous solutions under elevated pressures and temperatures. Of special interest is the method of hydrothermal crystallization, which allows the synthesis of large ZnO crystals at comparatively low (below 400°C) temperatures. The large number of experiments on growth of ZnO crystals from hydrothermal alkali media proves their pronounced polar growth along the *c*-axis, which is the consequence of the polarity of its crystal structure and the specific characteristics of the crystallization medium.

Irrespective of the growth method used, the ZnO crystals are always nonstoichiometric. The concentration of superstoichiometric Zn atoms at interstitials can attain 10^{15}–10^{19} at/cm^3 [5]. Less nonstoichiometric ZnO crystals can be obtained in two ways: first, by introducing oxygen into a crystal (ion implantation), i.e., by neutralizing the charge of the excessive Zn^{2+} ions, and second, by partial substitution of Zn^{2+} ions by ions having a lower positive charge (Li^+, H^+) during crystallization or special treatment of the grown crystals (annealing in Li-containing salts at the temperatures of about 700°C). The most effective method for decreasing nonstoichiometry of ZnO crystals is *in situ* doping with Li^+ ions, with the role of these ions being dependent on their position in the crystal lattice [6]. The Li^+ ions have approximately the same size as Zn^{2+} ions, $r(Li^+) = 0.73$ and $r(Zn^{2+}) = 0.74$ Å, and, thus, can both substitute Zn^{2+} ions at the cationic sites (Li'_{Zn}) or else they can enter the interstitials (Li_i^+). The substitution of Zn^{2+} ions by Li^+ at the cationic sites of the lattice results in the formation of the acceptor centers whose concentration increases in crystals grown under oxidative conditions. In this case, lithium diffusion is accompanied by the occurrence of the substitution reaction. As a result, lithium substitutes zinc in the crystal lattice, whereas during subsequent annealing, the interstitial zinc diffuses to the sample surface and is oxidized there. Donor centers arise in ZnO crystals because of the substitution of Zn^{2+} or O^{2-} ions at the lattice sites by impurity ions or because of their location at the interstitials. The typical donors in the ZnO lattice are the interstitial Li^+ and H^+ ions, i.e., Li_i^+ and H_i^+ [7].

The electrical conductivity of ZnO depends on the amount of Zn^{2+} ions with respect to O^{2-} (sample stoichiometry) and the real structure of the crystal (intrinsic defects associated with the presence of Zn at the interstitial, Zn_i^{2+}, or the defects associated with the oxygen vacancies V_O, playing the role of donors). The point defects (Zn_i, V_O) determine high conductivity of ZnO crystals; usually, the resistivity of crystals grown hydrothermally does not exceed 10^4 Ω cm.

Zincite crystals are rather sensitive to the presence of impurities in the growth systems; impurities can change the growth kinetics, habit, color, and various physical characteristics of the crystals over wide ranges. The impurities entering the cationic positions are elements of groups II and III of the Periodic System, whereas elements of group VII enter the anionic positions. Elements of groups I and V can play the role of acceptor impurities. Doping of ZnO with Li^+ ions sup-

1063-7745/02/47S1-S0086$22.00 © 2002 MAIK "Nauka/Interperiodica"

presses *n*-type conductivity and promotes the appearance of *p*-type conductivity.

In this article, we generalize the results obtained in our experiments on the solubility and crystallization kinetics of ZnO under hydrothermal conditions and analyze the results of hydrothermal experiments on growth of ZnO crystals performed by various researchers for several recent decades. To establish the growth mechanism in this case, we analyzed the structures of the individual faces of ZnO crystals and calculated the main characteristics of these faces which determine the crystal habit (the elemental composition, thicknesses, and reticular densities of the elementary layers of the face structure).

EXPERIMENTAL

Zincite single crystals were grown on seeding plates by method of direct temperature gradient in the ZnO–KOH–LiOH–H_2O system (the concentration of KOH solutions was 5–9 *m* and of LiOH solutions, 0.8–1.4 *m*, where *m* is molality (molar weight concentration, mol/1000 g H_2O). The experimental method and the apparatus used were similar to those described elsewhere [8]. The preliminary experiments were performed with the use of KOH, LiOH, NaOH, and NH_4OH aqueous solutions as mineralizers. The temperature in the growth zone ranged within 230–300°C; the temperature difference between the growth and dissolution zones (along the external wall of the autoclave) ranged within 5–75°C; the pressure varied within 50–350 MPa. The seeds were plane-parallel plates cut from hydrothermally grown bulk ZnO single crystals normally to the given crystallographic directions. Prior to experiments, the seeding plates were etched in the HCl and NaOH solutions to remove the layers disturbed during sawing of the samples.

The effect of impurities on growth and characteristics of ZnO single crystals was studied at a constant concentration of the mixed 5.15 *m* KOH + 1.2 *m* LiOH solution. The impurities (M^+, M^{2+}, and M^{3+}) were introduced into the crystallization medium in the form of various salts, oxides, and hydroxides (NH_4OH, NH_4Cl, LiF, LiOH, NaF, CdO, MnO, CoO, FeO, F_2O_3, Sc_2O_3, Mn_2O_3, Ga_2O_3, In_2O_3, etc.). The impurity content in the initial charge was varied from tenths of one up to 5 wt %.

The theoretical calculations and the analysis of the structure of the crystal faces were performed by the method described in [9] using the Diamond program.

In order to attain a composition close to stoichiometric, the crystals were either doped *in situ* with Li^+ during growth or subjected to high-temperature annealing in the presence of lithium carbonate.

Since doped ZnO crystals are characterized by exciton–phonon ultraviolet luminescence and luminescence in the long-wavelength range of the spectrum (caused by impurities), crystal quality was studied by optical and spectroscopic methods [1]. We do not consider here all the data on the physical properties of ZnO crystals studied. In some cases, we discuss only those physical characteristics which help us to understand the influence of impurities or the growth conditions on the growth kinetics and the quality of the crystals grown.

RESULTS AND DISCUSSION

Choice of Solvent

The analysis of the known data and the results of our experiments showed that ZnO crystals can be grown from alkali solutions under hydrothermal conditions. The KOH alkali is more preferable than NaOH because of the larger ion radius of K^+ and, thus, the lower probability of its incorporation into the ZnO lattice. The study of the cathodoluminescence spectra showed that ZnO crystals grown from KOH solutions, with the other conditions being the same, have better crystal structure than the ZnO crystals grown from NaOH solutions. A higher KOH concentration increases the ZnO solubility (Table 1). This table shows that the ZnO solubility in a KOH aqueous solution increases both at higher KOH concentrations and higher temperatures, which allows one to attain the necessary supersaturation $\Delta S'$ in the growth zone at the direct temperature difference Δt. The ZnO solubility at the constant temperature (t = 250°C) increases by an order of magnitude (from 0.124 to 1.281 *m*) with an increase in C_{KOH} from 3 to 10 *m*, which results in a higher supersaturation $\Delta S'$ in the growth zone ($\Delta S'$ 0.003, 0.011, 0.029 *m* at Δt = 10°C and C_{KOH} 3.07,5.15, and 10.0 *m*, respectively).

In pure KOH solutions, ZnO crystals grow at high rates (by about 1.5 times higher than in NaOH solutions). As a result, the grown crystals contain a larger number of intrinsic defects and are pronouncedly nonstoichiometric. High growth rates also complicate control of the growth process.

The introduction of NH_4OH increases growth rates and results in poorer crystal quality. The growth rate of the $(10\bar{1}0)$ face increases by almost five times, but this increase is accompanied by the initiation of skeletal growth.

Pure LiOH is too weak a solvent to provide the supersaturations necessary for growth at moderate temperatures (200–300°C) of hydrothermal crystallization.

The best solvents for ZnO are mixed KOH + LiOH solutions [1, 3, 4, 7, 8, 10–18]. The composition and concentration of mixed solutions are optimized based on the experimental data on the crystallization kinetics of zincites from 3–9 *m* KOH in the presence of 0.2–3.0 *m* LiOH solutions and the quality of the grown crystals. The use of mixed solutions ((5–6 *m*) KOH and (1–2 *m*) LiOH) allows one to grow ZnO crystals with the minimum halfwidths of the exciton band in the reflection spectra and the minimum luminescence intensity in the red range of the spectrum, which indicates the high quality of the grown crystals. With a fur-

Table 1. Solubility S' of zinc oxide in KOH aqueous solutions at 250–400°C

t, °C	C_{KOH}, m	S', m	Reference	t, °C	C_{KOH}, m	S', m	Reference
250	3.07	0.124	*	360	2.07	0.090	[4]
250	5.15	0.324	*	360	3.07	0.174	*
250	7.03	0.665	*	360	4.30	0.318	[4]
250	7.89	0.879	*	360	6.47	0.601	[4]
250	10.00	1.281	*	360	7.03	0.833	*
300	6.47	0.532	[4]	360	9.07	0.853	[4]
300	7.89	0.973	*	400	1.98	0.351	[10]
300	10.00	1.436	*	400	4.46	0.847	[10]
304	5.15	0.374	*	400	6.47	0.626	[4]
350	10.00	1.520	*	400	7.89	1.194	*
360	0.65	0.056	[4]	400	16.67	1.317	[10]

* Results obtained in the present study.

ther increase of KOH concentration, the growth rate remains constant within the measurement error; at an LiOH content in the solution up to $C_{LiOH} \sim 1.4$ m, the resistivity of the crystals increases from $10–10^2$ to 10^8 Ω cm. A further increase in the LiOH concentration in the solution does not change the resistivity.

Characterization of Grown ZnO Crystals

The ZnO crystals grown under hydrothermal conditions are usually faceted by two monohedra, (0001) and $(000\bar{1})$; the faces of the $\{10\bar{1}0\}$ hexagonal prism and the $\{10\bar{1}1\}$ and $\{10\bar{1}2\}$ faces of hexagonal pyramids. Sometimes the habit also has prismatic $\{11\bar{2}0\}$ faces. The crystal color varies from bright yellow or greenish yellow to yellowish brown. The yellowish color is not associated with the presence of impurities but depends on the specific properties of the crystallization medium (growth from alkali solutions occurs under reductive conditions), which results in nonstoichiometry. The resistivity of grown crystals ranged within $10^3–10^4$ Ω cm. The subsequent treatment of the crystals under the specified conditions indicated in [1] increased their resistivity up to 10^{11} Ω cm.

Since the initial mixed solutions contain lithium, the latter is also present in the crystals grown from these solutions. The specific features of hydrothermal synthesis allows one to synthesize ZnO crystals with relatively high Li^+ concentrations (>18 at/cm^3). At an Li content in the crystals of about 3×10^{-4}%, the resistivity is $\rho \sim 10^3$, and at an Li content of 1×10^{-3}% the resistivity equals $\rho \sim 10^9$ Ω cm [1, 19]. A considerable increase in resistivity of such crystals indicates that the majority of Li atoms occupy interstitials. At high Li concentrations, the condition of electroneutrality of the compound is met; i.e., the number of incorporated lithium ions is twice as large as the number of substituted zinc ions ($Zn^{2+} \longrightarrow 2Li^+$).

Various growth pyramids consist of crystalline material of considerably different quality. The samples cut from ⟨0001⟩ growth pyramids have higher quality than those cut from $\langle 000\bar{1} \rangle$ ones. This is confirmed by the data on the halfwidth of the main exciton reflection maxima, equal to 14 Å and 20–23 Å for the samples cut out from the ⟨0001⟩ and $\langle 000\bar{1} \rangle$ pyramids, respectively. The crystalline material of the ⟨0001⟩ growth pyramid is characterized by more intense exciton radiation, which indicates a smaller number of nonradiative centers in the growth pyramid of the $(000\bar{1})$ face compared to others.

The samples cut from the growth pyramid of the negative monohedron are characterized by considerably less intense yellow–orange luminescence than the samples cut from the ⟨0001⟩ growth pyramid. This indicates a small number of Li^+ ions in the acceptor state in the ⟨0001⟩ growth pyramid and is also confirmed by high conductivity of the samples ($\sigma > 0.05$ Ω^{-1} cm^{-1}). There is almost no thermoluminescence from the samples cut from the ⟨0001⟩ growth pyramid, which also indicates a large proportion of nonradiative recombination centers.

Structure of Main Habit-Forming Faces of ZnO Crystals

The probability of Zn-containing complex being incorporated into the surface of a growing crystal is determined by the face structure (chemical composition, reticular density, electric charge, etc.) and the physicochemical characteristics of the growth medium. The atomic structure of any face is characterized by an elementary layer—the minimum structural unit of the

thickness d/m, where d is the interplanar spacing and m is the integer dependent on the face symmetry.

According to [19, 20], an elementary layer is a layer of minimum thickness Δ that can be formed on the surface of a growing crystal. The structure of this layer consists of the minimum number of characteristic planar nets. These layers are repeated in the crystal structure with an interval of d/m. The elementary layer is a "planar molecular net" in the Bravais lattice. The reticular density of this net, $\rho_{(hkil)}$, can be determined by comparing it with the reference net,

$$\rho_{(hkil)} = \rho_0\Delta_{(hkil)}/\Delta_0, \quad (1)$$

where ρ_0 and Δ_0 are the constants of the latter net.

To understand the growth mechanism and the probability of the attachment of Zn-containing complexes to various faces of a ZnO crystal, one has to know the structure of the faces. We analyzed the structures of the (0001), $(000\bar{1})$, $(10\bar{1}0)$, $(10\bar{1}1)$, $(10\bar{1}2)$, and $(11\bar{2}0)$ faces of a zincite crystal (ZnO) by the method suggested in [9], constructed the schemes of the atomic structure of the faces, and determined the thicknesses $\Delta_{(hkil)}$ and reticular densities $\rho_{(hkil)}$ of the elementary layer and all the planar nets [20, 21].

Zincite is crystallized in sp. gr. $P6_3mc$. It has a framework structure consisting of $[ZnO_4]$ (or $[OZn_4]$) tetrahedra sharing the vertices. The unit-cell parameters are a = 3.249 Å and c = 5.207 Å. The atomic coordinates are

$$Zn_{[1]} = 1/3; 2/3; 0; \quad Zn_{[2]} = 2/3; 1/3; 1/2;$$

$$O_{[1]} = 1/3; 2/3; Z; \quad O_{[2]} = 2/3; 1/3; 1/2 + Z,$$

where $Z = 0.3817c$.

The $\rho_{(hkil)}$ and $\Delta_{(hkil)}$ values were calculated with the use of the (0001) reference face, whose projection onto the (0001) plane in shown in Fig. 1a. The structure of the elementary layer is clearly seen from its projection onto the face normal to the face analyzed. The elementary layer of the (0001) face is built by three planar nets (Figs. 1b–1d). The first one consists of $Zn_{[1]}$ atoms located at zero height Z, the second is built by $O_{[1]}$ atoms lying at height $Z = 0.3817c$, and the third consists of $Zn_{[2]}$ atoms lying at height $Z = 0.8817c$, with the first and third nets belonging to the neighboring elementary layers. The thickness of this elementary layer $\Delta_{(0001)}$ is equal to half the parameter c. The $\rho_{(hkil)}$ value is determined as the sum of the reticular densities of all the planar nets forming the layer. Thus, the value of $\rho_{(hkil)}$ for the (0001) faces equals

$$\rho_{(0001)} = 0.5L_{(Zn_{[1]})} + 1L_{(O)} + 0.5L_{(Zn_{[2]})} = 2,$$

where L are the planar nets occupied either by zinc, $Zn_{[1]}$ and $Zn_{[2]}$, or the oxygen, $O_{[1]}$ or $O_{[2]}$, depending on the choice of the origin.

The reticular densities and the thicknesses of the elementary layers of the (0001) and $(000\bar{1})$ faces are equal, with their values being 2.0 and 2.6 Å, respectively. The main difference in the structure of these planes reduces to different electric changes of their air–face interfaces. The surface of the positive (0001) monohedron consists of the net of Zn atoms and possesses a positive effective charge close to two. The $(000\bar{1})$ face, whose surface consists of the nets of O atoms, possesses a charge equal to minus two [22].

As an example, consider the corresponding calculation for the planar nets of the $(10\bar{1}0)$ face (the cleavage plane of the zincite structure). When constructing the atomic structure of the faces and all the constituent planar nets, it is convenient to analyze the distribution of labeled (i.e., numbered) atoms over the planar nets.

Now, substitute the atomic coordinates into the formula for the distance of an arbitrary point of the crystal structure from the nodal plane with the given Miller indices,

$$D = (P_1h + P_2k + P_3l)d_{(hkil)},$$

where D is the distance of this point from the nodal plane, $d_{(hkil)}$ is the interplanar spacing in the Bravais lattice (in the hexagonal setting), $P_1P_2P_3$ are the atomic coordinates of the points through which the planar net parallel to the nodal plane (face) passes, and $hkil$ are the Miller indices of the nodal net (face).

Now, determine the D/d value for each atom. For the $(10\bar{1}0)$ face with $d_{(10\bar{1}0)}$ = 2.817 Å and $P_1 = P_2 = 0$, we have $D_{(10\bar{1}0)} = 2.817P_1$, $P_1(Zn_{[1]}) = 1/3$, $P_1(Zn_{[2]}) = 2/3$, $P_1(O_{[1]}) = 1/3$, and $P_1(O_{[2]}) = 2/3$. Substituting the values of the constants ρ_0 and Δ_0 of the reference (0001) face and $\Delta_{(10\bar{1}0)}$ into Eq. (1), we have

$$\rho_{(10\bar{1}0)} = 2(2.82{:}2.6) = 2.17.$$

The structures of the main habit-forming faces of a ZnO single crystal are shown in Figs. 1a–1d, indicating the atomic composition, the sequence of the net alternation, and the spacing between the planar nets forming the given face of the crystal. One can readily see that the $(10\bar{1}0)$ face consists of pairs of alternating planar mixed (Zn,O) nets with the shortest spacing between them being equal to $1/3d_{(10\bar{1}0)}$. In this case, the elementary layer corresponds to translation between the planar nets of one type, i.e., $Zn_{[1]}O_{[1]}$–$(Zn_{[1]}O_{[1]})^t$ or, which is equivalent to the first case, $Zn_{[2]}O_{[2]}$–$(Zn_{[2]}O_{[2]})^t$ (the superscript t indicates a layer identical to the first one which is repeated via the translation $d_{(10\bar{1}0)}$). The elementary-layer thickness ($\Delta_{(10\bar{1}0)}$) equals the interplanar spacing $d_{(10\bar{1}0)}$ and has a value of 2.82 Å.

The calculated main characteristics of the elementary layers in the ZnO structure are shown in Fig. 2 and

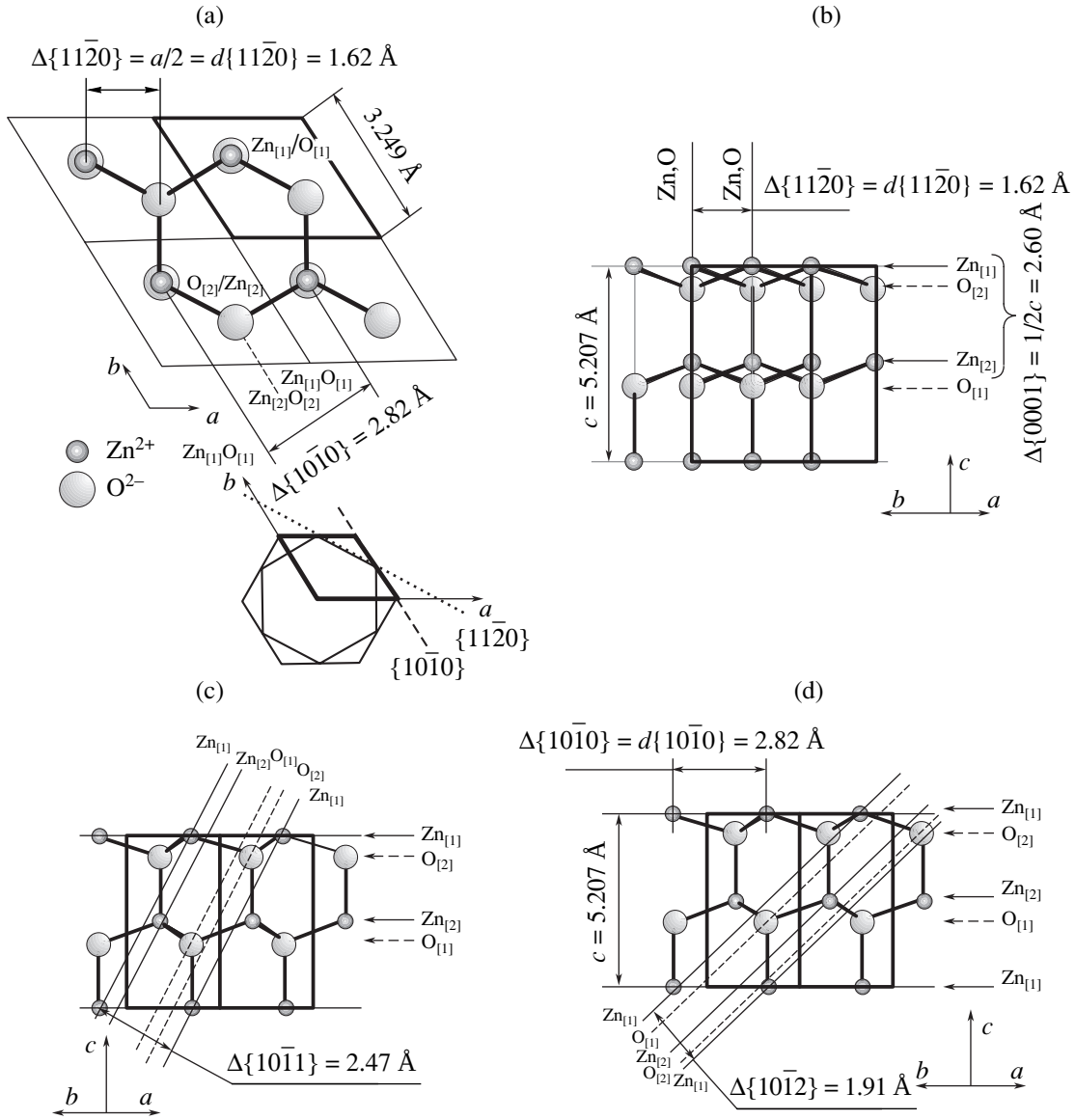

Fig. 1. ZnO crystal structure projected (a) onto the (0001) monohedron plane—the elementary layers of the $\{10\bar{1}0\}$ and $\{11\bar{2}0\}$ prisms are shown; (b) onto the $(10\bar{1}0)$ plane—the elementary layers of the (0001) monohedron and the $\{11\bar{2}0\}$ prism are shown; (c) onto the $(11\bar{2}0)$ plane—the elementary layer of the $\{10\bar{1}1\}$ pyramid is shown; and (d) onto the $(11\bar{2}0)$ plane—the elementary layer of the $\{10\bar{1}2\}$ pyramid is shown. The unit cell is indicated by solid lines.

Table 2. Table 2 indicates the elemental composition of each planar net of the elementary layer; the crystallographic positions of the $Zn_{[1]}$, $Zn_{[2]}$, $O_{[1]}$, and $O_{[2]}$ atoms; the sequence of their alternation; and also its simplified form (only the elemental composition of the planar net).

If the spacings between the nets drawn through the centers of the constituent atoms are small, it is possible to consider them as forming one corrugated net. Thus, for the faces of the $(10\bar{1}2)$ pyramid, the shortest spacing between the neighboring Zn and O nets is ~0.2 Å or $0.1\ d_{(10\bar{1}2)}$. These nets can conditionally be considered as one corrugated net of mixed (Zn,O) composition. For the elementary layer of another pyramid, $\{10\bar{1}1\}$, the spacing between the nets occupied by the same atoms ($Zn_{[1]}$ and $Zn_{[2]}$ or $O_{[1]}$ and $O_{[2]}$) equals 0.4 Å, which allows one to consider these nets as corrugated ones occupied by zinc and oxygen atoms, respectively.

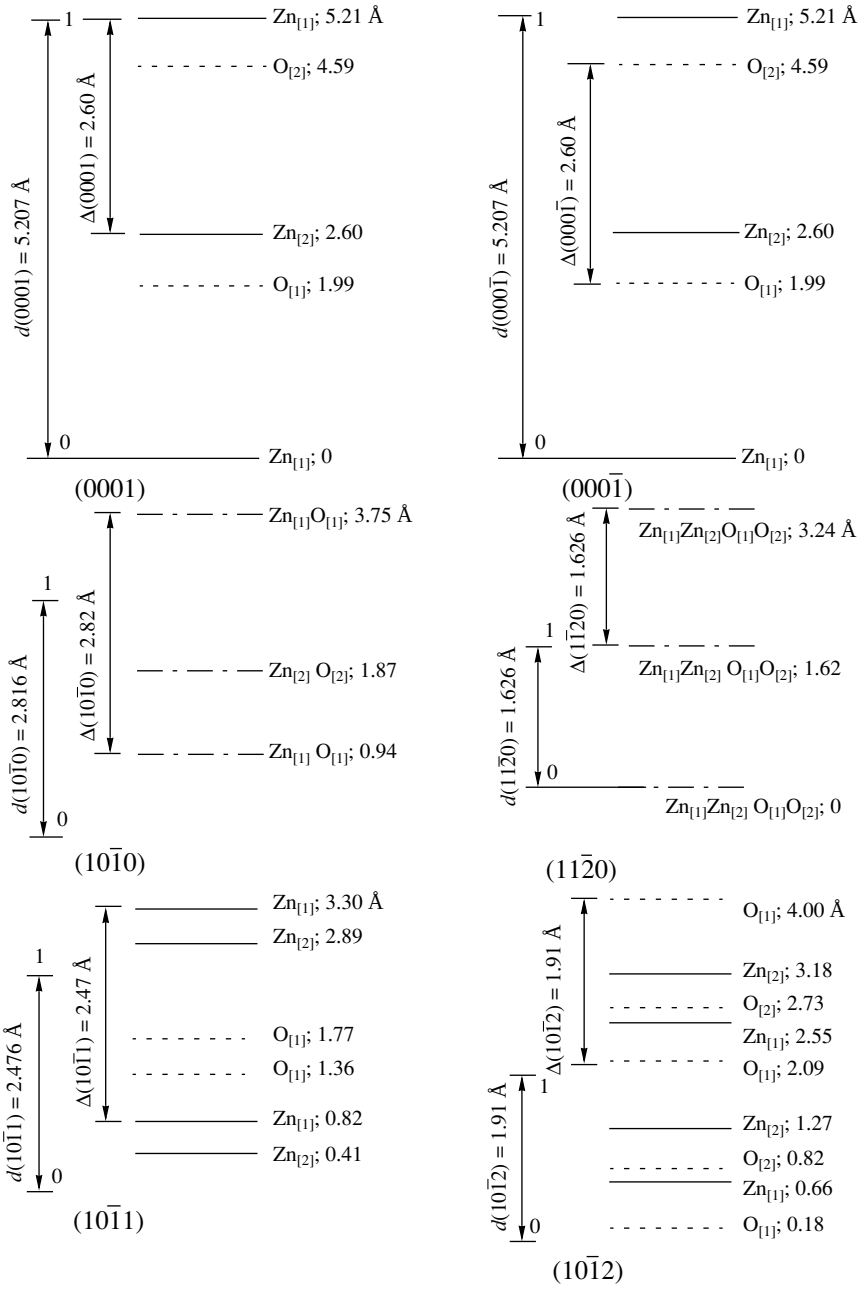

Fig. 2. Scheme of the atomic structures of the main habit-forming faces of zincite crystals (on the same scale). The thicknesses $\Delta_{(hkil)}$ of the elementary layers are indicated; on the right, the layer heights at which the planar nets passing through the centers of the corresponding atoms are indicated in Å. The nets of Zn atoms are shown by solid lines; those occupied by O atoms, by dashed lines; the nets of the mixed composition, by dotted and dashed lines.

The analysis of the structure of planar nets forming the ZnO structure and the corresponding graphical constructions show that only the faces of the hexagonal prisms of the first and second kind are characterized by the presence of mixed (Zn,O) nets. For the $\{10\bar{1}2\}$ pyramid, one can conditionally single out nets of mixed composition consisting of Zn and O atoms; however these nets are corrugated, with the distances between the planar nets passing through the centers of Zn atoms and planar nets passing through the centers of O atoms of the order of 0.2 Å. For all the remaining faces, the planar nets consisting only of Zn or O atoms alternate. Thus, as will be shown later, growth of the faces with the Zn and O nets depends on the charges of the species in the crystal-forming solution.

The calculations show that for ZnO crystals, the $\Delta_{(hkil)}$ and $\rho_{(hkil)}$ values of the main crystallographic sim-

Table 2. Calculated thicknesses Δ_{hkil} and reticular densities ρ_{hkil} of elementary layers of the main habit-forming faces of zincite crystals

(*hkil*) face	d_{hkil}, Å	Δ_{hkil}, Å	ρ_{hkil}, Å	Composition of elementary layer
(0001)	5.207	2.60	2	$Zn_{[1]}/O_{[2]}/Zn_{[2]}/O_{[1]}$/ (Zn/O/Zn)
$(000\bar{1})$	5.207	2.60	2	$O_{[1]}/Zn_{[2]}/O_{[2]}/Zn_{[1]}$/ (O/Zn/O)
$(10\bar{1}0)$	2.817	2.82	2.17	$Zn_{[1]}/O_{[2]}/Zn_{[2]}/O_{[1]}$/ (Zn,O/Zn,O)
$(11\bar{2}0)$	1.626	1.62	1.25	$Zn_{[1]}O_{[1]}Zn_{[2]}O_{[2]}$/ $Zn_{[1]}O_{[1]}Zn_{[2]}O_{[2]}$/ (Zn,O/Zn,O)
$(10\bar{1}1)$	2.476	2.47	1.90	$Zn_{[1]}Zn_{[2]}/O_{[1]}O_{[2]}$/ (Zn*/O*/Zn*)
$(10\bar{1}2)$	1.911	1.91	1.47	$Zn_{[1]}/O_{[1]}/Zn_{[2]}/O_{[2]}$/ (Zn,O)**/O/Zn/

Note: The sequence of elements in the alternating planar nets is given in the parentheses. The atomic positions are not indicated.

* Corrugated nets consisting of the equivalent atoms with the Zn–Zn or O–O distances equal to ~0.4 Å.

** Corrugated (Zn,O) net with the spacings between the Zn and O planes equal to ~0.2 Å (equivalent to 0.1 of the translation).

ple forms decrease in the sequence

$$\Delta_{(10\bar{1}0)} > \Delta_{(0001)} = \Delta_{(000\bar{1})} > \Delta_{(10\bar{1}1)} > \Delta_{(10\bar{1}2)} > \Delta_{(11\bar{2}0)};$$

$$\rho_{(10\bar{1}0)} > \rho_{(0001)} = \rho_{(000\bar{1})} > \rho_{(10\bar{1}1)} > \rho_{(10\bar{1}2)} > \rho_{(11\bar{2}0)}.$$

Since the reticular densities of the crystal faces are proportional to the elementary-layer thickness, whereas the growth rate of the faces is inversely proportional to the reticular density, one can draw the conclusion that, under ideal conditions (the absence of any additional components in the crystallization medium), the growth rates of the faces of a zincite vary in the row

$$V_{(10\bar{1}0)} < V_{(000\bar{1})} \sim V_{(0001)} < V_{(10\bar{1}1)} < V_{(10\bar{1}2)} < V_{(11\bar{2}0)}$$

and, therefore, the prevalence of these faces in the crystal habit is characterized by the reverse sequence. Indeed, the surface of a spontaneously grown crystal is formed by the faces of simple forms growing at a minimum rate, i.e., monohedra, a prism, and a first-order pyramid. The composition of the crystallization medium (the presence of complexes with various charges, the presence of impurities with different sorption ability, etc.) and the setting of the forced orientation (the presence of a seed with the given crystallographic orientation) change the theoretical sequence of variation of growth rates.

Mechanism of ZnO Crystallization

In alkali ZnO solutions, ZnO is dissolved with the formation of various oxy and hydroxy complexes of the $Zn(OH)_4^{2-}$, $ZnO(OH)^-$, and ZnO_2^{2-} types. According to [23], in hydrothermal strong alkali solutions, the transport of ZnO proceeds mainly as the transport of $Zn(OH)_4^{2-}$ species,

$$ZnO + 2OH^- + H_2O \longleftrightarrow Zn(OH)_4^{2-}. \quad (2)$$

During growth, the reaction should be the reverse of (2) with the formation of neutral ZnO particles. In this case, the probability of the attachment of ZnO particles to the faces of the positive (0001) and negative $(000\bar{1})$ monohedra should be equal. As a result, the growth rates should be approximately equal ($V_{(0001)} \cong V_{(000\bar{1})}$).

Different charges of the (0001) and $(000\bar{1})$ faces and different growth rates along the $\pm c$ directions lead to the assumption that the solution contains some charged particles or building units,

$$Zn(OH)_4^{2-} \longrightarrow Zn(OH)_2 + 2OH^-, \quad (3)$$

$$Zn(OH)_2 \longrightarrow 2H^+ + ZnO_2^{2-}. \quad (4)$$

The possible existence of such a growth mechanism of ZnO was indicated in [4]. The probability of the occurrence of reaction (4) in alkali solutions is rather high because of binding of H^+ ions in the presence of excessive OH^- ions and the formation of H_2O:

$$\begin{aligned} H^+ + OH^- &= H_2O, \\ K_5 &= [H^+][OH^-]. \end{aligned} \quad (5)$$

The constant of reaction (4) can be written as

$$K_4 = [H^+]^2[ZnO_2^{2-}]/[Zn(OH)_2]. \quad (6)$$

Substituting $[H^+] = K_5/[OH^-]$ into Eq. (6), we finally arrive at the equation

$$K_4 = K_5^2[ZnO_2^{2-}]/[OH^-]^2[Zn(OH)_2]$$

or

$$[ZnO_2^{2-}]/[Zn(OH)_2] = K_4[OH^-]^2/K_5^2.$$

It is seen that the concentration of ZnO_2^{2-} ions is higher, the higher the concentration of OH^- ions in the solution.

Now, it becomes obvious that it is ZnO_2^{2-} ions that are responsible for the polar growth of ZnO crystals. Then, the following reaction should occur on the surface of the (0001) face consisting of planar Zn^{2+} nets,

$$Zn^{2+}_{(sur)} + Zn^{2-}_{2(sol)} \longrightarrow 2ZnO_{(cryst)}, \quad (7)$$

whereas on the $(000\bar{1})$ surface consisting of the planar O^{2-} nets, the following reaction occurs:

$$O^{2-}_{(sur)} + ZnO^{2-}_{2(sol)} + 2H_2O \longrightarrow ZnO_{(cryst)} + 4OH^-. \quad (8)$$

The rate of reaction (7) between the oppositely charged particles should considerably exceed the rate of reaction (8). One can readily see that one elementary event of the interaction of the ZnO_2^{2-} species with the {0001} surface of the (0001) face results in "pinning" of two elementary structural units, whereas only one structural unit is pinned on the $(000\bar{1})$ face. The considerably higher growth rates along [0001] than along $[000\bar{1}]$ are confirmed experimentally: under the condition of infinitesimal impurity concentrations in alkali KOH solutions, the ratio of the growth rates $V_{(0001)}/V_{(000\bar{1})}$ varies within 1.50–2.28.

The growth rates of the (0001) and $(000\bar{1})$ faces show a tendency to increase with an increase in supersaturation (which corresponds to an increase in the OH^- ion concentration in the vicinity of the growth front). With an increase in the temperature difference Δt from 40 to 80°C, the growth rates $V_{(0001)}$ increase from 0.12 to 0.25 mm/day (24 h), whereas the growth rate $V_{(000\bar{1})}$, from 0.08 to 0.13 mm/day. At a mineralizer concentration of $C_{KOH} \sim 10$ *m*, the growth rates of the (0001) and $(000\bar{1})$ faces attain the maximum values and then, with a further increase in mineralizer concentration, remain constant [8].

An increase in $V_{(0001)}$ and $V_{(000\bar{1})}$ at higher temperatures and constant Δt and concentration C_{KOH} is consistent with an increase in the dissociation constants of KOH and NaOH at higher temperatures of hydrothermal solutions [24].

The specific nature of growth of ZnO crystals is determined by the chemical state of the medium and also by the crystallographic characteristics of a growing surface. Analysis of the available data shows that ZnO crystals can be grown over wide range of *t*, Δt, and C_{KOH} values.

Kinetics of ZnO Crystallization in Hydrothermal Alkali Solutions

Growth rates of all the main habit-forming faces of ZnO single crystals increases almost linearly with an increase in the concentration of an alkali (KOH) from 3 to 8 *m* in accordance with an increase in ZnO solubility (Table 1) and the supersaturation in the growth zone. At all the concentrations of the alkali, the maximum growth rate is recorded for the polar faces of the positive (0001) monohedron (curves *1* and *3* in Fig. 3). With an increase in temperature, the $V_{(0001)}/V_{(000\bar{1})}$ ratio also increases.

The introduction of Li^+ ions into the crystallization medium results in a decrease in the growth rates and a change of process. The growth rates of the main habit-forming faces (of monohedra) decrease by several times in comparison with the growth rates in pure KOH solutions. The presence of Li^+ ions changes the growth rate ratio of the monohedron and prism faces and also the habit of ZnO crystals because of a more intense (by 20–25% and, at higher Δt values, almost by an order of magnitude) suppression of the growth rate of the faces of the positive monohedron in comparison with $V_{(000\bar{1})}$. The reduction of the growth rates of the (0001) and $(10\bar{1}0)$ faces of ZnO crystals by almost an order of magnitude (caused by the introduction of lithium, 1.25 *m* LiOH, into the 5.15 *m* KOH solution at *t* = 300°C) is shown by dashed lines in Fig. 3. According to [13], lithium ions are adsorbed on the monohedron face, which reduces its free energy.

The data given in Figs. 4–6 were obtained in the studies of the growth kinetics at the constant concentration of the mixed solution selected as the optimum concentration upon a series of experiments, (5.0–5.2) *m* KOH + 1.2 *m* LiOH.

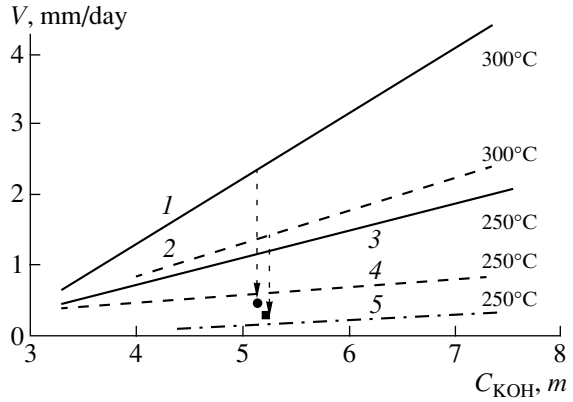

Fig. 3. Growth rates of the positive (0001) and negative $(000\bar{1})$ monohedra of ZnO single crystals as functions of the solution concentration at the constant growth temperature. (*1*, *3*) the KOH solution, the (0001) face; (*2*, *4*) the KOH solution, the $(000\bar{1})$ face; (*5*) the 5.15 *m* KOH + 1.2 *m* LiOH solution, the (0001) face; ● experimental point for $V_{(0001)}$, the 5.15 *m* KOH + 1.2 *m* LiOH solution, 300°C; ■ experimental point for $V_{(000\bar{1})}$; 5.15 *m* KOH + 1.2 *m* LiOH solution, 300°C. The vertical dashed lines show a decrease in the growth rates of the faces of the (0001) and $(000\bar{1})$ monohedra upon the introduction of lithium ions (1.2 *m* LiOH) into the growth system at 300°C.

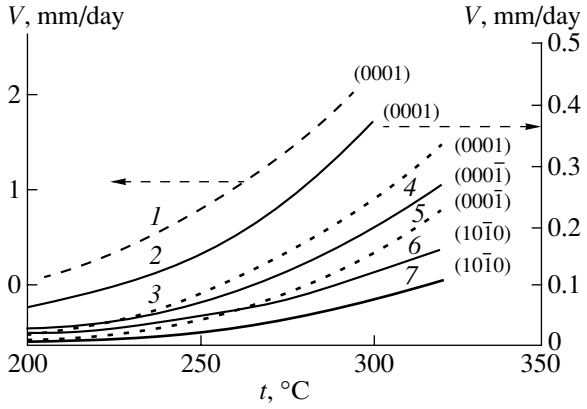

Fig. 4. Growth rates of the faces of monohedra and the $\{10\bar{1}0\}$ prism of ZnO single crystals in solutions (*1*) 5 *m* KOH and (*2–7*) 5.15 *m* KOH + 1.2 *m* LiOH as functions of temperature. Solid lines correspond to Δt = 75°C, dashed lines, to Δt = 50°C.

At a constant concentration of C_{LiOH} = 1.2 *m*, an increase in the KOH concentration up to 8.5 *m* results in an increase of the growth rates of all the main habit-forming faces of ZnO ({0001}, $\{10\bar{1}0\}$, $\{11\bar{2}0\}$, and $\{10\bar{1}1\}$) by a factor of about 1.5–3.0. However, at higher C_{KOH} values, the growth rates change only insignificantly, which shows that in the presence of lithium ions, ZnO crystals do not necessarily have to be grown from highly concentrated alkali solutions.

At the constant concentration of the KOH + LiOH solution, the growth rate varies with an increase in the temperature according to the parabolic law (Fig. 4). To compare the absolute values of the growth rates, Fig. 4 also shows the temperature dependence of $V_{(0001)}$ for ZnO crystallization from KOH solutions without Li impurities. The dependence of the growth rate on the supersaturation $\Delta S'$ at the constant temperature and solvent concentration is shown in Fig. 5. In the temperature range studied, $\Delta S'$ in the growth zone is independent of the temperature because of the linear variation of ZnO solubility with the temperature at the constant solvent concentration and Δt. The dependences in Fig. 5 are shown on two scales of the temperature difference corresponding to the Δt values—that inside the autoclave (Δt_{in}) and that along the outer wall of the autoclave (Δt_{out}). At growth temperatures ranging within 250–300°C, the dependence $\Delta S'/\Delta t$ is close to linear, which allows one to use the Δt values as "reduced" relative supersaturations while evaluating the growth rates of the crystals,

$$V_{(hkil)} = k(\Delta t - \Delta t_{cr}),$$

where k is the coefficient determined by the temperature and the crystallographic direction of crystallization, and Δt_{cr} is the critical temperature difference below which the growth rate is zero within the determination error.

The activation energies of growth of the (0001), $(000\bar{1})$, and $(10\bar{1}0)$ faces in the KOH + LiOH solutions are equal to 59 ± 3, 66 ± 3, and 68 ± 3 kJ/mol, respectively (Fig. 7), which indicates that the (0001) faces can also grow at somewhat lower critical supersaturations than the $\{10\bar{1}0\}$ and $(000\bar{1})$ faces. The activation energy of the growth process of the (0001) faces in KOH solutions without lithium impurities is considerably lower and equals 35 ± 3 kJ/mol (Fig 7, curve *1*).

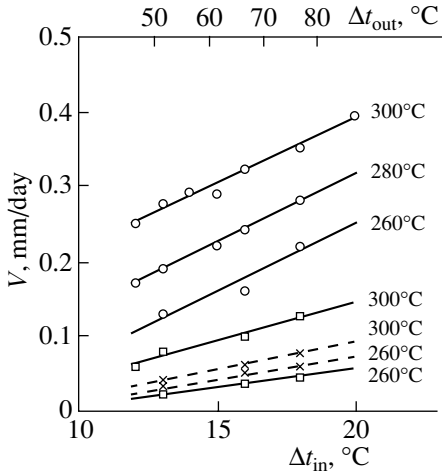

Fig. 5. Growth rates of the monohedron faces for ZnO as functions of the temperature gradient inside the autoclave (t_{in}) and along the outside wall of the autoclave (t_{out}) at different crystallization temperatures (the 5.15 *m* KOH + 1.2 *m* LiOH solution); ○ the (0001) face, × the $(000\bar{1})$ face, and □ the $(10\bar{1}0)$ face.

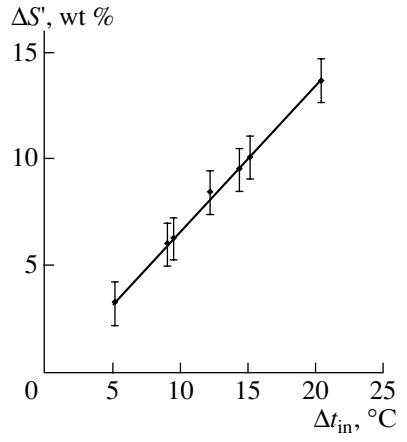

Fig. 6. Variation of solution supersaturation, $\Delta S' = (S'_{t2} - S'_{t1})$, in the growth zone with an increase in the temperature gradient Δt (S'_{t2} and S'_{t1} are the solubilities at the dissolution-zone and growth temperatures, respectively).

The calculated activation energies are of the same order of magnitude as the activation energies of growth of the (0001) faces of quartz crystals in the 0.5 *m* NaOH solution (84 kJ/mol), $(11\bar{2}0)$ faces of Al_2O_3 crystals in the 10% Na_2CO_3 solution (73 kJ/mol), and the $(10\bar{1}1)$ faces of calcite $CaCO_3$ (70 kJ/mol) calculated from the known data on growth kinetics of these compounds. The values thus obtained indicate that for ZnO and some other crystals grown under hydrothermal conditions, the activation energies are too high to provide the processes in the pure diffusion mode and correspond to the growth processes occurring in the diffusion–kinetic mode.

Lithium is the most important impurity in ZnO crystals; therefore, we analyze here the role of Li^+ ions in the growth process.

At the first stage of growth, the dissociation of lithium hydroxide proceeds according to the equation

$$LiOH \longleftrightarrow Li^+ + OH^-.$$

The above data on the growth rates lead to the assumption about the different character of the incorporation of lithium ions into different growth pyramids of ZnO crystals, which is determined, first and foremost, by the reduction–oxidation characteristics of the crystallization medium. The location of Li^+ ions at cationic sites of the lattice with the formation of Li'_{Zn} acceptor centers is characteristic of oxidative conditions, whereas the location of Li_i^+ ions in the interstitials is characteristic of reductive conditions [25]. In conventional growth experiments under hydrothermal conditions, reductive conditions are created as a result of the interaction of water with the autoclave material (metal) and the penetration of H^+ ions into the walls of Ag, Pt or Cu cans.

It is reasonable to assume that the polarity of the ZnO structure creates quasi-oxidative and quasi-reductive conditions at the (0001) and $(000\bar{1})$ faces, respectively. The incorporation of Li^+ into the (0001) face of the crystal can be represented as

$$Zn^{2+}_{(sur)} + Li^+_{(sol)} \longrightarrow Li^+_{Zn} + Zn^{2+}_i$$

or, in terms of quasi-chemical reactions [26], as

$$Zn^x_{Zn} + Li^+ \longrightarrow Li'_{Zn} + Zn^{2+}_i.$$

Thus, no doubt, the effective positive charge of the (0001) face diminishes, which, in turn, results in the lower probability of the attachment of negatively charged $Zn(OH)_4^{2-}$ and ZnO_2^{2-} complexes to the ZnO crystal. For the $(000\bar{1})$ face, we have

$$O^{2-}_{(sur)} + Li^+_{(sol)} \longrightarrow O^{2-},$$

$$O^x_{O(sur)} + Li^+ \longrightarrow O^x_O + Li_i^+.$$

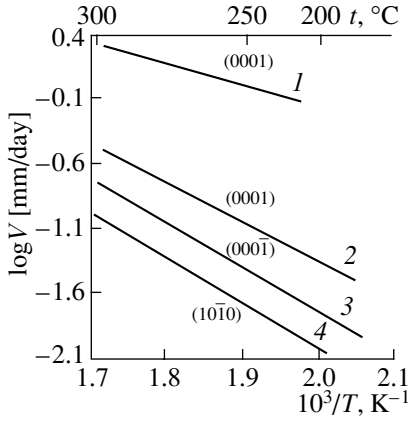

Fig. 7. Activation energies of the growth process of single crystals from the solutions: (*1*) 5 *m* KOH and (*2–4*) 5.15 *m* KOH + 1.2 *m* LiOH.

The above reaction results in a decrease of the negative charge of the $(000\bar{1})$ face and, therefore, to an increase in the growth rate. The incorporation of Li^+ into the $\langle 10\bar{1}0 \rangle$ growth pyramid seems to occur by the second mechanism, which results in the appearance of a weak positive charge and, thus, possible, more pronounced interaction of the face surface with the negatively charged species in the solution. In the growth process, the relationships between different forms of Li^+ incorporation into different positions in the lattice can vary; however, at high concentration of the Li^+, the electroneutrality condition is met in the crystal bulk—i.e., the number of lithium ions at the interstitials, Li_i^+, equals the number of lithium ions in the zinc positions, Li'_{Zn} [1, 26],

$$2Li^+ + Zn^x_{Zn} \longrightarrow Li_i^+ + Li'_{Zn} + Zn_i^{2+}.$$

A decrease in the growth rate of the (0001) face in the presence of Li^+ ions results in higher quality of the crystalline material and the formation of a smooth surface relief. The cathodoluminescence spectra of the samples cut from the $\langle 0001 \rangle$ and $\langle 000\bar{1} \rangle$ growth pyramids are characterized by the halfwidths of the main exciton reflection bands, 1.4 and 1.5–2.3 nm, respectively [10], which indicates that growth along the [0001] direction yields crystalline material of a higher quality.

Table 3 illustrates the effect of the introduction of various impurities on the growth rates of the main faces of ZnO crystals. The incorporation of Li^+ ions determines the well-developed faces of the positive (0001) monohedron and the $(10\bar{1}1)$ pyramid (Fig. 8a). The introduction of Fe and Mn impurities into the mixed (KOH + LiOH) solution results in considerable changes in the growth kinetics and the habit of ZnO crystals (Figs. 8b–8d). The ZnO:Fe crystals acquire the pyra-

Table 3. Growth rates of ZnO single crystals dependent on the main growth parameters (t, Δt, solvent composition, and presence of impurities)

Δt, °C	t, °C	Solution composition	Impurity content in the charge, wt %	V, mm/day		
				(0001)	$(000\bar{1})$	$(10\bar{1}0)$
75	250	KOH 5 *m*		0.96	0.44	–
75	300	KOH 5 *m*		2.05	1.08	–
50	250	KOH 5.15 *m* + LiOH 1.2 *m*		0.08	0.03	0.01
50	300	KOH 5.15 *m* + LiOH 1.2 *m*		0.25	0.16	0.07
40	280	KOH 5.15 *m* + LiOH 1.2 *m*		0.12	0.08	0.04
50	280	KOH 5.15 *m* + LiOH 1.2 *m*		0.15	0.09	0.05
75	280	KOH 5.15 *m* + LiOH 1.2 *m*		0.26	0.12	0.07
75	250	KOH 5.15 *m* + LiOH 1.2 *m*		0.10	0.06	0.04
75	300	KOH 5.15 *m* + LiOH 1.2 *m*		0.35	0.20	0.11
65	280	KOH 5.2 *m* + LiOH 1.2 *m* + NH_4OH 0.3 *m*	In, 2%			0.18
65	280	KOH 8 *m* + LiOH 1.2 *m* + NH_4OH 0.3 *m*		0.25	0.14	0.04
50	280	KOH 5.15 *m* + LiOH 1.2 *m*	Ni, 1.5%	0.18	0.11	0.05
50	280	KOH 5.15 *m* + LiOH 1.2 *m*	Cd, 2%	0.16	0.09	0.06
50	280	KOH 5.15 *m* + LiOH 1.2 *m*	Mn, 1.8%	0.05	0.04	0.02
50	280	KOH 5.15 *m* + LiOH 1.2 *m*	Fe, 1.2%	0.21	0.17	0.07

midal habit with weakly developed (0001) faces. Divalent Ni^{2+}, Cd^{2+}, Mn^{2+}, and Co^{2+} ions enter the ZnO lattice and substitute Zn in the cationic sites. The Ni^{2+}, Mn^{2+}, Fe^{2+}, and Fe^{3+} impurities give rise to crystal coloration. The introduction of nickel slightly increases the growth rates of both monohedra and, thus, also the crystal thickness along the *c* axis.

The introduction of Mn^{2+} impurity results in a twofold decrease in the growth rates of all the faces. In this case, the crystal habit is characterized by the well-developed faces of monohedra, a mirror-smooth surface relief, and weakly developed prismatic and pyramidal faces (Fig. 8d). The presence of Mn impurity does not affect the electrical properties of the crystal. The presence of Co^{2+} impurity (up to 0.15 wt %) does not change the growth kinetics. The Co^{2+}-doped crystals are green and have an emerald tint, which is associated with the electron transitions in the Co_{Zn}^{2+} ions substituting Zn at the cationic sites of the lattice. The illumination of these crystals with yellow–blue light results in red luminescence, and, therefore, the color of the Co-doped ZnO crystals can change from green

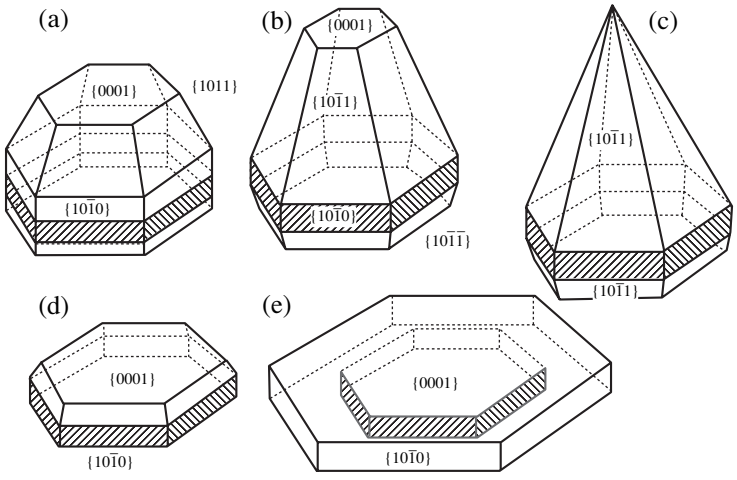

Fig. 8. Change in the habit of ZnO crystals grown on seed parallel to the (0001) plane in the presence of various impurities: (a) Li^+, (b, c) Fe^{2+}, (d) Mn^{2+}, and (e) In^{3+}. The prismatic faces of the initial seed are hatched.

under natural illumination to ruby red under the artificial illumination.

Iron impurity in ZnO crystals have three forms, Fe_{Zn}^{4+}, Fe_{Zn}^{3+}, and Fe_{Zn}^{2+}. The Fe_{Zn}^{4+} center can exist only in crystals with high resistivity, $\rho > \sim 10^{10}$ Ω cm. Trivalent iron located in the Fe_{Zn}^{3+} positions gives rise to a green color, whereas the presence of Fe_{Zn}^{2+} centers makes ZnO crystals black (in this case $\rho < \sim 10^3$ Ω cm). At the initial FeO concentration in the growth system exceeds FeO > ~2%, the crystal lattice of the grown crystals contains some defects (which results in disappearance of the exciton peaks in the reflection spectra). The thermal treatment of Fe-doped ZnO crystals results in the formation of $(Fe_{Zn}^{+} Li_{Zn}')$-type associates under the condition that the Li and Fe concentrations exceed $\sim 10^{-3}$ mol %. It is these clusters that are responsible for the intense ZnO luminescence in the red range of the spectrum [27].

At Fe concentrations up to several tenths of percent, the growth rates of the faces of the monohedra and prisms increase by the factor of 1.5–2.0. Higher concentrations of the Fe impurity make growth unstable and causes disorder in the crystal lattice of ZnO crystals. The exciton peaks in the reflection spectra of these crystals have very weak intensities, and the exciton luminescence is quenched. At liquid-nitrogen temperatures, the crystals are characterized by intense red luminescence. The presence of Fe impurity in ZnO crystals provides the formation of polar twins at the faces of the positive and negative monohedra and also an increase in the dislocation density from $10–10^3$ cm^{-2} to $10^5–10^7$ cm^{-2}.

The effect of In^{3+} impurity on growth and properties of ZnO crystals (Fig. 8e) synthesized by different methods was discussed earlier [1, 28]. It is essential that the growth kinetics under hydrothermal conditions depends on the presence of In^{3+} and NH_4^+ impurities: the growth rate of the hexagonal prism considerably increases, whereas the growth rates of the monohedron and pyramid faces drastically decrease. The grown layer is of a nonuniformly distributed bluish color; there are no signs of the polar growth because of the suppression of the growth rate along the $+c$ direction. The growth rate of the (0001) face increases with an increase in the In content in the initial charge up to ~2 wt % with respect to ZnO (Fig. 9). Doping of ZnO crystals with In^{3+} ions under hydrothermal conditions results in the substitution of Zn-positions by indium and formation of the point defects of the In_{Zn}^{+} type (which are, in fact, shallow donors). No associates of the $In_{Zn}^{+} Li_{Zn}'$ type (characteristic of the crystals grown from the vapor phase) are present in hydrothermally grown ZnO crystals, which can be associated with lower growth temperatures under hydrothermal conditions.

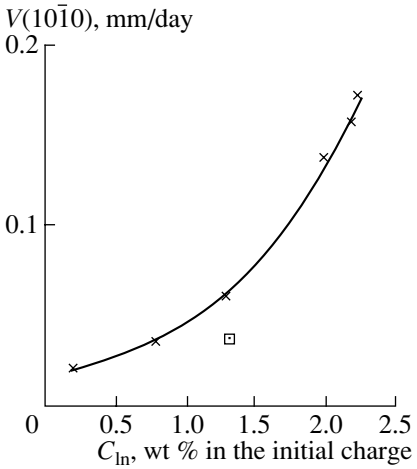

Fig. 9. Variation of the growth rate of the $(10\bar{1}0)$ face of ZnO single crystals grown on the (0001) seed in the presence of In at t = 250°C, Δt = 75°C; × the 5.15 *m* KOH + 1.2 *m* LiOH + 0.3 *m* NH_4OH solution; the 5.15 *m* KOH + 1.2 *m* LiOH solution.

CONCLUSIONS

Crystallization of zincite ZnO under hydrothermal conditions has been studied. The mechanism of crystal growth from hydrothermal alkali solutions is established based on the analysis of the crystallization kinetics and the atomic structure of ZnO. The experimental data on the crystallization kinetics of zincite are consistent with the assumptions on growth of crystals as a result of the interaction of the $[ZnO_2^{2-}]$ species in solution with the surfaces of the seeding zinc oxide single crystals with different effective charges and atomic structures.

The main habit-forming faces of zincite (ZnO) single crystals are analyzed in terms of crystal chemistry, and the characteristics of the elementary layers (compositions and thicknesses) for the faces of the (0001) and $(000\bar{1})$ monohedra, $\{10\bar{1}0\}$ and $\{11\bar{2}0\}$ hexagonal prisms, and $\{10\bar{1}1\}$ and $\{10\bar{1}2\}$ hexagonal pyramids are determined.

The mechanism of the influence of Li^+ ions on the polar growth of ZnO single crystals is considered. Upon partial substitution of Zn positions by lithium ions, the effective positive charge of the (0001) face decreases, which results in a decrease in the rate of incorporation of negatively charged Zn-containing complexes into the ZnO crystal. The capture of Li^+ ions by the surface of the negative monohedron reduces the total negative charge of the $(000\bar{1})$ face and, as a result,

increases the growth rate of ZnO single crystals along the $[000\bar{1}]$ direction.

The influence of the di- and trivalent metal impurities on the kinetics of zincite crystallization in hydrothermal alkali media is studied. The incorporation into the lattice of divalent metal ions (Ni^{2+}, Cd^{2+}, and Co^{2+}) barely changes the growth rate of the main habit-forming faces of ZnO single crystals. The introduction of Mn^{2+} and trivalent metal ions, Fe^{3+} and In^{3+}, results in considerable changes of the growth-rate ratios along the main crystallographic directions.

ACKNOWLEDGMENTS

This study was supported by the Russian Foundation for Basic Research, project no. 00-02-16463.

REFERENCES

1. I. P. Kuz'mina and V. A. Nikitenko, *Zinc Oxide: Growth and Optical Properties* (Nauka, Moscow, 1984).
2. W. Hirschwald, P. Bonasewicz, L. Ernst, *et al.*, in *Current Topics in Material Science*, Ed. by E. Kaldis (North-Holland, Amsterdam, 1981), Vol. 7, p. 143.
3. E. V. Kortunova and V. I. Lyutin, *Synthesis of Materials and Methods of Their Study* (VNIISIMS, Aleksandrov, 1997), Tr. Vseross. Nauchno-Issled. Inst. Sint. Miner. Syr'ya **24**, 31 (1997).
4. R. A. Laudise and E. D. Kolb, Am. Mineral. **48** (5/6), 642 (1963).
5. A. Scharovsky, Z. Phys. B **135**, 318 (1953).
6. Y. Y. Lauder, J. Phys. Chem. Solids **15**, 324 (1960).
7. S. Yasegawa and G. Ohara, J. Ceram. Assoc. Jpn. **75**, 255 (1967).
8. A. N. Lobachev, I. P. Kuz'mina, and O. A. Lazarevskaya, in *Hydrothermal Synthesis and Crystal Growth*, Ed. by A. N. Lobachev (Nauka, Moscow, 1982), p. 26.
9. N. Z. Evzikova, Zap. Vses. Mineral. O–va **94**, 129 (1965).
10. M. M. Lukina, Vestn. Akad. Nauk Kaz. SSR, No. 7, 47 (1968).
11. B. A. Laudise, E. D. Kolb, and A. J. Caporaso, J. Am. Ceram. Soc. **47**, 9 (1960).
12. I. P. Kuz'mina and V. F. Antonova, in *Crystal Growth*, Ed. by A. V. Shubnikov and N. N. Sheftal' (Nauka, Moscow, 1960), Vol. 4, p. 151.
13. D. E. Croxall, R. C. C. Ward, C. A. Wallace, *et al.*, J. Cryst. Growth **22**, 117 (1974).
14. E. D. Kolb, A. S. Kortell, B. A. Laudise, and A. R. Huston, Mater. Res. Bull. **2**, 1099 (1967).
15. A. N. Lobachev, I. P. Kuz'mina, Yu. V. Shaldin, *et al.*, in *Crystal Growth from High-Temperature Aqueous Solutions*, Ed. by A. N. Lobachev (Nauka, Moscow, 1977), p. 158.
16. M. M. Lukina and V. E. Khadzhi, in *Crystal Growth*, Ed. by N. N. Sheftal' and E. I. Givargizov (Nauka, Moscow, 1972), Vol. 9, p. 48.
17. L. N. Demianets, E. E. Komarova, I. P. Kuz'mina, *et al.*, Preprint No. 5, IK RAN (Institute of Crystallography, Russian Academy of Sciences, Moscow, 1992).
18. D. V. Kostomarov, L. N. Demianets, I. P. Kuzmina, and O. A. Lazarevskaya, in *Proceedings of Joint ISHR & ICSTR, 2001*, p. 326.
19. R. A. Laudise, in *Crystal Growth: an Introduction*, Ed. by P. Hartman (North-Holland, Amsterdam, 1973), Vol. 1, p. 162.
20. P. Hartmann, Z. Kristallogr. **119**, 65 (1963).
21. L. N. Demianets, D. V. Kostomarov, and I. P. Kuz'mina, Neorg. Mater. **38**, 171 (2002).
22. G. Heiland and P. Kunstmann, Surf. Sci. **13** (1), 72 (1969).
23. I. L. Khodakovskiĭ and A. E. Elkin, Geokhimiya, No. 10, 1490 (1975).
24. O. V. Bryzgalin, Geokhimiya, No. 8, 1184 (1985).
25. F. A. Kröger, *Chemistry of Imperfect Crystals* (Wiley, New York, 1964; Mir, Moscow, 1969).
26. G. Heiland and D. Kohl, Phys. Status Solidi A **49** (1), 27 (1978).
27. V. A. Nikitenko, K. É. Tarkpea, A. I. Tereshchenko, and I. P. Kuz'mina, Zh. Prikl. Spektrosk. **51**, 499 (1989).
28. L. N. Demianets and D. V. Kostomarov, Ann. Chim. Sci. Mater. **26**, 193 (2001).

Translated by L. Man

Crystallography Reports, Vol. 47, Suppl. 1, 2002, pp. S99–S104.

SOLUTION GROWTH

Growth and Properties of Nb- or Sn-Doped $KTiOPO_4$ Crystals

V. K. Yanovskiĭ*, V. I. Voronkova*, T. Yu. Losevskaya*, S. Yu. Stefanovich, S. A. Ivanov**, V. I. Simonov***, and N. I. Sorokina*****

** Moscow State University, Vorob'evy gory, Moscow, 119899 Russia*

e-mail: voronk@crysc24.phys.msu.su

*** Karpov Research Institute of Physical Chemistry, ul. Vorontsovo pole 10, Moscow, 103064 Russia*

**** Shubnikov Institute of Crystallography, Russian Academy of Sciences, Leninskiĭ pr. 59, Moscow, 117333 Russia*

Received February 20, 2001

Abstract—Single crystals of potassium titanyl phosphate, $KTiOPO_4$, doped with Nb or Sn to various doping levels are grown by crystallization from flux. Their atomic structure and physical properties are studied. It is found that both dopants greatly affect the configuration of titanium–oxygen polyhedra and, hence, the ferroelectric and nonlinear optical properties of the crystals. Superionic transitions with abrupt changes in electrical conductivity are observed in some crystals for the first time. *© 2002 MAIK "Nauka/Interperiodica".*

INTRODUCTION

Potassium titanyl phosphate, $KTiOPO_4$ (KTP), and some other related crystals and solid solutions are promising nonlinear optical materials that have been actively studied in recent years. Of great importance are also ferroelectric transitions and anomalously high ionic conductivity exhibited by these crystals. All these properties are sensitive to compositional changes and can be varied over wide ranges by substitutions. A number of works have studied KTP crystals with Ti partially replaced by Nb. It was shown that this substitution noticeably changes the crystal structure. In particular, $K_{1-x}Ti_{1-x}Nb_xOPO_4$ crystals were found to contain multiple vacancies in the K(1) and K(2) positions of the potassium cations [1] or in K(1) positions only [2]. Potassium can also be situated in three different positions, which are only partially occupied [3], while niobium largely occupies Ti(1) positions [1–3]. In this case, the concentration of additional vacancies in the potassium sublattice may be higher than that suggested by the condition of zero net charge [1]. The substitution of Ti by Nb increases the ionic conductivity [3, 4]. Moreover, it shifts the optical-absorption edge toward shorter wavelengths and enhances the birefringence; these effects favor using the crystals in nonlinear optics [5, 6].

Potassium stannyl phosphate, $KSnOPO_4$, is isostructural to KTP [7, 8]. These two compounds form a continuous set of $KTi_{1-x}Sn_xOPO_4$ solid solutions, whose structure and properties are still poorly understood, mainly due to the complexities of crystal growth. The nonlinear optical susceptibility is known to decrease with increasing x, virtually disappearing in $KSnOPO_4$ crystals [9–11]. This behavior results from changes in the degree of distortion of $(Ti,Sn)O_6$ polyhedra. A certain pattern in the distribution of Sn and Ti cations was observed in these solutions, larger Sn^{4+} cations with a low concentration occupying predominantly Ti(1) positions [12]. Furthermore, $KSnOPO_4$ crystals exhibit ferroelectric properties (Curie temperature 433°C) [13] and high ionic conductivity [14]. The electrical properties of $KTi_{1-x}Sn_xOPO_4$ solid solutions have yet to be investigated.

In this study, we grew KTP crystals doped with Nb or Sn to various doping levels and investigated their atomic structure, electrical conduction, and ferroelectric and nonlinear optical properties.

EXPERIMENTAL TECHNIQUES

The atomic structure and physical properties of $K_{1-x}Ti_{1-x}Nb_xOPO_4$ and $KTi_{1-x}Sn_xOPO_4$ solid solutions were studied on single crystals grown from flux in the K_2O–TiO_2–Nb_2O_5–P_2O_5 and K_2O–TiO_2–SnO_2–P_2O_5 quaternary systems, respectively. The crystals were grown in furnaces with Silit heaters; the temperature was controlled with an accuracy of ±0.5°C. The ingredients K_2CO_3, TiO_2, Nb_2O_5, SnO_2, and $NH_4H_2PO_4$ had reagent and extra-pure grades. The mixtures were first calcined at 700°C and then placed into 50-ml platinum crucibles and heated to 1100°C (for K_2O–TiO_2–Nb_2O_5–P_2O_5) or 1200°C (for K_2O–TiO_2–SnO_2–P_2O_5). This temperature was maintained for 24 h and then decreased to a value close to the liquidus point. Afterward, the temperature was lowered to 850°C at a rate of 1–2 °C/h. The remaining melt was poured out, and crystals grown in the bottom and on the walls of the crucible were cooled (together with the furnace) to room temperature and then rinsed in hot water to remove the residual solvent.

1063-7745/02/47S1-S0099$22.00 © 2002 MAIK "Nauka/Interperiodica"

The structure of the crystals was determined with a DRON-2.0 and a CAD-4F x-ray diffractometer. The neutron diffraction analysis was performed at the R2 Research Reactor in Studsvic (Sweden). The temperature dependence of the dielectric constant and conductivity was measured with a Tesla BM 431E bridge at 1 MHz on (001)-oriented plates cut from optically transparent, pure single crystals with deposited silver and gold electrodes. Second-harmonic generation (SHG) was studied by the Kurtz–Perry powder method, with the specimens heated to 900°C and cooled at a rate of 5–8°C/min. The melting points of the crystals were measured by differential thermal analysis (DTA), with the temperature varied at 10–20°C/min. The density of the crystals was measured by hydrostatic weighing in toluene. Their morphology was examined with a ZRG-3 optical goniometer. The chemical composition was checked with a Camebax SX-50 x-ray microanalyzer.

$K_{1-x}Ti_{1-x}Nb_xOPO_4$ CRYSTALS

KTP single crystals with Ti partially substituted with Nb were grown by spontaneous crystallization from melt. The starting mixtures contained 40 mol % of K_2O, 27 mol % of P_2O_5, and 33 mol % of $TiO_2 + Nb_2O_5$, with the individual TiO_2 and Nb_2O_5 contents given in Table 1. The crystals were mostly 5–10 mm in size. Their habits were basically typical of KTP crystals. However, raising the Nb content flattened them to an increasing extent. Also note that the {110} faces were absent from a large proportion of the crystals. The quality of the crystals was found to markedly deteriorate with the Nb content, in accordance with [5, 6]. Some crystals were light violet, but the color disappeared upon additional 30-min annealing in air at 300–600°C. The DTA data showed that the incongruent-melting temperature for crystals differing in composition was in the range 1120–1160°C.

Table 1. Composition of melts and $K_{1-x}Ti_{1-x}Nb_xOPO_4$ crystals

Experiment	Melt composition, mol %				Nb/(Nb + Ti) ratio, %	
	K_2O	TiO_2	Nb_2O_5	P_2O_5	melt	crystals
1	40	32	1	27	5.9	0.2
2	40	31	2	27	11.4	2.8
3	40	30	3	27	16.7	3.1
4	40	28	5	27	26.3	5.0
5	40	23	10	27	46.5	10.9

Table 2. Symmetry and unit-cell parameters of $K_{1-x}Ti_{1-x}Nb_xOPO_4$ crystals at three different temperatures

Temperature, °C	20	330	730
Space group	$Pna2_1$	$Pna2_1$	$Pnan$
a, Å	12.805 ± 0.001	12.859 ± 0.001	12.919 ± 0.002
b, Å	6.404 ± 0.001	6.433 ± 0.001	6.469 ± 0.001
c, Å	10.583 ± 0.001	10.576 ± 0.001	10.552 ± 0.001

We found that another, monoclinic, phase crystallizes from melts with Nb contents over 12 mol %. The phase is likely to be a nonstoichiometric compound; nevertheless, its composition is close to $K_2O : TiO_2 : Nb_2O_5 : P_2O_5 = 1 : 1 : 1 : 1$. The unit-cell parameters are a = 13.786(5) Å, b = 6.407(8) Å, c = 16.938(5) Å, and $\beta = 83°$ and a = 13.804(7) Å, b = 6.413(1) Å, c = 16.918(9) Å, and $\beta = 83°$ for crystals grown from melts with niobium oxide contents of 20 and 16.5 mol %, respectively.

The atomic structure of $K_{1-x}Ti_{1-x}Nb_xOPO_4$ crystals was examined by x-ray diffraction analysis at room temperature and by neutron diffraction analysis at high temperature.

A crystal grown in experiment 3 (Table 1) was selected for the x-ray diffraction analysis. A set of reflections was obtained with a CAD-4F diffractometer using a graphite monochromator. The structure was determined from 2699 independent reflections and 269 refined parameters (the final reliability factors were R = 1.45 and R_W = 1.92%). A detailed description of the survey conditions and complete crystallographic data are given in [3]. The model of the structure adopted implies that K cations can partially occupy three different positions. We found that niobium atoms partially substitute for titanium atoms only in Ti(1) positions, while Ti(2) positions remained occupied only by titanium atoms. From these data, the crystal composition can be represented as $K_{0.93}Ti_{0.96}Nb_{0.04}OPO_4$.

The neutron diffraction analysis was performed on crushed KTP : Nb crystals obtained in experiment 3 at three different temperatures: 20, 330, and 730°C (Table 2). We used a two-circle diffractometer whose analyzer was made up of 35 ^{3}He detectors. The intensity readings of each detector were statistically averaged and summed up. The monochromator consisted of two parallel (220)-oriented copper crystals. The wavelength was 1.470 Å, and the neutron flux on the specimen was 10^6 cm^{-2} s^{-1}. A specimen with a mass of about 5 g was placed in a vanadium container. Absorption corrections were made during data refinement. Scanning was performed over the 2θ range 4°–140° in 0.08° steps. The data obtained were processed by the Rietveld method using the FULLPROF program [15].

The results showed that the crystals are described by a polar space group at 20 and 330°C and by a nonpolar space group at 730°C. With increasing temperature, the a and b unit-cell parameters increase, while the c parameter decreases; this behavior had been observed in KTP [16] and $RbTiOPO_4$ [17] crystals. The findings

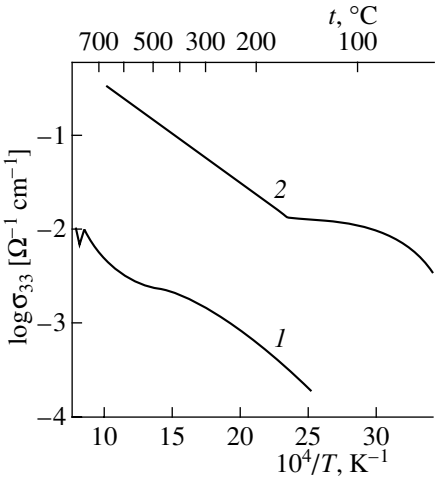

Fig. 1. Temperature dependence of the electrical conductivity σ_{33} of (*1*) KTP and (*2*) $K_{0.97}Ti_{0.97}Nb_{0.03}OPO_4$ crystals.

imply that the averaged composition of the crystals is $K_{0.94}Ti_{0.97}Nb_{0.03}OPO_4$.

The electrical conductivity of KTP:Nb crystals is greatly affected by the Nb content. It is more than an order of magnitude higher than that of undoped crystals, being equal to 5×10^{-2} Ω^{-1} cm^{-1} at 300°C for as few as 3 at. % of niobium (Fig. 1).

With such conductivities, it is unfeasible to measure the dielectric constant by conventional techniques. Therefore, ferroelectric phase transitions were mainly examined by measuring the temperature variation of the nonlinear optical susceptibility. Figure 2 shows the temperature dependence of SHG intensity for laser-irradiated KTP crystals and $K_{1-x}Ti_{1-x}Nb_xOPO_4$ crystals differing in x. Compared with undoped crystals, the ferroelectric-transition temperature decreases from 930 to 640°C even for $x = 0.02$; for $x = 0.11$, this temperature is 300°C.

It was revealed that some $K_{1-x}Ti_{1-x}Nb_xOPO_4$ crystals exhibit steps in electrical conductivity (and so in resistivity) along the c axis, a property typical of superionic conductors [18]. Figure 3 shows an example for a crystal with $x = 0.02$. The steps are found in the range from room temperature to 400°C; their magnitudes vary from ~10 to 300%. All the steps are accompanied by considerable temperature hysteresis, and their locations may greatly change from one heating–cooling cycle to another. The phenomenon involves no noticeable restructuring of the crystals. It is also worth noting that the steps become smoother upon long exposure of the crystals to air.

$KTi_{1-x}Sn_xOPO_4$ CRYSTALS

The Sn-doped KTP single crystals were grown by spontaneous crystallization from flux in the K_2O–TiO_2–SnO_2–P_2O_5 system. The composition of the starting melts and the results of the growth experiments are pre-

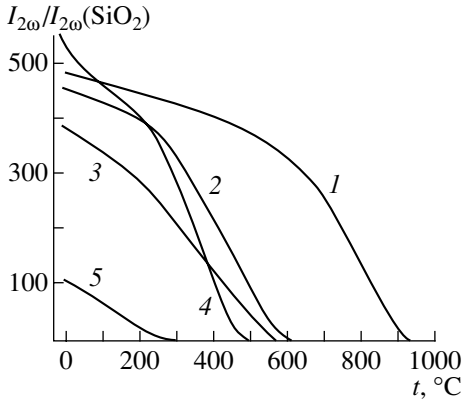

Fig. 2. Temperature dependence of SHG intensity for $K_{1-x}Ti_{1-x}Nb_xOPO_4$ crystals with x = (*1*) 0, (*2*) 0.02, (*3*) 0.03, (*4*) 0.05, and (*5*) 0.10.

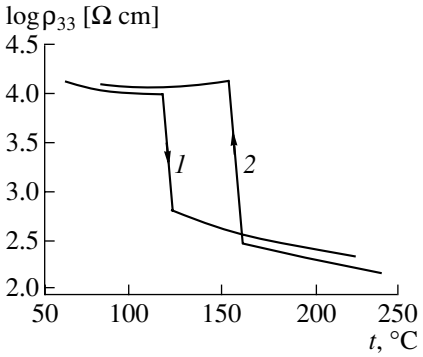

Fig. 3. Steps in the resistivity–temperature characteristics of a $K_{0.98}Ti_{0.98}Nb_{0.02}OPO_4$ crystal under (*1*) heating and (*2*) cooling.

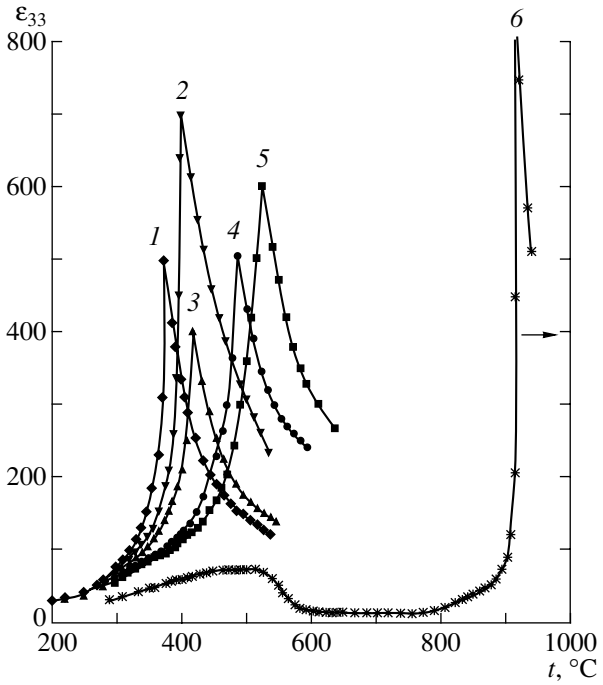

Fig. 4. Temperature dependence of the dielectric constant ε_{33} for $KTi_{1-x}Sn_xOPO_4$ crystals with x = (*1*) 1.00, (*2*) 0.42, (*3*) 0.40, (*4*) 0.28, (*5*) 0.16, and (*6*) 0.00.

Table 3. Composition of melts and $KTi_{1-x}Sn_xOPO_4$ crystals

Experiment	Melt composition, mol %				Sn/(Ti + Sn) ratio, %	
	K_2O	TiO_2	SnO_2	P_2O_5	melt	crystals
1	47.5	14	6	32.5	30	16
2	45	12	8	35	40	28
3	45	10	10	35	50	40
4	45	8	12	35	60	42
5	48.5	0	15	36.5	100	100

sented in Table 3. The mixtures were heated to 1200°C and kept at this temperature for 20 h. Melting was incomplete due to the high melting point of $KSnOPO_4$, which is close to 1370°C (DTA data). The partially melted mixture was cooled to 1000°C at a rate of 2°C/h and then to 850°C at a rate of 1°C/h. In doing so, we often observed the simultaneous crystallization of two different phases. One phase was orthorhombic, as with KTP crystals, and had a narrow crystallization field (especially at high Sn content). The other phase was rhombohedral and corresponded to $KTi_2(PO_4)_3$. The $KTi_{1-x}Sn_xOPO_4$ single crystals thus obtained were colorless, transparent, and about 3–5 mm in size. Their shape characteristics were somewhat different from those of undoped KTP crystals: the area of the {100} faces decreases with increasing Sn content, and the {110} faces are often absent.

The unit-cell parameters and crystal density evaluated from the x-ray diffraction patterns are shown in Table 4. It is seen that the substitution of Ti by Sn increases all the unit-cell parameters and the density. The Sn content of the crystals was determined by chemical analysis. It is worth noting that all the $KTi_{1-x}Sn_xOPO_4$ crystals showed high (4–7 at. %) concentrations of vacancies of K cations. The concentrations were almost unaffected by the composition of the melts and crystals (except for $KSnOPO_4$ crystals, in which the concentration approaches 15 at. %). Presumably, these vacancies are due to the intense evaporation of potassium during high-temperature crystal growth. It appears that zero net charge is maintained owing to the loss of an equivalent quantity of oxygen.

In order to ascertain how the substitution of Ti by Sn changes the structure, we performed x-ray diffraction analysis of a crystal grown from melt with 10 mol % of Sn (experiment 3 in Table 3) [19]. The unit-cell parameters refined by the least-squares method from 147 reflections are as follows: a = 12.831(1) Å, b = 6.410(1) Å, c = 10.584(1) Å, V = 870.50 Å^3, Z = 8, and space group $Pna2_1$. The occupancies determined indicate that x is close to 0.07. Being somewhat larger, Sn^{4+} cations (ionic radius 0.71 Å) substitute for Ti^{4+} cations (ionic radius 0.68 Å) nonuniformly: they are concentrated at Ti(2) positions. The occupancies of Ti(2) positions are 0.892 and 0.108 for Ti and Sn atoms, respectively; the corresponding occupancies of Ti(1) positions are 0.978 and 0.022, respectively.

Figure 4 shows the temperature dependence of the dielectric constant ε_{33} measured over the range from

Table 4. Unit-cell parameters and calculated density of $KTi_{1-x}Sn_xOPO_4$ crystals

Experiment	Sn content, x	Unit-cell parameters				ρ_{calc}, g/cm^3
		a, Å	b, Å	c, Å	V, Å^3	
1	0.16	12.853(3)	6.419(2)	10.595(3)	874.11	3.14
2	0.28	12.910(1)	6.453(5)	10.616(3)	884.33	3.20
3	0.40	12.965(4)	6.460(1)	10.642(2)	891.66	3.29
4	0.42	12.976(7)	6.455(8)	10.651(4)	892.05	3.33
5	1.00	13.145(3)	6.526(2)	10.738(3)	921.15	3.75

Table 5. Ferroelectric properties and electrical conductivity of $K_{1-x}Sn_xOPO_4$ crystals

Experiment	Crystal composition	T_C, °C	Electrical conductivity σ_{33} at 300°C, 10^{-5} Ω^{-1} cm^{-1}	Activation energy, eV	
				$T < T_C$	$T > T_C$
1	$KTiOPO_4$	934	1.7	0.31	
2	$K_{0.96}Ti_{0.84}Sn_{0.16}OPO_4$	540	4.0	0.09	0.55
3	$K_{0.94}Ti_{0.72}Sn_{0.28}OPO_4$	500	12	0.13	0.42
4	$K_{0.93}Ti_{0.60}Sn_{0.40}OPO_4$	430	19	0.21	0.55
5	$K_{0.94}Ti_{0.58}Sn_{0.42}OPO_4$	420	18	0.13	0.22
6	$K_{0.85}Sn_{0.99}OPO_4$	387	23	0.11	0.28

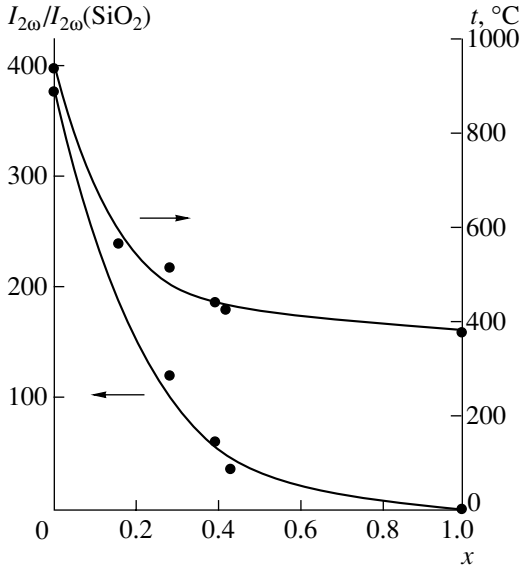

Fig. 5. SHG intensity $I_{2\omega}$ (at room temperature) and ferroelectric-transition temperature T_C as functions of Sn content for $KTi_{1-x}Sn_xOPO_4$ crystals.

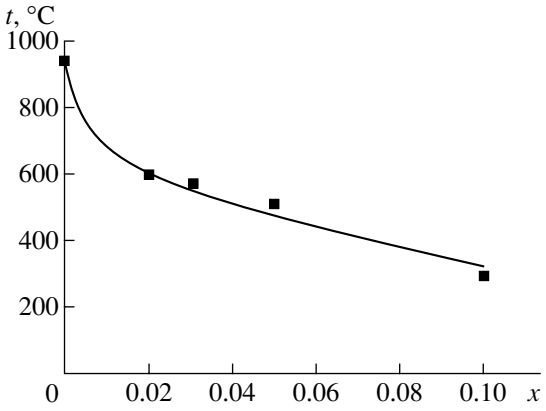

Fig. 6. Dependence of ferroelectric-transition temperature on Nb content for $K_{1-x}Ti_{1-x}Nb_xOPO_4$ crystals.

room temperature to 800°C for several values of x, including the case $x = 0$ [20]. All the crystals exhibit anomalies typical of second-order ferroelectric phase transitions, with the temperature decreasing with increasing Sn content. The Curie temperatures and other relevant data are given in Table 5. In all cases, the temperature dependence of $1/\varepsilon_{33}$ basically obeys the "rule of two" (the slope angle of the curve for temperatures approaching the phase-transition point is twice as large as that for temperatures exceeding the point.

The electrical conductivity σ_{33} of $KTi_{1-x}Sn_xOPO_4$ single crystals (measured at 1 MHz) is high, increasing with Sn content. At low temperatures, the conduction activation energy is 0.1–0.2 eV, which is typical of superionic conductors. At the ferroelectric-transition temperature, this energy increases approximately twofold. Some specimens exhibited abrupt (up to an order of magnitude) changes in conductivity when the temperature was decreased through the range of 550–400°C.

The temperature dependence of SHG intensity under laser irradiation was found to be as in ferroelectrics, for all the $KTi_{1-x}Sn_xOPO_4$ crystals. At room temperature, SHG intensity decreases with increasing x, especially for x between 0 and 0.4.

DISCUSSION AND CONCLUSIONS

The above data indicate that the substitution of Ti by Nb or Sn in KTP crystals has a surprisingly profound effect on the ferroelectric phase transitions, nonlinear optical properties, and ionic electrical conduction. As an example, Fig. 5 shows the dependence of SHG intensity and ferroelectric-transition temperature on Sn content for $KTi_{1-x}Sn_xOPO_4$ crystals. The sharpest changes in $I_{2\omega}$ and t_C occur at low Sn concentrations. Similar behavior is observed in Nb-doped crystals (Fig. 6).

It is worthwhile to correlate the changes in physical properties with the data on crystal restructuring. Table 6 lists the lengths of interatomic bonds in $(Ti,Sn)O_6$ octahedra for the case $x = 0.07$. Let us compare them with the corresponding data on KTP and $KSnOPO_4$ crystals [10]. The respective differences of the longest and the shortest bond, Δ, in $(Ti,Sn)(1)O_6$ octahedra of KTP, $KTi_{0.93}Sn_{0.07}OPO_4$, and $KSnOPO_4$ crystals make up the decreasing sequence 0.438 ⟶ 0.392 ⟶ 0.113 Å. For $(Ti,Sn)(2)O_6$ octahedra, the corresponding sequence is 0.363 ⟶ 0.286 ⟶ 0.004 Å. A similar pattern was observed for *cis*- and *trans*-(Ti,Sn)–O bonds. With the partial substitution of titanium by tin, the P–O distances in PO_4 tetrahedra change only slightly and the K–O distances in KO_8 and KO_9 polyhedra increase to some extent.

Similar changes were observed in $K_{0.94}Ti_{0.96}Nb_{0.04}OPO_4$ crystals. The average interatomic distances in $(Ti,Nb)O_6$ octahedra are approximately the same as above, with the octahedra distorted to a higher degree (see Table 7). In this case, the respective differences of the longest and the shortest bond, Δ, in KTP

Table 6. Lengths of interatomic bonds in $(Ti,Sn)O_6$ octahedra for $KTi_{0.93}Sn_{0.07}OPO_4$ crystals

Bond	Length, Å	Bond	Length, Å
(Ti,Sn)(1)–O(9)	1.744	(Ti,Sn)(2)–O(9)	2.048
O(10)	1.948	O(10)	1.793
O(1)	2.135	O(3)	2.045
O(2)	1.977	O(4)	1.987
O(5)	2.047	O(7)	1.978
O(6)	1.989	O(8)	1.995
Δ*	0.391	Δ*	0.255

* Δ is the difference of the longest and the shortest bond.

Table 7. Lengths of interatomic bonds in $(Ti,Nb)O_6$ octahedra for $K_{0.94}Ti_{0.96}Nb_{0.04}OPO_4$ crystals crystals

Bond	Length, Å	Bond	Length, Å
(Ti,Nb)(1)–O(9)	1.726	(Ti, Nb)(2)–O(9)	2.081
O(10)	1.962	O(10)	1.748
O(1)	2.145	O(3)	2.039
O(2)	1.969	O(4)	1.980
O(5)	2.047	O(7)	1.956
O(6)	1.989	O(8)	1.999
Δ*	0.419	Δ*	0.333

* Δ is the difference of the longest and the shortest bond.

and $K_{0.94}Ti_{0.96}Nb_{0.04}OPO_4$ crystals are 0.438 and 0.419 Å for $(Ti,Nb)(1)O_6$ octahedra and 0.363 and 0.333 Å for $(Ti,Nb)(2)O_6$ octahedra.

These data imply that the difference in ferroelectric and nonlinear optical properties between $KTi_{1-x}Sn_xOPO_4$ and $K_{1-x}Ti_{1-x}Nb_xOPO_4$ solid solutions is largely attributable to the different degrees of distortion of the octahedra MeO_6 (where *Me* stands for Ti, Sn, or Nb), whereas the ionic electrical conductivity is determined by the concentration of vacant positions in the potassium sublattice.

ACKNOWLEDGMENTS

The authors are grateful to Liu Wen for assistance in the growth of KTP : Sn single crystals, to O.A. Alekseeva and S.-G. Eriksson for valuable cooperation in the x-ray and neutron diffraction studies, and to S.A. Zver'kov for the chemical analysis of the crystals. This work was supported by the Russian Foundation for Basic Research, project nos. 00-02-17802 and 00-02-16059.

REFERENCES

1. P. A. Thomas and B. E. Watts, Solid State Commun. **73** (2), 97 (1990).
2. S. G. Moorthy, F. J. Kumar, C. Subramanian, *et al.*, Mater. Lett. **36**, 266 (1998).
3. O. A. Alekseeva, N. I. Sorokina, M. K. Blomberg, *et al.*, Kristallografiya **46** (2), 215 (2001) [Crystallogr. Rep. **46**, 176 (2001)].
4. P. U. M. Sastry, M. S. Somayazulu, and A. Sequiera, Mater. Res. Bull. **27**, 1385 (1992).
5. L. T. Cheng, L. K. Cheng, R. L. Harlow, and J. D. Bierlein, Appl. Phys. Lett. **64** (2), 155 (1994).
6. D. Y. Zhang, H. Y. Shen, W. Liu, *et al.*, J. Cryst. Growth **218**, 98 (2000).
7. V. I. Voronkova and V. K. Yanovskiĭ, Izv. Akad. Nauk SSSR, Neorg. Mater. **25** (9), 1579 (1989).
8. N. S. Slobodyanik, P. G. Nagornyĭ, V. V. Skopenko, and E. S. Lugovskaya, Zh. Neorg. Khim. **32** (7), 1724 (1987).
9. R. H. Jarman and S. G. Grubb, Proc. SPIE—Int. Soc. Opt. Eng. **968**, 108 (1988).
10. P. A. Thomas, A. M. Glazer, and B. E. Watts, Acta Crystallogr., Sect. B: Struct. Sci. **46**, 333 (1990).
11. M. L. F. Phillips, W. T. A. Harrison, and G. D. Stucky, Inorg. Chem. **29**, 3247 (1990).
12. S. J. Crennell, J. J. Owen, and A. K. Cheetham, Eur. J. Solid State Inorg. Chem. **28**, 397 (1991).
13. Sh. Furusawa, H. Yanagisawa, and Y. Ishibashi, J. Phys. Soc. Jpn. **62** (11), 4152 (1993).
14. H. Yanagisawa, H. Orihara, and Y. Ishibashi, J. Phys. Soc. Jpn. **63** (11), 4078 (1994).
15. T. Yu. Losevskaya, O. A. Alekseeva, V. K. Yanovskiĭ, *et al.*, Kristallografiya **45** (5), 809 (2000) [Crystallogr. Rep. **45**, 739 (2000)].
16. P. Delarue, C. Lecomte, M. Jannin, *et al.*, J. Phys.: Condens. Matter **11**, 4123 (1999).
17. P. Delarue, C. Lecomte, M. Jannin, *et al.*, Phys. Rev. B **58** (9), 5287 (1998).
18. T. Yu. Losevskaya, E. P. Kharitonova, V. I. Voronkova, *et al.*, Kristallografiya **44** (1), 95 (1999) [Crystallogr. Rep. **44**, 90 (1999)].
19. Liu Wen, N. I. Sorokina, V. I. Voronkova, *et al.*, Kristallografiya **45** (3), 423 (2000) [Crystallogr. Rep. **45**, 380 (2000)].
20. V. K. Yanovskiĭ and V. I. Voronkova, Phys. Status Solidi A **93** (2), 665 (1986).

Translated by A. Zolot'ko